2017 AAAS ANNUAL MEETING Serving Society Through Science Policy

Science

$15
21 OCTOBER 2016
sciencemag.org

AAAS

SCIENCE LESSONS FOR THE NEXT PRESIDENT

pp. 265 & 274

CONTENTS

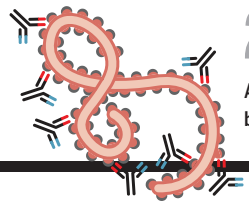

284
A dual-function antibody blocks Ebola virus infection

21 OCTOBER 2016 • VOLUME 354 • ISSUE 6310

NEWS

IN BRIEF

266 News at a glance

IN DEPTH

268 'GREEN HELL' HAS LONG BEEN HOME FOR HUMANS
By burning trees and tending crops, prehistoric people left a lasting mark on rainforests *By A. Curry*

269 ODD COMPUTER ZIPS THROUGH KNOTTY TASKS
Hybrid Ising machines survey universe of possible solutions for best answer *By A. Cho*

271 COLOMBIA PEACE DEAL BLOW DISMAYS ECOLOGISTS
Once encouraged by a cease-fire, scientists now reconsider venturing into rainforest *By L. Wade*

272 ARE LABMADE HUMAN EGGS COMING SOON?
Mouse eggs grown in vitro produce apparently healthy offspring, but clinical use is distant *By G. Vogel*

273 ALIEN FUNGUS BLIGHTS HAWAII'S NATIVE TREES
Big Island is under assault from deadly invader *By I. Vesper*

FEATURE

274 SCIENCE LESSONS FOR THE NEXT PRESIDENT
Election campaigns are light on science. But once a new president is in office, technical issues have a way of demanding attention
By D. Malakoff and J. Mervis

INSIGHTS

PERSPECTIVES

280 THE FIRST JAWS
A fossil fish helps to explain how jaws first evolved *By J. A. Long*
▸ REPORT P. 334

282 A PHOTORECEPTOR'S ON-OFF SWITCH
Light-induced protein interaction controls the signaling of a plant cryptochrome *By C. Fankhauser and R. Ulm*
▸ REPORT P. 343

283 MOLECULAR IMAGING AT 1-FEMTOSECOND RESOLUTION
Loss of a hydrogen atom from acetylene is observed with electron diffraction *By C.-Y. Ruan*
▸ REPORT P. 308

284 HITTING EBOLA, TO THE POWER OF TWO
Bispecific antibodies are engineered to thwart ebolavirus entry into cells
By A. F. Labrijn and P. W. H. I. Parren
▸ REPORT P. 350

286 WHY I KNOW BUT DON'T BELIEVE
Individuals hold interdependent beliefs that affect whether or not they accept scientific findings *By C. T. Butts*
▸ REPORT P. 321

287 A PLANKTON BLOOM SHIFTS AS THE OCEAN WARMS
Long-term data show how a widespread phytoplankton group responds to temperature changes
By A. Z. Worden and S. Wilken
▸ REPORT P. 326

289 PREDICTING THE BASIS OF CONVERGENT EVOLUTION
Convergent adaptive traits do not always arise from the same genetic changes *By J. T. Bridgham*
▸ REPORT P. 336

POLICY FORUM

290 IDENTIFYING THE POLICY SPACE FOR CLIMATE LOSS AND DAMAGE
Climate risk analysis must play a fundamental role *By R. Mechler and T. Schinko*

BOOKS *ET AL.*

293 STREET SMART
A physicist reveals the engineering marvels that underlie the modern metropolis *By S. Derrible*

294 THE BUSINESS OF DOING GOOD
A guide for aspiring entrepreneurs offers a data-driven approach to making a difference *By O. Bagasra*

LETTERS

295 PREMATURE DOWNGRADE OF PANDA'S STATUS
By D. Kang and J. Li

295 STOP PAKISTAN'S POLIO VACCINATION TAX
By S. A. Meo

296 CREATING A CULTURE OF ETHICS IN IRAN
By M. S. Rezaee-Zavareh et al.

296 TECHNICAL COMMENT ABSTRACTS

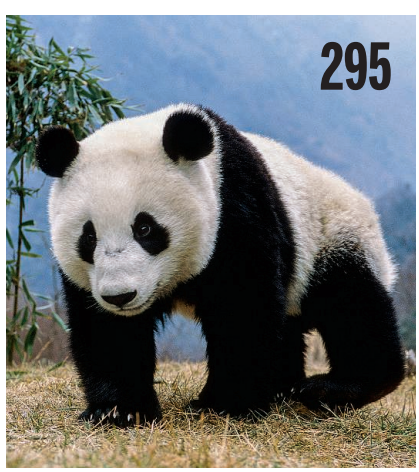

Downloaded from http://science.sciencemag.org/ on October 20, 2016

Published by AAAS

CONTENTS

334
Silurian jaws

21 OCTOBER 2016 • VOLUME 354 • ISSUE 6310

RESEARCH

IN BRIEF

297 From *Science* and other journals

REVIEW

300 **ORGANIC CHEMISTRY**
Metal-catalyzed reductive coupling of olefin-derived nucleophiles: Reinventing carbonyl addition *K. D. Nguyen* et al.
REVIEW SUMMARY; FOR FULL TEXT: dx.doi.org/10.1126/science.aah5133

RESEARCH ARTICLES

301 **STRUCTURAL BIOLOGY**
Structural basis for the gating mechanism of the type 2 ryanodine receptor RyR2 *W. Peng* et al.
RESEARCH ARTICLE SUMMARY; FOR FULL TEXT: dx.doi.org/10.1126/science.aah5324

REPORTS

302 **DEVICE TECHNOLOGY**
Subthreshold Schottky-barrier thin-film transistors with ultralow power and high intrinsic gain *S. Lee and A. Nathan*

305 **FORCE SPECTROSCOPY**
Molecular force spectroscopy with a DNA origami–based nanoscopic force clamp *P. C. Nickels* et al.

308 **CHEMICAL PHYSICS**
Ultrafast electron diffraction imaging of bond breaking in di-ionized acetylene *B. Wolter* et al.
▸ PERSPECTIVE P. 283

312 **METALLURGY**
Dynamic creation and evolution of gradient nanostructure in single-crystal metallic microcubes *R. Thevamaran* et al.

316 **SOLID-STATE PHYSICS**
Observation of a nematic quantum Hall liquid on the surface of bismuth *B. E. Feldman* et al.

321 **GROUP DYNAMICS**
Network science on belief system dynamics under logic constraints *N. E. Friedkin* et al.
▸ PERSPECTIVE P. 286

326 **PLANKTON DYNAMICS**
Physiological and ecological drivers of early spring blooms of a coastal phytoplankter *K. R. Hunter-Cevera* et al.
▸ PERSPECTIVE P. 287

329 **BIOMASS PROCESSING**
Formaldehyde stabilization facilitates lignin monomer production during biomass depolymerization *L. Shuai* et al.

334 **PALEONTOLOGY**
A Silurian maxillate placoderm illuminates jaw evolution *M. Zhu* et al.
▸ PERSPECTIVE P. 280

336 **EVOLUTION**
Predictable convergence in hemoglobin function has unpredictable molecular underpinnings *C. Natarajan* et al.
▸ PERSPECTIVE P. 289

339 **ENZYMOLOGY**
The biosynthetic pathway of coenzyme F430 in methanogenic and methanotrophic archaea *K. Zheng* et al.

343 **PLANT PHOTOBIOLOGY**
Photoactivation and inactivation of *Arabidopsis* cryptochrome 2 *Q. Wang* et al.
▸ PERSPECTIVE P. 282

347 **MICROBIOLOGY**
Intercellular communication and conjugation are mediated by ESX secretion systems in mycobacteria *T. A. Gray* et al.

350 **EBOLAVIRUSES**
A "Trojan horse" bispecific-antibody strategy for broad protection against ebolaviruses *A. Z. Wec* et al.
▸ PERSPECTIVE P. 284

354 **ANTIGEN PRESENTATION**
A large fraction of HLA class I ligands are proteasome-generated spliced peptides *J. Liepe* et al.

358 **MUCOSAL IMMUNITY**
A pathogenic role for T cell–derived IL-22BP in inflammatory bowel disease *P. Pelczar* et al.

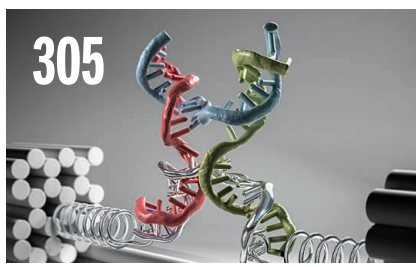

DEPARTMENTS

265 **EDITORIAL**
A short presidential reading list
By Jeremy Berg
▸ NEWS FEATURES P. 274

382 **WORKING LIFE**
Knocking on opportunity's door
By Diane Shao

ON THE COVER

Whoever wins the U.S. election on 8 November, Democrat (donkey) or Republican (elephant), the next president will confront issues that have science at their core, from sea-level rise to the emergence of new diseases. In this issue, *Science* discusses six concepts that deserve attention from the very top. See pages 265 and 274. *Illustration: Ricardo Martínez*

Science Staff 262
New Products 373
Science Careers 374

SCIENCE (ISSN 0036-8075) is published weekly on Friday, except the last week in December, by the American Association for the Advancement of Science, 1200 New York Avenue, NW, Washington, DC 20005. Periodicals mail postage (publication No. 484460) paid at Washington, DC, and additional mailing offices. Copyright © 2016 by the American Association for the Advancement of Science. The title SCIENCE is a registered trademark of the AAAS. Domestic individual membership and subscription (51 issues): $165 ($74 allocated to subscription). Domestic institutional subscription (51 issues): $1522; Foreign postage extra: Mexico, Caribbean (surface mail) $55; other countries (air assist delivery) $89. First class, airmail, student, and emeritus rates on request. Canadian rates with GST available upon request, GST #1254 88122. Publications Mail Agreement Number 1069624. **Printed in the U.S.A.**
Change of address: Allow 4 weeks, giving old and new addresses and 8-digit account number. **Postmaster:** Send change of address to AAAS, P.O. Box 96178, Washington, DC 20090–6178. **Single-copy sales:** $15.00 current issue, $20.00 back issue prepaid includes surface postage; bulk rates on request. **Authorization to photocopy** material for internal or personal use under circumstances not falling within the fair use provisions of the Copyright Act is granted by AAAS to libraries and other users registered with the Copyright Clearance Center (CCC) Transactional Reporting Service, provided that $35.00 per article is paid directly to CCC, 222 Rosewood Drive, Danvers, MA 01923. The identification code for *Science* is 0036-8075. *Science* is indexed in the *Reader's Guide to Periodical Literature* and in several specialized indexes.

Downloaded from http://science.sciencemag.org/ on October 20, 2016

Published by AAAS

Science
AAAS
1200 New York Avenue, NW, Washington, DC 20005
Clarendon House, Clarendon Road, Cambridge, UK CB2 8FH

Editor-in-Chief Jeremy Berg
Executive Editor Monica M. Bradford **News Editor** Tim Appenzeller
Deputy Editors Lisa D. Chong, Andrew M. Sugden(UK), Valda J. Vinson, Jake S. Yeston

Research and Insights

DEPUTY EDITOR, EMERITUS Barbara R. Jasny **SR. EDITORS** Caroline Ash(UK), Gilbert J. Chin, Julia Fahrenkamp-Uppenbrink(UK), Pamela J. Hines, Stella M. Hurtley(UK), Paula A. Kiberstis, Marc S. Lavine(Canada), Kristen L. Mueller, Ian S. Osborne(UK), Beverly A. Purnell, L. Bryan Ray, Guy Riddihough, H. Jesse Smith, Jelena Stajic, Peter Stern(UK), Phillip D. Szuromi, Sacha Vignieri, Brad Wible, Nicholas S. Wigginton, Laura M. Zahn **ASSOCIATE EDITORS** Brent Grocholski, Keith T. Smith **ASSOCIATE BOOK REVIEW EDITOR** Valerie B. Thompson **LETTERS EDITOR** Jennifer Sills **LEAD CONTENT PRODUCTION EDITORS** Harry Jach, Lauren Kmec **CONTENT PRODUCTION EDITORS** Jeffrey E. Cook, Chris Filiatreau, Cynthia Howe, Barbara P. Ordway, Catherine Wolner **SR. EDITORIAL COORDINATORS** Carolyn Kyle, Beverly Shields **EDITORIAL COORDINATORS** Aneera Dobbins, Joi S. Granger, Jeffrey Hearn, Lisa Johnson, Maryrose Madrid, Anita Wynn **PUBLICATIONS ASSISTANTS** Nida Masiulis, Dona Mathieu, Le-Toya Mayne Flood, Shannon McMahon, Scott Miller, Jerry Richardson, Alice Whaley(UK), Gwen Grant(UK), Brian White **EXECUTIVE ASSISTANT** Anna Bashkirova **ADMINISTRATIVE SUPPORT** Janet Clements(UK), Lizanne Newton(UK), Sarah Harrison (UK)

News

NEWS MANAGING EDITOR John Travis **INTERNATIONAL EDITOR** Richard Stone **DEPUTY NEWS EDITORS** Elizabeth Culotta, David Grimm, Eric Hand David Malakoff, Leslie Roberts **CONTRIBUING EDITOR** Martin Enserink(Europe) **SR. CORRESPONDENTS** Daniel Clery(UK), Jeffrey Mervis, Elizabeth Pennisi **NEWS WRITERS** Adrian Cho, Jon Cohen, Jennifer Couzin-Frankel, Carolyn Gramling, Jocelyn Kaiser, Catherine Matacic, Kelly Servick, Robert F. Service, Erik Stokstad(Cambridge, UK), Paul Voosen, Meredith Wadman **INTERNS** Jessica Boddy, Ben Panko **CONTRIBUTING CORRESPONDENTS** John Bohannon, Warren Cornwall, Ann Gibbons, Mara Hvistendahl, Sam Kean, Eli Kintisch, Kai Kupferschmidt(Berlin), Andrew Lawler, Mitch Leslie, Charles C. Mann, Eliot Marshall, Virginia Morell, Dennis Normile(Shanghai), Heather Pringle, Tania Rabesandratana(London), Emily Underwood, Gretchen Vogel(Berlin), Lizzie Wade(Mexico City) **CAREERS** Donisha Adams, Rachel Bernstein(Editor), Maggie Kuo **COPY EDITORS** Julia Cole, Dorie Chevlen, Jennifer Levin (Chief) **ADMINISTRATIVE SUPPORT** Jessica Adams

Executive Publisher Rush D. Holt
Publisher Bill Moran **Chief Digital Media Officer** Rob Covey

BUSINESS OPERATIONS AND PORTFOLIO MANAGEMENT DIRECTOR Sarah Whalen **PRODUCT DEVELOPMENT DIRECTOR** Will Schweitzer **PRODUCT DEVELOPMENT ASSOCIATE** Hannah Heckner **BUSINESS SYSTEMS AND FINANCIAL ANALYSIS DIRECTOR** Randy Yi **SENIOR SYSTEMS ANALYST** Nicole Mehmedovich **DIRECTOR, BUSINESS OPERATIONS & ANALYSIS** Eric Knott **MANAGER, BUSINESS OPERATIONS** Jessica Tierney **SENIOR BUSINESS ANALYST** Cory Lipman **BUSINESS ANALYSTS** David Garrison, Michael Hardesty Meron Kebede, Sandy Kim **FINANCIAL ANALYST** Drew Sher **DIRECTOR, COPYRIGHTS LICENSING SPECIAL PROJECTS** Emilie David **PERMISSIONS ASSOCIATE** Elizabeth Sandler **RIGHTS, CONTRACTS, AND LICENSING ASSOCIATE** Lili Kiser **RIGHTS & PERMISSIONS ASSISTANT** Alexander Lee

MARKETING DIRECTOR Elise Swinehart **ASSOCIATE MARKETING DIRECTOR** Stacey Burke Bowers **MARKETING ASSOCIATE** Steven Goodman **CREATIVE DIRECTOR** Scott Rodgerson **SENIOR ART ASSOCIATES** Paula Fry **ART ASSOCIATE** Kim Huynh

FULFILLMENT SYSTEMS AND OPERATIONS membership@aaas.org **MANAGER, MEMBER SERVICES** Pat Butler **SPECIALISTS** Terrance Morrison, Latasha Russell **MANAGER, DATA ENTRY** Mickie Napoleoni **DATA ENTRY SPECIALISTS** Brenden Aquilino, Fiona Giblin **MARKETING ASSOCIATE** Isa Sesay-Bah

PUBLISHER RELATIONS, EASTERN REGION Keith Layson **PUBLISHER RELATIONS, WESTERN REGION** Ryan Rexroth **SALES RESEARCH COORDINATOR** Aiesha Marshall **ASSOCIATE DIRECTOR, INSTITUTIONAL LICENSING OPERATIONS** Iquo Edim **SENIOR OPERATIONS ANALYST** Lana Guz **MANAGER, AGENT RELATIONS & CUSTOMER SUCCESS** Judy Lillibridge

WEB TECHNOLOGIES PORTFOLIO MANAGER Trista Smith **TECHNICAL MANAGER** Chris Coleman **PROJECT MANAGER** Nick Fletcher **DEVELOPERS** Ryan Jensen, Jimmy Marks, Brandon Morrison **BUSINESS ANALYST** Christina Wofford

DIGITAL MEDIA DIRECTOR OF ANALYTICS Enrique Gonzales **DIGITAL REPORTING ANALYST** Eric Hossinger **SR. MULTIMEDIA PRODUCER** Sarah Crespi **MANAGING DIGITAL PRODUCER** Alison Crawford **PRODUCER** Liana Birke **VIDEO PRODUCER** Chris Burns, Nguyên Khôi Nguyễn **DIGITAL SOCIAL MEDIA PRODUCER** Brice Russ

DIRECTOR OF OPERATIONS PRINT AND ONLINE Lizabeth Harman **DIGITAL/PRINT STRATEGY MANAGER** Jason Hillman **QUALITY TECHNICAL MANAGER** Marcus Spiegler **PROJECT ACCOUNT MANAGER** Tara Kelly **DIGITAL PRODUCTION MANAGER** Lisa Stanford **ASSISTANT MANAGER DIGITAL/PRINT** Rebecca Doshi **SENIOR CONTENT SPECIALISTS** Steve Forrester, Antoinette Hodal, Lori Murphy, Anthony Rosen **CONTENT SPECIALISTS** Jacob Hedrick, Kimberley Oster **ADVERTISING OPERATIONS SPECIALIST** Ashley Jeter

DESIGN DIRECTOR Beth Rakouskas **DESIGN EDITOR** Marcy Atarod **SENIOR DESIGNER** Chrystal Smith **GRAPHICS MANAGING EDITOR** Alberto Cuadra **GRAPHICS EDITOR** Garvin Grullón **SENIOR SCIENTIFIC ILLUSTRATORS** Chris Bickel, Katharine Sutliff **SCIENTIFIC ILLUSTRATOR** Valerie Altounian **INTERACTIVE GRAPHICS EDITOR** Jia You **SENIOR GRAPHICS SPECIALISTS** Holly Bishop, Nathalie Cary **PHOTOGRAPHY MANAGING EDITOR** William Douthitt **SENIOR PHOTO EDITOR** Christy Steele **PHOTO EDITOR** Emily Petersen

DIRECTOR, GLOBAL COLLABORATION, CUSTOM PUBLICATIONS, ADVERTISING Bill Moran **EDITOR, CUSTOM PUBLISHING** Sean Sanders: 202-326-6430 **ASSISTANT EDITOR, CUSTOM PUBLISHING** Jackie Oberst: 202-326-6463 **ADVERTISING MARKETING MANAGER** Justin Sawyers: 202-326-7061 science_advertising@aaas.org **ADVERTISING SUPPORT MANAGER** Karen Foote: 202-326-6740 **ADVERTISING PRODUCTION OPERATIONS MANAGER** Deborah Tompkins **SR. PRODUCTION SPECIALIST/GRAPHIC DESIGNER** Amy Hardcastle **SR. TRAFFIC ASSOCIATE** Christine Hall **SALES COORDINATOR** Shirley Young **ASSOCIATE DIRECTOR, COLLABORATION, CUSTOM PUBLICATIONS/CHINA/TAIWAN/KOREA/SINGAPORE** Ruolei Wu: +86-186 0082 9345, rwu@aaas.org **COLLABORATION/CUSTOM PUBLICATIONS/JAPAN** Adarsh Sandhu + 81532-81-5142 asandhu@aaas.org **EAST COAST/E. CANADA** Laurie Faraday: 508-747-9395, FAX 617-507-8189 **WEST COAST/W. CANADA** Lynne Stickrod: 415-931-9782, FAX 415-520-6940 **MIDWEST** Jeffrey Dembksi: 847-498-4520 x3005, Steven Loerch: 847-498-4520 x3006 **UK EUROPE/ASIA** Roger Goncalves: TEL/FAX +41 43 243 1358 **JAPAN** Katsuyoshi Fukamizu(Tokyo): +81-3-3219-5777 kfukamizu@aaas.org **CHINA/TAIWAN** Ruolei Wu: +86-186 0082 9345, rwu@aaas.org

WORLDWIDE ASSOCIATE DIRECTOR OF SCIENCE CAREERS Tracy Holmes: +44 (0) 1223 326525, FAX +44 (0) 1223 326532 tholmes@science-int.co.uk **CLASSIFIED** advertise@sciencecareers.org **U.S. SALES** Tina Burks: 202-326-6577, Nancy Toema: 202-326-6578 **EUROPE/ROW SALES** Sarah Lelarge **SALES ASSISTANT** Kelly Grace **JAPAN** Hiroyuki Mashiki(Kyoto): +81-75-823-1109 hmashiki@aaas.org **CHINA/TAIWAN** Ruolei Wu: +86-186 0082 9345 rwu@aaas.org **MARKETING MANAGER** Allison Pritchard **MARKETING ASSOCIATE** Aimee Aponte

AAAS BOARD OF DIRECTORS, CHAIR Geraldine L. Richmond **PRESIDENT** Barbara A. Schaal **PRESIDENT-ELECT** Susan Hockfield **TREASURER** David Evans Shaw **CHIEF EXECUTIVE OFFICER** Rush D. Holt **BOARD** Cynthia M. Beall, May R. Berenbaum, Carlos J. Bustamante, Stephen P.A. Fodor, Claire M. Fraser, Michael S. Gazzaniga, Laura H. Greene, Elizabeth Loftus, Mercedes Pascual

SUBSCRIPTION SERVICES For change of address, missing issues, new orders and renewals, and payment questions: 866-434-AAAS (2227) or 202-326-6417, FAX 202-842-1065. Mailing addresses: AAAS, P.O. Box 96178, Washington, DC 20090-6178 or AAAS Member Services, 1200 New York Avenue, NW, Washington, DC 20005

INSTITUTIONAL SITE LICENSES 202-326-6730 **REPRINTS:** Author Inquiries 800-635-7181 **COMMERCIAL INQUIRIES** 803-359-4578 **PERMISSIONS** 202-326-6765, permissions@aaas.org **AAAS Member Services** 202-326-6417 or http://membercentral.aaas.org/discounts

Science serves as a forum for discussion of important issues related to the advancement of science by publishing material on which a consensus has been reached as well as including the presentation of minority of conflicting points of view. Accordingly, all articles published in *Science*—including editorials, news and comment, and book reviews—are signed and reflect the individual views of the authors and not official points of view adopted by AAAS or the institutions with which the authors are affiliated.

INFORMATION FOR AUTHORS See pages 624 and 625 of the 5 February 2016 issue or access www.sciencemag.org/authors/science-information-authors

SENIOR EDITORIAL BOARD
Gary King, *Harvard University,* **Susan M. Rosenberg,** *Baylor College of Medicine,*
Ali Shilatifard, *Northwestern University Feinberg School of Medicine*

BOARD OF REVIEWING EDITORS (Statistics board members indicated with **(S)**)

Adriano Aguzzi, *U. Hospital Zürich*
Takuzo Aida, *U. of Tokyo*
Leslie Aiello, *Wenner-Gren Foundation*
Judith Allen, *U. of Edinburgh*
Sonia Altizer, *U. of Georgia*
Sebastian Amigorena, *Institut Curie*
Meinrat O. Andreae, *Max-Planck Inst. Mainz*
Paola Arlotta, *Harvard U.*
Johan Auwerx, *EPFL*
David Awschalom, *U. of Chicago*
Clare Baker, *University of Cambridge*
Nenad Ban, *ETH Zurich*
Franz Bauer, *Pontificia Universidad Católica de Chile*
Ray H. Baughman, *U. of Texas, Dallas*
David Baum, *U. of Wisconsin*
Carlo Beenakker, *Leiden U.*
Kamran Behnia, *ESPCI-ParisTech*
Yasmine Belkaid, *NIAID, NIH*
Philip Benfey, *Duke U.*
May Berenbaum, *U. of Illinois*
Gabriele Bergers, *U. of California, San Francisco*
Bradley Bernstein, *Massachusettes General Hospital*
Peer Bork, *EMBL*
Bernard Bourdon, *Ecole Normale Supérieure de Lyon*
Chris Bowler, *École Normale Supérieure*
Ian Boyd, *U. of St. Andrews*
Emily Brodsky, *U. of California, Santa Cruz*
Ron Brookmeyer, *U. of California Los Angeles* **(S)**
Christian Büchel, *U. Hamburg-Eppendorf*
Joseph A. Burns, *Cornell U.*
Carter Tribley Butts, *U. of California, Irvine*
Gyorgy Buzsaki, *New York U. School of Medicine*
Blanche Capel, *Duke U.*
Mats Carlsson, *U. of Oslo*
Ib Chorkendorff, *U. of Denmark*
David Clapham, *Children's Hospital Boston*
Joel Cohen, *Rockefeller U., Columbia U.*
James J. Collins, *MIT*
Robert Cook-Deegan, *Duke U.*
Lisa Coussens, *Oregon Health & Science U.*
Alan Cowman, *Walter & Eliza Hall Inst.*
Robert H. Crabtree, *Yale U.*
Roberta Croce, *Vrije Universiteit*
Janet Currie, *Princeton U.*
Jeff L. Dangl, *U. of North Carolina*
Tom Daniel, *U. of Washington*
Frans de Waal, *Emory U.*
Stanislas Dehaene, *Collège de France*
Robert Desimone, *MIT*
Claude Desplan, *New York U.*
Sandra Diaz, *Universidad Nacional de Cordoba*
Dennis Discher, *U. of Pennsylvania*
Gerald W. Dorn II, *Washington U. School of Medicine*
Jennifer A. Doudna, *U. of California, Berkeley*
Bruce Dunn, *U. of California, Los Angeles*
William Dunphy, *Caltech*
Christopher Dye, *WHO*
Todd Ehlers, *U. of Tuebingen*
David Ehrhardt, *Carnegie Inst. of Washington*
Tim Elston, *U. of North Carolina at Chapel Hill*
Jennifer Elisseeff, *Johns Hopkins U.*
Gerhard Ertl, *Fritz-Haber-Institut, Berlin*
Barry Everitt, *U. of Cambridge*
Ernst Fehr, *Johns Hopkins U.*
Anne C. Ferguson-Smith, *U. of Cambridge*
Michael Feuer, *The George Washington U.*
Toren Finkel, *NHLBI, NIH*
Kate Fitzgerald, *U. of Massachusetts*
Peter Fratzl, *Max-Planck Inst.*
Elaine Fuchs, *Rockefeller U.*
Daniel Geschwind, *UCLA*
Karl-Heinz Glassmeier, *TU Braunschweig*
Ramon Gonzalez, *Rice U.*
Elizabeth Grove, *U. of Chicago*
Nicolas Gruber, *ETH Zurich*
Kip Guy, *St. Jude's Children's Research Hospital*
Taekjip Ha, *U. of Illinois at Urbana-Champaign*
Wolf-Dietrich Hardt, *ETH Zurich*
Christian Haass, *Ludwig Maximilians U.*
Sharon Hammes-Schiffer, *U. of Illinois at Urbana–Champaign*
Michael Hasselmo, *Boston U.*
Martin Heimann, *Max-Planck Inst. Jena*
Yka Helariutta, *U. of Cambridge*
James A. Hendler, *Rensselaer Polytechnic Inst.*
Janet G. Hering, *Swiss Fed. Inst. of Aquatic Science & Technology*
Kai-Uwe Hinrichs, *U. of Bremen*
David Hodell, *U. of Cambridge*
Lora Hooper, *UT Southwestern Medical Ctr. at Dallas*
Tamas Horvath, *Yale University*
Raymond Huey, *U. of Washington*
Fred Hughson, *Princeton U.*
Auke Ijspeert, *EPFL Lausanne*
Stephen Jackson, *USGS and U. of Arizona*
Steven Jacobsen, *U. of California, Los Angeles*
Seema Jayachandra, *Northwestern U.*
Kai Johnsson, *EPFL Lausanne*
Peter Jonas, *Inst. of Science & Technology (IST) Austria*
Matt Kaeberlein, *U. of Washington*
William Kaelin Jr., *Dana-Farber Cancer Inst.*
Daniel Kahne, *Harvard U.*
Daniel Kammen, *U. of California, Berkeley*
Abby Kavner, *U. of California, Los Angeles*
Hitoshi Kawakatsu, *U. of Tokyo*
Masashi Kawasaki, *U. of Tokyo*
V. Narry Kim, *Seoul National U.*
Robert Kingston, *Harvard Medical School*
Etienne Koechlin, *Ecole Normale Suprieure*
Alexander Kolodkin, *Johns Hopkins U.*
Thomas Langer, *U. of Cologne*
Mitchell A. Lazar, *U. of Pennsylvania*
David Lazer, *Harvard U.*
Thomas Lecuit, *IBDM*
Virginia Lee, *U. of Pennsylvania*
Stanley Lemon, *U. of North Carolina at Chapel Hill*
Ottoline Leyser, *Cambridge U.*
Wendell Lim, *U.C. San Francisco*
Marcia C. Linn, *U. of California, Berkeley*
Jianguo Liu, *Michigan State U.*
Luis Liz-Marzan, *CIC biomaGUNE*
Jonathan Losos, *Harvard U.*
Ke Lu, *Chinese Acad. of Sciences*
Christian Lüscher, *U. of Geneva*
Laura Machesky, *CRUK Beatson Inst. for Cancer Research*
Anne Magurran, *U. of St. Andrews*
Oscar Marin, *CSIC & U. Miguel Hernández*
Charles Marshall, *U. of California, Berkeley*
C. Robertson McClung, *Dartmouth College*
Rodrigo Medellin, *U. of Mexico*
Graham Medley, *U. of Warwick*
Jane Memmott, *U. of Bristol*
Tom Misteli, *NCI*
Yasushi Miyashita, *U. of Tokyo*
Mary Ann Moran, *U. of Georgia*
Richard Morris, *U. of Edinburgh*
Alison Motsinger-Reif, *NC State U.* **(S)**
Thomas Murray, *The Hastings Center*
Daniel Neumark, *U. of California, Berkeley*
Kitty Nijmeijer, *U. of Twente*
Helga Nowotny, *European Research Advisory Board*
Rachel O'Reilly, *Warwick U.*
Joe Orenstein, *U. of California Berkeley & Lawrence Berkeley National Lab*
Harry Orr, *U. of Minnesota*
Pilar Ossorio, *U. of Wisconsin*
Andrew Oswald, *U. of Warwick*
Isabella Pagano, *Istituto Nazionale di Astrofisica*
Margaret Palmer, *U. of Maryland*
Steve Palumbi, *Stanford U.*
Jane Parker, *Max-Planck Inst. of Plant Breeding Research*
Giovanni Parmigiani, *Dana-Farber Cancer Inst.* **(S)**
John H. J. Petrini, *Memorial Sloan-Kettering Cancer Center*
Samuel Pfaff, *Salk Institute for Biological Studies*
Kathrin Plath, *U. of California, Los Angeles*
Joshua Plotkin, *U. of Pennsylvania*
Albert Polman, *FOM Institute AMOLF*
Philippe Poulin, *CNRS*
Jonathan Pritchard, *Stanford U.*
Wim van der Putten, *Netherlands Institute of Ecology*
David Randall, *Colorado State U.*
Sarah Reisman, *Caltech*
Felix Rey, *Institut Pasteur*
Trevor Robbins, *U. of Cambridge*
Jim Roberts, *Fred Hutchinson Cancer Research Ctr.*
Amy Rosenzweig, *Northwestern University*
Mike Ryan, *U. of Texas, Austin*
Mitinori Saitou, *Kyoto U.*
Shimon Sakaguchi, *Kyoto U.*
Miquel Salmeron, *Lawrence Berkeley National Lab*
Jürgen Sandkühler, *Medical U. of Vienna*
Alexander Schier, *Harvard U.*
Vladimir Shalaev, *Purdue U.*
Robert Siliciano, *Johns Hopkins School of Medicine*
Denis Simon, *Arizona State U.*
Uri Simonsohn, *U. of Pennsylvania*
Alison Smith, *John Innes Centre*
Richard Smith, *U. of North Carolina* **(S)**
John Speakman, *U. of Aberdeen*
Allan C. Spradling, *Carnegie Institution of Washington*
Jonathan Sprent, *Garvan Inst. of Medical Research*
Eric Steig, *U. of Washington*
Paula Stephan, *Georgia State U. and National Bureau of Economic Research*
Molly Stevens, *Imperial College London*
V. S. Subrahmanian, *U. of Maryland*
Ira Tabas, *Columbia U.*
Sarah Teichmann, *Cambridge U.*
John Thomas, *North Carolina State U.*
Shubha Tole, *Tata Institute of Fundamental Research*
Christopher Tyler-Smith, *The Wellcome Trust Sanger Inst.*
Herbert Virgin, *Washington U.*
Bert Vogelstein, *Johns Hopkins U.*
David Wallach, *Weizmann Inst. of Science*
Ian Walmsley, *U. of Oxford*
Jane-Ling Wang, *U. of California, Davis* **(S)**
David Waxman, *Fudan U.*
Jonathan Weissman, *U. of California, San Francisco*
Chris Wikle, *U. of Missouri* **(S)**
Ian A. Wilson, *The Scripps Res. Inst.* **(S)**
Timothy D. Wilson, *U. of Virginia*
Rosemary Wyse, *Johns Hopkins U.*
Jan Zaanen, *Leiden U.*
Kenneth Zaret, *U. of Pennsylvania School of Medicine*
Jonathan Zehr, *U. of California, Santa Cruz*
Len Zon, *Children's Hospital Boston*
Maria Zuber, *MIT*

BOOK REVIEW BOARD
David Bloom, *Harvard U.*, **Samuel Bowring,** *MIT,* **Angela Creager,** *Princeton U.,*
Richard Shweder, *U. of Chicago,* **Ed Wasserman,** *DuPont*

Published by AAAS

EDITORIAL

A short presidential reading list

Editor-in-Chief,
Science *Journals*

A new U.S. president will be sworn into office in less than 3 months. Because scientific issues cut across many aspects of modern life, in both the public and private sectors, the president has several challenges. He or she must ensure that the government has access to robust advice about scientific issues to guide policy development. The president must select, and the U.S. Senate must confirm, the leaders for agencies with a substantial science focus. Finally, the new president must set the tone regarding the importance of science in the nation's progress. Two short, 70-year-old documents outline many central issues that are still relevant today.

"...these...documents...lay out principles for the importance of science in society..."

The advisory role of science in the administration is held by the president's science adviser (formally, Assistant to the President for Science and Technology Policy). President Franklin Roosevelt established a precursor to this position during World War II with the appointment of Vannevar Bush as head of the Office of Scientific Research and Development. Bush was an engineer who had been a cofounder of the American Appliance Company (which later became the Raytheon Company), a faculty member at the Massachusetts Institute of Technology, and president of the Carnegie Institution of Washington. He is perhaps best known as the author of two seminal documents.

In 1945, Bush delivered "Science, The Endless Frontier"* as a report requested by President Roosevelt (likely at Bush's urging). This treatise detailed a compelling vision for the role of science in society, especially for basic science funded by the federal government. After an introduction, its subsequent chapters present many key elements of governmental science policy: "The War Against Disease" emphasizes the importance of broad and basic studies, as well as coordinated attacks on specific diseases; "Science and the Public Welfare" describes the role of science for job creation and the importance of academic basic research to complement research in industry; "Renewal of Our Scientific Talent" highlights the importance of training and recruiting talent in a manner that includes men, women, and those with limited economic means; "A Problem of Scientific Reconversion" describes the challenges of scientists transitioning from wartime to peacetime research and the open publication of scholarly results; and "The Means to the End" lists five principles for federal support of basic research with no expectation of immediate practical results, and concludes with a detailed outline for creating the National Research Agency. "Science, The Endless Frontier" presented a thoughtful outline for science in peacetime and, although many features of it were not implemented, its recommendations were reflected in the creation of the National Science Foundation in 1950.

In 1945, Bush also published "As We May Think"† in a popular magazine, *The Atlantic Monthly*. This strikingly prescient essay presents a crisp vision for the roles of machines in information storage and computation, and the need to convert large amounts of information into useful knowledge. Many features of his picture have come true—mostly in the past decade. Bush presented his ideas to inspire the citizenry to think about science and technology as a path to improving their futures, both with respect to extant tasks and futuristic ones.

As the president-elect considers many of the nation's challenges related to science, I have a simple suggestion: Read these two Vannevar Bush documents. They lay out principles for the importance of science in society, the interactions between academic and industrial science, the compelling nature of scientific discovery, and the importance of thinking with a long time horizon. This will provide a strong framework for selecting key leaders for the next administration and for being a good consumer of the information and advice that they provide. It will be an hour or two well spent.

–Jeremy Berg

*www.nsf.gov/about/history/vbush1945.htm †www.theatlantic.com/magazine/archive/1945/07/as-we-may-think/303881/

10.1126/science.aal2121

PHOTOS: (INSET) BROOKS KRAFT LLC/CORBIS/GETTY IMAGES; (TOP RIGHT) TERRY CLARK

Downloaded from http://science.sciencemag.org/ on October 20, 2016

Published by AAAS

NEWS

2,000,000,000,000

Number of galaxies in the observable universe—more than 10 times as many as previously estimated—according to a count reported in an upcoming study in *The Astrophysical Journal*.

IN BRIEF

Hunting is killing off hundreds of mammal species, including the black rhino.

Hunting driving many mammals to edge

Hundreds of mammals are being hunted to extinction, says a team of ecologists that has taken the first look at the effects of hunting on land mammals around the world. The researchers combed through the International Union for Conservation of Nature and Natural Resources's annual Red List of Threatened Species to see which of the 1169 land mammals listed faced extinction from hunting rather than, for example, habitat loss. Hunting is decimating populations of 301 species—including 126 primates, 26 bats, and 65 ungulates such as deer and wild pigs, the team reported this week in *Royal Society Open Science*. These mammal species play key roles in many different ecosystems, from large carnivores keeping plant-eating populations in check to mammals that shape the landscape by burrowing, foraging, or dispersing seeds. Hunting also disproportionately threatens large mammals: More than 60% of the threatened land mammal species weigh in at more than 1000 kilograms, among them rhinos and hippos. Those animals are especially vulnerable, because they tend to have smaller population sizes and longer times between generations. http://scim.ag/mammalext

AROUND THE WORLD

U.S.-Cuba biomed barrier falls

WASHINGTON, D.C. | Building on a historic December 2014 rapprochement, the U.S. Department of the Treasury this week authorized U.S. scientists to freely collaborate with Cuban counterparts on everything from cancer therapies to combatting the Zika virus. Previously, U.S. biomedical and public health scientists had to apply to the treasury's Office of Foreign Assets Control for a license to conduct research with Cuban colleagues; most licenses are valid for only 1 or 2 years, and renewals are time consuming, making it hard to sustain long-term collaborations. The rules, which went into effect 17 October, also make it easier for Cuban-made pharmaceuticals to undergo U.S. Food and Drug Administration (FDA) review, and allow FDA-approved Cuban drugs to be imported and sold. The U.S. government is also lifting restrictions that have mostly barred Cubans from receiving U.S. grants, scholarships, and research awards. One open question is whether Cuba's own regulations will pose constraints; another is whether many of Cuba's top scientists will embrace working with a country that sought to isolate them for so long. http://scim.ag/USCubabiomed

Downloaded from http://science.sciencemag.org/ on October 20, 2016

PHOTO: IMAGES OF AFRICA PHOTOBANK/ALAMY STOCK PHOTO

Published by AAAS

Oversight body debate heats up

LONDON | A controversial bill before U.K. Parliament proposes to create a UK Research and Innovation (UKRI) body to oversee the country's £6 billion in research funding. Last week, proponents and critics of the Higher Education and Research Bill gathered in a press briefing at London's Science Media Centre to lay out their cases. Proponents argue that a strong, independent voice would be the most effective advocate for scientists at a time of uncertainty over future budgets and the pending exit from the European Union. Opponents, meanwhile, worry that the bill's proposal to remove royal charters for universities and research councils, making it easier for the government to change or dissolve them, threatens to upend protections for independence and self-determination in science and higher education. The Public Bill Committee in the House of Commons completed its scrutiny of the bill on 18 October; after a vote by the House of Commons, the bill heads to the House of Lords. The target date for officially starting UKRI is April 2018. **http://scim.ag/UKoversight**

Brazil faces budget freeze

BRASÍLIA | Brazilian scientists are on high alert, thanks to a constitutional amendment bill proposed by the country's federal government that would put a cap on public spending for the next 20 years. The proposal, known as PEC 241, would make it illegal for all three branches of government—executive, legislative, and judicial—to raise their yearly expenditures above the rate of inflation, essentially freezing the federal budget at current levels for 2 decades. That "will be a disaster" for science, says the president of the Brazilian Academy of Sciences, Luiz Davidovich, in Rio de Janeiro. The current federal budget for science, technology, and innovation—$1.5 billion in 2016—is the lowest in 10 years, if corrected for inflation; government agencies have been cutting down on scholarships and grants, and research institutions across the country are struggling to pay even their electricity bills. Getting the bill approved in Congress before the end of this year is the top priority of Brazilian President Michel Temer, who took office on 31 August, following the impeachment of Dilma Rousseff. **http://scim.ag/Brazilcap**

Treaty to curb HFC emissions

KIGALI | On 15 October, world leaders gathered in Rwanda announced an agreement to curb the use of superpotent greenhouse gases used in air conditioners and refrigerators. The chemicals, called hydrofluorocarbons, or HFCs, have up to 2000 times the heat-trapping ability of carbon dioxide. The agreement comes nearly 30 years after the Montreal Protocol was created to protect the ozone layer by phasing out chemicals used in everything from hair spray to refrigerators. Emissions of those chemicals plunged as they were replaced by less-damaging alternatives, including HFCs—but those came with a heavy price. The new deal, which caps 7 years of negotiations, creates a three-tiered system: India, Pakistan, and four Gulf states would freeze HFC consumption in 2028 and set future reductions based on consumption between 2024 and 2026. China and other developing countries would halt growth in 2024, using 2020 to 2022 levels for a baseline. And the developed world would phase down the use of HFCs in 2019. At a time when the world is poised to add 700 million air conditioners by 2030, the agreement could prevent nearly 0.5°C in temperature rise over this century. **http://scim.ag/HFCtreaty**

FINDINGS

High altitude transforms blood

Even a brief time at high altitude can alter blood cells in ways that make it easier to cope with low-oxygen conditions, reports a study this month in the *Journal of Proteome Research*. The traditional explanation for how the body adjusts to oxygen-deprived high-altitude conditions is that it builds new red blood cells. But that can take weeks—whereas people are known to adapt within days. In the new study, researchers examined the blood of 21 volunteers acclimated to 5260 meters above sea level in the Bolivian Andes. The team found multiple changes affecting how tightly hemoglobin, the protein that transports oxygen, hangs onto its cargo, making it easier for the oxygen to be released to tissues that need it. The changes may persist for about 120 days—the life span of a red blood cell. It's a valuable finding not just for mountaineers, but also for doctors seeking to treat traumatic injuries by boosting blood's oxygen-carrying capacity. **http://scim.ag/altitudeblood**

Aspidella, one of the most common fossils of the enigmatic Ediacara biota.

PHOTO: LIDYA TARHAN

Puzzling fossils, preserved in a silica ocean

The so-called Ediacara biota—strangely shaped creatures that include Earth's oldest fossils of complex animals, dating to between 571 million to 541 million years ago—are found in rock layers on every continent except Antarctica. How the organisms became fossils in the first place has long puzzled scientists: Many of the biota were soft-bodied, and soft organisms tend to decay relatively rapidly after death rather than become preserved in the rock record. But a new study suggests that the Ediacaran oceans gave fossilization a boost: The waters were much more silica-rich than modern oceans, and that silica, concentrated between the sand grains that buried the organisms, likely precipitated out of the seawater and then covered and entombed the biota, researchers report this month in *Geology*. Unlike more selective fossilization, which can give a biased snapshot of the composition of an ecosystem, the precipitated silica would have covered the animals indiscriminately—so the Ediacaran fossil assemblages are likely accurate snapshots of what Ediacaran seafloor communities actually looked like.

Downloaded from http://science.sciencemag.org/ on October 20, 2016

Published by AAAS

ARCHAEOLOGY

‘Green hell’ has long been home for humans

By burning trees and tending crops, prehistoric people left a lasting mark on rainforests

By **Andrew Curry**, *in Jena, Germany*

For centuries, tropical rainforests were seen as the very definition of wilderness, largely untouched by humans. Spanish conquistadors called the Maya forest landscape a “green hell.” As late as the 1970s, anthropologists described Amazonian rainforests as a “counterfeit paradise,” arguing that their soil lacked the nutrients to sustain agriculture or complex human societies. “When I was starting school, there was this idea that the tropics were unlivable,” able to support only small groups of hunter-gatherers at most, says archaeologist Anabel Ford of the University of California in Santa Barbara (UCSB).

It’s now becoming clear, however, that human ancestors not only lived in the rainforest, but transformed it over tens of thousands of years. At Pantropica, a conference organized here this month by the Max Planck Institute for the Science of Human History, presentation after presentation highlighted how prehistoric people burned the forest, cleared it, farmed it, nurtured certain of its tree species, and even built cities in it, leaving lasting, if subtle, marks. “Tropical forests are long-term documents of human action,” says environmental archaeologist Chris Hunt of Liverpool John Moores University in the United Kingdom.

Although evidence of complex rainforest societies, and even cities, began emerging decades ago, the idea that human activity transformed the forest itself was slow to crystallize, because data were scarce. Acidic rainforest soils eat away bone, and tools and buildings made from organic materials like wood and bamboo rot quickly in warm, humid forests. Thick foliage obscures earthworks and structures.

But archaeologists have found clever ways to uncover ancient humans’ impact on today’s jungles. For example, powerfully fragrant ammonia from bird and bat guano preserved organic remains for millennia at Niah Cave on the island of Borneo, allowing Hunt to analyze a pollen record from inside the cave. He identified and counted the species represented in the pollen, noting some that sprout after forest fires. He found that the fires began only after modern humans arrived about 50,000 years ago, suggesting that people torched the forest, probably to make hunting easier and to promote useful “edge” plants and animals like bearded pigs. Then, about 11,000 years ago, pollen from a nearby site showed abundant wild rice and nonnative palms, showing that humans were selecting and importing useful species from other islands.

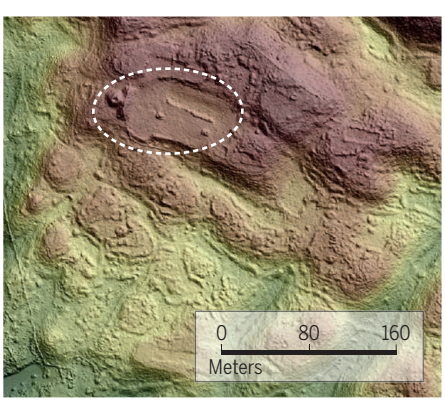

LiDAR images show a ceremonial pyramid (circled) with rectilinear and circular elements, in the pre-Columbian city of Angamuco in Mexico.

Thus this region, usually described as pristine, was in fact managed millennia ago. “It was shocking to me when I found out it wasn’t primary rainforest,” Hunt says. Pollen records from Australia and from Papua New Guinea’s Ivane Valley suggest a similar pattern of burning after humans arrived.

Researchers at the conference argued that slash-and-burn techniques, once thought to be environmentally destructive, were actually sustainable, part of a centuries-long forest management cycle practiced in many tropical forests. Modern Maya “forest gardeners” in Belize and Guatemala farm burn plots for a few years, then manage them for second-growth species like fruit trees, UCSB’s Ford says. She argues that a combination of arboriculture and cyclical agriculture

IMAGES: (TOP TO BOTTOM) STARLIGHTCHILD/WIKIMEDIA COMMONS; CHRIS FISHER/LEGACIES OF RESILIENCE PROJECT

Downloaded from http://science.sciencemag.org/ on Octob

Published by AAAS

Pollen from Borneo's Niah Cave shows that people began to burn nearby rainforest 50,000 years ago.

enabled the ancient Maya to support large populations in a sustainable way, and that the practice of burning the forest had begun with the first Native Americans in the area. "They are regularly burning fields, creating a cycle for reforestation," Ford says. "It's not that they're one with nature—they'd been recreating the forest across 8 millennia."

The legacy of ancient burning or clearing lingers in what may look like primeval forest today, Hunt says. Heavy concentrations of certain tree species, particularly useful or edible ones usually found near rivers but appearing far from streams, may signal ancient human forest management. One recent study estimated that 1.4% of Amazonian tree species make up more than 50% of the rainforest, with palm trees and other useful species dominating (*Science*, 18 October 2013, p. 325); the authors suspect that human hands crafted the unusual distribution.

Recently, researchers have found other signs of human disturbance in the Amazon: large patches of fertile "black earth," or terra preta—carbon-rich soil prized for farming today. Some argued that ancient people intentionally enriched nutrient-poor rainforest soils by burning vegetation and working charcoal and organic garbage into the ground. But most terra preta looks like places where people lived rather than farmed, with ample shards of pottery and bones, says archaeologist Manuel Arroyo-Kalin of University College London. He thinks ancient people could have boosted soil nutrients accidentally, simply by tossing their refuse in the same place for millennia.

> ***"Tropical forests are long-term documents of human action."***
>
> **Chris Hunt**, Liverpool John Moores University

New evidence, from the bones of early rainforest people, suggests they did grow surprising amounts of corn. At the conference, archaeologist Tiago Hermenegildo of the University of Cambridge in the United Kingdom presented data on carbon isotopes in bone collagen from more than 120 prehistoric individuals previously excavated from Amazonian sites. Corn uses a specific kind of photosynthesis, called C4 rare in rainforests, so carbon isotopes from people eating mostly corn look different from those who eat a more mixed diet.

At two Amazonian sites, Hermenegildo uncovered evidence of an unexpectedly corn-heavy diet. In the Brazilian site of Hatahara in the central Amazon, dated to between 750 and 1050 C.E., he detected the clear presence of corn in the remains of people thought to subsist mostly on fish and river turtles, suggesting that they planted corn to eat or ferment. For farmers from the Bolivian site of Llanos de Moxos, dated to between about 600 and 1400 C.E., corn was thought to be a secondary food source. But there, too, Hermenegildo found a strong signature from corn in human bones, and also in Muscovy ducks from the site. "They're using a lot of corn," he says, "so much they're feeding their animals with it."

Besides traces of agriculture, rainforests also bear the imprint of ancient cities far larger than anyone had guessed. Using laser scanners mounted on aircraft, or light detection and ranging (LiDAR), archaeologists have shown that Angkor Wat in Cambodia sprawled more than 3000 square kilometers and could have housed more than 750,000 people at its height in the 11th century C.E.

In Honduras, archaeologist Chris Fisher of Colorado State University in Fort Collins helped use LiDAR to discover traces of walls, earthen pyramids, and artificially leveled plazas with stone pavement: a sizable "lost city" dating to between 1000 and 1400 C.E., deep in what was thought to be untouched, impenetrable jungle. He also directed a LiDAR project that revealed the extent of Angamuco, a major urban center in Mexico built by the Purépucha culture that rivaled the great cities of the Aztec empire from 1000 C.E. until the arrival of the Spanish around 1500 C.E. "We can use these records to repopulate the Americas," Fisher says. "LiDAR enables us to see" cities in places once thought to be untouched.

The implications for modern rainforest management could be profound, as the evidence suggests that human activity helped shape some of today's supposed wildernesses. "Humans are not by nature incompatible with biological diversity," says anthropologist William Balée of Tulane University in New Orleans, Louisiana, who was not at the Jena meeting.

But others say the evidence for widespread human settlement in tropical forests has been overstated. "There was such a strong belief beforehand that you couldn't develop complex societies in the rainforest that when examples started to pop up the field immediately went to the other extreme," cautions Crystal McMichael, a paleobotanist at the University of Amsterdam who was not at the meeting. "In truth, it's probably somewhere in the middle." ■

Andrew Curry is a writer in Berlin.

COMPUTING

Odd computer zips through knotty tasks

Hybrid Ising machines survey universe of possible solutions for best answer

By **Adrian Cho**

A century-old theoretical model of magnetism is giving rise to a hybrid computer, part classical and part quantum, that may be capable of solving problems that overwhelm conventional computers. The so-called Ising machine, described in 100-bit and 2000-bit versions in two reports this week in *Science*, could tackle optimization problems that require finding the best solution among myriad possibilities, such as predicting how a protein will fold.

"This is an exciting development and something that we want to pursue," says Alán Aspuru-Guzik, a theoretical chemist at Harvard University who has studied using Ising machines to decipher protein folding. If the technology can be scaled up just a bit further, "it's going to start competing with classical computers," he predicts. Others are more ambivalent about the technology's prospects.

The machines take their name from the Ising model, which was developed in 1920 by German physicist Wilhelm Lenz and his student Ernst Ising to explain how magnetism arises. In a magnetic material, each atom acts like a little magnet. At high temperatures, the atoms point in random directions so that their magnetism cancels out. Below a certain temperature, the atoms point in the same direction, magnetizing the material. The Ising model aims to capture the transition from randomness to order by envisioning a regular array of "spins" that point up or down and randomly flip depending on the temperature. In the original model, neighboring spins interact so that they tend to point in the same direction. Lenz and Ising hoped to show how the spins would suddenly snap into the same orientation as the temperature fell—although the model turned out to be fiendishly difficult to analyze.

Curiously, many optimization problems can be mapped onto more general versions of the Ising model, in which any two spins can interact, not just neighbors, and the paired

Downloaded from http://science.sciencemag.org/ on October 20, 2016

Published by AAAS

spins can be set to favor alignment or opposition. For example, the spread of two contradictory opinions on the internet might be represented as an Ising model with up and down spins standing for opposite opinions. To solve a model, researchers must find the lowest energy configuration of the spins, or "ground state," in which the most interactions are satisfied (see graphic, right).

The challenge is finding that solution. On a conventional computer, the number of steps needed to solve the model is thought to blow up exponentially as the number of spins increases, making it among the hardest computational problems.

Now, two overlapping groups at Stanford University in Palo Alto, California, and at NTT Basic Research Laboratories in Atsugi, Japan, have developed optical machines specifically designed to solve, at least approximately, the Ising model. The method is the brainchild of Yoshihisa Yamamoto, an electrical engineer at Stanford who also founded the NTT group in 1983.

The devices rely on pulses of light generated by a widget called an optical parametric oscillator (OPO) when it is zapped with laser light. The pulses course around a single long loop of optical fiber like so many wooden horses on a carousel. Each pulse is the equivalent of an atomic spin in a traditional Ising model.

Each pulse also has a "phase," which describes whether the light waves oscillate in or out of step with the laser that zaps the OPO. The phase can be positive or negative, mimicking the up and down of a spin. As the pulses stream past, researchers measure their phases. They then use a very fast processor, which encodes the interaction constraints for the specific Ising model being analyzed, to calculate how the phases should change in order to lower the model's total energy. When the pulses circle back through the OPO on the next lap, scientists apply feedback to nudge their phases one way or the other. "In nanoseconds you have to figure out what the feedback to the next pulse will be," says Peter McMahon, an applied physicist at Stanford and lead author on one of the papers. After a few dozen laps, the phases evolve toward the ground state and stabilize.

Exactly how this happens remains a bit of a mystery, McMahon says. It appears crucial that each pulse start out in a quantum mechanical "squeezed state" in which its phase is, weirdly, both positive and negative at the same time, giving the system an inherent flexibility to search for solutions, he says.

Focusing on the basic technique, the Stanford group solved Ising models with up to 100 spins, using a conventional computer to check their work and see how close they were getting to ground state. Trying to scale up, the NTT group devised a 2000-spin system that solved a more limited group of problems. The devices aren't perfect. As the number of spins grows, they most often don't find the exact ground state, but only a low-energy approximation of it. However, for many purposes, that's good enough, Yamamoto says.

Others have built Ising machines, too. Researchers at Hitachi Ltd. in Tokyo have built a device in which each spin is represented by a transistor whose voltage can be high or low. D-Wave Systems of Burnaby, Canada, has built a chip in which each spin is a tiny ring of superconducting metal in which current can run one way or the other—or, thanks to the weirdness of quantum mechanics, both ways at once. D-Wave claims, controversially, that its machine can solve the Ising model faster than an ordinary computer thanks to quantum effects, which enable it to "tunnel" directly from one possible arrangement of spins to another (*Science*, 20 June 2014, p. 1330).

The optical Ising machines have a key advantage over the solid-state systems, says Hiroki Takesue, a physicist with the NTT group. In the Hitachi and D-Wave devices, the spins lie in a plane and only neighboring spins can interact directly. To mimic interactions with other, farther flung spins, a single spin in certain Ising problems has to be mapped onto a group of many spins on the chips. That reduces the size of the problems that the two companies' devices can handle, to about 150 spins for the Hitachi system and a few dozen for the D-Wave chip, Takesue says. In contrast, by allowing any spin to interact with any other, the optical machines can directly encode arbitrary Ising models. "Already with 2000 spins there may be some applications" such as optimizing the use of bandwidth in Wi-Fi and cellphone networks, Takesue says.

Some researchers say it isn't clear the Ising machines can best their primary competitors—conventional computers. "What is the case that you're going to do something faster this way than you could do it using just an ordinary digital computer?" says Scott Aaronson, a computer scientist at the University of Texas in Austin. "I never saw that satisfactorily addressed anywhere, and it's certainly not addressed in the present papers."

The researchers are working on such comparisons, which can be difficult. At least on one problem, the NTT machine seems to be 50 times faster than an ordinary computer, Takesue says. In the meantime, the teams are developing a compact version of the device that could be commercialized. They are also trying to make it accessible for other researchers to use remotely. "Sometime next year," Yamamoto says, "we will be able to connect our device to the internet." ■

Ising models made easy

Ising models map real-world optimization problems in terms of particles with spins, pointing up or down, and paired interactions that favor either aligned or opposing spins, such as in this eight-particle model. For the largest models, finding the optimum, lowest energy state can overwhelm conventional computers. But hybrid quantum-classical devices called Ising machines hold the promise to solve the problems easily.

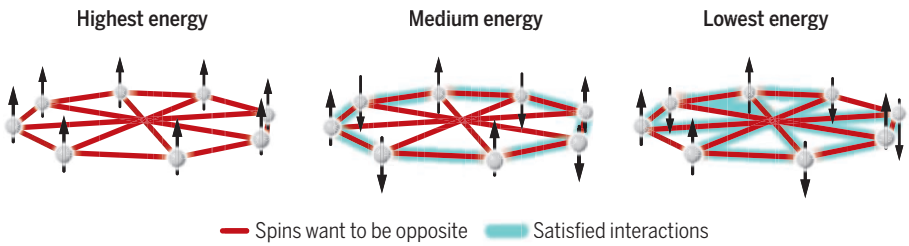

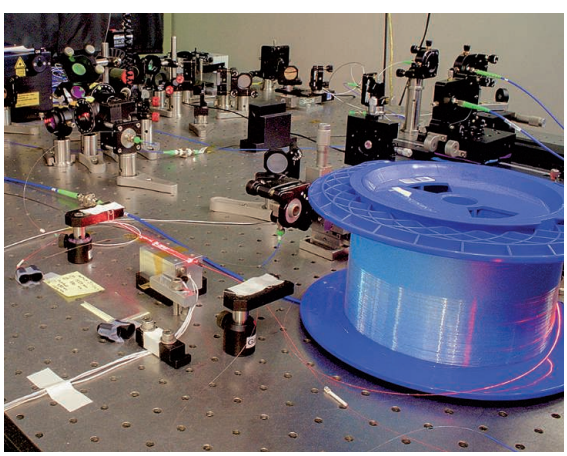

Ising machines compute by making pulses of light interact as they course through a spool of commercial optical fiber.

CREDITS: (DIAGRAM) V. ALTOUNIAN/*SCIENCE*; (PHOTO) ALIREZA MARANDI

Downloaded from http://science.sciencemag.org/ on October 20, 2016

Published by AAAS

LATIN AMERICA

Colombia peace deal blow dismays ecologists

Once encouraged by a cease-fire, scientists now reconsider venturing into rainforest

By **Lizzie Wade**

Under siege from deforestation and climate change, the last redoubt of the world's most poisonous frog is a dense patch of rainforest southwest of the Colombian city of Cali. How the golden poison dart frog is faring is largely a mystery: Experts on amphibians haven't dared venture into its habitat for decades, deterred by guerrilla fighters and other armed groups that once turned large swaths of Colombia into a war zone. But for a hopeful week, the threat finally seemed to have lifted.

On 26 September, Colombia's government and the Revolutionary Armed Forces of Colombia (FARC) signed an agreement ending 52 years of conflict—a feat that earned President Juan Manuel Santos the 2016 Nobel Peace Prize. As the fighters pledged to lay down their weapons, ecologist German Forero-Medina, science director of the Wildlife Conservation Society Colombia in Cali, and colleagues from the Zurich Zoo in Switzerland pressed ahead with a plan to check on the gold poison dart frog. But on 2 October, Colombians in a referendum narrowly rejected the peace accord, leaving Forero-Medina and other scientists wondering when it will truly be safe for fieldwork. "We're not in the era of peace that we expected to be in," he says. "The country is living with an incredible amount of uncertainty."

"Biologists are among the people who are saddest about the [referendum] results," says Susana Caballero, a biologist at the University of the Andes (Uniandes) in Bogotá. "There was so much hope that things could actually improve." She had recently taken 20 students into the previously inaccessible Chocó region along Colombia's Pacific coast, and she also hopes to help former guerrilla fighters find new livelihoods as field guides. Now, Caballero says, "That's all on standby."

Colombia has some of the richest biodiversity in the world, with more than 300 distinct ecosystems that are home to nearly 10% of the world's species. "There are zones that are incredibly interesting biologically," says Juan Posada, an ecologist at the University of El Rosario in Bogotá. The Chocó region, for example, is the wettest on the planet, soaking up about 16 meters of rain a year. But it has long been a battleground between leftist rebel groups like FARC and right-wing paramilitaries.

After Santos and FARC commander Rodrigo Londoño began peace negotiations 4 years ago, rural violence diminished. Even before a 23 June cease-fire, scientists started returning to some areas that were no-go zones. "In 2016 alone, scientists have discovered 100 new species in Colombia," says Hernando García, acting director of the Humboldt Institute, a biodiversity research center in Bogotá. "The majority of those species come from places that were closed to science because of the war."

FARC rebels in August watch a newscast at their encampment in Putumayo in Colombia. Earlier this month, citizens rejected a peace deal between FARC and the government, prompting some ecologists to hold off on fieldwork in areas still controlled by armed groups.

PHOTO: AP PHOTO/FERNANDO VERGARA

Scientists are also eager to study the aftermath of the conflict itself. Because the presence of armed groups slowed development, rebel territories "are some of the best protected and most intact regions," Posada says. Still, coca crops and illegal gold mining have led to rampant deforestation in many areas in the conflict zone. Until researchers investigate those regions for themselves, "it's hard to tell how good or bad" the conflict has been for the environment, says Daniel Cadena, a biologist at Uniandes.

Pablo Stevenson, an ecologist at Uniandes and director of the Macarena Ecological Research Center, recently returned to a field station he was forced to abandon in 2002, after armed rebels held a Japanese scientist hostage for several months. When Stevenson visited in July, for the first time in 14 years, he found that although some of the forest had been razed and replaced by illegal coca crops, healthy numbers of at least six monkey species still roamed near the station. With the signing of the cease-fire, Stevenson applied for permits to resume his research and began negotiations with local community leaders, who are affiliated with FARC. "We made those plans expecting peace," he says. In the wake of the referendum, he says, "I have no idea what's going to happen."

Santos has promised to continue peace negotiations and last week extended the cease-fire until the end of the year. Most researchers are optimistic that the country will not slide back into civil war. But they fear that a dragged-out peace process will divert the government from other domestic priorities, including more robust support for science. "In Colombia, many things got pushed to the side because we had to invest in the war," including science, Caballero says. According to the United Nations Educational, Scientific and Cultural Organization, Colombia spent a scant 0.19% of its gross domestic product on R&D in 2014, among the lowest in South America. Once the conflict ends, Posada says, "there might be more money for science and technology."

Despite the uncertainty, Forero-Medina is pressing forward with plans for fieldwork next month in the rainforest west of Cali. But his foreign colleagues are "a bit scared," so he is talking with local police and indigenous groups to find out what the situation is like on the ground. "From there, we'll make a final decision," he says. If it's not safe, the fate of the golden poison dart frog will remain unknown, for at least a little while longer. ■

Downloaded from http://science.sciencemag.org/ on October 20, 2016

Published by AAAS

STEM CELLS

Are labmade human eggs coming soon?

Mouse eggs grown in vitro produce apparently healthy offspring, but clinical use is distant

By **Gretchen Vogel**

There's no need to start rereading *Brave New World* just yet. But this week's announcement that biologists in Japan have grown mouse egg cells entirely in a lab dish gave new meaning to the term "test tube babies." The eggs, generated in a dish from two kinds of stem cells, gave rise to pups after being fertilized and implanted into rodent foster mothers. Stem cell biologist George Daley of Harvard Medical School in Boston calls it "a stunning achievement."

Beyond offering researchers a new way to study egg development, the feat suggests that scientists could someday make human eggs in the lab from almost any type of cell, including genetically altered ones. That may spark hope of new infertility treatments, but will also likely revive fears among those opposed to designer babies. "If a similar strategy proves successful in human pluripotent stem cells, then the options for reproductive biology, but also genetic modification of the germ line, are profound," Daley notes. But for now the method, which sometimes produced defective eggs and only rarely generated healthy pups, is far from making an impact in the clinic.

Reported in *Nature* this week by stem cell biologists Katsuhiko Hayashi and Mitinori Saitou at Kyoto University in Japan, the work builds on more than a decade of efforts to derive egg and sperm cells from pluripotent stem cells, which resemble cells in early embryos and can in theory become any tissue in the body. In 2012, Hayashi and Saitou made fertile egg cells from both mouse embryonic stem (ES) cells and induced pluripotent stem (iPS) cells, which are reprogrammed adult cells (*Science*, 5 October 2012, p. 24). But to accomplish the final steps of egg development, the researchers had to implant the precursor cells they had created into ovaries or even kidneys of a living mouse. Then, this summer, the scientists showed that they could keep fetal mouse ovaries growing in the lab and make them produce mature, fertile eggs.

The latest effort combines these strategies. First, the scientists used ES and iPS cells to make immature egg precursor cells. Then they inserted those precursors into clusters of cells taken from fetal mouse ovaries. They carefully cultured those cell clusters for more than a month.

Each cell cluster—a labmade ovary—produced on average more than 50 mature egg cells. Those eggs had higher rates of chromosome abnormalities than typical mouse eggs, but more than 75% had the correct number of chromosomes. The scientists mixed apparently normal eggs with mouse sperm, producing more than 300 two-cell embryos, which they then implanted into foster mothers. Only 11 of those embryos—3%—grew into full-term pups, compared with 62% for eggs taken from adult mice and fertilized in vitro. The pups from lab-grown eggs that did survive grew into fertile adults, and lived at least a year. But the researchers didn't look for subtle problems that may have affected the animals.

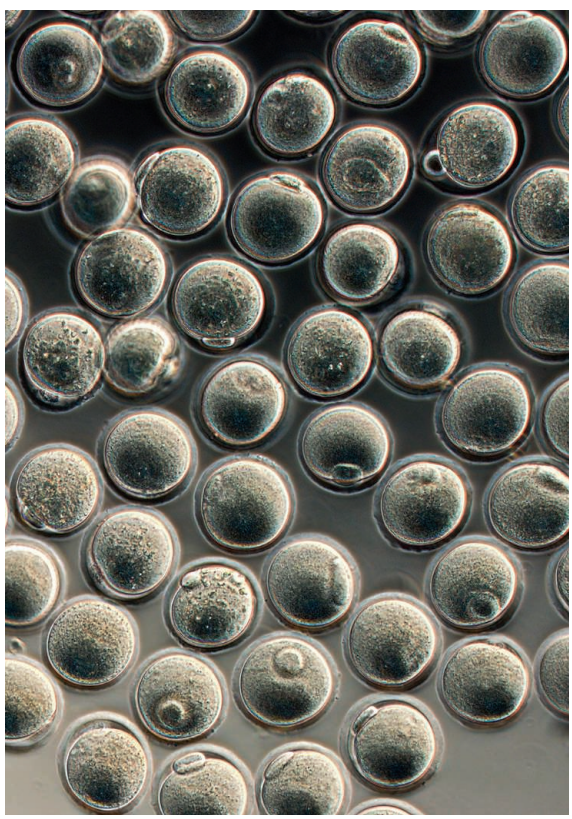

Mouse egg cells derived in the lab from embryonic stem cells.

If scientists could similarly transform female human ES or iPS cells into functional egg cells, they could offer new options for some cases of female infertility, as in women who have gone through egg-destroying chemotherapy. A more controversial application might be to try to generate egg cells from iPS cells derived from a man.

As a first step to any clinical use, the group is now testing the method on nonhuman primate stem cells, but they stress that it is far too early to count on any human applications. For one thing, work by other researchers has shown that mouse and human germ cells require different signals to develop. Another road block is the method's current need for ovary cells taken from a mouse fetus. Such human fetal cells are not readily available. Hayashi and Saitou suggest that it might be possible to derive similar cells from ES or iPS cells, but scientists have yet to turn human ES or iPS cells into any complex tissue type, and researchers know relatively little about early human ovary development.

Culturing human eggs from beginning to end could also take a much longer time: A mouse is born after just 3 weeks, whereas human pregnancy lasts 9 months. Other attempts to translate mouse stem cell research to human cells have stumbled because human cells take longer to grow and divide. And because cells in culture collect genetic damage over time, labmade human eggs might build up more harmful mutations. "We cannot exclude a risk of having a baby with a serious disease," Hayashi says.

Biologists are also divided on just how much insight the mouse work will provide into egg development. Allan Spradling, who studies oocyte development at the Carnegie Institution for Science in Baltimore, Maryland, cautions that any attempt to recreate a process as intricate as egg development is sure to leave out important factors that aren't yet understood. Yet because we can't study normal egg development in live human subjects, seeing it unfold in a dish is certain to be valuable, says Azim Surani, who studies germ cell development at the Gurdon Institute at the University of Cambridge in the United Kingdom. Combined with modern genetic tools, labmade eggs "can potentially tell us a lot." Those insights could have an impact in the clinic long before any such egg is used to produce a human baby. ■

PHOTO: O. HIKABE *ET AL.*, *NATURE* **538**, 7625 (20 OCTOBER 2016) © MACMILLIAN PUBLISHER LTD.

Downloaded from http://science.sciencemag.org/ on October 20, 2016

Published by AAAS

As ʻōhiʻa die off, species that rely on the trees for habitat, like the Hawaiian ʻiʻiwi, face hard times.

INVASIVE SPECIES

Alien fungus blights Hawaii's native trees

Big Island is under assault from deadly invader

By **Inga Vesper**, *on Big Island in Hawaii*

An ecological disaster is unfolding here on Hawaii's largest island. Along the South Kona Highway, near Keokea, lush emerald forest suddenly gives way to bleak stands of dead ʻōhiʻa, their bare limbs outstretched against the blue sky. Rapid ʻŌhiʻa Death (ROD), caused by an imported fungus, is causing Hawaii's iconic native tree to perish in droves. Some 20,000 hectares are now affected, according to a survey by the U.S. Department of Land and Natural Resources presented at the International Union for Conservation of Nature World Conservation Congress summit in Honolulu last month. A flurry of research to understand the invader—and find a way to stop it—is underway.

"People are heartbroken. To them, ʻōhiʻa are part of the family," says J.B. Friday, a forestry scientist at the University of Hawaii (UH) in Honolulu. "If we lose ʻōhiʻa, we'll lose a big part of Hawaiian culture."

Abundant across the archipelago, ʻōhiʻa are the only native tree in Hawaii that colonize lava flows. Their flowers are one of the few here that produce nectar for honey, and they provide habitat for several rare species of native birds and insects. The tree's extensive root network helps guide rainwater to underground aquifers. Researchers suspect that runoff is severe in areas where ROD has killed off ʻōhiʻa. As a result, ROD could threaten Hawaii's freshwater supplies, says Rob Hauff, a forester with the U.S. Division of Forestry and Wildlife in Honolulu.

The outbreak exploded in 2014, in dense ʻōhiʻa groves in Hilo Forest Reserve on Big Island's eastern side, and has worsened ever since. But the saga probably began imperceptibly, perhaps 20 years ago, when the fungus, *Ceratocystis fimbriata,* sneaked onto Big Island on imported plants. Strains of *C. fimbriata* have for decades ravaged mango, sweet potato, and pineapple crops in Asia and the United States. (Another *Ceratocystis* species infects Hawaiian pineapples.) Although Hawaii restricts the import of nonnative plants, pathogens can slip in with the new crop seeds and seedlings that are routinely brought in to improve local agriculture. "If only we knew [the source of *C. fimbriata*], we would be able to prevent people from moving that plant around or importing new ones," Friday says.

Rapid ʻŌhiʻa Death is now spreading fast across Hawaii's Big Island.

Characterizing the ROD strain might help researchers mount a defense for ʻōhiʻa, as well as determine whether other native plants or crops are vulnerable. Toward that end, Lisa Keith and colleagues at the U.S. Agricultural Research Service outpost in Hilo, Hawaii, are comparing the ROD strain's DNA to other *C. fimbriata* strains.

Scientists are also trying to unravel precisely how the fungus spreads. Ambrosia beetles, including several in the genera *Xyleborus* and *Xyleborinus*, appear to play a role. To find food, the beetles bore into ʻōhiʻa, scattering wood dust. Dust contaminated with the fungus is transported to new areas on clothing or on the wind, researchers believe. "Wind patterns correspond somewhat to [the outbreak pattern] and is the best theory currently of how it's spreading," Hauff says. Scientists are also investigating whether the fungus hitches a ride on the beetles themselves. "By understanding the routes of transmission, we can possibly disrupt transmission during a vulnerable stage in the disease cycle," says Curtis Ewing, an entomologist at UH in Hilo.

As scientists work out a strategy for combatting the fungus, the near-term goal is to contain it. They are encouraging locals to stop moving ʻōhiʻa wood and sawdust around the island, wipe ʻōhiʻa-cutting tools with alcohol, and use clean cars and gear before venturing into ʻōhiʻa forests.

Vigilance has also required cultural sacrifices. ʻŌhiʻa blossoms are popular for making leis for dances and festivals. At a festival here last spring, organizers banned the blossoms, forcing dancers to destroy their leis. The fear was that dancers would take leis to other islands and possibly spread ROD. "It took a great deal of education and some painful adjustments of tradition to adapt," says Samuel ʻOhukani'ohiʻa Gon, a senior scientist and cultural adviser in the Honolulu office of The Nature Conservancy, a nonprofit.

To get a sense of what's at stake beyond Big Island, there is no better place than Ka'ala bog forest reserve on Oahu. Here, millennia of ʻōhiʻa growth have created a swampy, springy soil that holds water like a sponge. Shrouded in a cool mist, the 445-hectare reserve sits high above Honolulu, where nearly half a million people depend on the upland forest for drinking water. All is quiet here except for the soft trills of ʻapapane, a rare honeycreeper. As far as scientists know, *Ceratocystis* hasn't jumped to Oahu. But the longer it takes to mount a defense against the fungus, the higher the odds that this refuge, too, will come under siege. ■

Inga Vesper is a journalist in London.

PHOTOS: (TOP TO BOTTOM) DANITA DELIMONT; HAWAII STATE DEPARTMENT OF LAND AND NATURAL RESOURCES VIA AP

Downloaded from http://science.sciencemag.org/ on October 20, 2016

Published by AAAS

Maintaining photosensitivity p. 282 ▸

How cities function on a daily basis p. 293

PERSPECTIVES

EVOLUTION

The first jaws

A fossil fish helps to explain how jaws first evolved

By **John A. Long**

Dinosaurs were once widely considered an evolutionary dead end without much bearing on the evolution of living animals. Yet, today it is clear that theropod dinosaurs gave rise to birds, and that dinosaurs are therefore still alive today. Similarly, placoderms, a group of extinct armored fishes, long held little or no interest to evolutionary biologists. However, discoveries from China are changing that by showing how important placoderms are to understanding the early assembly of the vertebrate body plan. On page 334 of this issue, Zhu *et al.* (*1*) report the discovery of a placoderm from Qujing in Yunnan, China, that fills a big gap in our understanding of how vertebrate jaws evolved.

The appearance of jaws in placoderms marks one of the great turning points in early vertebrate evolution. The first jawed fishes became the primary predators in the food chain and diversified into many feeding niches. Placoderms dominated the seas, rivers, and lakes of the Devonian period (~419 to 359 million years ago) and include the world's first megapredators, such as *Dunkleosteus*, which reached about 30 feet in length (*2*). However, until the Qujing site was discovered, the record of placoderms from the Silurian period (443 to 419 million years ago), when placoderms first appear in the fossil record, was very poor.

Zhu and colleagues have been excavating the Qujing site intensively for the past decade. They have made a series of intriguing discoveries, including the oldest

School of Biological Sciences, Flinders University, GPO Box 2100, Adelaide, South Australia 5001, Australia. Email: john.long@flinders.edu.au

***Qilinyu*, in the foreground and above, was part of a diverse fauna of early placoderms and bony fishes that lived in China about 425 million years ago. Their fossil remains reveal the early stages in the evolution of vertebrate jaws.**

Downloaded from http://science.sciencemag.org/ on October 20, 2016

Published by AAAS

known complete bony fish (osteichthyan), *Guiyu* (*3*), as well as the oldest known complete placoderms. One of these, *Entelognathus* (*4*), is arguably one of the most important fossils found in the past century. It bridges a huge morphological gap between the extinct placoderms and the living bony fishes (Osteichthyes, the clade that also includes tetrapods).

Entelognathus had a complex set of dermal bones forming the lower jaw, and large plates underneath the throat. Its lower jaw was formed by the dentary and infradentary bones, with an upper jaw formed by the premaxilla and maxilla. This jaw pattern is typical of all early osteichthyans and many tetrapods.

The *Entelognathus* jaw pattern posed a conundrum for evolutionary biologists. Were the first jaws complex structures made of many external dermal bones, as in *Entelognathus* and osteichthyans, or were the simple blade-like jaws of most placoderms the primitive condition? If the first jaws were complex, then this implied that the oldest known complete placoderm, *Entelognathus*, was far more advanced in its jaw structure than all later placoderms.

Various phylogenetic analyses posited *Entelognathus* as either a sister group to all crown gnathostomes (Osteichthyes and Chondrichthyes) (*4*), or a sister group to some placoderms and crown gnathostomes (*5*), or as the immediate sister group to Osteichthyes (*6*). Either way, it is regarded as the most derived of all placoderms from these analyses, yet is also the oldest known complete taxon of the group. As to whether placoderms are a single clade or a sequential set of clades (*7*), it seemed likely that only new discoveries of complete early placoderms could help to resolve this problem.

Zhu *et al.* now report the discovery of the placoderm *Qilinyu* (pronounced "chee-lin-you") at the Qujing site. This bizarre armored fish sports a flat extended rostrum, giving it a dolphin-shaped head. Yet, its most important feature is its jaws. Unlike *Entelognathus*, its lower jaw does not carry a complex set of external dermal bones. Instead, it has a simple bent blade-like jaw with a small palatal lamina and a large facial lamina (see the figure). In this respect, it more closely resembles other placoderms, whose lower jaws are mainly developed along the palatal aspect for biting. Like *Entelognathus*, *Qilinyu* possessed maxilla and premaxilla forming the upper jaw, demonstrating this as an early placoderm and osteichthyan pattern.

We can see in *Qilinyu* a new stage in placoderm jaw evolution, in which an external lamina of dermal bone begins to reinforce the jaw. This trend is more extensive in *Entelognathus*. The simple jaws of later placoderms are regarded as a primitive condition for jawed vertebrates because they had not yet evolved an outer covering of dermal bones. Thus, *Qilinyu* provides an elegant explanation for why other placoderms lack complex jaws and how the osteichthyan jaw evolved. It strengthens the case for homology between placoderm and osteichthyan jaw elements.

The cheek of *Qilinyu* also shows a bone found in *Entelognathus* and most early osteichthyans, the lacrimal, which is not present in any other placoderms. Furthermore, *Qilinyu* provides the first hard evidence that the earliest placoderms had paired pelvic fins. Recent work has shown that placoderms were the first vertebrates to have paired hind limbs and paired external genitalia (bony claspers), the latter formed by the same developmental process as for typical vertebrate limbs (*8*). The phylogenetic analysis places *Qilinyu* as one node further down the tree than *Entelognathus* (see the figure).

The next burning question at this node of vertebrate evolution is whether teeth evolved at the same time as or after the first jaws. Both *Entelognathus* and *Qilinyu* lack teeth on their jaws, as does a group of basal placoderms known as antiarchs (*9*). However, other placoderms called arthrodires did possess a relatively advanced tooth structure (see the figure) (*10*). It remains unclear why teeth evolved in some placoderms and not others, and whether or not tetrapod teeth were derived from placoderm teeth. Could this be the next big breakthrough that placoderm fossils help to resolve? ■

Placoderm fishes gave us jaws

Jaws first evolved in placoderms and later transformed into those found in osteichthyans and tetrapods.

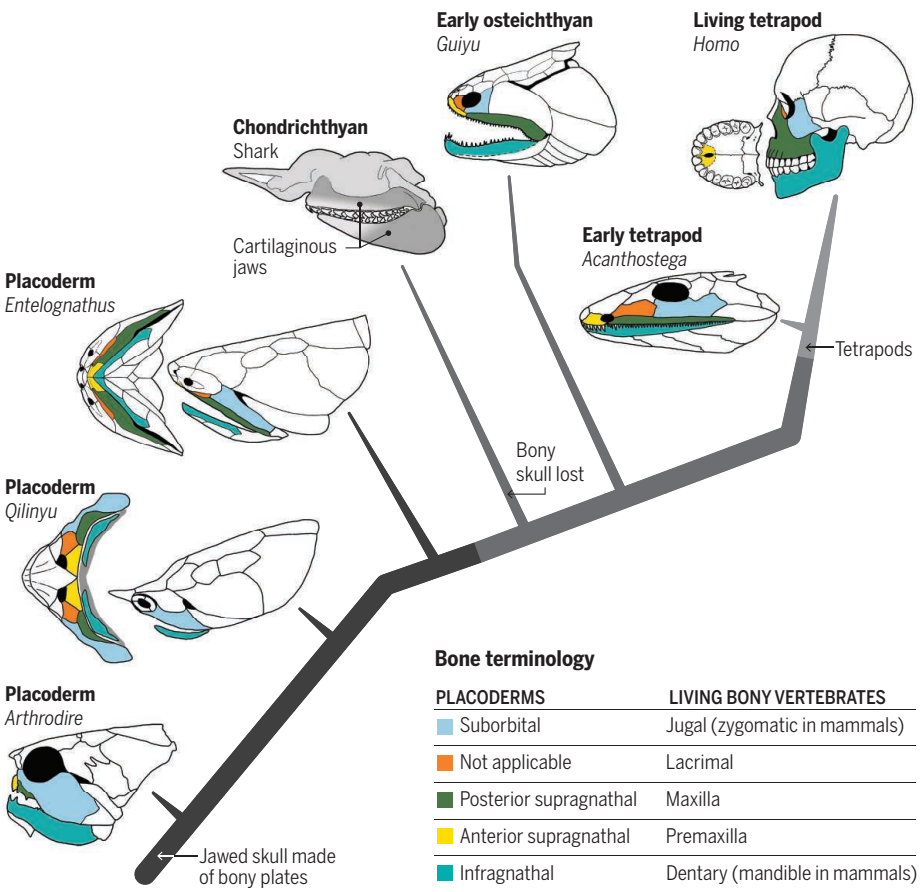

Bone terminology

PLACODERMS	LIVING BONY VERTEBRATES
Suborbital	Jugal (zygomatic in mammals)
Not applicable	Lacrimal
Posterior supragnathal	Maxilla
Anterior supragnathal	Premaxilla
Infragnathal	Dentary (mandible in mammals)

CREDIT: BRIAN CHOO/FLINDERS UNIVERSITY (ADPATED BY V. ALTOUNIAN/*SCIENCE*); (OPPOSITE PAGE) DINGHUA YANG/INSTITUTE OF VERTEBRATE PALAEONTOLOGY AND PALAEOANTHROPOLOGY

Downloaded from http://science.sciencemag.org/ on October 20, 2016

REFERENCES

1. M. Zhu *et al.*, *Science* **354**, 334 (2016).
2. J. Long, *The Rise of Fishes* (Johns Hopkins Univ. Press, Baltimore, 2011).
3. M. Zhu *et al.*, *Nature* **458**, 469 (2009).
4. M. Zhu *et al.*, *Nature* **502**, 188 (2013).
5. V. Dupret *et al.*, *Nature* **407**, 500 (2014).
6. J. Long *et al.*, *Nature* **517**, 196 (2015).
7. M. Brazeau, M. Friedman, *Nature* **520**, 490 (2015).
8. K. Trinajstic *et al.*, *Biol. Rev.* **90**, 467 (2014).
9. M. Rücklin *et al.*, *Nature* **491**, 748 (2012).
10. M. Smith, Z. Johanson, *Science* **299**, 1235 (2003).

10.1126/science.aai8828

Published by AAAS

CELL SIGNALING

A photoreceptor's on-off switch

Light-induced protein interaction controls the signaling of a plant cryptochrome

By **Christian Fankhauser**[1] *and* **Roman Ulm**[2]

Photoreceptors are present in all kingdoms of life. They fulfill a broad range of functions, including vision, photoprotection, and regulating growth and development (*1*). To maintain photosensitivity, photoreceptor-mediated signaling must be turned on and off in a timely fashion. For example, the signaling state of human visual rhodopsins is very short-lived, and patients with defective rhodopsin inactivation suffer from severe dark adaptation problems, illustrating the importance of inactivation mechanisms (*2*). On page 343 of this issue, Wang *et al.* (*3*) report a mechanism of controlling the signaling activity of a family of photoreceptors in plants. They show that cryptochromes are activated through blue light–induced homodimerization. This dimerization and all subsequent signaling events are blocked by the interaction between light-activated cryptochrome and a protein coined BLUE-LIGHT INHIBITOR OF CRYPTOCHROMES 1 (BIC1) (*3*). This system is proposed to control the fraction of cryptochrome photoreceptors engaged in cellular signaling, contributing to the maintenance of photosensitivity.

In insects and throughout the green lineage, cryptochromes are a family of blue-light photoreceptors. However, in mammals, cryptochromes do not function as photoreceptors but are part of the circadian oscillator (*4*). Presently, there is no evidence that animal cryptochromes act as homodimers in vivo; however, similar to plant cryptochromes, they signal through protein-protein interactions. The model plant *Arabidopsis thaliana* has two cryptochromes called CRY1 and CRY2, with the former primarily controlling blue light–regulated seedling establishment, whereas the latter controls photoperiod-mediated flowering (*4*). Plant cryptochromes have long been known to work as dimers (or oligomers) (*5*, *6*). The functional photoreceptor cry2 (CRY2 plus a chromophore) has a propensity of homo-oligomerizing in response to blue light, a feature that was exploited to design optogenetic tools (*7*). Wang *et al.* now provide several lines of evidence supporting blue light–induced dimerization as a central event in the activation of cryptochrome signaling in plants. They show that cry2 homodimerizes in response to blue-light absorption in plants, and BIC1 overexpression blocks light-regulated cry2 homodimerization, phosphorylation, and degradation, as well as interaction with downstream signaling partners such as the transcription factor CRYPTOCHROME-INTERACTING BASIC-HELIX-LOOP-HELIX 1 (CIB1) (*8*), blocking physiological responses (see the figure).

> ***"Outside of plants, the discovery of BIC1 may lead to further developments in the use of cryptochromes for optogenetics."***

Light-regulated dimerization has also been reported in several members of another blue light–photoreceptor family. LOV (light oxygen voltage) domain photoreceptors exist in plants, fungi, algae, and numerous prokaryotes. The photosensory LOV domains combine with various output domains, including protein kinase domains or DNA-binding domains. Light activation leads to dimerization of several "LOV-DNA binding domain" photoreceptors, enhancing photoreceptor affinity to target sequences (*9*–*11*). Interestingly, light triggers LOV-mediated homodimerization of the fungal white collar complex (WCC) photoreceptor, a circadian transcription factor. This induces VIVID, a negative regulator that interferes with WCC activity by forming competing heterodimers with WCC (*11*). However, light-induced dimerization is not a prerequisite for all LOV domain photoreceptors (*12*), and whether this happens for plant LOV domain photoreceptors such as the phototropins and ZEITLUPE remains unknown.

The ultraviolet B (UV-B)–photoreceptor UVR8 presents another example of regulation of the oligomeric state by light. In its ground state, UVR8 is a homodimer, and UV-B absorption leads to photoreceptor monomerization, a conformer that engages in subsequent signaling events through protein-protein interactions (*13*). The return to the ground state of UVR8 is facilitated by the interaction of the UVR8 monomer with REPRESSOR OF UV-B PHOTOMORPHOGENESIS 1 (RUP1) and RUP2, a pair of UV-B–induced proteins (*14*). This negative feedback system

[1]Centre for Integrative Genomics, Faculty of Biology and Medicine, University of Lausanne, 1015 Lausanne, Switzerland. [2]Department of Botany and Plant Biology, Section of Biology, Faculty of Science, University of Geneva, 1211 Geneva, Switzerland. Email: christian.fankhauser@unil.ch

Light switch

Light induces homodimerization of cry2 and subsequent signaling events, including its interaction with CIB and SPA proteins. The latter interaction stabilizes CONSTANS (CO); both interactions lead to flowering. BIC1 binds to cry2 and suppresses blue light–dependent cry2 dimerization and all light-induced–signaling events.

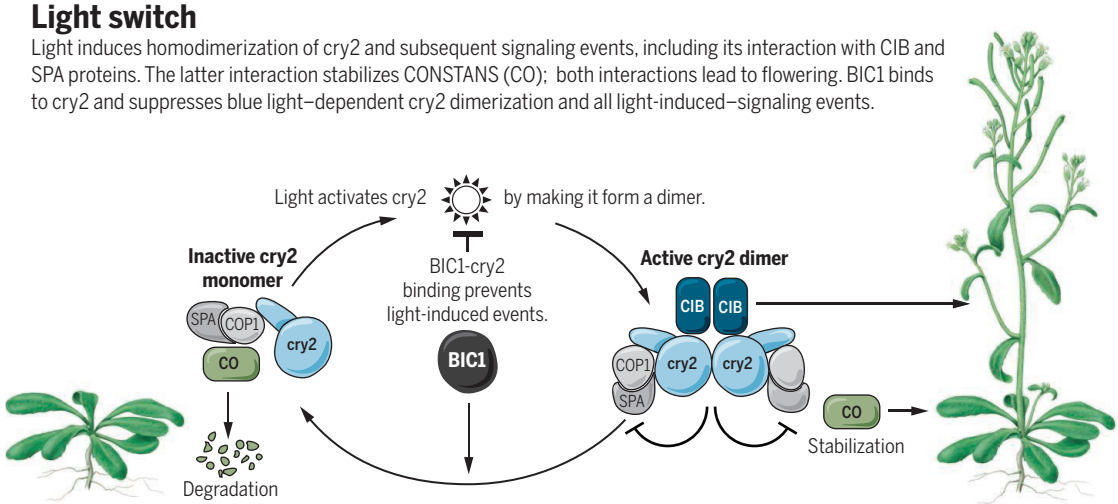

GRAPHIC: K. SUTLIFF/*SCIENCE*

Downloaded from http://science.sciencemag.org/ on October 20, 2016

Published by AAAS

ensures the presence of a pool of dimeric-inactive UV-B photoreceptors, which is probably essential to maintain UV-B sensitivity. The discovery of BIC1 and -2 as key regulators of the cryptochromes presents interesting analogies and differences with the UVR8-RUP system. By inhibiting cryptochrome dimerization, BICs prevent all subsequent signaling events (*3*). Given that expression of BIC1 and -2 is attenuated in cryptochrome mutants, there is also some evidence for a possible negative feedback loop coupling cryptochrome activation to the production of its negative regulators.

Light regulation of the oligomeric state and the regulation of this process by accessory proteins is crucial for the plant photoreceptors UVR8 and cryptochromes. Interestingly, in the former, monomers signal, whereas in the latter, homodimers do. Understanding how BIC expression and activity is regulated in vivo will be important to understand how the cryptochrome off-switch is wired, particularly whether it represents a node of cryptochrome signaling regulation modified by other environmental cues. It will also be exciting to learn about the exact mechanism of BIC action; in particular, are they primarily preventing dimerization by interacting with cryptochrome monomers or promoting the return to a monomeric state, or both? Outside of plants, the discovery of BIC1 may lead to further developments in the use of cryptochromes for optogenetics. Last, it will be interesting to test the evolutionary conservation of this newly discovered regulation of the active dimer state for animal cryptochrome activity. ■

REFERENCES

1. W. J. Gehring, *Wiley Interdiscip. Rev. Dev. Biol.* **3**, 1 (2014).
2. T. Orban, B. Jastrzebska, K. Palczewski, *Curr. Opin. Cell Biol.* **27**, 32 (2014).
3. Q. Wang *et al.*, *Science* **354**, 343 (2016).
4. I. Chaves, R. Pokorny, M. Byrdin, N. Hoang, T. Ritz, K. Brettel, L.-O. Essen, G. T. J. van der Horst, A. Batschauer, M. Ahmad, *Annu. Rev. Plant Biol.* **62**, 335 (2011).
5. G. Rosenfeldt, R. M. Viana, H. D. Mootz, A. G. von Arnim, A. Batschauer, *Mol. Plant* **1**, 4 (2008).
6. Y. Sang, Q. H. Li, V. Rubio, Y. C. Zhang, J. Mao, X. W. Deng, H. Q. Yang, *Plant Cell* **17**, 1569 (2005).
7. K. Zhang, B. Cui, *Trends Biotechnol.* **33**, 92 (2015).
8. H. Liu, X. Yu, K. Li, J. Klejnot, H. Yang, D. Lisiero, C. Lin, *Science* **322**, 1535 (2008).
9. U. Heintz, I. Schlichting, *eLife* **5**, e11860 (2016).
10. B. D. Zoltowski, L. B. Motta-Mena, K. H. Gardner, *Biochemistry* **52**, 6653 (2013).
11. E. Malzahn, S. Ciprianidis, K. Kaldi, T. Schafmeier, M. Brunner, *Cell* **142**, 762 (2010).
12. G. Rivera-Cancel, W. H. Ko, D. R. Tomchick, F. Correa, K. H. Gardner, *Proc. Natl. Acad. Sci. U.S.A.* **111**, 17839 (2014).
13. L. Rizzini, *J.-J. Favory, C. Cloix, D. Faggionato, A. O'Hara, E. Kaiserli, R. Baumeister, E. Schäfer, F. Nagy, G. I. Jenkins, R. Ulm*, *Science* **332**, 103 (2011).
14. M. Heijde, R. Ulm, *Proc. Natl. Acad. Sci. U.S.A.* **110**, 1113 (2013).

10.1126/science.aaj2077

GRAPHIC: C. BICKEL/*SCIENCE*

CHEMICAL PHYSICS

Molecular imaging at 1-femtosecond resolution

Loss of a hydrogen atom from acetylene is observed with electron diffraction

By **Chong-Yu Ruan**

We cannot yet watch all the steps of a gas-phase chemical reaction as it occurs, but we can come close. On page 308 of this issue, Wolter *et al.* (*1*) use an electron-imaging technique to capture the predissociated state of acetylene molecule just 9 fs after its ionization. On this time scale, the departing hydrogen atom and the remaining molecular fragment form an aloof complex in which the electronic coherence required to form bonds between the two is not yet fully lost. Imaging such transient states under different optical excitation conditions with high spatiotemporal resolution holds key information on selective photochemistry that may enable control of chemical reactions.

Normally, such diffraction experiments have been conducted with higher-energy electrons, as realized by Zewail and co-workers (*2*), or more recently with hard x-rays at free-electron laser facilities (*3*). However, the approach taken by Wolter *et al.* is more akin to diffraction of a photoelectron (*4*) that occurs entirely within the ionized molecule. The time resolution is incorporated by using the laser field as the clock to trigger and time both the chemical reaction and the photoelectron probe. By examining the far-field pattern of this self-diffraction over a specified energy window, an effective shutter speed (the time window over which the molecular scattering is recorded to form a snapshot) as low as 0.6 fs has been accomplished.

To see how this ultrahigh-speed imaging is possible, it is critical to understand the principles behind the conventional pump-probe experiments that ushered in the era of femtochemistry (*5*). In such a scheme, one short pulse (the "pump") is first used to initiate the chemical process and is followed by another short pulse (the "probe") interrogating its evolution. Making a molecular movie that encompasses the entire process requires the events to be reconstructed over different delays. However, the initiation must be abrupt, and good synchronization between the pump and probe pulses must be maintained within the desired time resolution, to

Department of Physics and Astronomy, Michigan State University, East Lansing, MI 48824, USA. Email: ruan@pa.msu.edu

Follow the fragments

Wolter *et al.*'s performed femtosecond imaging of an acetylene molecule ionizing it twice to form two fragments, HCC+ and H+ and breaks a C-H bond. This event is captured 9 fs after ionization by recording the far-field diffraction patterns produced by the emerging photoelectron waves with 0.6-fs time resolution.

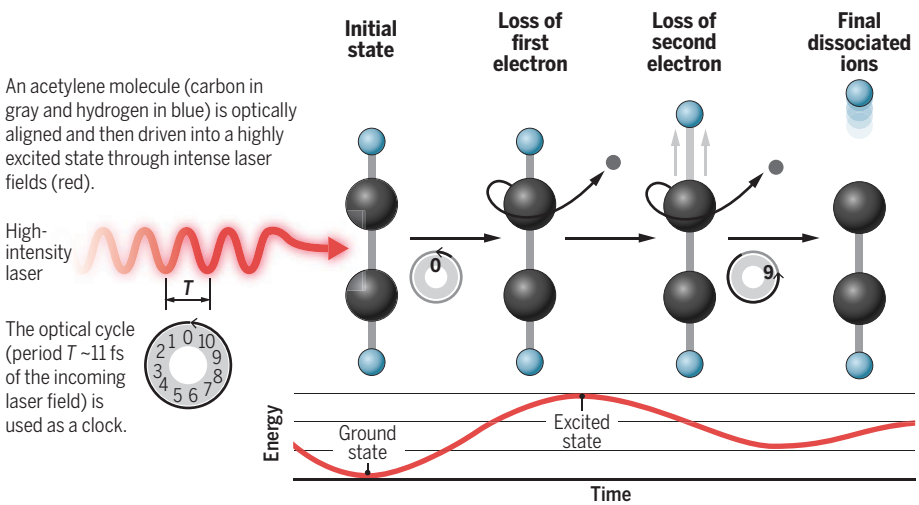

Downloaded from http://science.sciencemag.org/ on October 20, 2016

Published by AAAS

avoid jitter. Also, the physical processes under investigation must completely reset before each pump-probe cycle repeats in order to maintain a consistent causality between the reconstructed event sequences. For the time frames for molecular imaging reported by Wolter *et al.*, meeting these two conditions in conventional pump-probe studies is difficult because time jitter can easily set in at the 10-fs time scale. Also, image formation can be obscured because photoinduced molecular dissociation can proceed on multiple fragmentation pathways. These different outcomes normally can only be sampled statistically because tracking individual events is prohibited by the uncertainty principle.

In fact, the reported ~1-fs resolution is 10 times shorter than the optical cycles (~10 fs) of the mid-infrared pulses used to initiate the events. The ability to go beyond the traditional pulse-envelope–limited resolution and even sort out complex reactions is made possible by using "tagging" to isolate information. Taking their lead from coincidence schemes frequently used in the nuclear scattering experiments, Wolter *et al.* acquired the signals of both departing electrons and positive ions in their detection scheme to isolate specific excitation channels. Furthermore, given the precise timing of the optical field that also encodes a periodic time-energy (t-E) correlation on the departing electrons by way of high-field tunnel ionization, events can be delicately sorted out by analyzing the energy of the electrons arriving at the detectors.

From the knowledge of these correlations, post-collection analysis of events distributed over a 1-eV energy window (δE) yields a mere 0.2-fs shutter speed (δt), according to classical trajectory calculations of the tunnel-ionization process. This extremely high temporal resolution may at first glance appear to violate the uncertainty principle, that $\delta E \delta t > h$ (Planck's constant). In this case, it would impose an ~4-fs uncertainty in timing of the specific electron arriving at the detector if such a measurement were conducted.

However, the power of this resolution by correlation is not in sidestepping the uncertainty principle but in relying on the knowledge of the phase-space structure of the outgoing electrons. Although the overall phase space (t-E) of single electrons still extends over h, the exact correlation in t and E developed during the extraction process allows the identification of t by measuring E, to the precision of ~0.6 fs in this case. The penalty is taken in the sensitivity. The counting conducted in the specific energy-time window of the restricted electron phase space is scarce and relies on large statistical samplings, which fortunately is not prohibitive because of the nearly jitter-free nature of this imaging approach.

In spite of this exquisite demonstration of time resolution in molecular imaging, the technology in its current form is still limited in the dynamical range set by the optical cycle (~10 fs) and has a modest structure resolution. In terms of applications, these pros and cons seem to be orthogonal to the conventional ultrafast electron and x-ray diffraction technologies, which are more flexible in deployment but nonetheless face challenges in reaching the sub-10-fs time scale because of timing jitter.

However, the idea of improving resolution by tagging the events through correlation as demonstrated here is more general. In fact, the next generation of ultrafast electron-imaging technology development aims at circumventing the limitations posed by space-charge–driven expansion through actively controlling the beam dynamics (*6*). In one central aspect, the objective is to delicately shape the phase-space structure developed through the space-charge effect by designing new actively controlled optical components to reconstruct the electron pulse's phase space for optimizing performance (*7*). In another aspect, high-brightness beams created by controlling the photoemission can lead to highly compact electron pulses that can retrieve structural information in single shots, extending the pump-probe scheme to irreversible scenarios (*8*).

These strategies of dynamical phase-space control also provide means to encode information that can be used to improve the time resolution. For example, the phase-energy correlation developed through active fields used for pulse compression (*9*) can be exploited to resequence the events scrambled by timing jitter based on post-selection of pulse energy determined through diffraction itself. These various new developments, although operating in very different settings, share the key aspects of constraining and manipulating the phase space of the imaging electrons to transcend current resolution limits, presenting a bright future for electron-based ultrafast imaging technologies. ■

REFERENCES

1. B. Wolter *et al.*, *Science* **354**, 308 (2016).
2. R. Srinivasan, V. A. Lobastov, C. Y. Ruan, A. H. Zewail, *Helvetica Chim. Acta* **86**, 1761 (2003).
3. A. Barty, J. Küpper, H. N. Chapman, *Annu. Rev. Phys. Chem.* **64**, 415 (2013).
4. D. P. Woodruff, *J. Elec. Spec. Rel. Phen.* **126**, 55 (2002).
5. A. H. Zewail, *J. Phys. Chem. A* **104**, 5660 (2000).
6. E. Hall, S. Stemmer, H. Zheng, Y. Zhu, *Future of Electron Scattering and Diffraction. U.S. DOE Workshop Report* (2014); http://science.energy.gov/~/media/bes/pdf/reports/files/Future_of_Electron_Scattering.pdf.
7. J. Portman *et al.*, *Appl. Phys. Lett.* **103**, 253115 (2013).
8. G. Sciaini, R. J. D. Miller, *Rep. Prog. Phys.* **74**, 096101 (2011).
9. T. van Oudheusden *et al.*, *Phys. Rev. Lett.* **105**, 264801 (2010).

10.1126/science.aai8656

ANTIBODIES

Hitting Ebola, to the power of two

Bispecific antibodies are engineered to thwart ebola-virus entry into cells

By **Aran F. Labrijn**[1] *and* **Paul W. H. I. Parren**[1,2]

Passive immunotherapy with therapeutic antibodies is one of the most promising treatments for Ebola virus infection. Despite disappointing initial results using single monoclonal antibodies (mAbs) (*1*), successful post-exposure protection in nonhuman primate models of Ebola virus infection was eventually achieved using "designer polyclonals" that mixed individual mAbs (*2*). The efficacy of an optimized three-mAb cocktail (ZMapp) in protecting nonhuman primates (*3*) was the basis of its compassionate use and clinical evaluation during the 2014 to 2015 West African Ebola virus outbreaks. The limited protective breadth of available antibodies against specific ebolavirus species, however, raises concerns with respect to a general preparedness for filovirus outbreaks (*4*). On page 350 of this issue, Wec *et al.* (*5*) describe exploiting the powerful nature of bispecific antibodies (bsAbs)—the ability to recognize two different proteins or epitopes with a single antibody—to block entry of multiple ebolavirus species into cells. This may lead to the development of antiviral immunotherapy with cross-filovirus activity.

> ***"...bsAb technology may... provide exciting therapeutic opportunities..."***

Ebola virus, like other filoviruses, is unusual in that it bears a glycoprotein that exposes its receptor binding site only after entry and processing in an intracellular vesicle (endosome). Productive infection requires the virus to escape from the endosome by

[1]*Genmab, 3584 CM Utrecht, Netherlands.* [2]*Department of Immunohematology and Blood Transfusion, Leiden University Medical Center, 2333 ZA Leiden, Netherlands. Email: p.parren@genmab.com*

Downloaded from http://science.sciencemag.org/ on October 20, 2016

Published by AAAS

interacting with its receptor, an endosomal transporter protein (*6, 7*). Both the conserved nature of the viral glycoprotein's binding site for the host cell receptor and its critical role in filovirus infection would make it an attractive target for protective antibodies, were it not for the inaccessibility of the binding site to antibodies. Therefore, Wec *et al.* generated bsAbs that bear both the binding domain of a mAb specific for a conserved and exposed epitope present on all known ebolavirus glycoproteins, and the binding domain of an antibody that interrupts interaction between the cleaved viral glycoprotein and the endosomal transporter protein Niemann-Pick C1 (NPC1). Hence, the bsAb binds to the virus extracellularly and holds on while it enters the endosome. Once in the endosome, the second domain of the bsAb binds to the glycoprotein epitope that is revealed upon cleavage, and blocks viral entry into the host cell (see the figure). This "Trojan horse" approach could thus be used to outsmart the formidable fortifications of this lethal virus and create a single agent with an unprecedented effectiveness. Wec *et al.* show that the bsAb neutralized all known ebolaviruses in vitro and conferred postexposure protection against lethal challenge with multiple viruses in mouse models. The power of the bsAb approach is highlighted by the fact that simple mixtures of the parent antibodies were ineffective.

Wec *et al.* provide a dramatic example of the improvement that can be achieved by physically connecting an appropriate combination of antibody binding specificities. Indeed, therapeutic applications that are unique to bsAbs involve those in which the combination of two antibody specificities generates a new functionality not present in the parent antibodies. Because of the dependence on the two binding domains for activity, such antibodies have been termed "obligatory bsAbs" (*8*), a few examples of which now exist. In oncology, obligatory bsAbs are being used to redirect effector cells for the killing of tumor cells. Most of these bsAbs, including the marketed therapeutic bsAb blinatumomab, combine an agonistic antibody binding domain that recognizes a T cell co-receptor (CD3), with a binding domain that recognizes a tumor-associated antigen; thus, the T cells and tumor cell are brought together. In addition, the redirection of natural killer lymphocytes (*9*) to target tumor cells is also being pursued. Emicizumab, a bsAb that binds the blood clotting factors X and IXa, has been designed to replace the activity of factor VIII in patients with hemophilia A (*10*) and is currently in phase 3 clinical trials. In another application, bsAbs that can selectively activate or inhibit pairs of targets on a single cell are being developed. Examples include a bsAb directed against fibroblast growth factor receptor 1 (FGFR1) and βKlotho (KLB) to treat diabetes (thus, activating FGFR1 only in the presence of KLB) (*11*) and a bsAb that targets the epidermal growth factor receptor (EGFR) and the hepatocyte growth factor receptor (cMET) for cancer treatment (blocking both receptors to prevent treatment escape) (*12*). Also, the "hijacking" of transcytosis pathways (which transport macromolecules, in vesicles, through a cell barrier) would give bsAbs access to immunoprivileged sites such as the human brain (*13*), and represents another attractive application of obligatory bsAbs.

The design of new functionalities in a bsAb is not straightforward and may often combine knowledge-based and empirical approaches. As shown by Wec *et al.*, insights into the molecular mechanisms of filovirus infection, in combination with the availability of mAbs against the relevant epitopes, were critical in selecting the binding domains of the bsAb. As the biological activity of both arms of the bsAb occurs sequentially and does not require simultaneous binding, the relative epitope topology is likely to play a subordinate role in such applications and can thus be exploited by bsAb formats of different design (*8*). By contrast, for applications where simultaneous binding is a prerequisite, such as for selective agonists like emicizumab, the selection of binding arms of a bsAb is much more dependent on empirical approaches in which identifying just the right combination of binding specificities may require the screening of thousands of binding pairs. In addition, architecture of the selected bsAb format and positioning of the binding arms may impact the antibody's activity.

After decades of optimization, bsAb technology may finally start to deliver on its promise in which obligatory bsAbs with new functionalities provide exciting therapeutic opportunities, the design of which may only be limited by our imagination. ■

The bispecific's powers

Combining binding specificities into one antibody can lead to functionalities not present in the individual antibodies. An example of a bispecific antibody that blocks Ebola virus infection is shown.

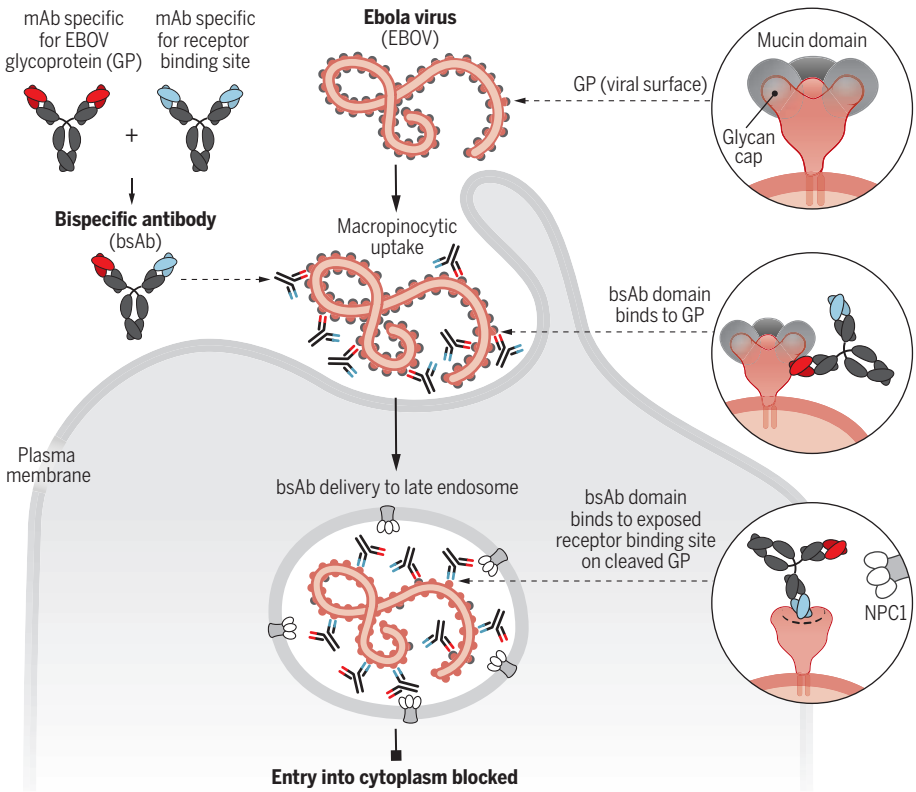

GRAPHIC: K. SUTLIFF/*SCIENCE*

REFERENCES AND NOTES

1. W. B. Oswald *et al.*, *PLOS Pathog.* **3**, e9 (2007).
2. L. Zeitlin *et al.*, *Curr. Opin. Virol.* **17**, 45 (2016).
3. X. Qiu *et al.*, *Nature* **514**, 47 (2014).
4. PREVAIL II Writing Group, Multi-National PREVAIL II Study Team, *N. Engl. J. Med.* **375**, 1448 (2016).
5. A. Z. Wec *et al.*, *Science* **354**, 350 (2016).
6. J. E. Carette *et al.*, *Nature* **477**, 340 (2011).
7. E. H. Miller *et al.*, *EMBO J.* **31**, 1947 (2012).
8. C. Spiess, Q. Zhai, P. J. Carter, *Mol. Immunol.* **67**, 95 (2015).
9. J. Bruenke *et al.*, *Br. J. Haematol.* **130**, 218 (2005).
10. M. Shima *et al.*, *N. Engl. J. Med.* **374**, 2044 (2016).
11. G. Kolumam *et al.*, *EBioMedicine* **2**, 730 (2015).
12. S. L. Moores *et al.*, *Cancer Res.* **76**, 3942 (2016).
13. Y. J. Yu *et al.*, *Sci. Transl. Med.* **3**, 84ra44 (2011).

ACKNOWLEDGMENTS

A.F.L. and P.W.H.I.P. are employees of Genmab, which develops therapeutic bispecific antibody products and technologies.

10.1126/science.aaj2036

Downloaded from http://science.sciencemag.org/ on October 20, 2016

Published by AAAS

BEHAVIOR

Why I know but don't believe

Individuals hold interdependent beliefs that affect whether or not they accept scientific findings

By **Carter T. Butts**

Despite extensive efforts at public science education, polling over the past 30 years has consistently shown that about 40 to 45% of Americans believe that humans were supernaturally created in the past 10,000 years (*1*). A natural interpretation of this finding is that U.S. science education is failing to reach nearly half of the population, and that widespread belief in recent human origins reflects basic scientific illiteracy. However, the reality is more complex (*2*): Many of those who reject evolutionary theory are aware of the scientific consensus on the subject, and such rejection is not always associated with low scientific literacy. Similar results have been found for beliefs regarding anthropogenic climate change (*3*). On page 321 of this issue, Friedkin *et al.* (*4*) provide a key step toward understanding this phenomenon by introducing a simple family of models for social influence among individuals with multiple, interdependent beliefs.

Current models for interpersonal influence are many and varied, reflecting differences in the purposes and time scales for which they are used. Of central importance is the time scale on which influence takes place, relative to the dynamics of the underlying network through which this influence is transmitted. Where these processes operate on similar time scales, social selection processes—such as whether people select partners who are similar to or different from them (*5*)—can interact with influence processes, requiring both to be modeled simultaneously (*6*).

Where network dynamics are slow compared to the influence process, the latter can be approximated by the evolution of individual states on a fixed network. Most social influence models operate in this regime (*7*–*10*), as does Friedkin *et al.*'s model (*4*). Both the latter (*4*) and the Friedkin-Johnsen model that it extends (*10*) can be used to model attitudes as well as beliefs in empirical propositions. They thus provide a flexible framework for modeling influence processes that evolve quickly relative to the dynamics of the underlying network.

Current models of social influence incorporate fairly detailed representations of social structure, but cognitive structure has been given short shrift. There are several competing frameworks for representing belief structures in the psychological literature (*11*–*13*), all of which support the notion of belief interdependence. Yet, most models of social influence consider only a single belief or treat multiple beliefs as cognitively independent. This limitation makes it difficult to account for the ways that belief dynamics can shape persuadability.

For instance, an individual who believes that human civilization is too insignificant to alter the global environment will tend to resist evidence for anthropogenic changes in atmospheric carbon dioxide concentration, because the former belief undermines the latter. If this same person is later persuaded (perhaps in an entirely different context) that human civilization can alter the global environment, he or she may become more likely to accept the notion that human activity has substantially increased atmospheric carbon dioxide levels. Similarly, belief structures can in some cases amplify the impact of social influence by leading persons persuaded to accept one proposition to immediately accept other propositions that follow from it.

The Friedkin *et al.* model addresses this problem by incorporating an "intrapersonal" influence mechanism, in which acceptance of one proposition influences the acceptance of others (see the figure). Connections among propositions are represented as a weighted network, providing a flexible means of specifying interdependent beliefs. The simplicity and extensibility of Friedkin *et al.*'s model make it a natural starting point for exploring further questions regarding belief structures and social influence. Perhaps foremost among these is the question of how influence on beliefs regarding the trustworthiness of evidence (evidentiary beliefs) affects social outcomes. Simulation studies have shown (*9*) that individuals' beliefs regarding the reliability or veracity of other individuals' testimony can radically alter both the probability of obtaining group consensus and the nature of the consensus view where obtained. Modeling what happens when such beliefs are themselves subject to social influence may provide a means of predicting the emergence of "epistemically closed" communities, whose extreme skepticism toward outside sources of evidence renders them vulnerable to persistent errors that are difficult to correct.

Individuals' beliefs can also affect the extent to which incoming information—whether from others' testimony or environmental sources—is attended to or perceived as relevant. For example, in the 1954 collective delusion known as the "Seattle windshield pitting epidemic" (*14*), persons who were alerted to the possibility of tiny defects in their windshields began seeking them. They then took the inevitable discovery of such flaws as confirmation

How beliefs interdepend

Friedkin *et al.*'s model shows that interdependence of different beliefs can cause groups to become strongly polarized despite being exposed to what should be moderating influences. Similar mechanisms may explain why some groups reject scientific findings, despite being aware of them.

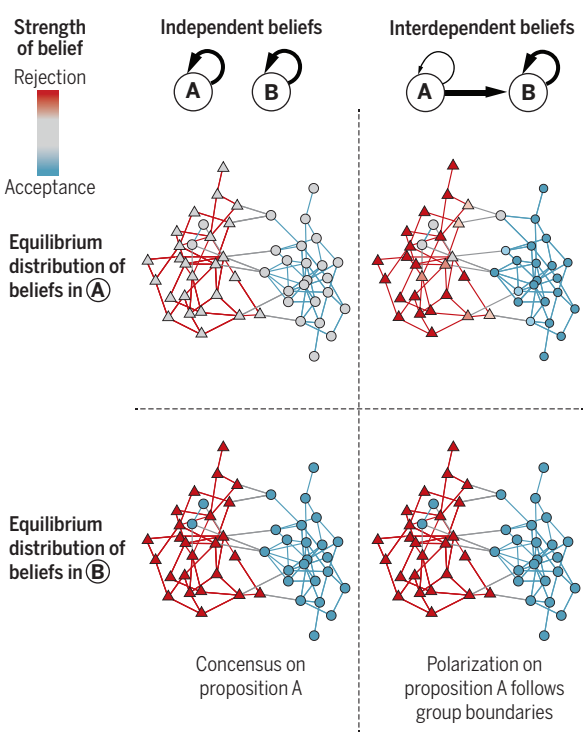

GRAPHIC: V. ALTOUNIAN/*SCIENCE*

Departments of Sociology, Statistics, and EECS and Institute for Mathematical Behavioral Sciences, University of California, Irvine, CA 92697, USA. Email: buttsc@uci.edu

Downloaded from http://science.sciencemag.org/ on October 20, 2016

Published by AAAS

of the theory that a novel and potentially hazardous mechanism was pitting windshields in the area. They communicated their discoveries to others, who conducted their own inspections, became convinced themselves, and continued to spread the belief to yet more persons. Further extensions to the current generation of models could help to identify the conditions that allow such phenomena to emerge and to explore how they might be inhibited.

An even more basic challenge is to model the effect of beliefs on information exchange itself. In the experimental settings in which models of the Friedkin-Johnsen type have been most frequently applied, it is reasonable to assume continuous communication surrounding the focal issue. In natural settings, however, communication is affected by many structural, contextual, and cultural factors, all of which may affect the potential for one individual to express his or her beliefs to another. Individuals' beliefs can also play a role in shaping communicative behavior, in some cases giving rise to systematic biases at the group level. For instance, Kitts (*15*) found that most members of ostensibly vegetarian communes did not actually consume a vegetarian diet, yet overwhelmingly believed their behavior to be exceptional.

Such examples of pluralistic ignorance arise when group members falsely believe themselves to be unusual in violating a group norm, and thus conceal their behavior and attitudes from others. This concealment then reinforces the false belief. Incorporating belief-dependent communication into the Friedkin *et al.* model would allow for treatment of this and other classes of emergent phenomena. ■

REFERENCES

1. Gallup, *Evolution, creationism, intelligent design*, Online Resource (2016); www.gallup.com/poll/21814/Evolution-Creationism-Intelligent-Design.aspx.
2. D. M. Kahan, *Polit. Psychol.* **36**, 1 (2015).
3. M. C. Nisbet, E. Markowitz, Americans' attitudes about science and technology: The social context for public communication, Commissioned Review (2016).
4. N. E. Friedkin, A. V. Proskurnikov, R. Tempo, S. E. Parsegov, *Science* **354**, 321 (2016).
5. J. M. McPherson, L. Smith-Lovin, J. M. Cook, *Annu. Rev. Sociol.* **27**, 415 (2001).
6. C. Steglich, T. A. B. Snijders, M. Pearson, *Sociol. Methodol.* **40**, 329 (2010).
7. D. Centola, M. Macy, *Am. J. Sociol.* **113**, 702 (2007).
8. J. A. Holyst, K. Kacperski, F. Schweitzer, *Annu. Rev. Comput. Phys.* **9**, 253 (2001).
9. C. T. Butts, *Comput. Math. Organ. Theory* **4**, 373 (1998).
10. N. E. Friedkin, E. C. Johnsen, *J. Math. Sociol.* **15**, 193 (1990).
11. N. Cruz, J. Baratgin, M. Oaksford, D. E. Over, *Front. Psychol.* **6**, 192 (2015).
12. B. Geurts, *Cognition* **86**, 223 (2003).
13. P. N. Johnson-Laird, R. M. J. Byrne, *Psychol. Rev.* **109**, 646 (2002).
14. N. Z. Medalia, O. N. Larsen, *Am. Sociol. Rev.* **23**, 180 (1958).
15. J. A. Kitts, *Soc. Psychol. Q.* **66**, 222 (2003).

10.1126/science.aaj1817

OCEANS

A plankton bloom shifts as the ocean warms

Long-term data show how a widespread phytoplankton group responds to temperature changes

By **Alexandra Z. Worden**[1,2] *and* **Susanne Wilken**[1]

Recent advances in sequencing technology have highlighted the extreme diversity of marine microbes and provided insights into their evolution (*1*–*3*). It remains unclear, however, how ocean microbial communities are responding to ongoing climate change. This is because pinpointing change with statistical rigor requires long-term studies that sample the same location or water mass repeatedly. On page 326 of this issue, Hunter-Cevera *et al.* (*4*) present a highly resolved long-term study of a widespread cyanobacterial phytoplankton group, *Synechococcus*. They show that the timing of the annual spring *Synechococcus* bloom has shifted in association with ocean warming.

About half of global primary production (photosynthetic CO_2 fixation) is performed by marine cyanobacteria and eukaryotic phytoplankton. Where marine time-series data are available, they have provided key insights into phytoplankton communities and overall ecosystem variability (*5*, *6*). These long-term studies are expensive and require a deep commitment to coherent methodologies and sampling. However, they also serve as the basis for hypotheses on how the phytoplankton populations that are essential for maintaining Earth's biosphere will respond to climate change (*1*, *7*).

The results of Hunter-Cevera *et al.* come from a concerted instrument development effort aimed at persistent presence in the environment. The study site, off the New England coast near Cape Cod, USA, is not one of the more noted climate-sensitive ocean regions, such as the Arctic. Rather, it is where the researchers could plug their in situ flow cytometer into one of the few existing cabled moorings, with electrical power and Internet lines running across the seafloor from shore. The main approach to marine flow cytometry has been to collect discrete water samples, preserve them, and analyze them in the laboratory. In contrast, the specially developed instrument at the Cape Cod site operates for months while submerged in the ocean. Challenges included continuous seawater flow-through, biofouling, winter weather, and analysis of data from vast numbers of individual cells for estimating phytoplankton division rates. The achievement of acquiring more than a decade of in situ, science-quality data in this way should not be underestimated.

A unique strength of the study is the robust estimation of *Synechococcus* cell division rates in nature. The short generation times of planktonic organisms necessitate high-resolution data sets (in this case, hourly measurements). Such data have been attained by just one other research group (*8*), through use of a shipboard continuous-flow cytometer. Hunter-Cevera *et al.* show that *Synechococcus* division rates increased throughout springtime and that loss rates tracked cell-division rates through most of the year. Ultimately, a slight imbalance between accelerated spring growth and the loss rate led to the net accumulation of *Synechococcus* cells that resulted in the bloom.

A specially developed flow-through cytometer has allowed collection of in situ data at the Cape Cod site for over a decade.

PHOTO: SEAN P. WHALEN/WOODS HOLE OCEANOGRAPHIC INSTITUTION

Most traditional measurements of phytoplankton cannot resolve closely correlated growth and loss rates, knowledge of which is needed to disentangle the intricacies of microbial dynamics that control bloom formation. The drivers behind bloom formation

[1]*Monterey Bay Aquarium Research Institute, Moss Landing, CA 95039, USA.* [2]*Integrated Microbial Biodiversity Program, Canadian Institute for Advanced Research, Toronto, Ontario M5G 1Z8, Canada. Email: azworden@mbari.org*

Downloaded from http://science.sciencemag.org/ on October 20, 2016

Published by AAAS

Phytoplankton blooms and ocean warming

Ocean sampling procedures are typically too short-term to capture the drivers behind phytoplankton blooms. Hunter-Cevera *et al*. overcame this limitation by using continuous data from a submerged flow cytometer. They were able to quantify changes in cell division rates of a phytoplankton group and connect a shift in bloom timing to increased water temperature.

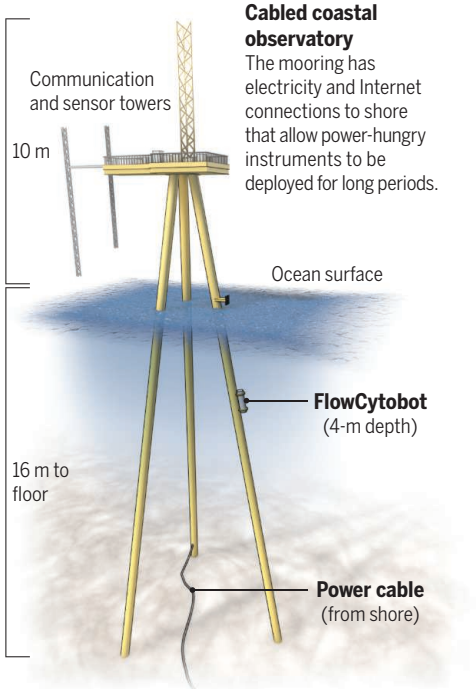

Cabled coastal observatory
The mooring has electricity and Internet connections to shore that allow power-hungry instruments to be deployed for long periods.

Dynamics of the phytoplankton bloom
Above 5°C, *Synechococcus* division rates (white arrows) increase and a temporary imbalance with loss rates (gray arrows) results in the bloom.

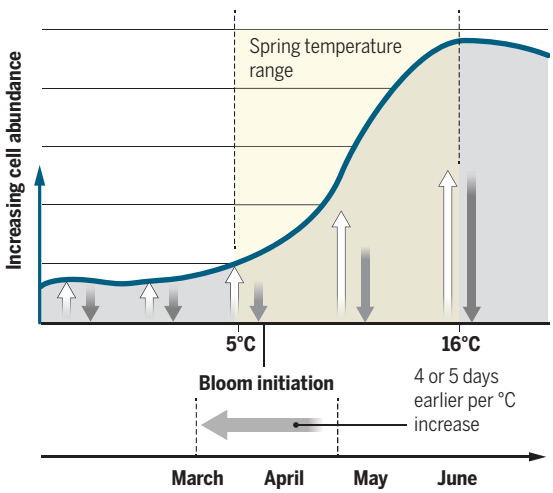

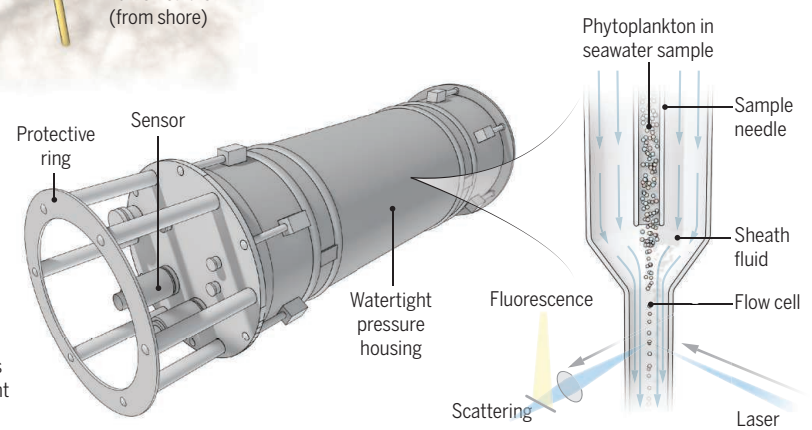

FlowCytobot
This in situ flow cytometer has the complexity of a traditional cytometer modified to fit inside a deployable pressure housing. In the clinical setting, cytometers count human blood cells; here, scatter and fluorescence properties of individual cells are used to quantify different phytoplankton groups.

may often involve such an imbalance, but whether it is caused by higher division rates (as observed here), and hence higher primary production, or a reduction in losses acting on slower-growing phytoplankton populations, has major implications for bloom productivity and carbon cycling.

Hunter-Cevera *et al*.'s study also reveals a temperature-induced shift in the timing of the *Synechococcus* spring bloom that is linked to ocean warming. The length of a time series needed to develop ecological understanding of a system and to relate shifts to climate change depends on the ocean region. Hunter-Cevera benefitted from the availability of a 100-year local water temperature record (*9*), which established a rise in temperature associated with climate change. In ocean regions with smaller seasonal transitions, variation is often more muted, and time-series data of less than 20 years do not typically resolve recurrent trends (*10*). Long-term sampling studies at specific geographical locations, like the Hawaii Ocean Time-series (HOT) and the Bermuda Atlantic Time-series Study (BATS), have provided comprehensive views of open-ocean seasonality (*4*, *5*). These studies form a baseline against which future trends can be compared. Still, detection of climate change effects on open-ocean productivity are thought to require more than three to four decades of data to separate these trends from natural ecosystem variability (*5*).

Hunter-Cevera *et al*. show that temperature (and possibly co-associated environmental factors) controls *Synechococcus* division rates and bloom timing, but the loss processes remain to be identified. If biological, as suggested by the authors, the specific cause of mortality—such as loss from viral lysis or predation—dictates the fate of the carbon contained in the phytoplankton biomass. The carbon can be released back into the atmosphere, be recycled in the microbial loop, move through marine food webs to higher trophic levels that support fisheries, and/or be exported to the deep sea (*1*).

The shift in timing of the bloom to earlier in spring could also reflect changes in the dominant *Synechococcus* clade(s). *Synechococcus* has considerable genetic diversity that cannot be discerned by flow cytometry but shapes the biology of different clades, including the nutrients they use (*11*). This in turn could affect forces of mortality acting on resident populations, especially given that viruses are highly specific to individual hosts (*12*) and predatory protists are thought to have prey specificities and strong temperature-related controls acting on them (*1*).

To predict the coupling of phytoplankton growth and mortality in future oceans, we thus need to understand the environmental factors and organismal interactions that underlie the observed correlations and imbalances. Does the agent of mortality respond directly to phytoplankton physiology as represented by cell division rates? Or are specific phytoplankton, their predators, and even infecting viruses, possibly controlled by the same or co-related environmental factors? Answering these questions is essential for gaining a mechanistic understanding of ecosystem change in the ocean and will require integration of future research efforts with time-series studies. ■

REFERENCES

1. A. Z. Worden *et al*., *Science* **347**, 1257594 (2015).
2. P. Bork *et al*., *Science* **348**, 873 (2015).
3. N. Kashtan *et al*., *Science* **344**, 416 (2014).
4. K. R. Hunter-Cevera *et al*., *Science* **354**, 326 (2016).
5. S. J. Giovannoni, K. L. Vergin, *Science* **335**, 671 (2012).
6. D. M. Karl, M. J. Church, *Nat. Rev. Microbiol.* **12**, 699 (2014).
7. M. J. Behrenfeld *et al*., *Nature* **444**, 752 (2006).
8. F. Ribalet *et al*., *Proc. Natl. Acad. Sci. U.S.A.* **112**, 8008 (2015).
9. S. W. Nixon, S. Granger, M. Buckley, B. K. Lamont, A. Rowell, *Estuaries* **27**, 397 (2004).
10. D. L. Rudnick, R. E. Davis, *Deep-Sea Res. I* **50**, 691 (2003).
11. D. J. Scanlan *et al*., *Microbiol. Mol. Biol. Rev.* **73**, 249 (2009).
12. M. Breitbart, *Ann. Rev. Mar. Sci.* **4**, 425 (2012).

10.1126/science.aaj1751

GRAPHIC: C. BICKEL/*SCIENCE*

Downloaded from http://science.sciencemag.org/ on October 20, 2016

Published by AAAS

EVOLUTION

Predicting the basis of convergent evolution

Convergent adaptive traits do not always arise from the same genetic changes

By **Jamie T. Bridgham**

Repeated evolution of similar traits in organisms facing the same ecological challenges has long captured the interest of evolutionary biologists (*1*–*4*). Naturally occurring examples of "convergent evolution" offer new opportunities to ask about predictability in evolution. Do complex genomes mean that there are endless possibilities for adapting to an ecological challenge? Or must evolution target the same genes, or even the same amino acids in the same proteins, in order to increase the fitness and therefore survival of different species facing similar challenges? Natarajan *et al.* (*5*), on page 336 of this issue, provide an example of an integrated approach to answer these questions. By using a combination of genetic data with experimental tests, they show that evolution of a new protein function in response to low-oxygen, high-altitude conditions can occur through different genetic mechanisms across a wide diversity of avian species living at high and low elevations.

Hemoglobin proteins found in different vertebrate species living either at low or high altitudes provide classic examples of convergent protein evolution. Natarajan *et al.* sequenced, expressed, and measured oxygen affinity for hemoglobins isolated from 56 species of birds clustered into related low- and high-altitude–species pairs. They found convergent evolution of high-oxygen affinity in proteins from high-elevation species. They then determined the genetic basis for this functional shift in hemoglobin oxygen affinity. Evolution of new protein functions is thought to be under biophysical constraint, limiting genetic changes to certain portions of proteins, or to specific amino acid substitutions (*6*, *7*), potentially making evolution largely predictable. On the other hand, evolutionary trajectories have been shown to be historically contingent, with possible evolutionary paths being dependent on the ancestral starting point (*8*, *9*), resulting in relatively unpredictable, distinct genetic changes in different lineages subjected to similar evolutionary pressures.

Were there common genetic changes in the hemoglobin from high-elevation–avian species? Amino acids were identified that diverged between low- and high-elevation–species pairs and were associated only with high-altitude environments. Although many amino acid differences were found between species pairs, only four were replicated in different lineages. Two of these positions are known to play key roles in protein function, yet these changes occurred in only two or three species pairs. The single most common substitution was found primarily in hummingbird species pairs but was also seen in one species of flowerpiercers. Was this change responsible for the convergent evolution of high-oxygen affinity? Natarajan *et al.* introduced the substitution from high-altitude–adapted species into a reconstructed ancestral hummingbird hemoglobin protein and found an increase in oxygen affinity. However, when they introduced the same substitution into more ancient avian hemoglobins, there was no change in protein function. Additional genetic differences prevented this substitution from having the same functional consequences in more distant ancestral backgrounds. They concluded that historical contingency constrained the potential evolutionary pathways for hemoglobin adaptation to high-altitude conditions.

Convergent evolution of high-oxygen affinity in hemoglobin from high-altitude–dwelling bird species (including some hummingbirds, shown) occurred through different amino acid substitutions. Historical contingency limits predictability.

Furthermore, a much wider taxonomic sampling, including perching birds and waterfowl, found many distinct and no common genetic substitutions in high-oxygen–affinity hemoglobins among the other high-altitude–adapted birds. By sampling many pairs of widely divergent avian lineages, Natarajan *et al.* discovered that although most high-altitude–adapted birds have hemoglobin with higher-oxygen affinity, this convergent evolution in protein function resulted from different genetic changes.

Evolutionary biologists have identified cases of predictable convergent evolution involving adaptations in single proteins (*6*, *7*), as well as cases in which evolutionary paths were less predictable because of historical differences in genetic backgrounds (*9*). The careful examination of convergent hemoglobin evolution across an extensive taxonomic scale by Natarajan *et al.* provides an elegant example of how the predictability of genetic evolution may change depending on the scale of the investigation.

They found contrasting results concerning genetic convergence depending on how closely related the species were. Among many hummingbirds, a single substitution was associated with high-altitude adaptation, and that amino acid substitution was sufficient to change hemoglobin oxygen affinity. However, no genetic convergence was seen between more distantly related high-altitude–adapted birds.

The genetic basis of convergent evolution may only be predictable when looking at the appropriate scale. Smaller-scale convergence between closely related organisms or specific proteins may occur through predictable genetic changes. Larger-scale convergence across taxonomic orders may only be predictable at larger genetic scales, targeting whole proteins or functional complexes (*10*, *11*). ■

Institute of Ecology and Evolution, 5289 University of Oregon, Eugene, OR 97403-5289, USA. Email: jamieb@uoregon.edu

REFERENCES

1. D. L. Stern, V. Orgogozo, *Science* **323**, 746 (2009).
2. J. B. Losos, *Evolution* **65**, 1827 (2011).
3. N. Gompel, B. Prud'homme, *Dev. Biol.* **332**, 36 (2009).
4. J. F. Storz, *Nat. Rev. Genet.* **17**, 239 (2016).
5. C. Natarajan, F. G. Hoffmann, R. E. Weber, C. C. Witt, J. F. Storz, *Science* **354**, 336 (2016).
6. D. L. Stern, *Nat. Rev. Genet.* **14**, 751 (2013).
7. C. R. Feldman, E. D. Brodie Jr., E. D. Brodie III, M. E. Pfrender, *Proc. Natl. Acad. Sci. U.S.A.* **109**, 4556 (2012).
8. S. Kryazhimskiy, D. P. Rice, E. R. Jerison, M. M. Desai, *Science* **344**, 1519 (2014).
9. L. I. Gong, M. A. Suchard, J. D. Bloom, *eLife* **2**, e00631 (2013).
10. J. R. Gallant *et al.*, *Science* **344**, 1522 (2014).
11. O. Tenaillon *et al.*, *Science* **335**, 457 (2012).

10.1126/science.aai7394

PHOTO: MALCOLM SCHUYL/ALAMY STOCK PHOTO

Downloaded from http://science.sciencemag.org/ on October 20, 2016

Published by AAAS

POLICY FORUM

CLIMATE POLICY

Identifying the policy space for climate loss and damage

Climate risk analysis must play a fundamental role

By **Reinhard Mechler**[1,2] *and* **Thomas Schinko**[1,3]

Currently planned greenhouse gas mitigation efforts would not prevent climate warming from going beyond 2°C as aspired to in the 2015 Paris Agreement (*1*), adding to climate-related impacts already under way (*2*). Although climate adaptation has been strengthened in the Paris Agreement, climate-related risks may exceed adaptation possibilities of communities and countries. To this effect, an important decision in the Paris Agreement was the endorsement of the Warsaw International Mechanism (WIM) for Loss and Damage (L&D) (*3*). This established L&D as a distinct pillar of climate negotiations, yet with an unclearly defined remit. With a policy framework yet to emerge, the 22nd Conference of the Parties of the United Nations Framework Convention on Climate Change (UNFCC) in November in Marrakesh will review the structure, mandate, and effectiveness of the WIM, first institutionalized in 2013. Risk science can provide a rationale and delineate a policy space for L&D, composed of curative measures for unavoided and unavoidable impacts, and transformative measures for avoiding and managing increasingly intolerable risks.

Climate risks considered by the WIM are associated with extreme events—flooding, droughts, heat waves, and cyclones—and slow-onset impacts, including sea level rise and melting glaciers. Lacking official definition, losses have been associated with irreversibility—e.g., fatalities from climate events or households stuck in disaster-induced poverty traps—whereas damages refer to impacts that can be alleviated. A useful distinction has been made between avoidable, unavoided, and unavoidable L&D (*4*).

[1]*International Institute for Applied Systems Analysis, Schlossplatz 1, 2361 Laxenburg, Austria.* [2]*Vienna University of Economics and Business, 1020 Vienna, Austria.* [3]*Wegener Center for Climate and Global Change, University of Graz, 8010 Graz, Austria. Email: mechler@iiasa.ac.at*

Discussion of the WIM has been contested (*5*) and wide-ranging (*6*). The Alliance of Small Island States (AOSIS), whose members face substantial climate-related stress, initiated the debate more than two decades ago, proposing that parties with historically high emissions take responsibility via some sort of compensation instrument. With endorsement from other vulnerable developing countries, AOSIS has been arguing for an international mechanism basically made up of two components: support for risk management, including insurance efforts, and a rehabilitation or compensatory component addressing increasingly negative impacts (*7*). Many developed countries concur in principle on the need to help those suffering from climate change impacts but have been unwilling to accept notions of liability and have stressed the need to institutionalize incentives for tackling risks (*8*), as, for example, suggested by the 2015 Sendai Framework for Disaster Risk Reduction (DRR) (*9*). These parties suggested covering the matter under adaptation, but the decision to have a stand-alone article of the Paris Agreement (Article 8) refer to the WIM came about only after developing countries insisted that L&D is distinct. Vulnerable countries celebrated the inclusion of the WIM in the agreement, whereas developed countries managed to include assurance that the WIM does not provide a basis for liability and compensation, which remain important background issues informing any potential implications of the WIM.

A CLIMATE-RISK SCIENCE PERSPECTIVE

Assessments of climate change impacts have shifted in focus from academic to more operational, including engagement of multiple stakeholders via novel risk analytical methods (*10*, *11*). Work had originally focused on tracing incremental impacts induced by global warming in order to identify "dangerous" anthropogenic interference for climate mitigation and adaptation purposes (IPCC's five reasons for concern) (*12*). An emergent perspective assesses risk as shaped by both climate variability and climate change and seeks to support climate risk management (CRM) at different scales (*13*). CRM aligns DRR, focused on sudden-onset hydrometeorological and geophysical events, with climate change adaptation (CCA), tackling slow-onset and sudden-onset climate-related impacts. CRM's overall remit is to anticipate, avoid, prevent, and finance risks as well as absorb remaining impacts.

CRM includes concern for CCA-DRR gaps—the difference between what we want or need and what we actually have and implement in terms of funds, technology, and knowledge for risk management (*14*). Socially desirable levels of CRM will generally be less stringent than technically and physically feasible because of a number of negotiated trade-offs; e.g., costly flood protection, even in well-protected countries, ends at 50- to 100-year flood recurrence levels. Considerations of risk preference (*15*) have entered the debate (and IPCC) to provide classifications of risk as acceptable (no additional action necessary), tolerable (action required considering costs and other constraints), and intolerable (action required irrespective of constraints) (*16*).

Risk and risk tolerance are socially constructed. Although the IPCC, with medium and high levels of confidence, has identified many regions as facing substantial stress from climate change–exacerbated risks, what constitutes acceptable, tolerable, and intol-

PHOTO: JEREMY SUTTON-HIBBERT/ALAMY STOCK PHOTO

Downloaded from http://science.sciencemag.org/ on October 20, 2016

Published by AAAS

One of the 33 atolls in the Republic of Kiribati, a small island state in the central Pacific, affected by an especially high tide.

erable is strongly determined by social, cultural, and economic determinants and often requires joint subjective and expert deliberation before being submitted to allocating responsibilities. Risk analysis has developed analytical procedures for negotiating and segregating risk according to risk preference ("risk layering") that have been used in the insurance industry and are being applied to climate risk issues to help allocate risks to multiple actors at various scales (*17*).

An important dimension requiring more attention is climate justice, which scientifically is linked with attributing impacts to anthropogenic climate change, identifying harm-doing and burden-sharing of benefits and costs. Burden-sharing has been necessary because many vulnerable countries are in need of international support for tackling adaptation gaps. The international community has shared such obligations under principles of distributive justice (*18*) not requiring climate attribution of risks for generating international support, such as via the Global Facility for Disaster Risk Reduction. There is a need to consider compensatory justice because of the unequal distribution of historical and current emissions, as well as potential irreversible loss (*19*). The IPCC has attributed trends in slow-onset climate change and some climate extremes to anthropogenic greenhouse gas emissions—also pointing out that risk causation is often multifactorial, with climate change and socioeconomic change as key risk drivers (*10*). Yet, although climate science has been making progress in climate attribution, linking anthropogenic emissions to impacts and to risks to people, property, and ecosystems remains complex, particularly for sudden-onset events (*20*). Both justice principles can be combined, yet balance needs attention. Many developing countries are worried that emphasis could be put on national responsibility for managing risks, rather than international law considerations associated with the "polluter pays" principle proportional to emissions contributions (*21*).

THE L&D RISK AND POLICY SPACE

Aligning emerging analytical insight, we build and extend a schematic scenario assessment of risks and CRM conducted by IPCC's 5th assessment report at regional scale and for groups of countries for slow and sudden-onset events (see the figure). The exemplary visualization applies the CRM framework to small island states faced with sea level rise and high–water level events. The IPCC considers today's risk as grave (medium), with further risk avoidance and reduction potential due to a considerable DRR-CCA gap (*22*). For example, technically and physically feasible DRR and CCA, such as elevating seawalls or maintaining coastal landforms, could bring risk down to acceptable levels today. Relying on national resources has generally not sufficed to reduce risk sufficiently in these countries, particularly for those in the Pacific, Caribbean, and Indian Oceans, and support from the international community has been required. In the near term, sea level rise will increase risks shaped by climate change and socioeconomic factors (increase of people and assets in harm's way). Although there is scope for DRR-CCA, some further risk is locked in already, with serious cost implications (e.g., costs associated with upgrading coastal protection). The risk has increased, and part of this cannot be reduced anymore (not all land is being protected from flooding). We term these additional measures and necessary costs curative. Over time, risk is projected to increase. Challenges and costs will increase to well-tested CCA and DRR measures, and for strong warming (4°C), risks become intolerable (*23*). Novel, transformative measures are increasingly needed, such as offering alternative livelihoods (e.g., switching from farming to services) and assisting with voluntary migration, as compared with curative support for forced migration.

Overall, with climate change amplifying risk, there is a legitimate case for international financial and operational support on L&D to tackle avoidable but increasingly intolerable loss and damage by picking up part of the burden from DRR and CCA domains (the transformative part); with feasible risk reduction becoming limited over

Downloaded from http://science.sciencemag.org/ on October 20, 2016

Published by AAAS

time, constraining societally desirable implementation pathways, measures for dealing with unavoided and unavoidable L&D, both tolerable and intolerable, will need further attention (the curative part).

BEYOND CURRENT DELIBERATIONS

A broad climate risk analysis perspective may provide a framework for negotiating responsibilities and leading to principled action. Action already under way can be integrated into the framework. What we call transformative action is seeing attention with pledges made by the G7 to support the "climate risk insurance" initiative, which aims to provide insurance cover for climate-related risks to an additional 400 million uninsured people in developing countries (*24*). This is connected to DRR support already granted for managing climate (and geophysical) variability via regional sovereign disaster risk insurance pools for Caribbean and Pacific island states, as well as countries in Central America and Africa. The transformative component to be further strengthened arises from efforts to broaden to comprehensive DRR, including risk prevention (e.g., coastal protection for low-lying islands) and preparedness (e.g., enhanced provision of functional flood early warning systems), and to build resilience, such as enabling farmers to take up-side risks (e.g., novel crop varieties with higher profits) in addition to better managing down-side risks.

It has been unclear whether the $300 million pledged for climate insurance is truly additional. Thus, better integrating CCA and DRR with transformative climate risk management efforts may ensure that intolerable risks are strongly acted upon via global solidarity, a keen demand by developing countries, rather than subsumed under country-driven approaches involving national responsibility. In adding L&D efforts to CRM, the distinction from support for DRR and CCA might be that the WIM covers increasingly intolerable risk building on some sort of an attribution signal (an extreme climate facility, to be triggered by attributed changes in underlying climate variability, is being discussed for the Africa drought risk insurance pool) (*25*). What we call curative action has not really seen direct action, although there is nascent debate on a climate displacement coordination facility, which may deal with planned migration and legal status for involuntary displacement of communities that permanently have lost homes or homelands.

There is a very important role for science in this contested political debate. The WIM Executive Committee recently decided to set up task forces with suggested participation of scientists on risk management (including transformational approaches) and displacement. Major scientific challenges remain, in particular to help better understand the physical and social limits of adaptation. Translating the largely schematic climate risk assessment into quantitative-qualitative projections of rising climate risks and associated costs of transformative and curative measures can help take the discourse on L&D forward, as well as motivate action toward the ambitious mitigation goals set in Paris. ■

Climate risk management options in small island states

The risk and policy space for Loss and Damage as applied to risks from sea level rise in small island states [adapted from (*2*, *22*, *23*)]. The scenarios identify classes of curative measures for unavoided and unavoidable impacts of sea level rise and transformative measures for avoiding and managing increasingly intolerable risks.

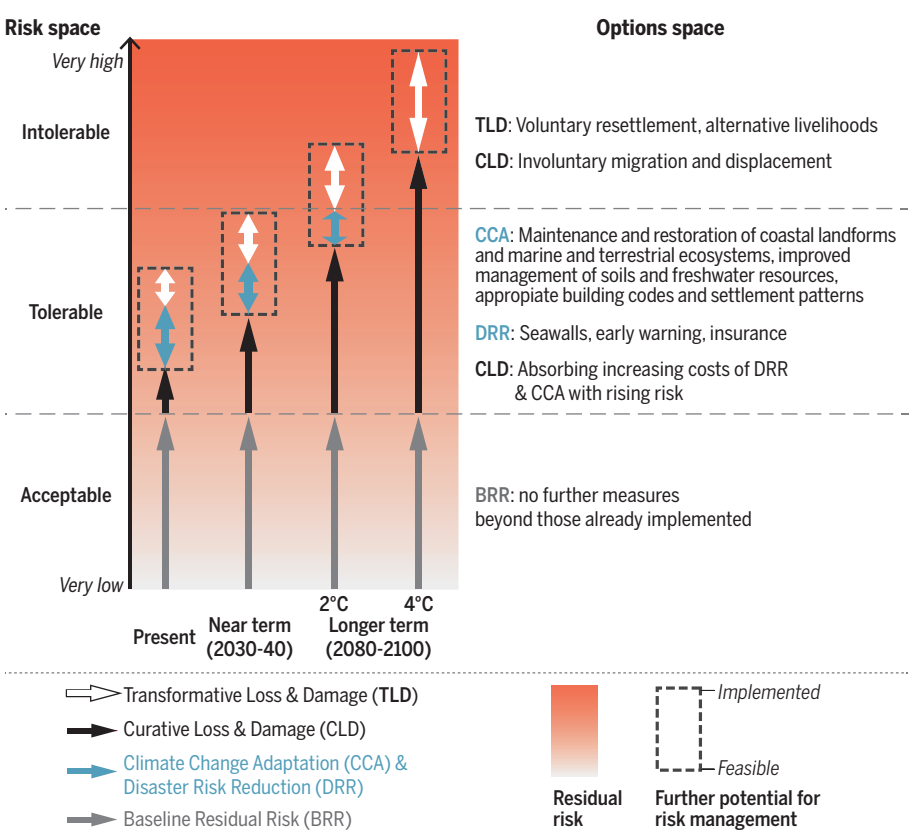

GRAPHIC: N. CARY/*SCIENCE*

REFERENCES AND NOTES

1. UNFCCC, Decision CP/2015/L.9 (UNFCCC, 2015).
2. IPCC, *Climate Change 2014. Synthesis Report. Summary for Policymakers* (Cambridge University Press, Cambridge, 2014).
3. UNFCCC, Decision 2/CP.19 (UNFCCC, 2013).
4. R. Verheyen, *Tackling Loss & Damage–A New Role for the Climate Regime?* (Climate and Development Knowledge Network, 2012).
5. K. van der Geest, K. Warner. *Int. J. Global Warming* **5**, 337 (2013).
6. R. James *et al.*, *Nat. Clim. Change* **4**, 938 (2014).
7. AOSIS, Proposal to the AWG-LCA Multi-Window Mechanism to Address Loss and Damage from Climate Change Impacts (AOSIS, 2008).
8. R. Roberts, S. Huq, *Int. J. Global Warming* **8**, 2 141 (2015).
9. UN, Sendai Framework for Disaster Risk Reduction 2015–2030 (A/CONF.224/CRP.1, UN, 2015).
10. C. B. Fields *et al.* Eds., *Climate Change 2014: Impacts, Adaptation, and Vulnerability, Part A: Global and Sectoral Aspects* (Cambridge Univ. Press, Cambridge, 2014).
11. R. Jones *et al.*, in (*10*), pp. 195–228.
12. J. Smith *et al.*, in *Climate Change 2001: Impacts, Adaptation, and Vulnerability*, J. J. McCarthy *et al.*, Eds. (Cambridge Univ. Press, Cambridge, 2001), pp. 914–967.
13. W. Travis, *B. Bates. Clim. Risk Manage.* **1**, 1 (2014).
14. M. Chambwera *et al.*, in (*10*), pp. 945–977.
15. German Advisory Council on Global Change (WBGU). *World in Transition: Strategies for Managing Global Environmental Risks* (Springer, Berlin, 1998).
16. K. Dow *et al.*, *Nat. Clim. Change* **3**, 305 (2013).
17. R. Mechler *et al.*, *Nat. Clim. Change* **4**, 235 (2014).
18. E. A. Posner, D. Weisbach, *Climate Change Justice* (Princeton Univ. Press, Princeton, NJ, 2010).
19. D. Roser *et al.*, *Clim. Change* **133**, 349 (2015).
20. C. Huggel *et al.*, *Nat. Clim. Change* **6**, 901 (2016).
21. M. J. Mace, M. Schaeffer, *Loss and Damage under the UNFCCC* (Climate Analytics, Berlin, 2013).
22. L. A. Nurse *et al.*, in (*10*), pp. 1613–1654.
23. UNFCCC, Decision FCCC/SB/2015/INF.1 (UNFCCC, 2015).
24. GIZ, "Climate risk insurance for strengthening climate resilience of poor people in vulnerable countries" (GIZ, Eschborn, 2015).
25. J. Syroka, R. Wilcox, *Planet@Risk* **3**, 146 (2015).

ACKNOWLEDGMENTS

The authors acknowledge research funding from the project ENHANCE (Enhancing Risk Management Partnerships for Catastrophic Natural Disasters in Europe) funded by the European Commission under the Seventh Framework Programme (grant agreement no. 308438), as well as from the Zurich Flood Resilience Alliance.

10.1126/science.aag2514

Downloaded from http://science.sciencemag.org/ on October 20, 2016

Published by AAAS

A specially built system that pumped liquid concrete from the ground up helped facilitate the rapid construction of the 163-story Burj Khalifa in Dubai.

ENGINEERING

Street smart

A physicist reveals the engineering marvels that underlie the modern metropolis

By **Sybil Derrible**

Science and the City
The Mechanics Behind the Metropolis
Laurie Winkless
Bloomsbury Sigma, 2016.
304 pp.

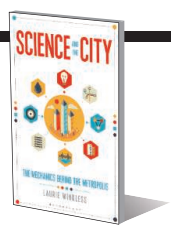

Books on cities appear almost monthly, but most focus on the history of particular cities or on urban planning or economics. Those that focus on the engineering of cities tend to concentrate on only one aspect: architecture, electricity, transportation, or water. No trade book has sought to cover all these engineering systems, much less in an entertaining way, until now.

From structural and electrical engineering to water and transportation engineering, in *Science and the City*, Laurie Winkless aptly describes how cities function on a daily basis in a manner that would be equally accessible to high-school students and practicing engineers. In one relatively short book, she manages to seamlessly cover everything from the definition of a kilowatt-hour to an explanation of how machine learning could have a lasting impact on traffic-signal timing.

Winkless is a physicist by education, and this comes across in the book. She delves all the way to the atomic level when writing about solar panels and reviews basic Newtonian physics when discussing trains and railways. Her tone, however, remains light and familiar, and technical descriptions are often infused with humor. For example, she refers to self-healing polymer plumbing systems as "a bit of a pipe-dream."

The book begins by focusing on buildings and, more particularly, on skyscrapers. After introducing the various materials used, she spends many pages discussing how the Burj Khalifa—the tallest building in the world at the moment—was designed and built, even including how live loads like wind were taken into account. (The initial designs, we learn, had the steplike recessions that taper the building's top arranged in a counterclockwise manner. But thanks to modeling and wind-tunnel testing, the recessions were instead arranged clockwise to promote greater stability.)

In chapter 2, Winkless moves on to electricity and power generation and distribution. She introduces renewable energy thoroughly and discusses the main technical challenge facing the power industry today: storage. After laying out the history of molten salts and hydroelectric power, she discusses recent developments in battery technology, from Elon Musk's Powerwall to Samsung's graphene-coated silicon battery. Here, she also gives us a short historical account of the "War of Currents" between Nikola Tesla and Thomas Edison. ("[L]ong ago, I lost my heart to a charismatic Serbian engineer," she cheekily begins.)

Winkless then moves on to urban water resources, writing about surface water and aquifers, pipes, water purification, and wastewater treatment. She narrows in on municipal waste treatment as an area ripe for innovation, citing recent advancements in membrane bioreactors and reverse osmosis. "Currently, around a third of all drinking water used in an urban home goes down the loo," she writes. "But, with some forward planning and a bit of investment, future buildings could instead utilise recycled greywater to do the job."

Regarding transportation, she details the various types of bridges and even gives us a crash course on traffic-flow theory. She also spends many pages explaining various car technologies—from biofuels to body design—and how they can be improved, and she concludes with a discussion of trains and urban rail systems.

Having covered the four main types of "hard" urban infrastructure, Winkless then discusses how sensors and Big Data are helping reshape how cities function. "At first glance, today's cities haven't changed all that much in the last 50 years," she writes. "If we dig a bit deeper though, we'll see that the city's DNA has been subtly but irreversibly altered, and it's mainly down to our love of data." From food distribution to high-frequency trading and GPS, she conservatively explains how data are changing the way city dwellers eat, commute, and work.

From the SpaceX Hyperloop to driverless cars, Winkless introduces many as-yet-unrealized technologies, but she does not speculate wildly about their potential. That is not to say she is not optimistic for the future: "The one thing I'm sure of," she writes "... is that science, engineering and technology will shape the way we build and interact with our cities, as they have done throughout history." ■

The reviewer is at the Complex and Sustainable Urban Networks (CSUN) Laboratory, University of Illinois at Chicago, Chicago, IL 60607, USA. Email: derrible@uic.edu

10.1126/science.aah7123

PHOTO: SHUTTERLK/SHUTTERSTOCK

Downloaded from http://science.sciencemag.org/ on October 20, 2016

Published by AAAS

ENTREPRENEURSHIP

The business of doing good

A guide for aspiring entrepreneurs offers a data-driven approach to making a difference

By **Omar Bagasra**

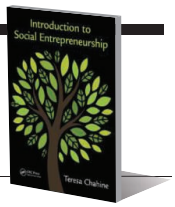

Introduction to Social Entrepreneurship
Teresa Chahine
CRC Press, 2016. 299 pp.

There is an increasing interest from the scientific and research community toward entrepreneurship for social good. Might it be possible to apply the scientific method to affect social change? Using the resources and knowledge available in a university setting, could we develop and test evidence-based solutions to the social problems facing our society?

In *Introduction to Social Entrepreneurship*, Teresa Chahine challenges us to do just that. Chahine, an environmental health scientist, teaches a course at Harvard that seeks to train students not just to analyze social problems but also to solve them. The book, based on the course, offers a step-by-step framework for thinking about the challenges facing our society and their solutions.

Chahine cautions the reader to begin by seeking to understand the root causes of a social challenge, rather than jumping in with ready-made solutions. "Any social entrepreneur who thinks he or she can enter a community with the perfect solution in mind and implement it as is will most likely fail," she writes.

Once you understand the challenge, the next step is to work with those most affected to develop an understanding of what a solution might look like. Whether you opt for door-to-door canvassing or roundtable focus groups, avoid overwhelming stakeholders by keeping questions accessible, she advises, and don't forget to listen: "If you're coming in with prejudgments or predeterminations, you won't hear what people have to say." Mix things up by asking questions in different ways, and be sure to include representatives from diverse groups.

In chapter 4, Chahine provides techniques to help aspiring social entrepreneurs brainstorm, prototype, create, and pilot-test solutions driven by end users. Push beyond conventional boundaries and don't be afraid to fail, she advises. This phase is "one of the most creative stages in social entrepreneurship."

The reviewer is at the Department of Biology, Claflin University, Orangeburg, SC 29115, USA, and the School of Medicine, University of South Carolina, Columbia, SC 29208, USA. Email: obagasra@claflin.edu

Next come the aspects of entrepreneurship with which the scientific community is least familiar. Once you formulate your solution, how do you get it to market? What channels will ensure it reaches your target audience? Establish a value proposition that aligns with your vision, mission, and values, Chahine advises, and use this to guide your market strategy. Identify the experience you want customers to associate with your product or service and build a brand that emphasizes these attributes in a "clear, catchy, and consistent" way.

"The more people you can mobilize ... the larger scale and depth your impact will have," writes Teresa Chahine.

What does success look like? Define your goals from the start and work backward toward achieving them, Chahine instructs. Set key performance indicators; measure the impact you have had on the social outcome according to the theory that links your product or service with the change you are trying to make.

There is more than one method to implement your solution in a financially viable way. The book provides examples of business models from for-profit to hybrid to nonprofit. Sketch out a process map of day-to-day operations that will be required to produce and deliver your solution, Chahine advises. Identify which operations you can standardize and automate, decentralize when possible, and leverage local resources.

Chahine walks the reader through various forms of financial and nonfinancial resources, ranging from traditional grants to crowdfunding campaigns to entrepreneurship contests. "Bootstrapping" and "lean start-ups" are among the buzzwords mentioned, but I had trouble conceptualizing how these might be useful in translating my own research into a social venture.

Chahine also provides helpful tips on how to structure a venture to ensure that a solution is scalable and that the organization will continue to thrive, even after its initial goals are met. She cautions readers to think twice before scaling, making sure to assess the resources that will be required and the potential strains that this will place on the venture.

Communication is key, both outside and inside an organization. Whether you're communicating through social media, through mailing lists, or in person, tailor your approach to the audience, Chahine suggests. But regardless, keep it simple, positive, and personal. "People will never forget the way you made them feel," she writes, quoting the late author Maya Angelou.

Chahine claims that one person can make a huge difference. She has clearly taken it upon herself to spark change. Given the growing interest in social justice, I think there is a chance this spark might grow. ■

10.1126/science.aai8940

Downloaded from http://science.sciencemag.org/ on October 20, 2016

PHOTO: STEPHEN DOREY ABIPP/ALAMY STOCK PHOTO

Published by AAAS

Edited by **Jennifer Sills**

Premature downgrade of panda's status

ACCORDING TO CHINA'S fourth giant panda survey, 1864 wild giant pandas now live in a habitat spanning 2,580,000 ha (*1*). As a result of the survey findings, the International Union for Conservation of Nature (IUCN) changed the classification of the giant panda from "endangered" to "vulnerable" (*2*). This downgrade was premature.

The Chinese government's protection efforts and the public's enthusiasm for the giant panda are directly related to the appeals of international organizations and conservation campaigns. The downgrade will likely reduce the public's enthusiasm for panda protection and may affect the government's protection policies and decision-making.

Furthermore, the IUCN's decision was based on the current number of giant pandas. However, the survey's conclusions were based on evidence of feces and bamboo stem fragments rather than direct encounters, which have been used in past surveys. For example, 30 giant pandas were encountered during the field survey in Wanglang Nature Reserve (one of the earliest giant panda nature reserves) in 1960s (*3*) and 13 dead individuals were found in a survey conducted during the large-scale bamboo flowering event that occurred in 1970s (*4*). It is possible that the methods used by the recent survey led to overestimated population numbers.

Habitat fragmentation is the most important threat to the sustainable survival of the giant panda. Today, giant panda populations are divided into 33 local populations (*1*), whereas in the 1990s, the number was about 24 (*5*). Habitat fragmentation is indisputably increasing. Even worse, there are currently no corridors between the fragmented habitat areas (*6*). Isolating the separated populations not only hinders gene exchange but also greatly increases the extinction risk of small populations. Of the current 33 local populations, 24 are at increased risk of extinction, which accounts for 12% (223 of 1864) of the panda population (*1*). The giant panda population increase, given such extreme habitat fragmentation, has a high genetic homogeneity, putting the species at higher risk.

The giant panda is now classified as "vulnerable" instead of "endangered," but the species remains at risk.

Given the continued threats to the giant panda population and its habitat, we cannot risk becoming complacent. The IUCN should reclassify the giant panda at the endangered level.

Dongwei Kang and Junqing Li*

College of Forestry, Beijing Forestry University, Beijing 100083, China.

*Corresponding author. Email: lijq@bjfu.edu.cn

REFERENCES

1. State Council Information Office of China (2015); www.scio.gov.cn/xwfbh/gbwxwfbh/fbh/Document/1395514/1395514.htm [in Chinese].
2. The IUCN Red List of Threatened Species (2016); www.iucnredlist.org/details/712/0.
3. Giant Panda Expedition of the Wanglang Nature Reserve, *Acta Zool. Sinica* **20,** 162 (1974).
4. Nanchong Teachers College and Wanglang Nature Reserve Survey Team on Giant Panda, *J. Nanchong Teach. Coll. Natural Sci.* **2,** 41 (1984).
5. S.J. O'Brien *et al.*, *Nature* **369,** 179 (1994).
6. The State Council Information Office of the People's Republic of China, "The State Forestry Administration held the fourth national giant panda survey results press conference" (2015); www.scio.gov.cn/xwfbh/gbwxwfbh/fbh/Document/1395514/1395514.htm [in Chinese].

10.1126/science.aaj1963

Stop Pakistan's polio vaccination tax

PAKISTAN IS ONE of three countries in the world where polio remains endemic (*1*). The country recorded more than 300 polio cases in 2014, the highest number since 1999 (*2*). In 2016, 14 cases have been reported (*3*). Although vaccinations could mitigate the spread of infection, many people in Pakistan are very suspicious of vaccines and those delivering them (*2*, *4*). Attempts by the government to overcome the stigma of vaccines have not been effective (*5*). The Pakistani public highly regards the advice of Islamic scholars. Although some scholars have misconceptions about polio campaigns, many are becoming more open to vaccination and its role in preventive medicine (*5*). This cultural shift has great potential. However, a new tax is stifling progress.

On 9 September, the government of Punjab, the most populated province of Pakistan, implemented a 0.9% infrastructure development tax on the polio vaccine (*6*). The tax does not affect international organizations such as UNICEF, who provide polio vaccines to Pakistani children for free (*7*), but it will hamper national anti-polio campaign efforts.

The Pakistan Armed Forces have recently flushed out militant groups from areas where vaccine programs have been unable to go in the past (*8*), and where polio cases have arisen as a result. Now is the time to mobilize polio teams and to capitalize on the support of clerics to educate local populations. The government should focus on making Pakistan polio free by immediately withdrawing the tax on the polio vaccination.

Sultan Ayoub Meo

Department of Physiology, College of Medicine, King Saud University, Riyadh 11461, Saudi Arabia. Email: smeo@ksu.edu.sa

REFERENCES AND NOTES

1. Global Polio Eradication Initiative (http://polioeradication.org/).
2. BBC News, "Pakistan could beat polio in months, says WHO" (2016); www.bbc.com/news/world-asia-36300034.
3. End Polio, "Polio cases district wise 2016" (www.endpolio.com.pk/polio-cases-district-wise-2016).

PHOTO: DESIGN PICS INC/ALAMY STOCK PHOTO

Downloaded from http://science.sciencemag.org/ on October 20, 2016

Published by AAAS

4. T. M. Khan, L. M. Chiau, *Lancet* **386**, 1733 (2015).
5. M. U. Khan *et al.*, *BMC Public Health* **15**, 1100 (2015).
6. Ary News, "Punjab govt imposes tax on life-saving vaccines" (2016); http://arynews.tv/en/punjab-govt-imposes-tax-on-life-saving-vaccines/.
7. UNICEF, Eradicating Polio (www.unicef.org/immunization/polio/).
8. The Guardian, "Pakistan sees huge drop in polio cases" (2015); www.theguardian.com/global-development/2015/jun/04/pakistan-drop-polio-military-operation.

ACKNOWLEDGMENTS

We thank the Deanship of Scientific Research, King Saud University, Riyadh, Saudi Arabia.

10.1126/science.aaa3158

Creating a culture of ethics in Iran

IN HIS IN Depth News story "In Iran, a shady market for papers flourishes" (16 September, p. 1197), R. Stone reports that an estimated 10% of all graduate theses are bought from dealers and then presented by students as their own work. A proposed law will make ghost authorship a crime for both the buyer and the seller. However, the legislation alone will not solve the problem of plagiarized work in Iran.

The number of Iranian universities, students, and scientific papers has grown quickly in recent years (*1*), with Iran achieving a global rank of 22 for the number of papers produced. However, Iran's rank for citations per paper is only 161 (*2*), and the country ranks second worldwide for the number of retracted papers (*2*). These data indicate that despite prolific publications, the quality of papers is lacking.

One explanation for this discrepancy could be the pressure placed on Iranian faculty members and their students to publish more papers to advance their careers (*3*, *4*). Desperation leads some of these students to turn to paper- and thesis-selling agencies. This problem can only be fully addressed by amending inappropriate metric tools used by universities and better preparing both professors and students to successfully complete their research projects and theses.

Iran's research institutions also need better policies for promoting academic ethics (*5*). Training in research ethics should be required in every Masters and Ph.D. program (*6*). Whereas most top universities have well-developed ethical codes for authorship, the first research ethical charter written by the Ministry of Science, Research, and Technology of Iran was issued in 2011 (*3*). Iranian students will not forgo thesis-selling agencies if research ethics are not integrated into the scientific culture through extensive training and modeling.

Mohammad Saeid Rezaee-Zavareh,[1,2] Zohrehsadat Naji,[3]* Payman Salamati[4]

[1]Student Research Committee, Baqiyatallah University of Medical Sciences, Tehran, Iran. [2]Scientometric Institute of Middle East Liver Diseases Center (MELD), Tehran, Iran. [3]Young Researchers and Elites Club, Science and Research Branch, Islamic Azad University, Tehran, Iran. [4]Sina Trauma and Surgery Research Center, Tehran University of Medical Sciences, Tehran, Iran.

*Corresponding author. Email: Zohrehsadat.Naji@gmail.com

REFERENCES

1. M. Farhadi, *Science* **349**, 1029 (2015).
2. M. S. Rezaee-Zavareh, P. Salamati, S. M. Alavian, *Lancet* **388**, 29 (2016).
3. Rules and Regulations, The Ministry of Science, Research and Technology of Iran (www.msrt.ir/fa/Pages/ubSitePages/Laws/rppc.aspx) [in Persian].
4. S. Ghazinoory, S. Ghazinoori, M. Azadegan-Mehr, *Sci. Eng. Ethics* **17**, 213 (2011).
5. B. Ataie-Ashtiani, *Science* **351**, 1273 (2016).
6. N. Nikravanfard, F. Khorasanizadeh, K. Zendehdel, *Dev. World Bioeth*. 10.1111/dewb.12122/abstract (2016).

10.1126/science.aal0019

NEXTGEN VOICES: SUBMIT NOW
DIVERSE EXPERIENCE

Add your voice to *Science*! Our new NextGen VOICES survey is now open:

In his Working Life "Doing science while black" (30 September, p. 1586), E. J. Smith talked about a researcher in his new lab who had mistaken him for a delivery man (http://science.sciencemag.org/content/353/6307/1586).

Have you ever been prejudged based on your appearance or background? What advice would you give to a scientist who had the same experience? What can institutions, professional societies, or individuals do to prevent such experiences in the science community?

To submit, go to www.sciencemag.org/news/nextgen-voices

Deadline for submissions is 4 November. A selection of the best responses will be published in the 6 January 2017 issue of *Science*. Submissions should be 100 words or less. Names will be withheld from printed responses upon request.

TECHNICAL COMMENT ABSTRACTS

Comment on "Reconciliation of the Devils Hole climate record with orbital forcing"

Isaac J. Winograd

Moseley *et al.* (Reports, 8 January 2016, p. 165) postulate an increase in dissolved thorium isotope ^{230}Th with depth below the water table as the explanation for the differing ages of Termination II. Flow of geothermal water through the Devils Hole caverns precludes this explanation. Deposition of younger secondary calcite into the initial porosity of the calcite comprising their cores is a plausible alternate explanation.

Full text at http://dx.doi.org/10.1126/science.aaf7718

Comment on "Reconciliation of the Devils Hole climate record with orbital forcing"

Tyler B. Coplen

Moseley *et al.*'s (Reports, 8 January 2016, p. 165) preferred–Termination-II age is subjective, as evidenced by variation in their Termination-II ages of 2500 years per meter. Termination-II-age bias decreases to zero at ~1.5 meters below the present-day water table, if one assumes linear variation with core-sample height. Maintaining the required gradient of thorium isotope ^{230}Th over 3.6 meters for 1000 years, much less 10,000 years, seems exceedingly unlikely.

Full text at http://dx.doi.org/10.1126/science.aaf8074

Response to Comments on "Reconciliation of the Devils Hole climate record with orbital forcing"

Gina E. Moseley, Yuri V. Dublyansky, R. Lawrence Edwards, Kathleen A. Wendt, Mathieu Pythoud, Pu Zhang, Hai Cheng, Yanbin Lu, Ronny Boch, Christoph Spötl

Winograd and Coplen question the thorium-230 distribution model proposed to explain the age bias observed with increasing depth during Termination II. We have evaluated both criticisms and find that all samples display virtually identical fabrics, argue that the modern setting is not analogous to the conditions during Termination II, and reiterate the robustness of our age models. Our conclusions remain unchanged.

Full text at http://dx.doi.org/10.1126/science.aaf8679

Downloaded from http://science.sciencemag.org/ on October 20, 2016

Published by AAAS

TECHNICAL COMMENT

PALEOCLIMATE

Comment on "Reconciliation of the Devils Hole climate record with orbital forcing"

Isaac J. Winograd

Moseley *et al*. (Reports, 8 January 2016, p. 165) postulate an increase in dissolved thorium isotope ^{230}Th with depth below the water table as the explanation for the differing ages of Termination II. Flow of geothermal water through the Devils Hole caverns precludes this explanation. Deposition of younger secondary calcite into the initial porosity of the calcite comprising their cores is a plausible alternate explanation.

Moseley *et al.*'s (*1*) postulated (not measured) increase in ^{230}Th with depth below the water table—invoked to explain the different published ages for Termination II (*1*–*3*)—is doubtful in consideration of the modern hydrodynamic setting of the two Devils Hole caverns. These caves, developed within a Paleozoic carbonate aquifer, are within 1 km of a major fault (*4*) that dams groundwater flow within the aquifer creating the spring-fed Ash Meadows oasis bordering the caverns on the west. Groundwater flow through the aquifer occurs solely via open fractures and faults (*4*); the caverns comprise such open major fissures that trend northeast-southwest and are of extensional tectonic origin (*5*). That groundwater in the caverns is moving toward the oasis is well documented based on (i) the hydraulic gradient between the caves and the springs and (ii) identity of the chemistry, stable isotopes, and temperature of cavern water with that discharging from the major springs (*4*, *6*, *7*).

Temperature surveys (*8*) to a depth of 32 m below the water table provide additional evidence of the hydrodynamic nature of the water column within these caverns. These surveys, in the larger of the two caves, documented the following: (i) vertical convective mixing during winter months; (ii) thermal stratification during summer months with possible periodic convective mixing; and (iii) "horizontal groundwater flows through discrete zones of high permeability." The temperature gradient during the summer months of minimal vertical convective mixing is about 0.14°C/32 m, or about 4.4°C/km. This gradient is a fraction of geothermal gradients elsewhere in the Great Basin, which vary from 20° to 50°C/km (*9*), but is similar to the very low gradients in other areas of upward flow of geothermal waters within fault zones (*10*). Additional evidence of active flow of water is provided by the chemical homogeneity of the water column between 5 and 38 m, as documented in table 1 of Plummer *et al.* (*11*), who noted, "Thermal convection and groundwater advection probably mix the water-table fluids to some depth along the fault plane." That the water column is dynamic is most easily comprehended by noting that the temperature of the water surface (33.5°C) is ~15° warmer than 18.5°C, the mean annual air temperature (*7*).

Briefly, several lines of evidence indicate that the caverns are not standpipes isolated from active flow in the carbonate aquifer; they comprise major avenues of water flow in the aquifer. Moseley *et al.*'s postulated buildup of ^{230}Th in the water column would be displaced by flow within the fissures and cannot be a valid explanation for the different ages of Termination II. During glacial terminations, the postulated buildup of ^{230}Th with depth below the water table is even more difficult to envision. During such times of transition from relatively wet to relatively dry climates, the water table in the caverns was several meters above modern (*12*), with likely greater than modern groundwater flow and chemical homogenization of the water column in the caverns.

Using seven observations gleaned from the Devils Hole literature and from Moseley *et al.* (*1*), I present below a plausible alternate explanation for the discrepancy in ages of Termination II. (i) Devils Hole mammillary calcite was precipitated under equilibrium conditions and constant aquifer temperature during at least the past 180 thousand years (ky) (*13*). (ii) The internal partial pressure of CO_2 in Devils Hole water (*11*) varies from 0.0123 to 0.0141 atm, or >30 times the modern atmospheric CO_2 and >50 times that during Termination II when CO_2 was ~230 parts per million by volume (ppmv) [figure 1 in (*1*)]. (iii) Outgassing of CO_2 is occurring in the upper 5 m of the water column, as indicated by the following data in table 1 of Plummer *et al.* (*11*). The pH and calcite saturation index is higher, and the log P_{CO_2} is lower at 5 m than at 25 and 37.5 m below the water table, leading Plummer *et al.* (*11*) to state, "More likely is the possible outgassing of CO_2 to the atmosphere in contact with the water table at Devils Hole…" (iv) The porosity of mammillary calcite formed at >20 m depth is <<1%, whereas the porosity of folia, formed at the water table via outgassing, may reach 15 to 20% (*12*). (v) Moseley *et al.*'s core DH_2-D was precipitated at an average rate 43% greater than DH_2-E, their slightly deeper core, and 54% greater than DH-2, which was deposited 21 m below the water table [supplementary materials of (*1*)]. (vi) Calcite comprising DH_2-D and DH_2-E precipitated at a rate 10 times their average growth rate in these cores after ~9 thousand years ago (ka) [figure 1 in (*1*)] when the water table declined close to modern levels (*12*), indicating that calcite formed close to the water table grows rapidly. (vii) Folia (not mammillary calcite) are present in Moseley *et al.*'s highest core (DH_2-D) between 121 and 116 ka, and in the next highest core (DH_2-E) at ~117 ka [table S1 in (*1*)], showing that during Termination II, calcite in both of these cores formed in the shallow zone of outgassing observed in the modern DH.

The observations listed above permit the conclusion that Moseley *et al.*'s U-series ages are inaccurate in the vicinity of terminations. This conclusion relies on a key assumption, namely, mammillary calcite precipitated in the upper few meters of the water column had significant (>5%) primary porosity due to outgassing with attendant rapid deposition of calcite, in contrast to the dense calcite (porosity <<1%) comprising cores deposited at depths >20 m below the water table (*2*). If this assumption is correct, then the younger U-series ages recorded by Moseley *et al.*'s cores during Termination II reflect the deposition of secondary (and younger) calcite into the initial porosity of the calcite comprising their cores. Notably, the 8- to 10-ky discrepancy in ages between their shallow cores and those deposited at depths >20 m (*2*, *3*) occurs during terminations because it is at this time that the water table is falling rapidly, outgassing is accelerated, and porous calcite is deposited in the upper few meters of the water column. The older age of Termination II in core DH_2-E than in DH_2-D is to be expected because DH_2-E, having been deposited 1.3 m deeper in the water column than DH_2-D, had less initial porosity. The conclusion outlined above can be verified or falsified by a thin-section examination of the cores. If correct, the segment of the cores covering Termination II will display numerous secondary growths of calcite within a matrix of crystal morphologies distinct from the dense elongate crystals typical of mammillary calcite deposited below 20 m. (*14*).

Emeritus, U.S. Geological Survey.
Email: ike.winograd@gmail.com

REFERENCES AND NOTES

1. G. E. Moseley *et al.*, *Science* **351**, 165–168 (2016).
2. I. J. Winograd *et al.*, *Science* **258**, 255–260 (1992).
3. I. J. Winograd *et al.*, *Quat. Res.* **66**, 202–212 (2006).
4. I. J. Winograd, W. Thordarson, "Hydrogeologic and hydrochemical framework, south-central Great Basin, Nevada-California, with special reference to the Nevada Test Site" (U.S. Geological Survey Professional Paper 712-C, USGS, 1975).
5. A. C. Riggs, W. J. Carr, P. T. Kolesar, R. J. Hoffman, *Quat. Res.* **42**, 241–254 (1994).
6. I. J. Winograd, F. J. Pearson Jr., *Water Resour. Res.* **12**, 1125–1143 (1976).

Downloaded from http://science.sciencemag.org/ on October 20, 2016

7. W. W. Dudley Jr., J. D. Larson, "Effects of irrigation pumping on desert pupfish habitats in Ash Meadows, Nye County, Nevada" (U.S. Geological Survey Professional Paper 927, USGS, 1976).
8. M. B. Hausner, K. P. Wilson, D. B. Gaines, S. W. Tyler, *Water Resour. Res.* **48**, W05513 (2012).
9. M. Nathenson, M. Guffanti, *J. Geophys. Res.* **93**, 6437–6450 (1988).
10. D. S. Chapmam, L. Rybach, *J. Geodyn.* **4**, 3–37 (1985).
11. L. N. Plummer, E. Busenberg, A. C. Riggs, *Aquat. Geochem.* **6**, 257–274 (2000).
12. B. J. Szabo, P. T. Kolesar, A. C. Riggs, I. J. Winograd, K. R. Ludwig, *Quat. Res.* **41**, 59–69 (1994).
13. T. Kluge, H. P. Affek, Y. Dublyansky, C. Spötl, *Earth Planet. Sci. Lett.* **400**, 251–260 (2014).
14. P. T. Kolesar, A. C. Riggs, in *Studies of Cave Sediments*, D. Sasowsky, J. Mylroie, Eds. (KluwerAcademic/Plenum Publishers, 2004), pp. 227–241.

ACKNOWLEDGMENTS

I thank T. B. Coplen and W. D. Sharp for helpful review comments.

28 March 2016; accepted 21 September 2016
10.1126/science.aaf7718

Downloaded from http://science.sciencemag.org/ on October 20, 2016

TECHNICAL COMMENT

PALEOCLIMATE

Comment on "Reconciliation of the Devils Hole climate record with orbital forcing"

Tyler B. Coplen

Moseley *et al.*'s (Reports, 8 January 2016, p. 165) preferred-Termination-II age is subjective, as evidenced by variation in their Termination-II ages of 2500 years per meter. Termination-II-age bias decreases to zero at ~1.5 meters below the present-day water table, if one assumes linear variation with core-sample height. Maintaining the required gradient of thorium isotope ^{230}Th over 3.6 meters for 1000 years, much less 10,000 years, seems exceedingly unlikely.

At Devils Hole Cave 2 in Nevada, Moseley *et al.* (*1*) obtained four carbonate cores at positions 0.8, 2.1, 4.5, and 5.5 m above the present-day water table, which they identified, respectively, as DH_2-E, DH_2-D, DH_2-G, and DH_2-J. With ^{230}Th age-dating and relative isotope-ratio measurements (*2*), they determined $\delta^{18}O$ time series (Fig. 1) from the two lower-elevation cores and from core DH-2, upon which the original Devils Hole chronology is based (*3*). The Termination-II ages—defined by Moseley *et al.* (*1*) as the time-series position at which $\delta^{18}O_{VPDB}$ (Vienna Pee Dee belemnite) = –15.7 per mil (‰)—differ among the cores. Specifically, the Termination-II ages of cores DH-2, DH_2-E, and DH_2-D are 139.4 ± 0.5, 133.8 ± 0.4, and 130.6 ± 0.4 thousand years ago (ka), respectively (Fig. 1), where uncertainties are mean ± 2 SD. These ages were derived from the midpoints of $\delta^{18}O_{VPDB}$ measurements between approximately –16.4 and –14.9‰ (three solid lines in Fig. 1), and they are anchored by nine ^{230}Th ages ranging between ~140.7 ± 0.5 and ~128.8 ± 0.4 ka. The Termination-II age from core DH-2 overlaps the "iconic" Devils Hole chronology, which is based on core DH-11 (*4*, *5*), as shown in figure 4 of (*1*).

If one assumes that core DH-2, which was precipitated at a depth of 21 m below the present-day water table, represents the heretofore accepted Devils Hole time series (Fig. 1), Termination-II ages of cores DH_2-E and DH_2-D are too low by ~5600 and 8800 years, respectively, based on measurements of Moseley *et al.* (*2*). Termination-II ages of cores DH_2-E and DH_2-D differ in elevation by 1.3 m and yet differ by ~3200 years in age. The Termination-II-age disparity between cores DH_2-E and DH_2-D of ~3200 years yields a decrease in age with height above the present-day water table of ~2500 years/m.

If one assumes a linear decrease in age with height above the present-day water table, the projected bias in Termination-II age increases to about –15 ka for core DH_2-G and to about –17 ka for core DH_2-J (Fig. 2), further assuming that Termination-II ages can be determined in these cores. The projected bias in Termination-II age with respect to DH-2 drops to zero at ~1.5 m below the present-day water table (Fig. 2). Therefore, had Moseley *et al.* (*1*) collected a core sample from ~1.5 m below the present-day water table, it potentially would have reproduced the heretofore accepted Devils Hole time series (*4*–*7*).

Moseley *et al.* (*1*) explain the Termination-II-age disparity among the time series (Fig. 1) as being due to the hypothesis that ^{230}Th increases down the water column in the Devils Hole hydrologic system selectively during terminations, namely during the period ~140 to 124 ka for Termination II (Fig. 1). About one-third of the age discrepancy attributed to the increase in ^{230}Th in the water column, hypothesized by Moseley *et al.* (*1*) during Termination II, occurs over an elevational distance of 1.3 m—that is, between cores DH_2-D and DH_2-E (Fig. 2). Potentially, the entire hypothesized ^{230}Th increase occurs over a distance of merely 3.6 m (Fig. 2), if one assumes a linear relationship. The maintenance over ~10,000 years of such a ^{230}Th gradient over 3.6 m (or even 1.3 m) near the top of a water column, subject to earth-tide-driven fluctuations of as much as 12 cm (*8*), is questionable.

The difference in age of Termination II is not the only problem that needs explanation. The $\delta^{18}O$ time series of DH_2-D and DH_2-E do not fully agree with those of DH-2 and DH-11. At 110 ka, the minimum $\delta^{18}O_{VPDB}$ value of core DH_2-D is more than 0.25‰ lower than that of DH-2 (Fig. 1) and DH-11 (*4*, *5*, *7*).

That Moseley *et al.*'s preferred age (132 ka) for Termination II, obtained from core DH_2-D, is subjective and unreliable is best seen by the time series for this core shown in figure 3 of (*1*), which shows events during Termination I, the best-dated portion of their record. The presently accepted date for Termination I is ~14 ka (*9*). The time series for core DH_2-D shown in figure 3 of (*1*) indicates an age for Termination I that is thousands of years younger than the accepted age. More disturbing is the absence of a post–10-ka plateau in the $\delta^{18}O_{VPDB}$ time series, a plateau present in all climate archives (e.g., ice cores, benthic $\delta^{18}O$, and speleothems) marking the relatively uniform Holocene climate. If Moseley *et al.*'s data cannot accurately record events during the past 15,000 years, why should readers accept their preferred age for Termination II, an event 100 millennia older?

These differences support the contention that the cores of Moseley *et al.* are composed, at least in part, of "mixed-age calcite." It would take a relatively small amount of calcite precipitated between ~90 and 13 ka in voids in DH_2-E and DH_2-D, which were formed at a shallow depth, to decrease

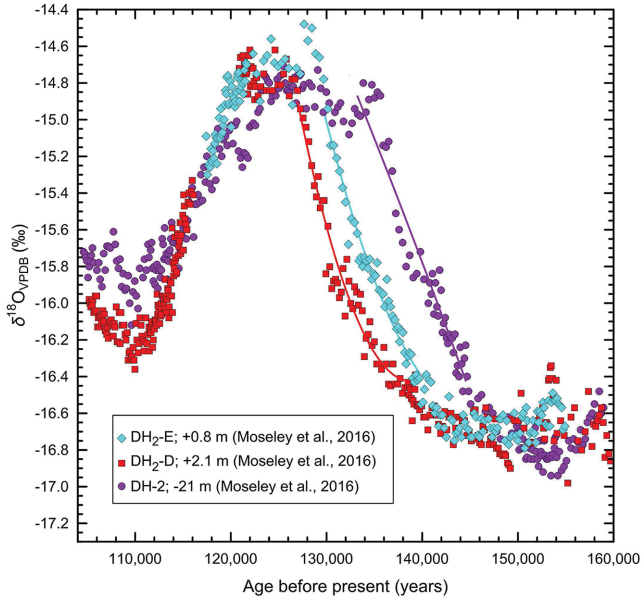

Fig. 1. Comparison of Devils Hole $\delta^{18}O$ time series. Core DH_2-E collected from Devils Hole Cave 2 at a distance above the water table of 0.8 m (*1*); core DH_2-D collected from Devils Hole Cave 2 at a distance above the water table of 2.1 m (*1*); core DH-2 collected from Devils Hole (*3*) at a depth of 21 m and reanalyzed by Moseley *et al.* (*1*). From measurements of Moseley *et al.* (*2*), the ages of the DH_2-E, DH_2-D, and DH-2 Termination-II midpoints, defined by $\delta^{18}O_{VPDB}$ = –15.7‰, are 130.6, 133.8, and 139.4 thousand years before the present.

U.S. Geological Survey, 431 National Center, Reston, VA 20192, USA.
Email: tbcoplen@usgs.gov

Downloaded from http://science.sciencemag.org/ on October 20, 2016

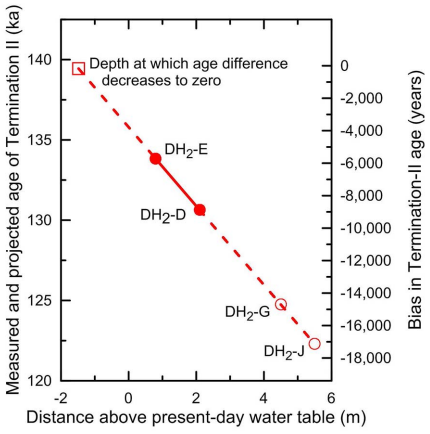

Fig. 2. Measured and projected Termination-II age as a function of distance above or below the present-day water table. Cores DH_2-E, DH_2-D, DH_2-G, and DH_2-J were collected from Devils Hole Cave 2 at a distance above the modern water table, respectively, of 0.8, 2.1, 4.5, and 5.5 m (*1*). Solid circles are measured values (*1*, *2*), open circles are projected values if one assumes linear bias in age with height above the water table, and the open square is a projected value assuming linear bias in age with height.

their apparent ages substantially. For example, if one assumes uniform uranium concentrations in the two end-members, 3% of a 13,000-year-old calcite would lower the apparent age of a 140,000-year-old calcite to 132 ka.

The explanation by Moseley *et al.* for the variation of Devils Hole Termination-II ages with depth beneath the water table in Devils Hole is based on a postulated (not measured) increase in ^{230}Th with depth during glacial terminations. As a rigorous test of their hypothesis, they should sample water in Devils Hole Cave 2 to a depth of 60 m, which is the depth of the deepest dated calcite sample discussed by them, and measure its ^{230}Th concentration. I look forward to publication of these ^{230}Th concentration measurements as well as the δ^{18}O time series of cores DH_2-G, and DH_2-J to learn whether the estimated biases in Termination-II ages (Fig. 2) are on target.

REFERENCES AND NOTES

1. G. E. Moseley *et al.*, *Science* **351**, 165–168 (2016).
2. National Oceanic and Atmospheric Administration, National Centers for Environmental Information; www.ncdc.noaa.gov/data-access/paleoclimatology-data.
3. I. J. Winograd, T. B. Coplen, B. J. Szabo, A. C. Riggs, *Science* **242**, 1275–1280 (1988).
4. I. J. Winograd *et al.*, *Science* **258**, 255–260 (1992).
5. J. M. Landwehr, W. D. Sharp, T. B. Coplen, K. R. Ludwig, I. J. Winograd, "The chronology for the δ^{18}O record from Devils Hole, Nevada, extended into the mid-Holocene" (U.S. Geological Survey Open-File Report 2011-1082, USGS, 2011); http://pubs.usgs.gov/of/2011/1082/.
6. K. R. Ludwig *et al.*, *Science* **258**, 284–287 (1992).
7. I. J. Winograd *et al.*, *Quat. Res.* **66**, 202–212 (2006).
8. W. W. Dudley Jr., J. D. Larson, "Effects of irrigation pumping on desert pupfish habitats in Ash Meadows, Nye County, Nevada" (U.S. Geological Survey Professional Paper 927, USGS, 1976).
9. L. E. Lisiecki, M. E. Raymo, *Paleoceanography* **20**, PA1003 (2005).

ACKNOWLEDGMENTS

This manuscript has benefited from reviews by I. J. Winograd (U.S. Geological Survey, Reston, Virginia) and W. D. Sharp (Berkeley Geochronology Center, Berkeley, California). The support of the U.S. Geological Survey National Research Program made this contribution possible.

1 April 2016; accepted 21 September 2016
10.1126/science.aaf8074

Downloaded from http://science.sciencemag.org/ on October 20, 2016

TECHNICAL RESPONSE

PALEOCLIMATE

Response to Comments on "Reconciliation of the Devils Hole climate record with orbital forcing"

Gina E. Moseley,[1]* Yuri V. Dublyansky,[1] R. Lawrence Edwards,[2] Kathleen A. Wendt,[1] Mathieu Pythoud,[2] Pu Zhang,[2] Hai Cheng,[2,3] Yanbin Lu,[2]† Ronny Boch,[1]‡ Christoph Spötl[1]

Winograd and Coplen question the thorium-230 distribution model proposed to explain the age bias observed with increasing depth during Termination II. We have evaluated both criticisms and find that all samples display virtually identical fabrics, argue that the modern setting is not analogous to the conditions during Termination II, and reiterate the robustness of our age models. Our conclusions remain unchanged.

In their Comments on our Report (*1*), Winograd (*2*) and Coplen (*3*) question the hypothesis that an increase in ^{230}Th concentration with depth in the Devils Hole aquifer [DH_{aq}, encompassing Devils Hole cave (DH) and Devils Hole no. 2 cave (DH-2)] caused erroneously old ages in deeper samples across Termination II (TII). Winograd's argument is based on the accuracy of the ^{230}Th ages produced for the shallow samples, whereas Coplen's argument is founded on a "challenging" depth gradient in ^{230}Th needed to maintain the age offset.

δ^{18}O time series produced over a depth range of 32.1 m within DH_{aq} demonstrate a linear (R^2 = 0.97) increase in age with depth for TII (*1*). Using well-understood ocean chemistry (*4*–*6*), Moseley *et al.* (*1*) and others (*7*, *8*) proposed a model for DH_{aq} whereby ^{230}Th produced in the water column is scavenged and transported downward by settling particles. Continuous reversible exchange between dissolved ^{230}Th and ^{230}Th adsorbed onto particles causes an increase in concentration with depth (*4*). Scavenging (*9*) of dissolved ^{230}Th onto calcite at the cave walls thus results in increasingly erroneously old ^{230}Th ages with depth. Similar to the oceans, it is possible that changes with time in the total sediment flux affected the radionuclide flux (*5*, *9*) and intensity of scavenging (*9*), hence providing a mechanism for the greater age biases observed during glacial terminations (*1*).

Winograd and Coplen do not dispute that an excess of ^{230}Th exists in the DH_{aq} [in (*10*), ^{230}Th ages are corrected for excess ^{230}Th]; in contrast to our model, however, Winograd argues that effective mixing and active flow in DH_{aq} precludes an increase in ^{230}Th concentration with depth (*2*), whereas Coplen questions the steepness of the ^{230}Th gradient (*3*).

Winograd's qualitative arguments are based on (i) temperature surveys in DH that suggest that convection occurs in winter and stratification in summer along with "horizontal groundwater flow" (*11*); (ii) low vertical thermal gradients characteristic of upward flow of geothermal water within fault zones; (iii) chemical homogeneity between 5 and 37.5 m depth (*12*); (iv) the difference between air and water temperatures; and, finally, (v) a statement about water transit times. Several lines of reasoning argue against these points.

Temperature measurements to −34 m in DH indicate that cold surface waters sink during the winter months, causing vertical convective mixing (*11*). This finding, however, is hardly relevant for our model because the roof collapse that opened DH to the surface occurred ~60,000 years ago (*12*); thus, modern winter conditions in DH are not analogous to the conditions that existed during TII. DH-2, which remains relatively enclosed with only two small (several m^2) openings, provides the closest modern analog for TII conditions; however, detailed studies of the water column have not yet been conducted. Observations in DH during the summer, when the air temperature is closer to that of the water, are thus the closest available analog to TII conditions, and these indicate very precisely the presence of a stable, stratified water column with a temperature gradient of 0.005°C m^{-1} (*11*) (i.e., no convective mixing).

Winograd *et al.* (*10*) estimated the transit time of water recharging ~80 km away and discharging at DH to be less than 2000 years. Based on these numbers, the transit time between the caves (5 years) was calculated to be within ^{230}Th age uncertainties (*1*); hence, differences in age for a specific event are unlikely to be caused by leads and lags in the arrival of the water. The transit time between the two caves may, however, be variable, and had it ever exceeded ^{230}Th age uncertainties (*1*), then the δ^{18}O time series for DH, which is downstream, should lag DH-2 [note that the flow direction is incorrect in (*2*)]. In fact, the data demonstrate the exact opposite (*1*). Winograd (*2*) implies that the flow velocity within the two caves is different from (faster than?) his average for the aquifer (*10*) and that the DH and DH-2 water bodies are not isolated standpipes. In such "active flow," he postulates that ^{230}Th would be displaced, preventing its accumulation with depth.

Assuming that Winograd's (*10*) transit time is correct, the average flow velocity in the groundwater system is on the order of $n \times 10^{-6}$ m s^{-1}, which is two orders of magnitude slower than the terminal velocity of settling fine-silt particles (*13*). Lateral laminar advective flow may thus deflect trajectories of settling particles in the direction of flow but cannot disturb the vertical ^{230}Th gradient. Furthermore, the presence of "dirty" calcite on the footwalls of both caves is evidence that the hydrodynamic nature of the DH_{aq} does not prevent the settling of particles (and hence the accumulation of ^{230}Th with depth). Similarly, oceans are not stagnant water bodies either, yet both shallow and deep waters maintain a ^{230}Th gradient (*4*–*6*).

Coplen outlines a case in which he assumes that sample DH-2_{spl} collected at −21 m relative to the present water table (r.w.t.) is the "heretofore accepted Devils Hole time series" (*3*). Justification for why DH-2_{spl} was chosen as the correct chronology over the other three samples deposited at +2.1 (DH_2-D), +0.8 (DH_2-E), or −30 (DH-11) m r.w.t. is, however, absent. We question the stance that DH-2_{spl} yields the "correct" chronology across TII on the basis that the glacial-interglacial transition in this δ^{18}O time series leads local dripstone records by ~8 thousand years (ky), of which the latter are in agreement with orbital forcing (*14*–*16*). Because the DH_{aq} and local dripstones received the same Pacific-sourced moisture during TII, the timing of δ^{18}O shifts at each site should be in agreement.

In Moseley *et al.* (*1*), age models for samples DH_2-D, DH_2-E, and $DH2_{spl}$ were constructed in OxCal (*17*, *18*) from high-resolution (100 μm) stable isotopes and a high density of precise [3 per mil (‰)] ^{230}Th ages in stratigraphic order, which had been analyzed using the most up-to-date techniques (*19*, *20*). Age-model indices (*21*) were ~100% in all cases. In keeping with previous discussions (*22*), and thus use of sample DH-11, which has a TII midpoint δ^{18}O value of −15.7‰ (Vienna Pee Dee belemnite) (*22*), Moseley *et al.* assigned the TII midpoint in each newly analyzed sample as the first point in the age model with a δ^{18}O value of −15.7 ± 0.08‰ (*23*). We consider our age modeling approach and allocation of TII-midpoint ages to be clear, logical, and reasonable.

Under the assumption that DH-2_{spl} is the correct chronology, Coplen states that the timing

[1]Institute of Geology, University of Innsbruck, Innrain 52, 6020 Innsbruck, Austria. [2]Department of Earth Sciences, University of Minnesota, 310 Pillsbury Drive SE, Minneapolis, MN 55455, USA. [3]Institute of Global Environmental Change, Xi'an Jiaotong University, Xi'an 710049, China.
*Corresponding author. Email: gina.moseley@uibk.ac.at
†Present address: Earth Observatory of Singapore, 639798, Singapore. ‡Present address: Institute of Applied Geosciences, Graz University of Technology, Rechbauerstraße 12, 8010 Graz, Austria.

Downloaded from http://science.sciencemag.org/ on October 20, 2016

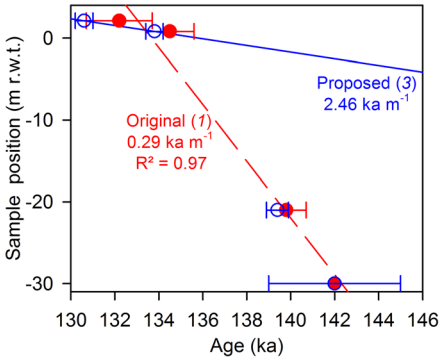

Fig. 1. The ages of the TII midpoint in samples at different depths/elevations relative to the present water table. Uncertainties are ± 2 SD. Linear trend lines are fitted through the original data set [red, n = 4 ^{230}Th ages (*1*)] and Coplen's newly proposed data set [blue, n ^{230}Th ages = 2 (*3*)].

Table 1. Ages for the TII midpoint in samples from different depths/elevations in DH and DH-2. Uncertainties are ± 2 SD.

	Modern position (m, r.w.t.)	Midpoint TII (ka) Moseley *et al.* (*1*)	Midpoint TII (ka) Coplen (*3*)	Difference (ka)
DH_2-D	+2.1	132.2 ± 1.5	130.6 ± 0.4	1.6
DH_2-E	+0.8	134.5 ± 1.1	133.8 ± 0.4	0.7
$DH2_{spl}$	−21	139.8 ± 0.9	139.4 ± 0.5	0.4
DH-11	−30	142 ± 3 (*22*)		

Table 2. U concentration and composition of DH-2 water. The samples were collected in February 2016, ~0.2 and 1.3 m below the modern water table. "Filtered" indicates that water samples were passed through a 0.2-μm pore filter to remove particles >0.2 μm. Uncertainties are ± 2 SD.

Approximate depth* (m)	$^{234}U/^{238}U$ (atomic × 10^{-6})	$\delta^{234}U^{\dagger}$ (‰)	^{234}U conc. (ag/g)	^{238}U conc. (ng/g)
−0.2 (filtered)	151.84 ± 0.11	1762.2 ± 2.0	460 ± 1	3.079 ± 0.005
−0.2 (unfiltered)	152.01 ± 0.10	1765.3 ± 1.9	461 ± 1	3.088 ± 0.005
−1.3 (filtered)	151.79 ± 0.11	1761.5 ± 2.1	461 ± 1	3.089 ± 0.005
−1.3 (unfiltered)	151.82 ± 0.11	1761.9 ± 2.1	460 ± 1	3.083 ± 0.005

*Depth relative to the water table during sampling. $^{\dagger}\delta^{234}U = ([^{234}U/^{238}U]_{activity} - 1) \times 1000$.

of TII recorded in shallower cores DH_2-D and DH_2-E is too young (*3*). Using "smoothed" versions [(figure 1 in (*3*)] of the age models of Moseley *et al.* (*1*), Coplen shifts the TII midpoints by up to 1600 years (Table 1) and calculates an age disparity of ~2.5 ky m^{-1} from the two shallowest cores (excluding the two deeper cores) (Fig. 1). The method of construction of Coplen's alternative age models is unclear; plus, we find no reason why a different approach to age modeling should be taken.

Moseley *et al.* (*1*) demonstrated a strong linear correlation (R^2 = 0.97) between age and depth that encompassed all four samples and yielded an age bias-depth gradient of 0.29 ky m^{-1} (Fig. 1). Similarly, a linear trend line fitted to Coplen's four TII-midpoint ages (R^2 = 0.95) would yield a gradient of 0.33 ky m^{-1}. Consequently, the age bias-depth gradient (~0.3 ky m^{-1}) is more realistic when all four samples across a depth range of 32.1 m are taken into consideration, rather than just two samples over a depth range of 1.3 m (2.5 ky m^{-1}).

Coplen (*3*) suggests that analysis of additional higher-elevation cores from +4.5 and +5.5 m r.w.t. should yield TII-midpoint ages of 124.6 and 122.1 ky, respectively, based on the 2.5 ky m^{-1} gradient (*3*). Indeed, we do intend to analyze additional cores from higher elevations above the present water table, although such work will take considerable time, effort, and resources. Likewise, a detailed study examining the cause for deviation of $\delta^{18}O$ values between shallow and deep samples at discrete time periods, such as 110 thousand years ago (ka) (*3*), reaches beyond the scope of this Response.

The suggestion that we analyze the ^{230}Th concentration with depth in DH-2 is indeed something that we have considered. Although it would be an interesting exercise, this must await a major effort to collect such water without introducing contamination from the nearby walls of the cave. We have, however, measured the ^{234}U concentration of shallow DH-2 water (Table 2) and find that it is 2.2 times that of seawater (*24*); thus, all other factors being equal, one would expect ^{230}Th concentrations in DH-2 water to be higher than a marine equivalent. Furthermore, as discussed, the modern water may not be analogous to TII water; thus, given that the age bias is only observed during glacial terminations, measurements on today's aquifer may not provide a suitable indication of the conditions that were present when the age-offset was created.

In summary, although several details of the DH_{aq} reversible ^{230}Th scavenging model require further study, arguments based on the hydrodynamic nature of the aquifer (*2*) and the ^{230}Th gradient (*3*) do not render the model invalid.

Winograd (*2*) furthermore proposes that the ages reported in (*1*) may represent "mixed ages" of older fast-growing calcite and younger calcite that subsequently filled pore spaces. He speculates that fast calcite growth, leading to higher porosity, was due to CO_2 outgassing in the upper ~5 m of the water column during TII. In support of this contention, he notes that samples displaying younger ages for TII formed much closer to the water table and that the water table was declining during the glacial-interglacial transition. Winograd rightly suggests that his assumption can be tested by thin-section examination (*2*).

Examination of the calcite fabrics that were deposited across TII in cores at +2.1, +0.8 and −21 m r.w.t. reveals virtually identical petrographic features (Fig. 2) generally consistent with previous observations (*25*). Mammillary calcite in all three samples has a compact fabric, comprising composite columnar crystals, each being a "bundle" of multiple rod-shaped (aspect ratio >20) crystallites. Primary growth zonation observed under epifluorescence indicates that the mammillary calcite surface advanced as multiple rhombohedral crystal terminations of crystallites 50 to 150 μm in size. Both the columnar crystals and the crystallites are tightly packed, and intervening pore spaces are absent. Aqueous fluid inclusions are very rare, and typically occur where several adjacent columnar crystals meet. The former show equant three-dimensional shapes and commonly preserve the morphology of cleavage rhombohedra (i.e., no sign of recrystallization).

There is thus no evidence of increased porosity in any of our samples across TII. The contention of Winograd (*2*) regarding "fast" calcite growth and development of porosity in mammillary calcite forming at shallow depth in DH_{aq} is not supported by petrographic evidence.

Furthermore, although the mammillary calcite in the shallow cores was, indeed, deposited on average slightly faster than its deeper counterpart during TII, the growth rates show no obvious relation to the water table decline (*1*). In fact, deposition seems to have slowed down rather than accelerated across TII, as would be expected if the deposition rate were controlled by progressively higher CO_2 outgassing in response to a declining water table. This suggests that CO_2 outgassing was not the primary factor controlling the kinetics of mammillary calcite deposition. This conclusion is consistent with previous findings (*12*) that "rate dependence on PCO_2 is small at CO_2 partial pressures in the range of that at Devils Hole."

REFERENCES AND NOTES

1. G. E. Moseley *et al.*, *Science* **351**, 165–168 (2016).
2. I. J. Winograd, *Science* **354**, 296 (2016).
3. T. B. Coplen, *Science* **354**, 296 (2016).
4. M. P. Bacon, R. F. Anderson, *J. Geophys. Res.* **87**, 2045–2056 (1982).

Downloaded from http://science.sciencemag.org/ on October 20, 2016

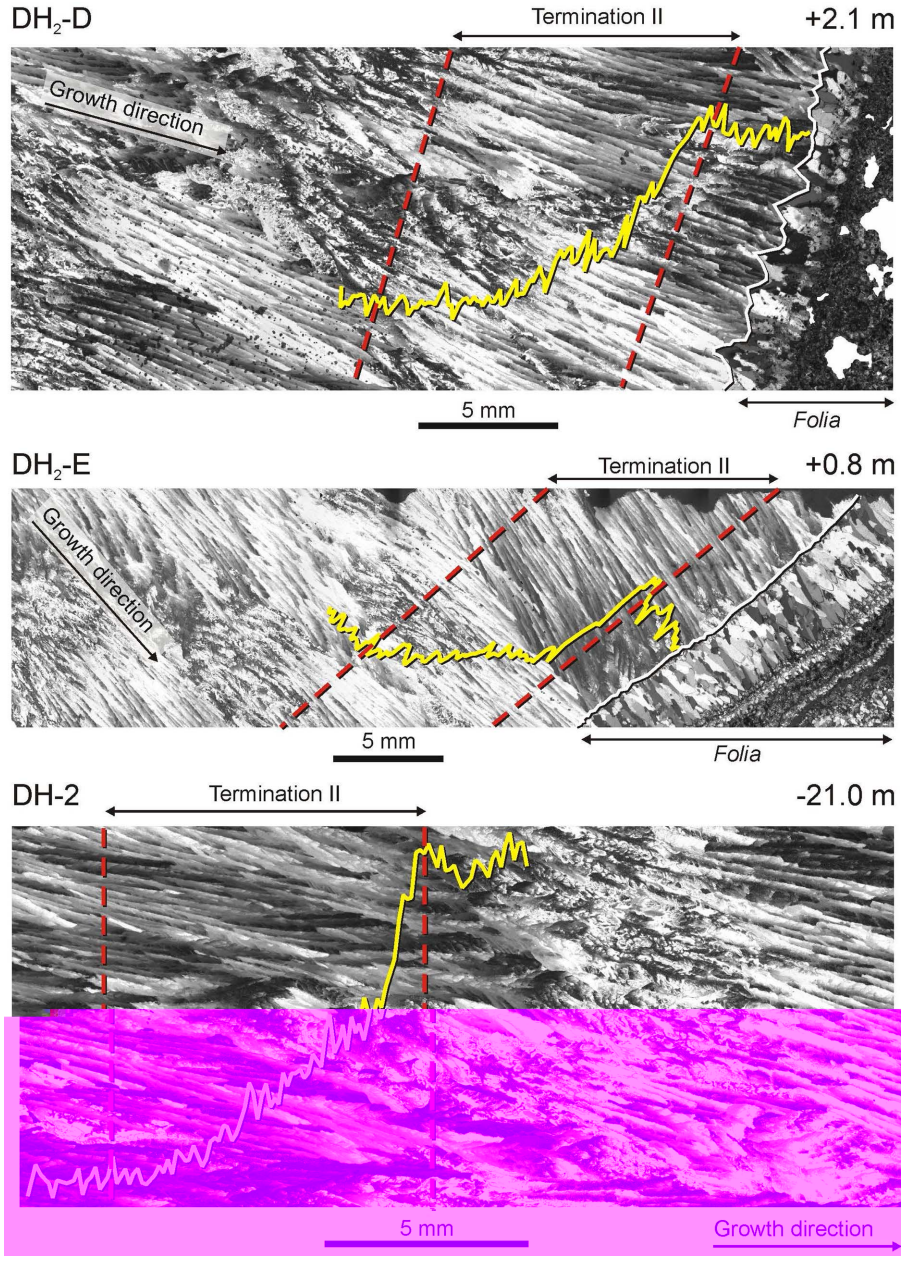

Fig. 2. Thin sections of samples at +2.1, +0.8, and −21 m relative to the present water table (transmitted light; nicols partially crossed). Calcite that was deposited during TII is located approximately within the bounds of the red dashed lines. The respective $\delta^{18}O$ curve (yellow) for each sample is superimposed on top of the thin section in its approximate position and shows an increase of ~2‰ (not to scale) across TII. The boundary between mammillary calcite (subaqueous) and folia (formed at the water table) in DH_2-D and DH_2-E is emphasized by a solid white line. The calcite fabric deposited during TII is identical to that deposited before TII and in the Eemian and does not vary between samples.

5. M. P. Bacon, C.-A. Huh, A. P. Fleer, W. G. Deuser, *Deep-Sea Res.* **32**, 273–286 (1985).
6. Y. Nozaki, H.-S. Yang, M. Yamada, *J. Geophys. Res.* **92**, 772–778 (1987).
7. R. L. Edwards, C. D. Gallup, *Science* **259**, 1626–1627 (1993).
8. N. J. Shackleton, *Nature* **362**, 596 (1993).
9. Y. Lao, R. F. Anderson, W. S. Broecker, *Paleoceanography* **7**, 783–798 (1992).
10. I. J. Winograd *et al.*, *Quat. Res.* **66**, 202–212 (2006).
11. M. B. Hausner, K. P. Wilson, D. B. Gaines, S. W. Tyler, *Water Resour. Res.* **48**, 5513 (2012).
12. L. N. Plummer, E. Busenberg, A. C. Riggs, *Aquat. Geochem.* **6**, 257–274 (2000).
13. R. Ferguson, M. Church, *J. Sediment. Res.* **74**, 933–937 (2004).
14. J. D. Shakun, S. J. Burns, P. U. Clark, H. Cheng, R. L. Edwards, *Geophys. Res. Lett.* **38**, L18701 (2011).
15. M. Cross *et al.*, *Quat. Sci. Rev.* **127**, 186–198 (2015).
16. M. S. Lachniet, R. F. Denniston, Y. Asmerom, V. J. Polyak, *Nat. Commun.* **5**, 3805 (2014).
17. C. B. Ramsey, *Quat. Sci. Rev.* **27**, 42–60 (2008).
18. C. Bronk Ramsey, S. Lee, *Radiocarbon* **55**, 720–730 (2013).
19. H. Cheng *et al.*, *Earth Planet. Sci. Lett.* **371-372**, 82–91 (2013).
20. C.-C. Shen *et al.*, *Geochim. Cosmochim. Acta* **99**, 71–86 (2012).
21. C. Bronk Ramsey, *Radiocarbon* **37**, 425–430 (1995).
22. I. J. Winograd, J. M. Landwehr, K. R. Ludwig, T. B. Coplen, A. C. Riggs, *Quat. Res.* **48**, 141–154 (1997).
23. C. Spötl, *Rapid Commun. Mass Spectrom.* **25**, 1683–1685 (2011).
24. M. B. Andersen, C. H. Stirling, B. Zimmermann, A. N. Halliday, *Geochem. Geophys. Geosyst.* **11**, 12 (2010).
25. P. T. Kolesar, A. C. Riggs, in *Studies of Cave Sediments*, D. Sasowsky, J. Mylroie, Eds. (Springer, Netherlands, 2007), pp. 227–241.

ACKNOWLEDGMENTS

This work was supported by the Austrian Science Fund (FWF) project no. FP263050 to C.S. and T 710-NBL to G.E.M., and in part by NSF grants 1337693 to R.L.E. and 1602940 to R.L.E. and H.C. This research was conducted under research permit numbers DEVA-2010-SCI-0004 and DEVA-2015-SCI-0006 issued by Death Valley National Park. We thank J. Wallraf for preparation of the thin sections and K. Wilson and R. Freeze for assistance in the field.

18 May 2016; accepted 21 September 2016
10.1126/science.aaf8679

Downloaded from http://science.sciencemag.org/ on October 20, 2016

RESEARCH

Structure of type 2 ryanodine receptor from porcine heart

Peng et al., *p. 301*

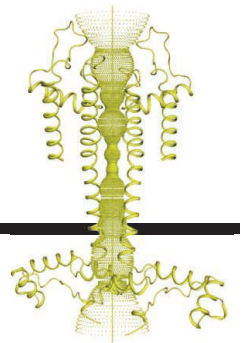

IN *SCIENCE* JOURNALS

Edited by **Stella Hurtley**

A native of the Andean highlands, the sparkling violetear hummingbird (*Colibri coruscans*)

EVOLUTION

Expect the unexpected

In convergent evolution, similar environmental conditions produce similar sets of adaptations. Does similar convergence exist in the molecular underpinnings of such morphological changes? Natarajan *et al.* looked across more than 50 species of birds that have adapted to different elevations to identify patterns of similarity in hemoglobin-oxygen binding affinity (see the Perspective by Bridgham). Increases in hemoglobin-oxygen binding affinity occurred in alpine species, but the molecular changes underlying the hemoglobin changes were variable. Thus, even in cases where adaptive phenotypic change is predictable, the molecular pathways to these changes may not be. —SNV

Science, this issue p. 336; see also p. 289

ANTIGEN PRESENTATION

New players in the repertoire

Antigen-presenting cells, such as macrophages and dendritic cells, activate immunological T cells by presenting them with antigens bound by major histocompatibility complexes (MHCs). The proteasome typically processes these antigens, which include peptides derived from both self and microbial origins. Liepe *et al*. now report that, surprisingly, a large fraction of peptides bound to class I MHC on multiple human cell types are spliced together by the proteasome from two different proteins. Such merged peptides might turn out to be useful in vaccine or cancer immunotherapy development. —KLM

Science, this issue p. 354

PAIN

Social transfer of pain in mice

Pain experienced by an individual can be modulated by social, cognitive, and emotional factors. In a group setting, can an individual experiencing pain affect other, pain-free individuals' behaviors and responses? Smith *et al.* explored this question in mice. They examined the responses of "bystander" animals housed in the same room, but not in the same cage, as animals experiencing hyperalgesia—a heightened sensitivity to pain—from tissue damage or withdrawal of opiates. The "bystander" animals also displayed hyperalgesia, which was mediated by olfactory cues. —PLY

Sci. Adv. 10.1126/sciadv.1600855 (2016).

GROUP DYNAMICS

Belief system dynamics

People tend to structure their beliefs in a way that appears consistent to them. But how do some beliefs within groups persist in the face of social pressure, whereas others change and, by changing, influence a cascade of other beliefs? Friedkin *et al*. developed a model that can describe complexes of attitudes in a group that interact and change (see the Perspective by Butts). Their model revealed how the changing views of the U.S. population on the existence of weapons of mass destruction in Iraq changed their views on whether the invasion by the United States was justified. —BJ

Science, this issue p. 321; see also p. 286

METALLURGY

A shocking transformation for silver

Clever processing of metals leads to technologically

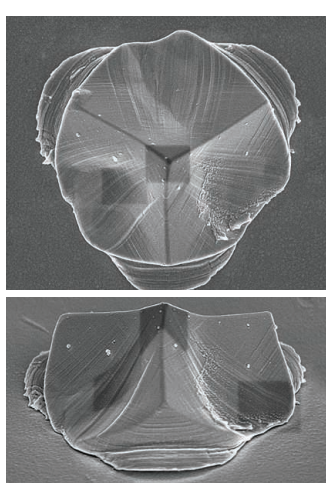

Silver microcubes deformed by high-velocity impact

CREDITS (TOP TO BOTTOM): PENG *ET AL.*; BRIAN ZWIEBEL; THEVAMARAN *ET AL.*

Published by AAAS

useful properties such as increased hardness and ductility. Thevamaran *et al*. fired specially synthesized silver cubes at a hard piece of silica, which produced a shock wave that dramatically changed the microstructure of the silver. The approach produced an extreme range in grain sizes that is useful for creating bendable yet strong metals. —BG

Science, this issue p. 312

MUCOSAL IMMUNITY

Sopping up IL-22 drives intestinal disease

The causes of inflammatory bowel disease (IBD) such as Crohn's disease and ulcerative colitis are likely complex and multifactorial, involving loss of epithelial cell integrity, chronic inflammation, and changes to the microbiota. Pelczar *et al*. investigated potential disease-driving mechanisms by studying IBD patients and mouse models. IBD patients express elevated levels of interleukin-22 binding protein (IL-22BP), which binds to the protein IL-22, preventing its tissue repair–promoting actions. Moreover, IBD development in mouse models requires IL-22BP. Lastly, IBD patients responding to therapy with antibodies against tumor necrosis factor–α exhibited reduced levels of IL-22BP but retained IL-22 expression, suggesting one mechanism by which this therapy may act. —KLM

Science, this issue p. 358

FORCE SPECTROSCOPY

Many tiny force sensors

Several techniques can measure forces on biomolecules, but the need to connect the molecule to the macroscopic world often limits the rate at which data can be taken. Nickels *et al*. created large arrays of nanoscale force sensors by using DNA origami structures. Single-stranded DNA molecules of different lengths attached to the molecule of interest acted as entropic springs, with shorter strands exerting more force. The authors used their setup to study the bending of DNA induced by the TATA-binding protein. —PDS

Science, this issue p. 305

CANCER

Metastasis casts a NET

Neutrophil extracellular traps, or NETs, are DNA structures that are produced by neutrophils in response to infection and can promote the spread of cancer in the presence of infection. Park *et al.* discovered that even in the absence of infection, metastatic breast cancer cells can stimulate neutrophils to form NETs, which further support the spread of metastasis. The authors also demonstrated an approach to breaking this vicious cycle by using nanoparticles coated with deoxyribonuclease I, an enzyme that breaks down the DNA NETs. This treatment was effective at reducing lung metastases in mice, demonstrating the potential of NETs as a therapeutic target. —YN

Sci. Transl. Med. **8**, 361ra138 (2016).

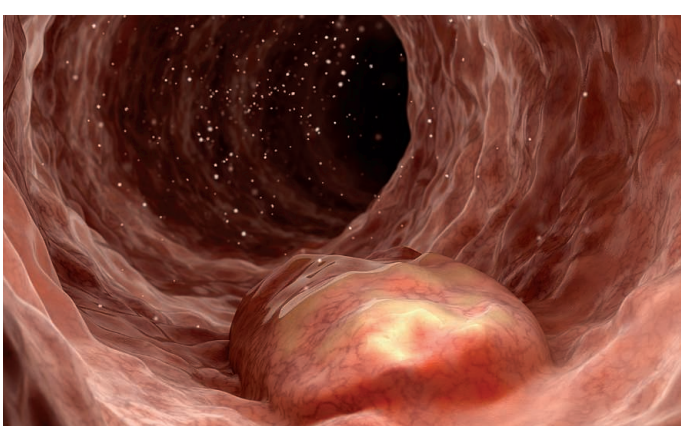

Illustration of an abnormal growth and inflammation in bowel disease

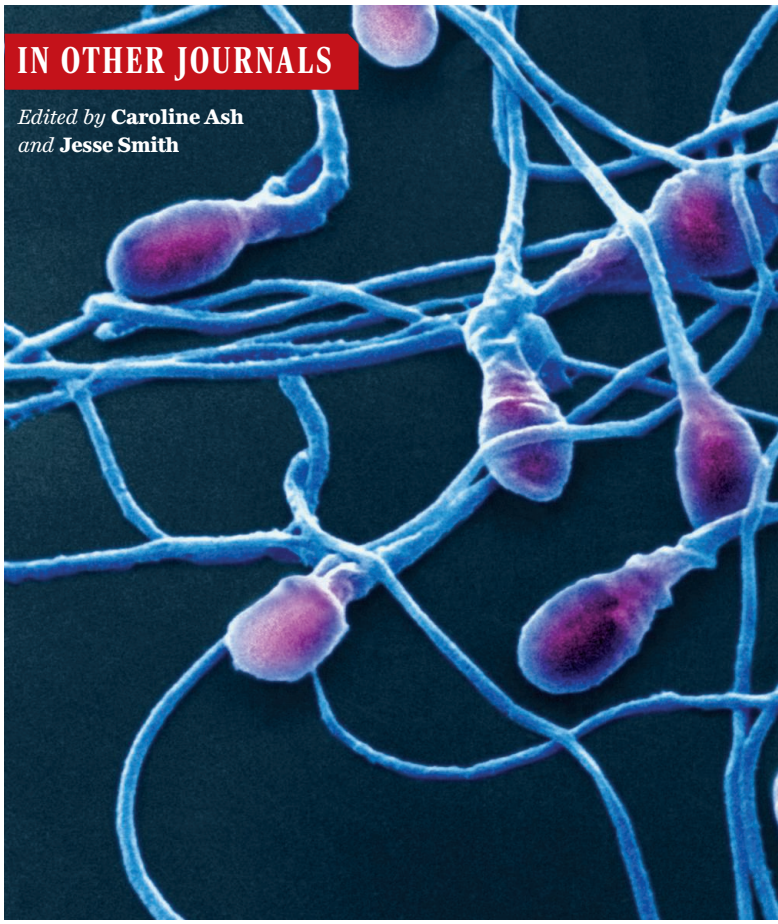

IN OTHER JOURNALS

Edited by **Caroline Ash** *and* **Jesse Smith**

T CELL MEMORY

Priming for T cell memory in tissues

During infections, dendritic cells prime T cell immunity and drive a subset of T cells to become long-lived memory cells. Memory T cells come in two flavors: those that circulate and those that establish long-term residency in tissues (Trm). Iborra *et al*. investigated the priming requirements of each type of cell in mice. Direct antigen presentation by dendritic cells is sufficient for generating circulating memory $CD8^+$ T cells. In contrast, $CD8^+$ Trm cells require antigen cross-presentation by dendritic cells that express DNGR-1, a protein receptor that binds necrotic cells. Without either DNGR-1 or cross-presenting dendritic cells, mice form few Trm cells in response to viral infection. —KLM

Immunity 10.1016/j.immuni.2016.08.019 (2016).

ENERGY EFFICIENCY

Better buildings' appetites for energy

Building codes targeting energy efficiency may not lead to obvious reductions in energy consumption, particularly compared with optimistic engineering predictions made before enacting the codes. Levinson studied homes in California where, since 1978, increasingly ambitious building regulations have targeted energy efficiency. But after controlling for factors such as home size, location, and occupant demographics; measuring consumption responses to temperature changes; and comparing with consumption in other states, newer homes built to meet California's stricter standards used no less energy than older ones. Although no direct impact on energy consumption was observed, the codes may have still had benefits, such as allowing residents

PHOTOS (FROM LEFT): SPRINGER MEDIZIN/SCIENCE SOURCE; DR. DAVID PHILLIPS/VISUALS UNLIMITED, INC.

Published by AAAS

PHOTO: DUBEY *ET AL.*, DEVELOPMENTAL CELL **38** (12 SEPTEMBER 2016) © CELL PRESS

REPRODUCTIVE BIOLOGY

Somatic cells raise sperm barriers

Sperm release is a potential target for contraception. Using time-lapse studies of sperm release from *Drosophila* testes ex vivo, Dubey *et al*. found that spermatid tails are released from the testes before the heads. Before ejection, spermatid heads attempt to penetrate the somatic cells of the testes but are repelled. Localized actin nucleation in the cortex of the somatic cell generates a mechanical barrier, preventing invasion. This response has similarities to the regulation of sperm release in mammals. —SEH

Dev. Cell **38**, 507 (2016).

Testes cells block sperm reentry with actin.

to stay more comfortably warm or cool for a given amount of energy consumption and corresponding greenhouse gas emissions. —BW

Amer. Econ. Rev. 10.1257/aer.20150102 (2016).

MATERIALS SCIENCE

Breaking the strongest of bonds

Boron carbide is an extremely hard ceramic used for applications such as bulletproof vests. Its exceptional properties are due to the bond strength in boron-carbon chains and clusters. Xie *et al.* show that the boron-carbon bond isn't quite as unbreakable as it may seem. The researchers found evidence for the complete destruction of 12-atom boron carbide clusters during laser-assisted evaporation while performing atom probe experiments. This result defies the expectation that these clusters are hard to break and may help explain the decrease in ballistic performance at high impact rates. —BG

Proc. Natl. Acad. Sci. U.S.A. 10.1073/pnas.1607980113 (2016).

MICROPOROUS COMPOUNDS

Creating a polybenzene network

Metal-organic framework (MOF) compounds are microporous materials in which inorganic centers are linked with organic ligands. Some network topologies, such as the diamond lattice, are formed by many MOFs, whereas others require specific linker positioning. One of the most difficult to form is the polybenzene (pbz) network that results from connecting phenyl rings via single carbon-carbon bonds into a three-dimensional network. Alezi *et al*. show that a six-connected hexagonal zirconium(IV) cluster can link a hexagonal ligand (a phenyl group substituted with carboxylate-terminated biphenyl groups) to form a pbz network. Structural studies verified an appropriate dihedral angle (70.5°) between the central phenyl ring of the linker and the hexagonal zirconium center. The material is not high-porosity but achieves high uptakes of methane at high pressures. —PDS

J. Am. Chem. Soc. 10.1021/jacs.6b08176 (2016).

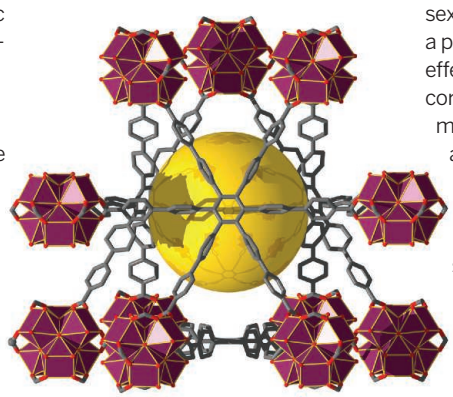

Cartoon of a zirconium-based metal-organic framework with the polybenzene (pbz) structure

CANCER THERAPY

A hat trick for differentiation therapy?

Most forms of acute myeloid leukemia (AML) are associated with a poor prognosis. One exception is acute promyelocytic leukemia, which is largely curable by two drugs, one originating from traditional Chinese medicine. Both drugs act by forcing leukemic precursor cells to differentiate into mature cell types that no longer divide. Given that all forms of AML are characterized by preleukemic myeloid cells whose differentiation is arrested, Sykes *et al.* performed an unbiased screen for compounds that induce myeloid differentiation. Unexpectedly, the most active compounds in mouse and human models were inhibitors of dihydroorotate dehydrogenase, an enzyme involved in pyrimidine biosynthesis. These inhibitors slowed AML development in mice and thus may merit further study as a therapy for the human disease. —PAK

Cell **167**, 171 (2016).

NEUROSCIENCE

Explaining gender differences in anxiety

Differences in the way brain neuronal circuits respond to the hormone oxytocin can explain gender-dependent variation in behavior. Li *et al.* found that a set of oxytocin-responsive neurons are anatomically similar in both sexes, but in males, they secrete a protein that antagonizes the effect of the stress-associated corticotropin-releasing hormone. This interaction provides an anti-anxiety effect with oxytocin that is not seen in females. Such signaling differences could underlie sex-dependent differences in social or emotional disorders and may reveal new mechanisms for therapeutic intervention. —LBR

Cell 10.1016/j.cell.2016.08.067 (2016).

Published by AAAS

ALSO IN *SCIENCE* JOURNALS

Edited by **Stella Hurtley**

BIOMASS PROCESSING

Formaldehyde protects and serves

The lignin found in plants is a desirable renewable feedstock for fuels and other useful compounds. Breaking down such a strong, energy-dense polymer, however, requires pretreatment of plant biomass under harsh conditions. These pretreatment steps often cause side reactions within the polymer itself, which lower the overall yields of lignin monomers. Shuai *et al*. used formaldehyde during pretreatment to block the reactive groups that lead to carbon-carbon linkages in lignin. This simple step stabilized lignin during pretreatment, resulting in dramatically improved yields. —NW

Science, this issue p. 329

ORGANIC CHEMISTRY

How to turn olefins into nucleophiles

The Grignard reaction has a storied place in the development of organic chemistry. Recognized by the Nobel Prize more than a century ago, this coupling of organomagnesium halides with carbonyl compounds remains a widely used route to carbon-carbon bonds. Nguyen *et al*. review an emerging alternative protocol that replaces the sensitive magnesium reagent with a catalytically activated olefin and a reductant such as hydrogen or an alcohol. In addition to safety and efficiency considerations, this class of reactions benefits from the high abundance and low cost of the olefins. —JSY

Science, this issue p. 300

STRUCTURAL BIOLOGY

Gating a calcium channel

The type 2 ryanodine receptor (RyR2) controls the release of calcium ions from the sarcoplasmic reticulum in cardiac cells—the initiating step in cardiac muscle contraction. Mutations in RyR2 are associated with cardiac diseases. Peng *et al*. used single-particle electron cryomicroscopy to determine the structure of RyR2 from porcine heart at 4.4-Å resolution with the calcium channel closed and at 4.2-Å resolution with the calcium channel open. The structures reveal how interdomain motions result in a conformational change in the cytoplasmic region of RyR2 that is transduced by a central domain to cause motions that open or close the channel. —VV

Science, this issue p. 301

SOLID-STATE PHYSICS

Relating interactions and nematicity

The electronic system in a strongly correlated material can sometimes be less symmetrical than the underlying crystal lattice. This loss of symmetry, caused by interactions and dubbed electronic nematicity, has been observed in a number of exotic materials. However, establishing a direct connection between the interactions and nematicity is tricky. Feldman *et al*. used scanning tunneling microscopy to image the wave functions of electrons on the surface of bismuth placed in an external magnetic field. The exchange interactions in the material caused a loss of symmetry, which was reflected in the orientations of the electrons' elliptical orbits. —JS

Science, this issue p. 316

DEVICE TECHNOLOGY

Almost-off transistors

Wearable devices and environmental sensors ideally should consume very little power to avoid the need for batteries that would have to be replaced. Lee and Nathan developed a thin-film transistor (TFT) from In-Ga-Zn-O thin films. To make the material less conductive, the films were fabricated to avoid oxygen vacancies. The TFT operated at ultralow power (less than 1 nW) and at switching voltages of less than 1 V with very high intrinsic gain. The devices work by changing the height of the so-called Schottky barrier formed between the semiconductor gate material and the metal drain contact. —PDS

Science, this issue p. 302

CHEMICAL PHYSICS

Acetylene's scission visualized by selfie

Can molecules take pictures of themselves? That is more or less the principle underlying laser-induced electron diffraction (LIED): A laser field strips an electron from a molecule and then sends it back to report on the structure of the remaining ion. Wolter *et al*. applied this technique to acetylene to track the cleavage of its C–H bond after double ionization (see the Perspective by Ruan). They imaged the full structure of the molecule and also distinguished more rapid dissociative dynamics when it was oriented parallel rather than perpendicular to the LIED field. —JSY

Science, this issue p. 308; see also p. 283

MICROBIOLOGY

Consenting mycobacteria

Mycobacteria encompass several slow-growing pathogens, including organisms that cause leprosy and tuberculosis. Mycobacteria use a component of their ESX (or Type VII) secretion system for a distinctive form of genetic exchange called distributive conjugal DNA transfer. Gray *et al.* investigated a quicker-growing model species, *Mycobacterium smegmatis*. They found that the secretory apparatus, ESX-4, is essential for DNA transfer into the recipient but is not required for donor cells to pass along their DNA. The ESX-1 secretory apparatus was required in the recipient for ESX-4 induction, but it did not appear to provide the physical channel for DNA. Rather, ESX-1 may secrete cell-surface "mating factor" receptors. More research will be needed to understand the details of this intriguing means of DNA exchange in mycobacteria. —CA

Science, this issue p. 347

PLANKTON DYNAMICS

Drivers of phytoplankton blooms

Despite decades of study, there is little evidence to link increases in phytoplankton growth in response to springtime warming with the dynamics of phytoplankton blooms. This lack of understanding makes it difficult to make predictions about global biogeochemical cycling in response to climate change. Hunter-Cevera *et al*. analyzed over a decade of data collected hourly from the New England shelf between 2003 and 2016 (see the Perspective by Worden and Wilken). Blooms now occur 20 days earlier than at the start of observations, because earlier springtime warming stimulates cell division earlier each year. Nevertheless, despite the shift in timing, predatory organisms in the food chain are still ready to consume the superabundance, which brings the blooms to an abrupt end each year. —CA

Science, this issue p. 326; see also p. 287

PALEONTOLOGY

Jaws from the jawless

Until a fossil called Entelognathus was found to contain a tripartite jaw a few years ago, it was believed that the skeletons of early osteichthyans (bony fish), the ancestors of all vertebrates, were derived

Published by AAAS

independently of those of the earlier placoderms (so-called jawless fish). Zhu *et al.* now describe a second Silurian placoderm that more securely bridges the jawless toothlike plates of placoderms to the development of the jawed condition that ultimately led to the three-boned jaw in ancestors of modern vertebrates (see the Perspective by Long). This finding upends the traditional belief that the two types of jaw were nonhomologous and sheds light on the evolution of the complex maxilla, a key component of diversification across many modern taxa, including humans. —SNV

Science, this issue p. 334; see also p. 280

PLANT PHOTOBIOLOGY

Turning off the blue-light response

In plants, blue light is perceived by cryptochromes, which, once activated, set off signaling events that regulate gene expression, circadian rhythms, and photomorphogenesis. Wang *et al*. now show that in the model plant *Arabidopsis*, one of the functions of activated cryptochromes, which are dimers or oligomers when active, is to activate production of the protein BIC1 (blue-light inhibitor of cryptochromes 1) (see the Perspective by Fankhauser and Ulm). BIC1 then favors monomerization and thus inactivation of the cryptochromes. This feedback loop resets the system so that blue-light responses can be turned off as well as turned on. —PJH

Science, this issue p. 343; see also p. 282

ENZYMOLOGY

Enzymes for making (or breaking) methane

The last enzymatic step of microbial methanogenesis, and the first step of microbial methane oxidation, relies on the nickel-containing tetrapyrrole coenzyme F430. The successful metabolic engineering of any organism to enzymatically consume methane thus also needs the appropriate machinery to synthesize this compound. Using comparative genomics, Zheng *et al*. identified several candidate genes responsible for coenzyme F430 biosynthesis. Cloning and expression of all the subsequent proteins in *Escherichia coli* confirmed the complete in vitro conversion of sirohydrochlorin into mature F430. —NW

Science, this issue p. 339

EBOLAVIRUSES

Treating Ebola with a Trojan horse

The recent major Ebola virus outbreak in West Africa highlighted the need for effective therapeutics against this and other filoviruses. Neutralizing ebolaviruses with antibodies is a challenge because the viruses bind their entry receptor, NPC1, inside the cell within endosomes rather than on the cell surface. Furthermore, enzymes in endosomes cleave the Ebola virus surface glycoprotein (GP) to reveal its receptor binding site. Wec *et al*. now report a bispecific antibody strategy targeting all known ebolaviruses that overcomes this problem (see the Perspective by Labrijn and Parren). They coupled an antibody specific for a conserved, surface-exposed epitope of GP to antibodies that recognize either NPC1 or the NPC1 binding site on GP. Treating mice therapeutically with these antibodies allowed them to survive otherwise lethal ebolavirus infection. —KLM

Science, this issue p. 350; see also p. 284

MICROBIOLOGY

Directing the movement of a pathogen

The opportunistic pathogen *Pseudomonas aeruginosa* is particularly resistant to antibiotic treatment when it forms biofilms. Biofilm formation requires both random migration (to enable adjustment to constantly changing conditions) and directed migration (also called chemotaxis). Xu *et al*. found that binding of the bacterial messenger cyclic diguanylate monophosphate to the adaptor protein MapZ suppressed random migration and biofilm formation by *P. aeruginosa* (see the Focus by Orr and Lee). Thus, the MapZ-associated pathway could potentially be targeted to prevent the chronic and hard-to-treat infections caused by *P. aeruginosa*.—WW

Sci. Signal. **9**, ra102 and fs16 (2016).

INFECTIOUS DISEASES

Persistent infections "interfere" with B cells

Certain pathogens, including HIV, hepatitis virus, and lymphocytic choriomeningitis virus (LCMV), cause persistent infections that are often associated with suboptimal antibody responses. Fallet *et al*., Moseman *et al*., and Sammicheli *et al*. found that up-regulation of type 1 interferon (IFN-1) in the early phase of LCMV infection in mice contributed to premature deletion of virus-specific B cells. Blocking IFN-1 prevented this B cell deletion. Although the studies agree that IFN-1 does not act directly on B cells, they find that distinct immune cells mediate IFN-1–dependent deletion of B cells, depending on the system examined. A related Focus by Laidlaw *et al*. highlights how targeting the IFN-1 pathway could restore B cell responses during persistent viral infections in humans. —AB

Sci. Immunol. 10.1126/sciimmunol.aah6817, 10.1126/sciimmunol.aah3565, 10.1126/sciimmunol.aah6789, and 10.1126/sciimmunol.aaj1836 (2016).

Published by AAAS

REVIEW SUMMARY

ORGANIC CHEMISTRY

Metal-catalyzed reductive coupling of olefin-derived nucleophiles: Reinventing carbonyl addition

Khoa D. Nguyen, Boyoung Y. Park, Tom Luong, Hiroki Sato, Victoria J. Garza, Michael J. Krische*

BACKGROUND: Since the discovery of the Grignard reaction more than a century ago, carbonyl addition mediated by premetalated reagents has played a central role in synthetic chemistry. Metal-catalyzed reductive coupling of π-unsaturated reactants with carbonyl compounds has emerged as an alternative to classical carbonyl addition. Although such processes bypass stoichiometric organometallic reagents and the issues of safety, selectivity, and waste associated with their use, in many cases the requisite terminal reductants are just as problematic as the organometallic reagents they replace. Catalytic reductive coupling via hydrogenation or transfer hydrogenation represents a more ideal strategy for carbonyl addition as relatively safe, inexpensive reductants with low molecular weights may be used (H_2 or 2-propanol). Carbonyl addition via hydrogen autotransfer is most ideal. In such processes, hydrogen embedded within a reactant alcohol mediates reductive coupling. By allowing alcohols to serve dually as reductant and proelectrophile (carbonyl precursor), this strategy completely bypasses the use of exogenous reductants, enabling byproduct-free carbonyl addition from the alcohol oxidation level—that is, the direct conversion of lower alcohols to higher alcohols. Alcohols are typically cheaper and more tractable than the corresponding carbonyl compounds, which is a further benefit of this approach. Ethylene ($H_2C{=}CH_2$) and α-olefins are the simplest π-unsaturated reactants and are manufactured on a vast scale at production volumes exceeded only by alkanes. Hence, the discovery and development of catalytic methods that exploit olefin-derived nucleophiles in byproduct-free carbonyl reductive coupling represents an especially important goal of chemical research.

ADVANCES: Methods for the metal-catalyzed reductive coupling of π-unsaturated reactants with carbonyl partners have expanded considerably in recent years. A broad palette of catalysts comprising diverse metals, ligands, and terminal reductants offers access to a surprising array of transformations. In addition to providing catalytic variants of classical carbonyl additions, the mechanisms availed by transition metal catalysts have unlocked broad, new capabilities and access to hitherto unavailable volumes of chemical space. Despite these advances, intermolecular catalytic reductive coupling of simple linear α-olefins with unactivated carbonyl partners remains an unmet and multifaceted challenge. Beyond defining active catalysts, the use of such abundant reactants mandates an additional consideration: the identification of terminal reductants that are equally inexpensive. Additionally, to avoid waste generation (a major issue in the context of large-volume chemical manufacture), byproduct-free methods for reductive coupling are highly preferred. Hence, processes mediated by elemental hydrogen or hydrogen autotransfer processes that exploit hydrogen embedded in the alcohol reactant itself are especially attractive. This latter class of catalytic C–C bond–forming processes was only recently discovered.

ON OUR WEBSITE

Read the full article at http://dx.doi.org/10.1126/science.aah5133

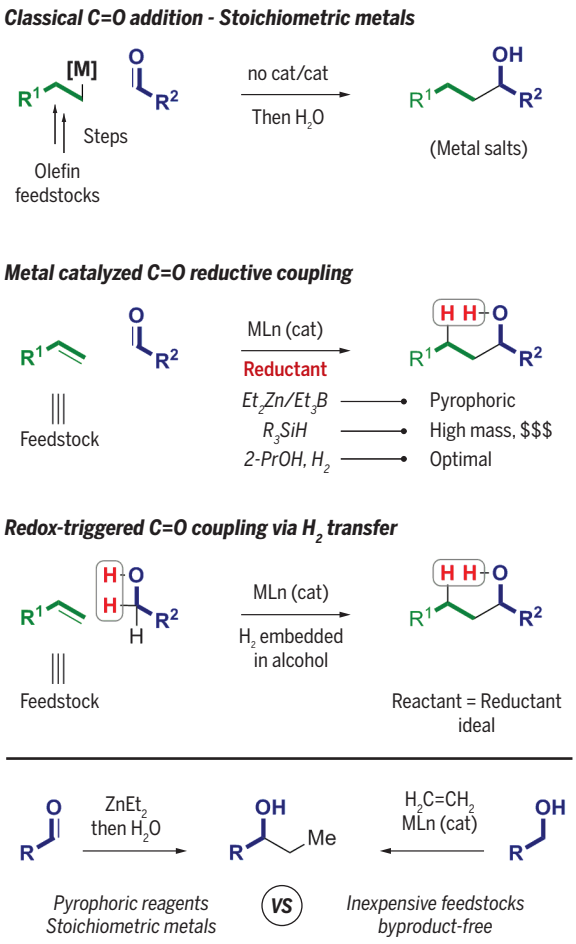

Evolution of carbonyl addition chemistry. The progression from (**top**) premetalated reagents, to (**top middle**) reductive couplings mediated by external reductants, and last, (**bottom middle**) byproduct-free reductive couplings powered by hydrogen autotransfer. (**Bottom**) Departure from preformed organometallic reagents in carbonyl addition.

OUTLOOK: The prototypical metal-catalyzed reductive C–C bond formation and largest-volume application of homogenous catalysis is hydroformylation (>10 million metric tons/year), which transforms olefins into aldehydes through reaction with carbon monoxide and hydrogen. Despite longstanding use of this chemistry, the concept of hydrogen-mediated reductive coupling underlying hydroformylation lay dormant for decades. Systematic efforts to exploit hydrogenation and transfer hydrogenation in reductive couplings to carbonyl compounds have only begun to emerge. The impact is clear: Reactions that traditionally have used organometallic reagents may now be conducted catalytically in the absence of premetalated reagents or stoichiometric byproducts. Among the numerous possibilities for growth in this area, the development of catalytic systems for the intermolecular reductive coupling of ethylene and simple linear α-olefins with unactivated carbonyl partners remains an important, elusive objective. Reactions conducted from the alcohol oxidation level via hydrogen autotransfer offer a promising approach to catalytic processes of this type. ■

The list of author affiliations is available in the full article online.
*Corresponding author. Email: mkrische@mail.utexas.edu
Cite this article as K. D. Nguyen *et al.*, *Science* 354, aah5133 (2016). DOI: 10.1126/science.aah5133

Downloaded from http://science.sciencemag.org/ on October 20, 2016

REVIEW

ORGANIC CHEMISTRY

Metal-catalyzed reductive coupling of olefin-derived nucleophiles: Reinventing carbonyl addition

Khoa D. Nguyen, Boyoung Y. Park, Tom Luong, Hiroki Sato, Victoria J. Garza, Michael J. Krische*

α-Olefins are the most abundant petrochemical feedstock beyond alkanes, yet their use in commodity chemical manufacture is largely focused on polymerization and hydroformylation. The development of byproduct-free catalytic C–C bond–forming reactions that convert olefins to value-added products remains an important objective. Here, we review catalytic intermolecular reductive couplings of unactivated and activated olefin-derived nucleophiles with carbonyl partners. These processes represent an alternative to the longstanding use of stoichiometric organometallic reagents in carbonyl addition.

Byproduct-free catalytic C–C bond–forming reactions of α-olefins are of great commercial interest. Hydroformylation (*1*, *2*) and single-site alkene polymerization (*3*) are now among the largest-volume applications of homogenous metal catalysis. Carbonyl compounds represent another abundant class of chemical feedstock that are derived from α-olefins via hydroformylation (oxo-products) (*1*, *2*) or Wacker oxidation (*4*). Despite the availability of α-olefins and carbonyl compounds, there is a striking paucity of catalytic processes for the coupling of these orthogonal feedstocks. Here, we review direct methods for the metal-catalyzed reductive coupling of olefins with carbonyl compounds. Transformations are cataloged according to their use of (i) unactivated or less activated olefins (α-olefins and styrenes), (ii) conjugated olefins (1,3-dienes, 1,3-enynes), and (iii) highly activated olefins (enones, acrylates, and vinyl azines) (Fig. 1). Multicomponent reactions, reductive couplings of allenes, reductive carboxylation, and carbonyl additions in which olefins are reduced in situ to form stoichiometric quantities of premetalated reagent—for example, through hydroboration or hydrozirconation—are not covered.

Department of Chemistry, University of Texas at Austin, Austin, TX 78712, USA.
*Corresponding author. Email: mkrische@mail.utexas.edu

α-Olefins and styrenes

Intermolecular catalytic reductive coupling of simple linear α-olefins with unactivated carbonyl partners remains an unmet challenge. Titanocene-catalyzed silane-mediated reductive cyclizations of 1,5-enones and enals were reported by Kablaoui and Buchwald (*5*, *6*) and Crowe and Rachita (*7*) in 1995; however, intermolecular variants remain elusive. The concept of transfer hydrogenative carbonyl addition introduced by our laboratory (*8*–*10*) provides an important inroad to this problem. Through the use of ruthenium(0) catalysts, vicinally oxygenated secondary alcohols serve dually as reductants and carbonyl precursors (Fig. 2) (*11*, *12*). Ethylene, propylene, 1-octene, styrene, and a host of other terminal olefins were found to engage in highly regio- and diastereoselective C–C coupling with 3-hydroxy-2-oxindoles to form the corresponding tertiary alcohols (*11*). The scope of this process was extended through the use of related osmium(0) catalysts (*12*), which promote the C–C couplings of ethylene and 1-octene with diols, α-ketols, or α-hydroxy esters by way of vicinal dicarbonyl intermediates. The collective data corroborate a catalytic mechanism involving oxametalacyclopentane formation via olefin-carbonyl oxidative coupling. Transfer hydrogenolysis of the metalacycle mediated by the reactant alcohol releases the product and regenerates the requisite carbonyl partner. As indicated in the general catalytic mechanism, carboxylic acid cocatalysts dramatically enhance rate and conversion in these processes (Fig. 2), an effect that may be attributed to intervention of 6-centered transition structures for both protonolytic cleavage of the metalacycle and substitution of the carboxylate ligand by the

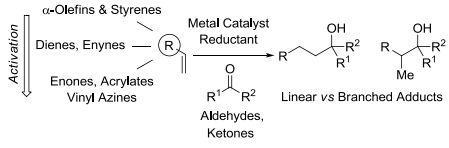

Fig. 1. Metal-catalyzed reductive coupling of unactivated and activated olefin-derived nucleophiles with carbonyl compounds.

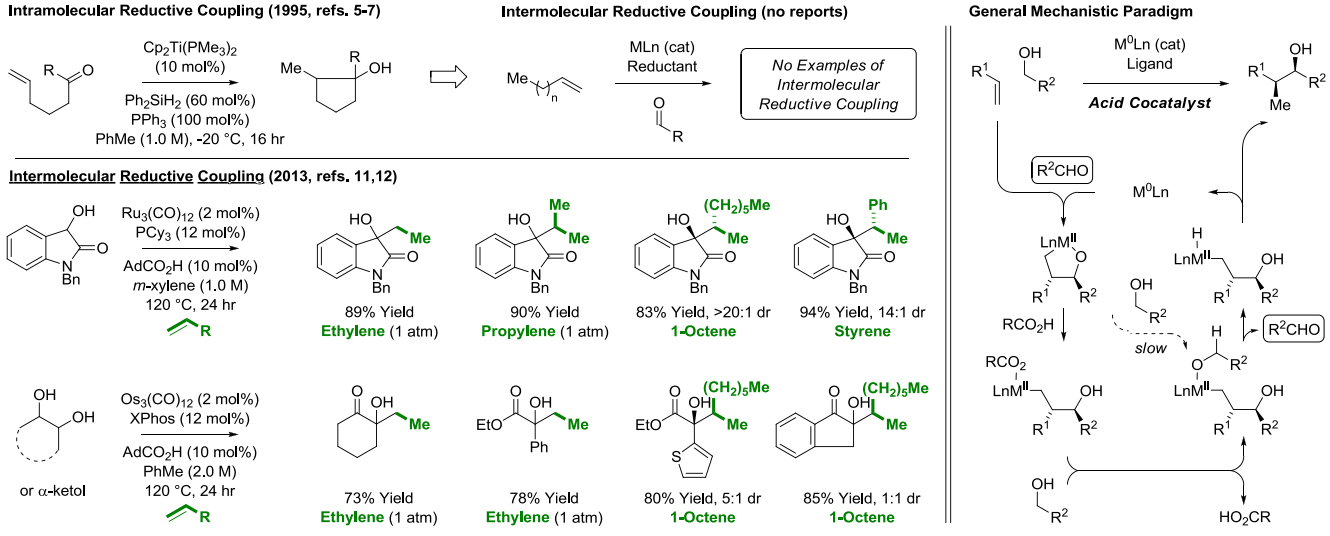

Fig. 2. Metal-catalyzed reductive coupling of α-olefins with carbonyl partners. $AdCO_2H$ refers to 1-adamantane carboxylic acid. X-Phos, 2-dicyclohexylphosphino-2′,4′,6′-triisopropylbiphenyl.

Downloaded from http://science.sciencemag.org/ on October 20, 2016

reactant alcohol at the metal center. Related C–C couplings of vinyl carboxylates with activated secondary alcohols result in metalacycle fragmentation to form products of vinyl transfer (*13*).

Anhydrides represent an alternate class of carbonyl electrophile that have proven effective in catalytic reductive couplings with styrenes and certain α-olefins (Fig. 3). After initial observations by Kokubo *et al.* (*14*), we reported a highly regioselective rhodium-catalyzed olefin-anhydride reductive coupling mediated by elemental hydrogen (*15*). Subsequently, an enantioselective variant of this process involving copper catalysts was developed by Bandar *et al.* (*16*). Oxidative coupling-metalacycle fragmentation pathways are proposed for the hydrogen-mediated processes, whereas the copper-catalyzed reactions are postulated to operate via olefin hydrometalation to form σ-benzyl copper intermediates. Whereas hydroacylations using aldehydes as acyl donors require chelating groups to suppress conversion of the transient acyl metal intermediates to catalytically inactive carbonyl complexes, the present anhydride reductive couplings overcome this limitation (*17*).

Recently, an iron-catalyzed Prins-Meerwein-Ponndorf-Verley–type olefin-aldehyde reductive coupling mediated by 2-propanol was reported by Zheng *et al.* (Fig. 4) (*18*). Deuterium-labeling studies corroborate a catalytic mechanism in which condensation of the aldehyde with 2-propanol triggers nucleophilic attack by the olefin. The nascent cation is reduced via internal hydride transfer. As anticipated on the basis of this nonconcerted or asynchronous oxonia-ene mechanism, olefins that best stabilize the developing cation are the most efficient reactants. The use of unactivated α-olefins in these couplings would represent a major advance.

Dienes and enynes

Butadiene (12×10^6 metric tons/year), isoprene (0.8×10^6 metric tons/year), and myrcene (30×10^3 metric tons/year) are important chemical feedstocks. The first intermolecular metal-catalyzed reductive coupling of dienes with carbonyl compounds, a process mediated by triethylborane, was reported by Kimura *et al.* in 1998 (Fig. 5) (*19*, *20*). Diverse dienes may be converted to the respective homoallylation products in good yields and excellent levels of *anti*-1,3-diastereoselectivity. Regioselectivity in favor of coupling to the more substituted olefin moiety is observed. A mechanism involving diene-carbonyl oxidative coupling to form transient oxo-nickelacycles is postulated (*19*, *20*). Corresponding ketone homoallylations were developed by using diethylzinc as the terminal reductant (*21*). Asymmetric variants of the nickel-catalyzed diene-aldehyde reductive couplings are limited to 1,4-diaryl-butadienes (*22*, *23*). Whereas rhodium-catalyzed diene-carbonyl reductive coupling mediated by elemental hydrogen requires use of α-ketoaldehydes (*24*), ruthenium catalysts promote the reductive coupling of diverse dienes to unactivated aldehydes via transfer hydrogenation (*25*); 2-propanol or formic acid may serve as terminal reductant, or remarkably, the reactant itself may serve dually as reductant

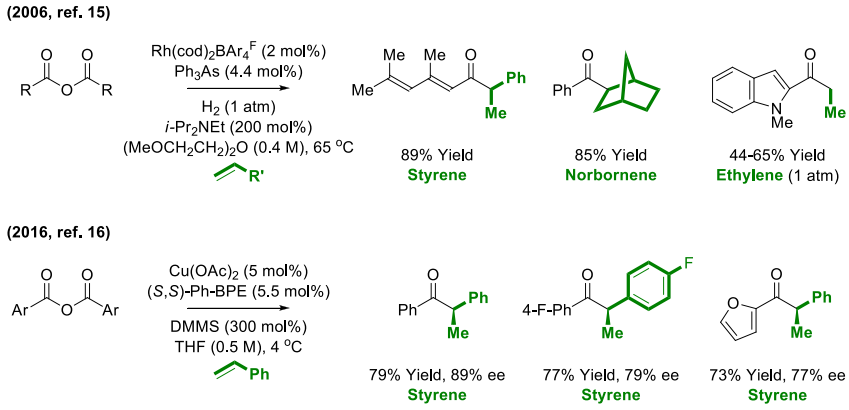

Fig. 3. Metal-catalyzed reductive coupling of olefins with anhydrides. (*S*,*S*)-Ph-BPE, 1,2-bis[(2*S*,5*S*)-2,5-diphenylphospholano]ethane; DMMS, dimethoxymethylsilane.

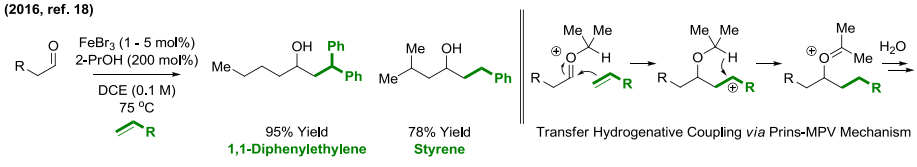

Fig. 4. Iron-catalyzed Prins-Meerwein-Ponndorf-Verley–type olefin-aldehyde reductive coupling.

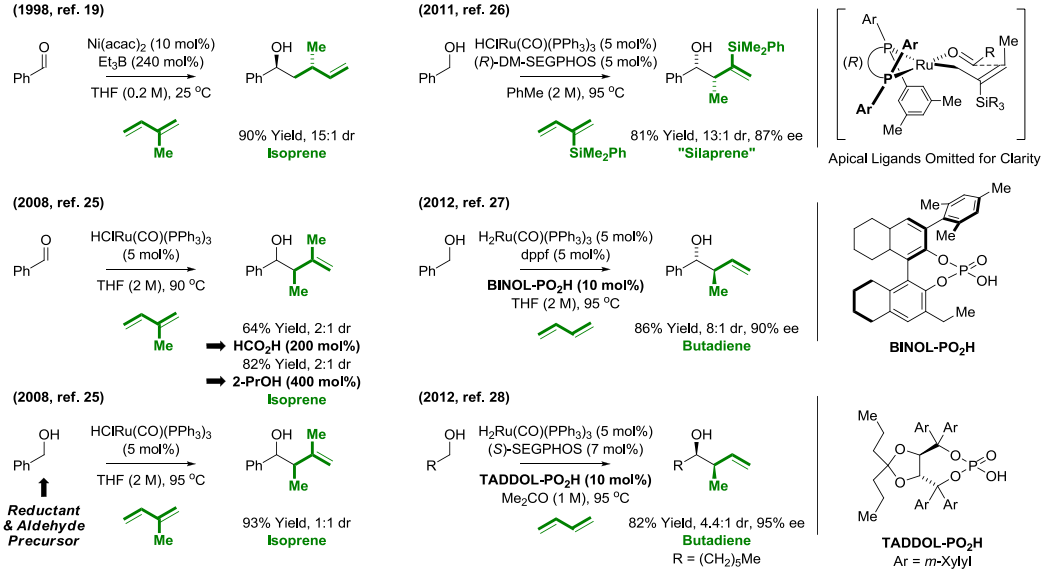

Fig. 5. Metal-catalyzed diene-carbonyl reductive coupling. dppf, 1,1-bis(diphenylphosphino)ferrocene; (*R*)-DM-SEGPHOS, (*R*)-(+)-5,5′–bis[di(3,5-xylyl)phosphino]-4,4′-bi-1,3-benzodioxole; (*S*)-SEGPHOS, (*S*)-(-)-5,5′-bis(diphenylphosphino)-4,4′-bi-1,3-benzodioxole; acac, acetylacetonate.

Downloaded from http://science.sciencemag.org/ on October 20, 2016

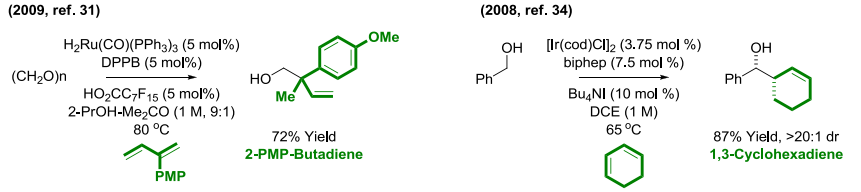

Fig. 6. Alternate regioselectivity and use of cyclic dienes in metal-catalyzed carbonyl reductive coupling. dppb, bis(diphenylphosphino)butane; biphep, 2,2′-bis(diphenylphosphino)-1,1′-biphenyl.

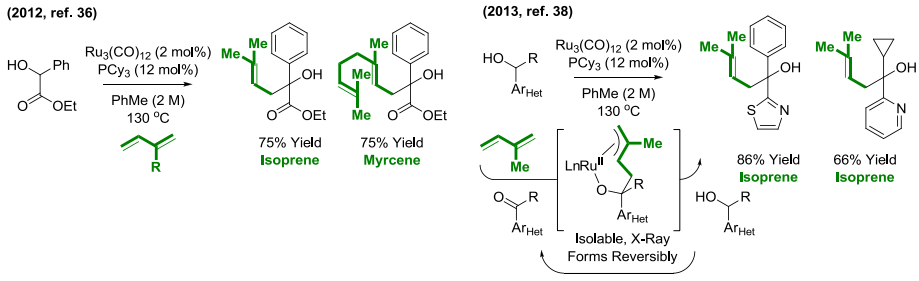

Fig. 7. Ruthenium(0)-catalyzed diene-ketone reductive coupling via hydrogen auto-transfer. PCy_3, tricyclohexylphosphine.

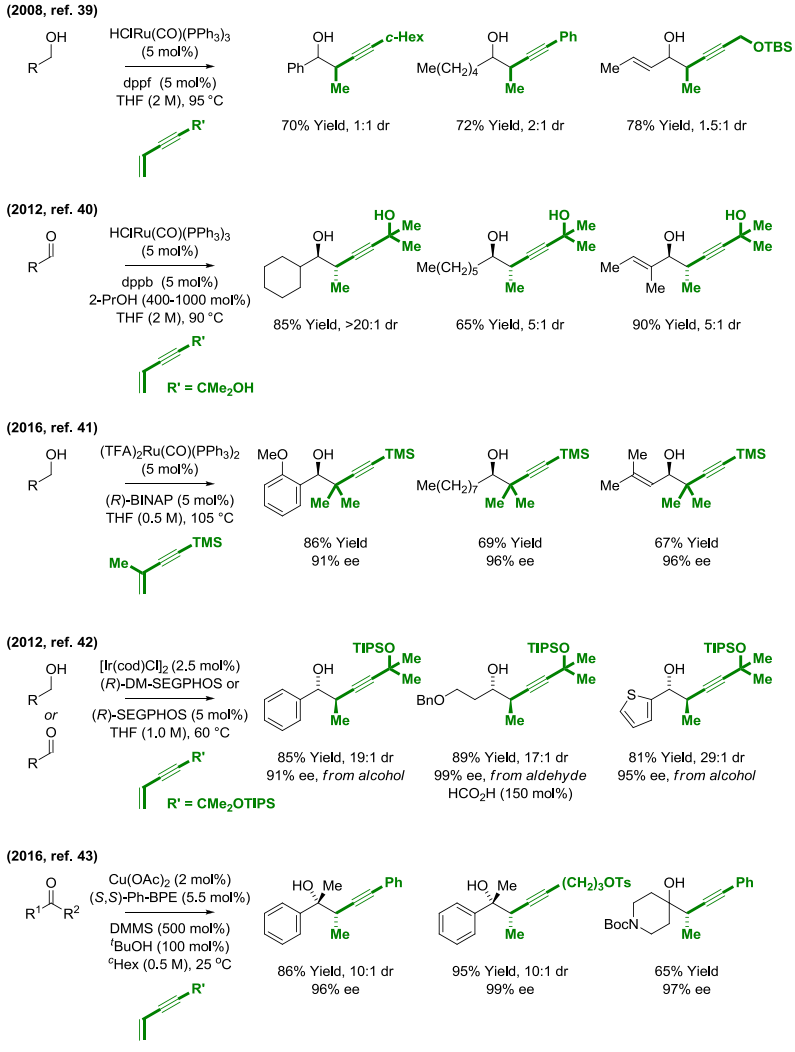

Fig. 8. Metal catalyzed enyne-carbonyl reductive coupling. DMMS, dimethoxymethylsilane; (*R*)-BINAP, (*R*)-(+)-2,2′-bis(diphenylphosphino)-1,1′-binaphthyl.

and carbonyl precursor. Enantioselective variants of the ruthenium-catalyzed reductive couplings have been developed (*26*–*29*). Whereas initial studies relied on the use of 2-silyl–substituted dienes to direct *syn*-diastereo and enantioselectivity (*26*), chiral phosphate counterions (*28*) enable access to either the *anti*- or *syn*-diastereomers with good control of enantioselectivity (*27*, *28*, *30*). The collective data are consistent with a catalytic mechanism in which alcohol dehydrogenation triggers diene hydrometalation (Fig. 5).

Ruthenium complexes that embody cationic character catalyze the reductive coupling of 2-substituted dienes to form all-carbon quaternary centers, as illustrated in 2-propanol–mediated reductive couplings with paraformaldehyde (Fig. 6) (*31*, *32*); a vacant or labile coordination site at the metal center facilitates reversible diene hydrometalation, enabling conversion of the kinetic π-allylruthenium isomer to the thermodynamically more stable, terminally disubstituted π-allyl species. Related hydrohydroxymethylations that directly use methanol (36×10^6 metric tons/year) as a coupling partner were reported for the first time by using an iridium catalyst and 1,1-disubstituted allenes as pronucleophiles (*33*). Indeed, iridium complexes also catalyze the reaction of dienes with carbonyl compounds to form secondary homoallylic alcohols (*33*, *34*). Cyclohexadiene (*34*) and butadiene (*35*) engage in either 2-propanol–mediated reductive coupling or, as shown, direct primary alcohol C–C coupling via hydrogen autotransfer (Fig. 6).

Ruthenium(0) catalysis enables reductive coupling of dienes with activated ketones from the secondary alcohol oxidation level via hydrogen autotransfer (Fig. 7) (*36*–*38*). Mechanistic studies corroborate a catalytic mechanism involving diene-carbonyl oxidative coupling to form an oxaruthenacycle. Hydrogen transfer from the secondary alcohol reactant mediates metalacycle hydrogenolysis, releasing the products of C–C coupling and regenerating the activated ketone to close the catalytic cycle. The regioselectivity of C–C coupling at the diene C4-position is distinct among diene-carbonyl reductive couplings. Beyond α-hydroxy esters (*36*), this process applies to 3-hydroxy-2-oxindoles (*37*) and heteroaryl-substituted secondary alcohols (*38*). In the latter case, the oxaruthenacycle intermediate was isolated and characterized, and reversible metalacycle formation was established through experiments involving diene exchange.

The reductive coupling of conjugated enynes with carbonyl compounds to form homopropargylic alcohols was first reported in 2008 (Fig. 8) (*39*). Through the use of the ruthenium catalyst derived in situ from $HClRu(CO)(PPh_3)_3$ and 1,1′-bis(diphenylphosphino)ferrocene (dppf), hydrogen is transferred from primary alcohols to 1,3-enynes to form aldehyde-allenylruthenium pairs that combine to deliver the products of C–C coupling as single regioisomers in the absence of stoichiometric byproducts. In corresponding 2-propanol–mediated reductive couplings of aldehydes with 2-propoxy–substituted enynes, good levels of *anti*-diastereoselectivity are achieved (*40*). The 2-propoxy

Downloaded from http://science.sciencemag.org/ on October 20, 2016

group of the product readily eliminates acetone upon exposure to aqueous sodium hydroxide to reveal the terminal alkyne. More recently, by using the chiral ruthenium complex derived in situ from $(TFA)_2Ru(CO)(PPh_3)_2$ and (*R*)-BINAP [(*R*)-(+)-2,2′-bis(diphenylphosphino)-1,1′-binaphthyl], the enantioselective C–C couplings of diverse primary alcohols with the commercially available 1,3-enyne, TMSC≡CC(Me)=CH_2, were reported (*41*). Metals other than ruthenium catalyze enyne-carbonyl reductive coupling. For example, an iridium catalyst with (*R*)-SEGPHOS [(*R*)-5,5′-bis(diphenylphosphino)-4,4′-bi-1,3-benzodioxole] or (*R*)-DM-SEGPHOS ligands catalyzes highly enantioselective enyne-carbonyl reductive coupling from the alcohol or aldehyde oxidation level (*42*). In the latter case, formic acid serves as terminal reductant. Last, copper complexes recently were found to catalyze the silane-mediated reductive coupling of 1,3-enynes with diverse ketones with excellent control of *syn*-diastereo- and enantioselectivity (Fig. 8) (*43*).

Acrylates, enones, and vinyl azines

The use of α,β-unsaturated carbonyl compounds as pronucleophiles in reductive couplings with carbonyl compounds is known as the "reductive aldol reaction" (*44*). After seminal studies by Revis and Hilty in 1987 on the rhodium-catalyzed reductive aldol reaction of acrylates with aldehydes and ketones mediated by silane (*45*), numerous processes of this type were developed by using different metal catalysts. We focus here on enantioselective intermolecular reductive aldol reactions (Fig. 9). Catalytic carbonyl reductive couplings of α,β-unsaturated carbonyl compounds that occur at the β-position are not covered (*46*).

The first enantioselective reductive aldol reaction was reported by Taylor *et al.* in 2000 (*47*). This reductive coupling of acrylic esters with aldehydes was catalyzed by a rhodium-BINAP catalyst by using Et_2MeSiH as the terminal reductant. High levels of enantioselectivity were accompanied by modest levels of *syn*-diastereoselectivity (Fig. 9). Mechanistic studies implicate hydrometalative pathways en route to rhodium enolates. Using an Ir(pybox) catalyst, improved *syn*-diastereo- and enantioselectivities were observed; however, inductively activated aldehydes are required (*48*). A remarkably general Rh(phebox) catalyst for asymmetric reductive aldol addition was subsequently reported by Nishiyama *et al.* (*49*). Uniformly high levels of *anti*-diastereoselectivity and enantioselectivity were observed across a diverse range of substrates, including additions to ketones (*50*). Ketone electrophiles are also accommodated by copper catalysts (*51*). The preceding examples of asymmetric reductive aldol coupling pair acrylate pronucleophiles with hydrosilane as terminal reductant. Vinyl ketones serve as pronucleophiles, with rhodium catalysts and H_2 as reductant (*52*). Substituting deuterium as the reductant leads to transfer of a single deuterium atom to the former enone β-position, which is consistent with a catalytic mechanism involving oxidative coupling followed by hydrogenolysis of the resulting metalacycle via σ-bond metathesis. Hydrometalative pathways cannot be excluded on the basis of these results; however, reversible hydrometalation–β-hydride elimination would be anticipated to diminish the extent of deuterium incorporation.

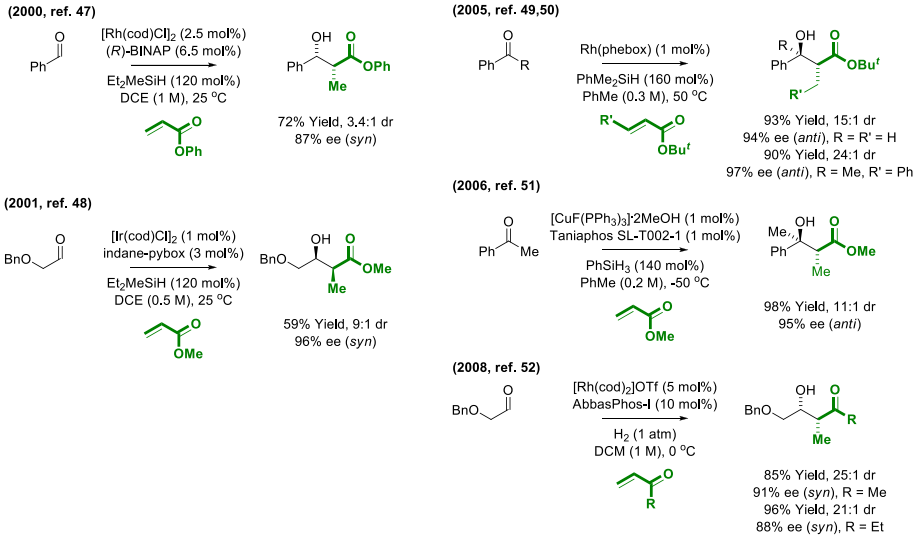

Fig. 9. Enantioselective metal-catalyzed reductive aldol reactions. The structures of indane-pybox, phebox, taniaphos, and AbbasPhos-I are provided in the cited references.

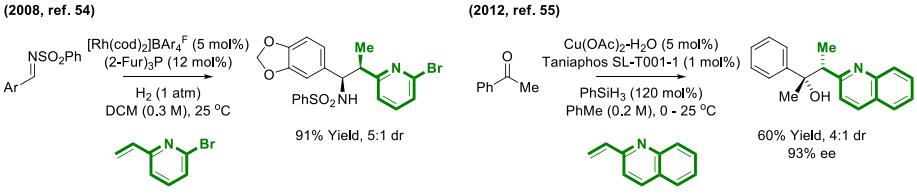

Fig. 10. Metal-catalyzed reductive coupling of vinyl azines.

Vinyl azines are isostructural with respect to α,β-unsaturated carbonyl compounds and, as described in the review literature (*53*), display analogous reactivity. However, their use as pronucleophiles in catalytic reductive coupling has only recently begun to be explored. In 2008, the first example of vinyl azine reductive coupling to a π-electrophile was achieved via rhodium-catalyzed hydrogenation of vinyl azines in the presence of imines (Fig. 10) (*54*). Good levels of *syn*-diastereoselectivity were observed. The Lam laboratory subsequently reported a copper-catalyzed coupling of vinyl azines to ketone electrophiles with good levels of *syn*-diastereoselectivity and excellent enantioselectivity (*55*). For both processes, optimal results are obtained by using vinyl azines in which both positions adjacent to nitrogen are substituted.

Conclusion and outlook

Intermolecular catalytic reductive coupling of simple linear α-olefins with unactivated carbonyl partners remains an important unmet challenge in chemical synthesis. For such abundant feedstocks, an additional consideration resides in identifying terminal reductants that are equally inexpensive and minimize or eliminate byproduct formation. Hence, byproduct-free processes mediated by elemental hydrogen or transfer hydrogenative C–C couplings of alcohol reactants are especially attractive. Conversely, processes mediated by reductants that are pyrophoric ($ZnEt_2$ and BEt_3) or those that are costly and mass-intensive (R_3SiH) can only be viewed as interim solutions. Despite the many unrequited challenges, progress made in the area of metal-catalyzed reductive coupling clearly shows that classical methods for carbonyl addition that traditionally have exploited stoichiometric organometallic reagents may be replaced with catalytic processes that bypass premetalated reagents (Fig. 11). It is our hope that this Review will inspire and guide future research aimed at unlocking carbonyl-addition chemistry beyond stoichiometric metals.

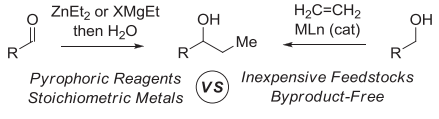

Fig. 11. A departure from preformed organometallic reagents in carbonyl addition.

REFERENCES AND NOTES

1. C. D. Frohning, C. W. Kohlpaintner, in *Applied Homogeneous Catalysis with Organometallic Compounds*, B. Cornils, W. A. Herrmann, Eds. (Wiley-VCH, 1996) pp. 29–104.
2. P. W. N. M. van Leeuwen, in *Homogeneous Catalysis: Understanding the Art* (Kluwer, 2004).

Downloaded from http://science.sciencemag.org/ on October 20, 2016

3. M. C. Baier, M. A. Zuideveld, S. Mecking, Post-metallocenes in the industrial production of polyolefins. *Angew. Chem. Int. Ed. Engl.* **53**, 9722–9744 (2014). doi: 10.1002/anie.201400799; pmid: 25146087
4. C. N. Cornell, M. S. Sigman, Recent progress in Wacker oxidations: Moving toward molecular oxygen as the sole oxidant. *Inorg. Chem.* **46**, 1903–1909 (2007). doi: 10.1021/ic061858d; pmid: 17348721
5. N. M. Kablaoui, S. L. Buchwald, Reductive cyclization of enones by a titanium catalyst. *J. Am. Chem. Soc.* **117**, 6785–6786 (1995). doi: 10.1021/ja00130a021
6. N. M. Kablaoui, S. L. Buchwald, Development of a method for the reductive cyclization of enones by a titanium catalyst. *J. Am. Chem. Soc.* **118**, 3182–3191 (1996). doi: 10.1021/ja954192n
7. W. E. Crowe, M. J. Rachita, Titanium-catalyzed reductive cyclization of δ,ε-unsaturated ketones and aldehydes. *J. Am. Chem. Soc.* **117**, 6787–6788 (1995). doi: 10.1021/ja00130a022
8. J. F. Bower, M. J. Krische, Formation of C–C bonds via iridium-catalyzed hydrogenation and transfer hydrogenation. *Top. Organomet. Chem.* **34**, 107–138 (2011). doi: 10.1007/978-3-642-15334-1_5; pmid: 21822399
9. A. Hassan, M. J. Krische, Unlocking hydrogenation for C–C bond formation: A brief overview of enantioselective methods. *Org. Process Res. Dev.* **15**, 1236–1242 (2011). doi: 10.1021/op200195m; pmid: 22125398
10. J. M. Ketcham, I. Shin, T. P. Montgomery, M. J. Krische, Catalytic enantioselective C–H functionalization of alcohols by redox-triggered carbonyl addition: Borrowing hydrogen, returning carbon. *Angew. Chem. Int. Ed. Engl.* **53**, 9142–9150 (2014). doi: 10.1002/anie.201403873; pmid: 25056771
11. E. Yamaguchi, J. Mowat, T. Luong, M. J. Krische, Regio- and diastereoselective C–C coupling of α-olefins and styrenes to 3-hydroxy-2-oxindoles by Ru-catalyzed hydrohydroxyalkylation. *Angew. Chem. Int. Ed. Engl.* **52**, 8428–8431 (2013). doi: 10.1002/anie.201303552; pmid: 23832830
12. B. Y. Park, T. Luong, H. Sato, M. J. Krische, Osmium(0) catalyzed C–C coupling of ethylene and alpha-olefins with diols, ketols or hydroxy esters via transfer hydrogenation. *J. Org. Chem.* **81**, 8585–8594 (2016). doi: 10.1021/acs.joc.6b01923; pmid: 27580269
13. B. Y. Park, T. Luong, H. Sato, M. J. Krische, A metallacycle fragmentation strategy for vinyl transfer from enol carboxylates to secondary alcohol C–H bonds via osmium- or ruthenium-catalyzed transfer hydrogenation. *J. Am. Chem. Soc.* **137**, 7652–7655 (2015). doi: 10.1021/jacs.5b04688; pmid: 26066660
14. K. Kokubo, M. Miura, M. Nomura, Rhodium-catalyzed reaction of benzoic anhydride with styrene under molecular hydrogen. *Organometallics* **14**, 4521–4524 (1995). doi: 10.1021/om00010a016
15. Y.-T. Hong, A. Barchuk, M. J. Krische, Branch-selective intermolecular hydroacylation: Hydrogen-mediated coupling of anhydrides to styrenes and activated olefins. *Angew. Chem. Int. Ed. Engl.* **45**, 6885–6888 (2006). doi: 10.1002/anie.200602377; pmid: 16991162
16. J. S. Bandar, E. Ascic, S. L. Buchwald, Enantioselective CuH-catalyzed reductive coupling of aryl alkenes and activated carboxylic acids. *J. Am. Chem. Soc.* **138**, 5821–5824 (2016). doi: 10.1021/jacs.6b03086; pmid: 27121395
17. J. C. Leung, M. J. Krische, Catalytic intermolecular hydroacylation of C–C π-bonds in the absence of chelation assistance. *Chem. Sci.* **3**, 2202–2209 (2012). doi: 10.1039/c2sc20350b
18. Y.-L. Zheng *et al*., Iron-catalyzed regioselective transfer hydrogenative couplings of unactivated aldehydes with simple alkenes. *Angew. Chem. Int. Ed. Engl.* **55**, 6315–6318 (2016). doi: 10.1002/anie.201602130; pmid: 27072872
19. M. Kimura, A. Ezoe, K. Shibata, Y. Tamaru, Novel and highly regio- and stereoselective nickel-catalyzed homoallylation of benzaldehyde with 1,3-dienes. *J. Am. Chem. Soc.* **120**, 4033–4034 (1998). doi: 10.1021/ja973847c
20. M. Kimura, Y. Tamaru, Nickel catalyzed reductive coupling of dienes and carbonyl compounds. *Top. Curr. Chem.* **279**, 173–207 (2007). doi: 10.1007/128_2007_121
21. M. Kimura *et al*., Nickel-catalyzed homoallylation of aldehydes and ketones with 1,3-dienes and complementary promotion by diethylzinc or triethylborane. *Angew. Chem. Int. Ed.* **38**, 397–400 (1999). doi: 10.1002/(SICI)1521-3773(19990201)38:3<397::AID-ANIE397>3.0.CO;2-Y
22. Y. Yang *et al*., Asymmetric reductive coupling of dienes and aldehydes catalyzed by nickel complexes of spiro phosphoramidites: Highly enantioselective synthesis of chiral bishomoallylic alcohols. *J. Am. Chem. Soc.* **129**, 2248–2249 (2007). doi: 10.1021/ja0693183; pmid: 17269780
23. Y. Sato, Y. Hinata, R. Seki, Y. Oonishi, N. Saito, Nickel-catalyzed enantio- and diastereoselective three-component coupling of 1,3-dienes, aldehydes, and silanes using chiral N-heterocyclic carbenes as ligands. *Org. Lett.* **9**, 5597–5599 (2007). doi: 10.1021/ol702543m; pmid: 18020355
24. H.-Y. Jang, R. R. Huddleston, M. J. Krische, A New catalytic C–C bond-forming hydrogenation: Reductive coupling of dienes and glyoxals under catalytic hydrogenation conditions. *Angew. Chem. Int. Ed. Engl.* **42**, 4074–4077 (2003). doi: 10.1002/anie.200351986; pmid: 12973774
25. F. Shibahara, J. F. Bower, M. J. Krische, Ruthenium-catalyzed C-C bond forming transfer hydrogenation: Carbonyl allylation from the alcohol or aldehyde oxidation level employing acyclic 1,3-dienes as surrogates to preformed allyl metal reagents. *J. Am. Chem. Soc.* **130**, 6338–6339 (2008). doi: 10.1021/ja801213x; pmid: 18444617
26. J. R. Zbieg, J. Moran, M. J. Krische, Diastereo- and enantioselective ruthenium-catalyzed hydrohydroxyalkylation of 2-silyl-butadienes: Carbonyl *syn*-crotylation from the alcohol oxidation level. *J. Am. Chem. Soc.* **133**, 10582–10586 (2011). doi: 10.1021/ja2046028; pmid: 21627316
27. J. R. Zbieg, E. Yamaguchi, E. L. McInturff, M. J. Krische, Enantioselective C–H crotylation of primary alcohols via hydrohydroxyalkylation of butadiene. *Science* **336**, 324–327 (2012). doi: 10.1126/science.1219274; pmid: 22442385
28. E. L. McInturff, E. Yamaguchi, M. J. Krische, Chiral-anion-dependent inversion of diastereo- and enantioselectivity in carbonyl crotylation via ruthenium-catalyzed butadiene hydrohydroxyalkylation. *J. Am. Chem. Soc.* **134**, 20628–20631 (2012). doi: 10.1021/ja311208a; pmid: 23234459
29. V. Komanduri, M. J. Krische, Enantioselective reductive coupling of 1,3-enynes to heterocyclic aromatic aldehydes and ketones via rhodium-catalyzed asymmetric hydrogenation: Mechanistic insight into the role of Brønsted acid additives. *J. Am. Chem. Soc.* **128**, 16448–16449 (2006). doi: 10.1021/ja0673027; pmid: 17177363
30. M. N. Grayson, M. J. Krische, K. N. Houk, Ruthenium-catalyzed asymmetric hydrohydroxyalkylation of butadiene: The role of the formyl hydrogen bond in stereochemical control. *J. Am. Chem. Soc.* **137**, 8838–8850 (2015). doi: 10.1021/jacs.5b04844; pmid: 26107070
31. T. Smejkal, H. Han, B. Breit, M. J. Krische, All-carbon quaternary centers *via* ruthenium-catalyzed hydroxymethylation of 2-substituted butadienes mediated by formaldehyde: Beyond hydroformylation. *J. Am. Chem. Soc.* **131**, 10366–10367 (2009). doi: 10.1021/ja904124b; pmid: 19594163
32. B. Sam, B. Breit, M. J. Krische, Paraformaldehyde and methanol as C_1 feedstocks in metal-catalyzed C–C couplings of π-unsaturated reactants: Beyond hydroformylation. *Angew. Chem. Int. Ed. Engl.* **54**, 3267–3274 (2015). doi: 10.1002/anie.201407888; pmid: 25430585
33. J. Moran, A. Preetz, R. A. Mesch, M. J. Krische, Iridium-catalysed direct C–C coupling of methanol and allenes. *Nat. Chem.* **3**, 287–290 (2011). doi: 10.1038/nchem.1001; pmid: 21430686
34. J. F. Bower, R. L. Patman, M. J. Krische, Iridium-catalyzed C–C coupling via transfer hydrogenation: Carbonyl addition from the alcohol or aldehyde oxidation level employing 1,3-cyclohexadiene. *Org. Lett.* **10**, 1033–1035 (2008). doi: 10.1021/ol800159w; pmid: 18254642
35. J. R. Zbieg, T. Fukuzumi, M. J. Krische, Iridium catalyzed hydro-hydroxyalkylation of butadiene: carbonyl crotylation. *Adv. Synth. Catal.* **352**, 2416–2420 (2010). doi: 10.1002/adsc.201000599; pmid: 21165157
36. J. C. Leung, L. M. Geary, T.-Y. Chen, J. R. Zbieg, M. J. Krische, Direct, redox-neutral prenylation and geranylation of secondary carbinol C–H bonds: C4-regioselectivity in ruthenium-catalyzed C–C couplings of dienes to α-hydroxy esters. *J. Am. Chem. Soc.* **134**, 15700–15703 (2012). doi: 10.1021/ja3075049; pmid: 22985393
37. T.-Y. Chen, M. J. Krische, Regioselective ruthenium catalyzed hydrohydroxyalkylation of dienes with 3-hydroxy-2-oxindoles: Prenylation, geranylation, and beyond. *Org. Lett.* **15**, 2994–2997 (2013). doi: 10.1021/ol401184k; pmid: 23721207
38. B. Y. Park, T. P. Montgomery, V. J. Garza, M. J. Krische, Ruthenium catalyzed hydrohydroxyalkylation of isoprene with heteroaromatic secondary alcohols: Isolation and reversible formation of the putative metallacycle intermediate. *J. Am. Chem. Soc.* **135**, 16320–16323 (2013). doi: 10.1021/ja4087193; pmid: 24156560
39. R. L. Patman, V. M. Williams, J. F. Bower, M. J. Krische, Carbonyl propargylation from the alcohol or aldehyde oxidation level employing 1,3-enynes as surrogates to preformed allenylmetal reagents: A ruthenium-catalyzed C–C bond-forming transfer hydrogenation. *Angew. Chem. Int. Ed. Engl.* **47**, 5220–5223 (2008). doi: 10.1002/anie.200801359; pmid: 18528831
40. L. M. Geary, J. C. Leung, M. J. Krische, Ruthenium-catalyzed reductive coupling of 1,3-enynes and aldehydes by transfer hydrogenation: Anti-diastereoselective carbonyl propargylation. *Chemistry* **18**, 16823–16827 (2012). doi: 10.1002/chem.201202446; pmid: 23147989
41. K. D. Nguyen, D. Herkommer, M. J. Krische, Ruthenium-BINAP catalyzed alcohol C–H *tert*-prenylation *via* 1,3-enyne transfer hydrogenation: Beyond stoichiometric carbanions in enantioselective carbonyl propargylation. *J. Am. Chem. Soc.* **138**, 5238–5241 (2016). doi: 10.1021/jacs.6b02279; pmid: 27079149
42. L. M. Geary, S. K. Woo, J. C. Leung, M. J. Krische, Diastereo- and enantioselective iridium-catalyzed carbonyl propargylation from the alcohol or aldehyde oxidation level: 1,3-enynes as allenylmetal equivalents. *Angew. Chem. Int. Ed. Engl.* **51**, 2972–2976 (2012). doi: 10.1002/anie.201200239; pmid: 22337340
43. Y. Yang, I. B. Perry, G. Lu, P. Liu, S. L. Buchwald, Copper-catalyzed asymmetric addition of olefin-derived nucleophiles to ketones. *Science* **353**, 144–150 (2016). doi: 10.1126/science.aaf7720; pmid: 27284169
44. H.-Y. Jang, M. J. Krische, "Metal-catalyzed reductive aldol coupling" in *Comprehensive Chirality*, H. Yamamoto, E. M. Carreira, Eds. (Elsevier, 2012), vol. 4, pp. 100–121.
45. A. Revis, T. K. Hilty, Novel synthesis of β-siloxy esters by condensation of carbonyls and trimethylsilane with α,β-unsaturated esters catalyzed by $RhCl_3$. *Tetrahedron Lett.* **28**, 4809–4812 (1987). doi: 10.1016/S0040-4039(00)96631-0
46. E. L. McInturff, J. Mowat, A. R. Waldeck, M. J. Krische, Ruthenium-catalyzed hydrohydroxyalkylation of acrylates with diols and α-hydroxycarbonyl compounds to form spiro- and α-methylene-γ-butyrolactones. *J. Am. Chem. Soc.* **135**, 17230–17235 (2013). doi: 10.1021/ja410533y; pmid: 24187991
47. S. J. Taylor, M. O. Duffey, J. P. Morken, Rhodium-catalyzed enantioselective reductive aldol reaction. *J. Am. Chem. Soc.* **122**, 4528–4529 (2000). doi: 10.1021/ja9944453
48. C.-X. Zhao, M. O. Duffey, S. J. Taylor, J. P. Morken, Enantio- and diastereoselective reductive aldol reactions with iridium-pybox catalysts. *Org. Lett.* **3**, 1829–1831 (2001). doi: 10.1021/ol015859f; pmid: 11405722
49. H. Nishiyama, T. Shiomi, Y. Tsuchiya, I. Matsuda, High performance of Rh(Phebox) catalysts in asymmetric reductive aldol reaction: High anti-selectivity. *J. Am. Chem. Soc.* **127**, 6972–6973 (2005). doi: 10.1021/ja050698m; pmid: 15884939
50. T. Shiomi, H. Nishiyama, Intermolecular asymmetric reductive aldol reaction of ketones as acceptors promoted by chiral Rh(Phebox) catalyst. *Org. Lett.* **9**, 1651–1654 (2007). doi: 10.1021/ol070251d; pmid: 17385871
51. J. Deschamp, O. Chuzel, J. Hannedouche, O. Riant, Highly diastereo- and enantioselective copper-catalyzed domino reduction/aldol reaction of ketones with methyl acrylate. *Angew. Chem. Int. Ed. Engl.* **45**, 1292–1297 (2006). doi: 10.1002/anie.200503791; pmid: 16425322
52. C. Bee, S. B. Han, A. Hassan, H. Iida, M. J. Krische, Diastereo- and enantioselective hydrogenative aldol coupling of vinyl ketones: Design of effective monodentate TADDOL-like phosphonite ligands. *J. Am. Chem. Soc.* **130**, 2746–2747 (2008). doi: 10.1021/ja710862u; pmid: 18266373
53. D. Best, H. W. Lam, C=N-containing azaarenes as activating groups in enantioselective catalysis. *J. Org. Chem.* **79**, 831–845 (2014). doi: 10.1021/jo402414k; pmid: 24341407
54. V. Komanduri, C. D. Grant, M. J. Krische, Branch-selective reductive coupling of 2-vinyl pyridines and imines via rhodium catalyzed C–C bond forming hydrogenation. *J. Am. Chem. Soc.* **130**, 12592–12593 (2008). doi: 10.1021/ja805056g; pmid: 18759388
55. A. Saxena, B. Choi, H. W. Lam, Enantioselective copper-catalyzed reductive coupling of alkenylazaarenes with ketones. *J. Am. Chem. Soc.* **134**, 8428–8431 (2012). doi: 10.1021/ja3036916; pmid: 22563725

ACKNOWLEDGMENTS

The Robert A. Welch Foundation (grant F-0038) and NIH–National Institute of General Medical Sciences (grant RO1-GM069445) are acknowledged for financial support. H.S. gratefully acknowledges a Japan Student Services Organization graduate student exchange fellowship.

10.1126/science.aah5133

Downloaded from http://science.sciencemag.org/ on October 20, 2016

RESEARCH ARTICLE SUMMARY

STRUCTURAL BIOLOGY

Structural basis for the gating mechanism of the type 2 ryanodine receptor RyR2

Wei Peng,* Huaizong Shen,* Jianping Wu,* Wenting Guo, Xiaojing Pan, Ruiwu Wang, S. R. Wayne Chen,† Nieng Yan†

INTRODUCTION: Ryanodine receptors (RyRs) are intracellular Ca^{2+} channels that control the release of Ca^{2+} from the sarco(endo)plasmic reticulum. Among the three mammalian RyR isoforms, RyR2 is primarily expressed in the heart and brain and is activated by Ca^{2+} influx by a mechanism known as calcium-induced calcium release. This Ca^{2+} release is fundamental to cellular processes ranging from muscle contraction to learning and memory.

RyRs are the largest known ion channels with a molecular mass of > 2 megadalton for a homotetramer. Each RyR protomer consists of a cytoplasmic region of over 4500 residues and a carboxyl terminal transmembrane (TM) domain. The four identical TM segments enclose a central ion-conducting pore, whereas the cytoplasmic regions serve as a scaffold for interactions with diverse ligands and protein modulators.

RyR channel gating involves a long-range allosteric mechanism. The structures of rabbit skeletal muscle RyR1 were determined at 3.8-Å resolution for the closed state and various lower resolutions for the potentially open states. Elucidating the gating mechanism of RyR requires structural determination of the open states at high resolution.

RATIONALE: RyR2 harbors more than 150 mutations associated with cardiac disorders, such as catecholaminergic polymorphic ventricular tachycardia type 1, idiopathic ventricular fibrillation, and sudden cardiac death. Structural elucidation of RyR2 may provide the molecular basis for understanding disease mechanisms and for the development of potential novel therapeutics. We purified endogenous RyR2 from porcine heart using glutathione *S*-transferase–fused FKBP12. To obtain the structure of RyR2 in the closed state, 5 mM EDTA was included throughout purification. To capture an open RyR2, the protein was purified in the presence of 20 μM Ca^{2+} and the compound 2,2′,3,5′,6-pentachlorobiphenyl (PCB95) that can stabilize RyR1 in the open state.

ON OUR WEBSITE

Read the full article at http://dx.doi.org/10.1126/science.aah5324

RESULTS: The electron microscopy (EM) maps for RyR2 were reconstructed to 4.4- and 4.2-Å resolutions for the closed and open states, respectively. Compared to the structure of RyR1, a number of armadillo repeats in the C terminus of the helical domain 2 were invisible in RyR2, likely due to intrinsic flexibility. At 20 μM Ca^{2+}, the cytoplasmic gate in the closed structure is dilated by approximately 8 Å, resulting in the shift of the constriction site from Ile4868 to Gln4864. The four Gln4864 residues enclose a gate with a diameter of approximately 4 Å, allowing Ca^{2+} passage in a single file.

CONCLUSION: Structure comparison of the open and closed RyR2 shows little intradomain rearrangement of the armadillo-containing cytoplasmic domains including the amino terminal domain, the Handle domain, and the Helical domain. Relative shifts between these domains result in the breathing motion of the periphery of the cytoplasmic canopy and the rotation of the Central domain. The horseshoe-shaped Central domain, with its convex side interacting with the three armadillo domains and its concave side wrapping around the cytoplasmic O-ring of the channel domain, serves as the primary transducer that integrates and translates the conformational changes of the cytoplasmic domains to channel gating. However, the mechanism of Ca^{2+} sensing and activation of RyR2 remains to be elucidated. ■

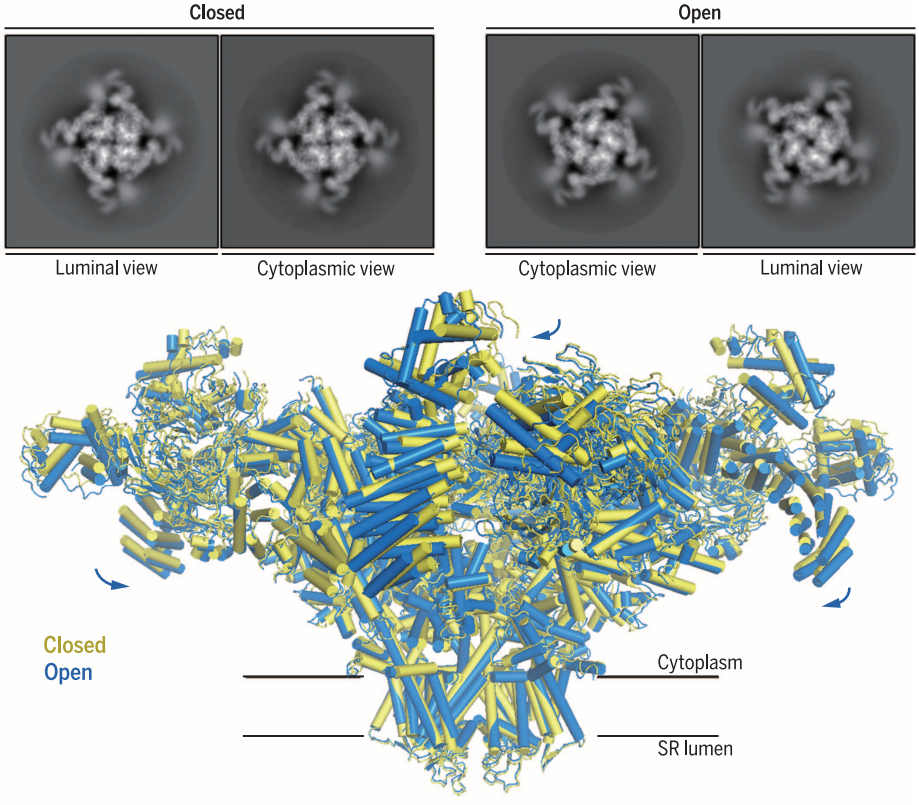

Cryogenic EM structures of RyR2 from porcine heart in both the closed and open states at near-atomic resolutions. (**Top**) Representative two-dimensional class averages of electron micrographs of the closed and open RyR2. (**Bottom**) The two structures are superimposed relative to the transmembrane domain. The blue arrows indicate the overall shifts of the cytoplasmic region from the closed state to the open state. SR, sarcoplasmic reticulum.

The list of author affiliations is available in the full article online.
*These authors contributed equally to this work.
†Corresponding author. Email: swchen@ucalgary.ca (S.R.W.C.); nyan@tsinghua.edu.cn (N.Y.)
Cite this article as W. Peng *et al.*, *Science* 354, aah5324 (2016). DOI: 10.1126/science.aah5324

Downloaded from http://science.sciencemag.org/ on October 20, 2016

RESEARCH ARTICLE

STRUCTURAL BIOLOGY

Structural basis for the gating mechanism of the type 2 ryanodine receptor RyR2

Wei Peng,[1,2]* Huaizong Shen,[1,2,3]* Jianping Wu,[1,2,3]* Wenting Guo,[4] Xiaojing Pan,[1,2] Ruiwu Wang,[4] S. R. Wayne Chen,[4]† Nieng Yan[1,2,3]†

RyR2 is a high-conductance intracellular calcium (Ca^{2+}) channel that controls the release of Ca^{2+} from the sarco(endo)plasmic reticulum of a variety of cells. Here, we report the structures of RyR2 from porcine heart in both the open and closed states at near-atomic resolutions determined using single-particle electron cryomicroscopy. Structural comparison reveals a breathing motion of the overall cytoplasmic region resulted from the interdomain movements of amino-terminal domains (NTDs), Helical domains, and Handle domains, whereas almost no intradomain shifts are observed in these armadillo repeats–containing domains. Outward rotations of the Central domains, which integrate the conformational changes of the cytoplasmic region, lead to the dilation of the cytoplasmic gate through coupled motions. Our structural and mutational characterizations provide important insights into the gating and disease mechanism of RyRs.

Ryanodine receptors (RyRs) are intracellular ion channels responsible for the rapid release of calcium (Ca^{2+}) ions from the sarcoplasmic/endoplasmic reticulum (SR/ER) into the cytoplasm, a key event in excitation-contraction coupling in skeletal and cardiac muscles (*1*–*5*). Among the three mammalian RyR isoforms, RyR2 is primarily expressed in the heart and brain and is activated by Ca^{2+} influx through a mechanism known as calcium-induced calcium release (CICR) (*6*–*10*). The RyR2-mediated Ca^{2+} release is fundamental to a number of cellular processes ranging from muscle contraction to learning and memory (*11*, *12*). Mutations in RyR2 are associated with cardiac disorders, such as catecholaminergic polymorphic ventricular tachycardia type 1 (CPVT1) and idiopathic ventricular fibrillation (IVF) (*13*–*17*).

Owing to their physiological and pathological importance, RyRs represent important targets for structural investigation. Electron microscopy (EM) has been the primary tool for structural elucidation of RyRs. The architecture and details of RyR1 have been gradually unveiled by EM analysis with increasing resolutions from below 20 to 3.8 Å (*18*–*26*). The near-atomic resolution structure of RyR1, which was captured in a closed state, revealed a hierarchical organization of the 2.2-megadalton tetrameric channel (*26*). Nine domains were resolved in the cytoplasmic region in each protomer, including four armadillo repeats–containing domains, the amino terminal domain (NTD), the Handle domain, the Helical domain, and the Central domain, three intertwined SPRY domains (the structural domains identified in SplA and RyRs), and two RyR domains designated P1 and P2 domains (Fig. 1A) (*26*). The armadillo repeats in the NTD, the Handle domain, and the Central domain together constitute a superhelical assembly in each protomer, which extensively interacts with the other super spiral formed by the Helical domain. In essence, the scaffold of the cytoplasmic domain is established by eight interconnected superhelical assemblies. Classification of the closed RyR1 structures (*24*, *25*) and the potentially open RyR1 structures at low resolutions (*25*, *27*, *28*) revealed thermal or "breathing" motions of this cytoplasmic canopy.

In side views, the NTDs, the Central domains, and the channel domain build up a central tower (*26*). The tetrameric channel domain contains a transmembrane region of the characteristic voltage-gated ion channel superfamily fold and an extended cytoplasmic O-ring in each protomer consisting of the elongated S6 segments ($S6_{Cyt}$), the zinc finger–containing carboxyl terminal domain (CTD), and a small globular cytoplasmic domain between S2 and S3 in the voltage sensor–like (VSL) domain, which we refer to as the VSL_{Cyt} domain hereafter. The Central domain contains a unique U-motif that hooks into the O-ring, whereas the concave face of the armadillo repeats in the Central domain wraps around the O-ring. We proposed that the Central domain may represent the primary transducer that integrates and translates the conformational changes of the cytoplasmic sensors induced by a variety of stimuli to the gating of the central pore (*26*, *27*).

Notwithstanding these exciting advances in the structural and mechanistic understanding of RyR1, a high-resolution structure in the open state is necessitated to reveal the molecular basis for the long-range allosteric gating mechanism. Furthermore, high-resolution structures of RyR2 are also required to better understand the mechanism and to develop novel therapeutics for the treatment of RyR2-associated diseases. Here, we report the cryogenic EM (cryo-EM) structures of porcine RyR2 (pRyR2) in both the open and closed states. Structural comparison and structure-guided mutational analysis provide important insights into the gating and disease mechanism of RyRs.

Structure determination of RyR2

Following the successful strategy for the purification of RyR1 and $Ca_v1.1$ complex from rabbit skeletal muscles (*26*, *29*, *30*), we used glutathione *S*-transferase (GST)–fused FKBP12 to purify RyR2 from porcine heart. Please refer to the supplementary materials for details of protein purification and cryosample preparation (fig. S1).

To obtain the structure of RyR2 in the closed state, 5 mM EDTA was included throughout purification. To capture an open RyR2, 20 μM Ca^{2+} was included throughout the purification (*23*, *31*). It was reported that the compound 2,2′,3,5′,6-pentachlorobiphenyl (PCB 95) stabilized RyR1 in the open state and increased [^{3}H]ryanodine binding to both RyR1 and RyR2 (*23*, *32*, *33*); we also added PCB 95. Despite the addition of excess GST-FKBP12 before size exclusion chromatography (SEC), the complex of GST-FKBP12 and RyR2 fell apart during SEC purification, indicating a weaker association of FKBP12 with RyR2 than with RyR1 (fig. S1, A and B).

The structures of RyR2 were determined at overall resolutions of 4.4 Å for the closed state and 4.2 Å for the open state (Fig. 1B, table S1, and figs. S1 and S2). Consistent with their 70% sequence similarity, the overall architecture and domain organization of RyR2 are identical to those of RyR1 (*26*) (Fig. 1, A and B, and fig. S4). As expected, no density was observed for FKBP12. In addition, a number of armadillo repeats in the C terminus of the Helical domain 2 (HD2) were invisible, likely due to intrinsic flexibility in the absence of FKBP12 (Fig. 1, C and D, and fig. S1, G and H).

Dilation of the S6 bundle leads to channel opening

In the presence of 20 μM Ca^{2+} and PCB 95, the dilation of the central pore was evident even during two-dimensional (2D) class average compared with the images obtained in the presence of 5 mM EDTA (Fig. 2A). When the pore domains of the two structures are superimposed, the conformation of structural elements on the luminal side, including the selectivity filter (SF), the pore helices, and the supporting helices on S5 and S6 (the turret, residues 4790 to 4840), remains nearly unchanged (Fig. 2B). The deviation occurs at residue Phe4854,

[1]State Key Laboratory of Membrane Biology, Tsinghua University, Beijing 100084, China. [2]Beijing Advanced Innovation Center for Structural Biology, Tsinghua University, Beijing 100084, China. [3]Tsinghua-Peking Joint Center for Life Sciences, School of Life Sciences and School of Medicine, Tsinghua University, Beijing 100084, China. [4]The Libin Cardiovascular Institute of Alberta, Department of Physiology and Pharmacology, University of Calgary, Calgary, Alberta, Canada, T2N 4N1.

*These authors contributed equally to this work. †Corresponding author. Email: swchen@ucalgary.ca (S.R.W.C.); nyan@tsinghua.edu.cn (N.Y.)

Downloaded from http://science.sciencemag.org/ on October 20, 2016

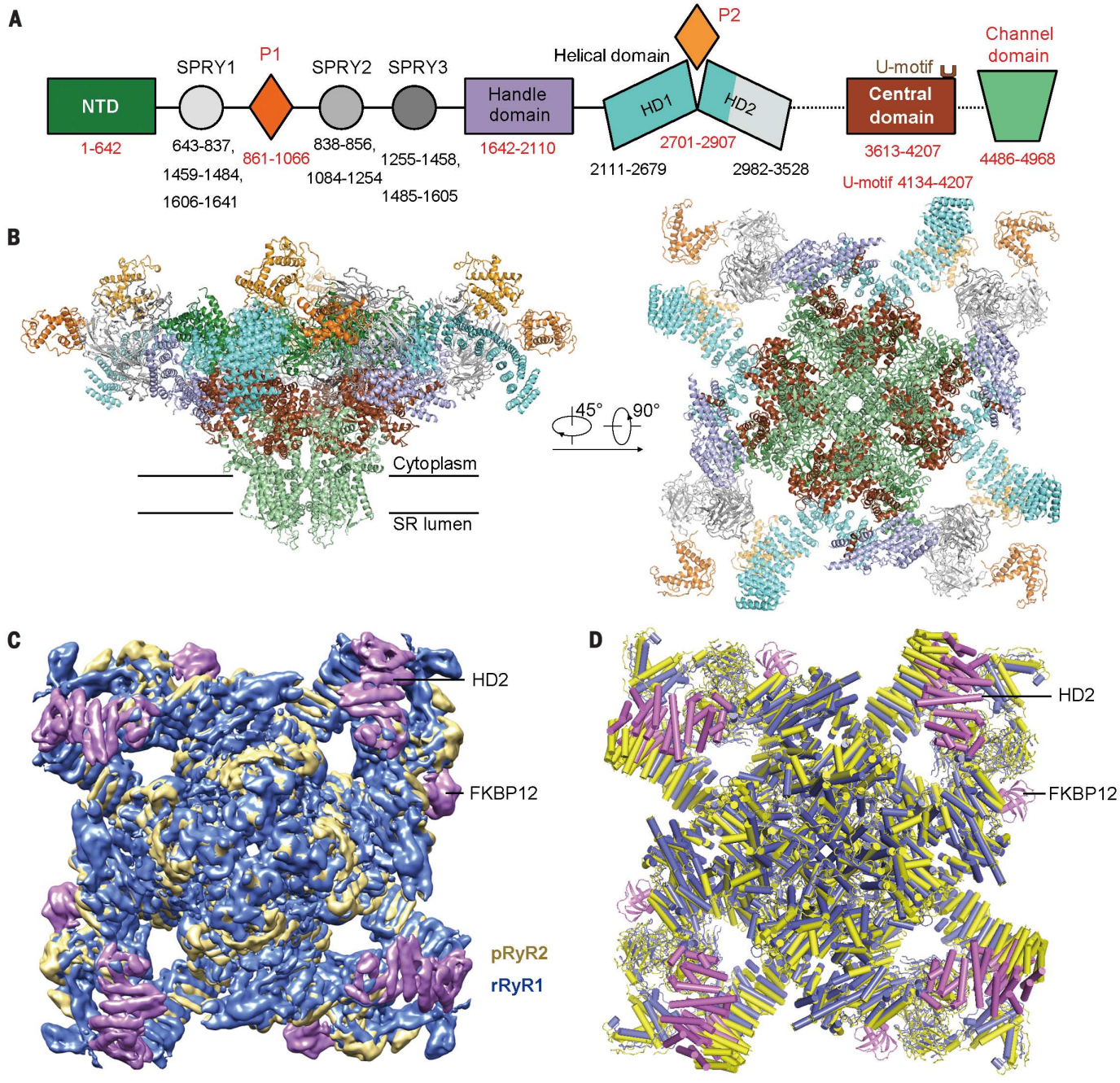

Fig. 1. The cryo-EM structure of RyR2 from porcine heart (pRyR2) in a closed state. (**A**) Domain organization of a pRyR2 protomer. The domain boundaries are indicated, with the reliably assigned boundaries labeled red. (**B**) The overall structure of the closed pRyR2 at a nominal resolution of 4.2 Å. The tetrameric structure of pRyR2 is domain-colored with the same scheme as in (A). (**C**) Comparison of the EM maps (low-pass filtered to 6-Å resolution) of pRyR2 and rRyR1 (rabbit RyR1). The FKBP12 and the carboxyl terminal half of the HD2 domain, shown in magenta, were resolved in rRyR1 but are invisible in pRyR2. (**D**) Structural comparison of pRyR2 (yellow) with rRyR1. The structures of rRyR1 (PDB code: 3J8H) and pRyR2 are superimposed relative to the channel domain. All structure figures were prepared with PyMol (*60*), and the EM maps were generated in Chimera (*61*). Single-letter abbreviations for the amino acid residues are as follows: A, Ala; C, Cys; D, Asp; E, Glu; F, Phe; G, Gly; H, His; I, Ile; K, Lys; L, Leu; M, Met; N, Asn; P, Pro; Q, Gln; R, Arg; S, Ser; T, Thr; V, Val; W, Trp; and Y, Tyr.

beyond which the four S6 segments tilt outward, resulting in the dilation of the intracellular gate by ~8 Å (Fig. 2B and Movie 1). Consequently, the pore constriction site is shifted from Ile4868 in the closed RyR2 to Gln4864 in the open structure. The four Gln4864 residues enclose a gate with a diameter of ~4 Å, allowing passage of Ca^{2+} ions in single file (Fig. 2, C to E). Therefore, the new structure obtained in the presence of 20 μM Ca^{2+} and PCB95 (2,2′,3,5′,6-pentachlorobiphenyl) represents an open conformation. Consistent with its critical location in the conduction pathway, mutating Gln4864 markedly or completely abolished channel activation by caffeine (fig. S5).

Internal stability and interdomain shifts of cytoplasmic domains

Determination of the pRyR2 structure in both the closed and open states offers the opportunity to characterize the structural elements responsible for the unique long-range allosteric gating mechanism of RyRs. When the two structures are

Downloaded from http://science.sciencemag.org/ on October 20, 2016

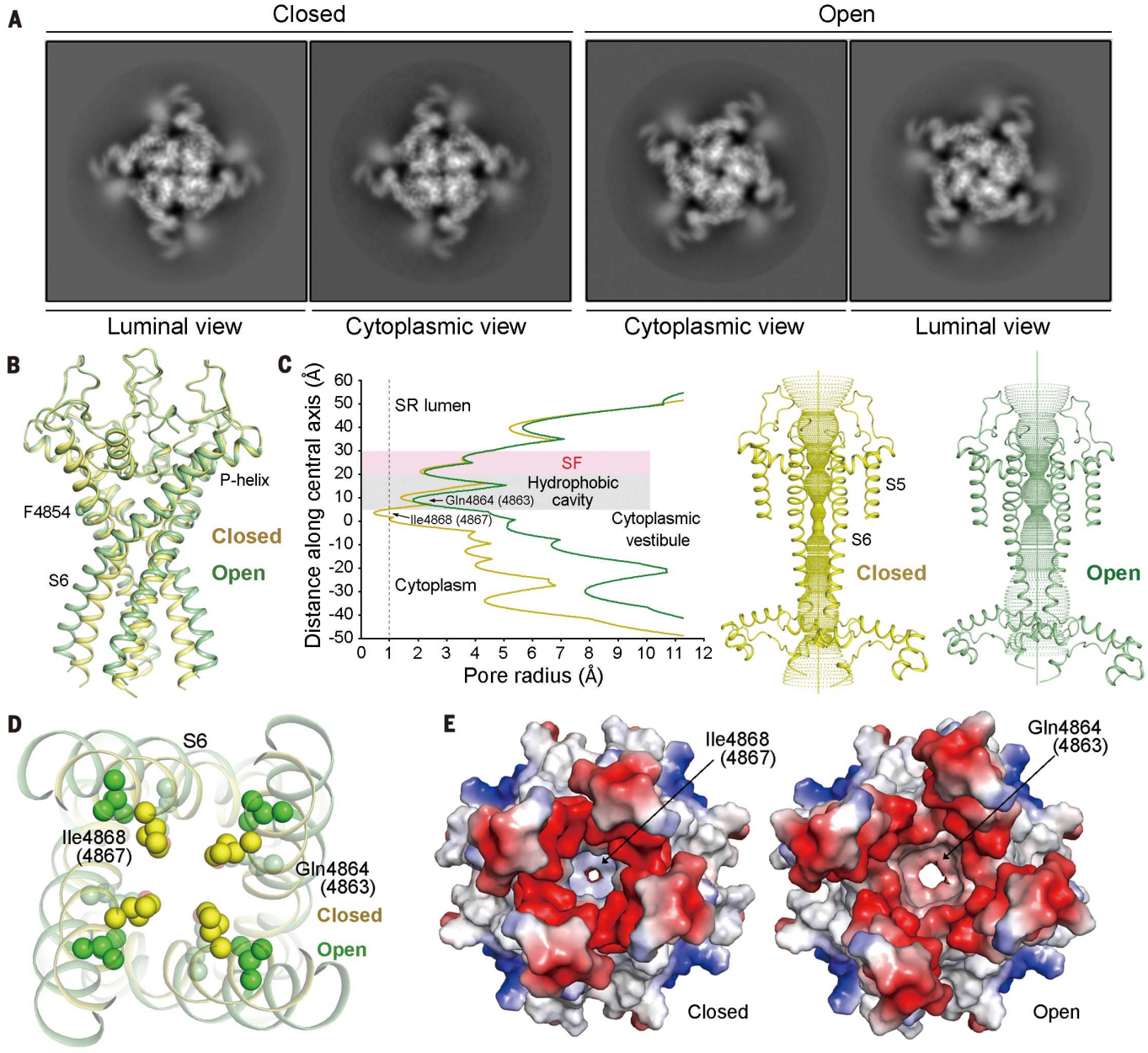

Fig. 2. Structural comparison of the open and closed RyR2. (**A**) Representative 2D class averages of cryo-EM images of the closed and open RyR2. Note the marked difference of the central pore. (**B**) Conformational changes of the S6 bundle of the channel domain in the open and closed RyR2 structures. The two structures are superimposed relative to the selectivity filter and its supporting turrets (residues 4790 to 4840). In this figure, the SR luminal side is placed on top, opposite to the presentations in other figures. (**C**) Pore radii of RyR2 in the open and closed states. (Left) The pore radii along the ion-conducting pathway, calculated by HOLE (*62*), are tabulated. The position of the S4-S5 helical axis is set as the origin of the *y* axis. Whereas Ile4868 in each protomer constitutes the intracellular gate in the closed RyR2, the constriction site is formed by Gln4864 in the open structure. The corresponding residue numbers in human RyR2 (hRyR2) are shown in brackets. The same applies to other figures. (Right) The channel passage is indicated by yellow (closed) and cyan (open) dots in the center of two diagonal protomers in each channel. (**D**) The dilation of the intracellular gate in the open RyR2. Shown here is the cytoplasmic view of the intracellular gate. The constriction residues in the closed and open states, Ile4868 and Gln4864, respectively, are shown as spheres and colored yellow in the closed and green in the open structures. (**E**) In the open pRyR2 structure, Gln4864 residues form the constriction site that allows passage of Ca^{2+} ion. Shown here are the cytoplasmic views of the pore domain. The surface electrostatic potential is calculated in PyMol. Please refer to fig. S3B for the EM maps of the discussed structural elements and fig. S5 for mutational characterizations of Gln4864.

superimposed relative to the channel domain, the overall structure undergoes intricate shifts (Fig. 3A, fig. S6, and Movie 1).

In the cytoplasmic region, the resolution of the peripheral structures, such as the three SPRY domains and P1 and P2 domains, is insufficient for detailed analysis, whereas the secondary structural elements of other domains are well-resolved. The NTD, the Handle domain, and the HD1 domain exhibit nearly no intradomain rearrangements between the closed and open RyR2 structures when compared individually (Fig. 3B). Therefore, the overall motion of the cytoplasmic region may result from domain-wise displacement and relative shifts between domains.

Downloaded from http://science.sciencemag.org/ on October 20, 2016

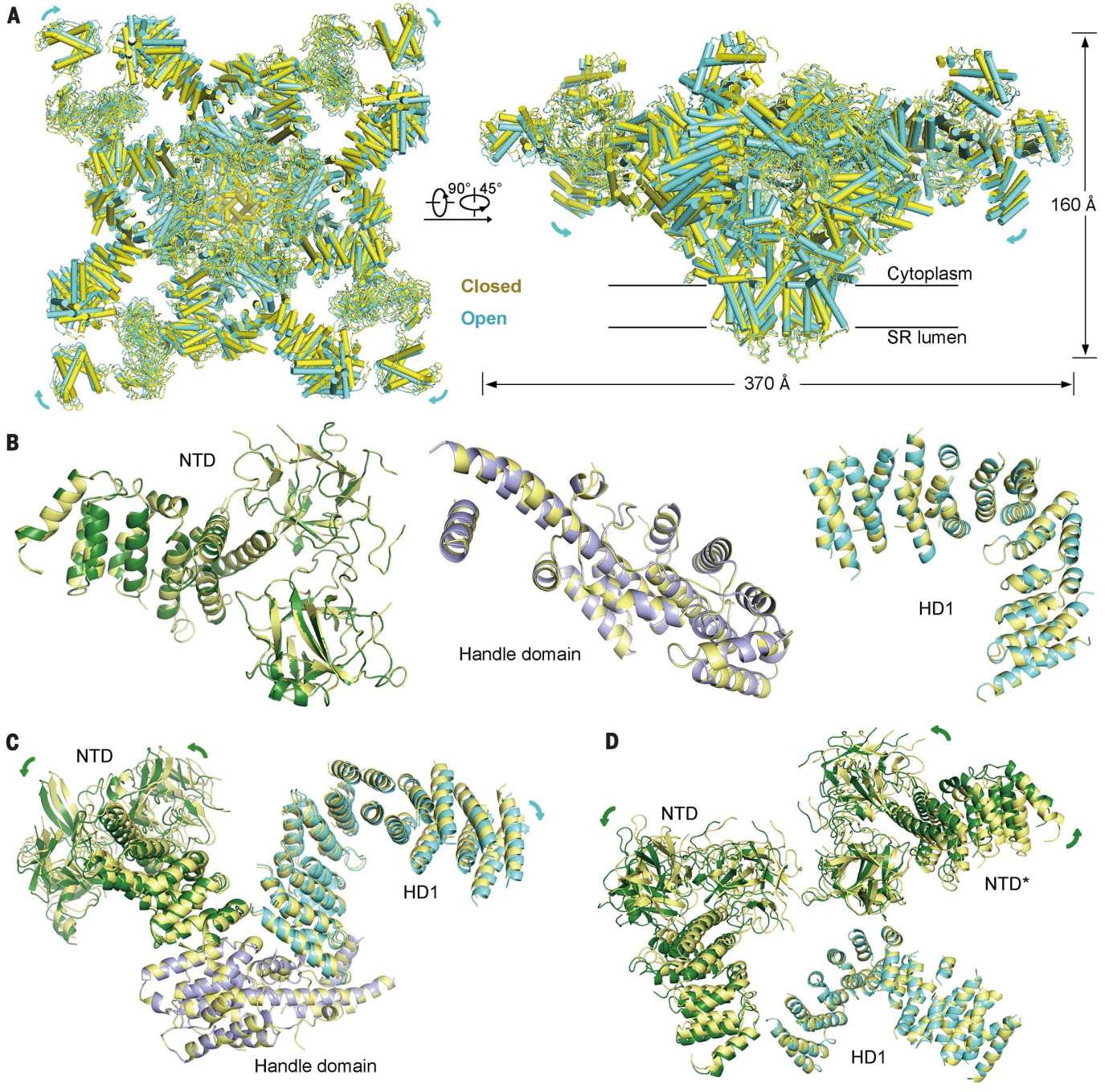

Fig. 3. Structural shifts of the cytoplasmic domains between the closed and open RyR2. (**A**) Overall conformational changes between the open and closed RyR2. The two structures are superimposed relative to the channel domain. The cyan arrows indicate the overall shifts of the cytoplasmic domains from the closed to the open state. (**B**) Almost no intradomain rearrangements of the NTD, the Handle domain, and the HD1 between the open and closed RyR2. The domains in the open RyR2 are colored the same as in Fig. 1B, whereas those in the closed structure are colored yellow. (**C**) The motions of NTD and HD1 relative to the Handle domain. The structures are superimposed relative to the Handle domain. The arrows indicate the motion directions of NTD and HD1. (**D**) Movement of NTDs within the same protomer and from the neighboring protomer relative to HD1. The structures are superimposed against HD1. Please refer to Movie 1 for the morph illustrating the conformational changes between the open and closed RyR2.

It has been previously analyzed in detail that each interface in the cytoplasmic region generally involves more than two domains (*26*). Such clustered interactions may be important for the coupled conformational changes among domains. From the closed to open state, the periphery of the cytoplasmic canopy constituted by the Helical domains, the SPRY domains, and the P1 and P2 domains undergoes a combination of downward rocking toward the SR lumen and clockwise rotation when viewed from the cytoplasmic side. On the contrary, the inner circle enclosed by the NTDs appears to rotate upward and counterclockwise (Fig. 3C; fig. S6, A and B; and Movie 1). The opposing motion directions between the outer and inner rings are in a sense achieved by twisting the two ends of the helical assembly formed by the NTD, Handle domain, and Helical domain in each protomer (Fig. 3C and Movie 1).

One HD1 domain simultaneously interacts with two NTDs from neighboring protomers (Fig. 3D).

Downloaded from http://science.sciencemag.org/ on October 20, 2016

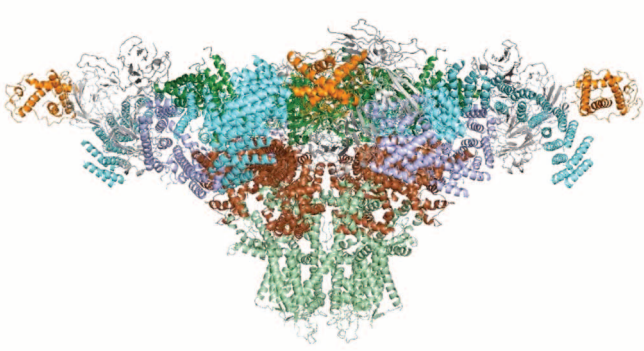

Movie 1. Conformational changes of RyR2 between the closed and open states. The morph was generated using the cryo-EM structures of the closed and open pRyR2. The structure is domain-colored as in Fig. 1B. To generate the morph, the two structures were superimposed in PyMol relative to the channel domain. Forty intermediates were then generated using the crystallography and NMR system (*63*). The morphs were merged and displayed in PyMol using the "mset" command. The same was applied to Movies 2 to 4 and movies S1 to S4. Specific views are shown in each movie. In the side views, the luminal side is placed at the bottom.

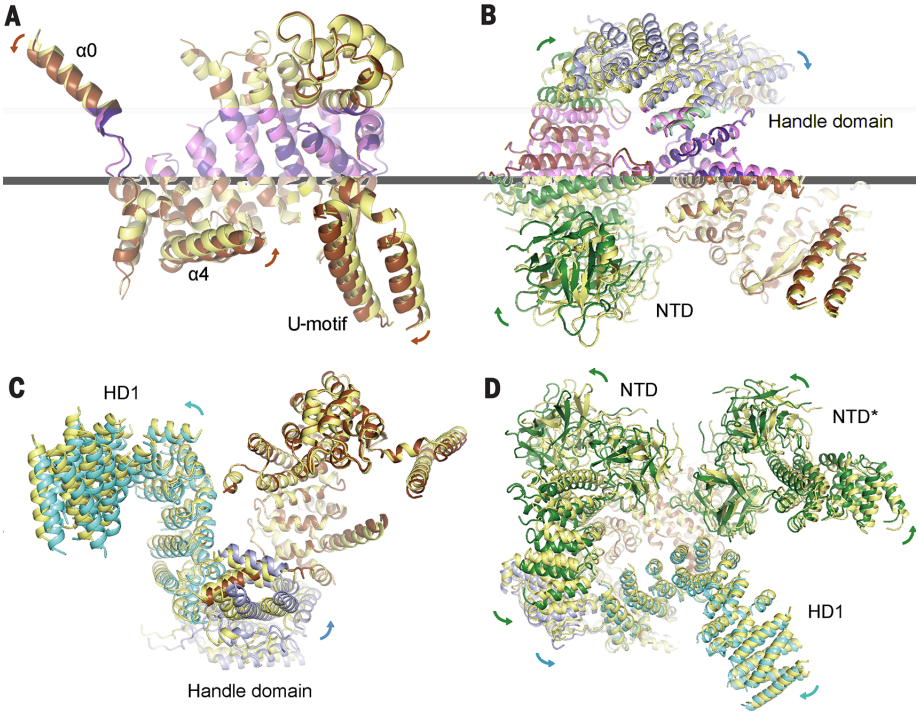

Fig. 4. Intra- and interdomain shifts of the Central domain. All the structural comparisons in this figure are made relative to the Central domain. (**A**) Intradomain shifts of the Central domain. The backbone of the horseshoe-shaped armadillo repeats within the Central domain remains nearly unchanged, whereas the edges exemplified by the U-motif and α4 helix fold toward the concave side. (**B**) The conformational changes of NTD and the Handle domain relative to the Central domain. (**C**) The shifts of the Handle and HD1 domains relative to the Central domain. (**D**) The motions of the NTDs from two adjacent protomers and the Handle domain within the same protomer relative to the Central domain. Please refer to Movie 2 and movies S1 to S3 for the morphs illustrating the conformational changes and relative displacement of domains described in this figure when the structures are compared relative to the channel domain.

The four NTDs and four HD1 domains also complete a closed ring. In the cytoplasmic view, the combined relative motions of NTDs and HD1s result in contraction and expansion of the ring accompanying pore closure and opening, respectively (Fig. 3D; fig. S6, A and B; and Movie 1). Despite the pronounced overall structural shifts, there are only minor relative motions between the NTD, Handle domain, and HD1 when the domains are compared pairwise (Fig. 3, C and D). The major structural rearrangements occur at the interface between these domains and the Central domain.

Twisting of the Central domain

When the structures of the Central domain in the closed and open RyR2 are superimposed, the backbone of the armadillo repeats remains nearly unchanged. The auxiliary motifs, including the preceding helix α0, a capping helix α4 that is located on top of the concave face of the armadillo repeats, and the U-motif on the C-terminal end, slightly fold toward the center of the concave surface (Fig. 4A).

Whereas the concave surface of the Central domain wraps up the cytoplasmic O-ring of the channel domain, the two edges of the convex side contact two neighboring NTDs and one Helical domain, respectively. In addition, despite the distance in the primary sequence, the N-terminal helical repeats of the Central domain appear to be the continuation of the C-terminal repeats of the Handle domain in the 3D structure, and the flanking α0 helix is sandwiched by two helices in the Handle domain.

When the structures are superimposed relative to the Central domain, the consecutive helical repeats of the NTD and the Handle domain appear to rock around the interface between the Handle domain and the Central domain. Consequently, the NTD, which is on the distal end, undergoes a larger degree rotation (Fig. 4B and movie S1). Importantly, there are only insignificant changes of the interface between HD1 and Central domain, suggesting coupled motions of these domains during channel opening (Fig. 4C and movie S2). This observation implicates that structural shifts of the Helical domain may directly induce the concordant movement of the Central domain.

In the context of the RyR2 tetramer, the Central domain appears to slightly swirl around an axis encompassed by its horseshoe-shaped armadillo repeats. The clockwise screw of the Central domain in the cytoplasmic view, which is concordant with the clockwise rotation of the Helical domain, synchronizes with the expansion of the central tower consisting of the channel domain, the Central domain, and the NTD during channel opening (Movies 1 and 2). Meanwhile, the interface between the Central domain and the two neighboring NTDs undergoes marked rearrangements (Fig. 4D and movie S3).

Coupled changes between the Central domain and channel domain

The swirl of each Central domain results in the outward motion of the $S6_{Cyt}$ segments through intricate interactions between the channel domain and the Central domain (Fig. 5A and Movie 3). The U-motif of the Central domain hooks into the cytoplasmic O-ring of the channel domain. Consistent with their extensive interactions, there is no relative motion between the U-motif and the CTD. The displacement of the U-motif thus leads to coupled outward shifts of the CTD and its preceding $S6_{Cyt}$ (Fig. 5B and Movie 3). Accompanying this dilation, the central pore axis is

Downloaded from http://science.sciencemag.org/ on October 20, 2016

shortened by approximately 3 Å in the open RyR2 (Fig. 5A).

There is a minor relative movement between VSL_{Cyt} and CTD, whereas the backbone of VSL remains rigid during channel opening (Fig. 5, B and C). In addition to the contacts between VSL_{Cyt} and the U-motif, the cytoplasmic tip of VSL may contact the EF-hand motif of the neighboring Central domain in the closed structure. This interaction no longer exists in the open structure (movie S4). In the closed RyR1 and RyR2 structures, the S4-S5 linker constrains the cytoplasmic gate formed by the S6 tetrahelical bundle at the boundary between the SR membrane and cytoplasm, reinforcing the closure of the channel (*26*). In the open RyR2, the S4-S5 linker moves closer to the VSL domain, resulting in an expansion of the S4-S5 ring that releases the constriction to the cytoplasmic gate (Fig. 5, B and C). We predicted that interactions among the four CTDs may facilitate closure of the S6 bundle (*26*). Indeed, the adjacent CTDs no longer interact with each other in the open RyR2, whereas the U-motif from the neighboring Central domain still contacts the CTD (Fig. 5D and movie S4).

The concerted movements of U-motif, CTD, and $S6_{Cyt}$ segment requires the rigidity of CTD, which is provided by the zinc finger motif at the joint between CTD and S6 segment (*26*). Supporting this notion, single point mutations of the zinc-coordinating residues, C4888H, C4891H, and H4908C, all abolished the response of RyR2 to caffeine activation (Fig. 5E and fig. S7). Only H4913C retains the sensitivity to caffeine as wild type (WT), suggesting that the 4913 position is relatively more adaptable than other positions in coordinating Zn binding in the CTD (the corresponding residue numbers in human RyR2 are labeled and referred to in all functional assay-related figures and texts).

Discussion

The recently reported 3.8-Å-resolution cryo-EM structure of RyR1-FKBP12 complex in the closed state revealed domain organization and atomic details of the largest ion channels (*26*). Comparison of the near-atomic-resolution structures of the open and closed RyR2 presented here identifies the Central domain as the primary transducer of conformational changes that controls the opening and closure of the channel domain, confirming our previous conjecture (*26*, *27*). The Central domain is surrounded by a second tier of transmitters, including NTDs and the Handle and Helical domains, which provide a scaffold for interactions with a multitude of peripheral domains and channel modulators. The Central domains undergo both intradomain contraction and domain-wise rotation that collectively result in the outward tilting of the pore-forming S6 segments through extensive interactions between the Central domain and channel domain, primarily through the U-motif and the CTD. Consistent with the pivotal role of the Central domain in channel gating, a single point mutation E3987A in mouse RyR2 or E3885A in rabbit RyR3, located within the Central domain, reduced the sensitivity of single RyR channels to cytosolic Ca^{2+} activation by a factor of 1000 to 10,000 (*34*, *35*). However, deleting the entire EF-hand motif in the Central domain does not affect cytosolic Ca^{2+} activation of single RyR2 channels, suggesting that the EF-hand is unlikely to be the cytosolic Ca^{2+} sensor (*36*). Detailed understanding of the role of the Central domain in cytosolic Ca^{2+} activation of RyR2 will have to await atomic-resolution structures of RyRs, which may unveil the binding sites for Ca^{2+}.

One unexpected feature is the little intradomain shifts of the armadillo repeats–containing domains. The VSL domain also remains rigid during channel opening. Furthermore, the U-motif of the Central domain and the CTD form a stable structural unit that has literally no internal rearrangement during pore opening. In a sense, these rigid domains represent individual modules, whereas the Central domain is a relatively flexible joint. The overall conformational changes are achieved through the relative motions between these modules. This analysis predicts that some ligands and modulators may target interfaces of these modules to induce conformational changes, a scenario that awaits further structural and biochemical characterizations.

Mutations in human RyR2 are associated with a range of debilitating diseases such as CPVT1, IVF, and sudden cardiac death (*15*, *17*). More than 100 disease-associated missense mutations and deletions can be mapped onto all major domains in the structure of RyR2 (fig. S8A). Mutations that are located on the surface may disrupt interactions between RyR and its modulators (fig. S8A). The HD1, the Central domain, and the channel domain represent major disease hot spots in addition to NTD (*5*, *26*, *37*) (fig. S8, A and B). Supporting the importance of interactions among domains, one type of mutations and deletions clusters at domain interfaces. These mutations may alter the ability of RyRs to sense chemicals/modulators or to propagate conformational changes that are required for ion channel regulation and gating (fig. S8, C to F).

On the other hand, the coupled motion of the Helical domain and Central domain suggests that shifts of the Helical domain may be directly translated to the structural changes of the Central domain (movie S2). As the Helical domains are positioned on the edge of the cytoplasmic canopy and contact multiple peripheral domains (Fig. 1B), conformational changes of the Helical domains can be achieved through mechanical forces exerted by the upstream $Ca_v1.1$ complex or the neighboring RyR molecules, as in the case of RyR1 (*38*–*43*). This analysis provides a clue to understanding the molecular basis for excitation-contraction coupling in skeletal muscles.

The $S6_{Cyt}$ segment contains a large number of negatively charged or polar residues (Glu, Asp, and Gln) and one positively charged residue (R4875) (Fig. 6A). Mutational studies suggested that mouse RyR2-R4874 may form intersubunit salt bridges with D4868 and E4872 (Fig. 6B) (*44*). Mutating these key residues dramatically diminished the activation of RyR2 by caffeine (Fig. 6C and fig. S9A). It has recently been shown that the E4872A mutation selectively and completely abolishes luminal,

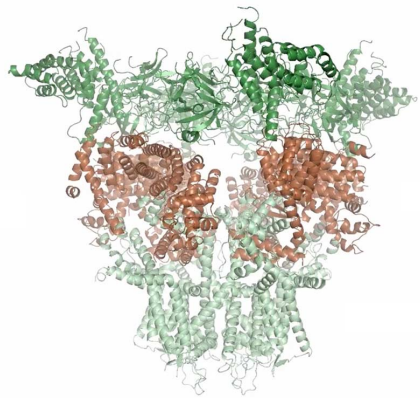

Movie 2. Conformational changes of the "central tower" between the open and closed RyR2. The rotations of the Central domains are evident in the luminal view.

Movie 3. Conformational changes of the channel domain and the Central domain during pore opening. For visual clarity, only two diagonal protomers are shown.

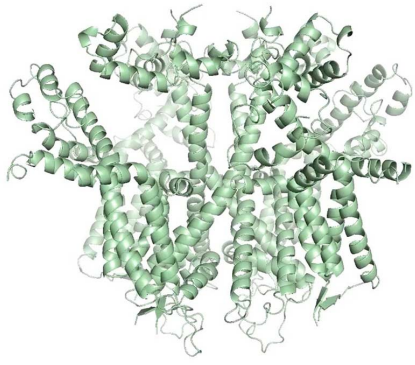

Movie 4. Potential rearrangement of interactions between the $S6_{Cyt}$ residues from adjacent protomers. The resolutions do not allow accurate assignment of the side chains of negatively charged residues. These side groups are modeled to facilitate discussion of the potential rearrangement of the interactions during pore opening. It remains to be elucidated whether Ca^{2+} ions play a role in the rearrangement of the interactions among the charged and polar residues in the $S6_{Cyt}$ segment.

Downloaded from http://science.sciencemag.org/ on October 20, 2016

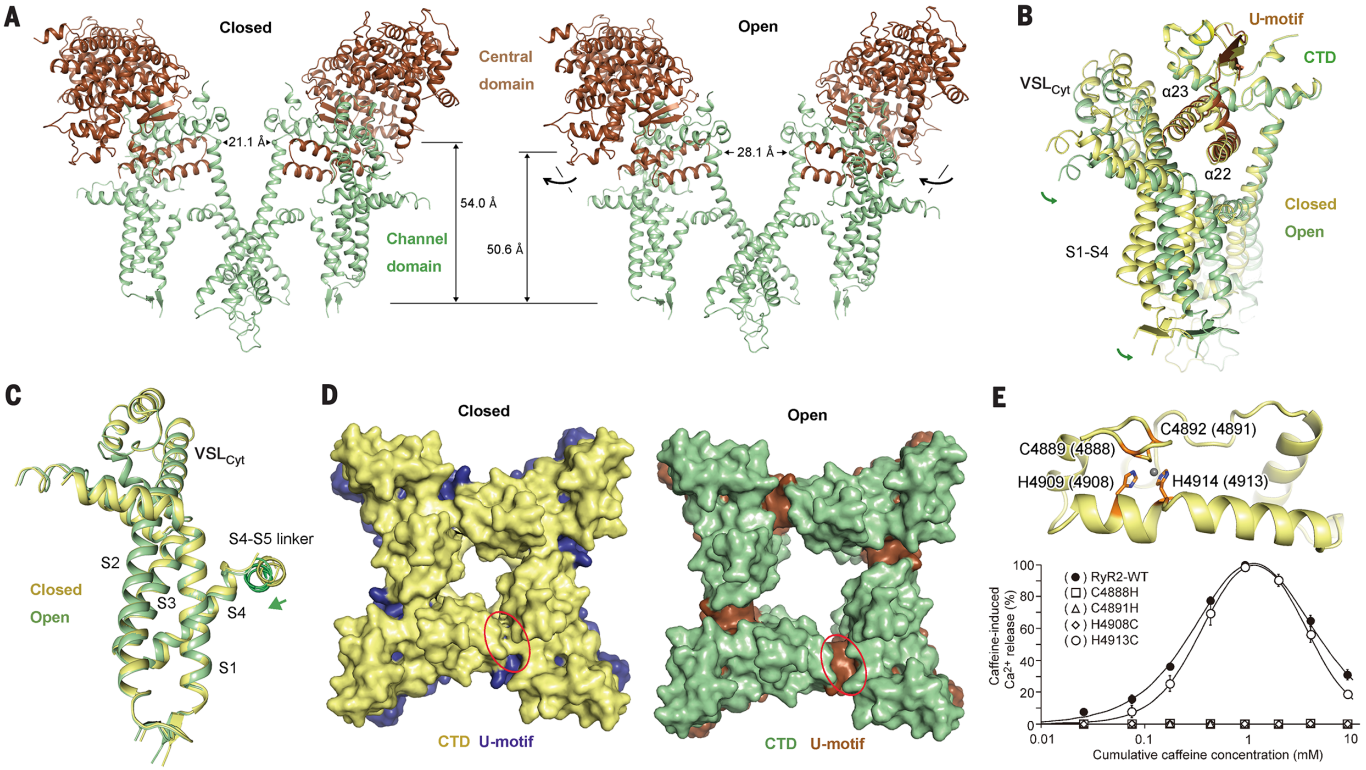

Fig. 5. The carboxyl terminal domain (CTD) couples the conformational changes of the Central domain and channel domain of RyR2. (**A**) The rotations of individual Central domains pull the $S6_{Cyt}$ segments outward through the interactions between the U-motif and CTD. (**B**) The helical hairpin in the U-motif of the Central domain forms a stable structural unit with the CTD. The structures are superimposed relative to CTD. (**C**) The VSL domain remains almost rigid during pore opening. The superimposition of the VSL domain of the open and closed structures shows little intradomain rearrangement, whereas the S4-S5 linker undergoes lateral shifts that relax the constriction to the S6 bundle at the cytoplasmic gate in the closed RyR. (**D**) The outward expansion of the CTDs and U-motifs accompanies rearrangements of the interactions between adjacent CTDs and between CTD and the U-motif from a neighboring protomer. (**E**) The integrity of the zinc finger in CTD is essential for RyR2 function. Mutations C4888H, C4891H, and H4908C completely abolish the activation of RyR2 by caffeine, whereas the H4913C mutant remains sensitive to caffeine activation (residue numbering of human and mouse RyR2). See fig. S7 for details of the mutational analysis and Movie 3 and movie S4 for the conformational changes discussed in this figure when the structures are compared relative to the channel domain.

but not cytosolic, Ca^{2+} activation of mouse RyR2. Further, introducing metal binding His residues at this site converts RyR2 from a luminal Ca^{2+}-gated channel to a luminal Ni^{2+}-gated channel (*44*). These data strongly suggest that a $S6_{Cyt}$ region encompassing the E4872 residue contains a cation binding pocket that may contribute to RyR2 activation by luminal Ca^{2+}. However, the composition of this putative cation binding pocket is unknown. Despite the fact that the densities for the negatively charged residues are invisible in the cryo-EM structures, those of the backbones and of the side chain of R4875 in pRyR2 (corresponding to R4874 in human and mouse RyR2) are discernible. Structural comparison of the closed and open states reveals that residue R4874 moves away from E4872, while E4878 may move close to E4872 in the open state (these residue numbers corresponding to those in mouse and human RyR2) (Fig. 6B). This suggests that, in addition to E4872, E4878 may also be involved in luminal Ca^{2+} activation of RyR2. Indeed, mutating mouse RyR2-E4878 markedly reduced luminal Ca^{2+} activation of RyR2 (Fig. 6D and fig. S9B). Atomic resolution structures of RyR2 in the presence of high concentrations of Ca^{2+} will be required to understand the structural basis of luminal Ca^{2+} activation of RyR2.

A number of questions remain to be investigated. The structure of the open pRyR2 was obtained in the presence of Ca^{2+} and PCB 95. However, no densities were identified for these ligands in the reconstruction. The bottleneck in the improvement of resolution in part resides in the flexibility of the protein, particularly in the absence of FKBP12 or FKBP12.6. Comparison of RyR1 and RyR2 suggests highly conserved sequences of the structural elements involved in interactions with FKBP12 in the NTD, SPRY1, and Handle domains (fig. S10) (*26*, *45*–*47*). Therefore, the basis underlying the markedly different affinities of FKBP12 binding to RyR1 and RyR2 remains to be determined (*48*, *49*).

Materials and methods

Expression and purification of GST-FKBP12 and GST-FKBP12.6

Both FKBP12 and FKBP12.6 can bind to RyR2, but the two isoforms show distinct binding affinities, particularly to the dog RyR2 (*48*). As the sequence of porcine FKBP12 or FKBP12.6 is not available in public domain, we used human FKBP12 and FKBP12.6 for affinity purification of pRyR2 based on the previous protocol for purification of rabbit RyR1 (rRyR1) (*26*). The cDNAs encoding human FKBP12/12.6 were cloned into pGEX-4T-2 vector with a C-terminal 6×His tag. The plasmids were transformed into BL21 (DE3) strain for protein overexpression. When OD_{600} reached 1.0, the temperature was adjusted to 16°C, and 0.2 mM IPTG was added for induction overnight. Cells collected by centrifugation were resuspended in lysis buffer solution (25 mM Tris-HCl, pH 8.0, and 150 mM NaCl). After removal of cell debris by centrifugation at 22,000 g for 1 hour, the supernatant was loaded to Ni^{2+}-NTA resin (Qiagen). Sequentially washed by the W1 buffer containing 25 mM Tris-HCl, pH 8.0 and 300 mM NaCl, and W2 buffer containing 25 mM Tris-HCl, pH 8.0 and 20 mM imidazole, the target protein was eluted by the buffer containing 25 mM Tris-HCl, pH 8.0 and 300 mM imidazole. Anion exchange chromatography (SOURCE 15Q, GE Healthcare) was performed for further purification. As GST-FKBP12 appeared to have a better solution behavior, we used the GST-FKBP12-His protein as bait to pull-down pRyR2.

Preparation of sarcoplasmic reticulum membrane from porcine heart

A single porcine heart was diced into small pieces, and resuspended in five volumes of homogenization buffer containing 25 mM Tris, pH 7.5, 150 mM

Downloaded from http://science.sciencemag.org/ on October 20, 2016

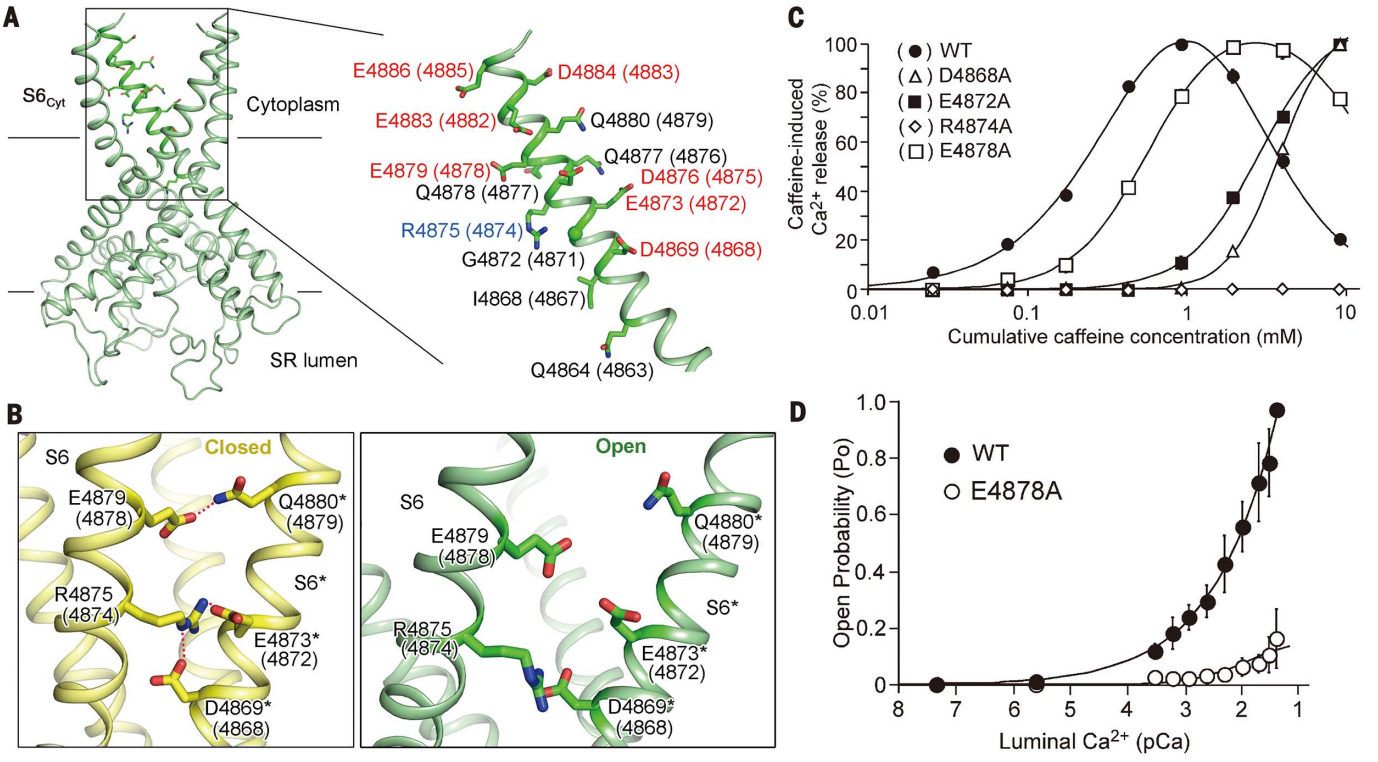

Fig. 6. The putative luminal Ca^{2+} activation sites. (**A**) The $S6_{Cyt}$ segments are enriched in charged and polar residues. The densities for the side groups of the negatively charged residues are largely invisible due to radiation damage. They are modeled in this figure to facilitate discussion. (**B**) Potential rearrangement of interactions between two neighboring $S6_{Cyt}$ helices in the open and closed pRyR2 structures. The putative hydrogen bonds are represented by red dotted lines. (**C**) Ca^{2+} release–cumulative caffeine concentration relationships. The amplitude of caffeine-induced Ca^{2+} release at each caffeine concentration was normalized to that of the maximum release for each experiment. Data shown are mean ± SEM ($n = 3$ separate experiments). (**D**) Single point mutation E4878A (corresponding to E4879 in pRyR2) leads to decreased sensitivity to luminal Ca^{2+} activation. The relationships between the open probability (Po) and luminal Ca^{2+} concentrations (pCa) of single RyR2-WT (solid circles) and E4878A mutant channels (open circles) are shown. Data points shown are mean ± SEM from 5 to 7 channels.

NaCl, 5 mM EDTA, and the protease inhibitor cocktail (0.2 mM PMSF, 1.3 μg/ml aprotinin, 0.7 μg/ml pepstatin, and 5 μg/ml leupeptin). Fifteen cycles of homogenization were performed with a blender (JYL-C010, Joyoung). The debris was removed by low-speed centrifugation (6000 g) for 6 min. The supernatant was then centrifuged at high speed (20,000 g) for 1 hour. The pellet was resuspended in two volumes of homogenization solution and flash frozen in liquid nitrogen.

Purification of pRyR2 by GST-FKBP12

The pRyR2 was purified following the same strategy for the purification of rabbit RyR1 (*26*) and the $Ca_v1.1$ complex (*29*). The porcine sarcoplasmic reticulum membrane (1/4 of total membrane from a single heart) was solubilized at 4°C for 2 hours in the homogenization buffer (mentioned above) plus 4% CHAPS, 1% soybean lecithin, and 2 mM DTT. Approximately 3-4 mg of GST-FKBP12 was added to the extraction system. After ultrahigh speed centrifugation (200,000 g), the supernatant was applied to GS4B (GE Healthcare) column. To obtain pRyR2 in closed state, the resin was washed with buffer similar to the homogenization buffer, except that the NaCl concentration was changed to 1 M, and 2 mM DTT and 0.1% Digitonin were supplemented. The complex was eluted by 75 mM Tris-HCl, pH 8.0, 150 mM NaCl, 10 mM GSH, 0.1% Digitonin, 2 mM DTT, 5 mM EDTA, and protease inhibitors. The eluted protein was concentrated before size exclusion chromatography (SEC, Superose 6 10/300 GL, GE Healthcare) in the buffer containing 25 mM Tris, pH 7.5, 300 mM NaCl, 0.1% Digitonin, 2 mM DTT, 5 mM EDTA, and protease inhibitors. The pRyR2 fractions were concentrated to approximately 0.1 mg/ml for EM sample preparation.

To capture pRyR2 in an open state, a similar protocol was used, except that EDTA was omitted. Instead, 20 μM $CaCl_2$ and 20 μM PCB 95 were supplemented to GS4B eluent. After SEC, additional 10 μM PCB 95 was added before concentrating the pRyR2 fractions.

Cryo-EM image collection

Cryo-EM grids were prepared using Vitrobot Mark IV (FEI). Aliquots (3 μl each) of pRyR2 protein were placed on glow-discharged copper grids covered with continuous carbon film (Zhongjingkeyi Technology Co. Ltd.). Grids were immediately blotted for 1.5 s and flash-frozen in liquid ethane. Cryo-EM images were acquired with a Titan Krios (FEI) operated at 300 kV. FEI Falcon-II direct electron detector was mounted and the pixel size was 1.05 Å at a nominal magnification of 75,000. Defocus value varied from −1.5 to −3.0 μm. Each image was dose-fractionated to 19 frames with a total electron dose of 44 $e^-/Å^2$ for a total exposure time of 1.2 s. EPU package (FEI) and AutoEMation package (*50*) upgraded recently were used for automated data collection.

Image processing

Frames of each image were aligned and summed using whole-image motion correction program MotionCorr (*51*). CTFFIND3 was adopted to calculate the contrast transfer function parameters (*52*). Particles were auto-picked by RELION1.4 and rechecked manually (*53*). Two- and three-dimensional classifications and refinements were all performed using RELION1.4 (*53*). In total, 213,595 particles from 4,439 micrographs were selected for the closed pRyR2. After 2D and 3D classification with C1 symmetry, 91,076 particles were selected for refinement with RyR1 (EMD accession number 2807) (*26*) as initial model. Combined with local angular search, a second round of 3D classification with C4 symmetry was performed using generated pRyR2 model from the prior refinement. 48,454 particles were finally chosen for refinement, which gave rise to an electron density map of 4.4 Å according to the gold-standard Fourier shell correlation (FSC) 0.143 criterion. A local mask of channel domain improved the resolution to 4.2 Å. Local resolution was estimated using ResMap (*54*).

Downloaded from http://science.sciencemag.org/ on October 20, 2016

With regard to the reconstruction of open pRyR2, 589,270 particles were picked from 9662 micrographs. Subsequent procedures were similar to those described above, and 133,196 particles were used for final refinement. The calculated resolution is 4.5 Å and 4.3 Å (with a local mask of channel domain). Particle polishing was performed for particle based beam-induced motion correction and radiation-damage weighing. Subsequent refinement using the polished particles further improved the resolution of 3D reconstruction to 4.2 Å and 4.1 Å (with a local mask of channel domain). Please refer to fig. S2 for the workflow of image processing.

Model building and structure refinement

Sequence alignment was done at www.ebi.ac.uk/Tools/msa/clustalo. The output file was then further processed at http://espript.ibcp.fr/ESPript/cgi-bin/ESPript.cgi (*55*). The structure of RyR1 (PDB code 3J8H) (*26*) was used for homologous model building of the closed pRyR2 and manually adjusted in COOT (*56*). The open pRyR2 was built based on the structure of closed pRyR2. Structure refinement was performed using PHENIX (*57*) in real space with secondary structure and geometry restrained.

Caffeine-induced Ca^{2+} release in HEK293 cells

Mouse RyR2 cDNA was used for transfection of HEK293 cells and electrophysiological studies of RyR2 (the corresponding residue numbers in human RyR2 are labeled instead in all functional assay figures for clarity). Cytosolic Ca^{2+} concentration in transfected HEK293 cells was measured using the fluorescence Ca^{2+} indicator dye Fluo-3 AM (Molecular Probes). HEK293 cells grown for 18 to 20 hours after subcultures were transfected with 12 μg of WT or mutant RyR2 cDNAs. Cells grown for 18 to 20 hours after transfection were washed four times with PBS and incubated in KRH (Krebs-Ringer-Hepes, 125 mM NaCl, 5 mM KCl, 1.2 mM KH_2PO_4, 6 mM glucose, 1.2 mM $MgCl_2$, 2 mM $CaCl_2$ and 25 mM HEPES, pH 7.4) buffer without $MgCl_2$ and $CaCl_2$ at room temperature for 40 min and at 37°C for 40 min. After being detached from culture dishes by pipetting, cells were collected by centrifugation at 1000 rpm for 2 min in a Beckman TH-4 rotor. Cell pellets were loaded with 10 μM Fluo-3 AM in high-glucose Dulbecco's Modified Eagle Medium at room temperature for 60 min, followed by washing with KRH buffer plus 2 mM $CaCl_2$ and 1.2 mM $MgCl_2$ (KRH+ buffer) three times and resuspended in 150 μl KRH+ buffer plus 0.1 mg/ml BSA and 250 μM sulfinpyrazone. The Fluo-3 AM loaded cells were added to 2 ml (final volume) KRH+ buffer in a cuvette. The fluorescence intensity of Fluo-3 AM at 530 nm was measured before and after repeated additions of various concentrations of caffeine (0.025 to 5 mM) in an SLM-Aminco series 2 luminescence spectrometer (SLM Instruments) with 480 nm excitation at 25°C. The peak levels of each caffeine-induced Ca^{2+} release were determined and normalized to the highest level (100%) of caffeine-induced Ca^{2+} release for each experiment.

Single channel recordings in planar lipid bilayers

Recombinant RyR2 WT and E4878A mutant channels were purified from cell lysate prepared from HEK293 cells transfected with the RyR2 WT or the E4878A mutant cDNA by sucrose density gradient centrifugation, as described previously (*35*, *58*). Heart phosphatidylethanolamine (50%) and brain phosphatidylserine (50%) (Avanti Polar Lipids), dissolved in chloroform, were combined and dried under nitrogen gas and resuspended in 30 μl of *n*-decane at a concentration of 12 mg lipid per ml. Bilayers were formed across a 250-μm hole in a Delrin partition separating two chambers. The trans chamber (800 μl) was connected to the head stage input of an Axopatch 200A amplifier (Axon Instruments, Austin, TX). The cis chamber (1.2 ml) was held at virtual ground. A symmetrical solution containing 250 mM KCl and 25 mM Hepes (pH 7.4) was used for all recordings, unless indicated otherwise. A 4-μl aliquot (~1 μg protein) of the sucrose density gradient-purified recombinant RyR2 WT or E4878A mutant channels was added to the cis chamber. Spontaneous channel activity was always tested for sensitivity to EGTA and Ca^{2+}. The chamber to which the addition of EGTA inhibited the activity of the incorporated channel presumably corresponds to the cytosolic side of the Ca^{2+} release channel. The direction of single channel currents was always measured from the luminal to the cytosolic side of the channel, unless mentioned otherwise. Recordings were filtered at 2500 Hz. Data analyses were carried out using the pclamp 8.1 software package (Axon Instruments). Free Ca^{2+} concentrations were calculated using the computer program Fabiato and Fabiato (*59*).

REFERENCES AND NOTES

1. I. N. Pessah, A. L. Waterhouse, J. E. Casida, The calcium-ryanodine receptor complex of skeletal and cardiac muscle. *Biochem. Biophys. Res. Commun.* **128**, 449–456 (1985). doi: 10.1016/0006-291X(85)91699-7; pmid: 3985981
2. M. Inui, A. Saito, S. Fleischer, Purification of the ryanodine receptor and identity with feet structures of junctional terminal cisternae of sarcoplasmic reticulum from fast skeletal muscle. *J. Biol. Chem.* **262**, 1740–1747 (1987). pmid: 3805051
3. K. P. Campbell *et al*., Identification and characterization of the high affinity [3H]ryanodine receptor of the junctional sarcoplasmic reticulum Ca^{2+} release channel. *J. Biol. Chem.* **262**, 6460–6463 (1987). pmid: 2437119
4. E. F. Rogers, F. R. Koniuszy, J. Shavel Jr., K. Folkers, Plant insecticides. I. Ryanodine, a new alkaloid from *Ryania speciosa* Vahl. *J. Am. Chem. Soc.* **70**, 3086–3088 (1948). doi: 10.1021/ja01189a074; pmid: 18882544
5. Z. Yuchi, F. Van Petegem, Ryanodine receptors under the magnifying lens: Insights and limitations of cryo-electron microscopy and x-ray crystallography studies. *Cell Calcium* **59**, 209–227 (2016). doi: 10.1016/j.ceca.2016.04.003; pmid: 27103405
6. K. Otsu *et al*., Molecular cloning of cDNA encoding the Ca^{2+} release channel (ryanodine receptor) of rabbit cardiac muscle sarcoplasmic reticulum. *J. Biol. Chem.* **265**, 13472–13483 (1990). pmid: 2380170
7. J. Nakai *et al*., Primary structure and functional expression from cDNA of the cardiac ryanodine receptor/calcium release channel. *FEBS Lett.* **271**, 169–177 (1990). doi: 10.1016/0014-5793(90)80399-4; pmid: 2226801
8. M. Endo, Calcium release from the sarcoplasmic reticulum. *Physiol. Rev.* **57**, 71–108 (1977). pmid: 13441
9. P. S. McPherson, K. P. Campbell, Characterization of the major brain form of the ryanodine receptor/Ca^{2+} release channel. *J. Biol. Chem.* **268**, 19785–19790 (1993). pmid: 7690041
10. D. M. Bers, Sarcoplasmic reticulum Ca release in intact ventricular myocytes. *Front. Biosci.* **7**, d1697–d1711 (2002). doi: 10.2741/A873; pmid: 12086924
11. M. Fill, J. A. Copello, Ryanodine receptor calcium release channels. *Physiol. Rev.* **82**, 893–922 (2002). doi: 10.1152/physrev.00013.2002; pmid: 12270947
12. M. J. Berridge, Dysregulation of neural calcium signaling in Alzheimer disease, bipolar disorder and schizophrenia. *Prion* **7**, 2–13 (2013). doi: 10.4161/pri.21767; pmid: 22895098
13. S. G. Priori *et al*., Mutations in the cardiac ryanodine receptor gene (hRyR2) underlie catecholaminergic polymorphic ventricular tachycardia. *Circulation* **103**, 196–200 (2001). doi: 10.1161/01.CIR.103.2.196; pmid: 11208676
14. S. G. Priori *et al*., Clinical and molecular characterization of patients with catecholaminergic polymorphic ventricular tachycardia. *Circulation* **106**, 69–74 (2002). doi: 10.1161/01.CIR.0000020013.73106.D8; pmid: 12093772
15. S. G. Priori, S. R. Chen, Inherited dysfunction of sarcoplasmic reticulum Ca^{2+} handling and arrhythmogenesis. *Circ. Res.* **108**, 871–883 (2011). doi: 10.1161/CIRCRESAHA.110.226845; pmid: 21454795
16. P. J. Laitinen *et al*., Mutations of the cardiac ryanodine receptor (RyR2) gene in familial polymorphic ventricular tachycardia. *Circulation* **103**, 485–490 (2001). doi: 10.1161/01.CIR.103.4.485; pmid: 11157710
17. A. Medeiros-Domingo *et al*., The RYR2-encoded ryanodine receptor/calcium release channel in patients diagnosed previously with either catecholaminergic polymorphic ventricular tachycardia or genotype negative, exercise-induced long QT syndrome: A comprehensive open reading frame mutational analysis. *J. Am. Coll. Cardiol.* **54**, 2065–2074 (2009). doi: 10.1016/j.jacc.2009.08.022; pmid: 19926015
18. M. Radermacher *et al*., Cryo-EM of the native structure of the calcium release channel/ryanodine receptor from sarcoplasmic reticulum. *Biophys. J.* **61**, 936–940 (1992). doi: 10.1016/S0006-3495(92)81900-8; pmid: 1316182
19. M. Radermacher *et al*., Cryo-electron microscopy and three-dimensional reconstruction of the calcium release channel/ryanodine receptor from skeletal muscle. *J. Cell Biol.* **127**, 411–423 (1994). doi: 10.1083/jcb.127.2.411; pmid: 7929585
20. R. D. Zühlke, G. S. Pitt, K. Deisseroth, R. W. Tsien, H. Reuter, Calmodulin supports both inactivation and facilitation of L-type calcium channels. *Nature* **399**, 159–162 (1999). doi: 10.1038/20200; pmid: 10335846
21. M. Samsó, T. Wagenknecht, P. D. Allen, Internal structure and visualization of transmembrane domains of the RyR1 calcium release channel by cryo-EM. *Nat. Struct. Mol. Biol.* **12**, 539–544 (2005). doi: 10.1038/nsmb938; pmid: 15908964
22. I. I. Serysheva *et al*., Subnanometer-resolution electron cryomicroscopy-based domain models for the cytoplasmic region of skeletal muscle RyR channel. *Proc. Natl. Acad. Sci. U.S.A.* **105**, 9610–9615 (2008). doi: 10.1073/pnas.0803189105; pmid: 18621707
23. M. Samsó, W. Feng, I. N. Pessah, P. D. Allen, Coordinated movement of cytoplasmic and transmembrane domains of RyR1 upon gating. *PLOS Biol.* **7**, e1000085 (2009). doi: 10.1371/journal.pbio.1000085; pmid: 19402748
24. R. Zalk *et al*., Structure of a mammalian ryanodine receptor. *Nature* **517**, 44–49 (2015). doi: 10.1038/nature13950; pmid: 25470061
25. R. G. Efremov, A. Leitner, R. Aebersold, S. Raunser, Architecture and conformational switch mechanism of the ryanodine receptor. *Nature* **517**, 39–43 (2015). doi: 10.1038/nature13916; pmid: 25470059
26. Z. Yan *et al*., Structure of the rabbit ryanodine receptor RyR1 at near-atomic resolution. *Nature* **517**, 50–55 (2015). doi: 10.1038/nature14063; pmid: 25517095
27. X. C. Bai, Z. Yan, J. Wu, Z. Li, N. Yan, The Central domain of RyR1 is the transducer for long-range allosteric gating of channel opening. *Cell Res.* **26**, 995–1006 (2016). doi: 10.1038/cr.2016.89; pmid: 27468892
28. R. Wei *et al*., Structural insights into Ca^{2+}-activated long-range allosteric channel gating of RyR1. *Cell Res.* **26**, 977–994 (2016). doi: 10.1038/cr.2016.99; pmid: 27573175
29. J. Wu *et al*., Structure of the voltage-gated calcium channel Cav1.1 complex. *Science* **350**, aad2395 (2015). doi: 10.1126/science.aad2395; pmid: 26680202
30. J. Wu *et al*., Structure of the voltage-gated calcium channel Cav1.1 at 3.6 A resolution. *Nature* **537**, 191–196 (2016). doi: 10.1038/nature19321
31. G. Meissner, E. Darling, J. Eveleth, Kinetics of rapid calcium release by sarcoplasmic reticulum. Effects of calcium, magnesium, and adenine nucleotides. *Biochemistry* **25**, 236–244 (1986). doi: 10.1021/bi00349a033; pmid: 3754147

Downloaded from http://science.sciencemag.org/ on October 20, 2016

32. P. W. Wong, W. R. Brackney, I. N. Pessah, Ortho-substituted polychlorinated biphenyls alter microsomal calcium transport by direct interaction with ryanodine receptors of mammalian brain. *J. Biol. Chem.* **272**, 15145–15153 (1997). doi: 10.1074/jbc.272.24.15145; pmid: 9182535
33. P. W. Wong, I. N. Pessah, Ortho-substituted polychlorinated biphenyls alter calcium regulation by a ryanodine receptor-mediated mechanism: Structural specificity toward skeletal- and cardiac-type microsomal calcium release channels. *Mol. Pharmacol.* **49**, 740–751 (1996). pmid: 8609904
34. S. R. Chen, K. Ebisawa, X. Li, L. Zhang, Molecular identification of the ryanodine receptor Ca^{2+} sensor. *J. Biol. Chem.* **273**, 14675–14678 (1998). doi: 10.1074/jbc.273.24.14675; pmid: 9614063
35. P. Li, S. R. Chen, Molecular basis of Ca^{2+} activation of the mouse cardiac Ca^{2+} release channel (ryanodine receptor). *J. Gen. Physiol.* **118**, 33–44 (2001). doi: 10.1085/jgp.118.1.33; pmid: 11429443
36. W. Guo *et al.*, The EF-hand Ca^{2+} binding domain is not required for cytosolic Ca^{2+} activation of the cardiac ryanodine receptor. *J. Biol. Chem.* **291**, 2150–2160 (2016). doi: 10.1074/jbc.M115.693325; pmid: 26663082
37. C. C. Tung, P. A. Lobo, L. Kimlicka, F. Van Petegem, The amino-terminal disease hotspot of ryanodine receptors forms a cytoplasmic vestibule. *Nature* **468**, 585–588 (2010). doi: 10.1038/nature09471; pmid: 21048710
38. E. Rios, G. Brum, Involvement of dihydropyridine receptors in excitation-contraction coupling in skeletal muscle. *Nature* **325**, 717–720 (1987). doi: 10.1038/325717a0; pmid: 2434854
39. T. Tanabe, K. G. Beam, B. A. Adams, T. Niidome, S. Numa, Regions of the skeletal muscle dihydropyridine receptor critical for excitation-contraction coupling. *Nature* **346**, 567–569 (1990). doi: 10.1038/346567a0; pmid: 2165570
40. C. Franzini-Armstrong, F. Protasi, V. Ramesh, Shape, size, and distribution of Ca^{2+} release units and couplons in skeletal and cardiac muscles. *Biophys. J.* **77**, 1528–1539 (1999). doi: 10.1016/S0006-3495(99)77000-1; pmid: 10465763
41. F. Protasi, C. Franzini-Armstrong, B. E. Flucher, Coordinated incorporation of skeletal muscle dihydropyridine receptors and ryanodine receptors in peripheral couplings of BC3H1 cells. *J. Cell Biol.* **137**, 859–870 (1997). doi: 10.1083/jcb.137.4.859; pmid: 9151688
42. F. Protasi, C. Franzini-Armstrong, P. D. Allen, Role of ryanodine receptors in the assembly of calcium release units in skeletal muscle. *J. Cell Biol.* **140**, 831–842 (1998). doi: 10.1083/jcb.140.4.831; pmid: 9472035
43. C. C. Yin, L. G. D'Cruz, F. A. Lai, Ryanodine receptor arrays: Not just a pretty pattern? *Trends Cell Biol.* **18**, 149–156 (2008). doi: 10.1016/j.tcb.2008.02.003; pmid: 18329877
44. W. Chen *et al.*, The ryanodine receptor store-sensing gate controls Ca^{2+} waves and Ca^{2+}-triggered arrhythmias. *Nat. Med.* **20**, 184–192 (2014). doi: 10.1038/nm.3440; pmid: 24441828
45. H. Masumiya, R. Wang, J. Zhang, B. Xiao, S. R. Chen, Localization of the 12.6-kDa FK506-binding protein (FKBP12.6) binding site to the NH2-terminal domain of the cardiac Ca^{2+} release channel (ryanodine receptor). *J. Biol. Chem.* **278**, 3786–3792 (2003). doi: 10.1074/jbc.M210962200; pmid: 12446682
46. R. Wang *et al.*, Localization of the dantrolene-binding sequence near the FK506-binding protein-binding site in the three-dimensional structure of the ryanodine receptor. *J. Biol. Chem.* **286**, 12202–12212 (2011). doi: 10.1074/jbc.M110.194316; pmid: 21262961
47. Z. Yuchi *et al.*, Crystal structures of ryanodine receptor SPRY1 and tandem-repeat domains reveal a critical FKBP12 binding determinant. *Nat. Commun.* **6**, 7947 (2015). doi: 10.1038/ncomms8947; pmid: 26245150
48. L. H. Jeyakumar *et al.*, FKBP binding characteristics of cardiac microsomes from diverse vertebrates. *Biochem. Biophys. Res. Commun.* **281**, 979–986 (2001). doi: 10.1006/bbrc.2001.4444; pmid: 11237759
49. H. B. Xin, K. Rogers, Y. Qi, T. Kanematsu, S. Fleischer, Three amino acid residues determine selective binding of FK506-binding protein 12.6 to the cardiac ryanodine receptor. *J. Biol. Chem.* **274**, 15315–15319 (1999). doi: 10.1074/jbc.274.22.15315; pmid: 10336416
50. J. Lei, J. Frank, Automated acquisition of cryo-electron micrographs for single particle reconstruction on an FEI Tecnai electron microscope. *J. Struct. Biol.* **150**, 69–80 (2005). doi: 10.1016/j.jsb.2005.01.002; pmid: 15797731
51. X. Li *et al.*, Electron counting and beam-induced motion correction enable near-atomic-resolution single-particle cryo-EM. *Nat. Methods* **10**, 584–590 (2013). doi: 10.1038/nmeth.2472; pmid: 23644547
52. J. A. Mindell, N. Grigorieff, Accurate determination of local defocus and specimen tilt in electron microscopy. *J. Struct. Biol.* **142**, 334–347 (2003). doi: 10.1016/S1047-8477(03)00069-8; pmid: 12781660
53. S. H. W. Scheres, RELION: Implementation of a Bayesian approach to cryo-EM structure determination. *J. Struct. Biol.* **180**, 519–530 (2012). doi: 10.1016/j.jsb.2012.09.006; pmid: 23000701
54. A. Kucukelbir, F. J. Sigworth, H. D. Tagare, Quantifying the local resolution of cryo-EM density maps. *Nat. Methods* **11**, 63–65 (2014). doi: 10.1038/nmeth.2727; pmid: 24213166
55. X. Robert, P. Gouet, Deciphering key features in protein structures with the new ENDscript server. *Nucleic Acids Res.* **42** (W1), W320–W324(2014). doi: 10.1093/nar/gku316; pmid: 24753421
56. P. Emsley, B. Lohkamp, W. G. Scott, K. Cowtan, Features and development of Coot. *Acta Crystallogr. D Biol. Crystallogr.* **66**, 486–501 (2010). doi: 10.1107/S0907444910007493; pmid: 20383002
57. P. D. Adams *et al.*, PHENIX: A comprehensive Python-based system for macromolecular structure solution. *Acta Crystallogr. D Biol. Crystallogr.* **66**, 213–221 (2010). doi: 10.1107/S0907444909052925; pmid: 20124702
58. D. Jiang *et al.*, Enhanced store overload-induced Ca^{2+} release and channel sensitivity to luminal Ca^{2+} activation are common defects of RyR2 mutations linked to ventricular tachycardia and sudden death. *Circ. Res.* **97**, 1173–1181 (2005). doi: 10.1161/01.RES.0000192146.85173.4b; pmid: 16239587
59. A. Fabiato, F. Fabiato, Calculator programs for computing the composition of the solutions containing multiple metals and ligands used for experiments in skinned muscle cells. *J. Physiol.* **75**, 463–505 (1979). pmid: 533865
60. W. L. DeLano, The PyMOL Molecular Graphics System on World Wide Web; www.pymol.org (2002).
61. E. F. Pettersen *et al.*, UCSF Chimera—A visualization system for exploratory research and analysis. *J. Comput. Chem.* **25**, 1605–1612 (2004). doi: 10.1002/jcc.20084; pmid: 15264254
62. O. S. Smart, J. M. Goodfellow, B. A. Wallace, The pore dimensions of gramicidin A. *Biophys. J.* **65**, 2455–2460 (1993). doi: 10.1016/S0006-3495(93)81293-1; pmid: 7508762
63. A. T. Brunger, Version 1.2 of the crystallography and NMR system. *Nat. Protoc.* **2**, 2728–2733 (2007). doi: 10.1038/nprot.2007.406; pmid: 18007608

ACKNOWLEDGMENTS

We thank J. Lei and X. Li for technical support. We thank the Tsinghua University Branch of the China National Center for Protein Sciences (Beijing) for providing facility support. The computation was completed on the "Explorer 100" cluster system of Tsinghua National Laboratory for Information Science and Technology. This work was supported by funds from the Ministry of Science and Technology of China (2015CB9101012014, 2016YFA0500402, and ZX09507003006), the National Natural Science Foundation of China (project 31321062), the Canadian Institutes of Health Research (MOP-123506 to S.R.W.C.), and the Heart and Stroke Foundation of Canada (G-16-00014214 to S.R.W.C.). W.G. was supported by the Alberta Innovates–Health Solutions Graduate Studentship Award. S.R.W.C. is an Alberta Innovates–Health Solutions Scientist and was supported in part by the Heart and Stroke Foundation/Libin Cardiovascular Institute Professorship in Cardiovascular Research. The research of N.Y. was supported in part by an International Early Career Scientist grant from the Howard Hughes Medical Institute and an endowed professorship from Bayer Healthcare. The atomic coordinates of pRyR2 in the closed and open states have been deposited in the Protein Data Bank with the accession codes 5GO9 and 5GOA, respectively. The corresponding maps have been deposited in the Electron Microscopy Data Bank with the accession codes EMD-9528 and EMD-9529, respectively.

SUPPLEMENTARY MATERIALS

www.sciencemag.org/content/354/6310/aah5324/suppl/DC1
Figs. S1 to S10
Table S1
Movies S1 to S4
References

13 July 2016; accepted 14 September 2016
Published online 22 September 2016
10.1126/science.aah5324

Downloaded from http://science.sciencemag.org/ on October 20, 2016

REPORTS

DEVICE TECHNOLOGY

Subthreshold Schottky-barrier thin-film transistors with ultralow power and high intrinsic gain

Sungsik Lee and Arokia Nathan*

The quest for low power becomes highly compelling in newly emerging application areas related to wearable devices in the Internet of Things. Here, we report on a Schottky-barrier indium-gallium-zinc-oxide thin-film transistor operating in the deep subthreshold regime (i.e., near the OFF state) at low supply voltages (<1 volt) and ultralow power (<1 nanowatt). By using a Schottky-barrier at the source and drain contacts, the current-voltage characteristics of the transistor were virtually channel-length independent with an infinite output resistance. It exhibited high intrinsic gain (>400) that was both bias and geometry independent. The transistor reported here is useful for sensor interface circuits in wearable devices where high current sensitivity and ultralow power are vital for battery-less operation.

Thin-film transistors (TFTs) based on amorphous oxide semiconductors (AOSs), such as indium-gallium-zinc-oxide (i.e., In-Ga-Zn-O or IGZO), have been shown to be a highly promising candidate for large-area electronics because of their high mobility, low-temperature processability, and wide band gap, hence high transparency and low OFF current, compared with the ubiquitous silicon thin-film technology and more recently the organic family (*1*–*8*). For deployment of TFTs in mobile devices, such as wearables, low voltage and low power are crucial because the operation of the wearable device is challenged by the limited battery lifetime even if it is augmented with energy harvesting (*9*–*12*). Other TFT technologies are unlikely to meet these requirements because of their higher quiescent power (table S2) (*1*–*8*, *13*–*16*).

The approach used here to achieve ultralow power is to operate the transistor in the deep subthreshold regime, i.e., near the OFF state. Within this regime, the saturation drain current (I_{DS}) of the Schottky barrier (SB) TFT is independent of drain voltage (V_{DS}), yielding an infinite output resistance (i.e., $r_o = \partial V_{DS}/\partial I_{DS} \rightarrow \infty$). Indeed, the magnitude of the current is scaled geometrically only by the channel width (W) as opposed to the channel width-to-length ratio (W/L) as in conventional transistors (see inset of Fig. 1B). The insulated gate provides an effective means of modulating the SB height at the source contact and hence the thermionic emission (TE) and thermionic field emission (TFE) properties. Thus, the emission current into the channel is determined by the reverse saturation current of the Schottky diode at the source, which in turn is modulated by the gate voltage. As a result, the SB-TFT yields a large intrinsic gain that is independent of both geometry and bias. This bias independence of intrinsic gain and zero input current by virtue of the insulated gate makes the SB-TFT capture the best of the bipolar junction transistor (BJT) and metal-oxide-semiconductor field-effect transistor (MOSFET) technology families (table S4) (*16*–*18*).

To form a Schottky contact at the source/drain contact of the IGZO TFT, we decreased the electron concentration of the IGZO film by using a high oxygen-gas partial pressure relative to argon, i.e., $P_{ox} = O_2/(O_2 + Ar)$, during the radio frequency (RF) sputtering process, with subsequent thermal annealing for a more reliable contact (Fig. 1A and fig. S1). Here, a high P_{ox} serves to compensate oxygen vacancies (V_{ox}), which act as electron donors (*7*, *19*, *20*). Indeed, in the measured output characteristics, the MC-IGZO TFT (at P_{ox} = 15%) provided Schottky characteristics at low V_{DS}, whereas the LC-IGZO TFT (at P_{ox} = 4%) showed the usual ohmic behavior (fig. S2). At higher V_{DS}, both devices show current saturation (Fig. 1B). More important, the SB-TFT (i.e., MC-IGZO TFT) has a much flatter output curvature compared to the ohmic device, yielding a much higher r_o. In particular, the output characteristics of the ohmic device had a L dependence (fig. S2). In contrast, the output characteristics of the SB-TFT were almost independent of L (Fig. 1B). This can be explained with the saturation drain-current (I_{sat}) relation as (*21*–*23*)

$$I_{sat} = A_J J_{sat}(V_{GS}) \exp\left(-\frac{\varphi_{B0}}{v_{th}}\right)\left(1 - \exp\left(-\frac{V_{DS}}{nv_{th}}\right)\right) \quad (1)$$

where n is the ideality factor (~1.7 of the examined device); A_J is the contact area, where electrons are emitted through TE-TFE rather than the drift-diffusion process; v_{th} is the thermal voltage (i.e., k_BT/q, where k_B is Boltzmann's constant, T is the absolute temperature, and q is the elementary charge); and J_{sat} is the saturation current density as a function of gate voltage (V_{GS}). I_{sat} is linearly proportional to A_J, and scales with W. In addition, the term $(1 - \exp(-V_{DS}/nv_{th}))$ is almost unity in the saturation regime because $V_{DS} >> nv_{th}$ at 300 K, and thus is independent of V_{DS}. These are consistent with the results in Fig. 1B. Besides, Fig. 1, C to E, show input characteristics, in which a conceptual color-bar of output power consumption (P_{out}) for a 1-V supply, normalized with W, is shown, clearly indicating each operational regime (Fig. 1F). In particular, as seen in Fig. 1E, the SB-TFT has a higher transconductance (g_m). This can be explained with its smaller subthreshold slope (SS) ~ 0.28 V/decade compared to the ohmic device (Fig. 1D, fig. S2, and table S1). Because the intrinsic gain (A_i) of a transistor is defined as $g_m r_o$, the SB-TFT provides a higher A_i associated with its higher r_o and g_m compared to the ohmic device (table S3).

To theoretically explain the results of the SB-TFT, we describe its operating principle in Fig. 2. At a given V_{GS}, the nonlinear response of the drain current at $V_{DS} < V_{tran}$ (the transition voltage) suggests a forward-biased Schottky diode at the drain junction (Fig. 2A). Here, the electron collection is modulated with V_{GS} through an effective SB lowering at the drain side ($\Delta\varphi_{BD}$) (Fig. 2B). When $V_{DS} > V_{tran}$, I_{DS} becomes firmly saturated because of the reverse-biased Schottky diode at the source (Fig. 2C). This regime satisfies the condition of $L >> W_D$, suggesting a negligible image-charge effect from the drain to source, where W_D is the depletion width at the drain (Fig. 2C and fig. S5A). Thus, the SB lowering at the source ($\Delta\varphi_{BS}$) is mainly a function of V_{GS} modulating the current density expressed as

$$J_{sat}(V_{GS}) = J_0 \exp\left(\frac{\Delta\varphi_{BS}(V_{GS})}{v_{th}}\right) \quad (2)$$

Here, J_0 is a reference current density. As seen in Fig. 2D, the intercept ($\Delta\varphi_0$) ~ 0.165 V can be considered as an initial SB lowering corresponding to the reference current at $V_{GS} = V_{ref}$ (the reference voltage). An effective SB-lowering (e.g., $\Delta\varphi_{BS}$) approximation is used to account for changes in the SB width (W_S) and, hence, the degree of the quantum mechanical tunneling (fig. S5C) (*23*).

Based on the theory discussed along with Fig. 2, the output characteristics of the SB device for different V_{GS} (ranging from 0 to 1 V, in steps of 0.1 V) were measured (movie S1) and modeled (Fig. 3A). The results show good agreement with each other. Figure 3B shows the transfer characteristics for V_{DS} of 0.5 and 1 V. They are nearly identical, implying current saturation for $V_{DS} > V_{tran}$ ~ 0.48 V. Also, it shows an exponential dependency on V_{GS}, which can be explained with Eq. 2 where $\Delta\varphi_{BS}(V_{GS}) = \zeta_0(V_{GS} - V_{ref}) + \Delta\varphi_0$. ζ_0 is a coefficient that describes the sensitivity of barrier lowering to V_{GS}. The retrieved r_o and g_m for V_{DS} = 1 V are shown as a function of V_{GS} (Fig. 3C). Both follow an exponential law with an opposite proportionality on V_{GS}, as described in Eqs. 3 and 4. Their

Electrical Engineering Division, Department of Engineering, University of Cambridge, 9 JJ Thomson Avenue, Cambridge CB3 0FA, UK.
*Corresponding author. Email: an299@cam.ac.uk

Downloaded from http://science.sciencemag.org/ on October 20, 2016

product gives a signal amplification factor, i.e., intrinsic gain (A_i):

$$r_o = n\frac{v_{th}}{A_J J_{B0}}\exp\left(\frac{-\zeta_0(V_{GS}-V_{ref})-\Delta\varphi_0}{v_{th}}\right)\exp\left(\frac{v_{sat}}{nv_{th}}\right) \quad (3)$$

$$g_m = \zeta_0\frac{A_J J_{B0}}{v_{th}}\exp\left(\frac{\zeta_0(V_{GS}-V_{ref})+\Delta\varphi_0}{v_{th}}\right) \quad (4)$$

$$A_i = \zeta_0 n\exp\left(\frac{v_{sat}}{nv_{th}}\right) \quad (5)$$

where $J_{B0} = J_0\exp(-\varphi_{B0}/v_{th})$ (eqs. S17 to S21). As seen in Eq. 5, A_i is not a function of either bias (e.g., V_{GS}, V_{DS}) or geometry (e.g., W and L), but rather is a function of intrinsic parameters (e.g., ζ_0, n, v_{th}, and a saturation voltage v_{sat}). So, it is just a constant, unlike the ohmic device. With Eq. 5, A_i is calculated as ~450 with the retrieved values of intrinsic parameters (fig. S6), which is consistent with measurements (Fig. 3D). Here, A_i of the SB-TFT is at least an order of magnitude higher compared to the ohmic IGZO TFT (table S3) or a typical Si-MOSFET (*17*, *18*). Because the SB-TFT operates at low voltage and low current, it is also electrically stable over time (fig. S7). The low power and high-gain performance of the SB-TFTs were applied to a common source amplifier as demonstrated in Fig. 4 (movie S2). As seen in Fig. 4, A and B, the TFT-2 (load), whose V_{ref} (and V_T) was shifted to negative because of light stress,

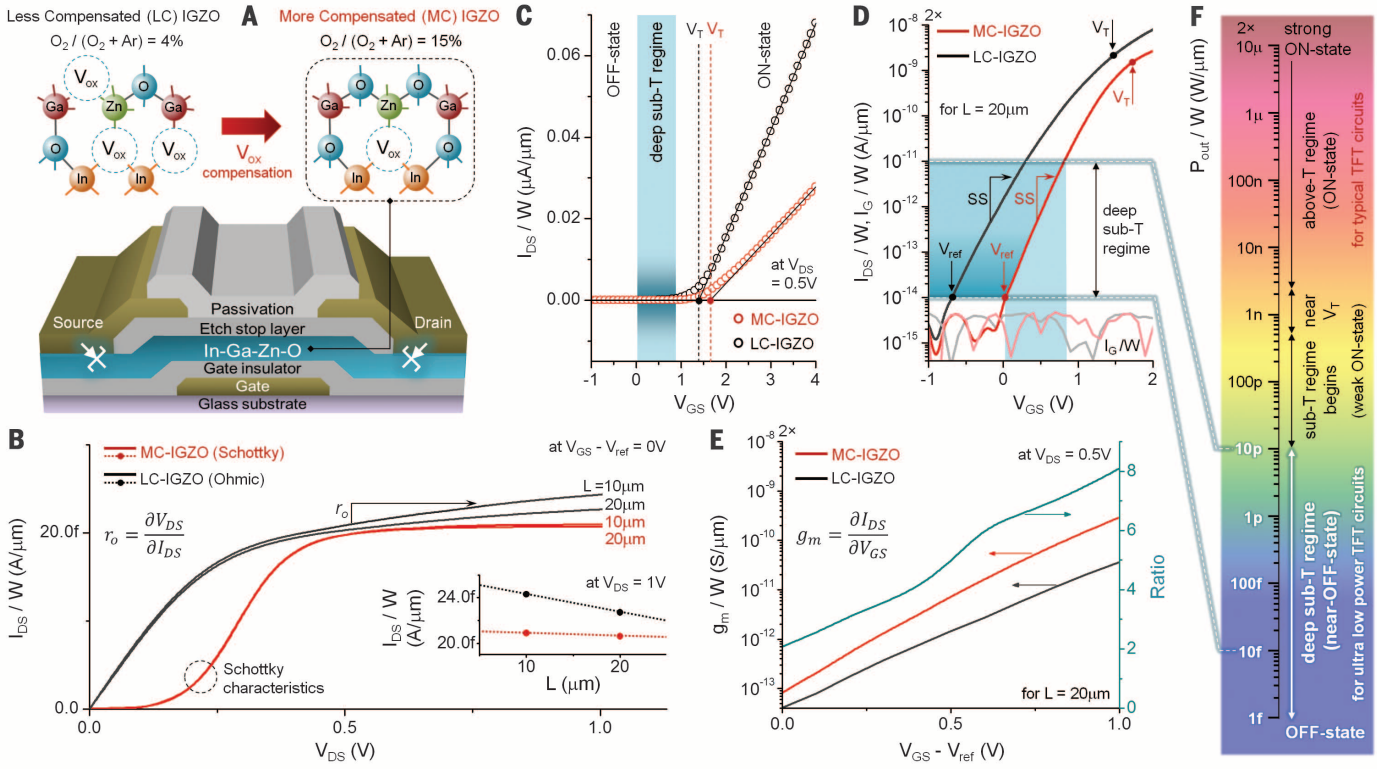

Fig. 1. Device structure and basic electrical characteristics. (**A**) Schematic cross-section of the examined device [inset: Illustration of atomic structures for less compensated (LC) and more compensated (MC) IGZO films, respectively]. (**B**) Measured I_{DS}/W versus V_{DS} for MC and LC devices (inset: I_{DS}/W versus L). Measured input characteristics: (**C**) in linear scale, indicating V_T (the threshold voltage), and (**D**) in logarithmic scale, indicating V_{ref}, respectively (I_G is a gate leakage current). (**E**) Measured g_m/W of each device along with the ratio between them. (**F**) Conceptual color bar of P_{out} normalized with W for 1-V supply. Here, the sub-T and above-T denote the subthreshold and above-threshold, respectively.

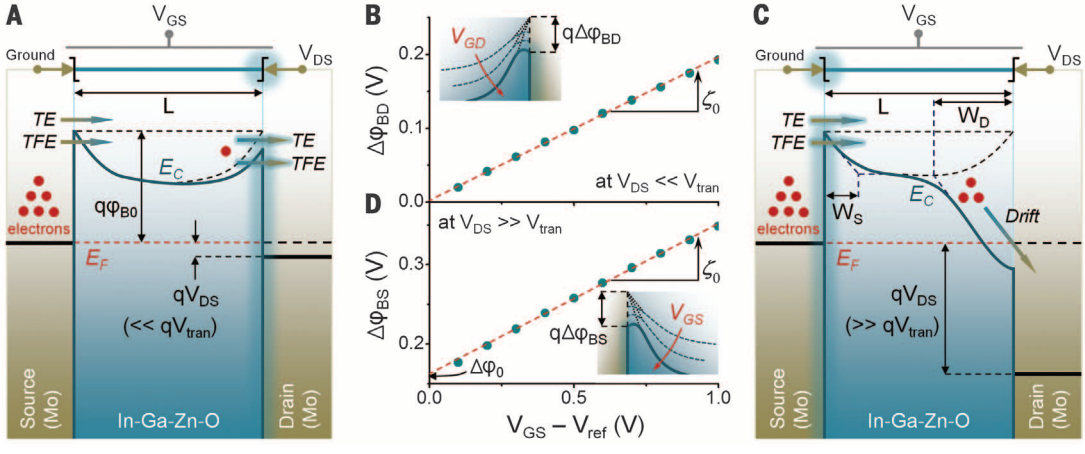

Fig. 2. Operating principle of the deep subthreshold SB-TFT. (**A**) Band diagram along L when $V_{DS} < V_{tran}$. (**B**) Retrieved $\Delta\varphi_{BD}$ at drain contact as a function of V_{GS} calibrated with V_{ref}, i.e., $V_{GS} - V_{ref}$. (**C**) Band diagram along L when $V_{DS} > V_{tran}$. (**D**) Extracted $\Delta\varphi_{BS}$ at source contact as a function of $V_{GS} - V_{ref}$. Here, E_C and E_F denote the conduction band minima and Fermi level, respectively. [Insets in (A) and (C) are equivalent circuit representations, and those of (B) and (D) are schematic diagrams to describe the bias-dependent SB lowering, respectively.]

Downloaded from http://science.sciencemag.org/ on October 20, 2016

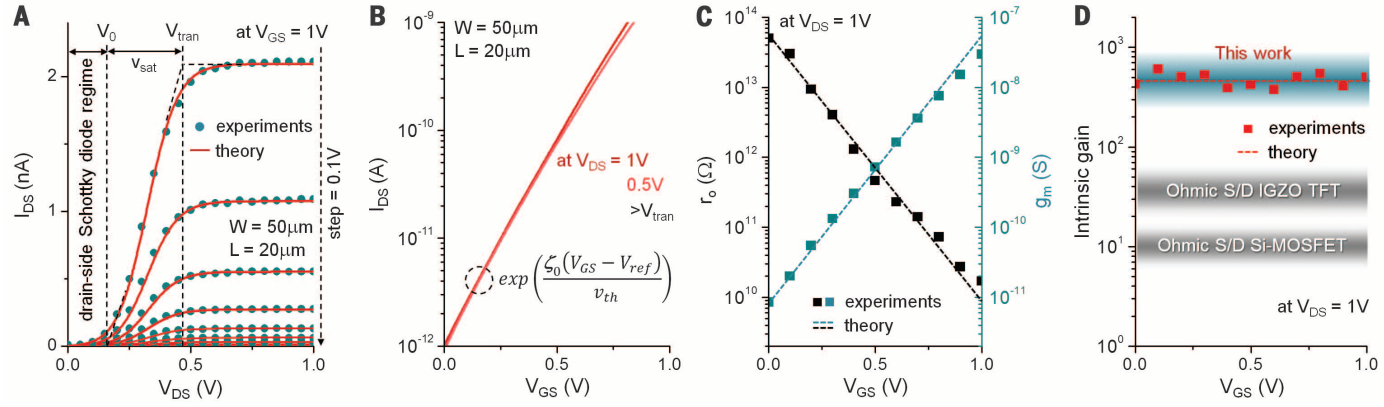

Fig. 3. Modulation characteristics and small-signal parameters of the SB-TFT in the deep subthreshold regime. (**A**) Measured I_{DS} versus V_{DS} for a different V_{GS} along with theoretical prediction. Here, V_0 is a threshold at which the source-side Schottky diode starts dominating. (**B**) Transfer characteristics for V_{DS} = 0.5 and 1 V. (**C**) Experimental values of r_o and g_m as a function of V_{GS} along with theoretical prediction (dashed lines). (**D**) Measured A_i of the SB-TFT as a function of V_{GS}.

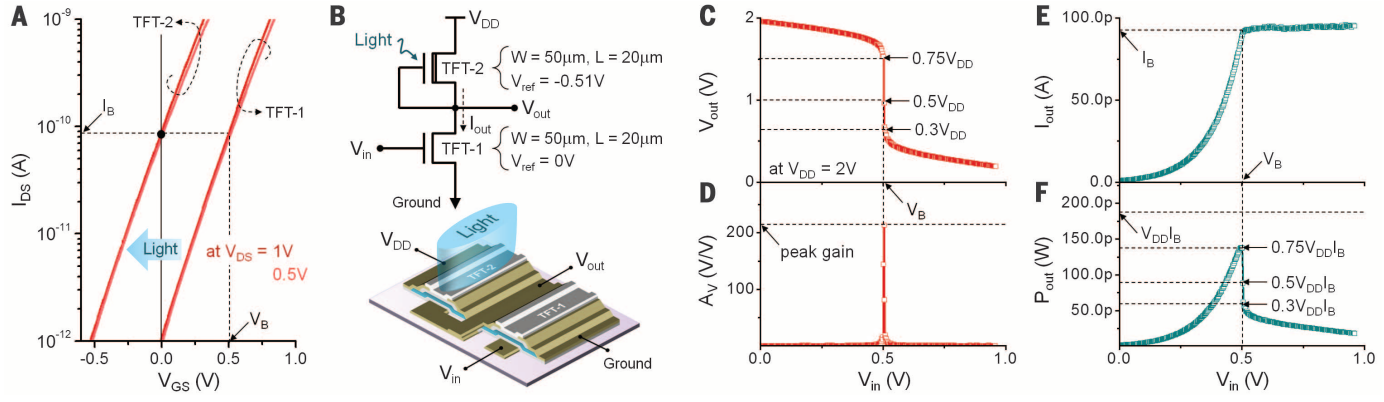

Fig. 4. Circuit-level demonstrations with the SB-TFTs. (**A**) Transfer characteristics of TFT-1 (driver) and TFT-2 (depletion load due to light stress), where I_B and V_B are determined as ~90 pA and ~0.5 V, respectively. (**B**) Common-source circuit and its three-dimensional view. (**C**) Measured output voltage (V_{out}) as a function of input voltage (V_{in}) while using 2-V supply (V_{DD}), (**D**) A_V, (**E**) output current (I_{out}), and (**F**) P_{out} versus V_{in}, respectively.

was used as a depletion load (fig. S8) (*24*). Alternatively, a TFT with a larger W as a design parameter can also be employed (fig. S9A). As shown in Fig. 4D, the circuit exhibits a high voltage gain (A_V) >220, and its output-power consumption (P_{out}) is very low, <150 pW (Fig. 4F). Thus, it can even be driven by a nanowatt power source.

Our deep subthreshold operating SB-TFT is fundamentally an ultralow-power and high-gain device, which opens up possibilities for innovative system design in many applications, including wearables and implantable devices, where low-power and low-current analog signal processing are essential requirements. In addition, the operating principle of the SB-TFT in the deep subthreshold regime (i.e., near-OFF-state) brings together the best of two transistor families: the bias independence of gain of the BJT and the zero input current of the MOSFET (table S4). Thus, the SB-TFT will bring about a new design paradigm for near-OFF-state sensor interfaces and analog front-end circuits (figs. S10 to S12).

REFERENCES AND NOTES

1. K. Nomura *et al.*, *Science* **300**, 1269–1272 (2003).
2. J. F. Wager, *Science* **300**, 1245–1246 (2003).
3. K. Nomura *et al.*, *Nature* **432**, 488–492 (2004).
4. R. Martins *et al.*, *Adv. Mater.* **23**, 4491–4496 (2011).
5. S. Lee, S. Jeon, R. Chaji, A. Nathan, *Proc. IEEE* **103**, 644–664 (2015).
6. E. Fortunato, P. Barquinha, R. Martins, *Adv. Mater.* **24**, 2945–2986 (2012).
7. Y. J. Tak *et al.*, *Sci. Rep.* **6**, 21869 (2016).
8. J. F. Wager, B. Yeh, R. L. Hoffman, D. A. Keszler, *Curr. Opin. Solid State Mater. Sci.* **18**, 53–61 (2014).
9. H. Nishide, K. Oyaizu, *Science* **319**, 737–738 (2008).
10. P. D. Mitcheson, E. M. Yeatman, G. K. Rao, A. S. Holmes, T. C. Green, *Proc. IEEE* **96**, 1457–1486 (2008).
11. J. M. Donelan *et al.*, *Science* **319**, 807–810 (2008).
12. R. J. M. Vullers, R. van Schaijk, I. Doms, C. Van Hoof, R. Mertens, *Solid-State Electron.* **53**, 684–693 (2009).
13. T. Kodaira *et al.*, *J. Soc. Inf. Disp.* **16**, 107–111 (2008).
14. H. Gleskova, S. Wagner, W. Soboyejo, Z. Suo, *J. Appl. Phys.* **92**, 6224 (2002).
15. T. Sekitani, U. Zschieschang, H. Klauk, T. Someya, *Nat. Mater.* **9**, 1015–1022 (2010).
16. R. Chaji, A. Nathan, *Thin Film Transistor Circuits and Systems* (Cambridge Univ. Press, 2013).
17. B. Razavi, *Design of Analog CMOS Integrated Circuits* (McGraw-Hill, New York, 2001).
18. A. S. Sedra, K. C. Smith, *Microelectronic Circuits* (Oxford Univ. Press, New York, 2007).
19. A. Janotti, C. G. Van de Walle, *Appl. Phys. Lett.* **87**, 122102 (2005).
20. S. Lany, A. Zunger, *Phys. Rev. B* **72**, 035215 (2005).
21. S. M. Sze, *Physics of Semiconductor Devices* (Wiley, Hoboken, NJ, ed. 2, 1981).
22. S. Lee, S. Jeon, A. Nathan, *J. Disp. Technol.* **9**, 883–889 (2013).
23. Y. Umemoto, W. J. Schaff, H. Park, L. F. Eastman, *Appl. Phys. Lett.* **62**, 1964 (1993).
24. S. Lee, A. Nathan, S. Jeon, J. Robertson, *Sci. Rep.* **5**, 14902 (2015).

ACKNOWLEDGMENTS

S.L and A.N. contributed equally to this work. We thank the Engineering and Physical Sciences Research Council under Project EP/M013650/1; European Union (EU) under Projects DOMINO 645760, ORAMA 246334, 1D-NEON 685758-2, BET-EU 692373; and Danbond under Project 69191 for their generous support. We also thank X. Cheng and J. Li (Cambridge University) for stimulating discussions. All data are available in the main text, supplementary materials, and the Cambridge University's repository.

SUPPLEMENTARY MATERIALS

www.sciencemag.org/content/354/6310/302/suppl/DC1
Materials and Methods
Supplementary Text
Figs. S1 to S12
Tables S1 to S4
Movies S1 and S2
References (*25*–*38*)

6 July 2016; accepted 20 September 2016
10.1126/science.aah5035

Downloaded from http://science.sciencemag.org/ on October 20, 2016

FORCE SPECTROSCOPY

Molecular force spectroscopy with a DNA origami–based nanoscopic force clamp

Philipp C. Nickels,[1] Bettina Wünsch,[2] Phil Holzmeister,[2]* Wooli Bae,[1] Luisa M. Kneer,[1] Dina Grohmann,[2]† Philip Tinnefeld,[2]‡ Tim Liedl[1]‡

Forces in biological systems are typically investigated at the single-molecule level with atomic force microscopy or optical and magnetic tweezers, but these techniques suffer from limited data throughput and their requirement for a physical connection to the macroscopic world. We introduce a self-assembled nanoscopic force clamp built from DNA that operates autonomously and allows massive parallelization. Single-stranded DNA sections of an origami structure acted as entropic springs and exerted controlled tension in the low piconewton range on a molecular system, whose conformational transitions were monitored by single-molecule Förster resonance energy transfer. We used the conformer switching of a Holliday junction as a benchmark and studied the TATA-binding protein–induced bending of a DNA duplex under tension. The observed suppression of bending above 10 piconewtons provides further evidence of mechanosensitivity in gene regulation.

The single-molecule force spectroscopy techniques that are most widely used to study minute forces and mechanical properties of biomolecules are atomic force microscopy and optical and magnetic tweezers. These methods have helped to explore the unfolding and folding of proteins (*1*, *2*), the elasticity of DNA (*3*), and the folding trajectory of proteins in force clamp configurations (*4*). Despite this success, two limitations persist. One is the low data throughput arising from the serial nature of conventional force spectroscopy. Recent attempts to overcome this problem include the development of increased parallel data acquisition in magnetic tweezer experiments (*5*) and centrifuge force microscopes (*6*). The second limitation is the requirement of a physical connector to a micrometer-sized object that enables interaction with the macroscopic world (*7*). These typically long and flexible connector molecules are an intrinsic feature of all established techniques and make them susceptible to drift and noise. Further, they prevent the investigation of DNA-interacting systems that induce only minor conformational changes, such as many gene-regulatory proteins (e.g., transcription factors). One previous attempt to reduce noise involved the use of DNA origami bundles as rigid spacers in optical traps (*8*). Regardless, any tether prohibits access to biologically relevant complex environments such as the inside of living cells.

A promising approach toward the complete removal of the invasive connection is the construction of autonomous, nanoscopic manipulation tools. Earlier efforts on the molecular scale to sense forces autonomously, although not in an adjustable fashion, include simple nanomechanical DNA devices (*9*–*11*) and intracellular protein force sensors (*12*). In this work, we used programmable DNA self-assembly (*13*–*18*) to construct a nanoscopic device that overcomes both limitations. Extending prestressed DNA origami tensegrity (*19*), we used the entropic spring behavior of single-stranded DNA (ssDNA) to exert defined and tunable forces on molecular systems. Conceptually, the ssDNA connects the system of interest with two immobile anchor points (Fig. 1A). By adjusting the number of bases between the fixed anchor points, the contour length of the ssDNA can be changed, directly affecting the entropic force acting on the system under study. The fixed distance imparted by the rigid DNA structure and the given contour length of the ssDNA provide an approximately constant force over time (supplementary text, section S1) (*20*). In analogy to the nomenclature of established constant-force experiments, we call our device a nanoscopic force clamp.

In the experimental realization, the ssDNA spring spans the gap of a rigid, bracket-shaped DNA origami clamp and is part of the long scaffold strand that forms the backbone of the DNA origami structure (Fig. 1B). For our design, we located the multiple cloning site (MCS) of the M13mp18 scaffold in the middle of the spring, which allowed us to insert and probe any DNA sequence of interest by means of standard cloning procedures. Additional ssDNA scaffold was stored in reservoir loops on both ends of the clamp. This enabled us to cost-efficiently build multiple objects with ssDNA springs of different lengths, permitting a flexible design with adjustable force (*19*). Individual structures were

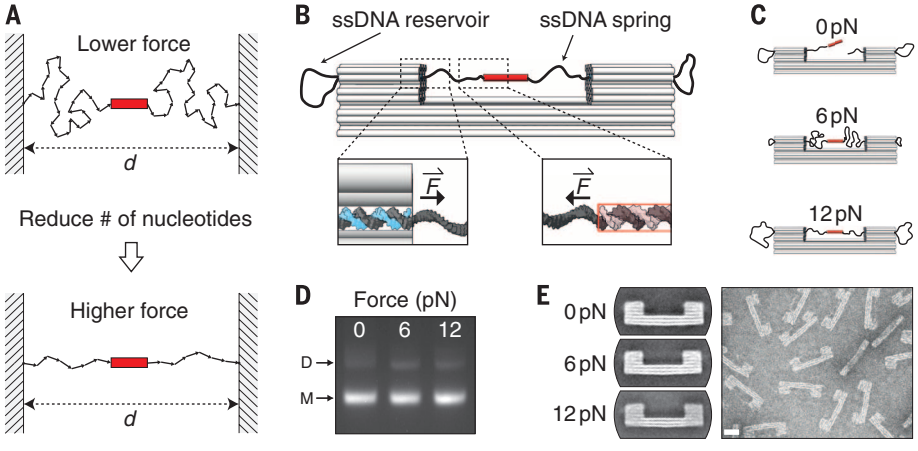

Fig. 1. DNA origami force clamp. (**A**) ssDNA connects the molecular system of interest (red rectangle) with two immobile anchor points. Reducing the number of nucleotides spanning the distance *d* leads to a smaller number of adoptable conformations of the ssDNA chain and thus results in a higher entropic force. (**B**) Structure of the DNA origami force clamp. ssDNA exits the clamp duplexes in a shear conformation (left inset; scaffold in dark gray and staple in blue) and spans the 43-nm gap. ssDNA reservoirs are located on each side of the clamp. The system of interest (here a DNA duplex) is probed in shear conformation (right inset; scaffold in dark gray and complementary DNA in light gray). *F*, force. (**C**) For each constant-force variant (three variants are shown here), individual origami samples were assembled. (**D**) Agarose gel of the three variants after annealing, with the monomer (M) and dimer (D) bands of the origami structure highlighted. (**E**) Average TEM micrographs of the three variants (left) and a single negative-stain TEM image of the 6-pN variant (right). Scale bar, 20 nm.

[1]Faculty of Physics and Center for NanoScience, Ludwig-Maximilians-Universität, Geschwister-Scholl-Platz 1, 80539 München, Germany. [2]Institut für Physikalische und Theoretische Chemie, Braunschweig Integrated Centre of Systems Biology, and Laboratory for Emerging Nanometrology, Technische Universität Braunschweig, Rebenring 56, 38106 Braunschweig, Germany.
*Present address: Bayer AG, Engineering and Technology, Enabling Technologies, Chempark E41, 51368 Leverkusen, Germany.
†Present address: Department of Biochemistry, Genetics and Microbiology, Institute of Microbiology, University of Regensburg, 93053 Regensburg, Germany. ‡Corresponding author. Email: p.tinnefeld@tu-braunschweig.de (P.T.); tim.liedl@physik.lmu.de (T.L.)

Downloaded from http://science.sciencemag.org/ on October 20, 2016

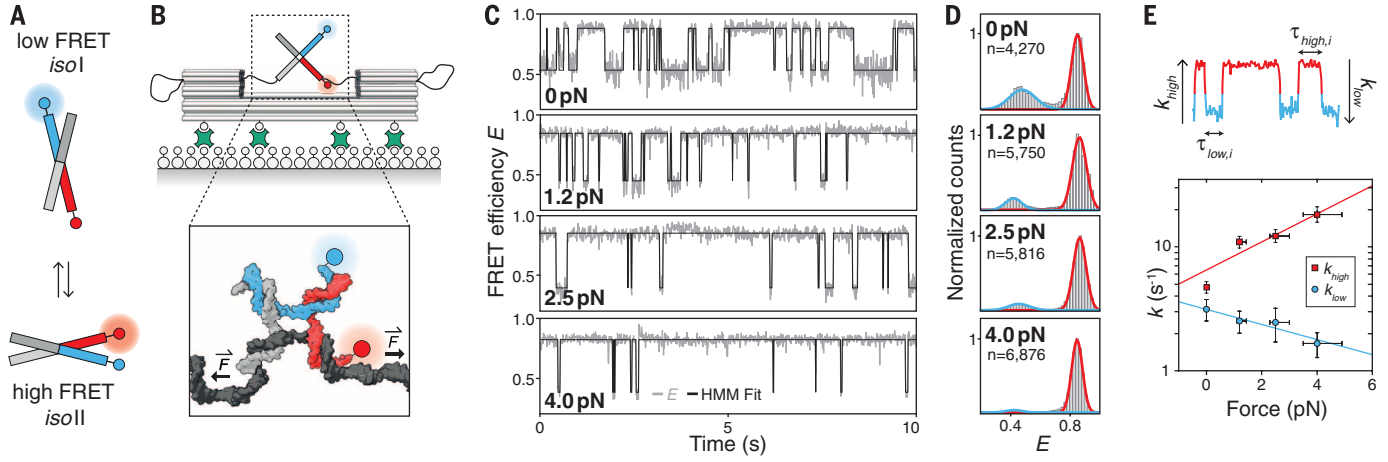

Fig. 2. Holliday junction conformer transitions under force. (**A**) Schematic of the Holliday junction (HJ) switching between two stacked isomers. Cy3 donor, blue; Cy5 acceptor, red. (**B**) Force clamps were immobilized on a bovine serum albumin–covered glass surface by biotin-streptavidin coupling. The HJ system is mounted in the force clamp with one of the four HJ strands being the scaffold (black strand in the inset). (**C**) FRET efficiency E traces (gray line) and two-state hidden Markov fit (HMM, black line). (**D**) Histograms over all recorded FRET traces, with Gaussian fits for the two FRET populations in blue (low FRET) and red (high FRET). Only traces with >20 transitions were included in the analysis; n is the total number of transitions. (**E**) Dwell times for both states ($\tau_{low,i}$ and $\tau_{high,i}$) were extracted for each trace. Transition rates (k_{low} and k_{high}) were first extracted from a monoexponential decay fit for each dwell time histogram, then averaged and plotted (semilog plot) as a function of force. Red squares, low to high FRET (k_{high}); blue circles, high to low FRET (k_{low}). Solid lines are exponential fits, where the exponent relates the rates to the applied force. The y-axis error is the standard error of each average rate; the x-axis error is the uncertainty of the calculated force (fig. S15).

assembled for each chosen length of the ssDNA spring with a distinct subset of only 10 oligonucleotides (staple strands) (Fig. 1C and figs. S1 to S3). For a zero-force control, we enzymatically cut the single-stranded spring to release any tension from the region of interest (Fig. 1C).

To calculate the resulting force for a given contour length, we approximated the ssDNA as a purely entropic spring by using a modified freely jointed chain model (*3*) with the contour length $L_C = N \times L_B$, with N being the number of nucleotides and L_B the length per single base (supplementary text, section S1). For L_B, we used 6.3 ± 0.8 Å, a value obtained from a length comparison of five different crystal structures of ssDNA segments (*21*).

We thermally annealed the force clamp structure, producing ~10^{12} force clamps in a single one-pot reaction. The chosen annealing ramp avoided temperatures above 65°C to minimize thermal degradation of the scaffold (fig. S4 and supplementary text, section S2) (*20*). We confirmed successful assembly by means of agarose gel electrophoresis (Fig. 1D and fig. S5), bulk Förster resonance energy transfer (FRET) experiments (fig. S6), and transmission electron microscopy (TEM) (Fig. 1E and figs. S7 to S13).

To demonstrate the functionality and sensitivity of our force clamp, we cloned a sequence into the scaffold that, together with three other oligonucleotides, forms the well-studied four-way Holliday junction (HJ) (*22*). In the presence of magnesium, the HJ forms an X-like structure by pairwise coaxial stacking of its helical arms. The chosen sequence is known to constantly switch between the two stacking conformers iso I and iso II (Fig. 2A) (*22*), a process that can be efficiently monitored with the help of a donor-acceptor FRET pair positioned on two of the arms (Fig. 2B and fig. S14). We chose four force variants ranging from 0 to 4.0 pN and confirmed their successful assembly (figs. S15 to S23). We immobilized these structures on a coverslip surface and monitored donor-acceptor pair intensities from individual force clamps over time in a confocal single-molecule setup with alternating laser excitation (ALEX) (*20*, *23*).

Exemplary FRET traces and FRET histograms from thousands of transitions are shown in Fig. 2, C and D, for each constant-force experiment (more traces are shown in figs. S24 and S25). A low-FRET population was centered at the FRET efficiency E = 0.42 (corresponding to iso I), and a high-FRET population was centered at E = 0.85 (corresponding to iso II). With increasing force, the equilibrium shifted toward the iso II conformation with almost no low-FRET population remaining at 4.0 pN. We used two-state hidden Markov modeling (*24*) to calculate the transition rates between the low- and high-FRET conformations for each of the forces. The transition rate from low to high FRET (k_{high}) increased from 4.7 ± 0.4 s^{-1} at 0 pN to 18.3 ± 1.4 s^{-1} at 4.0 pN. Meanwhile, the transition rate from high to low FRET (k_{low}) decreased from 3.2 ± 0.6 s^{-1} at 0 pN to 1.7 ± 0.4 s^{-1} at 4.0 pN (Fig. 2E). These rate changes are in good agreement with reported values from combined FRET and optical and magnetic tweezer measurements (*22*, *25*). Importantly, the heterogeneity of the HJ (*26*) was preserved in our measurements (fig. S26), indicating that the force clamp itself did not influence the dynamics of the HJ.

Next, we studied the force dependency of the TATA-binding protein (TBP)–induced bending of a DNA duplex. Such DNA distortions are an integral function of many transcription factors and DNA binding proteins. Although the correlation between transcriptional regulation and chromosome organization is well known, it has been challenging to quantify the impact of the DNA condensation state and the chromosome organization (e.g., the extent of strain in the DNA) on transcription factors such as TBP.

TBP is found in the archaeal and eukaryotic domains of life. It recognizes the minor groove of the adenine- and thymidine-rich TATA box in the core promoter sequence and introduces a severe ~90° bend in the DNA. Together with transcription factor B [TFB/TF(II)B], TBP is responsible for the site-specific recruitment and orientation of RNA polymerases at the transcription start site. To date, force measurements of this system have been futile, at least partly because the TBP-induced changes in the DNA topology are not easily detectable through the long tethers that are unavoidable in standard force spectroscopy experiments. Fluorescence readout in combination with our high-throughput method helped us to circumvent this problem.

We used TBP from the hyperthermophilic archaeal organism *Methanocaldococcus jannaschii* (MjTBP) (Fig. 3A), which bends the promoter DNA in one step without the need for the second transcription initiation factor TFB/TF(II)B (*27*), and inserted into the scaffold a promoter sequence, derived from the *Sulfolobus* spindle-shaped virus 1 (SSV) T6 gene promoter, that contains a TATA box motif and is recognized by MjTBP (Fig. 3B and fig. S27). We chose six force clamp variants ranging from 0 to 11.4 pN and confirmed their successful assembly (figs. S28 to S40). The complementary

Downloaded from http://science.sciencemag.org/ on October 20, 2016

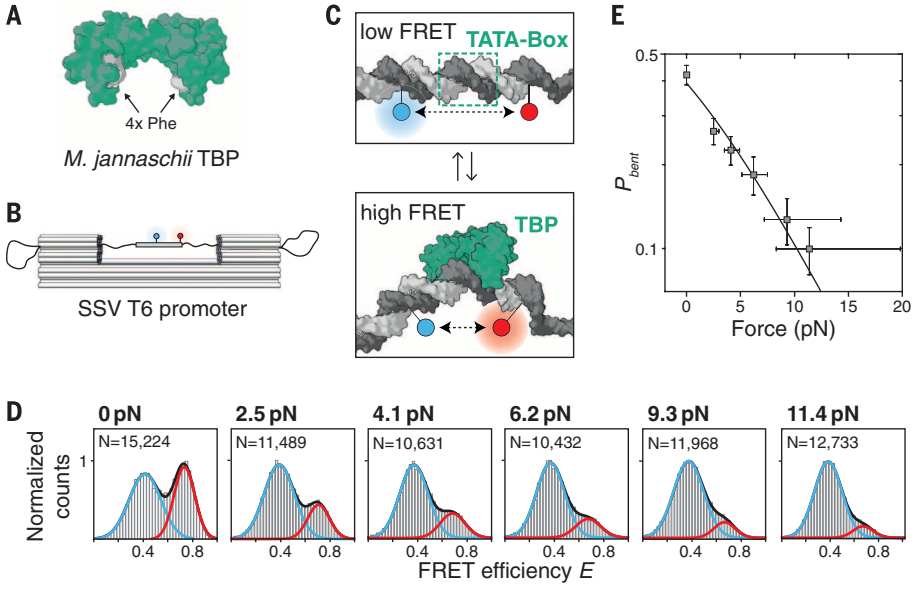

Fig. 3. TBP-induced DNA bending under force. (**A**) TBP from *M. jannaschii* (MjTBP; Protein Data Bank ID, 2Z8U) (*29*). Two pairs of phenylalanines (Phe) located in the DNA binding domain promote DNA bending. (**B**) The SSV T6 promoter, including the TATA box, mounted on the force clamp. Atto532 donor, blue; Atto647n acceptor, red. (**C**) TBP binds the minor groove of the TATA box and bends the duplex by almost 90°, thus changing the distance between the donor and acceptor. (**D**) FRET histograms and Gaussian fits for the low-FRET (blue) and high-FRET (red) populations. *N* is the number of molecules measured for each force. (**E**) Semilog plot of the probability of the bent state P_{bent} as a function of force. The solid line is a Boltzmann distribution fit. The *y*-axis error is the standard error of P_{bent}; the *x*-axis error is the uncertainty of the calculated force (fig. S28).

strand of the 51–base-pair–long SSV T6 promoter was hybridized to the scaffold during folding. Bending was monitored by single-molecule FRET measurements of a donor-acceptor pair flanking the TATA box (Fig. 3C and fig. S27). We chose in-solution over surface measurements to greatly increase the data acquisition throughput (*28*). Fluorescence bursts of the donor and acceptor were recorded before and after the addition of MjTBP.

Figure 3D shows histograms of the FRET efficiency with MjTBP for the six different forces. Each histogram includes data from at least 10,000 measured force clamps, although the average recording time per sample was only ~30 min. All histograms show a bimodal distribution with a low-FRET population centered at E = 0.42 (corresponding to the undistorted state) and a high-FRET population centered at E = 0.74 (corresponding to the bent state). The high-FRET population disappeared gradually with increasing force, and the TBP-induced bending was almost completely suppressed at 11.4 pN (full histograms for E and stoichiometry are shown in fig. S41). We calculated the probability of the bent state P_{bent} from its relative occurrence within the bimodal FRET distribution and plotted P_{bent} as a function of force (Fig. 3E). P_{bent} is well described by the difference in free energy between the unbent and bent states, expressed through a Boltzmann distribution (Fig. 3E and supplementary text, section S3) (*20*). An estimate of the change in binding affinity and Gibbs free energy is given in fig. S42.

Our DNA origami force clamp serves as a new tool to quantify the sensitivity of transcription factor–induced distortion to DNA tension and thus to chromosome organization. This adds information to the growing picture of transcriptional regulation and protein-DNA interactions in general. Our nanoscopic force clamp expands the range of available single-molecule force spectroscopy techniques and makes new molecular systems accessible to sensitive force spectroscopy analysis. The self-assembling clamps are easy to prepare and can be used to study any DNA-interacting and DNA-modifiable system (e.g., proteins conjugated with short DNA tethers). The simple operation and highly increased throughput compared with standard techniques facilitate the generation of force spectroscopy data in a dynamic range of 0 to 12 pN, which easily can be extended to ~50 pN (supplementary text, section S4) (*20*). Given that our method provides the flexibility to perform both on-surface and in-solution experiments, we envision moving from elaborate and costly single-molecule tools toward simple and readily adaptable ensemble assays.

REFERENCES AND NOTES

1. M. S. Kellermayer, S. B. Smith, H. L. Granzier, C. Bustamante, *Science* **276**, 1112–1116 (1997).
2. M. Rief, M. Gautel, F. Oesterhelt, J. M. Fernandez, H. E. Gaub, *Science* **276**, 1109–1112 (1997).
3. S. B. Smith, Y. Cui, C. Bustamante, *Science* **271**, 795–799 (1996).
4. J. M. Fernandez, H. Li, *Science* **303**, 1674–1678 (2004).
5. N. Ribeck, O. A. Saleh, *Rev. Sci. Instrum.* **79**, 094301 (2008).
6. K. Halvorsen, W. P. Wong, *Biophys. J.* **98**, L53–L55 (2010).
7. K. C. Neuman, A. Nagy, *Nat. Methods* **5**, 491–505 (2008).
8. E. Pfitzner *et al.*, *Angew. Chem. Int. Ed. Engl.* **52**, 7766–7771 (2013).
9. H. Shroff *et al.*, *Nano Lett.* **5**, 1509–1514 (2005).
10. W. Shen, M. F. Bruist, S. D. Goodman, N. C. Seeman, *Angew. Chem. Int. Ed. Engl.* **43**, 4750–4752 (2004).
11. H. Gu, W. Yang, N. C. Seeman, *J. Am. Chem. Soc.* **132**, 4352–4357 (2010).
12. C. Grashoff *et al.*, *Nature* **466**, 263–266 (2010).
13. N. C. Seeman, *Nature* **421**, 427–431 (2003).
14. P. W. K. Rothemund, *Nature* **440**, 297–302 (2006).
15. S. M. Douglas *et al.*, *Nucleic Acids Res.* **37**, 5001–5006 (2009).
16. Y. Ke *et al.*, *J. Am. Chem. Soc.* **131**, 15903–15908 (2009).
17. E. S. Andersen *et al.*, *Nature* **459**, 73–76 (2009).
18. S. M. Douglas *et al.*, *Nature* **459**, 414–418 (2009).
19. T. Liedl, B. Högberg, J. Tytell, D. E. Ingber, W. M. Shih, *Nat. Nanotechnol.* **5**, 520–524 (2010).
20. Materials and methods are available as supplementary materials on *Science* Online.
21. M. C. Murphy, I. Rasnik, W. Cheng, T. M. Lohman, T. Ha, *Biophys. J.* **86**, 2530–2537 (2004).
22. S. Hohng *et al.*, *Science* **318**, 279–283 (2007).
23. J. Ross *et al.*, *J. Phys. Chem. B* **111**, 321–326 (2007).
24. S. A. McKinney, C. Joo, T. Ha, *Biophys. J.* **91**, 1941–1951 (2006).
25. F. E. Kemmerich *et al.*, *Nano Lett.* **16**, 381–386 (2016).
26. C. Hyeon, J. Lee, J. Yoon, S. Hohng, D. Thirumalai, *Nat. Chem.* **4**, 907–914 (2012).
27. A. Gietl *et al.*, *Nucleic Acids Res.* **42**, 6219–6231 (2014).
28. A. N. Kapanidis *et al.*, *Acc. Chem. Res.* **38**, 523–533 (2005).
29. N. Adachi, M. Senda, R. Natsume, T. Senda, M. Horikoshi, *Genes Cells* **13**, 1127–1140 (2008).

ACKNOWLEDGMENTS

We thank H. Gaub, A. Gietl, A. Maier, I. MacPherson, J. Lipfert, M. Pilo-Pais, J. Rädler, O. Saleh, and T. Zhang for discussions and S. Kempter and G. Schwake for technical assistance. S. Schulz kindly prepared the MjTBP. This work was supported by the Deutsche Forschungsgemeinschaft [grant LI 1743/2-1, grant TI 329/6-1, grant GrK1952/1 ("Metrology for Complex Nanosystems"), Nanosystems Initiative Munich, grant SFB 1032 (TPA6), and grant SFB 960 (TPA7)], the Braunschweig International Graduate School of Metrology, the European Commission [Framework Programme 7–EScoDNA grant agreement no. 317110 and European Research Council grant agreement no. 336440 for ORCA (Optical Responses Controlled by DNA Assembly)], and the Boehringer Ingelheim Foundation. P.C.N., B.W., and P.H. performed the experiments. P.C.N., D.G., P.T., and T.L. designed the research. P.C.N., B.W., P.H., L.M.K., W.B., P.T., and T.L. analyzed the data. P.C.N. and W.B. prepared the figures. P.C.N., P.T., D.G., and T.L. wrote the manuscript. All authors edited the manuscript. The authors declare that they have no competing interests. Additional data described in this work can be found in the supplementary materials.

SUPPLEMENTARY MATERIALS

www.sciencemag.org/content/354/6310/305/suppl/DC1
Materials and Methods
Supplementary Text
Figs. S1 to S42
Custom M13mp18-Based Scaffold Sequences
References (*30*–*40*)

19 July 2016; accepted 6 September 2016
10.1126/science.aah5974

Downloaded from http://science.sciencemag.org/ on October 20, 2016

CHEMICAL PHYSICS

Ultrafast electron diffraction imaging of bond breaking in di-ionized acetylene

B. Wolter,[1]* M. G. Pullen,[1]* A.-T. Le,[2] M. Baudisch,[1] K. Doblhoff-Dier,[3] A. Senftleben,[4] M. Hemmer,[1,5] C. D. Schröter,[6] J. Ullrich,[6,7] T. Pfeifer,[6] R. Moshammer,[6] S. Gräfe,[8,9] O. Vendrell,[5,10] C. D. Lin,[2] J. Biegert[1,11]†

Visualizing chemical reactions as they occur requires atomic spatial and femtosecond temporal resolution. Here, we report imaging of the molecular structure of acetylene (C_2H_2) 9 femtoseconds after ionization. Using mid-infrared laser–induced electron diffraction (LIED), we obtained snapshots as a proton departs the $[C_2H_2]^{2+}$ ion. By introducing an additional laser field, we also demonstrate control over the ultrafast dissociation process and resolve different bond dynamics for molecules oriented parallel versus perpendicular to the LIED field. These measurements are in excellent agreement with a quantum chemical description of field-dressed molecular dynamics.

Ultrafast imaging of atomic motion in real time during transitions in molecular structure is a prerequisite to disentangling the complex interplay between reactants and products (*1*, *2*) because the movements of all atoms are coupled. Ultrafast absorption and emission spectroscopic techniques have uncovered numerous insights in chemical reaction dynamics (*3*, *4*) but are limited by their reliance on local chromophores and their associated ladders of quantum states rather than global structural characterization.

Reaction imaging at the molecular level requires a combination of few-femtosecond temporal and picometer spatial measurement resolution (*5*). Among the many techniques that are currently under intense development, x-ray scattering can reach few-femtosecond pulse durations at photon energies of 8.3 keV (1.5 Å) (*6*) with a demonstrated measurement resolution of 3.5 Å (*7*). Challenges for such photon-based approaches are the coarse spatial resolution and the low scattering cross sections, especially for gas-phase investigations. Electron scattering (*8*) provides much-larger-interaction cross sections and smaller de Broglie wavelengths but suffers from space charge broadening, which decreases the temporal resolution. Consequently, measurements have demonstrated 7-pm spatial and 100-fs temporal resolution (*9*, *10*) in gas-phase experiments. Remedies to improve temporal resolution include relativistic electron acceleration (*11*) or electron bunch compression (*12*) with 100- and 28-fs limits, respectively. Compared with such incoherent scattering of electrons from an electron source off a molecular target, laser-induced electron diffraction (LIED) is a self-imaging method based on coherent electron scattering (*13*–*17*). In LIED, one electron is liberated from the target molecule through tunnel ionization and then accelerated in the field and rescattered off its molecular ion, acquiring structural information. The electron recollision process occurs within one optical cycle of the laser field and permits the mapping of electron momenta to recollision time (*18*, *19*).

Here, we used LIED to image an entire hydrocarbon molecule [acetylene (C_2H_2)] at 9 fs after ionization-triggered dissociation and visualize the departure of a proton. Our methodology combined mid-infrared (mid-IR) LIED with single-molecule coincidence detection in a reaction microscope (*20*–*22*) and used an additional laser control field to impulsively align the molecule (supplementary materials). The laser control field, a 1700-nm pulse, was sent before the 3100-nm LIED pulse and oriented the rotationally cold C_2H_2 molecule parallel or perpendicular to the LIED field depending on the time delay. The 3100-nm pulse triggered molecular dissociation and, at the same time, collected structural snapshots of the entire C_2H_2 molecule. The alignment-dependent dynamics (*23*) were structurally imaged for both orientations. We chose C_2H_2 because it is one of the best-studied hydrocarbons (*24*–*27*) and offers the numerous degrees of freedom and multitude of structural dynamics found also in larger and more complex molecules (*1*, *28*, *29*). Because of the strong field nature of LIED, many different fragmentation channels and ionization states occur simultaneously. Our specific implementation of mid-IR LIED with single-molecule coincidence detection provides a remedy because post-selection of data regains channel selectivity.

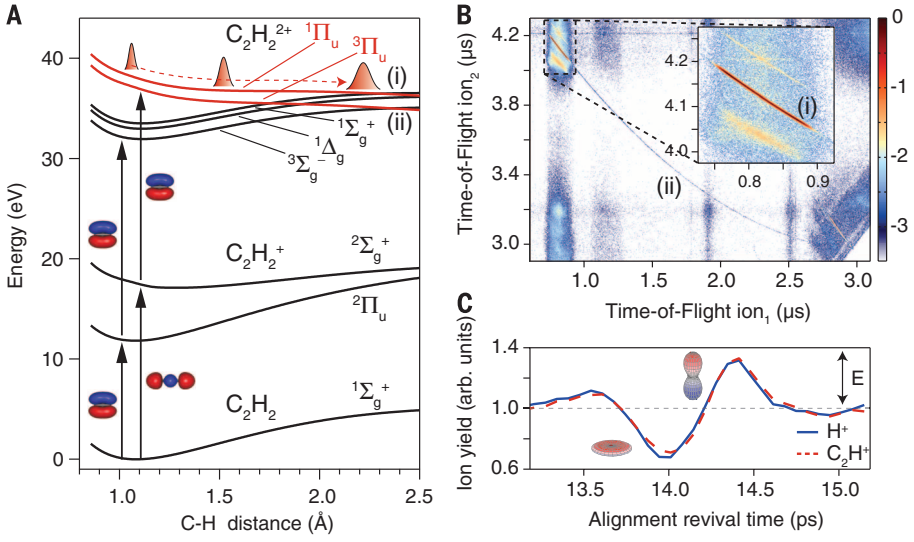

Fig. 1. Identification of the relevant states leading to proton ejection. (**A**) The calculated relevant energy levels and possible pathways (*34*) leading to dissociation of C_2H_2 and departure of one proton (*26*, *35*). The calculation is detailed in the supplementary materials. Two main pathways are identified, one leading to dissociative PES and fast dissociation (i), the other via metastable states to slow dissociation (ii). (**B**) These pathways are identified in the PIPICO analysis and (**C**) exhibit alignment-dependent fragment yields. (B) is shown here for perpendicularly oriented C_2H_2; the parallel case is provided in fig. S4.

[1]ICFO–Institut de Ciencies Fotoniques, The Barcelona Institute of Science and Technology, 08860 Castelldefels, Barcelona, Spain. [2]J. R. Macdonald Laboratory, Physics Department, Kansas State University, Manhattan, KS 66506-2604, USA. [3]Leiden Institute of Chemistry, Gorlaeus Laboratories, Leiden University, Post Office Box 9502, 2300 RA Leiden, Netherlands. [4]Universität Kassel, Institut für Physik und CINSaT, Heinrich-Plett-Str. 40, 34132 Kassel, Germany. [5]Center for Free-Electron Laser Science, Deutsches Elektronen-Synchrotron (DESY), Centre for Ultrafast Imaging (CUI), 22607 Hamburg, Germany. [6]Max-Planck-Institut für Kernphysik, Saupfercheckweg 1, 69117 Heidelberg, Germany. [7]Physikalisch-Technische Bundesanstalt (PTB), Bundesallee 100, 38116 Braunschweig, Germany. [8]Institute for Physical Chemistry, Friedrich-Schiller University Jena, 07743 Jena, Germany. [9]Abbe Center of Photonics, Friedrich-Schiller-University Jena, 07743 Jena, Germany. [10]Department of Physics and Astronomy, Aarhus University, 8000 Aarhus C, Denmark. [11]Institució Catalana de Recerca i Estudis Avançats (ICREA), Pg. Lluís Companys 23, 08010 Barcelona, Spain.
*These authors contributed equally to this work. †Corresponding author. Email: jens.biegert@icfo.eu

Downloaded from http://science.sciencemag.org/ on October 21, 2016

Using this capability, we specifically chose to isolate and examine the dissociation of the C_2H_2 dication ($C_2H_2^{2+} \rightarrow H^+ + C_2H^+$) because it results in a proton H^+ and an ethynyl C_2H^+ moiety. This prototypical dissociation pathway is interesting because it presents one of the fastest expected proton motions and can proceed via two different pathways.

The relevant cuts through the potential energy surface (PES) of C_2H_2 along one C–H direction are shown in Fig. 1A, including states that are relevant for the desired dissociation channel of $C_2H_2^{2+}$ (*30*, *31*) at the present experimental conditions by using a 65-fs (6.3 cycle), 3100-nm pulse (*32*, *33*) with a peak intensity of (65 ± 16) TW/cm^2. The pulse parameters were chosen in order to position the experiment in the sequential double ionization (SDI) regime in which the LIED imaging electron is ejected independently from the first electron in a second tunnel ionization step before scattering off the C_2H_2 dication (supplementary materials). It is known (*26*, *30*, *31*) that the resulting pair of proton H^+ and ethynyl C_2H^+ moiety originates via different possible pathways from the $C_2H_2^{2+}$ dication: (i) The first dissociative excited singlet and triplet states, the $^1\Pi_u$ and the $^3\Pi_u$ states, can be reached through ionization from the σ_g type highest occupied molecular orbital (HOMO)–1 of the neutral ground state ($1\sigma_g^2$, $1\sigma_u^2$, $2\sigma_g^2$, $2\sigma_u^2$, $3\sigma_g^2$, $1\pi_u^2$, $1\pi_u^2$) followed by tunnel ionization from the π_u type HOMO of the excited cationic $^2\Sigma_g^+$ state (*26*, *34*); (ii) the dication possesses a long-lived metastable triplet state [$^3\Sigma_g^-$ lifetime 108 ns (*35*)] and two metastable singlet states ($^1\Sigma_g^+$ and $^1\Delta_g$) that can be reached via sequential tunnel ionization of two π_u electrons. In this case, first one electron tunnels from the HOMO of the neutral ground state ($^1\Sigma_g^+$), populating the singly ionic doublet $^2\Pi_u$ state; then, a second electron tunnels from the HOMO of the singly ionic ground state to populate one of the aforementioned dicationic states. We were interested in the direct dissociation channel that leads to fast proton loss. A simple estimation of the initial speed of the C–H bond elongation, which is based on the curvature of the $^3\Pi_u$ PES, yields an initial elongation velocity of 9 pm/fs from the initial C–H bond length of 1.07 Å in the Frank-Condon region.

To obtain the clearest possible conditions for imaging the direct proton loss channel, and to investigate its dependence on the LIED field, we impulsively aligned the C_2H_2 molecule with an additional 1700-nm, 98-fs pulse focused to a peak intensity of (20 ± 5) TW/cm^2 into the interaction region of the 3100-nm LIED pulse. Having ensured that the 1700-nm pulse did not induce ionization, we could distinguish between the different pathways from a photo-ion/photo-ion coincidence (PIPICO) analysis of our data, which is shown in Fig. 1B (here for perpendicularly oriented C_2H_2). The diagonally sloping line (Fig. 1B, top left to bottom right) shows a very pronounced section [Fig. 1B, top left corner, (i) centered around 0.8 μs/4.1 μs], which corresponds to direct dissociation of the dication from its excited $^1\Pi_u$ and $^3\Pi_u$ states. Section (ii) of this line [Fig. 1B, top left corner 1.0 μs/4.0 μs to bottom right corner 2.6 μs/3.1 μs] is much weaker and is identified with the dication's meta-stable states $^3\Sigma_g^-$, $^1\Delta_g$, and $^1\Sigma_g^+$ (*35*). The proton-ethynyl pairs of the fast deprotonation channel are accompanied by two shallow lines, above and below, respectively associated with reactions involving a ^{13}C atom and a neutral product that is not detected with the reaction microscope: $C_2H_2^{2+} \rightarrow H^+ + C_2^+ + H$. Both of these processes, as well as the slow proton loss channel, occur with a probability two orders of magnitude lower than that for the fast proton loss channel. Nevertheless, we explicitly excluded those channels by isolating the three-dimensional (3D) momentum distribution of the electrons that correspond to the reaction moieties originating from the fast proton loss channel. This permits extraction of structural information only from electrons that rescattered off the H^+ and C_2H^+ fragment pairs from direct dissociation. Additional support to identify population of the fast proton ejection channel (i) stems from measurements of the fragment pair ion yield ($H^+ + C_2H^+$) as a function of delay between alignment and LIED pulse. The results are shown in Fig. 1C and are in excellent agreement with previous work (*36*) in which this temporal dependence was used to identify the two different dication fragmentation channels.

Having identified the direct proton ejection channel (via $^1\Pi_u$ and $^3\Pi_u$), we turned to extracting structural information from its scattered electrons. Our LIED methodology (*20*) permits use of momentum coincidence arguments to associate the scattering electron to only the moieties of the fast proton loss channel. Applying such constraints to the data analysis reduces the event rate by a factor of 83, but the elimination of the general electron scattering background ensures that the resulting momentum map of the electrons bears only structural information

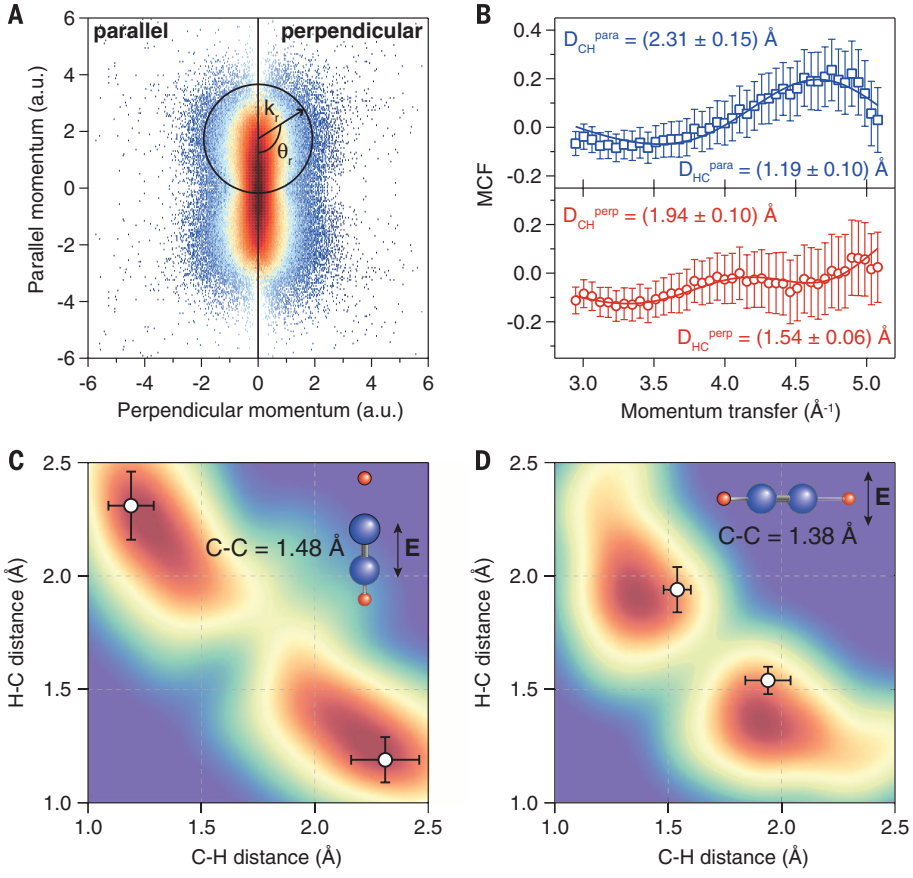

Fig. 2. Measurement of bond distances with LIED. (**A**) The electron momentum distribution in coincidence with the moieties corresponding to the fast proton loss channel. The left half shows data for parallel aligned C_2H_2, and the right half shows data for perpendicularly aligned C_2H_2. (**B**) The MCF for both cases, parallel (top, blue) and perpendicular (bottom, red). Error bars are derived from the experiment based on Poissonian statistics (supplementary materials). (**C** and **D**) Experimental data (white data points with error bars extracted from the MCF fit) overlaid with numerical results (density plot) for cuts through the 3D solution space at the location of its minima. The locations of these cuts correspond to C–C distances of 1.48 Å for the parallel case (C) and 1.38 Å for the perpendicular case (D). (C) shows elongation of one C–H bond to more than twice the equilibrium bond length, corresponding to bond breakage, whereas the other C–H bond is still bound. (D) represents a more symmetric scenario, nearing heterolytic cleavage of one of the two C–H bonds.

Downloaded from http://science.sciencemag.org/ on October 21, 2016

of the dissociating C_2H_2 dication (Fig. 2A); the left half of the image shows data for parallel oriented C_2H_2, and the right half of the image shows data for perpendicularly oriented C_2H_2. These momentum maps correspond to the doubly differential electron scattering cross section measured under the influence of the mid-IR LIED field. However, molecular structure is extracted from the field-free molecular differential cross section (mDCS), which is to say that we need to correct for the influence of the mid-IR field. Operating LIED with the 3100-nm pulse in the deep tunneling regime permits application of the semiclassical model (*18*, *37*) in order to determine the vector potential of the LIED field at the time of rescattering for a given electron energy. The vector potential presents the LIED field's influence on the rescattering electron as an offset from zero (field-free) momentum that is simply subtracted from the measurement. The mDCS is then extracted by recording the number of counts along the circumference of a circle whose radius corresponds to the scattering momentum and whose origin is shifted by the vector potential from zero momentum; we show an example in black in Fig. 2A for an electron kinetic energy of 50 eV. Information about the position of the molecule's nuclei is encoded as energy modulations onto the mDCS due to scattering interference. To make these oscillations directly visible, we calculated the molecular contrast factor (MCF), a renormalized quantity, from the mDCS (supplementary materials).

Shown in Fig. 2B are the resulting MCFs for both perpendicularly oriented (Fig. 2B, red circles) and parallel oriented (Fig. 2B, blue squares) C_2H_2. Striking differences are immediately apparent between the MCFs of both orientations, indicating that different structures are observed. The positions of the individual scattering centers, and hence atomic distances, are extracted by calculating MCF patterns for a wide range of possible positions. Comparing the measured MCF with these patterns, we obtained the full 3D solution space (minimum fitted χ^2 value as a function of the C–C distance and two C–H distances) of the instant condition of the molecular wave packet at the time of the electron's return. The solution space is obtained without assumptions such as partially frozen nuclei or linear elongation and includes independent symmetric as well as asymmetric elongation of C–H bonds.

We obtained two different solutions, one for the parallel and one for the perpendicular case, and present 2D cuts through the 3D solution space at those positions: The solution for the parallel case for which we measure a C–C bond length of (1.48 ± 0.11) Å, a value 23% greater than the 1.204 Å equilibrium bond length (*38*) in neutral C_2H_2, is shown in Fig. 2C. Associated C–H distances are (2.31 ± 0.15) Å and (1.19 ± 0.10) Å, corresponding to 118 and 12% elongations, respectively, relative to the 1.06 Å equilibrium value (*38*). This difference, in which one proton has more than doubled its distance to its neighbor, is a clear signature of departure of a proton and hence bond cleavage. The scenario is markedly different for the perpendicular case, in which we measured a C–C bond elongation of 16% from the equilibrium value to (1.38 ± 0.06) Å. The measured C–H distances of (1.94 ± 0.10) Å and (1.54 ± 0.06) Å are shown in Fig. 2D. The more symmetric scenario of C–H bond elongations by 83 and 45% from their equilibrium value is understandable considering that the molecule is aligned perpendicular to the control field when being imaged with the LIED electrons; the molecule is not asymmetrically pulled apart by the strong laser field. This approximates an imaging scenario under quasi–field-free conditions (Fig. 3B). The measured disparity of C–H distances for different alignments provides a means of controlling bond cleavage and proton loss, depending on molecular orientation.

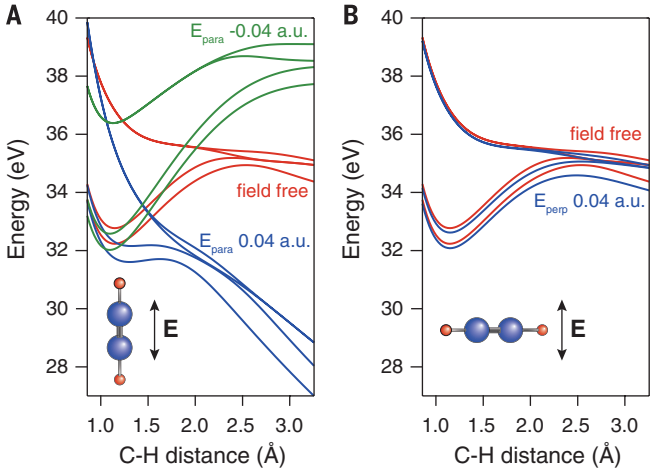

Fig. 3. PES of the C_2H_2 dication with the mid-IR LIED field. (**A** and **B**) The field-free case is shown in red. (A) shows how the PESs Stark-shift when dressed by a mid-IR LIED field aligned with the molecular axis. For one field direction ($E > 0$), all dication PESs are strongly dissociative (blue), whereas for the other field direction ($E < 0$), the PESs present a bound scenario. The trend is exactly reversed for the other C–H bond. (B) shows the doubly degenerate scenario for alignment perpendicular to the mid-IR LIED field, for which we find slight PES shifts but not the dramatic Stark shifts shown in (A).

Next, we sought to explain the difference in imaged structures between the parallel and perpendicularly aligned molecules. We turned to mixed quantum chemistry and semiclassical ab initio molecular dynamics calculations so as to realistically describe the molecular wave packet in the dressing mid-IR field with varying polarization direction as a function of time (supplementary materials). Shown in Fig. 3 is how the PESs of the dication are modified for parallel (Fig. 3A) and perpendicularly oriented (Fig. 3B) molecules in the presence of the LIED field. In Fig. 3, A and B, only the dication's ground states ($^3\Sigma_g^-$ and the near-degenerate singlet states $^1\Delta_g$, $^1\Sigma_g^+$) and the $^1\Pi_u$ and $^3\Pi_u$ excited states are shown, for clarity. For the parallel case (Fig. 3A), we found a stable equilibrium when the LIED field is directed to pull the hydrogen atom toward the carbon atom (Fig. 3A, green). Once the LIED field direction reverses, half a cycle later, all PESs (Fig. 3A, blue) become strongly dissociative, and the C–H bond is broken within 8 fs. Internuclear separation for only one of the two C–H bonds is shown in Fig. 3; the exact opposite scenario occurs at the same time for the other C–H bond (exchange blue with green PESs). In total, during one LIED field cycle (10.3 fs for 3100 nm), one C–H is always broken, whereas the other C–H bond is only elongated. We found excellent agreement with our measured C–C bond length, which is elongated during both half cycles of the LIED field. The calculation yields a C–C bond length of 1.45 Å, which is in excellent agreement with our measured value of (1.48 ± 0.11) Å. The perpendicular case is different because no preferential axis is induced by the LIED field, and hence there are two degenerate cases. Thus, no LIED field direction dependence and only minimal modification of the field-free PESs are exhibited in Fig. 3B. This scenario leads to slower bond dynamics, with eventual breakup. The computed smaller C–C elongation to 1.40 Å agrees with the measured bond length of (1.38 ± 0.06) Å. The simulations show that the C–C bond and the second C–H bond undergo vibration throughout the course of the LIED pulse, yet they stay bound within the temporal range of one optical cycle (10.3 fs).

Because the LIED field does not noticeably distort the PESs in the perpendicular orientation, the C_2H_2 dication behaves like a quasi–field-free electronic system and can be imaged as such. Moreover, the dependence of proton loss dynamics on alignment permits control over the speed and visualization of molecular dissociation.

Having corroborated the dependence of proton loss on alignment, we next linked the measured structures to the times when the snapshots were taken. In our experiment, we analyzed electrons with 50 eV return energy because they yielded the highest number of counts for the largest angular coverage and hence the best scattering momentum transfer. On the basis of the semiclassical model (*18*, *37*), which pertains well for our Keldysh parameter of $\gamma = 0.31$, we can determine the time of return and the backscattering energy for the scattering electron. We only have to consider the long trajectory pathway because of its much higher ionization probability as compared with the short trajectory. We show in Fig. 4A that these electrons have reencountered the target after 9.15 fs (10.3 fs correspond to one optical cycle at 3100 nm) and

Downloaded from http://science.sciencemag.org/ on October 21, 2016

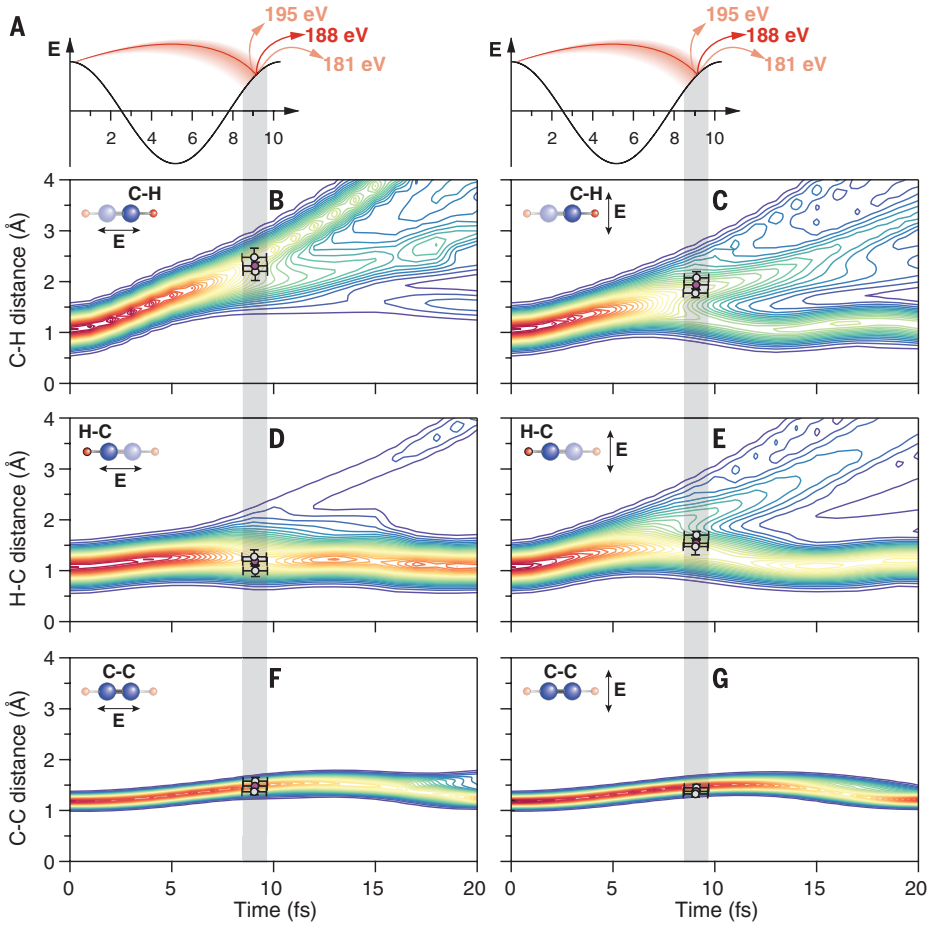

Fig. 4. Temporal dynamics of C_2H_2 resolved for the different bonds and as a function of alignment. (**A**) Temporal range imaged for electron energies ranging up to 195 eV, in accordance with the semiclassical rescattering model. (**B** to **G**) Mixed quantum-classical dynamical calculations are shown below for [(B), (D), and (F)] parallel and [(C), (E), and (G)] perpendicularly aligned C_2H_2. Extracted bond distances from the snapshots taken between 9.1 and 9.2 fs are overlaid onto the calculations and exhibit excellent agreement by being well positioned within the theoretical distribution; the results corresponding to Fig. 2 are shown in pink, and error bars are determined based on the semiclassical rescattering model (supplementary materials). Differences for bond elongation between the [(B) and (D)] parallel and [(C) and (E)] perpendicular cases are clearly resolved.

backscatter with a maximum energy of 188 eV. We additionally analyzed our measurement for two closely neighboring energies of 48 and 52 eV, which correspond to backscattering energies of 181 and 195 eV and for which we achieve high count rates with excellent signal-to-noise ratio. The overall temporal spread is negligible because these three measurements interrogated the molecular structure during a short span between 9.1 and 9.2 fs, as indicated by the vertical gray bars in Fig. 4. The experimental results for the three scattering energies (Fig. 4, circles with error bars) are overlaid with calculated values for all bond distances and for all orientations. The calculated values are based on modeling the experimental conditions with ab initio molecular dynamics simulations that take the modification of the dication states of C_2H_2 by the LIED field fully into account. The simulated evolution of the corresponding probability distribution on the dissociative excited dication state over a time span of 20 fs is shown in Fig. 4, B to G. For parallel orientation (Fig. 4, B, D, and F), the molecule experiences the full LIED field strength along its molecular axis and gets maximally distorted. This scenario corresponds to rapid elongation of one C–H bond (Fig. 4B) and breakage, which is defined at twice its equilibrium distance, after 8 fs. The other C–H bond (Fig. 4D) experiences elongation in the presence of the LIED field, and the C–C bond (Fig. 4F) moves with a period longer than the LIED field's optical cycle. The dynamics change markedly for perpendicular orientation (Fig. 4, C, E, and G), which closely approximates a quasi–field-free imaging scenario (Fig. 3B). We found that the C–C bond undergoes a very similar excursion as that of the parallel case because of the stiffness of the bond. The two C–H bonds, however, show strong probabilities to both oscillate in phase with the LIED field, with some small probability for dissociation. This behavior makes sense, over the shown time range, because there is no preferential direction of the external field that would bias the dynamics of one C–H bond as compared with the other.

The measured snapshots are overlaid (Fig. 4, B, D, and F, circles) with all figures for the parallel case and exhibit excellent agreement with the expected behavior of the molecule. The result from Fig. 2C is indicated by the pink solid circle. Similarly, we show the perpendicular case in Fig. 4, C, E, and G, and found equally excellent agreement with the measurement shown in Fig. 2D.

On the basis of these findings, we can corroborate the full spatiotemporal structure of dicationic C_2H_2 9 fs after ionization. The snapshots of the spatiotemporal structure were taken with an estimated 0.6-fs temporal resolution and are capable of distinguishing the different kinetic behaviors of the molecule when field-ionized parallel or perpendicular to the LIED field. In the parallel case, the snapshots show that one of the hydrocarbon bonds is heterolytically cleaved with the proton 1.24 Å away from its equilibrium position. The perpendicular case snapshots reveal the molecular structure in the quasi–field-free scenario for the dissociative dication.

As a future step, we envision application of our implementation of LIED to triggering and imaging of ultrafast structural transformations over a longer time scale—for example, with two separate pulses as pump and probe, and with molecules with more complex structures. Prospects include structural and spatial isomerization and especially proton tautomerization, a key chemical and biological process that is largely obscured from x-ray scattering techniques.

REFERENCES AND NOTES

1. R. G. Woolley, *J. Mol. Struct. THEOCHEM* **230**, 17–46 (1991).
2. A. H. Zewail, *J. Phys. Chem. A* **104**, 5660–5694 (2000).
3. H. Xu, T. Okino, K. Yamanouchi, *J. Chem. Phys.* **131**, 151102 (2009).
4. J. C. Polanyi, A. H. Zewail, *Acc. Chem. Res.* **28**, 119–132 (1995).
5. M. Chergui, A. H. Zewail, *ChemPhysChem* **10**, 28–43 (2009).
6. M. P. Minitti *et al.*, *Phys. Rev. Lett.* **114**, 255501 (2015).
7. K. Ayyer *et al.*, *Nature* **530**, 202–206 (2016).
8. A. A. Ischenko, S. A. Aseyev, Eds., Time-resolved electron diffraction: For chemistry, biology and materials science, in *Advances in Imaging and Electron Physics* (Elsevier, 2014), vol. 184; www.sciencedirect.com/science/article/pii/B9780128001455210010.
9. P. Zhang, J. Yang, M. Centurion, *New J. Phys.* **16**, 083008 (2014).
10. C. Gerbig, A. Senftleben, S. Morgenstern, C. Sarpe, T. Baumert, *New J. Phys.* **17**, 043050 (2015).
11. S. Manz *et al.*, *Faraday Discuss.* **177**, 467–491 (2015).
12. A. Gliserin, M. Walbran, F. Krausz, P. Baum, *Nat. Commun.* **6**, 8723 (2015).
13. T. Zuo, A. D. Bandrauk, P. B. Corkum, *Chem. Phys. Lett.* **259**, 313–320 (1996).
14. M. Lein, J. P. Marangos, P. L. Knight, *Phys. Rev. A* **66**, 051404 (2002).
15. M. Meckel *et al.*, *Science* **320**, 1478–1482 (2008).
16. C. D. Lin, A.-T. Le, Z. Chen, T. Morishita, R. Lucchese, *J. Phys. At. Mol. Opt. Phys.* **43**, 122001 (2010).
17. C. I. Blaga *et al.*, *Nature* **483**, 194–197 (2012).
18. P. B. Corkum, *Phys. Rev. Lett.* **71**, 1994–1997 (1993).
19. S. Baker *et al.*, *Science* **312**, 424–427 (2006).
20. M. G. Pullen *et al.*, *Nat. Commun.* **6**, 7262 (2015).
21. B. Wolter *et al.*, *Phys. Rev. X* **5**, 021034 (2015).
22. M. G. Pullen *et al.*, *Nat. Commun.* **7**, 11922 (2016).
23. P. M. Kraus *et al.*, *Science* **350**, 790–795 (2015).
24. X. Xie *et al.*, *Phys. Rev. Lett.* **109**, 243001 (2012).
25. A. S. Alnaser *et al.*, *Nat. Commun.* **5**, 3800 (2014).

Downloaded from http://science.sciencemag.org/ on October 21, 2016

26. B. Gaire *et al.*, *Phys. Rev. A* **89**, 013403 (2014).
27. H. Ibrahim *et al.*, *Nat. Commun.* **5**, 4422 (2014).
28. G. A. Worth, L. S. Cederbaum, *Annu. Rev. Phys. Chem.* **55**, 127–158 (2004).
29. J. M. Bowman, *Science* **319**, 40–41 (2008).
30. E. M.-L. Ohrendorf, F. Tarantelli, L. S. Cederbaum, *J. Chem. Phys.* **92**, 2984 (1990).
31. R. Thissen *et al.*, *J. Chem. Phys.* **99**, 6590 (1993).
32. J. Biegert, P. K. Bates, O. Chalus, *IEEE J. Sel. Top. Quantum Electron.* **18**, 531–540 (2012).
33. M. Baudisch *et al.*, *J. Opt.* **17**, 094002 (2015).
34. K. Doblhoff-Dier, M. Kitzler, S. Gräfe, *Phys. Rev. A* **94**, 013405 (2016).
35. M. Alagia *et al.*, *J. Chem. Phys.* **136**, 204302 (2012).
36. X. Xie *et al.*, *Phys. Rev. Lett.* **112**, 163003 (2014).
37. J. L. Krause, K. J. Schafer, K. C. Kulander, *Phys. Rev. Lett.* **68**, 3535–3538 (1992).
38. W. M. Haynes, Ed., *CRC Handbook of Chemistry and Physics*, (CRC Press, ed. 94, 2013); www.crcpress.com/CRC-Handbook-of-Chemistry-and-Physics-94th-Edition/Haynes/9781466571143.

ACKNOWLEDGMENTS

We acknowledge financial support from the Spanish Ministry of Economy and Competitiveness (MINECO), through the "Severo Ochoa" Programme for Centres of Excellence in R&D (SEV-2015-0522), grants FIS2014-56774-R and FIS2014-51478-ERC; the Catalan Institució Catalana de Recerca I Estudis Avançats; Agencia de Gestió d'Ajuts Universitaris i de Recerca (AGAUR) with grant SGR 2014-2016; the Fundació Cellex Barcelona; the European Union's Horizon 2020 research and innovation program under LASERLAB-EUROPE (EU-H2020 654148); COST Actions MP1203, XUV/X-ray light and fast ions for ultrafast chemistry (XLIC); the Marie Sklodowska-Curie grant agreement 641272; and the European Research Council through ERC-2013 Advanced Grant 338580. B.W. was supported by AGAUR (FI-DGR 2013–2015). M.G.P. was supported by the ICFONEST+ program, partially funded by the Marie Curie cofunding of Regional, National and International Programs—COFUND (FP7-PEOPLE-2013-COFUND) action of the European Commission. A.-T.L. and C.D.L. are supported by the Chemical Sciences, Geosciences, and Biosciences Division, Office of Basic Energy Sciences, Office of Science, U.S. Department of Energy, under grant DE-FG02-86ER13491. We thank D. Zalvidea, M. Sclafani, and A. Stolow for helpful and inspiring discussions.

SUPPLEMENTARY MATERIALS

www.sciencemag.org/content/354/6310/308/suppl/DC1
Supplementary Text
Figs. S1 to S5
References (*39*–*62*)

13 June 2016; accepted 19 September 2016
10.1126/science.aah3429

METALLURGY

Dynamic creation and evolution of gradient nanostructure in single-crystal metallic microcubes

Ramathasan Thevamaran,[1]* Olawale Lawal,[1] Sadegh Yazdi,[1] Seog-Jin Jeon,[2] Jae-Hwang Lee,[3] Edwin L. Thomas[1]*

We demonstrate the dynamic creation and subsequent static evolution of extreme gradient nanograined structures in initially near–defect-free single-crystal silver microcubes. Extreme nanostructural transformations are imposed by high strain rates, strain gradients, and recrystallization in high-velocity impacts of the microcubes against an impenetrable substrate. We synthesized the silver microcubes in a bottom-up seed-growth process and use an advanced laser-induced projectile impact testing apparatus to selectively launch them at supersonic velocities (~400 meters per second). Our study provides new insights into the fundamental deformation mechanisms and the effects of crystal and sample-shape symmetries resulting from high-velocity impacts. The nanostructural transformations produced in our experiments show promising pathways to developing gradient nanograined metals for engineering applications requiring both high strength and high toughness—for example, in structural components of aircraft and spacecraft.

Creating ultrastrong materials that are also tough enough to resist failure has always been a challenge to material scientists and engineers. In metals, decreasing the grain sizes to the nanoscale has been shown to result in ultrastrong nanocrystalline metals (*1*, *2*). This improvement, however, comes at the cost of increased susceptibility to catastrophic brittle failure as strain localizes in nanocrystalline metals and forms cracks under tensile loading. It has recently been shown (*3*–*6*) that the creation of spatial gradients in grain structure can potentially alleviate the catastrophic failure through progressive ductile behavior under applied uniform tensile stresses. Previous methods for creating a gradient nanograined (GNG) structure require multistep surface mechanical grinding (*3*) or surface mechanical attrition treatment (SMAT) (*5*). Surface mechanical grinding results in a GNG structure with grain sizes increasing from the nanocrystalline (~20 nm) to the coarse-grained (~10 μm) scales from the surface to the interior over a depth of ~0.5 mm, leading to a gradient of grain size ~0.02 (*3*). The SMAT has been shown to produce a GNG structure with grains increasing in size from the ~100-nm nanocrystals to the ~35-μm coarse grains over a depth of ~120 μm, leading to a gradient of grain size ~0.3 (*5*). We demonstrate effective creation of an extreme GNG structure with a single-step, high-velocity-impact process. The high strain rates, pressure, and strain gradients during impact create the GNG structure with a gradient of grain size ~1, where the grain size varies from ~10 to ~500 nm over a distance of ~500 nm. We also show that the high elastic energy stored in the material due to impact triggers a continuous (static) recrystallization process that takes place over the course of weeks at room temperature.

A clear understanding of the fundamental deformation mechanisms in materials exposed to high-velocity impacts and shock compressions is critical to the development of advanced protective technologies for applications in automobile and aircraft crashes (*7*), sport-related collisions (*8*), and body and vehicle armors (*9*). Impact and shock compression are also used for advanced material processing techniques such as shot peening (*10*), laser shock peening (*11*), and explosive welding (*12*). Supersonic velocity microparticle impacts are especially relevant in cold spray technologies (*13*), collision of undetectable small-sized space debris and micrometeorites with spacecraft (*14*), and microparticle impacts on turbine blades (*15*). However, to date, most of the studies on the nano- and micrograins of metals have been limited to quasi-static loading rates of micropillars (*1*, *2*, *16*), due to the challenges in conducting short–time-scale experiments on small-sized samples.

Laser-driven shockwaves have recently been used to probe material responses at small length scales and short time scales (*17*, *18*). Here, we use an advanced laser-induced projectile impact testing (α-LIPIT) apparatus (*19*, *20*) to selectively launch individual single-crystal silver (Ag) microcubes at supersonic velocities (~400 ms^{-1}) and allow them to directly impact a rigid impenetrable target (Fig. 1A). The laser ablation of a gold (Au) thin film produces Au vapor—trapped between the glass substrate and the thin cross-linked polydimethylsiloxane (PDMS) layer—that locally expands the PDMS layer and launches the room-temperature projectile (Ag microcube) at controlled velocities that are proportional to the laser pulse energy (*20*). The PDMS layer also thermally isolates the Ag projectile during laser ablation. This technique allows the sample to deform in an unconstrained manner and enables us to investigate the roles that the intrinsic crystal symmetries and the extrinsic microcube-shape symmetries play on resulting deformations, when the microcube impacts along specific crystal-symmetry directions (Fig. 1, C to E).

[1]Department of Materials Science and NanoEngineering, Rice University, Houston, TX 77005, USA. [2]Department of Polymer Science and Engineering, University of Massachusetts, Amherst, MA 01003, USA. [3]Department of Mechanical and Industrial Engineering, University of Massachusetts, Amherst, MA 01003, USA.
*Corresponding author. Email: thevamaranr@rice.edu (R.T.); elt@rice.edu (E.L.T.)

Downloaded from http://science.sciencemag.org/ on October 21, 2016

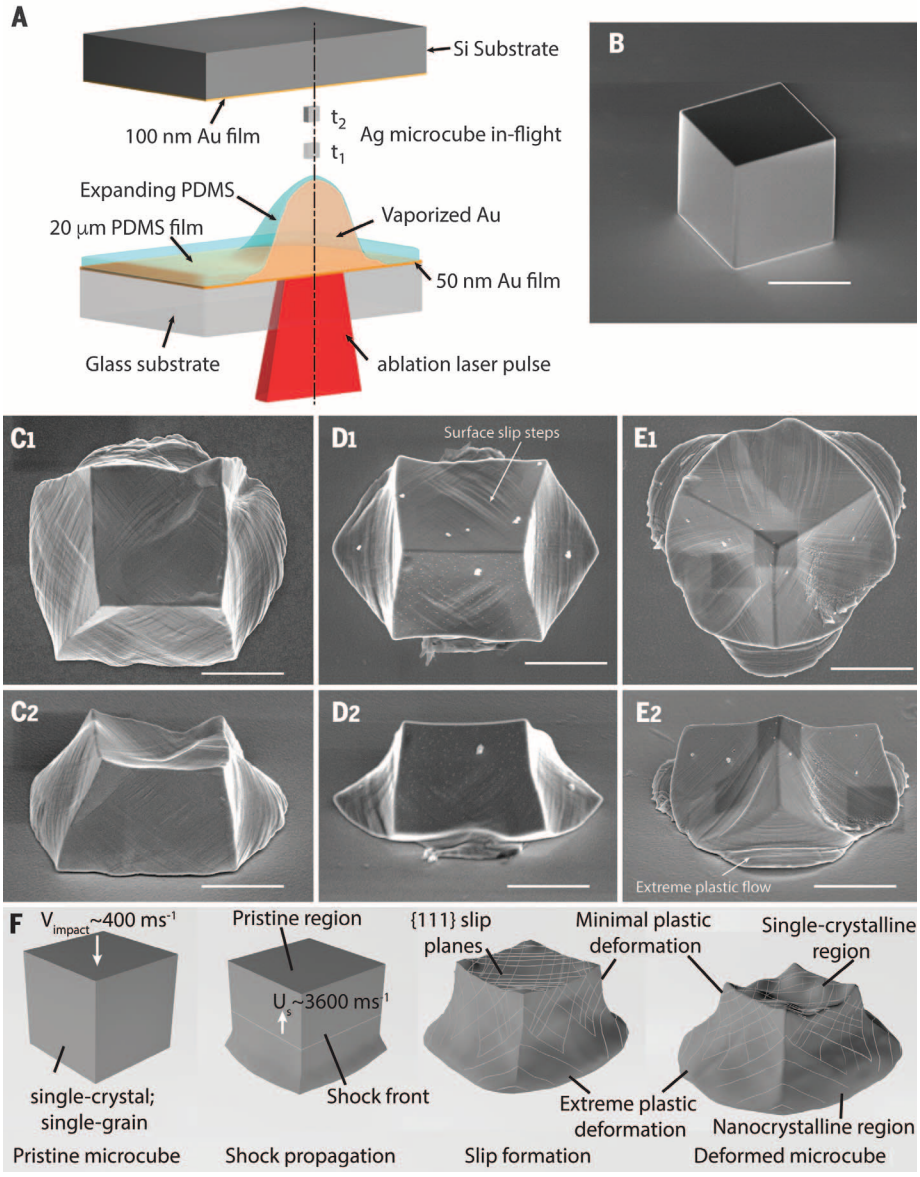

Fig. 1. The LIPIT of single-crystal Ag microcubes. (**A**) A schematic of the α-LIPIT experiment. (**B**) Scanning electron microscopy (SEM) image of a pristine single-crystal Ag microcube. (**C** to **E**) Top and side (at 60° tilt) views of the deformed Ag microcubes showing the crystal and deformation symmetries resulting from high-velocity impact, when impacted approximately along the (C) [100], (D) [110], and (E) [111] directions (all scale bars indicate 1 μm). (**F**) Illustrations of the sequence of deformations in the Ag microcube during high-velocity impact along the [100] crystal-symmetry direction.

Recent advances in the synthesis of Ag nano/microcubes (*21*) enable us to synthesize near–defect-free single crystals in near-perfect cubic geometry (Fig. 1B) and in large quantities. Our bottom-up synthesis contrasts the commonly used top-down sample preparation techniques based on focused ion beam (FIB) milling, which result in substrate bound samples in limited quantities that contain surface damage and gallium contamination incurred from ion milling. We used a seed-growth process with control of oxygen in the reaction environment (*20*) to synthesize the near-monodispersed single-crystal Ag microcubes (cube edge ~1.4 μm) for this study (*20*). Ag is a face-centered-cubic (fcc) metal having space group $Fm\bar{3}m$ (no. 225) that can serve as a model for investigating the dynamic deformation behavior of fcc metals. Moreover, the low-stacking-fault energy of Ag (19 mJ/m^2) (*22*) reduces the mobility of dislocations, which in turn activates numerous intriguing microstructural processes to accommodate large imposed strains such as the formation of stacking faults, partial dislocations, deformation twins, and shear bands, in addition to the conventional slips and cross-slips found in fcc metals having high-stacking-fault energy (*23*–*26*).

For impacts approximately along the [100], [110], and [111] crystal-symmetry directions, the deformed samples exhibit distinct deformation features that reflect the interplay of intrinsic and extrinsic symmetries. The extrinsic cubic geometry of the sample guides the plastic deformation to follow the cube's symmetries and results in *p4mm*, *p2mm*, and *p3m* plane point group symmetries (fig. S1) (*20*), as seen in the top views of the deformed samples corresponding to the impacts along the [100], [110], and [111] directions, respectively (Fig. 1, C1 to E1). The average pressure rise of more than 9 GPa during the high-strain-rate (>10^8 s^{-1}) impact far exceeds (>150x) the 60-MPa (*27*) yield strength of Ag. This generates a hydrodynamic stress state that results in severe plasticity at the impacted side of the sample as the material deforms with no resistance to shear (*20*, *28*).

The initial compressional shock wave generated during impact rapidly attenuates as it moves toward the top region of the sample due to interactions with free-surface reflections (tensile waves). This results in large deformations at the bottom region of the sample but far less at the top region, approximately retaining its initial shape. As the amplitude of the propagating compressive stress wave reduces to a few times the yield strength of the material, plastic deformation via crystallographic slips ensues, governed by the intrinsic fcc-lattice symmetry (Fig. 1F, fig. S3, and tables S3 to S5) (*20*). We observe clear evidence of parallel surface slip steps on the cube's surfaces after impact due to the exiting dislocation avalanches (Fig. 1, C to E).

The deformed geometry also indicates high axial and transverse strain gradients during deformation. For example, the impact along the [100] direction (impact on a cube face) results in the nominal lateral strains of ~1.45 and ~0.25 at the bottom and top sides of the samples, with greater than 8 × 10^5/m lateral strain gradient along the height direction (fig. S4 and table S6) (*20*). These observed characteristic deformations suggest that extreme micro- and nanostructural changes must occur within the crystal.

To investigate the nanostructural changes within the sample, we performed transmission electron microscope (TEM) and selective area diffraction (SAD) analyses on a sample impacted along the ~[100] direction (Fig. 2A) soon after the impact (~20 hours from impact to TEM analysis). The varying SAD patterns (Fig. 2, B1 to B4) indicate a strong gradient in grain size along the height of the sample. The top region exhibits a single-crystalline diffraction pattern with negligible distortion arising in the probed ~200-nm-diameter region (Fig. 2, B1 and B2), whereas the bottom impacted region exhibits a nanocrystalline diffraction pattern (Fig. 2B4). The high-resolution TEM (HRTEM) images obtained at the bottom region of the sample show nanocrystalline grains that are ~10 nm in size (Fig. 2, C and D). The presence of nanocrystalline structure in the region that underwent severe plastic flow suggests that there may have been dynamic recrystallization during the impact. The nearly adiabatic compression within the short impact time (~1.5 ns) generates material heating and leads to dynamic recrystallization as deformation twinning and strain-induced grain boundary migrations

Downloaded from http://science.sciencemag.org/ on October 20, 2016

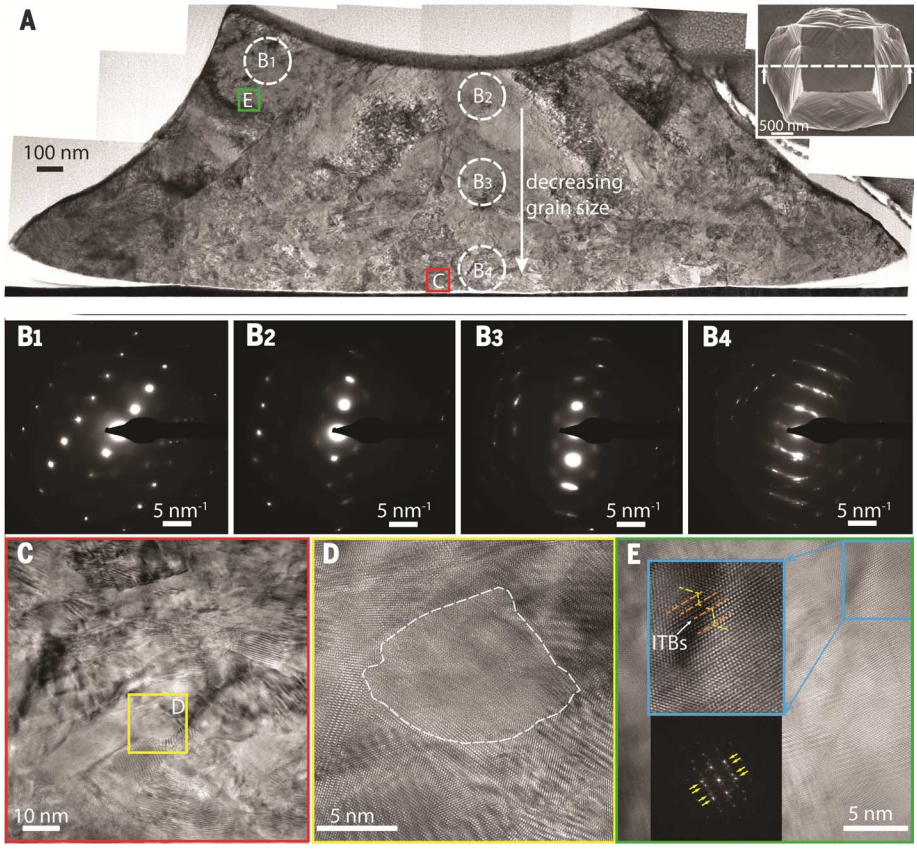

Fig. 2. Deformation modes and GNG structure formation in impacted Ag microcube, examined 20 hours after impact. (**A**) A cross-sectional image of an Ag microcube impacted along the ~[100] direction; image is produced by stitching several bright-field TEM (BF-TEM) images (inset shows an SEM image of the impacted sample with a horizontal white dashed line indicating the location from which the TEM lamella was obtained). (**B1** to **B4**) SAD patterns taken along the increasingly highly deformed regions showing a variation from ~single-crystalline structure in the top region to the nanocrystalline structure at the bottom region. (**C**) HRTEM image of the bottom region showing nanocrystalline grains. (**D**) Magnified HRTEM image of a nanocrystal grain at a different orientation compared to its surrounding. (**E**) HRTEM image of the top region of the sample showing deformation twins [insets show the incoherent twin boundaries (ITBs) and the fast Fourier transform (FFT) of the selected region exhibiting twin spots].

occur during deformation (*29*, *30*). The average sample temperature is estimated to rise by ~350 K during impact (*20*), because of the rapid and nearly adiabatic plastic deformation that does not provide enough time for the sample to dissipate heat into the Au-coated Si substrate. Higher temperatures may occur locally, but the overall shape and texture of the deformed cube rule out the possibility of melting. Nanoscale incoherent deformation twins found in the sample (Fig. 2E) and the continuously varying orientation of grains, characterized by varying convergent beam electron diffraction (CBED) patterns, also signify the highly localized deformations in the sample.

We performed TEM analysis on a sample impacted along the [100] direction 8 days after impact and found substantial nanostructural recovery in the form of recrystallization. Two distinct regions are evident in Fig. 3A: the recrystallized highly deformed bottom region and the top less-deformed region. The highly deformed bottom region of this sample now shows 30- to 150-nm-sized grains (Fig. 3B and fig. S5), which have recrystallized from the less-than-10-nm-sized grains evident in the sample investigated 20 hours after impact. We also found several subgrains and a high density of dislocations in these grains (Fig. 3C) that suggests a system that is still far from equilibrium. The top-center region and the left- and right-side regions of the sample cross section exhibit distinct slip planes at ~30° and ~150° to the horizontal impact plane, which correspond to the {111} crystal planes in the pristine fcc lattice (Fig. 3A). Although the slip planes also exist in the sample shown in Fig. 2, the recrystallization in the top region of the sample allows them to be seen more clearly, as in Fig. 3A. Additionally, consistent with the presence of the strong strain gradient, the thickness of the shear bands bounded by these slip planes gradually reduces from the top region (~25-nm-thick bands) and becomes so thin as to be nearly indistinguishable near the most highly deformed bottom region (Fig. 3D and fig. S6).

The evolution of the GNG structure in the material is also evident in the distinct electron diffraction patterns obtained in three different regions that have undergone different extents of deformation and recrystallization. The top region shows a pattern that is similar to a single crystal with small distortions caused by the numerous closely spaced slip systems (Fig. 3E1). The bottom-center region that was highly deformed and recrystallized shows the characteristics of a nanocrystalline structure (Fig. 3E2), and the bottom-side region that underwent the most severe plastic flow exhibits diffraction characteristics of even smaller, highly misoriented nanocrystalline grains (Fig. 3E3).

Such extreme deformations occurring over a short time scale result in high energy storage in the newly formed nanocrystalline grains with high elastic strain and grain misorientations. The stored elastic energy and the recrystallization nucleus formed during dynamic recrystallization together set the stage for continuous (static) recrystallization (*30*, *31*). The continuous recrystallization at room temperature results in drastic changes in the nanostructure of the sample: The GNG structure formed as a result of impact evolves through grain coarsening by glide and climb dislocation movements, dislocation accumulation at subgrain boundaries, and coalescence of subgrains at low-angle grain boundaries, all of which contribute to decreasing the stored elastic energy (*30*). It is remarkable that the continuous recrystallization process occurs predominantly due to the stored mechanical energy without any external thermal annealing, in contrast to previous studies (*30*, *31*) that have used thermal annealing at ~573 K for 30 s to induce continuous recrystallization in highly deformed Ag.

To further probe recrystallization, we prepared a TEM lamella of another Ag microcube impacted along the [100] direction 44 days after impact. It shows much coarser-grained structure, indicating that the static recrystallization has continued (Fig. 4). The middle region of the sample has a large (~850 nm) grain with an aspect ratio of ~1, whereas the adjacent regions contain elongated grains [up to ~1700 nm in length and ~300 nm in width; equivalent diameter ~100 to 750 nm (fig. S7)] inclined at ~27° (right) and ~10° (left) with respect to the impact plane. These unique grain shapes and their preferential orientations imply that the midregion of the impacted cube has experienced a nearly isotropic state of stress due to initial shock compression and the large number of {111} slip bands crisscrossing in multiple directions, whereas the side regions have been deformed by {111} slip bands oriented predominantly on a preferred plane. The diffraction pattern (Fig. 4C) obtained in a highly deformed region exhibits the characteristics of a single-crystal grain structure, implying a near-complete nanostructural recovery from the prior severely deformed nanocrystalline state observed immediately after impact. However, it should be noted that the nanostructural recovery in the form of continuous recrystallization has transformed these single-crystal grains into entirely new orientations compared

Downloaded from http://science.sciencemag.org/ on October 20, 2016

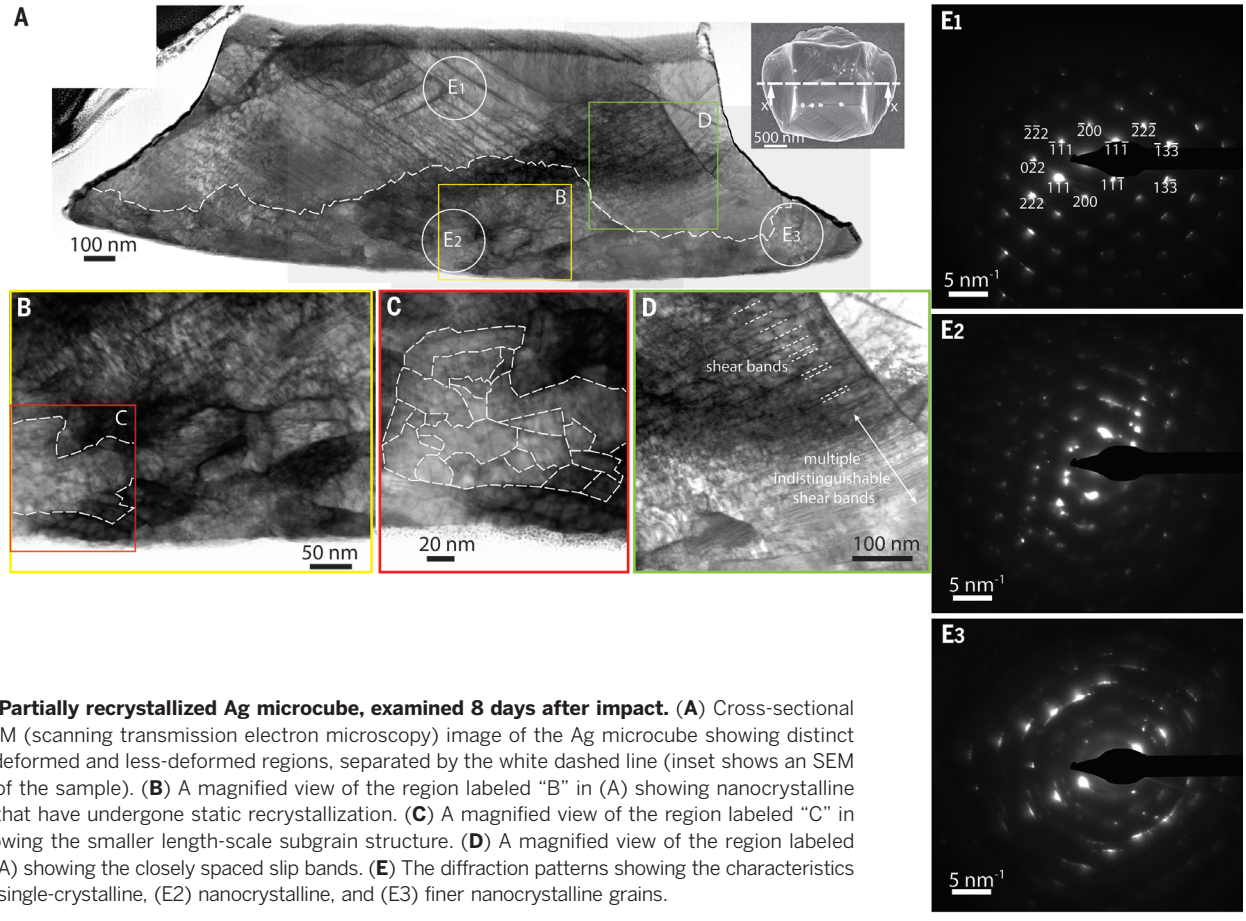

Fig. 3. Partially recrystallized Ag microcube, examined 8 days after impact. (**A**) Cross-sectional BF-STEM (scanning transmission electron microscopy) image of the Ag microcube showing distinct highly deformed and less-deformed regions, separated by the white dashed line (inset shows an SEM image of the sample). (**B**) A magnified view of the region labeled "B" in (A) showing nanocrystalline grains that have undergone static recrystallization. (**C**) A magnified view of the region labeled "C" in (B) showing the smaller length-scale subgrain structure. (**D**) A magnified view of the region labeled "D" in (A) showing the closely spaced slip bands. (**E**) The diffraction patterns showing the characteristics of (E1) single-crystalline, (E2) nanocrystalline, and (E3) finer nanocrystalline grains.

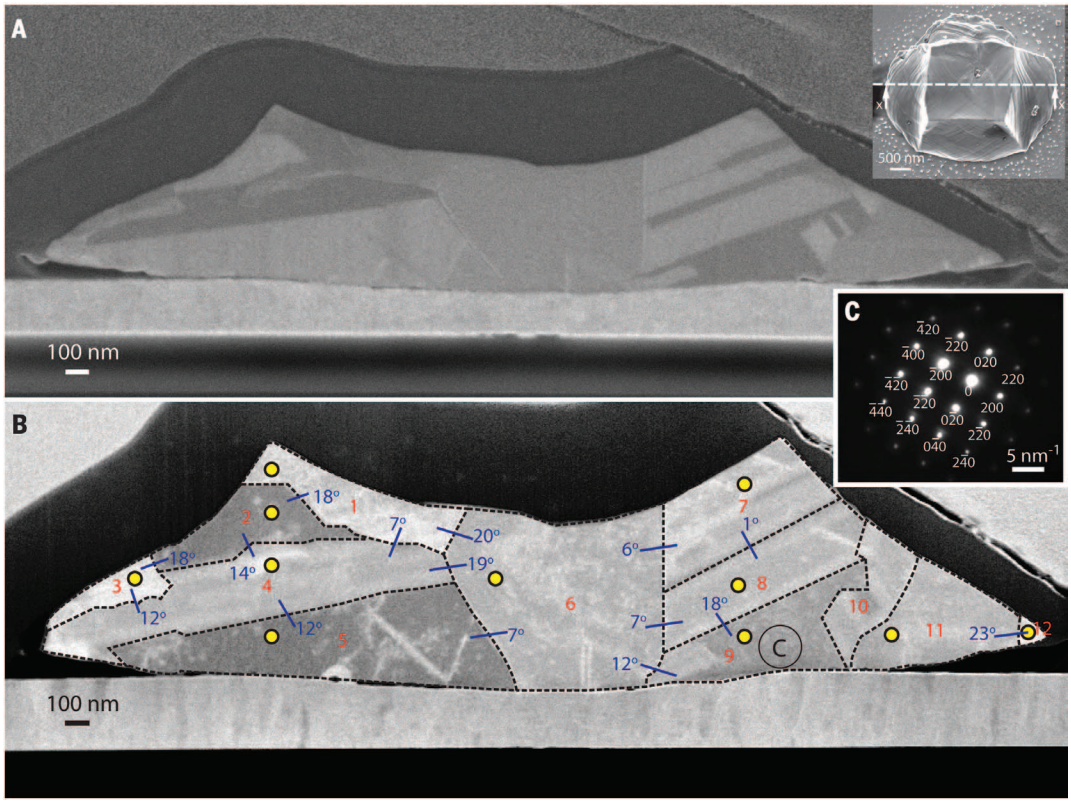

Fig. 4. A highly recrystallized Ag microcube examined 44 days after impact showing a larger grain structure. (**A**) An SEM image showing the channeling contrast arising from differently oriented grains (inset shows the SEM image of the sample). (**B**) Annular darkfield-STEM image of the lamella showing the larger grain structure with high-angle rotations between adjacent grains (the yellow spots indicate the locations where the CBED patterns were obtained for grain orientation measurements). (**C**) SAD pattern of the previously highly deformed bottom region (labeled as "C" in B) currently exhibiting the characteristics of fully recovered single-crystalline structure.

Downloaded from http://science.sciencemag.org/ on October 20, 2016

to the overall single-crystal orientation of the initial microcube. CBED analysis performed on the sample showed large misorientations between adjacent grains that exhibit high contrast (Fig. 4B and table S7) (*20*) and a gradually varying CBED pattern within each of those grains, consistent with a structure at a lower length scale containing defects and small subgrain misorientations.

Upon impact, the pristine single-crystal single-grain Ag microcube undergoes an extreme deformation trajectory of micro- and nanostructural changes due to the high-strain-rate deformation: a highly deformed external geometry and creation of nanoscale grains and strong spatial gradients in grain size along the height of the sample. Such a GNG structure has been shown to result in a new gradient-plasticity strengthening and toughening mechanism in metals with spatial gradients in stress and strain under uniform overall deformations (*6*). Because of the correlation between the yield strength and the grain size, application of a uniform external load to a material with GNG structure still leads to different strain distributions in different-sized grains, resulting in a spatial gradient of strain and stress (*6*). This strengthening and toughening mechanism, which is distinct from the commonly known strain-gradient plasticity, prevents catastrophic failure through progressive yielding and strain hardening (*4*–*6*).

Our observations of recrystallization driven by the stored elastic energy suggest a microstructural evolution path that progresses from nanocrystalline toward single crystal. The recrystallization processes also soften the hard and brittle nanocrystalline material that results from dynamic deformation (*31*). Therefore, the GNG-structured metal with intermediate states of recrystallization should have desirable strength and toughness for mechanical applications requiring high fatigue life and survivability in extreme environments such as automobile and aircraft crashes, sport-related collisions, and body and vehicle armors. The recrystallization process can be retarded by the addition of alloying elements that preferentially segregate to grain boundaries for thermodynamic nanostructure stabilization (*32*).

The GNG-structured materials made by a single-step high-strain-rate process, particularly in metallic alloy systems that have the ability to retard continuous recrystallization even at high temperatures (*32*), will be useful for applications requiring ultrahigh strength and toughness. Our studies also demonstrate that controlling the impact orientation will provide additional control over tailoring the GNG structure and hence the mechanical properties of the resultant material. Additionally, our findings suggest important roles played by both the intrinsic crystal symmetries and the extrinsic sample geometries, inspiring further fundamental investigations to understand the interplay of intrinsic and extrinsic symmetries.

REFERENCES AND NOTES

1. M. D. Uchic, D. M. Dimiduk, J. N. Florando, W. D. Nix, *Science* **305**, 986–989 (2004).
2. J. R. Greer, J. T. M. De Hosson, *Prog. Mater. Sci.* **56**, 654–724 (2011).
3. T. H. Fang, W. L. Li, N. R. Tao, K. Lu, *Science* **331**, 1587–1590 (2011).
4. K. Lu, *Science* **345**, 1455–1456 (2014).
5. X. Wu, P. Jiang, L. Chen, F. Yuan, Y. T. Zhu, *Proc. Natl. Acad. Sci. U.S.A.* **111**, 7197–7201 (2014).
6. Z. Zeng, X. Li, D. Xu, L. Lu, H. Gao, T. Zhu, *Extrem. Mech. Lett.* **2015** (2015); www.sciencedirect.com/science/article/pii/S2352431615001261.
7. J. D. Reid, *Thin-walled Struct.* **24**, 285–313 (1996).
8. T. W. McAllister *et al*., *Ann. Biomed. Eng.* **40**, 127–140 (2012).
9. P. Hazell, *Armour: Materials, Theory, and Design* (CRC Press, 2015).
10. S. Dai, Y. Zhu, Z. Huang, *Vacuum* **125**, 215–221 (2016).
11. C. Montross, *Int. J. Fatigue* **24**, 1021–1036 (2002).
12. F. Findik, *Mater. Des.* **32**, 1081–1093 (2011).
13. R. C. Dykhuizen *et al*., *J. Therm. Spray Technol.* **8**, 559–564 (1999).
14. E. Grossman, I. Gouzman, R. Verker, *MRS Bull.* **35**, 41–47 (2010).
15. T. J. Carter, *Eng. Fail. Anal.* **12**, 237–247 (2005).
16. M. J. Burek *et al*., *Mater. Sci. Eng. A* **528**, 5822–5832 (2011).
17. G. Youssef *et al*., *J. Appl. Phys.* **113**, 084309 (2013).
18. H. A. Colorado *et al*., *J. Appl. Phys.* **114**, 233510 (2013).
19. J.-H. Lee, P. E. Loya, J. Lou, E. L. Thomas, *Science* **346**, 1092–1096 (2014).
20. Materials and methods are available as supplementary materials on *Science* Online.
21. S.-J. Jeon, J.-H. Lee, E. L. Thomas, *J. Colloid Interface Sci.* **435**, 105–111 (2014).
22. E. B. Tadmor, N. Bernstein, *J. Mech. Phys. Solids* **52**, 2507–2519 (2004).
23. S. Buzzi, M. Dietiker, K. Kunze, R. Spolenak, J. F. Löffler, *Philos. Mag.* **89**, 869–884 (2009).
24. W. Heye, G. Wasserman, *Scr. Metall.* **2**, 205–207 (1968).
25. H. Paul, J. H. Driver, C. Maurice, A. Piatkowski, *Acta Mater.* **55**, 575–588 (2007).
26. I. J. Beyerlein, L. S. Tóth, C. N. Tomé, S. Suwas, *Philos. Mag.* **87**, 885–906 (2007).
27. D. R. Smith, F. R. Fickett, *J. Res. Natl. Inst. Stand. Technol.* **100**, 119 (1995).
28. A. M. Meyers, *Dynamic Behavior of Materials* (Wiley, 1994).
29. J. A. Hines, K. S. Vecchio, *Acta Mater.* **45**, 635–649 (1997).
30. R. D. Doherty *et al*., *Mater. Today* **1**, 14–15 (1998).
31. H. Paul, J. H. Driver, C. Maurice, A. Piatkowski, *Acta Mater.* **55**, 833–847 (2007).
32. T. Chookajorn, H. A. Murdoch, C. A. Schuh, *Science* **337**, 951–954 (2012).

ACKNOWLEDGMENTS

This work was financially supported by the George R. Brown School of Engineering, Rice University. We thank D. Pham for his help in constructing 3D illustrations. We also acknowledge the useful discussions with E. Ringe, Electron Microscopy Center, Rice University.

SUPPLEMENTARY MATERIALS

www.sciencemag.org/content/354/6310/312/suppl/DC1
Material and Methods
Figs. S1 to S7
Tables S1 to S7
References

19 May 2016; accepted 22 September 2016
10.1126/science.aag1768

SOLID-STATE PHYSICS

Observation of a nematic quantum Hall liquid on the surface of bismuth

Benjamin E. Feldman,[1]* Mallika T. Randeria,[1]* András Gyenis,[1]* Fengcheng Wu,[2] Huiwen Ji,[3] R. J. Cava,[3] Allan H. MacDonald,[2] Ali Yazdani[1]†

Nematic quantum fluids with wave functions that break the underlying crystalline symmetry can form in interacting electronic systems. We examined the quantum Hall states that arise in high magnetic fields from anisotropic hole pockets on the Bi(111) surface. Spectroscopy performed with a scanning tunneling microscope showed that a combination of single-particle effects and many-body Coulomb interactions lift the six-fold Landau level (LL) degeneracy to form three valley-polarized quantum Hall states. We imaged the resulting anisotropic LL wave functions and found that they have a different orientation for each broken-symmetry state. The wave functions correspond to those expected from pairs of hole valleys and provide a direct spatial signature of a nematic electronic phase.

Nematic electronic states represent an intriguing class of broken-symmetry phases that can spontaneously form as a result of electronic correlations (*1*, *2*). They are characterized by reduced rotational symmetry relative to the underlying crystal lattice and have attracted considerable interest in systems such as two-dimensional electron gases (2DEGs) (*3*–*5*), strontium ruthenate (*6*), and high-temperature superconductors (*7*–*12*). The sensitivity of electronic nematic phases to disorder results in short-range ordering and the formation of domains, making them difficult to study using global measurements that average over microscopic configurations. The effect of perturbations, such as crystalline strain, may be used to show a propensity for nematic order—that is, to provide evidence that vestiges of nematic behavior survive even in the presence of material imperfections (*1*). However, it is difficult to quantitatively correlate the experimental evidence of ordering with a microscopic description of the electronic states and the interactions responsible for nematic behavior. To put the study of nematic electronic phases on more quantitative ground,

[1]Joseph Henry Laboratories and Department of Physics, Princeton University, Princeton, NJ 08544, USA. [2]Department of Physics, University of Texas, Austin, TX 78712, USA. [3]Department of Chemistry, Princeton University, Princeton, NJ 08544, USA.
*These authors contributed equally to this work. **†Corresponding author. Email: yazdani@princeton.edu**

Downloaded from http://science.sciencemag.org/ on October 20, 2016

it is therefore important not only to perform local measurements, but also to find a material system for which theory can fully characterize the underlying broken-symmetry states and the electronic interactions.

Multivalley 2DEGs with anisotropic band structure have been anticipated as a model platform to explore nematic order in the quantum Hall regime (*13*–*17*). The key idea is that Coulomb interactions can spontaneously lift the valley degeneracy in materials with low disorder and thereby break rotational symmetry. In contrast to previously studied metallic nematic phases, this leads to a gapped nematic state with quantized Hall conductance. We examined such a 2DEG on the surface of single crystals of bismuth (Bi), which is one of the cleanest electronic systems, with a bulk mean free path reaching 1 mm at low temperatures (*18*). Interest in Bi has recently been rekindled by bulk measurements showing phase transitions and anisotropic behavior, possibly related to nematic electronic phenomena, in the presence of large magnetic fields (*19*–*22*). We focus here on the (111) surface of Bi, for which strong Rashba spin-orbit coupling results in a rich 2DEG consisting of spin-split surface states that produce multiple electron and hole pockets (*23*, *24*). Scanning tunneling microscope (STM) images (Fig. 1A) show that the in situ cleaved Bi(111) surface has large (>200 nm × 200 nm) atomically ordered terraces that are separated by steps oriented along high-symmetry crystallographic directions (*25*). Angle-resolved photoemission spectroscopy (ARPES) measurements (*23*, *24*, *26*, *27*) of this surface show that its Fermi surface consists of a hexagonal electron pocket at the Γ point, three additional elongated electron pockets around the M points, and six anisotropic hole pockets along the Γ-M directions (Fig. 1B, inset). The multiply degenerate anisotropic valleys and the low disorder of the Bi(111) surface make it an ideal system to search for nematic electronic behavior using the STM.

In the absence of magnetic field, spectroscopic measurements of the Bi(111) surface with the STM (Fig. 1B) show features in the tunneling conductance G that are related to van Hove singularities of the density of states (DOS), such as the sharp peak at energy E = 220 meV and the abrupt drop at 33 meV. These features correspond to the upper band edges of the surface states along the Γ-M direction (*25*, *28*, *29*). In the presence of a large magnetic field B, the electron and hole states of the Bi(111) surface are quantized into Landau levels (LLs), each with degeneracy geB/h, where e is the electron charge, h is Planck's constant, and g accounts for the degeneracy arising from the valley degree of freedom (g = 6 for holes). At high magnetic field, the STM spectra show a series of sharp peaks (Fig. 1B) whose evolution with magnetic field can be used to distinguish between electron- and hole-like LLs, which disperse in energy with positive or negative slopes, respectively, as a function of magnetic field (Fig. 1, C and D). They do not exhibit avoided crossings, and the total conductance is additive when they cross, which suggests independent tunneling into each LL. LL spectroscopy on thin Bi(111) films was recently reported (*28*) but did not show evidence of symmetry breaking, which is the focus of our work.

Our first key observation is that the surface-state LLs do not disperse linearly with magnetic field. Instead, they are pinned to the Fermi level until they are fully occupied, as is clearly shown for the hole states in Fig. 1D. Such behavior is rarely observed in LL spectroscopy of ungated samples performed using a STM (*30*), and it indicates that the surface charge density is held constant in our system. Electron LLs exhibit pinning only when there are no proximal hole states, whereas they otherwise cross straight through the hole LLs at the Fermi level. This difference in behavior signals an intriguing competition between electron- and hole-like states in a magnetic field, and suggests charge rearrangement between pockets (*29*). We focus below on the hole states, for which the orbital index N_h is straightforward to assign, with the highest-energy peak corresponding to N_h = 0 closely matched to the zero-field drop in conductance at 33 meV. Using the values of the field and filling factor at which LLs cross the Fermi

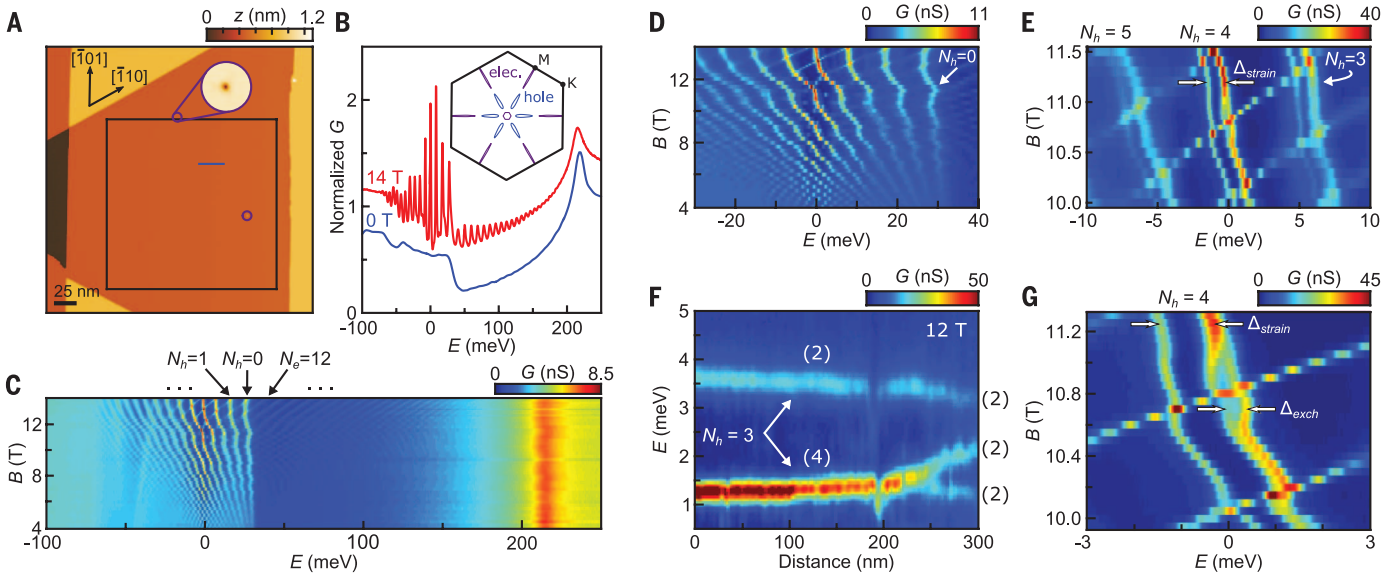

Fig. 1. Landau levels (LLs) of the Bi(111) surface states. (**A**) A typical cleaved Bi(111) surface, with crystallographic axes labeled. The data in (E) and (G) are an average of spectra measured along the blue line, and the conductance maps in Fig. 3 were performed in the area denoted by the black box. Surface defects are circled in purple; the inset shows a zoom-in on one defect (inset z height scale, 1.3 Å). (**B**) Conductance G as a function of energy E at magnetic field B = 0 (blue) and at 14 T (red). The curves are offset by 0.5 for clarity. At B = 0, the data are taken at temperature $T \approx 4$ K. All other data throughout the manuscript are measured at 250 mK. The inset is a diagram of the Bi(111) first Brillouin zone, showing the electron (purple) and hole (blue) Fermi pockets of the surface states. (**C**) Landau fan diagram of $G(E, B)$ that shows crossing electron- and hole-like LLs. The data are averaged over a 20-nm line, with individual spectra showing almost no spatial variation on this energy scale. Select orbital indices N_e and N_h of the respective electron and hole LLs are labeled. (**D**) Higher-energy resolution measurement of $G(E, B)$ that clearly shows Fermi-level pinning of each hole LL. (**E**) High-resolution measurement of $G(E, B)$ in a region where the LLs corresponding to N_h = 3, 4, and 5 each show splitting into a two-fold degenerate and a four-fold degenerate LL peak. Data are averaged over the blue line in (A). (**F**) Line cut of spectra showing strain-induced splitting of the six-fold degenerate N_h = 3 LL into two or three peaks, depending on position. Numbers in parentheses denote the degeneracy of each broken-symmetry state. (**G**) Zoom-in on $G(E, B)$ in the same location as in (E). The four-fold degenerate peak further splits into two distinct LLs as it crosses the Fermi level, indicating broken symmetry states arising from exchange interactions. Arrows mark Δ_{strain} and Δ_{exch}.

Downloaded from http://science.sciencemag.org/ on October 21, 2016

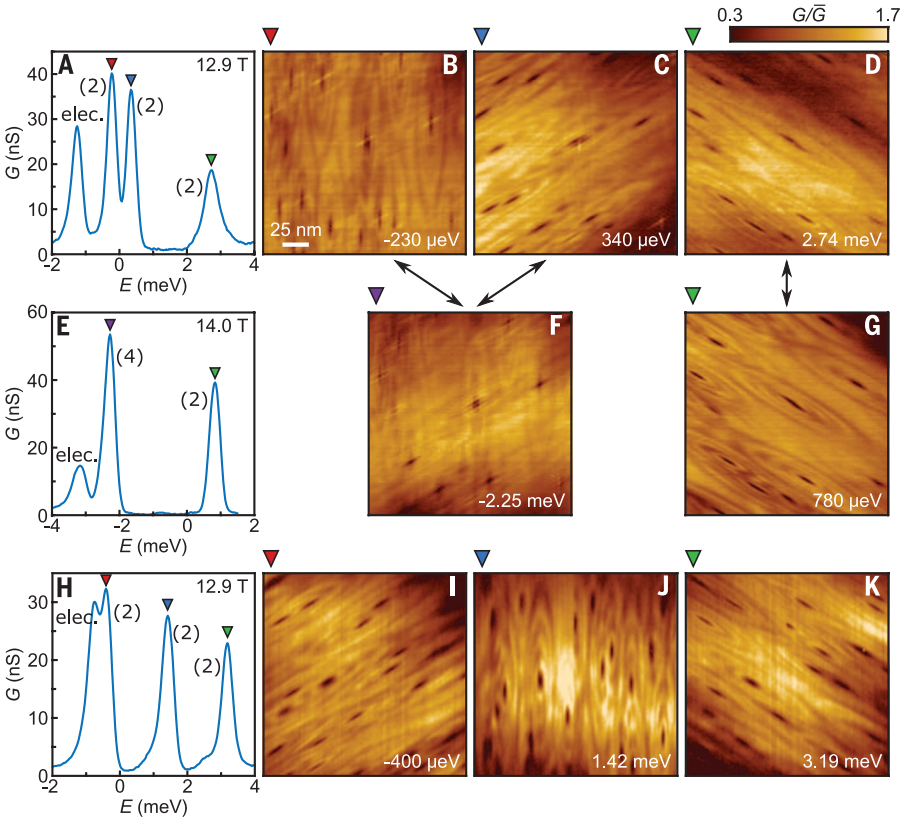

Fig. 2. Rotational symmetry breaking and local domains of a nematic electronic phase. (**A**) Average conductance spectrum at 12.9 T, measured over a 100-nm line cut (which exhibits little spatial dependence) near the start of the line cut in Fig. 1F, showing three broken-symmetry hole LLs, two of which are split by exchange interactions at the Fermi level. (**B** to **D**) Spatial maps of conductance normalized by its average value $G/\overline{G}$ at energies corresponding to the three split hole LL peaks. Ellipses of reduced conductance are centered on surface defects, with different orientations at each energy. (**E**) Average conductance spectrum at 14 T, measured in the same location as in (A). The spectrum shows restored symmetry of the exchange-split LLs in (A) to produce a four-fold degenerate LL. (**F**) Spatial map of $G/\overline{G}$ at the energy of the four-fold degenerate LL peak, which shows ellipses with two orientations. (**G**) Spatial map of $G/\overline{G}$ at the energy of the two-fold degenerate LL peak that is split from the four-fold degenerate peak by strain, showing the same unidirectional behavior as in (D). The spatial maps in (F) and (G) are measured in the same area as (B) to (D). (**H**) Average conductance spectrum (measured over a 100-nm line cut that exhibits little spatial dependence) at 12.9 T in a location about 1 μm away from the region shown in (A) to (G). (**I** to **K**) Spatial maps of $G/\overline{G}$ in the new location at energies corresponding to the three split hole LL peaks. The energetic order of the three directions is different, with the first two orientations switched, demonstrating the presence of domains. For all conductance spectra, the electron LLs are labeled, and the hole LL degeneracy is denoted in parentheses near each peak.

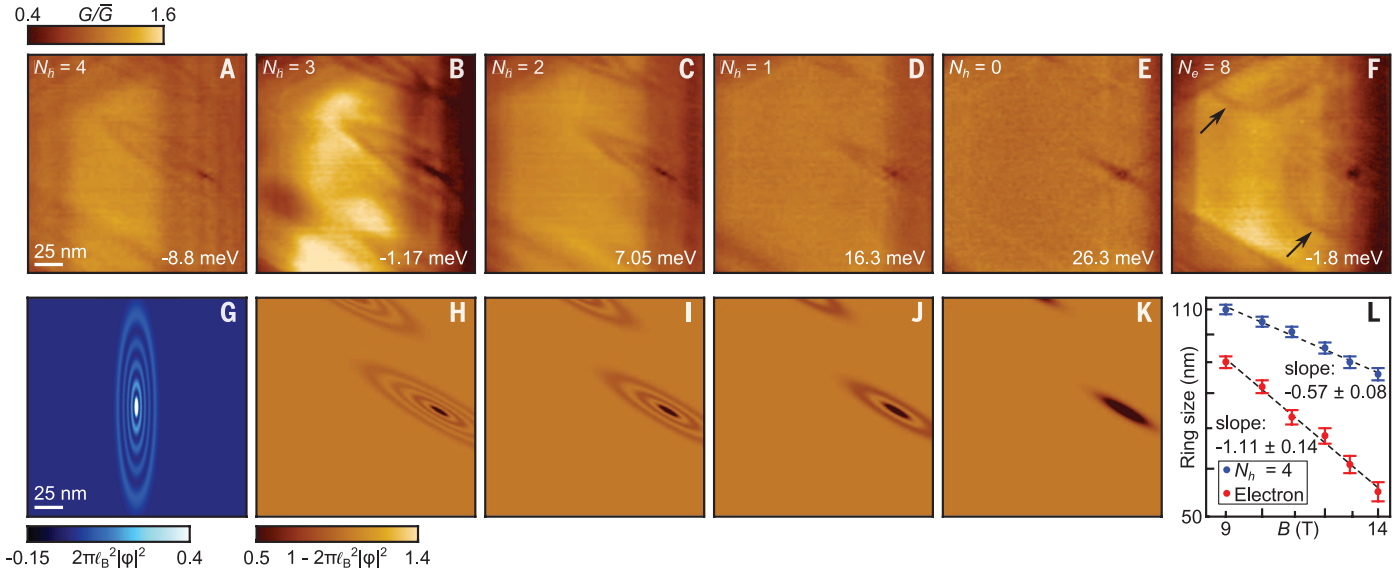

Fig. 3. Isolated anisotropic cyclotron orbits and theoretical modeling. (**A** to **E**) Spatial maps of $G/\overline{G}$ at 14 T in the area denoted by the black box in Fig. 1A, at energies corresponding to the strain-induced broken-symmetry hole LL for orbital indices N_h = 0 to 4. Isolated anisotropic cyclotron orbits are present around surface defects. (**F**) Spatial map of $G/\overline{G}$ in the same area at the energy of the N_e = 8 LL, showing circular rings of suppressed conductance (black arrows) that occur around the same surface defects. The weak elliptical feature around the lower defect is related to a missing cyclotron orbit from the N_h = 3 LL at a nearby energy. The trapezoidal feature in the background conductance results from the shape of the terrace because the LL visibility is suppressed near step edges. (**G**) Amplitude $2\pi l_B^2|\varphi_{4,4}(\mathbf{r})|^2$ of the $m = N_h = 4$ cyclotron orbit wave function. (**H** to **K**) Simulated maps of the expected conductance, $1-2\pi l_B^2|\varphi_{N,N}(\mathbf{r})|^2$, with individual cyclotron orbits centered on the surface defects circled in Fig. 1A. The size and shape of the simulated conductance are a good match to the data in (B) to (E). (**L**) Semimajor axis size of the cyclotron orbits for N_h = 4 (blue) and ring size of those from electron LLs near the Fermi level (red) as a function of magnetic field. Dashed lines are fits to the field dependence of the extracted sizes.

Downloaded from http://science.sciencemag.org/ on October 21, 2016

level, we determine the hole surface density to be $p \approx 7.1 \times 10^{12}$ cm^{-2} (*29*).

High-resolution spectroscopic measurements provide an indication that both single-particle effects and electron-electron interactions break the six-fold symmetry of the hole LLs. Evidence of symmetry breaking can be seen in Fig. 1E, which shows the field evolution of the conductance spectra in one region of the sample where the LLs corresponding to N_h = 3, 4, and 5 are each split into two peaks with different amplitudes, indicating a lifting of the six-fold valley degeneracy of each level to form two- and four-fold degenerate LLs. The fact that the splitting (characterized by a gap Δ_{strain}) occurs away from the Fermi level indicates that it is a single-particle effect. The very weak dependence of Δ_{strain} on magnetic field and orbital index and the fact that we observe different magnitude gaps in different regions of the sample suggest that local strain underlies this partial symmetry breaking (*29*). As an illustration of the spatial dependence of this behavior, we show in Fig. 1F a spectroscopic line cut from a region of the sample in which the six-fold degeneracy of the N_h = 3 LL is lifted to produce either two or three broken-symmetry states, depending on location within the sample.

Electron-electron interactions further lift the LL degeneracy and are manifested in spectroscopic measurements by the appearance of energy gaps when the LLs cross the Fermi level. Figure 1G shows a high-resolution measurement of the Fermi-level crossing of the N_h = 4 LL (in the same area as in Fig. 1E), where over a range of 0.5 T, the four-fold degenerate peak develops an exchange energy gap (Δ_{exch} = 450 μeV) that is coincident with the Fermi level. Although there are spatial variations in the exact magnitude of the gaps between the broken-symmetry LLs, exchange interactions consistently enhance gaps between LLs that are already split by strain and induce a gap between previously degenerate levels when they cross the Fermi level. The magnitude of the exchange gap is consistent with that estimated theoretically for the hole pockets of Bi(111), and it is not related to an Efros-Shlovskii Coulomb gap (*29*). These observations demonstrate that a combination of a single-particle effect, likely strain, and many-body interactions lift the six-fold valley degeneracy of the hole LL to produce three broken-symmetry states.

We performed spectroscopic mapping with the STM to directly visualize the underlying quantum Hall wave functions and to demonstrate the breaking of crystalline symmetry in these phases. Conductance maps at energies corresponding to each of the three broken-symmetry hole LLs show anisotropic ellipse-like features that point along high-symmetry crystal axes, with relative angles rotated by 120° with respect to each other (Fig. 2, A to D). The elliptical features are centered on atomic-scale surface defects, and the same defects produce rings in all three directions. This suggests that ellipse orientation is not associated with symmetry breaking from the defect itself, which is further confirmed by atomic-resolution topographs (*29*). As we show below, the three different directionalities arise from cyclotron orbits in pairs of hole valleys that are elongated in the same direction. More important, such spatially resolved measurements enable us to directly visualize the spontaneous breaking of the LL degeneracy by electron-electron interactions. By tuning the magnetic field to adjust the occupancy of two of the three broken symmetry states, we can contrast spatial maps of the LLs with and without exchange splitting. The measurements in Fig. 2, E to G, obtained in the same region as those in Fig. 2, A to D, show that the elliptical features in the conductance maps can occur as a superposition of two different orientations, indicating that the symmetry between these two orientations is not broken in the absence of

Downloaded from http://science.sciencemag.org/ on October 21, 2016

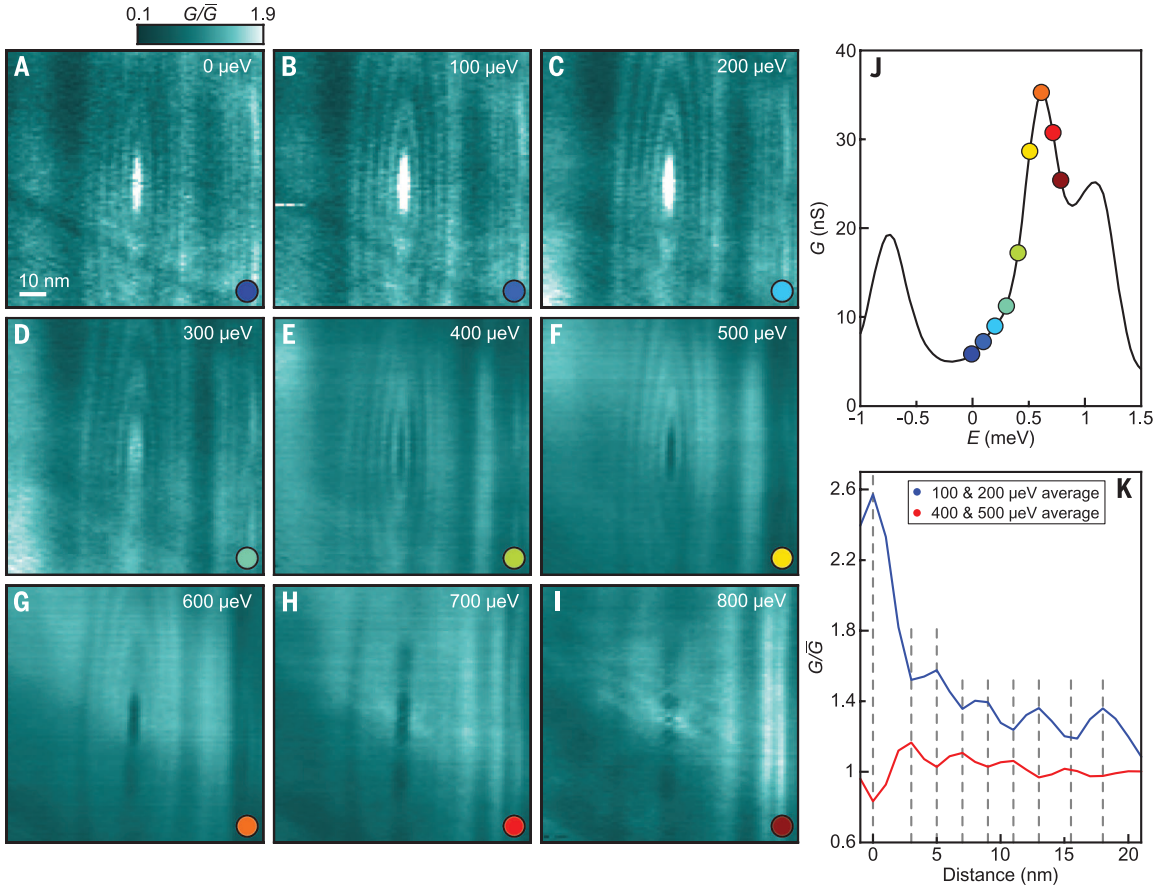

Fig. 4. Energy shift of the cyclotron orbits. (**A** to **I**) Spatial maps of $G/\overline{G}$ around an isolated impurity at B = 10 T with energy spaced by 100 μeV throughout one broken-symmetry N_h = 4 LL peak. These maps show the shift to lower energy of the $m = N$ cyclotron orbit. (**J**) Corresponding conductance spectrum (averaged over a 12 nm × 2.5 nm area centered about 5 nm underneath the defect) marked with colored circles for each mapped energy. (**K**) Oscillations of $G/\overline{G}$ along the semiminor axis, averaged over 100 and 200 μeV (blue) and over 400 and 500 μeV (red), respectively, highlighting the contrast reversal in the maps.

an exchange gap. A comparison of Fig. 2F with Fig. 2, B and C, clearly shows that unidirectional elliptical features emerge as the exchange gap opens, providing a direct manifestation of nematic valley-polarized states on the Bi(111) surface.

Another key feature of a nematic electronic phase without long-range order is the presence of domains, which we observe in our system by performing spatially resolved spectroscopy with the STM. We find that the sequence in energy of the three broken-symmetry hole LL states can change depending on the location within the sample. An example of this behavior can be seen by contrasting the spectrum and corresponding conductance maps in Fig. 2, A to D, to those measured about 1 μm away, shown in Fig. 2, H to K. These data reveal that the orientations of the two broken-symmetry states corresponding to the first two peaks in the spectra have switched between the two locations on the Bi surface. Thus, our STM measurements not only show that electron-electron interactions drive nematic behavior, but also illustrate the formation of local nematic domains.

We show below that the elliptical features in our STM conductance maps arise from cyclotron orbit wave functions of the broken-symmetry quantum Hall phases that are pinned by surface defects. To characterize these features in detail, we studied them in an area with few surface defects (box in Fig. 1A) and examined their dependence on orbital index at a constant magnetic field (14 T) around the same defects (circled in Fig. 1A). The conductance maps shown in Fig. 3, A to E, were obtained at the energies of the strain-induced broken-symmetry LLs for N_h = 0 to 4, and they revealed concentric ellipses of suppressed conductance similar to those in Fig. 2, with a consistent orientation for all the orbital indices. The size of the outermost ring increased with increasing orbital index, as did the number of concentric rings of suppressed conductance. Around these same surface defects, we observed approximately circular rings in conductance maps measured at the nearby electron LL peak (Fig. 3F), which further confirms that the defects themselves do not break rotational symmetry.

The rings of suppressed conductance for both electron and hole LLs can be understood as a consequence of cyclotron orbits that are shifted in energy because of the sharp potential produced by the atomic surface defects. In the symmetric gauge, the cyclotron orbits of each LL can be labeled by a second orbital quantum number m (*31*, *32*). Only the $m = N$ cyclotron orbit has weight at the defect, so it is the only state whose energy is shifted by the defect potential, which we modeled as a delta function (*29*). Without the defect, conductance maps measured at the LL peak would include DOS contributions from all cyclotron orbits, and no spatial variation would be expected. However, because the $m = N$ orbit is shifted to a different energy by the defect, it becomes visible as a decreased conductance in the shape of the wave function when measurements are performed at the unperturbed LL energy.

A theoretical model of cyclotron orbit wave functions for the surface states of Bi(111) can be used to capture the elliptical features in the STM conductance maps near individual defects with excellent accuracy. The anisotropy of the surface state hole pockets is reflected in their cyclotron orbit wave function, as exemplified by the $m = N_h = 4$ state, whose amplitude $2\pi l_B^2|\varphi_{4,4}(\mathbf{r})|^2$ (where $l_B = \sqrt{\hbar/eB}$ is the magnetic length) is plotted in Fig. 3G. The number of elliptical features in these wave functions increases with orbital index and is a reflection of the spatial oscillations of the $m = N_h$ wave function, which is proportional to a Laguerre polynomial with $N_h + 1$ peaks (*29*). Using the defects marked in Fig. 1A as the centers of such cyclotron orbits, we simulated the expected conductance pattern by subtracting $2\pi l_B^2|\varphi_{N,N}(\mathbf{r})|^2$ from a uniform background (Fig. 3, H to K). The similarity to the experimental data in Fig. 3, B to E, for different N_h states is remarkable, especially given that the only adjustable fit parameter is the anisotropy of the hole pocket effective mass. We extract a ratio of 5 for the hole pocket anisotropy, in good agreement with previous ARPES measurements (*23*, *26*, *27*) and calculations (*33*). Our model also captures the field dependence of the cyclotron orbit size of the hole LL for $N_h = 4$, as well as that of the electron LLs near the Fermi level. Figure 3L shows the experimentally measured size of the outermost rings for both sets of orbits. They follow the expected $1/\sqrt{B}$ or $1/B$ scaling for hole and electron LLs, respectively, which reflects the dependence of the cyclotron orbit wave functions on magnetic length and orbital index (*29*).

On the basis of the model described above, we anticipate that the suppression we have detected in the conductance maps at the LL peaks should be accompanied by an enhanced conductance relative to the background at other energies. An example of such contrast reversal is shown in Fig. 4, A to I, which displays conductance maps near an isolated defect over a range of energies within one broken-symmetry LL peak with orbital index $N_h = 4$ (Fig. 4J). The maps measured at the LL peak and at higher energies show ellipses of suppressed conductance that correspond to a missing cyclotron orbit, whereas at lower energies, such maps show ellipses of higher conductance that indicate the lower energy to which this orbit has been shifted by the defect potential. This reversal of the contrast is clearly illustrated by the energy-averaged line cuts shown in Fig. 4K, which demonstrate that the cyclotron orbit energy has been lowered by about 300 μV by this particular defect. Examining different defects, we have found evidence for both attractive and repulsive potentials from the contrast reversal in the conductance maps (*29*).

Our measurements are in the clean regime where signatures of isolated cyclotron orbits are visible around individual defects, in contrast to previous studies of DOS modulations from drift states moving along equipotential lines in the disordered limit (*34*–*36*). Cyclotron orbits that are shifted in energy by an isolated defect have been explored in graphene (*32*), and other measurements have indirectly probed the size and shape of cyclotron orbits (*36*–*38*) by examining LL spatial dependence caused by potential modulations. We performed direct two-dimensional mapping of isolated cyclotron orbits, which enabled us to visualize nematic order on the Bi(111) surface, where the anisotropic hole mass leads to anisotropic cyclotron orbits.

The Bi(111) 2DEG represents an interesting venue to explore electron-electron interactions within anisotropic valleys. The ability to bring the lowest hole-like LL to the Fermi level, either by external gating or doping, may allow for direct visualization of fractional quantum Hall states and Wigner crystallization with a STM. In addition, the boundaries between different nematic domains are expected to harbor low-energy edge modes that are analogous to topologically protected states (*13*). The ability to generate a valley-polarized nematic phase that can be externally tuned with strain makes Bi(111) surface states ideally suited for controlled engineering of anisotropic physical properties. The predicted semimetal-to-semiconductor transition with decreasing thickness in bulk Bi (*18*) means that the transport properties of thin Bi(111) crystals will be dominated by the surface states, yielding further prospects for integration into devices that exploit the unique physical properties reported here.

REFERENCES AND NOTES

1. E. Fradkin, S. A. Kivelson, M. J. Lawler, J. P. Eisenstein, A. P. Mackenzie, *Annu. Rev. Cond. Matt. Phys.* **1**, 153–178 (2010).
2. S. A. Kivelson, E. Fradkin, V. J. Emery, *Nature* **393**, 550–553 (1998).
3. M. P. Lilly, K. B. Cooper, J. P. Eisenstein, L. N. Pfeiffer, K. W. West, *Phys. Rev. Lett.* **83**, 824–827 (1999).
4. R. R. Du *et al.*, *Solid State Commun.* **109**, 389–394 (1999).
5. A. S. Mayorov *et al.*, *Science* **333**, 860–863 (2011).
6. R. A. Borzi *et al.*, *Science* **315**, 214–217 (2007).
7. Y. Ando, K. Segawa, S. Komiya, A. N. Lavrov, *Phys. Rev. Lett.* **88**, 137005 (2002).
8. V. Hinkov *et al.*, *Science* **319**, 597–600 (2008).
9. J.-H. Chu *et al.*, *Science* **329**, 824–826 (2010).
10. T. M. Chuang *et al.*, *Science* **327**, 181–184 (2010).
11. E. P. Rosenthal *et al.*, *Nat. Phys.* **10**, 225–232 (2014).
12. K. Fujita *et al.*, *Science* **344**, 612–616 (2014).
13. D. A. Abanin, S. A. Parameswaran, S. A. Kivelson, S. L. Sondhi, *Phys. Rev. B* **82**, 035428 (2010).
14. A. Kumar, S. A. Parameswaran, S. L. Sondhi, *Phys. Rev. B* **88**, 045133 (2013).
15. X. Li, F. Zhang, A. H. MacDonald, *Phys. Rev. Lett.* **116**, 026803 (2016).
16. Y. P. Shkolnikov, S. Misra, N. C. Bishop, E. P. De Poortere, M. Shayegan, *Phys. Rev. Lett.* **95**, 066809 (2005).
17. T. M. Kott, B. Hu, S. H. Brown, B. E. Kane, *Phys. Rev. B* **89**, 041107 (2014).
18. P. Hofmann, *Prog. Surf. Sci.* **81**, 191–245 (2006).
19. L. Li *et al.*, *Science* **321**, 547–550 (2008).
20. Z. Zhu, A. Collaudin, B. Fauque, W. Kang, K. Behnia, *Nat. Phys.* **8**, 89–94 (2012).
21. R. Küchler *et al.*, *Nat. Mater.* **13**, 461–465 (2014).
22. A. Collaudin, B. Fauque, Y. Fuseya, W. Kang, K. Behnia, *Phys. Rev. X* **5**, 021022 (2015).
23. C. R. Ast, H. Höchst, *Phys. Rev. Lett.* **87**, 177602 (2001).
24. Y. M. Koroteev *et al.*, *Phys. Rev. Lett.* **93**, 046403 (2004).
25. I. K. Drozdov *et al.*, *Nat. Phys.* **10**, 664–669 (2014).
26. T. Hirahara *et al.*, *Phys. Rev. Lett.* **97**, 146803 (2006).
27. Y. Ohtsubo *et al.*, *Phys. Rev. Lett.* **109**, 226404 (2012).
28. H. Du *et al.*, *Nat. Commun.* **7**, 10814 (2016).

Downloaded from http://science.sciencemag.org/ on October 21, 2016

29. See supplementary materials on *Science* Online.
30. S. Becker *et al.*, *Phys. Rev. Lett.* **106**, 156805 (2011).
31. A. H. MacDonald, https://arxiv.org/abs/cond-mat/9410047 (1994).
32. A. Luican-Mayer *et al.*, *Phys. Rev. Lett.* **112**, 036804 (2014).
33. K. Saito, H. Sawahata, T. Komine, T. Aono, *Phys. Rev. B* **93**, 041301 (2016).
34. K. Hashimoto *et al.*, *Phys. Rev. Lett.* **101**, 256802 (2008).
35. D. L. Miller *et al.*, *Nat. Phys.* **6**, 811–817 (2010).
36. Y.-S. Fu *et al.*, *Nat. Phys.* **10**, 815–819 (2014).
37. K. Hashimoto *et al.*, *Phys. Rev. Lett.* **109**, 116805 (2012).
38. Y. Okada *et al.*, *Phys. Rev. Lett.* **109**, 166407 (2012).

ACKNOWLEDGMENTS

We thank D. A. Abanin, S. A. Kivelson, S. A. Parameswaran, S. L. Sondhi, and A. Yacoby for helpful discussions. Work at Princeton was supported by the Gordon and Betty Moore Foundation as part of the EPiQS initiative (GBMF4530) and by the U.S. Department of Energy (DOE) Office of Basic Energy Sciences. Facilities at the Princeton Nanoscale Microscopy Laboratory are supported by NSF grant DMR-1104612, NSF-MRSEC programs through the Princeton Center for Complex Materials (DMR-1420541, LPS and ARO-W911NF-1-0606), ARO-MURI program W911NF-12-1-0461, and the Eric and Wendy Schmidt Transformative Technology Fund at Princeton. Also supported by a Dicke fellowship (B.E.F.), a NSF Graduate Research Fellowship (M.T.R.), and DOE Division of Materials Sciences and Engineering grant DE-FG03-02ER45958 and Welch foundation grant F1473 (F.W. and A.H.M.).

SUPPLEMENTARY MATERIALS

www.sciencemag.org/content/354/6310/316/suppl/DC1
Materials and Methods
Supplementary Text
Figs. S1 to S8
Tables S1 and S2
References (*39*–*43*)

18 May 2016; accepted 23 September 2016
10.1126/science.aag1715

GROUP DYNAMICS

Network science on belief system dynamics under logic constraints

Noah E. Friedkin,[1]* Anton V. Proskurnikov,[2,3] Roberto Tempo,[4] Sergey E. Parsegov[5]

Breakthroughs have been made in algorithmic approaches to understanding how individuals in a group influence each other to reach a consensus. However, what happens to the group consensus if it depends on several statements, one of which is proven false? Here, we show how the existence of logical constraints on beliefs affect the collective convergence to a shared belief system and, in contrast, how an idiosyncratic set of arbitrarily linked beliefs held by a few may become held by many.

Converse [(*1*), p. 207] defined a belief system as "a configuration of ideas and attitudes in which the elements are bound together by some form of constraint or functional interdependence." The existence of belief systems is widely accepted and a subject of interest in the scientific community (*2*–*4*), but there are still unresolved puzzles. According to cognitive consistency theory, inconsistent beliefs cause tension that individuals seek to resolve (*5*, *6*). Thus, if an individual's certainty of belief on the truth of one statement is altered, the alteration may propagate changes of the individual's certainties of beliefs on the truth of other statements. Individual-level, independent adjustments of certainties of belief (*7*–*14*) do not suffice to explain the existence of shared beliefs in a population of individuals. Some additional, natural, social control and coordination mechanism is required. Public dispute on global warming is a prominent case in which individuals have varying certainties of belief on the truth values of a logically interdependent set of statements, which has implications for reaching a conclusion that collective action is required to mitigate global warming. Debates in economics on appropriate macroeconomic policy, and debates in politics on acceptable legislation, are also examples of interpersonal influences modifying individuals' certainties of belief on multiple interdependent statements. A critical open problem is the theoretical integration of theory on cognitive consistency and theory on interpersonal influence systems. We report a generalization of the Friedkin-Johnsen model (*15*–*17*) that achieves this integration. When individuals' beliefs on multiple statements are being influenced, the Friedkin-Johnsen model assumes that a change of belief on one statement does not affect beliefs on other statements. We develop and apply a more realistic model on the dynamics of belief systems in which individuals' certainties of belief on a set of interdependent true or false statements are being changed by network mechanisms of interpersonal influence.

A shared logic constraint structure on a set of truth statements (e.g., if X is true, then Y and Z are true) does not imply belief consensus. It will polarize a population into two opposing ideological factions when high certainty of belief on one central statement implies high certainties of belief on all other statements, and low certainty of belief on that central statement implies low certainties of belief on all other statements. One faction accepts the premise of the central statement and thus accepts all the other statements as true; the other rejects the premise of the central statement and thus rejects all the other statements as false. How can we better understand the dynamics of belief systems in which individuals' certainties of belief are modified by network mechanisms of interpersonal influence toward a consensus on a set of interdependent beliefs?

An analyzable problem on belief system dynamics can be posed as follows. Let us start from a state of heterogeneity in a population of individuals (i) with various levels of certainty of belief on the truth values of two or more truth statements and (ii) with a common set of logical constraints that associate these statements. In this population, levels of certainty of belief about one statement are associated with levels of certainty of belief about another statement and, more generally, an individual's level of certainty of belief about one statement is some mixture of that individual's certainty of beliefs about other statements. Let each individual's certainty about each statement be subject to disturbance. Cognitive consistency theory posits that the disturbance will cause a within-individual change that recalibrates their certainties of beliefs to achieve consistency. Let each individual in this population be embedded in a social network that allows interpersonal influences on individuals' beliefs. With such a network, cognitive consistency effects are now competing with effects of other individuals' displayed beliefs.

In our model (Fig. 1), individual nodes have different certainties of belief on multiple truth statements, which may be changed through their interactions with others. The nodes may vary in their levels of closure-openness to influence. Each node's integration of their own and others' displayed certainties of belief may be subject to logical interdependencies among statements. These interdependencies can be expressed as a matrix of logic constraints.

The dynamics of this n-individual belief system on m truth statements is defined by the tensor matrix equation (*18*)

$$\mathbf{X}(k+1) = \mathbf{AWX}(k)\mathbf{C}^T + (\mathbf{I} - \mathbf{A})\mathbf{X}(0)$$

where $k = 0, 1, \ldots$. The $\mathbf{X}(0)$ is a $n \times m$ matrix of n individuals and m truth statements with truth values (true or false) on which individuals have heterogeneous certainties of belief in the $[0, 1]$ interval, such that $x_{ij} = 0.50$ corresponds to an i with maximum uncertainty on the truth value of statement j of the m statements; $x_{ij} = 1$ corresponds to an i with

[1]Center for Control, Dynamical-Systems and Computation and Department of Sociology, University of California, Santa Barbara, CA, USA. [2]Engineering and Technology Institute (ENTEG), University of Groningen, Netherlands. [3]The Institute of Problems of Mechanical Engineering of Russian Academy of Sciences (IPME RAS) and ITMO University, Saint Petersburg, Russia. [4]National Research Council (CNR-IEIIT), Torino, Italy. [5]V.A. Trapeznikov Institute of Control Sciences of the Russian Academy of Sciences (ICS RAS), Moscow, Russia.
*Corresponding author. Email: friedkin@soc.ucsb.edu

Downloaded from http://science.sciencemag.org/ on October 21, 2016

maximum certainty that the truth value of statement j is true; and $x_{ij} = 0$ corresponds to an i with maximum certainty that the truth value of statement j is false. A simple one-to-one correspondence (bijective function) exists between individuals' emotive attitudes toward statements and their certainties of belief on statements. These two forms of evaluative orientation to truth statements are not the same, but are naturally associated. That is, the stronger i's positive attitude toward a statement, the greater i's certainty of belief that a statement is true, and the stronger i's negative attitude toward a statement, the greater i's certainty of belief that a statement is false. The **C** is, in the simplest case, a $m \times m$ matrix of interdependencies among the m truth statements $\left(0 \le c_{ij} \le 1 \; \forall ij, \sum_{j=1}^{m} c_{ij} = 1 \; \forall i\right)$. The **W** is a $n \times n$ matrix of weights, each row i of which corresponds to individual i's allocations of weights to the n individuals' displayed certainties of belief $\left(0 \le w_{ij} \le 1 \, \forall ij, \sum_{j=1}^{n} w_{ij} = 1 \, \forall i\right)$. The **A** is a $n \times n$ diagonal matrix with values $(0 \le a_{ii} \le 1, \; a_{ii} = 1 - w_{ii} \; \forall i)$ that correspond to individual i's level of openness (maximally 1) or closure (minimally 0) to interpersonal influences on i's certainties of belief. The supplementary materials contain a deeper introduction to the mathematical analysis of the model and references to publications with tests of the predictions of the interpersonal influence mechanism that it assumes.

We next show how the 1992–2003 fluctuations of the U.S. population's certainties of belief on truth statements involved in the decision to invade Iraq may be understood. During the period 1992 to 2002, U.S. public opinion polls indicated that a slight majority supported an invasion of Iraq, and that a strong majority favored waiting for the conclusion of UN inspections on the status of Iraq's weapons of mass destruction (*19*–*22*). In January 2003, President Bush's State of the Union address included a threat assessment of Iraq's weapons and intentions. He stated, "We will consult, but let there be no misunderstanding: If Saddam Hussein does not fully disarm for the safety of our people, and for the peace of the world, we will lead a coalition to disarm him." In February 2003, Colin Powell, the highly respected U.S. Secretary of State and former Chairman of the Joint Chiefs of Staff, spoke to the UN Security Council. Polling just prior to the speech indicated that a strong majority of the public viewed Powell's forthcoming speech as an important factor in settling their minds about an attack on Iraq (*23*). The speech (*24*) presented a logic structure on three truth statements:

Statement 1. Saddam Hussein has a stockpile of weapons of mass destruction.

Statement 2. Saddam Hussein's weapons of mass destruction are real and present dangers to the region and to the world.

Statement 3. A preemptive invasion of Iraq would be a just war.

It was a logic structure in which high certainty of belief on statement 1 implies high certainty of belief on statements 2 and 3. Powell concluded his speech with the words, "We must not shrink from whatever is ahead of us. We must not fail in our duty and our responsibility to the citizens of the countries that are represented by this body." In March 2003, the U.S. government announced that "diplomacy has

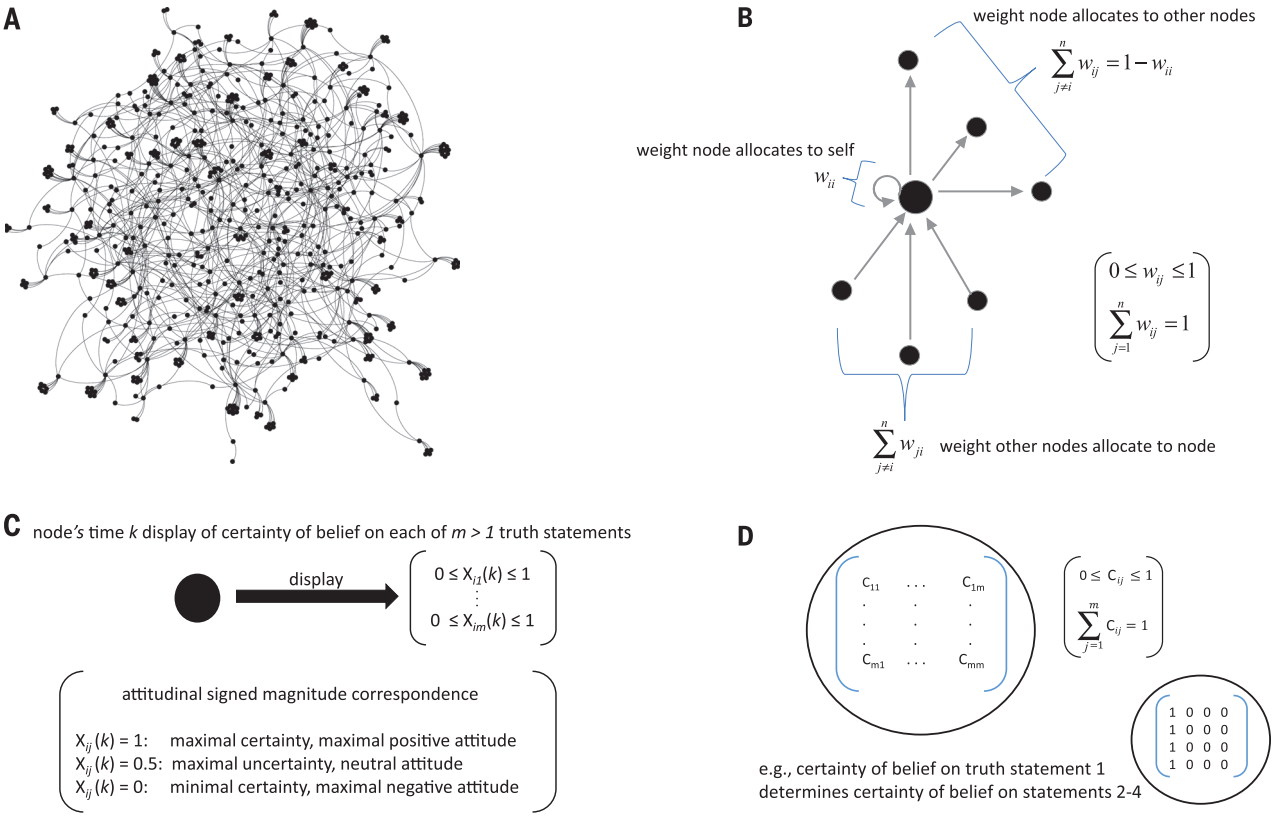

E tensor matrix equation of belief system dynamics

$$\mathbf{X}(k+1) = \mathbf{AWX}(k)\mathbf{C}^T + (\mathbf{I} - \mathbf{A})\mathbf{X}(0), \; k = 0, 1, \ldots$$

$$\left(\mathbf{A}_{n \times n}, \; a_{ii} = 1 - w_{ii} \; \forall i, \; a_{ij} = 0 \; \forall i \neq j\right)$$

Fig. 1. Model of belief system structure and dynamics. (**A**) An influence network, (**B**) with nodes that are allocators of influence to other nodes, (**C**) whose certainties of belief on multiple truth statements are influenceable, (**D**) under the condition of logical interdependencies among the statements, (**E**) based on a weighted averaging mechanism that is updating each node's certainty of belief on each truth statement.

Downloaded from http://science.sciencemag.org/ on October 20, 2016

failed" and that it would proceed without UN Security Council approval with a "coalition of the willing." President Bush spoke to the American public and announced Operation Iraqi Freedom. He stated, "The people of the United States and our friends and allies will not live at the mercy of an outlaw regime that threatens the peace with weapons of mass murder." The 2003 invasion of Iraq began a few days later. In the immediate March-May aftermath of the invasion, polling indicated a surge to strong majority support of the preemptive invasion. With the failure to find any evidence of weapons of mass destruction in Iraq, polling indicated that a strong majority of the public believed that the Iraq War was based on incorrect assumptions (*25*). In September 2005, Colin Powell acknowledged that his UN speech was based on flawed intelligence reports.

Two events underlie the fluctuation of public opinion on the war. The first event set up a logic structure and a conclusion. If statement 1 is true, then statements 2 and 3 are true, and the available evidence indicates that statement 1 is without doubt true. The ensuing public discourse elevated the belief that an invasion was justified. The invasion occurred. The second event, no weapons of mass destruction were found, altered the conclusion of the logic structure. The ensuing public discourse elevated the belief that the invasion was unjustified. For if statement 1 is false, then statements 2 and 3 are also false, and the available evidence indicates that statement 1 is without doubt false.

Applying the Fig. 1 model, consider a population that (i) is attentive to Powell's UN speech logic structure, (ii) maximally open to interpersonal influence, (iii) accepts its logic structure, and (iv) is connected in a regular influence network structure that allows direct or indirect flows of influence from every individual i to every individual j of the population. If this population has a high certainty on statement 1, then the belief system dynamics will generate a consensus that a preemptive invasion is a just war for any distribution of certainties of belief on statements 2 and 3. And if an event occurs that proves statement 1 false, then the population's certainty belief on all three statements will be dramatically lowered.

Figure 2 illustrates the different results of belief dynamics with and without the logic structure in which statements 2 and 3 certainties of belief depend on statement 1 certainty of belief. The colored lines distinguish individual temporal trajectories of belief on each of the three statements. Figure 2A is a population without such a logic structure. Its distinctive distributions of certainty of belief on the three statements are independent. The population converges to consensus on each statement. A high-certainty consensus is reached on the truth of statement 1. A consensus is reached that entails near maximum uncertainty on the truth of statement 2. A high-certainty consensus is reached that statement 3 is false. Figure 2B is a population with the logic structure. Its distinctive distributions

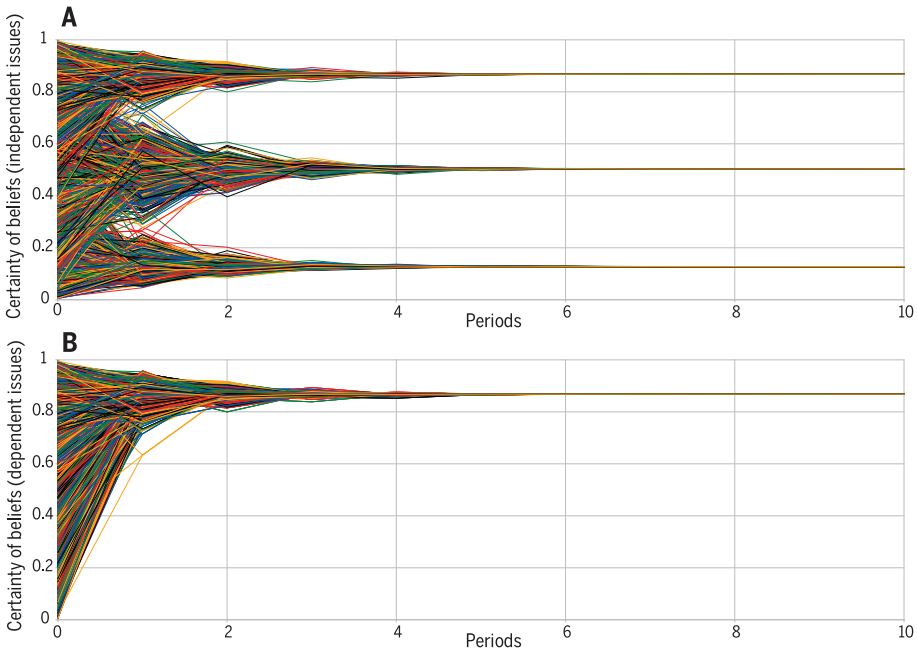

Fig. 2. Belief heterogeneity on three truth statements is reduced by the interpersonal influence system. The form of the reduction depends on the presence or absence of a belief constraint structure. (**A**) The three statements of belief are independent

$$\mathbf{C} = \begin{pmatrix} 1 & 0 & 0 \\ 0 & 1 & 0 \\ 0 & 0 & 1 \end{pmatrix}.$$

(**B**) Certainties of belief on statement 1 constrain certainties of belief on statements 2 and 3

$$\mathbf{C} = \begin{pmatrix} 1 & 0 & 0 \\ 1 & 0 & 0 \\ 1 & 0 & 0 \end{pmatrix}.$$

The supplementary materials provide the technical details on this figure.

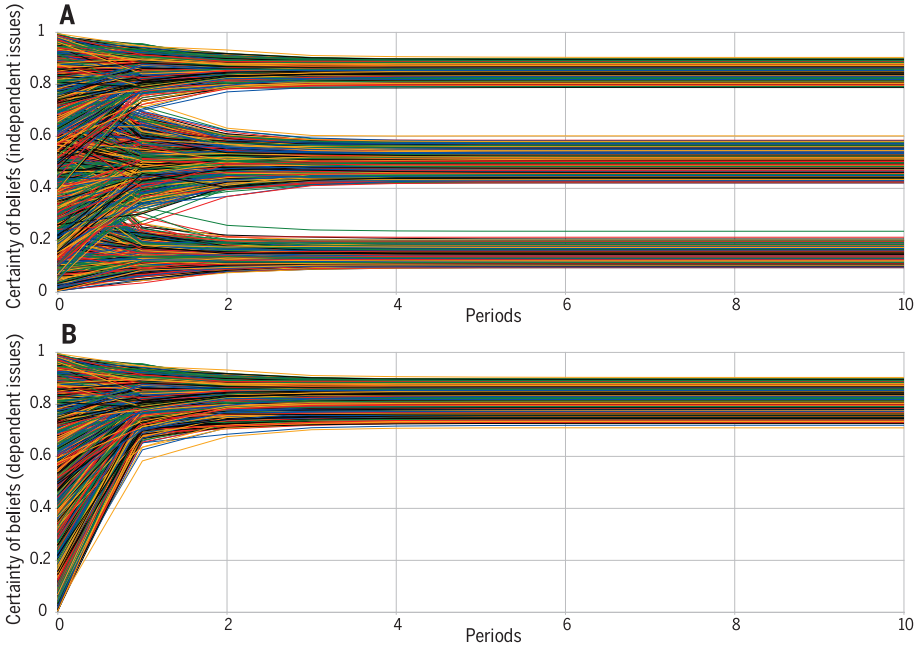

Fig. 3. When people are more wedded to their initial beliefs, the interpersonal influence system reduces, but does not eliminate, belief heterogeneity on the three statements. The form of the reduction depends on the presence or absence of a belief constraint structure. (**A**) The three statements of belief are independent. (**B**) Certainties of belief on statement 1 constrain certainties of belief on statements 2 and 3.

Downloaded from http://science.sciencemag.org/ on October 20, 2016

of certainty of belief on the three statements are interdependent. A high-certainty consensus is reached that all three statements are true.

Figure 3 relaxes the assumption that individuals' levels of openness to interpersonal influence are all maximal and introduces a level of closure to interpersonal influence that modestly anchors individuals on their initial beliefs. In contrast to the belief trajectories of Fig. 2, the effect of such anchorage is a maintained heterogeneity of beliefs under the same conditions of initial belief and network connectivity that generated the consensus results of Fig. 2. It can be shown that with more markedly heterogeneous levels of closure to influence, the evolution of the belief system is disorganized.

Figures 2B and 3B elucidate the conditions under which substantial shifts of public opinion occur when a highly influenceable public accepts a government's logic structure on truth statements. The next three figures illustrate alternate realizations of belief system dynamics on the same truth statements.

Figure 4 considers an alternative system with the same structure as Figs. 2B and 3B, but one in which the influence system overrides the implications of the logic structure. It contains an intransigent faction of k skeptics, maximally closed interpersonal influence, with identical and uniform low confidence (0.10) on all three truth statements. All other $n-k$ individuals are maximally open to influence. Thus, the intransigent faction is composed of individuals (i) who reject the $n-k$ others' high certainty of belief on the truth of statement 1, (ii) who are substantially less certain on the truth of statement 2 than the $n-k$ others, and (iii) who are as skeptical as the $n-k$ others' on statement 3. Figure 4 shows that the temporal movement is toward a consensus of diminished confidence on statements 1 and 2. More generally, if k intransigent individuals have identical beliefs $\mathbf{z} = (z_1, z_2, z_3)$, then the beliefs of the open-minded individuals converge to the row vector $\mathbf{zC}^T$. In Fig. 4, the beliefs z_i are uniform $z_1 = z_2 = z_3 = 0.10$, and thus the whole community reaches consensus. For nonuniform certainties of belief of the intransigent individuals $z_1 \neq z_2 \neq z_3$, in general $\mathbf{zC}^T \neq \mathbf{z}$, and the final beliefs of the intransigent and open-minded individuals may disagree.

Figure 5 considers an alternative system with the same initial distribution of beliefs and influence network as Fig. 2B, but one with a cross-pressure logic structure in which statements 1 and 3 are independent competing determinants of the statement 2 appraisal of a real and present danger,

$$\mathbf{C} = \begin{pmatrix} 1 & 0 & 0 \\ 0.80 & 0 & 0.20 \\ 0 & 0 & 1 \end{pmatrix}.$$

The cross-pressure coefficients c_{21} and c_{23} in row 2 of the logic structure (depending on their values) determine the direction and extent of movement of statement 2 beliefs. If the row 2 values of this logic structure were reversed, $c_{21} = 0.20$ and $c_{23} = 0.80$, then the movement of public opinion would gravitate toward a rejection of statement 2 that Saddam Hussein's weapons of mass destruction are real and present dangers to the region and to the world.

Our final illustration relaxes the assumption of a common logic structure and considers a small-scale system of $n = 6$ policy-makers engaged in debate on the three truth statements under the condition of two competing logic structures

$$\mathbf{C}_1 = \begin{pmatrix} 1 & 0 & 0 \\ 1 & 0 & 0 \\ 1 & 0 & 0 \end{pmatrix} \text{ and } \mathbf{C}_2 = \begin{pmatrix} 1 & 0 & 0 \\ 1 & 0 & 0 \\ 0 & 0 & 1 \end{pmatrix}.$$

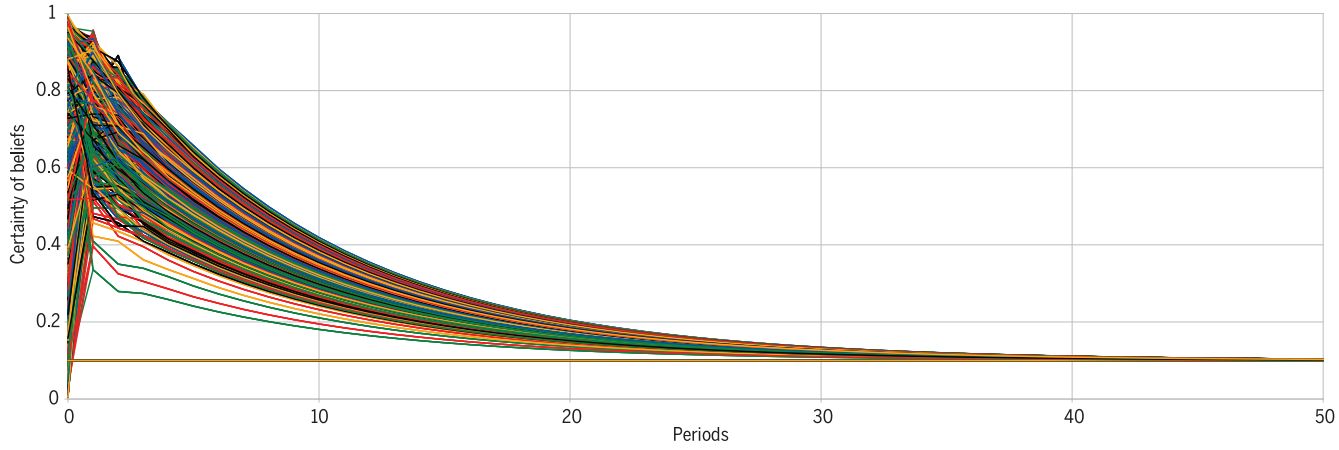

Fig. 4. A faction of intransigent skeptics overrides the belief constraint structure and generates a consensus that all three statements are false.

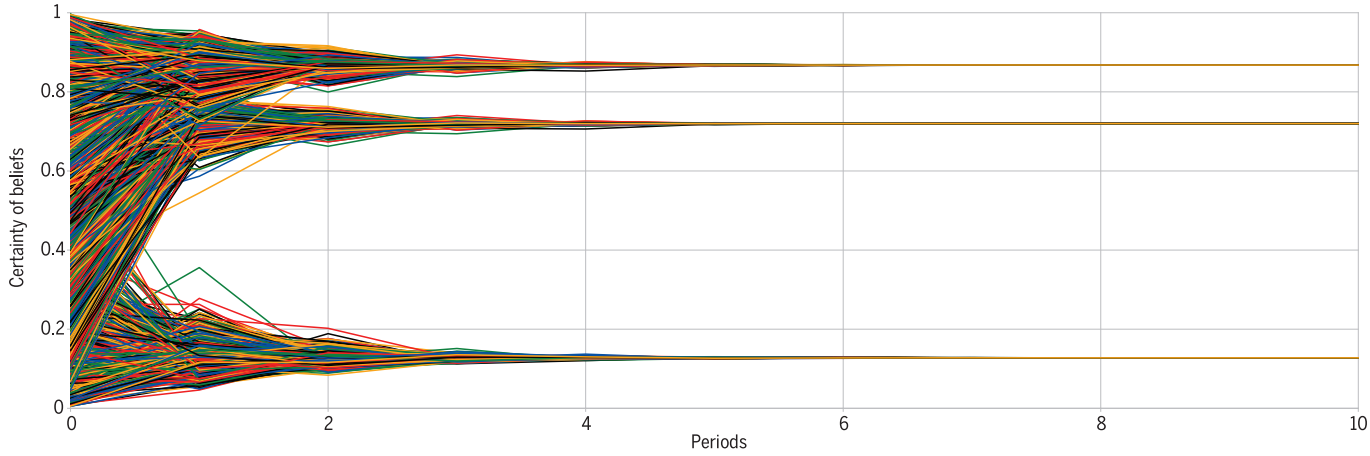

Fig. 5. Belief system dynamics with a cross-pressure logic structure in which statements 1 and 3 are independent competing determinants of the statement 2 appraisal of a real and present danger.

Downloaded from http://science.sciencemag.org/ on October 20, 2016

For three decision-makers, the position on statement 1 determines the conclusion on statements 2 and 3. For the other three decision-makers, their conclusion on statement 3 is not determined by their position on statement 1. Let the initial beliefs of the six policy-makers be consonant with initial certainties of the larger population of citizens in which the policy group is situated,

$$\mathbf{X}(0) = \begin{pmatrix} 0.96 & 0.56 & 0.16 \\ 0.94 & 0.54 & 0.14 \\ 0.92 & 0.52 & 0.12 \\ 0.88 & 0.48 & 0.08 \\ 0.86 & 0.46 & 0.06 \\ 0.84 & 0.44 & 0.04 \end{pmatrix};$$

that is, each decision-maker has high certainty that statement 1 is true, uncertainty on the truth of statement 2, and high certainty that statement 3 is false, as in our previous illustrations. If all six of these decision-makers are motivated to reach consensus, and maximally open to interpersonal influence, then the belief-system dynamics are determined by the two logic structures, $\mathbf{C}_1$ and $\mathbf{C}_2$, and the individuals' $\mathbf{W}$ matrix of $i \xrightarrow{w_{ij}} j$ allocated weights to other individuals' displayed positions on the statements. Let this matrix be

$$\mathbf{W} = \begin{bmatrix} 0 & 0.80 & 0.20 & 0 & 0 & 0 \\ 0.50 & 0 & 0.50 & 0 & 0 & 0 \\ 0.20 & 0.80 & 0 & 0 & 0 & 0 \\ 0 & 0.80 & 0 & 0 & 0.10 & 0.10 \\ 0 & 0.80 & 0 & 0.10 & 0 & 0.10 \\ 0 & 0.80 & 0 & 0.10 & 0.10 & 0 \end{bmatrix},$$

where the block partition indicates that individuals 1 to 3 are processing information based on the $\mathbf{C}_1$ logic structure and individuals 4 to 6 are processing information based on the $\mathbf{C}_2$ logic structure. Note that the $i \xrightarrow{w_{ij} > 0} j$ weights are dense among individuals with the same logic structure and that individual 2 with the $\mathbf{C}_1$ logic structure is allocated disproportionate weight by the five other members. The generalization of the basic equation for the competing structures is presented as eqs. 23 and 24 in the supplementary materials, and we discuss the stability in models with multiple dependency constraints in supplementary text S.2.3.3. Figure 6 shows the certainty of belief trajectories for each of the six individuals on each of three statements. With low diversity of initial opinion on each statement and an influence network in which one individual has high influence centrality, a consensus is rapidly reached that is consistent with the $\mathbf{C}_1$ logic structure. With its dampened opportunity for a vigorous debate on the merits of the $\mathbf{C}_2$ decoupling of statement 3 from statement 1, this group illustrates the potential hazards of the "groupthink" systems (*26*) that have been associated with policy-decision fiascoes.

In conclusion, truth statement interdependencies matter, and their manifestations may be diverse when individuals are embedded in an interpersonal influence system that is modifying individuals' certainties of belief. Belief system dynamics depend on the topology of truth statements' interdependencies and the topology of the influence network in which individuals are embedded. Interpersonal influence networks set up a complex system.

Individuals' certainties of belief may be elevated or dampened, beliefs about different objects may be linked, and shared belief systems may be generated. The information environment to which individuals are responding by updating their belief systems includes other individuals who are displaying their certainties of beliefs on the same truth statements. Individuals who are exposed to such social information may have heterogeneous levels of closure or openness to interpersonal influence, they may vary in who is included in the subsets of individuals whose certainties of beliefs are visible to them, and they may vary in the weights allocated to particular individuals' displayed positions. The influence network that is assembled by individuals' allocations of weights allows both direct and indirect interpersonal influences on individuals' certainties of belief on multiple truth statements.

Although possible realizations of belief system dynamics are infinite, a parsimonious, analytically tractable, general theory may cover them. Special cases include systems in which no logical interdependencies exist among truth statements, no interpersonal influences exist among individuals of the system, or no consensus is possible. The model posits two individual-level information integration processes in which a logic constraint structure is nested in an interpersonal influence process. Dynamic information environments, which include information on other individuals' certainties on multiple truth statements, continuously activate self-organizing cognitive consistency processes. If such continuous activation is a source of individual-level stress, then buffering defenses to the disturbances of the information environment may occur. Such individual defense responses include a reduced openness to interpersonal influence, a restructuring of the allocated weights to sources of information, or a flight into a local environment in which the individual is exposed only to self-confirming information. Currently, the model does not consider such defense responses. The mathematics of the model allow a calibration of the influence network and logic constraint structures of a population; that is, an inference on what logic structure is consistent with observed trajectories of belief.

Belief system dynamics occur in both large-scale populations and in small groups. Their implications are especially potent in the debates that arise in small policy groups, whose decisions affect the collective actions of governments and other organizations and, in turn, the security and welfare of numerous individuals. The hazard rate of policy fiascoes may be reduced with a more detailed attention to (i) structural features of small-group interpersonal influence systems and (ii) applications of formal rules of debate

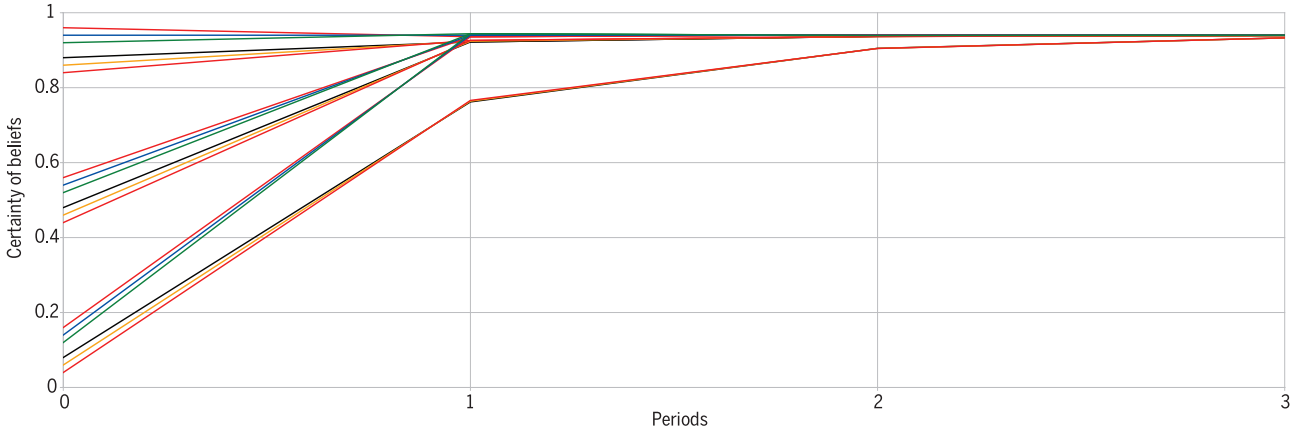

Fig. 6. Belief system dynamics in a small policy group of six individuals engaged in debate on the three truth statements under the condition of two competing logic structures. In one, the position on statement 1 determines the conclusion on statements 2 and 3. In the other, the conclusion on statement 3 is not determined by the position on statement 1. With its quick dismissal of the latter, this group illustrates the "groupthink" systems that have been associated with policy-decision fiascoes.

Downloaded from http://science.sciencemag.org/ on October 20, 2016

that can regulate these systems. The field of science on this is in its infancy.

REFERENCES AND NOTES

1. P. E. Converse, in *Ideology and Its Discontents*, D. E. Apter, Ed. (The Free Press of Glencoe, 1964), pp. 206–261.
2. E. H. Spicer, *Science* **174**, 795–800 (1971).
3. J.-B. Michel *et al.*, *Science* **331**, 176–182 (2011).
4. E. Griffiths, *Towards a Science of Belief Systems* (Palgrave Macmillan, 2014).
5. L. Festinger, *A Theory of Cognitive Dissonance* (Stanford Univ. Press, 1957).
6. B. Gawronski, F. Strack, Eds., *Cognitive Consistency: A Fundamental Principle in Social Cognition* (Guilford, 2012).
7. M. H. DeGroot, *J. Am. Stat. Assoc.* **69**, 118–121 (1974).
8. R. Axelrod, *J. Conflict Resolut.* **41**, 203–226 (1997).
9. N. E. Friedkin, *A Structural Theory of Social Influence* (Cambridge Univ. Press, 1998).
10. D. A. Snow, S. A. Soule, H. Kriesi, Eds., *The Blackwell Companion to Social Movements* (Blackwell, 2004).
11. V. Blondel, J. Hendrickx, J. Tsitsiklis, *IEEE Trans. Automat. Contr.* **54**, 2586–2597 (2009).
12. A. Flache, M. W. Macy, *J. Math. Sociol.* **35**, 146–176 (2011).
13. P. V. Marsden, Ed., *Social Trends in American Life: Findings from the General Social Survey Since 1972* (Princeton Univ. Press, 2012).
14. C. Altafini, *IEEE Trans. Automat. Contr.* **58**, 935–946 (2013).
15. N. E. Friedkin, E. C. Johnsen, *Social Influence Network Theory: A Sociological Examination of Small Group Dynamics* (Cambridge Univ. Press, 2011).
16. P. Frasca, H. Ishii, C. Ravazzi, R. Tempo, *Eur. J. Control* **24**, 2–13 (2015).
17. N. E. Friedkin, *IEEE Control Systems* **35**, 40–51 (2015).
18. S. E. Parsegov, A. V. Proskurnikov, R. Tempo, N. E. Friedkin, *IEEE Trans. Automat. Contr.* (2016); published online at http://ieeexplore.ieee.org/document/7577815/
19. www.gallup.com/poll/7303/public-iraq-fails-inspections-second-un-resolution-needed-war.aspx
20. www.gallup.com/poll/7408/public-taking-waitandsee-attitude-un-inspections.aspx
21. www.people-press.org/2003/01/16/public-wants-proof-of-iraqi-weapons-programs/
22. http://usatoday30.usatoday.com/news/world/iraq/2003-03-16-poll-iraq_x.htm
23. www.gallup.com/poll/7720/powells-un-appearance-important-public.aspx
24. www.washingtonpost.com/wp-srv/nation/transcripts/powelltext_020503.html
25. www.pewresearch.org/2008/03/19/public-attitudes-toward-the-war-in-iraq-20032008/
26. I. L. Janis, *Groupthink: Psychological Studies of Policy Decisions and Fiascoes* (Houghton Mifflin, 1982).

ACKNOWLEDGMENTS

N.E.F. acknowledges the financial support of the U.S. Army Research Laboratory and the U.S. Army Research Office under grant no. W911NF-15-1-0577. A.V.P. acknowledges Russian Science Foundation project 14-29-00142 hosted by IPME RAS, under whose financial support the results from section S2.3.2 were obtained. Partial financial support was also provided by European Research Council grant ERCStG-307207 hosted by the University of Groningen. R.T. acknowledges the financial support of the National Research Council of Italy. S.E.P. acknowledges the financial support of Russian Science Foundation project 16-11-00063 hosted by the V.A. Kotelnikov Institute of Radio Engineering and Electronics of the Russian Academy of Sciences.

SUPPLEMENTARY MATERIALS

www.sciencemag.org/content/354/6310/321/suppl/DC1
Supplementary Text
Fig. S1
References (*27*–*34*)

31 May 2016; accepted 7 September 2016
10.1126/science.aag2624

PLANKTON DYNAMICS

Physiological and ecological drivers of early spring blooms of a coastal phytoplankter

Kristen R. Hunter-Cevera,[1] Michael G. Neubert,[1] Robert J. Olson,[1] Andrew R. Solow,[2] Alexi Shalapyonok,[1] Heidi M. Sosik[1]*

Climate affects the timing and magnitude of phytoplankton blooms that fuel marine food webs and influence global biogeochemical cycles. Changes in bloom timing have been detected in some cases, but the underlying mechanisms remain elusive, contributing to uncertainty in long-term predictions of climate change impacts. Here we describe a 13-year hourly time series from the New England shelf of data on the coastal phytoplankter *Synechococcus*, during which the timing of its spring bloom varied by 4 weeks. We show that multiyear trends are due to temperature-induced changes in cell division rate, with earlier blooms driven by warmer spring water temperatures. *Synechococcus* loss rates shift in tandem with division rates, suggesting a balance between growth and loss that has persisted despite phenological shifts and environmental change.

Marine phytoplankton account for one-half of global primary production. Of considerable interest and concern is how climate change may affect this production. Increased temperature, ocean acidification, and altered nutrient delivery all have the potential to affect phytoplankton dynamics, including the timing and magnitude of blooms, which can dominate seasonal productivity (*1*, *2*). There is evidence of current and ongoing changes in plankton phenology (*3*–*5*), with potentially substantial ecological consequences for marine systems (*6*).

Recently, there has been uncertainty about the detection of trends in phytoplankton biomass and how possible trends relate to climate change (*7*–*9*). The uncertainty arises in part from difficulties in species-level detection of phytoplankton. Many studies use bulk measurements that reflect a composite of the phytoplankton community (*10*). These measurements (such as chlorophyll concentration) can mask taxon-specific changes and obscure the mechanisms that govern responses to climate change. Another challenge lies in the need to observe and measure phytoplankton at appropriate time scales to elucidate those mechanisms. Ecological interactions and physiological responses of phytoplankton are rapid (on the order of minutes to hours). To adequately capture population dynamics, we must sample at this frequency, but also for extended durations because identification of seasonal, yearly, or decadal trends requires time series of these lengths.

We address this lack of temporal and taxonomic resolution for the picophytoplankter *Synechococcus* by using observations of individual cells and their properties from an automated submersible flow cytometer, FlowCytobot (FCB) (*11*) , deployed at the Martha's Vineyard Coastal Observatory (MVCO). FCB has been deployed at MVCO since 2003, with year-round observations beginning in 2007. The data consist of a 13-year time series of hourly measurements of *Synechococcus* concentration and cell properties.

At MVCO, *Synechococcus* concentration exhibits a strong seasonal cycle, with low concentrations in winter and early spring, followed by a two- to three-order-of-magnitude bloom event in late spring (Fig. 1A). The population fluctuates around a slowly declining trend during summer and early fall and then declines sharply in late fall. Although this classic pattern (*12*) is stable from year to year, we found that the timing of the spring bloom varied by up to 4 weeks within our time series, and in particular we noted a trend of earlier blooms from 2003 to 2012 (~20-day advance) and later blooms from 2013 to 2015. We quantified these shifts by determining the day of the year at which the concentration first exceeds threshold concentration levels (Fig. 2B and fig. S1). Concurrent observations of temperature (Fig. 1D) show that earlier blooms coincide with warmer spring conditions (Fig. 2A and fig. S2). For each degree increase of the mean temperature in April, the spring bloom advances 4 to 5 days. The water at MVCO has been warming (fig. S3) in a manner consistent with the multidecadal trend in this region (*13*). Large seasonal and interannual variations are superimposed on these warming trends.

Numerous studies have identified correlations between temperature and *Synechococcus* concentration across a range of ocean conditions (*12*, *14*–*17*). In particular, there is evidence that the spring bloom begins in northeast U.S. and Canadian waters when the temperature exceeds

[1]Biology Department, Woods Hole Oceanographic Institution, Woods Hole, MA 02543, USA. [2]Marine Policy Center, Woods Hole Oceanographic Institution, Woods Hole, MA 02543, USA.
***Corresponding author. Email: hsosik@whoi.edu**

Downloaded from http://science.sciencemag.org/ on October 20, 2016

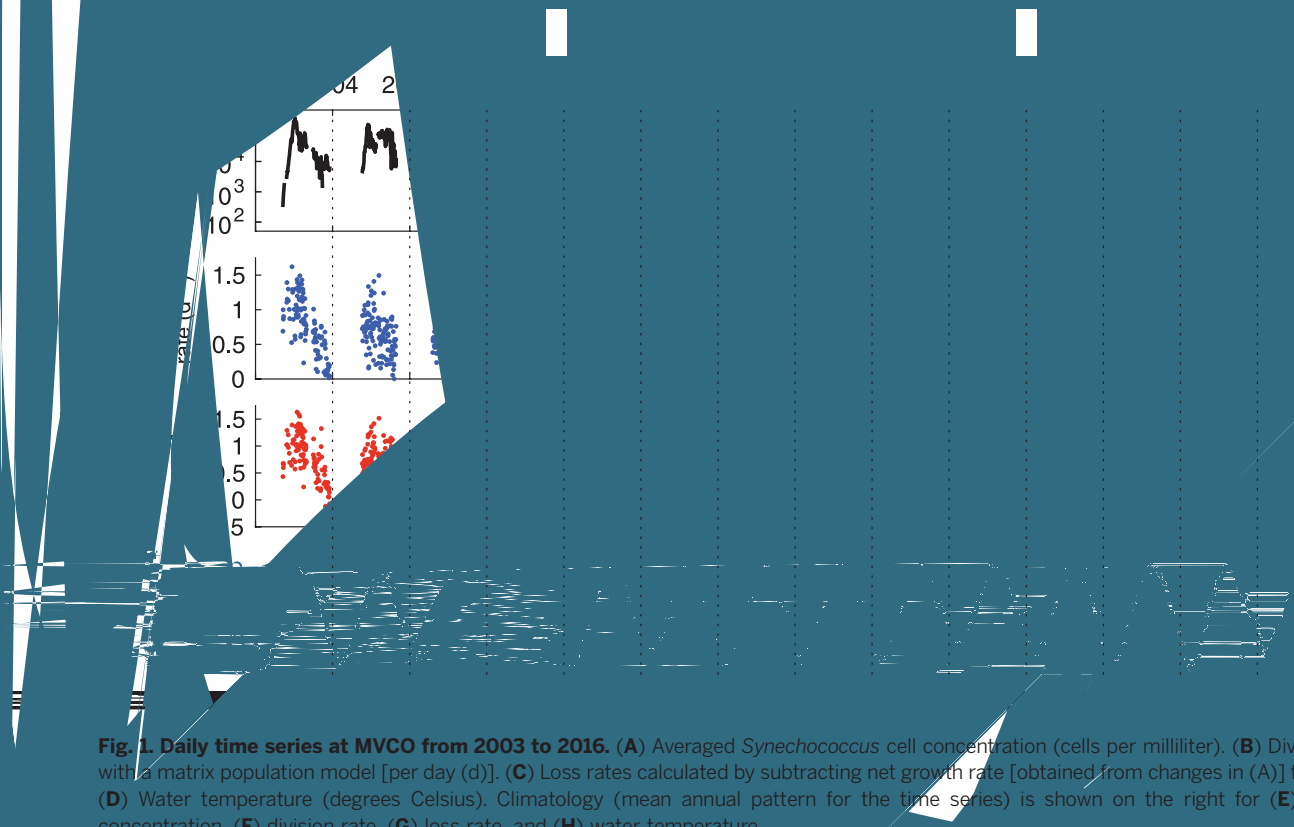

Fig. 1. Daily time series at MVCO from 2003 to 2016. (**A**) Averaged *Synechococcus* cell concentration (cells per milliliter). (**B**) Division rates estimated with a matrix population model [per day (d)]. (**C**) Loss rates calculated by subtracting net growth rate [obtained from changes in (A)] from division rate (B). (**D**) Water temperature (degrees Celsius). Climatology (mean annual pattern for the time series) is shown on the right for (**E**) *Synechococcus* cell concentration, (**F**) division rate, (**G**) loss rate, and (**H**) water temperature.

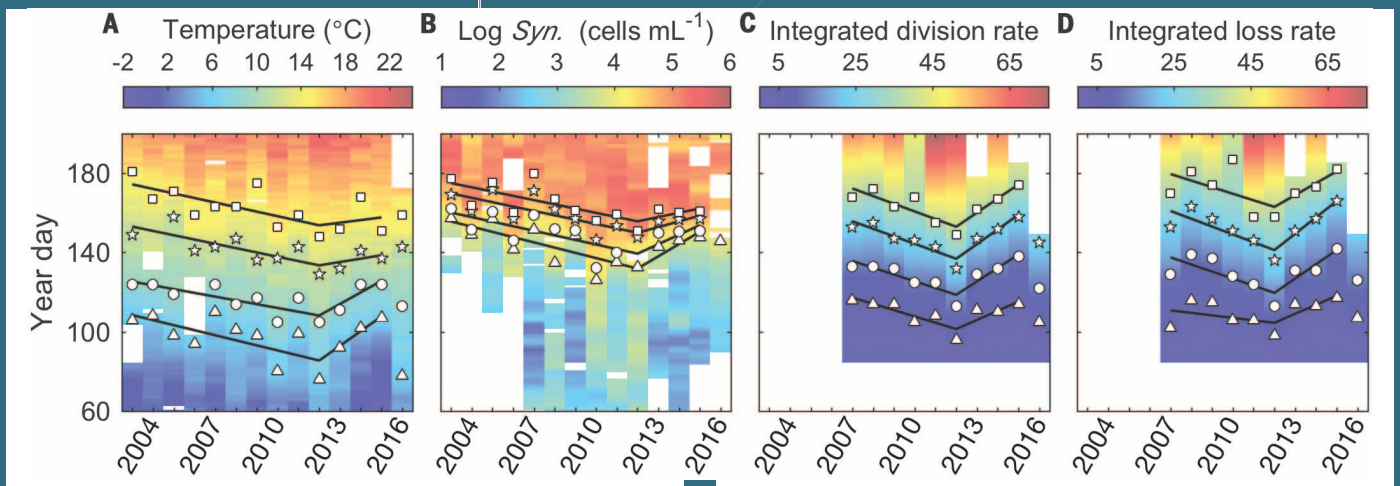

Fig. 2. Multiyear trends showing spring temperature changes and *Synechococcus* bloom shifts from 2003 to 2016. The data are shown by day of the year (vertical axis), with values denoted by color. (**A**) Temperature. Markers indicate the day in each year when water temperature first exceeds 6° (triangles), 9° (circles), 12° (stars), or 15°C (squares). (**B**) *Synechococcus* cell concentration. Markers indicate the day in each year when cell concentration exceeds 8×10^3 (triangles), 1.6×10^4 (circles), 4.8×10^4 (stars), or 9.6×10^4 (squares) cells ml^{-1}. (**C**) Integrated division rate (cumulative summed division rate starting at year day 85). Markers indicate the day in each year when the integrated division rate exceeds values of 4 (triangles), 12 (circles), 24 (stars) or 36 (squares). (**D**) Integrated loss rate (cumulative summed loss rate starting at year day 85). Markers indicate the day in each year when the integrated loss rate exceeds values of 4 (triangles), 12 (circles), 24 (stars), or 36 (squares). Solid lines in each panel represent best fits from a piecewise linear regression model between year-day threshold crossings (as denoted by the markers) and year. Parallel lines reflect insensitivity to the choice of threshold and a shift in only the timing, not in the shape, of the spring bloom trajectory.

Downloaded from http://science.sciencemag.org/ on October 20, 2016

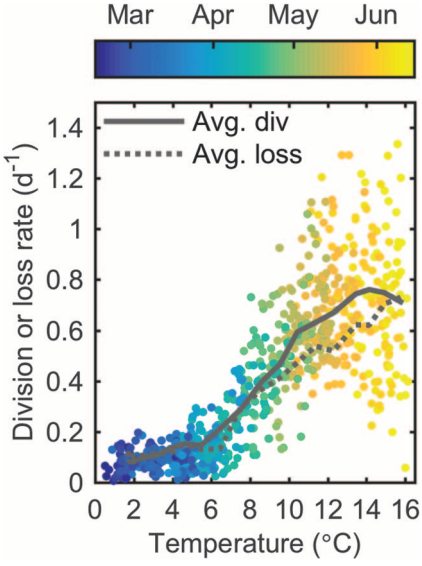

Fig. 3. Relationship between division rates and temperature between 1 February and 15 June for all data points (2003–2016). Colors indicate day of the year. The solid line is the relationship between the weekly climatology of division rate and the weekly climatology of temperature. The dashed line is the relationship between the weekly climatology of loss rate and the weekly climatology of temperature.

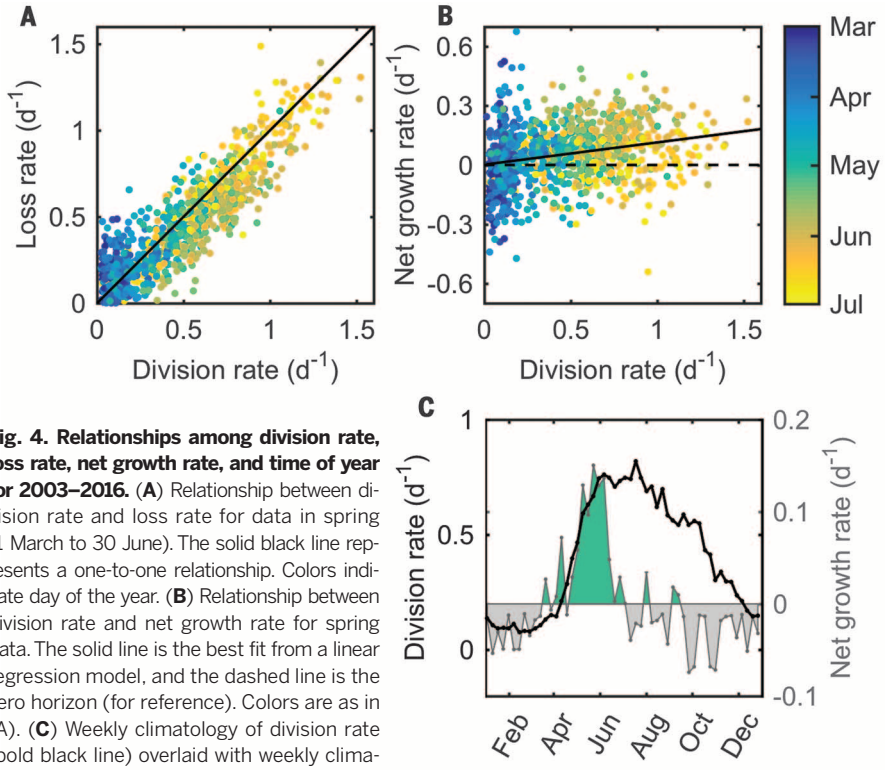

Fig. 4. Relationships among division rate, loss rate, net growth rate, and time of year for 2003–2016. (**A**) Relationship between division rate and loss rate for data in spring (1 March to 30 June). The solid black line represents a one-to-one relationship. Colors indicate day of the year. (**B**) Relationship between division rate and net growth rate for spring data. The solid line is the best fit from a linear regression model, and the dashed line is the zero horizon (for reference). Colors are as in (A). (**C**) Weekly climatology of division rate (bold black line) overlaid with weekly climatology of net growth rate (thin gray line). Periods of positive (negative) net growth rate are indicated with green (gray) shading.

species (*23*, *24*). The model relies only on changes in cell size and not on changes in cell concentration, which are often decoupled from division rate (fig. S4) as a result of cell loss or advection. Isolating the contribution of cell division is critical, because the net population growth rate is typically much lower than the division rate as a result of the tight coupling between primary producers and consumers in planktonic ecosystems (*25*). In combination with sustained, high-resolution in situ observations, this model makes it possible to produce the multiyear records of daily division rate (Fig. 1B) that are required to understand phenological shifts.

Model-estimated division rates reflect a composite response of the entire *Synechococcus* population. Natural populations are often composed of more than one *Synechococcus* type, and multiple genotypes are known to coexist at MVCO (*26*, *27*). Types can differ in physiological characteristics, such as temperature growth response or tolerance (*20*). Nonetheless, we find that *Synechococcus* division rates exhibit a pronounced seasonality, suggesting strong environmental drivers for the entire population. The division rate is as low as 0.1 day^{-1} in winter and as high as 1.4 day^{-1} in spring (Fig. 1B), increasing rapidly after water temperature exceeds ~5°C (Fig. 3). The increase slows or stops once water temperature reaches ~16°C in spring. The shape of the relationship between temperature and division rate strongly resembles that of the relationship for cultured *Synechococcus* (*19*, *20*). During spring, a single clade-I genotype makes up the majority of the population (*26*). A cultured MVCO isolate belonging to this clade exhibits the same relationship between division rate and temperature as we report here for the natural population (*17*) (fig. S5). No other environmental factor (light or nutrients) shows such a strong relationship with in situ division rate in spring (fig. S6). Together, these results support the view that temperature is the main factor limiting *Synechococcus* division during late winter and spring (*17*).

Our second main result is that the phenological shifts of the spring bloom are caused by temperature-induced shifts in the timing of the division rate increase (fig. S2). Specifically, the date at which population growth potential (computed as the integrated division rate for each day in spring; methods and fig. S7) reached threshold values advanced over the warming period 2003–2012 but retreated when spring temperatures cooled in 2013–2015 (Fig. 2C). The record-warm conditions in 2012 mark a transition between periods of advancing and retreating that are coincident across threshold crossings for spring temperature, *Synechococcus* concentration, and integrated division rate. In conjunction with the temperature dependence of the division rate in spring (Fig. 3), this result supports the conclusion that shifts in the timing of spring blooms reflect a direct physiological response to shifts in the onset of seasonal warming.

If division rates were the only factor affecting bloom phenology, we would expect not only a shift in timing, but also a change in the rate of increase in cell concentration. In fact, only the timing has shifted, whereas the rate of increase in cell concentration has not changed systematically (Fig. 2B). The stability of the bloom trajectory suggests that population losses have also shifted in tandem with growth (Fig. 2D and fig. S7). To illustrate this, we calculated bulk *Synechococcus* loss rates by subtracting the division rate from the net growth rate. The loss rates closely track division rates in magnitude over the entire time series (Fig. 1C), but during the spring bloom, the loss rate is on average ~ 0.15 day^{-1} lower than the division rate (Fig. 4A). It is this slight imbalance persisting for several months that leads to a steady blooming phase. The narrow margin by which *Synechococcus* can essentially "outgrow" their losses in spring makes this a critical time for cells to accumulate.

Our third main result, that loss rates closely track division rates, suggests that the dominant losses are biological (e.g., viral lysis and grazing) rather than physical in nature. It is unlikely that advection of spatial patches, for instance, would produce this tight correspondence year after year.

Beyond the connection to climate, our findings provide important insights into the ways that physiology and environmental factors interact to control phytoplankton blooms, a classic problem that has been the subject of recent controversy (*28*). Considering bulk properties of phytoplankton, Behrenfeld and Boss (*29*) have recently argued that, despite decades of study, no evidence has emerged linking bloom dynamics to physiological factors that regulate phytoplankton division rates. This led them to conclude that

Downloaded from http://science.sciencemag.org/ on October 20, 2016

bloom dynamics depend principally on the impact of consumers, a long-recognized control of phytoplankton abundance (*30*). Our findings for *Synechococcus* agree with those of Behrenfeld and Boss in so far as division rates (and, by inference, loss rates) are roughly 10 times the accumulation (net growth) rates. Our results differ, however, in that we find a significant positive correlation between division and accumulation rates over the course of the spring bloom (Fig. 4, B and C). This correlation was not detected by Behrenfeld and Boss, and perhaps should not be expected to be evident in the satellite-based observations of chlorophyll concentration that they analyzed (*29*). Those observations aggregate the entire phytoplankton community over a relatively large region of the ocean and mask individual responses of different taxa.

Our observations, made at a much smaller spatial scale and with much finer taxonomic and temporal resolution than that of satellite data, reveal a connection between division rates and the bloom dynamics of *Synechococcus*. Consumers (including grazers, viruses, and parasites) certainly play a major role in shaping the bloom's trajectory, but the bloom is triggered by an environmental factor, the seasonal temperature rise, which leads to increases in the *Synechococcus* division rate (Fig. 3). The bloom persists until the division rate plateaus (Fig. 4B), at which point losses overtake division and the bloom begins to decline.

We were able to diagnose the importance of temperature in regulating the dynamics of a ubiquitous marine primary producer, *Synechococcus,* by exploiting a 13-year time series comprising data on millions of individual cells and their traits. This allowed us to not only quantify the relationship between temperature and cell division in a natural population, but also to document how that relationship is the basis for a dramatic phenological shift affecting both *Synechococcus* and their consumers. It remains to be seen whether this ecological coupling will hold as warming trends continue in the decades to come.

REFERENCES AND NOTES

1. K. R. Arrigo, D. Worthen, A. Schnell, M. P. Lizotte, *J. Geophys. Res. Oceans* **103**, 15587–15600 (1998).
2. P. Martin *et al.*, *Deep Sea Res. Part I Oceanogr. Res. Pap.* **58**, 338–349 (2011).
3. R. Ji, M. Edwards, D. L. Mackas, J. A. Runge, A. C. Thomas, *J. Plankton Res.* **32**, 1355–1368 (2010).
4. K. H. Wiltshire *et al.*, *Estuaries Coasts* **33**, 295–310 (2010).
5. M. Kahru, V. Brotas, M. Manzano-Sarabia, B. G. Mitchell, *Glob. Change Biol.* **17**, 1733–1739 (2011).
6. M. Edwards, A. J. Richardson, *Nature* **430**, 881–884 (2004).
7. A. McQuatters-Gollop *et al.*, *Nature* **472**, E6–E7, discussion E8–E9 (2011).
8. W. W. Gregg, C. S. Rousseaux, *J. Geophys. Res. Oceans* **119**, 5921–5933 (2014).
9. D. G. Boyce, M. Dowd, M. R. Lewis, B. Worm, *Prog. Oceanogr.* **122**, 163–173 (2014).
10. D. A. Siegel *et al.*, *Remote Sens. Environ.* **135**, 77–91 (2013).
11. R. J. Olson, A. A. Shalapyonok, H. M. Sosik, *Deep Sea Res. Part I Oceanogr. Res. Pap.* **50**, 301–315 (2003).
12. J. B. Waterbury, S. W. Watson, F. W. Valois, D. G. Franks, *Can. Bull. Fish. Aquat. Sci.* **214**, 71–120 (1986).
13. S. W. Nixon, S. Granger, B. A. Buckley, M. Lamont, B. Rowell, *Estuaries* **27**, 397–404 (2004).
14. N. S. R. Agawin, C. M. Duarte, S. Agusti, *Mar. Ecol. Prog. Ser.* **170**, 45–53 (1998).
15. W. K. W. Li, *Limnol. Oceanogr.* **43**, 1746–1753 (1998).
16. A.-Y. Tsai, K.-P. Chiang, J. Chang, G.-C. Gong, *Aquat. Microb. Ecol.* **51**, 263–274 (2008).
17. K. R. Hunter-Cevera *et al.*, *Proc. Natl. Acad. Sci. U.S.A.* **111**, 9852–9857 (2014).
18. W. K. W. Li, W. G. Harrison, E. J. H. Head, *Proc. R. Soc. London Ser. B* **273**, 1953–1960 (2006).
19. L. R. Moore, R. Goericke, S. W. Chisholm, *Mar. Ecol. Prog. Ser.* **116**, 259–275 (1995).
20. J. Pittera *et al.*, *ISME J.* **8**, 1221–1236 (2014).
21. M. R. Landry, R. P. Hassett, *Mar. Biol.* **67**, 283–288 (1982).
22. R. E. McDuff, S. W. Chisholm, *Limnol. Oceanogr.* **27**, 783–788 (1982).
23. M. Dugenne *et al.*, *Front. Microbiol.* **5**, 485 (2014).
24. F. Ribalet *et al.*, *Proc. Natl. Acad. Sci. U.S.A.* **112**, 8008–8012 (2015).
25. A. Calbet, M. R. Landry, *Limnol. Oceanogr.* **49**, 51–57 (2004).
26. K. R. Hunter-Cevera, thesis, Massachusetts Institute of Technology and Woods Hole Oceanographic Institution (2014).
27. K. R. Hunter-Cevera, A. F. Post, E. E. Peacock, H. M. Sosik, *Microb. Ecol.* **71**, 276–289 (2016).
28. A. Fischer *et al.*, *Oceanography* **27**, 222–235 (2014).
29. M. J. Behrenfeld, E. S. Boss, *Annu. Rev. Mar. Sci.* **6**, 167–194 (2014).
30. K. Banse, in *Primary Productivity and Biogeochemical Cycles in the Sea*, P. G. Falkowski, A. D. Woodhead, K. Vivirito, Eds. (Springer, 1992), pp. 409–440.

ACKNOWLEDGMENTS

We thank E. T. Crockford, E. Peacock, J. Fredericks, the MVCO Operations Team, the captain and mate of the R/V *Tioga*, and P. Henderson of the Woods Hole Oceanographic Institution (WHOI) Nutrient Analytical Facility for logistical and analytical support. We thank S. W. Chisholm and J. Waterbury for discussions and comments on the manuscript. This work was supported by U.S. NSF grants OCE-0119915, OCE-0530830, OCE-1031256, DEB-1145017, and DEB-1257545; NASA grants NNX11AF07G and NNX13AC98G; Gordon and Betty Moore Foundation grant GGA#934; the Investment in Science Fund, given primarily by WHOI Trustee and Corporation Members; and a National Defense Science and Engineering graduate fellowship from the U.S. Department of Defense. Data used in this study were deposited in the Dryad Digital Repository (http://dx.doi.org/10.5061/dryad.jm8s7).

SUPPLEMENTARY MATERIALS

www.sciencemag.org/content/354/6310/326/suppl/DC1
Materials and Methods
Figs. S1 to S8
References (*31*–*33*)

10 April 2016; accepted 9 September 2016
10.1126/science.aaf8536

BIOMASS PROCESSING

Formaldehyde stabilization facilitates lignin monomer production during biomass depolymerization

Li Shuai,[1] Masoud Talebi Amiri,[1] Ydna M. Questell-Santiago,[1] Florent Héroguel,[1] Yanding Li,[2,3] Hoon Kim,[2,4] Richard Meilan,[5] Clint Chapple,[6] John Ralph,[2,3,4] Jeremy S. Luterbacher[1]*

Practical, high-yield lignin depolymerization methods could greatly increase biorefinery productivity and profitability. However, development of these methods is limited by the presence of interunit carbon-carbon bonds within native lignin, and further by formation of such linkages during lignin extraction. We report that adding formaldehyde during biomass pretreatment produces a soluble lignin fraction that can be converted to guaiacyl and syringyl monomers at near theoretical yields during subsequent hydrogenolysis (47 mole % of Klason lignin for beech and 78 mole % for a high-syringyl transgenic poplar). These yields were three to seven times those obtained without formaldehyde, which prevented lignin condensation by forming 1,3-dioxane structures with lignin side-chain hydroxyl groups. By depolymerizing cellulose, hemicelluloses, and lignin separately, monomer yields were between 76 and 90 mole % for these three major biomass fractions.

Lignin is an abundant natural polymer, accounting for 15 to 30 weight % (wt %) of lignocellulosic biomass (*1*, *2*). Unlike cellulose and hemicellulosic polysaccharides, the other major constituents of biomass, lignin primarily consists of methoxylated phenylpropanoid (guaiacyl and syringyl) subunits. This structure gives lignin an energy density 30% greater than that of polysaccharide polymers and makes it one of the few natural large-scale sources of aromatic compounds (*3*, *4*). These properties make lignin-derived monomers useful precursors for renewable aromatic chemicals and drop-in fuels (*3*, *4*).

The longstanding interest in lignin valorization has translated into few commercial processes because of the lack of practical high-yield lignin depolymerization methods that can be used while upgrading biomass polysaccharides. Promising biorefinery fractionation or pretreatment processes—such as those using water (*5*), alcohol (*6*), tetrahydrofuran (THF) (*7*), ionic liquids (IL) (*8*), and γ-valerolactone (GVL) (*9*, *10*)—use high temperatures and/or inexpensive mineral acids (such as H_2SO_4 and HCl) that facilitate the removal of lignin and hemicelluloses (*5*, *11*). A large-scale source of lignin could likely come from a process using these technologies (*4*). However, the

Downloaded from http://science.sciencemag.org/ on October 20, 2016

use of acid and/or high temperatures during lignin extraction leads to severe and irreversible condensation that dramatically affects its upgrading. Specifically, under the extraction conditions, lignin ether bonds are cleaved, and stable carbon-carbon (C–C) bonds are formed. The proposed mechanism involves the formation of highly reactive lignin side-chain (benzylic) carbocations that attack electron-rich lignin aromatic rings (Fig. 1A) (*12*, *13*).

The most prevalent lignin depolymerization strategy is the direct hydrogenolysis of native lignin in biomass. Such processes usually involve mixing a heterogeneous metal catalyst with solid untreated biomass in a batch reactor, cleaving ether bonds in near theoretical yields to produce ~45 to 55 mole % (mol %) of monomers, along with enzyme-digestible pulps (*14*–*17*). Issues such as catalyst recovery and mass transfer limitations have nevertheless restricted the large-scale implementation of this method. The hydrogenolysis of extracted lignin could avoid these drawbacks and be implemented in a continuous process. However, the use of extracted lignin has led to monomer yields of typically 5 to 20 mol %, which is 3 to 10 times lower than those obtained from direct hydrogenolysis of native lignin due to the lignin degradation and condensation experienced during extraction (Fig. 1A) (*18*, *19*). Oxidation of benzylic hydroxyl groups on cellulolytic enzyme lignin (CEL) (extracted from biomass by means of ball-milling and repeated enzymatic steps), followed by formic acid–catalyzed β-aryl ether cleavage, resulted in near theoretical yields of lignin monomers (50 mol %, ≈61 wt % because of added oxygen) (*20*). However, large-scale quantities of uncondensed CEL lignin are currently impossible to produce industrially. The use of GVL as a solvent for extracting lignin from corn (*Zea mays*) stover was shown to partially conserve lignin's β-ether bonds owing to its ability to solubilize lignin under mild conditions (*21*). Even this method led to yields below 70% of theoretical for corn stover and below 40% for maple (*Acer* spp.) wood, presumably because of lignin condensation reactions that occurred during its extraction (*21*).

Extracting a soluble and uncondensed lignin substrate during biomass pretreatment could facilitate the production of lignin monomers and be compatible with current biorefining strategies. The major challenge in developing such a process is to prevent interunit C–C coupling during extraction (Fig. 1A). Our strategy was to attempt to block the reactive benzylic positions with a protecting agent during pretreatment. We report here that using formaldehyde (FA) to stabilize lignin during extraction leads to near theoretical yields of lignin monomers after hydrogenolysis of the extracted product. These yields were three to seven times higher than those obtained when using the analogous method without FA (Fig. 1). Evidence suggests that FA actually hinders the formation of C–C linkages through two mechanisms. First, in an acidic, water-deficient environment, FA reacts to form a stable six-membered 1,3-dioxane (acetal) structure with the 1,3-diols (and their α- and γ-hydroxyl groups) on lignin side-chains (Fig. 1B), blocking the formation of benzylic cations. Second, the electron-rich positions at the positions ortho or para to methoxyl groups on the aromatic ring are the most reactive for electrophilic aromatic substitution by (protonated) FA to form hydroxymethyl groups, blocking these reactive positions.

For initial tests, we used a model lignin dimer (veratrylglycerol-β-guaiacyl ether, VG, **1**) (Fig. 2A), representing the predominant phenol-etherified β–O–4-linked (β-aryl ether) units with their characteristic and available α- and γ-hydroxyl groups (*22*). Without FA, **1** depolymerized to form **3** and **4** through **2**, as was consistent with a prior report (Fig. 2, A and C) (*12*). The low yield of **3** (40%) compared with **4** (95%) after 7 hours was likely due to condensation reactions similar to those observed with real lignin. In the presence of FA, **1** was rapidly converted to **5** and **6** (Fig. 2, B and D). Comparison of two-dimensional heteronuclear single-quantum coherence nuclear magnetic resonance (2D HSQC NMR) spectra of pure **1** and the derived products obtained in the presence of FA (Fig. 2, E and F) revealed the formation of the 1,3-dioxane structures [FA-derived C/H pairs in Fig. 2 are colored in red; two pairs of peaks are seen for all of the product's C/H correlations for the two (syn and anti, or threo and erythro) isomers], with chemical shift data matching those previously reported for **1** and the free-phenolic analogs of the acetals **5** (*23*).

After the acid treatment of **1**, as in a typical biomass fractionation process, a hydrogenolysis step was performed to produce monomers (*22*). Using the products from the reaction without FA, **3** was quantitatively converted to veratrylpropyl compounds **7** (Fig. 2A and fig. S1, B, C, and D), with the low overall yields (43%) confirming the loss of over half of the product **3** to condensation products before hydrogenolysis. In contrast, hydrogenolysis of the product mixture obtained in the presence of FA produced veratrylpropyl compounds **8** in 85% yield along with 87% for guaiacyl compounds **9** (Fig. 2B and fig. S1). This substantial increase in yield with FA addition (85 versus 43%) reflects the stabilizing effect that FA has on real lignin (Fig. 1).

We observed the hydroxymethylation of aromatic rings with FA via the additional ring methylation in several VG **1** reaction products (**8** and **9**) and when reacting several lignin monomers with FA followed by hydrogenolysis (fig. S2). Hydroxymethylation appears to act as a secondary lignin stabilization mechanism, as demonstrated with condensation studies using vanillyl alcohol, which can polymerize like lignin but cannot form a dioxane structure with FA (*22*).

We used beech (*Fagus grandifolia*) wood (particle size, <0.45 mm; moisture content, 5.7%) to test the effect of FA during the extraction of real lignin using similar reaction conditions (*22*). HSQC spectra from lignin extracted in the presence of FA (Fig. 3A, right) revealed the presence of the 1,3-dioxane structures analogous to those observed with model compounds (Fig. 2F). Without FA addition, no dioxane structure signals were observed, and signals characteristic of the native lignin side-chains were also absent (Fig. 3A, left). This disappearance was consistent with the results of previous studies of lignin condensation (*24*, *25*). In addition, the color of

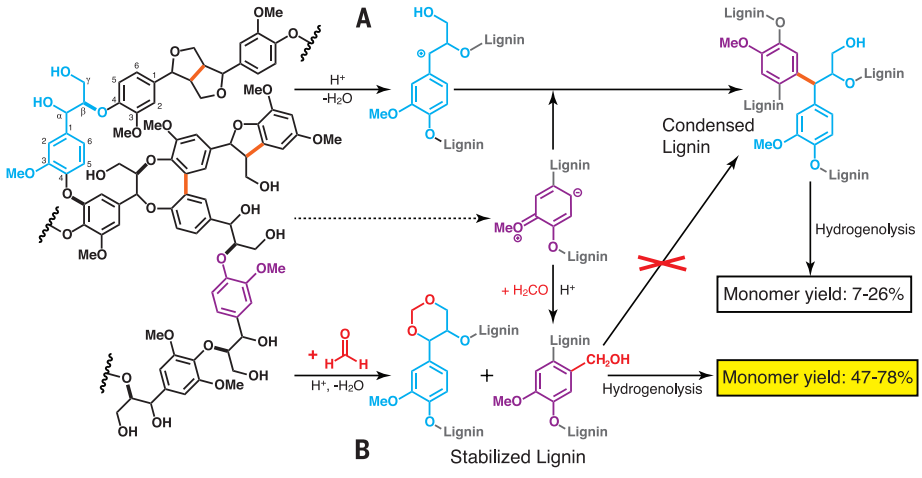

Fig. 1. Lignin monomer production by extraction followed by hydrogenolysis. (**A**) Lignin extraction, condensation, and hydrogenolysis in a standard acidic process. (**B**) Lignin extraction, stabilization with FA, and hydrogenolysis. Monomer yields, on a molar basis, are based on native Klason lignin. Bold bonds are those formed during the radical coupling reactions of lignification. The bonds highlighted in orange represent interunit C–C linkages.

[1]Laboratory of Sustainable and Catalytic Processing, Institute of Chemical Sciences and Engineering, École Polytechnique Fédérale de Lausanne (EPFL), CH-1015 Lausanne, Switzerland. [2]U.S. Department of Energy (DOE) Great Lakes Bioenergy Research Center, Wisconsin Energy Institute, University of Wisconsin, Madison, WI 53726, USA. [3]Department of Biological Systems Engineering, University of Wisconsin, Madison, WI 53706, USA. [4]Department of Biochemistry, University of Wisconsin, Madison, WI 53706, USA. [5]Department of Forestry and Natural Resources, Purdue University, West Lafayette, IN 47907, USA. [6]Department of Biochemistry, Purdue University, West Lafayette, IN 47907, USA.
***Corresponding author. Email: jeremy.luterbacher@epfl.ch**

Downloaded from http://science.sciencemag.org/ on October 21, 2016

the lignin obtained in the presence of FA was substantially lighter than that obtained in its absence, serving as a qualitative indicator of reduced condensation (fig. S3). We also tested the effect of FA in a similar manner using an extremely high-S poplar, to be described below. In this case, all of the features of the 1,3-dioxane-derivatized and purified lignin, along with some hydroxymethylation of the ring, could be readily discerned and assigned with the aid of model compounds run under the same conditions (Fig. 3B).

Lignin monomer identification and quantification are described extensively in the supplementary materials (*22*). Five major lignin monomers were identified in the products without FA addition, or from the direct hydrogenolysis of native lignin (Fig. 3, C and D, and fig. S4), that were all consistent with previous reports (*16*). With FA addition, five additional methylated monomers were identified (Fig. 3, C and D, and figs. S4 and S5) (*22*). The addition of FA did not substantially affect lignin removal, but final monomer yields after hydrogenolysis of the extracted lignin were remarkably elevated (Fig. 3B). Without FA addition, hydrogenolysis of the extracted lignin resulted in a monomer yield of 7%, which is consistent with previous studies (*26*). With FA addition, the highest yield was 47% after hydrogenolysis of the extraction liquor (Fig. 3B). We attribute the increased monomer yield obtained with FA primarily to the same stabilization mechanism observed with the model lignin dimer (Figs. 1 and 2). This yield (47%) was comparable with the yield of 48% obtained through direct hydrogenolysis of the

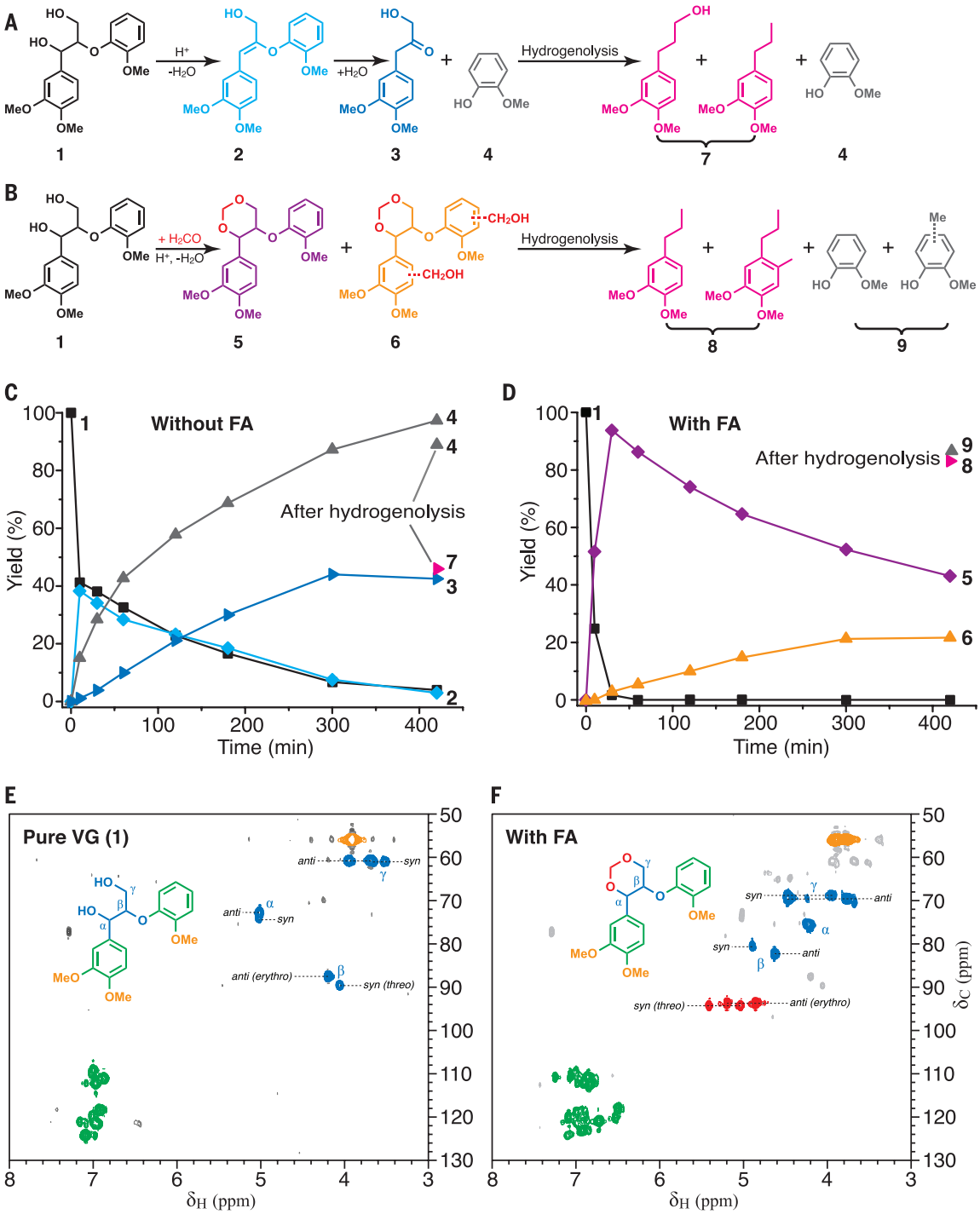

Fig. 2. Acid-catalyzed depolymerization of veratrylglycerol-β-guaiacyl ether 1. (**A**) Without FA. (**B**) With FA. (**C**) Time course of reaction (A). (**D**) Time course of reaction (B). (**E**) 2D HSQC NMR spectrum of pure VG **1**. (**F**) 2D HSQC NMR spectrum of the product mixture resulting from reaction (B) after 30 min. δ_H, proton NMR chemical shift (in parts per million); ΔC, carbon NMR chemical shift (in parts per million).

Downloaded from http://science.sciencemag.org/ on October 21, 2016

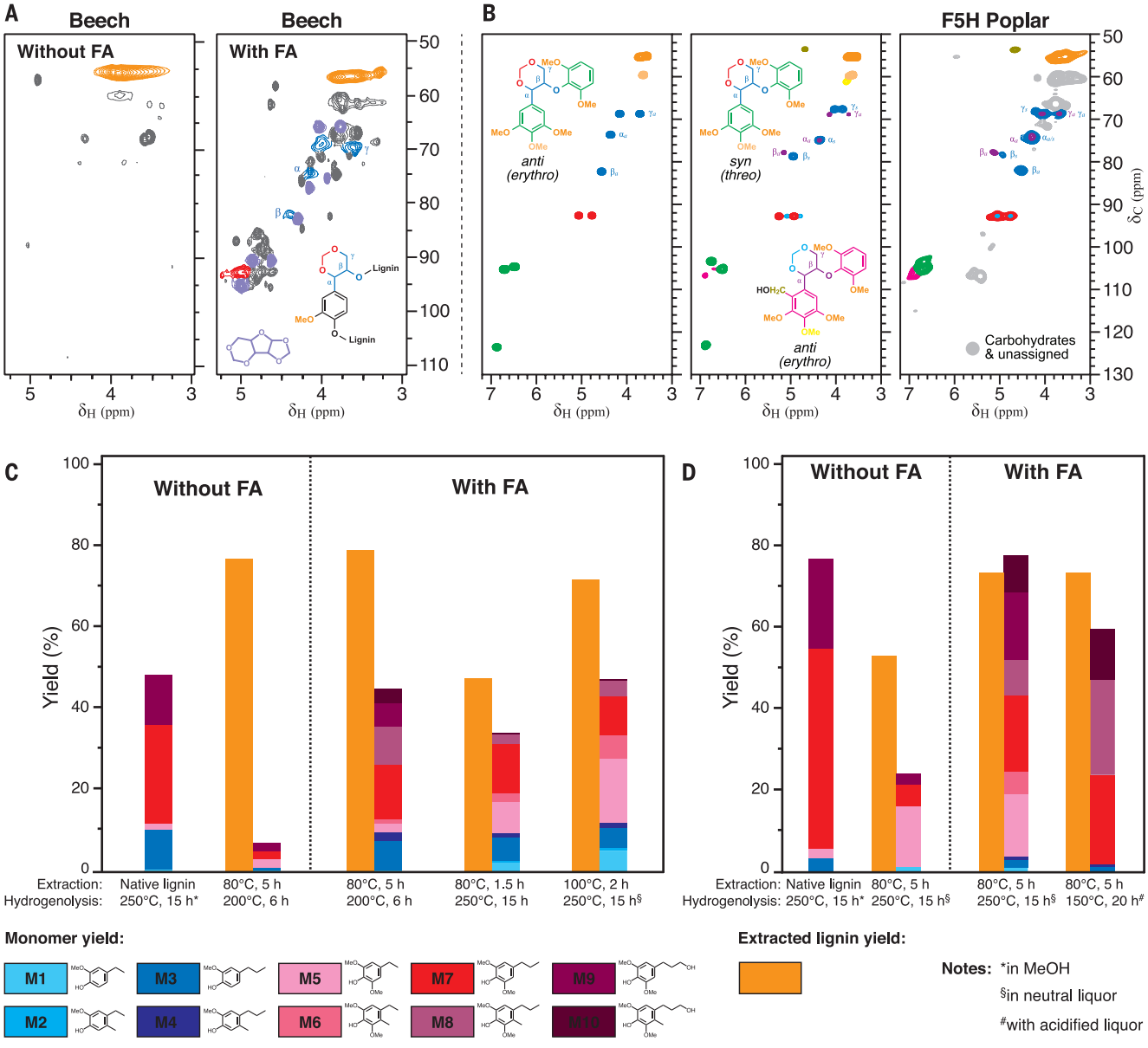

Fig. 3. Production of lignin monomers from lignocellulosic biomass. (**A**) 2D HSQC NMR spectra of lignin extracted from beech wood in the absence and presence of FA. Signals attributed to diformyl-xylose (fig. S6) are highlighted in light purple. (**B**) The same extraction by using high-syringyl F5H-poplar (after a precipitative purification of the lignin, right), and assignments from authentic syringyl model compounds for the produced dioxanes. (**C**) Lignin monomer yields from beech wood (table S1, entries 1 to 5). (**D**) Lignin monomer yields from high-syringyl F5H-poplar (table S1, entries 14, 15, 16, and 22).

wood (*14*, *16*) and with the yields obtained by using established lignin monomer analysis methods, including derivatization followed by reductive cleavage (DFRC) (*27*) and nitrobenzene oxidation (NBO) (fig. S7) (*28*).

We applied this method to softwood (spruce, *Picea abies*) (particle size, <1.5 mm; moisture content, 6.6%) and obtained a yield of 21%—the same yield obtained with direct hydrogenolysis (table S1). These relatively low monomer yields are consistent with previous reports using softwoods (*15*, *16*) and likely are due in part to the higher native levels of interunit C–C linkages in softwoods as compared with hardwoods.

Our strategy for improving lignin monomer yields is to hinder the formation of C–C linkages during lignin extraction. Thwarting the production of such linkages by altering the native lignin could further increase yields (*3*, *29*). Overexpression of the *ferulate 5-hydroxylase* gene in poplar (*Populus* spp., F5H-poplar) (particle size, <1 mm; moisture content, 6.7%) yields lignin that has a high content of syringyl units (98.3%) and reduced native interunit C–C linkages (88.8% β–O–4 linkages, 4.2% β–1 linkages, and 7.1% β–β linkages) (fig. S8). Because of the high-S nature of this lignin, there was a simpler array of major products, and using FA stabilization, we obtained lignin monomer yields of up to 78% after hydrogenolysis of the extracted substrate (Fig. 3D). This yield was comparable with that obtained through direct hydrogenolysis of F5H-poplar (77%). In contrast, a monomer yield of only 24.5% was obtained from its native wood lignin without FA addition. Furthermore, monomer selectivities from the isolated soluble F5H-poplar lignin were quantitative, which was confirmed with gel permeation chromatography of the lignin before and after hydrogenolysis. After hydrogenolysis, the broad lignin oligomer peak (molecular weight ≈ 2900 g/mol) had disappeared, and essentially only a single monomer peak remained (fig. S9).

Downloaded from http://science.sciencemag.org/ on October 21, 2016

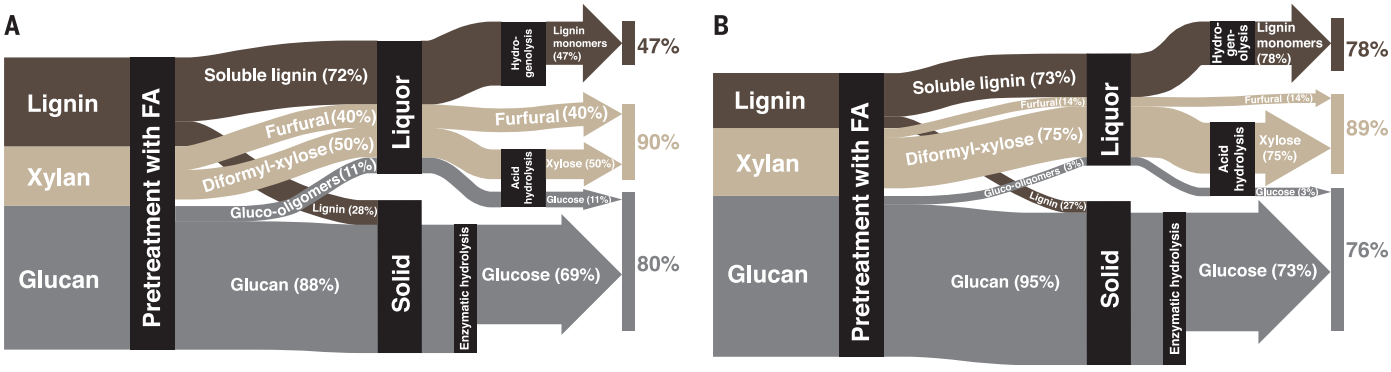

Fig. 4. Mass balance of polysaccharide (glucan and xylan) and lignin fractions of biomass. (**A**) Beech wood (table S1, entry 3). (**B**) F5H-poplar wood (table S1, entry 16). The corresponding reaction conditions are summarized in table S3.

These advantages illustrate the potential benefits of optimizing lignin biosynthesis for improved lignin valorization.

Selectively hydrogenating only the extracted upgradeable lignin, as opposed to recalcitrant lignin and other biomass derivatives, could facilitate continuous processing and increase the selective use of H_2 by avoiding the hydrogenation of recalcitrant lignin or other biomass fractions. FA-extracted lignin can also be converted to monomers at 150°C (instead of 250°C) if acid is present to break the 1,3-dioxane ring structure (Fig. 3C); direct hydrogenolysis of F5H-poplar at 150°C under neutral conditions leads to negligible monomer production. Under acidic conditions, direct hydrogenolysis leads to lower yields (48 versus 60%) than with FA extraction (table S1) and to substantial loss of the polysaccharide fraction of biomass (table S2). The comparison demonstrates the advantages of using FA-extracted lignin to generate monomers separately from the polysaccharides at low hydrogenolysis temperatures.

In contrast to direct biomass hydrogenolysis, extracting a soluble stabilized lignin fraction before its hydrogenolysis is compatible with most polysaccharide depolymerization approaches. With FA present, 40% of xylan was dehydrated into furfural, and 50% reacted with FA to form diformyl-xylose (structure given in Fig. 3A and fig. S6), which could be converted back to xylose under aqueous acidic conditions (Fig. 4 and supplementary materials, section S2.3) (*22*). High yields of glucose (80%) were obtained after enzymatic hydrolysis of the leftover solids, which required further treatment in an aqueous dilute acid solution (1 wt % H_2SO_4) to remove grafted FA on the surface of substrates (supplementary materials, section S2.3) (*22*). Therefore, the treatment of beech wood under acidic conditions in the presence of FA leads to overall yields of 47% lignin monomers (theoretical yield for its β-ether content), 80% glucose, 40% furfural, and 50% xylose (90% overall yield from xylan) (Fig. 4A). With F5H-poplar, yields of 78% lignin monomers, 76% glucose, 14% furfural, and 75% xylose (89% overall yield from xylan) were obtained.

These results suggest that lignin upgrading could be easily integrated into current biorefinery schemes, especially considering that FA is a relatively inexpensive bulk chemical that can be produced from biomass-derived syngas or methanol, either sourced biologically or from lignin methoxyl groups (*14*). Furthermore, we estimated that FA consumed for stabilizing lignin represented ~1.9 wt % of the original biomass, with the remaining FA being recoverable (supplementary materials, section S2.4) (*22*). Studies with ^{13}C-labeled FA demonstrated that FA consumed by lignin ended up either as methyl groups on the lignin aromatic rings or as methane after hydrogenolysis (supplementary materials, section S2.4) (*22*). Although processes exist for converting methane back to FA, we estimated that the cost of replacing FA would be 9% of the cost of monomers (supplementary materials, section S2.4) (*22*).

REFERENCES AND NOTES

1. J. Zakzeski, P. C. A. Bruijnincx, A. L. Jongerius, B. M. Weckhuysen, *Chem. Rev.* **110**, 3552–3599 (2010).
2. J. Ralph *et al.*, *Phytochem. Rev.* **3**, 29–60 (2004).
3. R. Rinaldi *et al.*, *Angew. Chem. Int. Ed. Engl.* **55**, 8164–8215 (2016).
4. A. J. Ragauskas *et al.*, *Science* **344**, 1246843 (2014).
5. J. S. Luterbacher, D. M. Alonso, J. A. Dumesic, *Green Chem.* **16**, 4816–4838 (2014).
6. X. Pan *et al.*, *Biotechnol. Bioeng.* **90**, 473–481 (2005).
7. T. Y. Nguyen, C. M. Cai, R. Kumar, C. E. Wyman, *ChemSusChem* **8**, 1716–1725 (2015).
8. H. Tadesse, R. Luque, *Energy Environ. Sci.* **4**, 3913–3929 (2011).
9. L. Shuai, Y. M. Questell-Santiago, J. S. Luterbacher, *Green Chem.* **18**, 937–943 (2016).
10. J. S. Luterbacher *et al.*, *Science* **343**, 277–280 (2014).
11. L. Shuai, J. Luterbacher, *ChemSusChem* **9**, 133–155 (2016).
12. M. R. Sturgeon *et al.*, *ACS Sustain. Chem. Eng.* **2**, 472–485 (2014).
13. K. Shimada, S. Hosoya, T. Ikeda, *J. Wood Chem. Technol.* **17**, 57–72 (1997).
14. N. Yan *et al.*, *ChemSusChem* **1**, 626–629 (2008).
15. T. Parsell *et al.*, *Green Chem.* **17**, 1492–1499 (2015).
16. S. Van den Bosch *et al.*, *Energy Environ. Sci.* **8**, 1748–1763 (2015).
17. J. M. Pepper, Y. W. Lee, *Can. J. Chem.* **47**, 723–727 (1969).
18. V. M. Roberts *et al.*, *Chemistry* **17**, 5939–5948 (2011).
19. C. Xu, R. A. D. Arancon, J. Labidi, R. Luque, *Chem. Soc. Rev.* **43**, 7485–7500 (2014).
20. A. Rahimi, A. Ulbrich, J. J. Coon, S. S. Stahl, *Nature* **515**, 249–252 (2014).
21. J. S. Luterbacher *et al.*, *Energy Environ. Sci.* **8**, 2657–2663 (2015).
22. Materials and methods are available as supplementary materials on *Science* Online.
23. S. Ralph, J. Ralph, L. Landucci, NMR database of lignin and cell wall model compounds (2009); www.glbrc.org/databases_and_software/nmrdatabase.
24. L. Shuai *et al.*, *Bioresour. Technol.* **101**, 3106–3114 (2010).
25. H. L. Trajano *et al.*, *Biotechnol. Biofuels* **6**, 110 (2013).
26. H. Wang, M. Tucker, Y. Ji, *J. Appl. Chem.* **2013**, 1–9 (2013).
27. S. D. Karlen *et al.*, *Sci. Adv.* 10.1126/sciadv.1600393 (2016).
28. Y. Li, T. Akiyama, T. Yokoyama, Y. Matsumoto, *Biomacromolecules* **17**, 1921–1929 (2016).
29. J. J. Stewart, T. Akiyama, C. Chapple, J. Ralph, S. D. Mansfield, *Plant Physiol.* **150**, 621–635 (2009).

ACKNOWLEDGMENTS

This work was supported by the Swiss Competence Center for Energy Research: Biomass for a Swiss Energy Future through the Swiss Commission for Technology and Innovation grant KTI.2014.0116; by the Swiss National Science Foundation through grant PYAPP2_154281; and by EPFL. J.R., Y.L., and H.K. were funded by the DOE Great Lakes Bioenergy Research Center (DOE BER Office of Science DE-FC02-07ER64494). R.M. and C.C. were funded by the Center for Direct Catalytic Conversion of Biomass to Biofuels (C3Bio), an Energy Frontier Research Center funded by the DOE Office of Science, Office of Basic Energy Sciences, award DE-SC0000997. We thank M. Studer for providing us with beech and spruce wood. All data are provided in the supplementary materials. J.S.L. and L.S. are inventors on European patent application EP 16 165 180.7 submitted by EPFL, which covers methods for producing lignin monomers from biomass during biomass depolymerisation. C.C. is an inventor on U.S. patent 6610908 held by the Purdue Research Foundation, which covers manipulation of lignin composition in plants by using a tissue-specific promoter.

SUPPLEMENTARY MATERIALS

www.sciencemag.org/content/354/6310/329/suppl/DC1
Materials and Methods
Supplementary Text
Figs. S1 to S22
Tables S1 to S11
References (*30*–*45*)

8 May 2016; accepted 14 September 2016
10.1126/science.aaf7810

Downloaded from http://science.sciencemag.org/ on October 21, 2016

PALEONTOLOGY

A Silurian maxillate placoderm illuminates jaw evolution

Min Zhu,[1,2]* Per E. Ahlberg,[3]* Zhaohui Pan,[1,2] Youan Zhu,[3] Tuo Qiao,[1] Wenjin Zhao,[1] Liantao Jia,[1] Jing Lu[1]

The discovery of *Entelognathus* revealed the presence of maxilla, premaxilla, and dentary, supposedly diagnostic osteichthyan bones, in a Silurian placoderm. However, the relationship between these marginal jaw bones and the gnathal plates of conventional placoderms, thought to represent the inner dental arcade, remains uncertain. Here we report a second Silurian maxillate placoderm, which bridges the gnathal and maxillate conditions. We propose that the maxilla, premaxilla, and dentary are homologous to the gnathal plates of placoderms and that all belong to the same dental arcade. The gnathal-maxillate transformation occurred concurrently in upper and lower jaws, predating the addition of infradentary bones to the lower jaw.

Macromeric dermal skeletons incorporating jaw bones are found in the clade Osteichthyes (bony fishes and tetrapods) and the paraphyletic group Placodermi (jawed stem gnathostomes). Osteichthyans have a maxilla, premaxilla, and dentary, all with facial laminae, whereas placoderms have supposedly nonhomologous gnathal plates that lack facial laminae. *Entelognathus* from the Late Silurian (Ludlow) Xiaoxiang vertebrate fauna (*1*, *2*) of Yunnan, China, revealed the presence of maxilla, premaxilla, dentary, and infradentaries (*3*–*7*) in a vertebrate with a dermal skeleton otherwise typical of placoderms (*2*, *8*). Phylogenetic analyses place *Entelognathus* near the top of the gnathostome stem group, but it is uncertain whether the apparent homology of the jaw bones in *Entelognathus* and osteichthyans is supported by phylogenetic congruence (*2*, *8*–*11*). Here we describe a second maxillate placoderm from the Xiaoxiang fauna (Figs. 1 and 2; figs. S1 to S7; and fig. S8, A and B), which illuminates the evolution of the dermal jaw (*12*–*15*), resolves the phylogenetic uncertainty around *Entelognathus*, and provides a comparative context for the bizarre facial morphology of the latter genus.

The holotype of *Qilinyu rostrata* (gen. et sp. nov.) (*16*) (Fig. 1 and figs. S2 to S4) represents a three-dimensionally preserved fish. It is 126 mm in length as preserved, with an estimated total body length of more than 20 cm. In general terms, *Qilinyu* combines arthrodire-like and antiarch-like characteristics (*17*–*24*).

The most conspicuous feature of *Qilinyu* is its moderately developed rostrum in front of the domed cranial vault, which is suggestive of a dolphin-like head profile. Apart from this rostrum and the presence of two pairs of postorbital plates and paired central plates, the skull roof is similar to that of *Entelognathus* (*2*). The mouth and nostrils are located on the flattened ventral surface of the head. The eyes of *Qilinyu* are small and laterally positioned. Unlike in *Entelognathus*, the sclerotic ring is not fused with the skull roof and dermal cheek.

The maxilla and premaxilla (Figs. 1 and 2A and figs. S1 to S5) bear both facial and palatal laminae, as in *Entelognathus* (*2*). There are no dermal bones internal to them in the oral cavity. Immediately behind the upper jaw in the holotype, the perichondrally ossified Meckelian cartilage (Fig. 1, B and D and figs. S2B and S4A) is preserved in articulation with the mouth closed. No dermal lower jaw bones are preserved in the holotype. However, in specimen V20733.1 (Fig. 2A and figs. S5, D and E, and S6G), an L-shaped dentary bone in internal aspect is preserved, slightly displaced. A further four dentaries preserved in external aspect (Fig. 2, B and C, and fig. S6, C to F) show a tuberculate area with three divisions (palatal lamina, facial lamina, and a depressed posterior division bearing smaller tubercles) and a posterolateral unornamented process. Left and right dentaries do not meet in the midline; a "step" in the anterior margin of the Meckelian cartilage marks the position of the mesial extremity of the dentary. Infradentaries are absent.

The dermal cheek, opercular region, and trunk armor show a combination of characteristics shared with *Entelognathus* (for example, the presence of a jugal) (*2*) and antiarchs (the absence of an opercular cartilage) (*22*, *25*), as well as distinct features (three median dorsal plates) (Fig. 1, A and C and figs. S1; S2; S5, D and E; and S6B). For a full description, see the supplementary text. The long trunk armor and flattened ventral surface create a somewhat antiarch-like appearance.

Qilinyu provides the first detailed evidence of paired appendages in maxillate placoderms. The pectoral fin is covered by minute scales resembling the trunk scales of some early antiarchs (*26*). The anterolateral margin of the scale cover appears to be the true leading edge of the

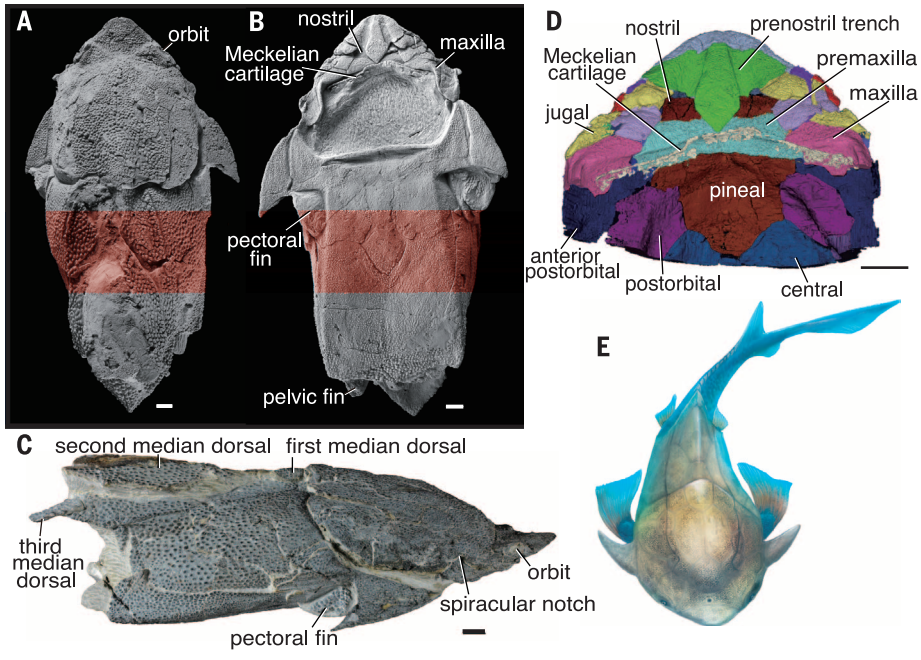

Fig. 1. *Qilinyu rostrata* (gen. et sp. nov.), a 423-million-year-old fish from the Kuanti Formation (late Ludlow, Silurian) of Qujing, Yunnan. (**A** to **C**) Holotype V20732, a three-dimensionally preserved specimen with skull and trunk armor, shown in dorsal (A), ventral (B), and lateral (C) views. (**D**) Skull in ventral view, as revealed by the computed microtomography restoration of the holotype. (**E**) Life restoration. Scale bars, 5 mm.

[1]Key Laboratory of Vertebrate Evolution and Human Origins of Chinese Academy of Sciences, Institute of Vertebrate Paleontology and Paleoanthropology, Chinese Academy of Sciences, PO Box 643, Beijing 100044, China. [2]College of Earth Science, University of Chinese Academy of Sciences, Beijing, 100049, China. [3]Subdepartment of Evolution and Development, Department of Organismal Biology, Uppsala University, Norbyvägen 18A, SE-752 36 Uppsala, Sweden.
*Corresponding authors. E-mail: zhumin@ivpp.ac.cn (M.Z.); per.ahlberg@ebc.uu.se (P.E.A.)

Downloaded from http://science.sciencemag.org/ on October 20, 2016

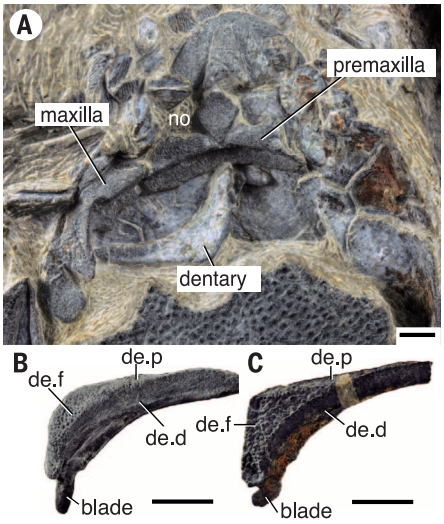

Fig. 2. Dentary specimens of *Qilinyu rostrata* (gen. et sp. nov). (**A**) Part of an articulated specimen (V20733.2) in ventral view, showing the slightly displaced dentary. (**B** and **C**) Ventral view of dentaries of specimens V20735.2 (B) and V20735.1 (C). de.d, depressed area of dentary; de.f, facial lamina of dentary; de.p, palatal lamina of dentary; no, nostril. Scale bars, 10 mm.

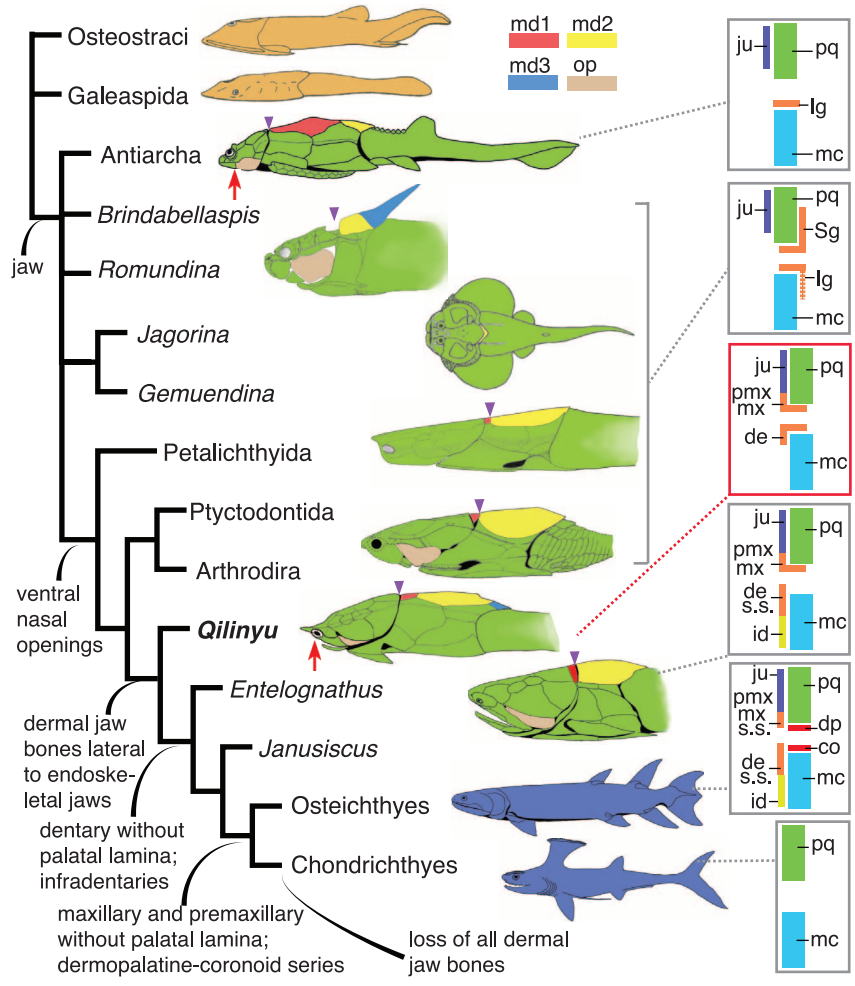

Fig. 3. Summary phylogeny showing the transformation of the dermal jaw bones from a gnathal to a maxillate condition. This phylogeny is simplified from the strict consensus tree of the 1248 most parsimonious trees (fig. S10). co, coronoid series; de, dentary; dp, dermopalatine series; id, infradentary; lg, infragnathal; ju, jugal; mc, Meckelian cartilage; md1 to md3, first to third median dorsal plate; mx, maxilla; op, opercular; pmx, premaxilla; pq, palatoquadrate; Sg, supragnathal; s.s., sensu stricto. Brown body color, jawless stem gnathostome (ostracoderm); green body color, jawed stem gnathostome (placoderm); blue body color, crown gnathostome. Red arrows, mouth position; purple arrowheads, division between head and trunk armor.

fin, but considering the hydrodynamic balance of the fish, we assume that the fin must have had a broad posterodistal brim without scale cover (Fig. 1E and fig. S1). The pelvic fin (Fig. 1B and fig. S2B) is also covered by minute scales and located immediately behind the ventral wall of the trunk armor. A large plate medial to the pelvic fin is interpreted as the dermal pelvic plate (fig. S2B).

Maximum parsimony and Bayesian inference analyses, using a data set with 372 characters and 104 taxa, place *Qilinyu* consistently as the sister group of *Entelognathus*, *Janusiscus*, and crown gnathostomes (Fig. 3, figs. S9 to S11, and data S1 and S2). According to the Bayesian analysis (fig. S11), the antiarchs, with which *Qilinyu* shares many similarities, are positioned at the base of jawed vertebrates, successively followed by *Brindabellaspis* (*27*), *Romundina* (*9*), and the *Jagorina-Gemuendina* clade (*18*), all of which bear dorsal nasal openings positioned near the eyes. However, this phylogenetic resolution at the base of jawed vertebrates is lost in the maximum parsimony analysis (figs. S9 and S10).

Qilinyu expands our understanding of maxillate placoderms, previously represented only by *Entelognathus* (*2*). *Qilinyu* has a different body shape, with a ventrally positioned mouth and nostrils that are suggestive of a benthic feeder. The immobile eyes of *Entelognathus* are absent in *Qilinyu*, which has small and apparently mobile eyes of conventional placoderm type. Most importantly, the character combination of *Qilinyu* and its phylogenetic position as the most basal maxillate vertebrate illuminate the relationship between the marginal jaw bones of osteichthyans and the gnathal plates of placoderms (*17*–*19*, *22*).

Entelognathus and *Qilinyu* have maxillae and premaxillae that carry broad palatal laminae. This contrasts with the crown-group osteichthyan condition, where these bones essentially lack palatal laminae (*6*, *19*). The dentary of *Entelognathus* has only a narrow biting edge, whereas that of *Qilinyu* has a narrow palatal lamina. Again, the crown osteichthyan condition is a biting edge. We infer that the maxilla, premaxilla, and dentary all originally had laminae that extended into the oral cavity and were lost prior to the osteichthyan crown group node.

Neither *Entelognathus* nor *Qilinyu* has any dermal jaw bones internal to the marginal arcade. Both holotypes have the mouth wholly or partly closed, showing that this is a genuine absence and not a taphonomic loss. Placoderms typically carry one dermal bone on the Meckelian cartilage (infragnathal), one on the palatoquadrate (posterior supragnathal), and one on the ethmoid (anterior supragnathal) (*17*–*24*, *28*). These bones lack facial laminae and have been homologized with the inner dental arcade (coronoids, ectopterygoids, dermopalatines, and vomers) of osteichthyans (*2*, *17*, *18*, *22*). However, in number and anteroposterior position relative to the mandibular arch, they actually resemble the dentary, maxilla, and premaxilla; the osteichthyan inner arcade always contains a greater number of bones. In *Entelognathus* and *Qilinyu*, the inner arcade is absent and the marginal bones carry oral laminae that—especially in the upper jaw—correspond precisely in position to the gnathal plates of placoderms. The only major difference is that the marginal jaw bones of *Entelognathus* and *Qilinyu* have facial laminae, whereas placoderm gnathal plates do not.

We are thus faced with two alternative homology hypotheses. The traditional identification of the placoderm gnathals with the inner

Downloaded from http://science.sciencemag.org/ on October 20, 2016

dental arcade (*2*, *17*, *18*, *22*) implies that the three gnathals were lost at the internode between arthrodires and *Qilinyu* and replaced with three new bones that occupied essentially the same positions but were slightly more external. Alternatively, if the gnathals are identified with the outer dental arcade, these bones remained in place and acquired facial laminae. Given the overall pattern stability of the dermal skeleton, the second hypothesis seems more probable. It also does not require the inner dental arcade to be acquired in placoderms, lost in *Qilinyu* and *Entelognathus*, and then reevolved in osteichthyans. In any case, the boundary between inner and outer arcades is not completely rigid: For example, in the early tetrapod *Discosauriscus*, the posterior coronoid (a bone of the inner arcade) contributes to the external face of the lower jaw (*29*).

Under our new hypothesis, the dermal jaw bones form part of the overall pattern conservation of the dermal skeleton from placoderms to osteichthyans (*2*, *4*). In their earliest form, the gnathal plates seen, for example, in antiarchs and arthrodires were entirely oral and lacked facial laminae. Facial laminae were acquired at the internode below *Qilinyu*. Between *Qilinyu* and *Entelognathus*, the dentary lost its oral lamina, and the lower jaw acquired an external covering of infradentary bones. Between *Entelognathus* and crown osteichthyans, the maxilla and premaxilla lost their palatal (i.e., oral) laminae, and a new inner arcade of coronoids, ectopterygoids, dermopalatines, and vomers evolved.

This picture of gradual transformation underscores the emerging view of osteichthyans as the more conservative clade of crown gnathostomes (*2*, *9*–*11*, *30*), contrasting with the historically dominant perception of chondrichthyans as primitive and informative about ancestral gnathostome conditions (*17*, *18*). We predict that future discoveries from the Xiaoxiang fauna will continue to fuel the debate about jawed vertebrate origins and challenge long-held beliefs about their evolution.

REFERENCES AND NOTES

1. M. Zhu *et al.*, *Nature* **458**, 469–474 (2009).
2. M. Zhu *et al.*, *Nature* **502**, 188–193 (2013).
3. P. L. Forey, *Proc. R. Soc. London Ser. B* **208**, 369–384 (1980).
4. J. G. Maisey, *Cladistics* **2**, 201–256 (1986).
5. H.-P. Schultze, in *The Skull*, vol. 2, J. Janke, B. K. Hall, Eds. (Univ. of Chicago Press, 1993), pp. 189–254.
6. H. Botella, H. Blom, M. Dorka, P. E. Ahlberg, P. Janvier, *Nature* **448**, 583–586 (2007).
7. M. Friedman, M. D. Brazeau, *J. Vertebr. Paleontol.* **30**, 36–56 (2010).
8. M. D. Brazeau, M. Friedman, *Nature* **520**, 490–497 (2015).
9. V. Dupret, S. Sanchez, D. Goujet, P. Tafforeau, P. E. Ahlberg, *Nature* **507**, 500–503 (2014).
10. J. A. Long *et al.*, *Nature* **517**, 196–199 (2015).
11. S. Giles, M. Friedman, M. D. Brazeau, *Nature* **520**, 82–85 (2015).
12. P. E. Ahlberg, J. A. Clack, *Trans. R. Soc. Edinb. Earth Sci.* **89**, 11–46 (1998).
13. G. H. Sperber, *Craniofacial Development* (B.C. Decker, 2001).
14. C. A. Sidor, *Paleobiology* **29**, 605–640 (2003).
15. S. H. Lee, O. Bédard, M. Buchtová, K. Fu, J. M. Richman, *Dev. Biol.* **276**, 207–224 (2004).
16. Materials and methods and supplementary text are available as supplementary materials on *Science* Online.
17. E. A. Stensiö, *Kungl.Svenska Vetenskap. Hand.* **9**, 1–419 (1963).
18. E. A. Stensiö, in *Traité de Paléontologie*, J. Piveteau, Ed. (Masson, 1969), vol. 4(2), pp. 71–692.
19. E. Jarvik, *Basic Structure and Evolution of Vertebrates*, vol. 1 (Academic Press, 1980).
20. D. F. Goujet, *Proc. Linn. Soc. N. S. W.* **107**, 211–243 (1984).
21. B. G. Gardiner, *J. Vertebr. Paleontol.* **4**, 379–395 (1984).
22. G. C. Young, *Zool. J. Linn. Soc.* **88**, 1–57 (1986).
23. P. Janvier, *Early Vertebrates* (Clarendon Press, 1996).
24. G. C. Young, *Annu. Rev. Earth Planet. Sci.* **38**, 523–550 (2010).
25. G. C. Young, *Palaeontology* **27**, 635–661 (1984).
26. M. Zhu, X. Yu, B. Choo, J. Wang, L. Jia, *Biol. Lett.* **8**, 453–456 (2012).
27. G. C. Young, *Palaeontogr. Abt. A* **167**, 10–76 (1980).
28. M. Rücklin *et al.*, *Nature* **491**, 748–751 (2012).
29. J. Klembara, *Philos. Trans. R. Soc. Lond. B Biol. Sci.* **352**, 257–302 (1997).
30. A. Pradel, J. G. Maisey, P. Tafforeau, R. H. Mapes, J. Mallatt, *Nature* **509**, 608–611 (2014).

ACKNOWLEDGMENTS

We thank X. Lu, J. Zhang, C.-H. Xiong, C.-Y. Xiong, J. Xiong, Q. Deng, and Q. Wen for specimen preparation and field work; Y.-M. Hou and X. Huang for computed tomography scanning and rendering; and D. Yang and Q. Zeng for artwork. This work was supported by Major Basic Research Projects of China (grant 2012CB821902), the National Natural Science Foundation of China (grant 41530102), the National Major Scientific Instrument and Equipment Development Project of China (grant 2011YQ03012), and the Chinese Academy of Sciences (grant QYZDJ-SSW-DQC002; Funds for Paleontology Fieldwork and Fossil Preparation). P.E.A. and Y.Z. were supported by Swedish Research Council grant 2014-4102 and a Wallenberg Scholarship from the Knut and Alice Wallenberg Foundation, both awarded to P.E.A. The phylogenetic data used in the paper, as well as information about the specimen provenance and repository, are archived in the supplementary materials.

SUPPLEMENTARY MATERIALS

www.sciencemag.org/content/354/6310/334/suppl/DC1
Materials and Methods
Supplementary Text
Figs. S1 to S12
Table S1
References (*31*–*227*)
Data S1 and S2

16 June 2016; accepted 31 August 2016
10.1126/science.aah3764

EVOLUTION

Predictable convergence in hemoglobin function has unpredictable molecular underpinnings

Chandrasekhar Natarajan,[1] Federico G. Hoffmann,[2] Roy E. Weber,[3] Angela Fago,[3] Christopher C. Witt,[4] Jay F. Storz[1]*

To investigate the predictability of genetic adaptation, we examined the molecular basis of convergence in hemoglobin function in comparisons involving 56 avian taxa that have contrasting altitudinal range limits. Convergent increases in hemoglobin-oxygen affinity were pervasive among high-altitude taxa, but few such changes were attributable to parallel amino acid substitutions at key residues. Thus, predictable changes in biochemical phenotype do not have a predictable molecular basis. Experiments involving resurrected ancestral proteins revealed that historical substitutions have context-dependent effects, indicating that possible adaptive solutions are contingent on prior history. Mutations that produce an adaptive change in one species may represent precluded possibilities in other species because of differences in genetic background.

A fundamental question in evolutionary genetics concerns the extent to which adaptive convergence in phenotype is caused by convergent or parallel changes at the molecular sequence level. This question has important implications for understanding the inherent repeatability (and, hence, predictability) of molecular adaptation. One especially powerful approach for addressing this question involves the examination of phylogenetically replicated changes in protein function that can be traced to specific amino acid replacements. If adaptive changes in protein function can only be produced by a small number of possible mutations at a small number of key sites—representing "forced moves" in genotype space—then evolutionary outcomes may be highly predictable. Alternatively, if adaptive changes can be produced by numerous possible mutations—involving different structural or functional mechanisms, but achieving equally serviceable results—then evolutionary outcomes may be more idiosyncratic and unpredictable (*1*–*4*). The probability of replicated substitution at the same site in different species may be further reduced by context-dependent mutational effects (epistasis), because a given mutation will only contribute to adaptive convergence if it retains a beneficial effect across divergent genetic backgrounds (*4*).

To assess the pervasiveness of parallel molecular evolution and to investigate its causes, we examined replicated changes in the oxygenation properties of hemoglobin (Hb) in multiple bird

[1]School of Biological Sciences, University of Nebraska, Lincoln, NE 68588, USA. [2]Department of Biochemistry, Molecular Biology, Entomology, and Plant Pathology and Institute for Genomics, Biocomputing, and Biotechnology, Mississippi State University, Mississippi State, MS 39762, USA. [3]Zoophysiology, Department of Bioscience, Aarhus University, DK-8000 Aarhus, Denmark. [4]Department of Biology and Museum of Southwestern Biology, University of New Mexico, Albuquerque, NM 87131, USA.
***Corresponding author. E-mail: jstorz2@unl.edu**

Downloaded from http://science.sciencemag.org/ on October 20, 2016

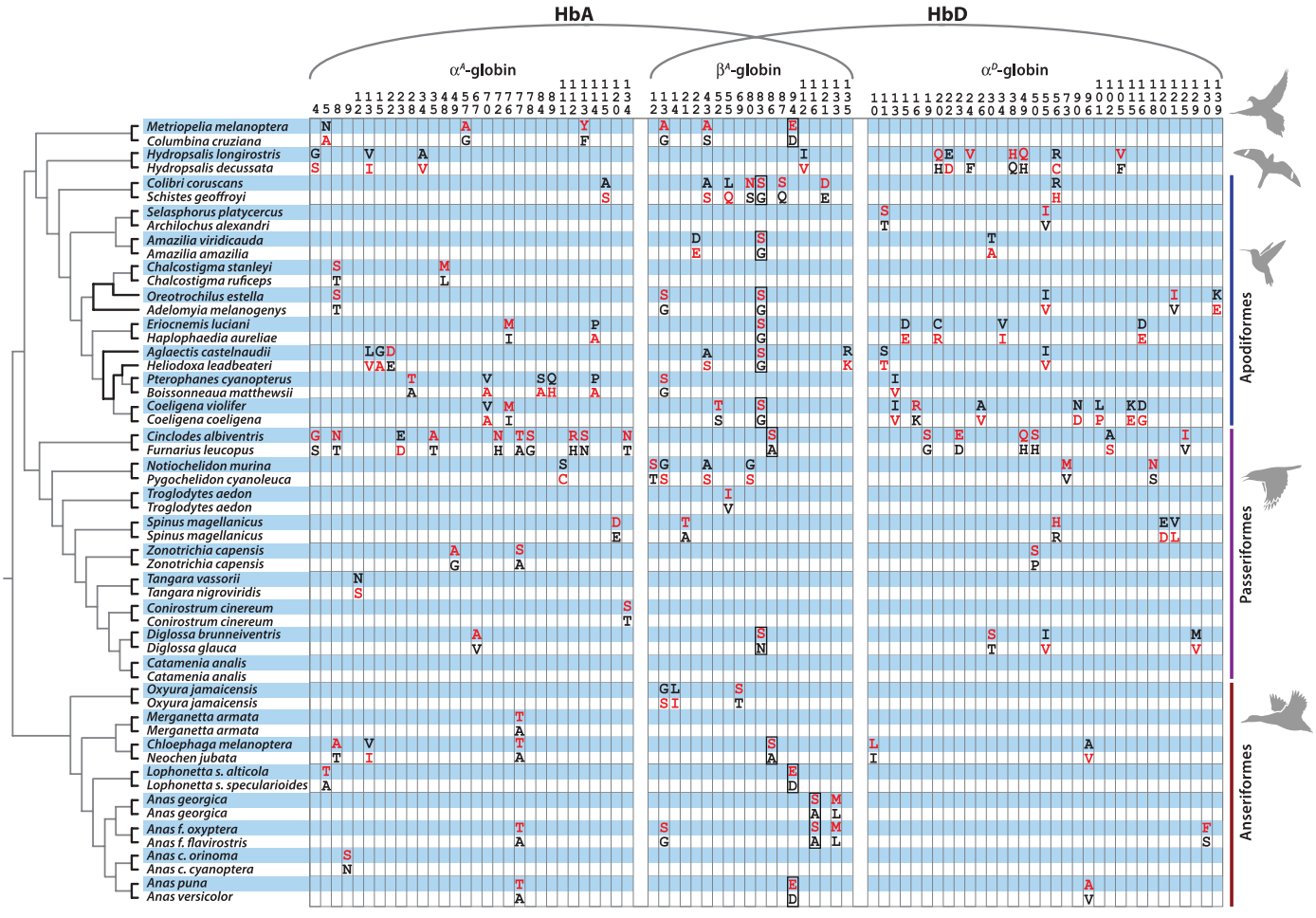

Fig. 1. Amino acid differences that distinguish the Hbs of each pair of high- and low-altitude taxa. Derived (nonancestral) amino acids are shown in red lettering, and rows corresponding to high-altitude taxa are shaded in blue. Subunits of the major HbA isoform are encoded by the α^A- and β^A-globin genes, whereas those of the minor HbD isoform are encoded by the α^D- and β^A-globin genes. Phylogenetically replicated β-chain replacements that contribute to convergent increases in Hb-O_2 affinity (N/G83S, A86S, D94E, and A116S) are outlined. Single-letter abbreviations for the amino acid residues are as follows: A, Ala; C, Cys; D, Asp; E, Glu; F, Phe; G, Gly; H, His; I, Ile; K, Lys; L, Leu; M, Met; N, Asn; P, Pro; Q, Gln; R, Arg; S, Ser; T, Thr; V, Val; and Y, Tyr.

species that have independently colonized high-altitude environments. Specifically, we tested whether high-altitude taxa have convergently evolved derived increases in Hb-O_2 affinity, and we assessed the extent to which such changes are attributable to parallel amino acid substitutions. We performed comparisons of Hb function in 56 avian taxa making up 28 pairs of high- and low-altitude lineages (table S1). The comparisons involved pairs of species or conspecific populations that are native to different altitudes.

Under severe hypoxia, an increased Hb-O_2 affinity can help sustain tissue O_2 delivery by safeguarding arterial O_2 saturation while simultaneously maintaining the pressure gradient for O_2 diffusion from capillary blood to the tissue mitochondria, so altitude-related changes in Hb function likely have adaptive relevance (*5*, *6*). Evolutionary increases in Hb-O_2 affinity can be caused by amino acid mutations that increase intrinsic O_2 affinity and/or mutations that suppress the sensitivity of Hb to the inhibitory effects of allosteric effectors such as Cl^- ions and organic phosphates (*5*, *7*).

In a highly influential paper on biophysical mechanisms of protein evolution, Perutz (*7*) predicted that adaptive changes in functional properties of vertebrate Hb are typically attributable to "a few replacements at key positions." According to Perutz, amino acid substitutions that can be expected to make especially important contributions to evolutionary changes in Hb-O_2 affinity involve heme-protein contacts (affecting intrinsic heme reactivity), intersubunit contacts (affecting the oxygenation-linked, allosteric transition in quaternary structure), and binding sites for allosteric effectors (*7*). If Perutz is correct that adaptive modifications of Hb function are typically attributable to a small number of substitutions at key positions, then it follows that the same mutations will be preferentially fixed in different species that have independently evolved Hbs with similar functional properties. For example, in high-altitude vertebrates that have convergently evolved elevated Hb-O_2 affinities, Perutz's hypothesis predicts that parallel amino acid substitutions should be pervasive.

Most bird species express two tetrameric ($\alpha_2\beta_2$) Hb isoforms in adult red blood cells: (i) the major hemoglobin A (HbA) isoform, which incorporates α-chain products of the α^A-globin gene, and (ii) the minor HbD isoform, which incorporates products of the closely linked α^D-globin gene. Both isoforms share the same β-chain subunits. By cloning and sequencing the adult-expressed globin genes, we identified all amino acid differences that distinguish the Hbs of each pair of high- and low-altitude taxa. The comparative sequence data revealed phylogenetically replicated replacements at numerous sites in the α^A-, α^D-, and β^A-globins (Fig. 1 and figs. S1 and S2).

After identifying the complete set of Hb substitutions that distinguish each pair of high- and low-altitude taxa, we experimentally assessed how many of the replicated amino acid replacements actually contributed to convergent changes in Hb function. To characterize the functional mechanisms that are responsible for evolved changes in Hb-O_2 affinity, we measured P_{50} (the O_2 partial pressure at which Hb is 50% saturated) of purified Hbs in the presence and absence of Cl^- ions and the organic phosphate inositol hexaphosphate (IHP) (*8*). We focus on measures of P_{50} in the

Downloaded from http://science.sciencemag.org/ on October 20, 2016

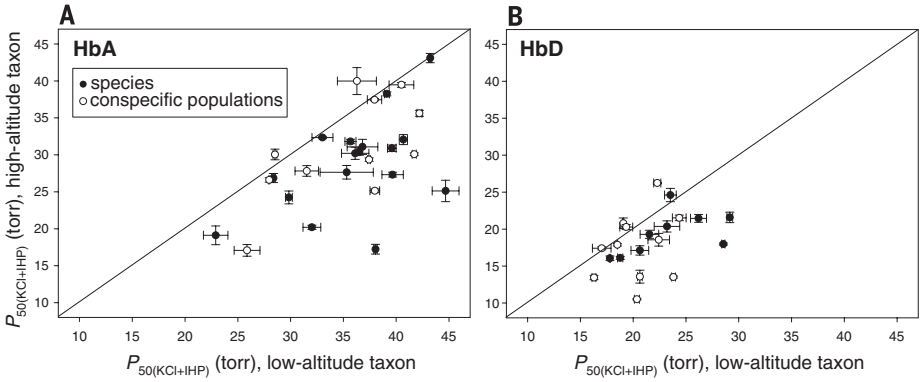

Fig. 2. Convergent increases in Hb-O_2 affinity in high-altitude Andean birds. (**A**) Plot of $P_{50(KCl+IHP)}$ (± 1 SE) for HbA in 28 matched pairs of high- and low-altitude taxa. Data points that fall below the diagonal line ($x = y$) denote cases in which the high-altitude member of a given taxon pair possesses a higher Hb-O_2 affinity (lower P_{50}). Comparisons involve replicated pairs of taxa, so all data points are phylogenetically independent. (**B**) Plot of $P_{50(KCl+IHP)}$ (± 1 SE) for the minor HbD isoform in a subset of the same taxon pairs in which both members of the pair express HbD. $P_{50(KCl+IHP)}$, O_2 partial pressure at which Hb is 50% saturated in the presence of chloride and inositol hexaphosphate.

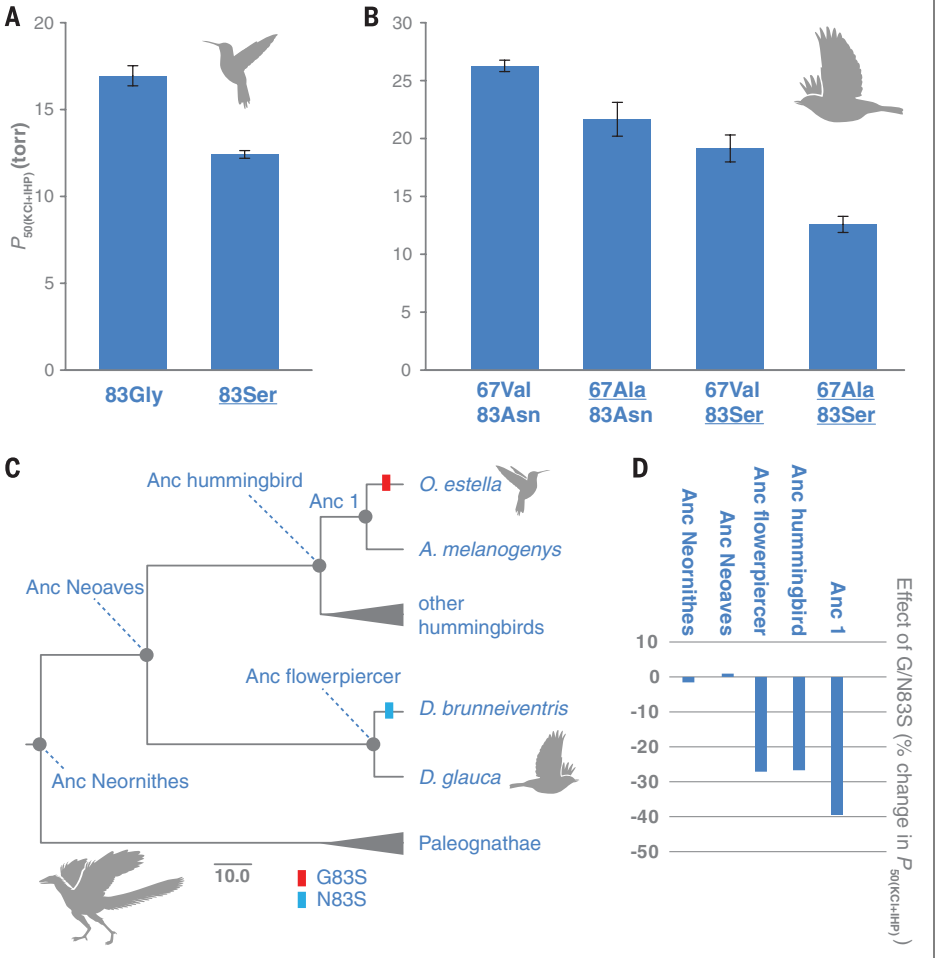

Fig. 3. Phenotypic effects of substitutions at β83 are conditional on genetic background. (**A**) The engineered G83S mutation produced a significant reduction in $P_{50(KCl+IHP)}$ (increase in Hb-O_2 affinity) in the reconstructed Hb of the hummingbird ancestor. (**B**) The engineered A67V and N83S mutations produced additive reductions in $P_{50(KCl+IHP)}$ in the reconstructed Hb of the flowerpiercer ancestor. Underlining indicates derived (nonancestral) amino acids. (**C**) Diagrammatic tree with time-scaled branch lengths showing internal nodes that we targeted for ancestral protein resurrection. Scale bar, 10 million years. (**D**) N/G83S mutations produced significant increases in Hb-O_2 affinity (expressed as reductions in $P_{50(KCl+IHP)}$) in the ancestors of hummingbirds and flowerpiercers. Substitutions at the same site produced no detectable effects in Anc Neoaves or Anc Neornithes.

presence of Cl^- and IHP, because this experimental treatment is most relevant to in vivo conditions in avian red blood cells.

HbD exhibited uniformly higher O_2 affinities than HbA in all examined taxa (table S2), consistent with results of previous studies (*9*–*13*). This consistent pattern of isoform differentiation suggests that up-regulating the expression of HbD could provide a ready means of increasing blood O_2 affinity. However, our results demonstrate that this regulatory mechanism does not play a general role in hypoxia adaptation, because there was no consistent trend of increased HbD expression among high-altitude taxa (Wilcoxon signed-rank test, $Z = -0.775$, $P = 0.441$, $n = 26$; table S3 and fig. S3).

Phylogenetically independent comparisons involving all 28 taxon pairs revealed that highland natives have generally evolved an increased Hb-O_2 affinity relative to that of their lowland counterparts, a pattern that is consistent for both HbA (Wilcoxon's signed-rank test, $Z = -4.236$, $P < 0.0001$, $n = 28$; Fig. 2A and table S2) and HbD ($Z = -2.875$, $P = 0.0041$, $n = 20$; Fig. 2B and table S2). In all pairwise comparisons in which the high-altitude taxa exhibited significantly higher Hb-O_2 affinities ($n = 22$ taxon pairs for HbA and 15 taxon pairs for HbD), the measured differences were almost entirely attributable to differences in intrinsic O_2 affinity, rather than differences in sensitivity to Cl^- or IHP (table S4). Thus, genetically based increases in Hb-O_2 affinity were not generally associated with a diminution of allosteric regulatory capacity (i.e., O_2 affinity could still be modulated by erythrocytic changes in anion concentrations), in contrast to the case with some high-altitude mammals (*5*, *14*, *15*).

Results of experiments based on both native Hb variants and engineered, recombinant Hb mutants revealed that only a subset of replicated replacements actually contributed to convergent increases in Hb-O_2 affinity in high-altitude taxa (table S5). These include replicated replacements at just four β-chain sites: N/G83S, A86S, D94E, and A116S. β116 is an $\alpha_1\beta_1$ intersubunit contact, and β94 plays a key role in allosteric proton binding; neither of the other replicated replacements—and few of the affinity-enhancing nonreplicated replacements—involved heme contacts, intersubunit contacts, or canonical binding sites for allosteric effectors.

Our experiments revealed a striking pattern of convergence in the oxygenation properties of Hb in high-altitude natives (Fig. 2, A and B), and, in several cases, convergent increases in Hb-O_2 affinity were caused by parallel substitutions at key residues that mediate protein allostery (e.g., D94E in the β-chains of high-altitude ground doves and waterfowl; Fig. 1 and table S5). However, in the majority of cases, convergent increases in Hb-O_2 affinity were attributable to nonreplicated substitutions and/or parallel substitutions at sites that are not considered "key residues" (e.g., N/G83S in the β-chains of high-altitude hummingbirds and flowerpiercers; Fig. 1). Clearly, evolutionary increases in Hb-O_2 affinity can be produced by amino acid substitutions at numerous sites.

Downloaded from http://science.sciencemag.org/ on October 20, 2016

These findings expose a clear demarcation between the realms of chance and necessity at different hierarchical levels. At the level of biochemical phenotype, and even at the level of functional mechanism, evolutionary changes are highly predictable. At the amino acid level, in contrast, predictability breaks down.

In addition to the many-to-one mapping of genotype to phenotype, the phylogenetic distribution of affinity-enhancing parallel substitutions suggests another possible explanation for the limited contribution of such substitutions to convergent functional changes in the Hbs of distantly related species. The most striking functional parallelism at the amino acid level was concentrated in the hummingbird clade. Replicated G83S substitutions contributed to convergent increases in Hb-O_2 affinity in multiple high-altitude hummingbird species (table S5 and fig. S4) (*16*), and a convergent substitution at the same site (N83S) occurred in one other (nonhummingbird) high-altitude species: the black-throated flowerpiercer, *Diglossa brunneiventris*. One possible explanation for this phylogenetically concentrated pattern of parallelism is that the mutation's phenotypic effect is conditional on genetic background, so the same mutation produces different effects in different species.

To test this hypothesis, we used ancestral sequence reconstruction in combination with site-directed mutagenesis to test the effect of β83 substitutions in a set of distinct genetic backgrounds. We first resurrected HbA of the common ancestor of hummingbirds ("Anc hummingbird") (figs. S5 to S7), and we confirmed that G83S has a significant affinity-enhancing effect on this ancestral genetic background (Fig. 3A). This result is consistent with the affinity-enhancing effect of G83S in numerous descendant lineages of high-altitude hummingbirds (table S5 and fig. S4). In similar fashion, we resurrected HbA of the common ancestor of the high- and low-altitude flowerpiercers ("Anc flowerpiercer") to test the effect of N83S (fig. S7). Hbs of the two flowerpiercers differed at two sites because of substitutions in the *D. brunneiventris* lineage (V67A in α^A-globin, in addition to N83S in β^A-globin; Fig. 1). We therefore synthesized a total of four recombinant Hb mutants, representing each possible genotypic combination of the two substituted sites, to measure the relative contributions of V67A and N83S to the evolved increase in Hb-O_2 affinity in *D. brunneiventris* (table S2 and fig. S4). The tests showed that both mutations increased Hb-O_2 affinity in an additive fashion (Fig. 3B). We then engineered the same N83S mutation into resurrected ancestral Hbs representing two far more ancient nodes in the avian phylogeny: the reconstructed common ancestor of Neoaves ("Anc Neoaves") and the common ancestor of all extant birds ("Anc Neornithes") (Fig. 3C and figs. S5, S7, S8, and S9). In contrast to the highly significant effects of N/G83S in hummingbird and flowerpiercer Hbs, N83S produced no detectable effect in Anc Neoaves or Anc Neornithes (Fig. 3D and table S6). The ancestral hummingbird and flowerpiercer Hbs contained 18 and 32 amino acid states, respectively, that were not present in Anc Neornithes (fig. S7), representing net sequence differences that accumulated over a ~100-million-year time period. The context-dependent effects of N/G83S indicate that lineage-specific substitutions in the ancestry of hummingbirds and flowerpiercers produced a genetic background in which mutations at β83 could contribute to an adaptive increase in Hb-O_2 affinity. This adaptive solution was apparently not an option in the deeper ancestry of birds and may also represent a precluded possibility in contemporary, high-altitude members of other avian lineages.

These findings reveal a potentially important role of contingency in adaptive protein evolution. In different species that are adapting to the same selection pressure, the set of possible amino acids at a given site that have unconditionally beneficial effects may be contingent on the set of antecedent substitutions that have independently accumulated in the history of each lineage. Consequently, possible options for adaptive change in one species may be foreclosed options in other species.

REFERENCES AND NOTES

1. D. L. Stern, V. Orgogozo, *Science* **323**, 746–751 (2009).
2. J. B. Losos, *Evolution* **65**, 1827–1840 (2011).
3. D. L. Stern, *Nat. Rev. Genet.* **14**, 751–764 (2013).
4. J. F. Storz, *Nat. Rev. Genet.* **17**, 239–250 (2016).
5. R. E. Weber, *Respir. Physiol. Neurobiol.* **158**, 132–142 (2007).
6. J. F. Storz, G. R. Scott, Z. A. Cheviron, *J. Exp. Biol.* **213**, 4125–4136 (2010).
7. M. F. Perutz, *Mol. Biol. Evol.* **1**, 1–28 (1983).
8. Materials and methods are available as supplementary materials on *Science* Online.
9. M. T. Grispo *et al.*, *J. Biol. Chem.* **287**, 37647–37658 (2012).
10. Z. A. Cheviron *et al.*, *Mol. Biol. Evol.* **31**, 2948–2962 (2014).
11. S. C. Galen *et al.*, *Proc. Natl. Acad. Sci. U.S.A.* **112**, 13958–13963 (2015).
12. C. Natarajan *et al.*, *PLOS Genet.* **11**, e1005681 (2015).
13. J. C. Opazo *et al.*, *Mol. Biol. Evol.* **32**, 871–887 (2015).
14. J. F. Storz, A. M. Runck, H. Moriyama, R. E. Weber, A. Fago, *J. Exp. Biol.* **213**, 2565–2574 (2010).
15. C. Natarajan *et al.*, *Mol. Biol. Evol.* **32**, 978–997 (2015).
16. J. Projecto-Garcia *et al.*, *Proc. Natl. Acad. Sci. U.S.A.* **110**, 20669–20674 (2013).

ACKNOWLEDGMENTS

This work was funded by grants from the U.S. NIH (HL087216), the U.S. NSF (IOS-0949931, MCB-1517636, and MCB-1516660), and the Danish Council for Independent Research (10-084-565 and 4181-00094). We thank E. Petersen, H. Moriyama, and A. Kumar for assistance in the laboratory and C. Meiklejohn and K. Montooth for helpful suggestions. All experimental data are tabulated in the supplementary materials, and sequence data are archived in GenBank under accession numbers KX240692 to KX241466.

SUPPLEMENTARY MATERIALS

www.sciencemag.org/content/354/6310/336/suppl/DC1
Materials and Methods
Figs. S1 to S9
Tables S1 to S6
References (*17*–*33*)

19 April 2016; accepted 20 July 2016
10.1126/science.aaf9070

ENZYMOLOGY

The biosynthetic pathway of coenzyme F430 in methanogenic and methanotrophic archaea

Kaiyuan Zheng, Phong D. Ngo, Victoria L. Owens, Xue-peng Yang,* Steven O. Mansoorabadi†

Methyl-coenzyme M reductase (MCR) is the key enzyme of methanogenesis and anaerobic methane oxidation. The activity of MCR is dependent on the unique nickel-containing tetrapyrrole known as coenzyme F430. We used comparative genomics to identify the coenzyme F430 biosynthesis (*cfb*) genes and characterized the encoded enzymes from *Methanosarcina acetivorans* C2A. The pathway involves nickelochelation by a nickel-specific chelatase, followed by amidation to form Ni-sirohydrochlorin *a*,*c*-diamide. Next, a primitive homolog of nitrogenase mediates a six-electron reduction and γ-lactamization reaction before a Mur ligase homolog forms the six-membered carbocyclic ring in the final step of the pathway. These data show that coenzyme F430 can be synthesized from sirohydrochlorin using Cfb enzymes produced heterologously in a nonmethanogen host and identify several targets for inhibitors of biological methane formation.

Methanogenic archaea are a major player in the global carbon cycle, producing nearly 1 billion metric tons of methane annually (*1*, *2*). The terminal step of methanogenesis is catalyzed by methyl-coenzyme M reductase (MCR) and involves the conversion of coenzyme B (CoB-SH) and methyl-coenzyme M (MeS-CoM) to the mixed heterodisulfide CoB-S-S-CoM and methane (*3*) (Fig. 1). MCR uses the unique nickel-containing tetrapyrrole coenzyme F430 to carry out its catalytic function (*4*) (Fig. 1). Recently, anaerobic methanotrophic archaea (ANME) have been shown

Department of Chemistry and Biochemistry, Auburn University, Auburn, AL 36849, USA.
*Present address: School of Food and Biological Engineering, Zhengzhou University of Light Industry, Zhengzhou 450002, China.
†Corresponding author. Email: som@auburn.edu

Downloaded from http://science.sciencemag.org/ on October 20, 2016

PLANT PHOTOBIOLOGY

Photoactivation and inactivation of *Arabidopsis* cryptochrome 2

Qin Wang,[1,2]* Zecheng Zuo,[1,3]* Xu Wang,[1,2]* Lianfeng Gu,[1] Takeshi Yoshizumi,[4] Zhaohe Yang,[1] Liang Yang,[1,3] Qing Liu,[1,2,3] Wei Liu,[3] Yun-Jeong Han,[5] Jeong-Il Kim,[5] Bin Liu,[6] James A. Wohlschlegel,[7] Minami Matsui,[4] Yoshito Oka,[1,4]† Chentao Lin[1,2]†

Cryptochromes are blue-light receptors that regulate development and the circadian clock in plants and animals. We found that *Arabidopsis* cryptochrome 2 (CRY2) undergoes blue light–dependent homodimerization to become physiologically active. We identified BIC1 (blue-light inhibitor of cryptochromes 1) as an inhibitor of plant cryptochromes that binds to CRY2 to suppress the blue light–dependent dimerization, photobody formation, phosphorylation, degradation, and physiological activities of CRY2. We hypothesize that regulated dimerization governs homeostasis of the active cryptochromes in plants and other evolutionary lineages.

The *Arabidopsis* genome encodes two cryptochromes (CRYs), CRY1 and CRY2, which act as photoreceptors mediating blue-light inhibition of hypocotyl elongation and long-day (LD) stimulation of floral initiation (*1*–*4*). CRYs regulate light responses by interacting with CRY signaling partners, such as CIBs (cryptochrome-interacting basic helix-loop-helixes) and COP1/SPA (constitutive photomorphogenic 1/suppressor of PhyA-105), to regulate blue light–responsive gene expression changes and photophysiology responses (*5*–*7*). Homodimers are the physiologically active form of plant CRYs, but it has remained unclear how light affects CRY dimerization or photoactivation (*8*, *9*). Photoactivated CRYs are also expected to undergo inactivation to maintain sustainable photosensitivity of the cell, which may be accomplished by thermal relaxation or other mechanisms (*10*).

We reasoned that identification of possible negative regulators of CRYs may help to elucidate the photoactivation and inactivation mechanisms of CRYs. We therefore screened for such genes in the *Arabidopsis* FOX (full-length cDNA overexpressing gene hunting system) library, which contains transgenic lines individually overexpressing about 10,000 independent full-length *Arabidopsis* cDNAs (*11*). We identified multiple FOX lines (*bic1D-1*, *bic1D-2*, and *bic1D-3*) that overexpress the same gene and exhibit similar phenotypes resembling that of the *cry1cry2* mutant (*12*), including blue light–insensitive hypocotyl growth, reduced blue-light stimulation of anthocyanin accumulation and gene expression, and delayed floral initiation in LD photoperiod (Fig. 1 and figs. S1 and S2). The corresponding FOX gene was identified and referred to as *BIC1* (*Blue-light Inhibitor of Cryptochromes 1*, At3G52740), which has an *Arabidopsis* homolog referred to as *BIC2* (At3G44450) (fig. S3). BIC1 and BIC2 appear to be nuclear proteins (fig. S4).

Independent transgenic lines overexpressing various BIC fusion proteins under control of either the constitutive promoters or the respective *BIC* promoters recapitulated the light-insensitive phenotypes of the BIC1-overexpressing FOX lines and the *cry1cry2* mutant (Fig. 1 and fig. S1). The *bic1* and *bic2* monogenic mutants showed no obvious phenotypic alterations, whereas the *bic1bic2* double mutant and the *BIC* RNA interference lines exhibited phenotypes mimicking that of the CRY-overexpressing plants (Fig. 1 and figs. S2, S5, and S6), which suggests that BIC1 and BIC2 act redundantly to inhibit the function of CRYs. Analyses of the genetic interactions between the *BIC* and *CRY* genes support this hypothesis (fig. S7): Neither *bic1bic2* mutation nor BIC overexpression altered the blue light–insensitive phenotypes of the *cry1cry2* mutant (fig. S7, D to F), whereas overexpression of BIC1 or BIC2 effectively suppressed the blue light–hypersensitive phenotype of plants overexpressing CRY2 (fig. S7G).

The *cry1cry2* mutation and BIC1 overexpression caused similar transcriptome changes in response to blue light (Fig. 2 and table S2), which suggests that BICs inhibit early photoreactions of CRYs. As reported previously (*13*–*16*), CRY1 and CRY2 underwent blue light–dependent phosphorylation and the phosphorylated CRY2 was degraded rapidly (Fig. 3, A to E, and fig. S8, upshifted bands). However, neither blue light–dependent phosphorylation of CRYs nor blue light–dependent degradation of CRY2 (*15*, *16*) was detected in the plants overexpressing BIC1 or BIC2 (Fig. 3, A to E, and fig. S8); hence, BICs inhibit CRY phosphorylation. Consistent with those results, the *bic1bic2* mutant plants grown in blue or white light accumulated lower levels of CRY2 (Fig. 1, G to J), which seems physiologically hyperactive because the *bic1bic2* mutant is hypersensitive to blue light (Fig. 1, A to C). The BIC-overexpressing plants grown in blue or white light accumulated higher levels of CRY2 (Fig. 1, G to J), which appears mostly inactive because the BIC-overexpressing plants are insensitive to blue light (Fig. 1, A to C).

BICs also inhibit the blue light–induced formation of CRY2 photobodies (Fig. 3 and fig. S9), which is another early photoreaction of CRY2 (*17*–*19*). Figure 3 shows that CRY2-YFP (CRY2 fused to yellow fluorescent protein) formed photobodies within 60 s of blue-light exposure in the nucleus of the wild-type *Arabidopsis* protoplasts, whereas no CRY2-YFP photobodies were detected in the protoplasts overexpressing BIC1 or BIC2 after blue-light illumination for up to 60 min (Fig. 3, F and H). In both darkness and light, BIC1 interacted with CRY2 in yeast or HEK293T (human embryonic kidney) cells via the conserved CRY-interacting domain of BIC1 and the photolyase homologous region of CRY2 (Fig. 4, B and F, and fig. S10). The results of the coimmunoprecipitation (co-IP) experiments indicate that blue light enhances BIC1-CRY2 interaction in plants. BIC1 coimmunoprecipitated CRY2 in seedlings exposed to blue light, but little BIC1-CRY2 complex was coprecipitated in the dark (Fig. 4A). This observation suggests that BIC1 might interact with photoexcited CRY2 to inhibit its activity.

Homodimers are the physiologically active form of plant CRYs (*8*, *9*), but the effect of light on CRY dimerization has not been detected in previous studies (*9*, *20*). This could be explained by, among other interpretations, light-independent CRY dimerization or masking effects of regulatory proteins, such as BICs, on the light-dependent CRY dimerization (*9*, *20*). We reexamined the blue-light dependence of CRY2 dimerization using multiple approaches. In the first experiment, we coexpressed Flag-CRY2 and Myc-CRY2 in HEK293T cells (*21*–*24*) and tested the interaction between the two differentially tagged CRY2s by co-IP assay. In the absence of blue light, antibody to Flag coprecipitated little Myc-CRY2 from HEK293T cells expressing similar amounts of Flag-CRY2 and Myc-CRY2 (Fig. 4B and fig. S12A). In contrast, antibody to Flag coprecipitated increasing amounts of Myc-CRY2 from HEK293T cells exposed to blue light for 10 to 120 min, thereby demonstrating the light-dependent CRY2 homodimerization in the absence of BIC or other plant proteins (Fig. 4B and fig. S12A). In a control experiment, human CRYs (hCRY1 and hCRY2) exhibited light-independent dimerization (Fig. 4C and fig. S12D), which appears consistent with the light-independent activity of hCRYs in cultured HEK293T cells (*25*). The blue light–dependent CRY2 dimerization was also detected by the two-hybrid assay in yeast cells (fig. S11) and the bimolecular fluorescence complementation (BiFC) assay in *Arabidopsis* protoplasts (Fig. 3, G and I, and fig. S9). The BiFC assays revealed a more complex behavior of the intermolecular interaction of CRY2:

[1]Basic Forestry and Proteomics Research Center, Fujian Agriculture and Forestry University, Fuzhou 350002, China. [2]Department of Molecular, Cell and Developmental Biology, University of California, Los Angeles, CA 90095, USA. [3]College of Plant Science, Jilin University, Changchun 130062, China. [4]Biomass Engineering Research Division, RIKEN, Kanagawa 230-0045, Japan. [5]Department of Biotechnology and Kumho Life Science Laboratory, Chonnam National University, Gwangju 61186, Republic of Korea. [6]Institute of Crop Sciences, Chinese Academy of Agricultural Sciences, Beijing 10081, China. [7]Department of Biological Chemistry, University of California, Los Angeles, CA 90095, USA. *These authors contributed equally to this work. **†Corresponding author. Email: yoshitooka@fafu.edu.cn (Y.O.); clin@mcdb.ucla.edu (C.L.)**

Downloaded from http://science.sciencemag.org/ on October 20, 2016

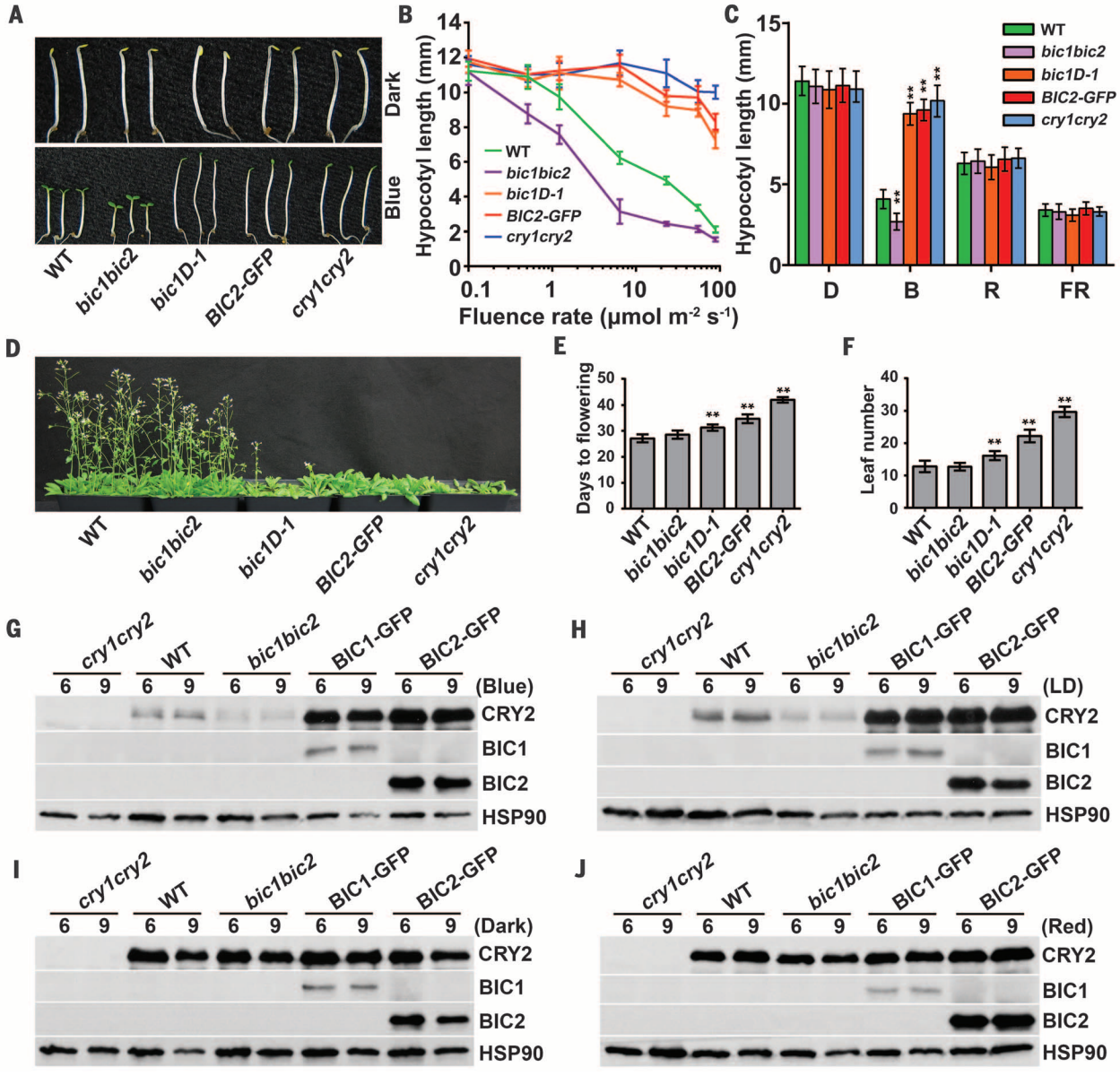

Fig. 1. BIC1 and BIC2 suppress the functions of *Arabidopsis* cryptochromes. (**A**) Five-day-old seedlings overexpressing BIC1 (*bic1D-1*) or BIC2-GFP (*BIC2-GFP*) and *cry1cry2* or *bic1bic2* mutant seedlings grown in continuous blue light (4 μmol m^{-2} s^{-1}) or dark; WT, wild type. (**B**) Hypocotyl lengths of 5-day-old seedlings grown under continuous blue light with fluence rates of 0.1 to 100 μmol m^{-2} s^{-1}. (**C**) Hypocotyl lengths of indicated genotypes grown in the dark (D), under blue light (B; 10 μmol m^{-2} s^{-1}), under red light (R; 10 μmol m^{-2} s^{-1}), or under far-red light (FR; 5 μmol m^{-2} s^{-1}) for 5 days. (**D**) Plants of indicated genotypes grown in LD photoperiods (16 hours light, 8 hours dark) for 31 days. (**E** and **F**) Days to flowering (E) and number of rosette leaves at the time of flowering (F) of the indicated genotypes grown in LD. (**G** to **J**) Immunoblots of samples prepared from seedlings grown in continuous blue light (30 μmol m^{-2} s^{-1}) (G), LD photoperiods (H), darkness (I), or continuous red light (30 μmol m^{-2} s^{-1}) (J) for 6 or 9 days were probed with antibodies to CRY2, GFP, or HSP90 (loading control). Data in (B), (C), (E), and (F) are means ± SD ($n > 20$); $^{**}P < 0.01$.

The BiFC signal resulting from the interaction between nYFP-CRY2 (N terminus of YFP fused to CRY2) and cCFP-CRY2 (C terminus of cyan fluorescent protein fused to CRY2) was detected regardless of blue-light treatment, whereas the fluorescent photobodies resulting from the interaction between nYFP-CRY2 and cCFP-CRY2 were detected only after blue-light treatment (Fig. 3, G and I, and fig. S9).

Because photoexcited CRY2 is known to oligomerize into photobodies (*18*, *19*, *23*, *24*), it is possible that in darkness nYFP-CRY2 and cCFP-CRY2 interact weakly in a manner sufficient to reconstitute the fluorescent BiFC signal but insufficient to enable oligomerization of CRY2 into photobodies. In response to blue light, nYFP-CRY2 and cCFP-CRY2 may interact with higher affinity to reconstitute not only the fluorescent BiFC signals but also fluorescent photobodies. To test this interpretation, we used co-IP assays to examine effects of blue light on CRY2 dimerization or oligomerization in plants coexpressing GFP-CRY2 (CRY2 fused to green fluorescent protein) and Myc-CRY2 (Fig. 4D). Antibody to GFP coprecipitated little Myc-CRY2 in etiolated seedlings, whereas the same antibody coprecipitated abundant Myc-CRY2 in etiolated seedlings exposed to blue light for 5 to 10 min (Fig. 4D). Similarly, the blue light–specific CRY2 homodimerization was also detected in adult plants (fig. S12B). We conclude that the high-affinity CRY2 dimerization is a photoreaction in plant cells.

We next investigated the effects of BIC1 on blue light–dependent CRY2 dimerization using

Downloaded from http://science.sciencemag.org/ on October 20, 2016

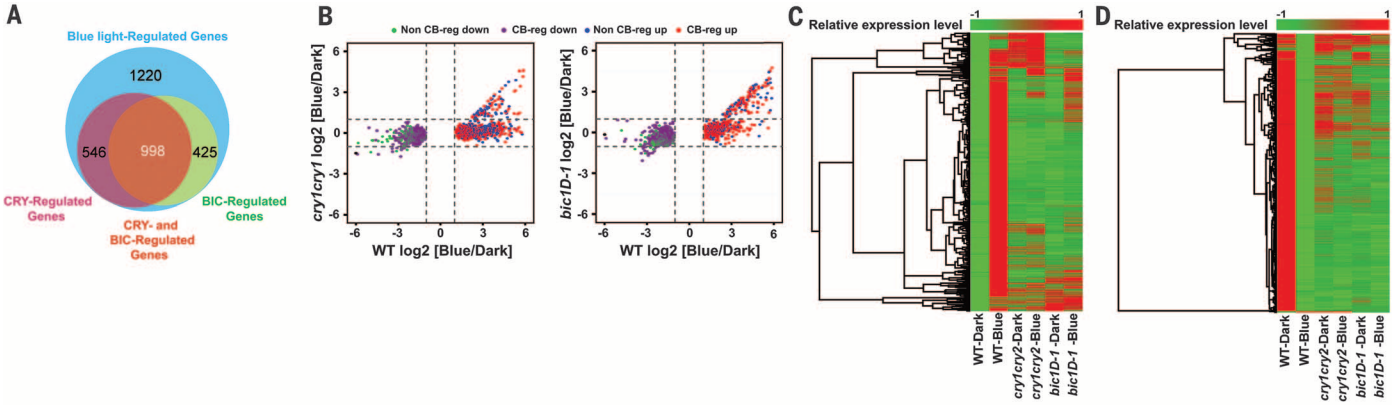

Fig. 2. CRY and BIC regulate similar transcriptome changes in response to blue light. (**A**) Venn diagram depicting overlaps among blue light–regulated, CRY-regulated, and BIC-regulated genes determined by RNA sequencing. Five-day-old etiolated seedlings were exposed to blue light (20 μmol m^{-2} s^{-1}) or kept in the dark for 2 hours. The blue light–regulated genes are defined as those that showed a factor of >2 change of mRNA [fold change (FC) > 2, $P < 0.01$, false discovery rate < 0.01; see table S2 for details] between light- and dark-treated wild-type plants. The blue light–regulated genes that showed 200% reduction of FC or changed significance to $P > 0.01$ in *cry1cry2* or *bic1D-1* are defined as CRY-regulated and BIC-regulated genes, respectively; those that showed similar change in both *cry1cry2* and *bic1D-1* are defined as CRY- and BIC-regulated ("CB-reg") genes. (**B**) Scatterplot showing plots of log2 (FC) of wild-type (*x* axis) versus log2 (FC) of *cry1cry2* or *bic1D-1* (*y* axis). The dashed lines indicate log2 (FC) = 1 and −1. The colored dots (see key at top) indicate up-regulated or down-regulated genes not co-regulated by CRY and BIC1 ("Non CB-reg") and genes that are co-regulated by CRY and BIC1 ("CB-reg"). (**C** and **D**) Hierarchical clustering (GENE-E) of the change of expression of blue light–induced genes (C) and blue light–repressed genes (D) detected in the indicated genotypes. Scale bars at top indicate relative expression levels of mRNA.

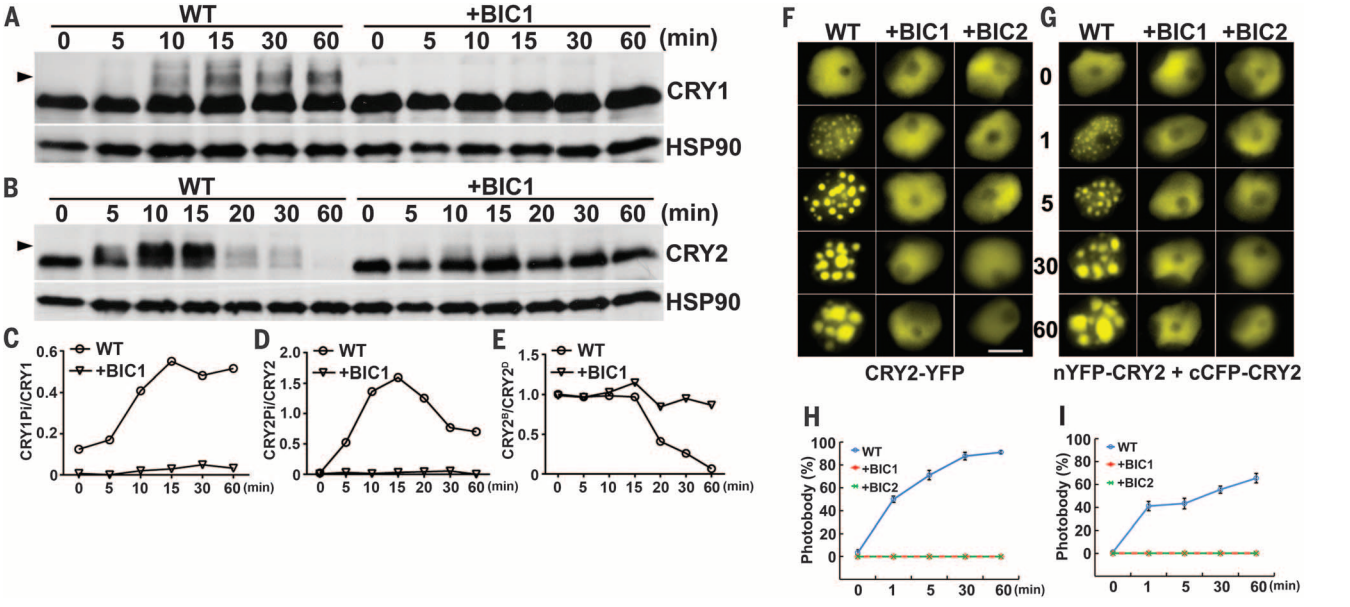

Fig. 3. BIC1 and BIC2 inhibit early photoreactions of cryptochromes. (**A** and **B**) BIC1 inhibits blue light–dependent phosphorylation of CRY1 and CRY2 and blue light–dependent degradation of CRY2. Immunoblots of samples prepared from 7-day-old etiolated seedlings (WT, wild type; +BIC1, BIC1-overexpressing) exposed to blue light (30 μmol m^{-2} s^{-1}) for the indicated times were probed with antibodies to CRY1, CRY2, or HSP90 (loading control). Arrowheads indicate upshift bands of the phosphorylated CRYs. (**C** to **E**) Quantification of band intensities, showing CRY phosphorylation [(C), CRY1Pi/CRY1; (D), CRY2Pi/CRY2] or CRY2 degradation [(E), $CRY2^B/CRY2^D$]. (**F**) BIC inhibition of CRY2 photobodies. Protoplasts isolated from 4-week-old plants of indicated genotypes were transfected to express CRY2-YFP, exposed to blue light (20 μmol $m^{-2}s^{-1}$) for 0 to 60 min, fixed in 1% formaldehyde, and examined by a fluorescence microscope. Scale bar, 5 μm. (**G**) BiFC assay showing the blue light–independent (dispersed fluorescence) and blue light–dependent (photobodies) interactions between nYFP-CRY2 and cCFP-CRY2. Protoplasts transfected to express nYFP-CRY2 and cCFP-CRY2 were exposed to blue light and analyzed as in (F). (**H**) The CRY2-YFP photobody of the experiment shown in (F) was digitized and quantified; 30 nuclei per sample were counted, and the percentage of protoplasts containing photobodies was calculated (±SD; $n = 3$). (**I**) Same as (H) but for the nYFP-CRY2/cCFP-CRY2 photobody shown in (G).

the multiple assays described above. We first examined dimerization of Flag-CRY2 and Myc-CRY2 in HEK293T cells coexpressing BIC1. Figure 4B shows that in the cells coexpressing BIC1, antibody to Flag coprecipitated only residual Myc-CRY2 even after blue-light treatment for up to 120 min, thereby demonstrating that BIC1 suppresses blue light–dependent CRY2 dimerization. The specificity of BIC1 inhibition of CRY2 dimerization is verified by the result that CIB1, which also interacts with photoexcited CRY2 (*6*, *26*), did not inhibit blue light–dependent CRY2 dimerization (Fig. 4E). The BIC1 inhibition of blue light–dependent CRY2 dimerization was also detected by the trihybrid assay in yeast cells (fig. S11) and by the BiFC photobody assay in *Arabidopsis* cells (Fig. 3, G and I, and fig. S9). Because physiologically active CRY2 dimers or oligomers are expected to interact with their signaling partners, such as CIB1 and SPA1 (*7*), we used co-IP assays to test the effects of BIC1 on the blue light–dependent

Downloaded from http://science.sciencemag.org/ on October 20, 2016

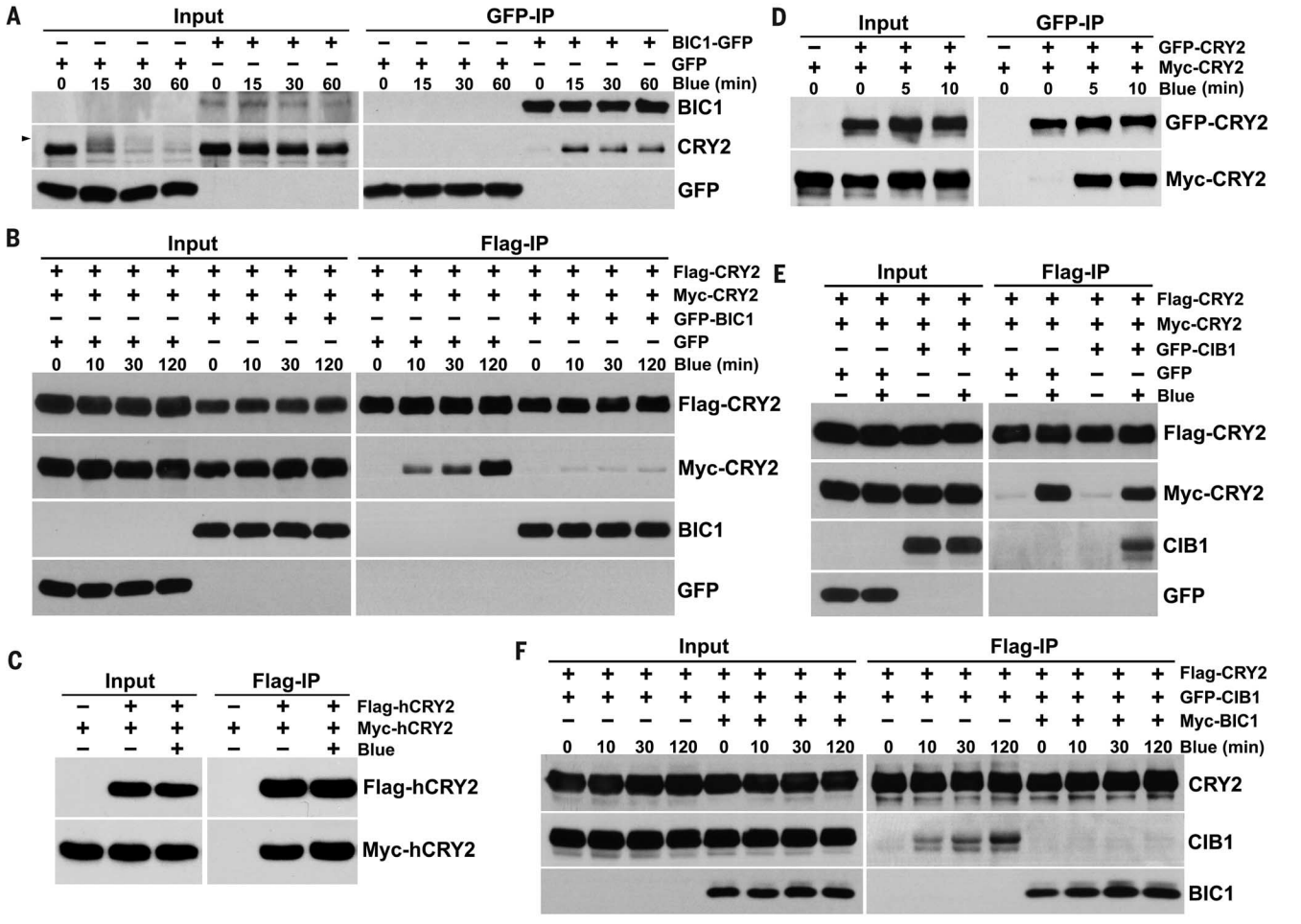

Fig. 4. BIC1 interacts with CRY2 to inhibit blue light–dependent CRY2 dimerization and CRY2-CIB1 interaction. (**A**) Seven-day-old etiolated seedlings expressing *35S::BIC1-GFP* or *35S::GFP* (control) were exposed to blue light (30 μmol m^{-2} s^{-1}) for 0 to 120 min and immunoprecipitated by GFP-trap beads. The IP (BIC1) and co-IP signals (CRY2) were detected by immunoblots probed with antibodies to GFP and CRY2, respectively. (**B**) HEK293T cells were cotransfected to express the indicated proteins, exposed to blue light (180 μmol m^{-2} s^{-1}) for 0 to 120 min, and immunoprecipitated by antibody to Flag (Flag-IP). The IP signal (Flag-CRY2) or the co-IP signals (Myc-CRY2 and BIC1) were detected by immunoblots probed with antibodies to Flag or to Myc and GFP, respectively. (**C**) Co-IP assays showing light-independent dimerization of human CRY2 (hCRY2) in HEK293T cells. (**D**) Seven-day-old etiolated transgenic seedlings coexpressing the indicated proteins were exposed to blue light (30 μmol m^{-2} s^{-1}) for 0 to 10 min and immunoprecipitated by the GFP-trap beads. The IP signal (GFP-CRY2) and the co-IP signal (Myc-CRY2) were detected by immunoblots probed with antibodies to GFP or Myc, respectively. (**E**) HEK293T cells transfected to express the indicated fusion proteins were kept in the dark (–Blue) or exposed to blue light (180 μmol m^{-2} s^{-1}) for 2 hours (+Blue) and analyzed by co-IP assay as in (B). (**F**) HEK293T cells coexpressing the indicated proteins were exposed to blue light (180 μmol m^{-2} s^{-1}) for 0 to 120 min. The IP signal (CRY2) or the co-IP signals (CIB1 and BIC1) were detected by immunoblots probed with antibodies to Flag or to GFP and Myc, respectively.

CRY2-CIB1 and CRY2-SPA1 interactions. As expected, coexpression of BIC1 suppressed the blue light–dependent CRY2-CIB1 interaction (Fig. 4F) and CRY2-SPA1 interaction (fig. S12C), which explains how inhibition of CRY dimerization by BIC1 suppresses CRY2-dependent photoresponses of plants.

Homodimerization appears to be a common mechanism of photoreceptors (*27*–*29*). Our study supports a hypothesis that plant CRYs exist as inactive monomers in the absence of light, whereas photoexcited CRYs form active homodimers or oligomers that interact with CRY-signaling proteins to trigger transcriptome changes responsible for photomorphogenesis; the BIC proteins interact with CRYs to prevent CRY homodimerization and thereby maintain the appropriate homeostasis of the active and inactive pools of CRYs and sustainability of cellular photosensitivity (fig. S12E). It would be interesting to examine whether photoinsensitive mammalian CRYs and photosensitive insect CRYs undergo circadian phase–dependent and light-dependent dimerization, respectively.

REFERENCES AND NOTES

1. M. Ahmad, A. R. Cashmore, *Nature* **366**, 162–166 (1993).
2. H. Guo, H. Yang, T. C. Mockler, C. Lin, *Science* **279**, 1360–1363 (1998).
3. A. R. Cashmore, *Cell* **114**, 537–543 (2003).
4. A. Sancar, *Chem. Rev.* **103**, 2203–2237 (2003).
5. H.-Q. Yang *et al.*, *Cell* **103**, 815–827 (2000).
6. H. Liu *et al.*, *Science* **322**, 1535–1539 (2008).
7. H. Liu, B. Liu, C. Zhao, M. Pepper, C. Lin, *Trends Plant Sci.* **16**, 684–691 (2011).
8. G. Rosenfeldt, R. M. Viana, H. D. Mootz, A. G. von Arnim, A. Batschauer, *Mol. Plant* **1**, 4–14 (2008).
9. Y. Sang *et al.*, *Plant Cell* **17**, 1569–1584 (2005).
10. D. M. Shcherbakova, A. A. Shemetov, A. A. Kaberniuk, V. V. Verkhusha, *Annu. Rev. Biochem.* **84**, 519–550 (2015).
11. T. Ichikawa *et al.*, *Plant J.* **48**, 974–985 (2006).
12. T. C. Mockler, H. Guo, H. Yang, H. Duong, C. Lin, *Development* **126**, 2073–2082 (1999).
13. D. Shalitin *et al.*, *Nature* **417**, 763–767 (2002).
14. D. Shalitin, X. Yu, M. Maymon, T. Mockler, C. Lin, *Plant Cell* **15**, 2421–2429 (2003).
15. Q. Wang *et al.*, *Mol. Plant* **8**, 631–643 (2015).
16. X. Yu *et al.*, *Plant Cell* **19**, 3146–3156 (2007).
17. P. Más, P. F. Devlin, S. Panda, S. A. Kay, *Nature* **408**, 207–211 (2000).
18. X. Yu *et al.*, *Plant Cell* **21**, 118–130 (2009).
19. L. J. Bugaj, A. T. Choksi, C. K. Mesuda, R. S. Kane, D. V. Schaffer, *Nat. Methods* **10**, 249–252 (2013).

Downloaded from http://science.sciencemag.org/ on October 20, 2016

20. X. Yu *et al.*, *Proc. Natl. Acad. Sci. U.S.A.* **104**, 7289–7294 (2007).
21. J. Gao *et al.*, *Proc. Natl. Acad. Sci. U.S.A.* **112**, 9135–9140 (2015).
22. U. V. Pedmale *et al.*, *Cell* **164**, 233–245 (2016).
23. A. Taslimi *et al.*, *Nat. Commun.* **5**, 4925 (2014).
24. I. Ozkan-Dagliyan *et al.*, *J. Biol. Chem.* **288**, 23244–23251 (2013).
25. E. A. Griffin Jr., D. Staknis, C. J. Weitz, *Science* **286**, 768–771 (1999).
26. M. J. Kennedy *et al.*, *Nat. Methods* **7**, 973–975 (2010).
27. L. Rizzini *et al.*, *Science* **332**, 103–106 (2011).
28. M. Heijde, R. Ulm, *Proc. Natl. Acad. Sci. U.S.A.* **110**, 1113–1118 (2013).
29. C.-H. Chen, B. S. DeMay, A. S. Gladfelter, J. C. Dunlap, J. J. Loros, *Proc. Natl. Acad. Sci. U.S.A.* **107**, 16715–16720 (2010).

ACKNOWLEDGMENTS

Q.W., Y.O., and C.L. are inventors on a patent application (U.S. Serial No. 62/360,862). Supported by NIH grants GM56265 (C.L.) and GM089778 and GM112763 (J.A.W.), Rural Development Administration of Republic of Korea grant PJ01104001 (J.-I.K.), Biomass Engineering Program of RIKEN (M.M.), the Special Postdoctoral Researcher Program of RIKEN (Y.O.), National Natural Science Foundation of China grants 31500991 (Q.W.), 31570674 (L.G.), 31422041 (B.L.), and 31371411 (Z.Z.), and Fujian 2011 Program (2015-75). We thank K. Shuai, H. Goto, and H. Shimada for technical assistance, and UCLA-FAFU (Fujian Agriculture and Forestry University) Joint Research Center on Plant Proteomics, Haixia Institute of Science and Technology, and Fujian Provincial Key Laboratory of Haixia Applied Plant Systems Biology for institutional support.

SUPPLEMENTARY MATERIALS

www.sciencemag.org/content/354/6310/343/suppl/DC1
Materials and Methods
Figs. S1 to S12
Tables S1 and S2
References (*30*–*38*)

18 April 2016; accepted 29 August 2016
10.1126/science.aaf9030

MICROBIOLOGY

Intercellular communication and conjugation are mediated by ESX secretion systems in mycobacteria

Todd A. Gray,[1,2]* Ryan R. Clark,[1] Nathalie Boucher,[1] Pascal Lapierre,[1] Carol Smith,[1] Keith M. Derbyshire[1,2]*

Communal bacterial processes require intercellular communication mediated by secretion systems to coordinate appropriate molecular responses. Intercellular communication has not been described previously in mycobacteria. Here we show that the ESX secretion-system family member ESX-4 is essential for conjugal recipient activity in *Mycobacterium smegmatis*. Transcription of *esx4* genes in the recipient requires coculture with a donor strain and a functional ESX-1 apparatus in the recipient. Conversely, mutation of the donor ESX-1 apparatus amplifies the *esx4* transcriptional response in the recipient. The effect of ESX-1 on *esx4* transcription correlates with conjugal DNA transfer efficiencies. Our data show that intercellular communication via ESX-1 controls the expression of its evolutionary progenitor, ESX-4, to promote conjugation between mycobacteria.

Mycobacteria have elaborate cell envelopes and use ESX secretion systems to transport substrates across their diderm cell structure (*1*). Mycobacteria encode as many as five paralogous *esx* loci (*2*). Each *esx* locus encodes components for its own membrane transporter, secretion substrates, powering adenosine triphosphatase (ATPase), and other proteins that contribute structural or regulatory functions. Although they are homologous, the ESX conserved components (*ecc*) encoded by each locus are specific to their individual secretory apparatus (*3*) and are not functionally redundant, as phenotypes arise from mutations in individual paralogs. ESX secretion activity is required for virulence in pathogenic mycobacteria (*4*–*6*). However, the full range of functions of the various *esx* loci remains unknown.

[1]Wadsworth Center, New York State Department of Health, P.O. Box 22002, Albany, NY 12201-2002, USA. [2]Department of Biomedical Sciences, University at Albany, State University of New York, Albany, NY 12201-02002, USA.
*Corresponding author. Email: todd.gray@health.ny.gov (T.A.G.); keith.derbyshire@health.ny.gov (K.M.D.)

Mycobacterium smegmatis is a fast-growing saprophytic and nonpathogenic species that has been used as a model for slow-growing pathogenic species (*7*). *M. smegmatis* has three *esx* loci that encode the ESX-1, ESX-3, and ESX-4 secretion apparatuses. In *M. smegmatis*, the ESX-1 apparatus is required for distributive conjugal transfer (DCT), a distinct gene transfer process that occurs between independent and genetically distinct donor and recipient strains and results in progeny with mosaic genomes (fig. S1) (*8*–*11*). Mutations that inactivate ESX-1 in either the donor or recipient strains of *M. smegmatis* alter conjugal DNA transfer efficiencies. A direct model, in which ESX-1 is proposed to serve as the conduit for DNA traversing from the donor strain into the recipient, is ruled out by the finding that *esx1* mutations in the donor strain increase DNA transfer efficiencies up to 100-fold (*9*). Conversely, ESX-1 mutations in the recipient reduce DNA transfer to undetectable levels (*8*). Recent findings further show that genes determining donor or recipient mating identity in DCT have been mapped to a cluster of six of the 25 *esx1* genes (*11*). The disparate roles for the various ESX secretion apparatuses, in both slow- and fast-growing mycobacteria, indicate that they mediate secretion of substrates that function in diverse pathways.

The *esx4* loci appear to encode only the essential core components of a functional ESX apparatus and lack *eccA* and *espG* genes that are functionally important for substrate secretion and processing in other ESX systems (*12*, *13*). This observation and the absence of any identified activity for ESX-4 led to the speculation that it is a vestigial locus (*5*). Loci encoding ESX-4 secretion systems are also found in other Actinobacteria and Firmicutes, which suggests that ESX-4 is the progenitor ESX (*2*, *3*). In spite of its ancestral status, conserved composition, and broad distribution, a functional role for ESX-4 has not been identified.

Here we report mapping of a transposon insertion in the recipient *esx4* locus that abolished conjugation (Fig. 1). The transposon inserted into the recipient ortholog of *Msmeg_1536*, encoding a dedicated Ftsk-SpoIIIE-ATPase, $EccC_4$ (the subscript "4" indicates the associated *esx* locus), whose paralogs in other *esx* loci are required for function of their respective ESX apparatus (*1*, *14*). To ensure that the transposon insertion resulted in a null phenotype, we created a precise deletion of $eccC_4$ in the recipient, and it too was defective for DCT (Fig. 1). To formally rule out any possibility of ESX-4 secretion activity, we created a precise deletion of *Msmeg_1535*, encoding the ESX-4 transporter, $EccD_4$. The recipient $EccD_4$ mutant was also transfer-defective (Fig. 1). Deletion of $eccC_4$ or $eccD_4$ from the donor strain, however, did not abrogate conjugation (Fig. 1). This recipient-specific requirement for ESX-4 is also seen with *esx1* mutants in DCT, although the increase in transfer efficiency seen with ESX-1 donor mutants was not evident with the loss of ESX-4 in the donor.

Only one gene is exclusive to *esx4* (Fig. 1B). *Msmeg_1537* is of unknown function and is conserved in position in all *esx4* loci, but homologs are not found in other paralogous *esx* loci. The conserved presence of this gene within the *esx4* locus led us to hypothesize that it is necessary for ESX-4 function. We created a deletion mutant of *Msmeg_1537* in the recipient strain and found that this mutant strain was also defective for DCT, producing no transconjugants. Complementation by ectopic expression of *Msmeg_1537* restored conjugation (Fig. 1).

Together, these data show that ESX-4 is essential for DCT in the recipient but not the donor

Downloaded from http://science.sciencemag.org/ on October 20, 2016

and that DCT is a sensitive and reliable assay for ESX-4 function. Thus, ESX-1 and ESX-4 have nonredundant roles in the same biological pathway. ESX-4 function cannot compensate for ESX-1 mutations and vice versa. Although the traditional *oriT*-based conjugation systems have evolved as a donor function encoded by a specific mobile element for self-propagation, all of the genes that have thus far been identified as necessary for mycobacterial DCT are recipient-specific.

Conjugation is a tightly regulated biological process that requires coordinated gene expression (*15*–*17*). We hypothesized that a subset of genes involved in DCT would respond to the presence of the opposite mating type. We used RNA profiling to detect key transcriptional programs that were activated or silenced upon coculture of donor and recipient strains. The many single-nucleotide polymorphisms (SNPs) between donor and recipient genomes act as strain-specific identifiers for the mRNAs and allowed us to perform strain-specific expression profiling (Fig. 2A). cDNA libraries were prepared from mRNA isolated from donor and recipient cells grown under mating conditions in either monoculture or coculture (fig. S2A). After library sequencing, reads were mapped back to each reference genome, and the embedded SNPs were used to identify which strain produced the mapped read. All genes were evaluated for their transcript levels under mating conditions relative to their levels from monoculture to identify the transcripts that responded to the presence of the opposite mating type (fig. S3).

During coculture of wild-type (WT) *M. smegmatis* strains, one of the most highly induced transcripts was from the *esx4* locus (Fig. 2B, fig. S2B, and table S1). *esx4* transcripts were elevated only in the recipient strain, as can be observed in the heat map of *esxUT* (Fig. 2B), the tandem gene pair encoding the primary WXG100 secretion substrates of ESX-4. Notably, the paralogous *esx1* and *esx3* WXG100 genes—*esxBA* and *esxGH*, respectively—did not transcriptionally respond in either strain to coculture with their mating partner (Fig. 2B). Therefore, coculture of donor and recipient strains specifically increased transcript levels of a recipient locus required for conjugation. The specific conditions required for the expression of *esx4* locus genes (in this case, coculture of a mating pair) may explain why identification of ESX-4 expression and function has been elusive. Overexpression of the sigma factor, SigM, has been associated with increased transcription of *esxUT* in *M. tuberculosis* (*18*, *19*), but our *M. smegmatis* DCT RNA sequencing (RNA-seq) analyses detected no transcriptional change in *sigM* or conserved genes of its regulon.

We then tested whether ESX-1 function affected transcriptional profiles in DCT mating conditions. The *esx1*-encoded Ftsk-SpoIIIE-ATPase ortholog of $eccC_4$ (*1*), $eccC_{b1}$, was deleted in the donor and recipient strains for use as mating partners with WT strains. Coculture of the $\Delta eccC_{b1}$ donor with a WT recipient induced transcription of the recipient WT *esx4* locus (Fig. 2B), as expected for mutated ESX-1 donors, which are known to perform DCT (*9*). In contrast, the pairing of the WT donor with the $\Delta eccC_{b1}$ recipient failed to induce *esx4* transcription in this recipient strain (Fig. 2B). ESX-1 function in the recipient strain is required for DCT (*8*). Therefore, the recipient *esx4* locus transcriptionally responds only in conjugation-proficient mating pairs. Our RNA-seq analyses show that recipient *esx4* gene transcripts are induced only upon coculture with the donor strain and that the induction requires a functional recipient ESX-1 secretion system.

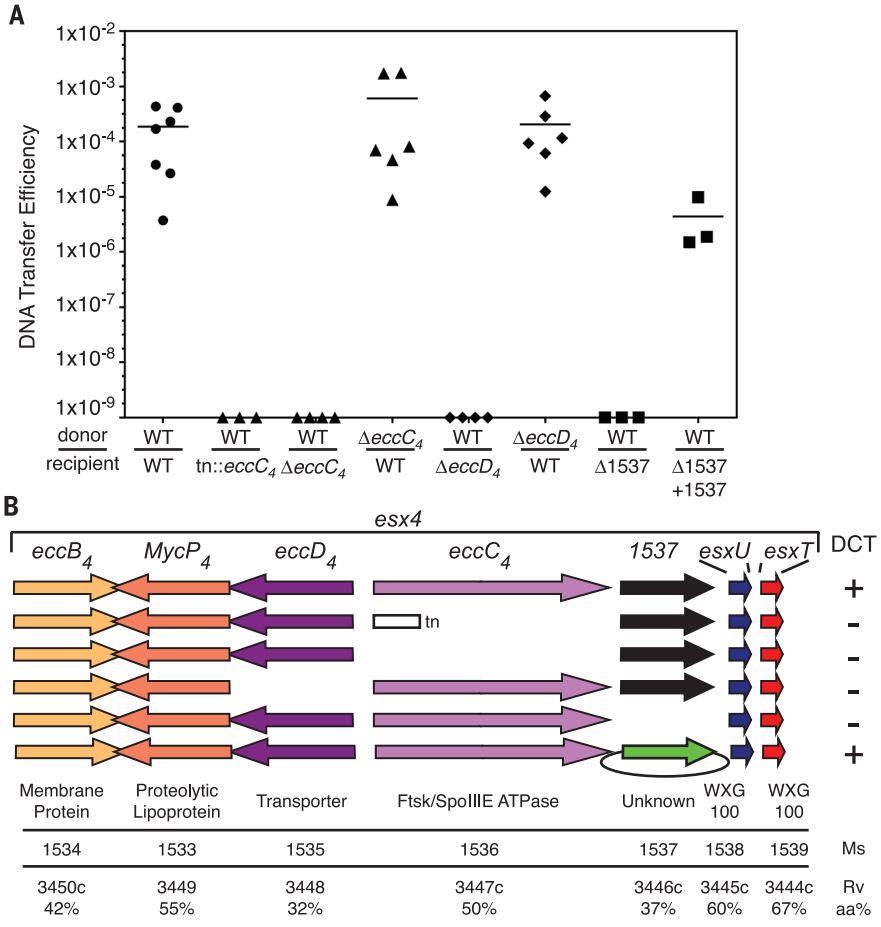

Fig. 1. Recipient ESX-4 is required for mycobacterial conjugation. (**A**) DNA transfer efficiencies (transconjugants per donor cell) show that DCT requires an intact *esx4* locus in the recipient strain. Transconjugants were not recovered in matings that lacked a recipient ESX-4 component. Mating-pair genotypes are indicated for donor and recipient, above and below the line, respectively. (**B**) Schematic showing the conserved gene content and order of *esx4* loci. ESX nomenclature of the encoded proteins is shown above the arrows (*ecc* designates an ESX essential core protein). The gene specific to *esx4* is indicated by its *M. smegmatis* gene name, *Msmeg_1537*. Recipient locus mutations are summarized by a transposon insertion (tn), a deletion (the absence of an arrow), or a complementing plasmid (green arrow with oval). *M. smegmatis* (Ms) and *M. tuberculosis* (Rv) gene numbers and amino acid identities (aa%) and the putative function of the encoded proteins are shown below each gene.

We used the highly responsive bicistronic *esxUT* transcript in quantitative reverse transcription polymerase chain reaction (qRT-PCR) assays to independently validate and quantify our global SNP-specific RNA-seq profiles (fig. S2B). DCT mating assays were repeated, with duplicate samples being processed for conjugal DNA transfer efficiency (Fig. 3A) and qRT-PCR (Fig. 3B). We used a polymorphic BstUI cleavage site to show that the induced *esxUT* transcript is exclusively from the recipient strain (Fig. 3C). The WT mating pair showed a 30-fold increase of the *esxUT* transcript relative to parental monocultures (Fig. 3B). The ESX-1 dependence in the recipient was corroborated, as *esxUT* was increased less than six-fold in the $\Delta eccC_{b1}$ mutant. This level was slightly elevated relative to our RNA-seq data (Fig. 2B), although it is unclear whether this is normal variation in the assay, the *rpoB* qRT-PCR internal control, or an unknown factor. The accentuated recipient *esxUT* transcriptional response to the ESX-1 mutant donor strain indicated by RNA-seq data (Fig. 2B) was corroborated by qRT-PCR, which showed a 221-fold induction (Fig. 3B). Thus, coculture induction of ESX-4 corresponds to the reported effects of ESX-1 on conjugation: Recipient ESX-1 mutants do not induce recipient ESX-4 and do not produce transconjugants (*8*), whereas donor ESX-1 mutants hyperinduced recipient ESX-4 and are hyperconjugative (*9*). These results indicate that ESX-1 acts upstream of

Downloaded from http://science.sciencemag.org/ on October 20, 2016

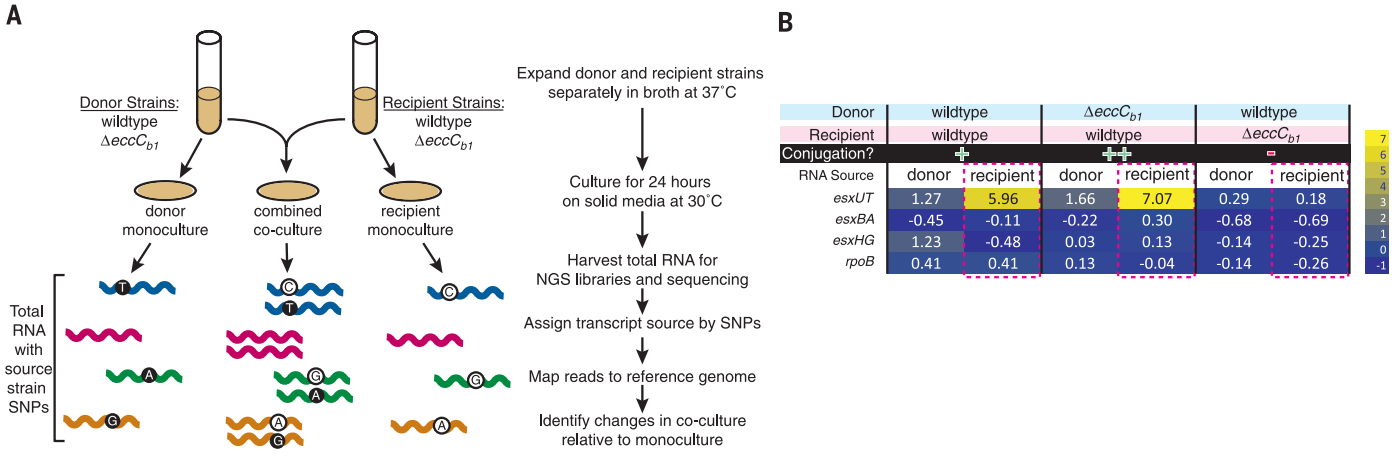

Fig. 2. Coculture with donor induces recipient *esx4* transcript levels and requires recipient ESX-1 activity. (**A**) Experimental design for SNP-guided RNA-seq of DCT. The ESX-1$_{mut}$ strains have targeted deletions of *eccC$_{b1}$*, encoding the ATPase required for ESX-1 secretion activity and required in the recipient for conjugation. The four strains were grown individually and in mixed cultures of WT × WT, WT × ESX-1$_{mut}$, or ESX-1$_{mut}$ × WT. Conditions, processing, and analysis are as indicated at right. (**B**) Heat-map cells of WXG100 genes from *esx4* (*esxUT*), *esx1* (*esxBA*), and *esx3* (*esxHG*), with changes upon coculture shown as log$_2$ insets. For each mating, the donor and recipient genotypes are shown, and the conjugal mating proficiencies are indicated. A housekeeping gene (*rpoB*) is included as an independent expression control.

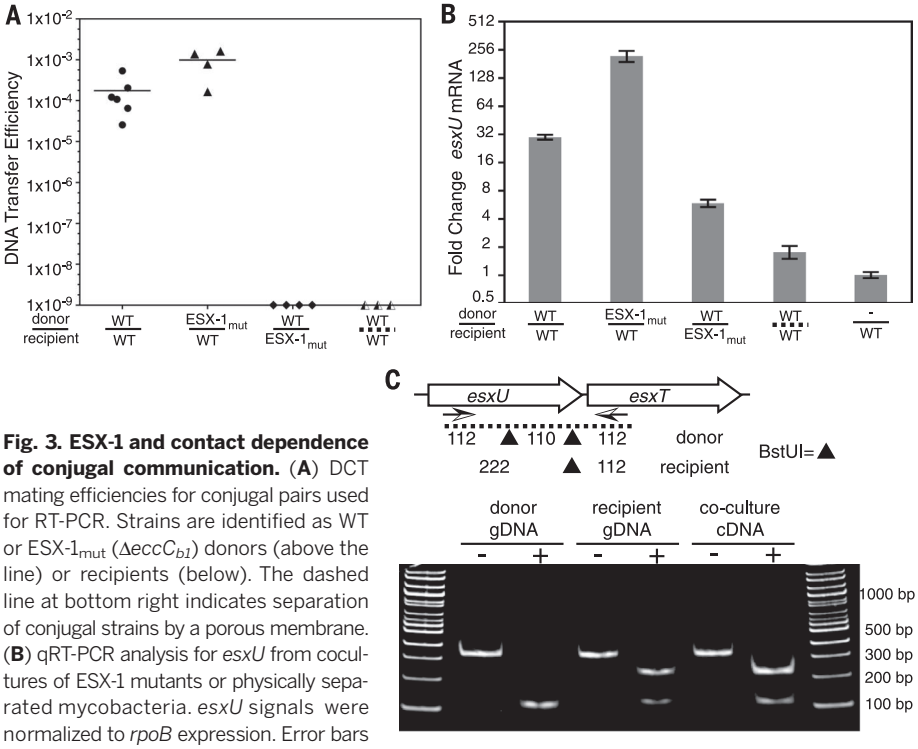

Fig. 3. ESX-1 and contact dependence of conjugal communication. (**A**) DCT mating efficiencies for conjugal pairs used for RT-PCR. Strains are identified as WT or ESX-1$_{mut}$ (Δ*eccC$_{b1}$*) donors (above the line) or recipients (below). The dashed line at bottom right indicates separation of conjugal strains by a porous membrane. (**B**) qRT-PCR analysis for *esxU* from cocultures of ESX-1 mutants or physically separated mycobacteria. *esxU* signals were normalized to *rpoB* expression. Error bars indicate SD (*n* = 3). (**C**) RT-PCR and restriction fragment length polymorphism analysis of BstUI fragments identifies recipient origin of the elevated *esxUT* transcripts. Arrows below the genetic map indicate the primers used for amplification, and the sites of BstUI cleavage are indicated by triangles. Monoculture genomic DNA (gDNA) controls show the expected parental patterns upon digestion (+) with BstUI. Digestion of coculture-derived cDNA shows a recipient pattern. bp, base pairs.

ESX-4 in DCT, directing the induction of *esx4* gene expression that results from mating-pair interactions.

The transfer of DNA between participating cells during DCT clearly requires physical contact, yet the communication might occur by diffusible signals. We performed coculture under typical DCT mating conditions. However, we separated the donor and recipient strains with a 0.45-μm filter membrane intended to allow transit of soluble signaling molecules but prevent cell-cell contact. qRT-PCR analysis revealed that recipient cells cultured with this porous separation did not show an *esxUT* transcriptional response to the underlying donor strain (Fig. 3B). These data indicated that direct cell-cell contact is needed to initiate the *esx4* transcriptional response. We speculate that ESX-1 secretes cell-surface mating identifiers, receptor proteins, and/or tethering scaffolds. One possibility consistent with our data is that ESX-1 secretes a cell surface receptor in both strains: In the recipient, a yet unknown ligand binding to this receptor initiates a signal cascade that induces ESX-4 necessary for DCT (fig. S4). Thus, disabling ESX-1 function in the donor strain would prevent its receptor secretion from competing for ambient ligand, resulting in hyperactivation of the recipient *esx4* locus. Candidates for potential involvement are encoded by the subset of *esx1* genes that constitute the mating identity locus (*mid*) (*11*).

Strain-specific RNA-seq during coculture also identified expression changes in genes that are not involved in DCT. Thus, coculture responses between these mycobacterial strains may not be limited to conjugation. Some of the largest transcriptional changes were dependent on ESX-1. The concept that ESX systems function in intercellular communication among mycobacteria has implications for other mycobacterial species and for intercellular communication in infection.

REFERENCES AND NOTES

1. A. M. Abdallah *et al.*, *Nat. Rev. Microbiol.* **5**, 883–891 (2007).
2. N. C. Gey van Pittius *et al.*, *Genome Biol.* **2**, research0044.1 (2001).
3. W. Bitter *et al.*, *PLOS Pathog.* **5**, e1000507 (2009).
4. R. Simeone, D. Bottai, R. Brosch, *Curr. Opin. Microbiol.* **12**, 4–10 (2009).
5. E. J. Stoop, W. Bitter, A. M. van der Sar, *Trends Microbiol.* **20**, 477–484 (2012).
6. T. Tan, W. L. Lee, D. C. Alexander, S. Grinstein, J. Liu, *Cell. Microbiol.* **8**, 1417–1429 (2006).
7. M. U. Shiloh, P. A. DiGiuseppe Champion, *Curr. Opin. Microbiol.* **13**, 86–92 (2010).

Downloaded from http://science.sciencemag.org/ on October 20, 2016

8. A. Coros, B. Callahan, E. Battaglioli, K. M. Derbyshire, *Mol. Microbiol.* **69**, 794–808 (2008).
9. J. L. Flint, J. C. Kowalski, P. K. Karnati, K. M. Derbyshire, *Proc. Natl. Acad. Sci. U.S.A.* **101**, 12598–12603 (2004).
10. L. M. Parsons, C. S. Jankowski, K. M. Derbyshire, *Mol. Microbiol.* **28**, 571–582 (1998).
11. T. A. Gray, J. A. Krywy, J. Harold, M. J. Palumbo, K. M. Derbyshire, *PLOS Biol.* **11**, e1001602 (2013).
12. P. A. DiGiuseppe Champion, M. M. Champion, P. Manzanillo, J. S. Cox, *Mol. Microbiol.* **73**, 950–962 (2009).
13. E. N. Houben, K. V. Korotkov, W. Bitter, *Biochim. Biophys. Acta* **1843**, 1707–1716 (2014).
14. S. E. Converse, J. S. Cox, *J. Bacteriol.* **187**, 1238–1245 (2005).
15. G. Koraimann, M. A. Wagner, *Front. Cell. Infect. Microbiol.* **4**, 54 (2014).
16. P. K. Singh, W. J. Meijer, *FEMS Microbiol. Lett.* **358**, 119–128 (2014).
17. G. M. Dunny, R. P. Berntsson, *J. Bacteriol.* **198**, 1556–1562 (2016).
18. N. Agarwal, S. C. Woolwine, S. Tyagi, W. R. Bishai, *Infect. Immun.* **75**, 452–461 (2007).
19. S. Raman *et al.*, *J. Bacteriol.* **188**, 8460–8468 (2006).

ACKNOWLEDGMENTS

We thank J. Wade for valuable discussions and technical assistance and the Wadsworth Center Core Facilities for Media and Bioinformatics. Primary data can be found in the supplementary materials, and RNA-seq data sets have been deposited at the National Center for Biotechnology Information with accession number SRP080861. This work was supported by National Institute of Allergy and Infectious Diseases grants R01AI097191 and R21AI07258 (to K.M.D. and T.A.G.). R.R.C. generated strains, performed conjugation, and carried out RT-PCR experiments; N.B. identified the initial transposon mutant, constructed mutants, and performed conjugation assays; C.S. prepared RNA-seq libraries; P.L. analyzed RNA-seq data; K.M.D. contributed study design and data analyses; T.A.G. contributed study design, targeted mutations, and data analyses; and K.M.D. and T.A.G. wrote the manuscript.

SUPPLEMENTARY MATERIALS

www.sciencemag.org/content/354/6310/347/suppl/DC1
Material and Methods
Figs. S1 to S4
Tables S1 and S2
References (*20*–*22*)

6 May 2016; accepted 31 August 2016
10.1126/science.aag0828

EBOLAVIRUSES

A "Trojan horse" bispecific-antibody strategy for broad protection against ebolaviruses

Anna Z. Wec,[1]* Elisabeth K. Nyakatura,[2]* Andrew S. Herbert,[3]* Katie A. Howell,[4] Frederick W. Holtsberg,[4] Russell R. Bakken,[3] Eva Mittler,[1] John R. Christin,[5] Sergey Shulenin,[4] Rohit K. Jangra,[1] Sushma Bharrhan,[1] Ana I. Kuehne,[3] Zachary A. Bornholdt,[6] Andrew I. Flyak,[7] Erica Ollmann Saphire,[6,8] James E. Crowe Jr.,[7,9,10]† M. Javad Aman,[4]† John M. Dye,[3]† Jonathan R. Lai,[2]† Kartik Chandran[1]†

There is an urgent need for monoclonal antibody (mAb) therapies that broadly protect against Ebola virus and other filoviruses. The conserved, essential interaction between the filovirus glycoprotein, GP, and its entry receptor Niemann-Pick C1 (NPC1) provides an attractive target for such mAbs but is shielded by multiple mechanisms, including physical sequestration in late endosomes. Here, we describe a bispecific-antibody strategy to target this interaction, in which mAbs specific for NPC1 or the GP receptor–binding site are coupled to a mAb against a conserved, surface-exposed GP epitope. Bispecific antibodies, but not parent mAbs, neutralized all known ebolaviruses by coopting viral particles themselves for endosomal delivery and conferred postexposure protection against multiple ebolaviruses in mice. Such "Trojan horse" bispecific antibodies have potential as broad antifilovirus immunotherapeutics.

The development of therapeutics targeting Ebola virus (EBOV) and other filoviruses is a global health priority. The success of ZMapp—a cocktail of three monoclonal antibodies (mAbs) targeting the EBOV surface glycoprotein GP—in reversing Ebola virus disease in nonhuman primates (NHPs) has underscored the promise of antiviral immunotherapy (*1*). However, most available mAbs have a narrow antiviral spectrum, because they recognize variable surface-exposed GP epitopes (*2*). ZMapp protects against EBOV but not against other filoviruses with known epidemic potential, including the ebolaviruses Bundibugyo virus (BDBV) and Sudan virus (SUDV) and the more divergent marburgviruses. Given the scientific and logistical challenges inherent in developing a separate mAb cocktail for each filovirus, as well as the need for preparedness against newly emerging or engineered viral variants, broadly protective antifilovirus immunotherapies are highly desirable. A few mAbs have shown cross-neutralization and protection in rodents, indicating that cross-species protection by a single molecule is possible; however, such antibodies are rare (*3*–*8*).

An unusual feature of cell entry by filoviruses is the proteolytic cleavage of GP in endosomes to reveal "cryptic" epitopes (*9*, *10*), including the receptor-binding site (RBS) that engages the critical intracellular receptor, Niemann-Pick C1 (NPC1) (fig. S1) (*11*–*18*). Engagement of NPC1's second luminal domain, NPC1-C, by this highly conserved RBS in cleaved GP (GP_{CL}) is required for cell entry and infection by all filoviruses (*11*, *19*–*21*). Consistent with this, MR72, an RBS-specific mAb isolated from a Marburg virus (MARV) disease survivor, blocked GP_{CL}-NPC1 interaction in vitro and broadly neutralized viruses bearing in vitro cleaved GP_{CL} (*15*, *22*, *23*). However, MR72 failed to neutralize infection by uncleaved ebolaviruses, likely because it could not gain access to late endosomes, where the GP_{CL} RBS becomes unmasked (*15*). Therefore, the development of broadly protective immunotherapies targeting the GP_{CL}-NPC1 interaction is challenged by the endosomal sequestration of this virus-receptor complex.

We envisioned a bispecific antibody (bsAb)–engineering strategy to block intracellular GP_{CL}-NPC1 interaction by a "Trojan horse" mechanism. We reasoned that, by coupling receptor or RBS–targeting mAbs to a delivery mAb directed against a broadly conserved epitope in uncleaved GP, virions themselves could be coopted to transport bsAbs to the appropriate endosomal compartments (Fig. 1, A and B). To block the filovirus-receptor interaction, we chose mAbs targeting both its viral and host facets: MR72, a human mAb that recognizes the GP_{CL} RBS (above), and mAb-548, a novel murine mAb that engages human NPC1-C. mAb-548 bound with picomolar affinity to an NPC1-C epitope that overlaps the GP_{CL}-binding interface and blocked GP_{CL}–NPC1-C association in vitro at pH 5.5, the presumptive pH of late endosomes (figs. S1 and S2). mAb-548 resembled MR72 in its lack of neutralizing activity against uncleaved viruses (Fig. 2, A and B, and fig. S6), likely because NPC1 is absent from the cell surface (*11*, *24*). To deliver mAb-548 and MR72 to endosomes, we selected the macaque mAb FVM09, which recognizes a conserved linear

[1]Department of Microbiology and Immunology, Albert Einstein College of Medicine, Bronx, NY 10461, USA. [2]Department of Biochemistry, Albert Einstein College of Medicine, Bronx, NY 10461, USA. [3]U.S. Army Medical Research Institute of Infectious Diseases, Fort Detrick, MD 21702, USA. [4]Integrated Biotherapeutics Inc., Gaithersburg, MD 20878, USA. [5]Department of Cell Biology, Albert Einstein College of Medicine, Bronx, NY 10461, USA. [6]Department of Immunology and Microbial Science, The Scripps Research Institute, La Jolla, CA 10550, USA. [7]Department of Pathology, Microbiology and Immunology, Vanderbilt University, Nashville, TN 37235, USA. [8]The Skaggs Institute for Chemical Biology, The Scripps Research Institute, La Jolla, CA 10550, USA. [9]Department of Pediatrics, Vanderbilt University, Nashville, TN 37232, USA. [10]Vanderbilt Vaccine Center, Vanderbilt University, Nashville, TN 37232, USA.
*These authors contributed equally to this work. **†Corresponding author. Email: kartik.chandran@einstein.yu.edu (K.C.); jon.lai@einstein.yu.edu (J.R.L.); john.m.dye1.civ@mail.mil (J.M.D.); javad@integratedbiotherapeutics.com (M.J.A.); james.crowe@vanderbilt.edu (J.E.C.)**

Downloaded from http://science.sciencemag.org/ on October 20, 2016

epitope in the GP glycan cap of all known ebolaviruses (Fig. 1A and fig. S4) (*8*). FVM09 does not neutralize infection and confers limited in vivo protection against EBOV (*8*).

The heavy- and light-chain variable domains (V_H and V_L, respectively) of FVM09 were fused to mAb-548 and MR72 by using the dual–variable domain immunoglobulin (DVD-Ig) design strategy (*25*). The DVD-Ig format was chosen as a test case because it allows bivalent binding of both combining sites but does not use long polypeptide linkers that may be susceptible to proteolysis or immunogenic presentation. The FVM09~548 and FVM09~MR72 DVD-Igs could be readily isolated from transiently transfected human embryonic kidney 293 (HEK293) cells (fig. S3A). Size-exclusion chromatography–multiangle light scattering indicated a monodisperse population of monomers, with some higher aggregate present (fig. S3, B and C). Each DVD-Ig could bind to EBOV GP via the FVM09 "outer" variable domains, with no loss of affinity relative to the parent FVM09 immunoglobulin G (IgG), as determined by biolayer interferometry (BLI) (Fig. 1C and table S1). FVM09~548 could recognize human NPC1-C, by means of its "inner" variable domains, with a subpicomolar equilibrium dissociation constant (K_D). The MR72 variable domains also retained subnanomolar affinity toward GP_{CL} in the DVD-Ig format. Two-phase binding studies, in which each DVD-Ig was first exposed to EBOV GP and then to NPC1-C or GP_{CL} (Fig. 1D), indicated that there were no steric restrictions to engagement of both combining sites.

We tested the DVD-Igs for their capacity to neutralize infection in human cells by recombinant vesicular stomatitis viruses bearing EBOV GP (rVSV–EBOV GP) or control nonfilovirus glycoproteins derived from VSV and Andes hantavirus (Fig. 2, A and B, and fig. S5) (*26*). Both FVM09~548 and FVM09~MR72 specifically and potently neutralized rVSV–EBOV GP, whereas the parental mAbs FVM09, mAb-548, and MR72 had little or no neutralizing activity. Equimolar mixtures of the "delivery" IgG, FVM09, with each receptor-RBS–targeting IgG (mAb-548 or MR72) also did not neutralize infection (Fig. 2, A and B); this indicated that DVD-Ig antiviral activity requires the physical linkage of delivery and receptor-RBS–binding specificities. Overall, the DVD-Ig half-maximal inhibitory concentration (IC_{50}) values were in the nanomolar range, similar to the measured K_D of the FVM09-GP complex but higher than those of the mAb-548–NPC1-C and MR72-GP_{CL} complexes.

The GP_{CL}-NPC1 interaction is conserved among filoviruses (*11*, *15*, *21*, *27*, *28*), and thus, we postulated that the DVD-Igs would exhibit broad neutralizing activity. rVSVs bearing GP proteins from the four other ebolaviruses were sensitive to neutralization by both DVD-Igs, whereas rVSV–MARV GP was resistant (Fig. 2, C, D, and G), consistent with the known specificity of FVM09 toward ebolaviruses (*8*). We next tested the DVD-Igs against authentic EBOV, BDBV, and SUDV (Fig. 2, E and F). Each ebolavirus was neutralized by both receptor- and RBS-targeting DVD-Igs but not by the individual parent IgGs (Fig. 2G and fig. S6).

The success of antibody therapeutics has fueled the development of a panoply of optimized bsAb architectures, several of which (including the DVD-Ig) are in clinical trials (*29*). To explore the generality of our strategy to other formats, we generated an FVM09*MR72 "asymmetric IgG" using the DuoBody platform (figs. S7 and S8) (*30*). FVM09*MR72 broadly neutralized rVSVs bearing ebolavirus GPs, albeit with reduced potency against SUDV GP, possibly because of its loss of bivalent recognition of GP and/or GP_{CL}. Nonetheless, these results illustrate that endosomal targeting of the ebolavirus-receptor interaction is amenable to other bispecific-antibody formats.

Our observation that bsAbs combining two nonneutralizing antibodies could confer potent neutralization implied critical roles for both binding specificities. This hypothesis is supported by three pieces of evidence. First, the activity of the DVD-Igs against rVSV–EBOV GP particles containing two point mutations in the FVM09 epitope was greatly reduced (Fig. 3A and fig. S9).

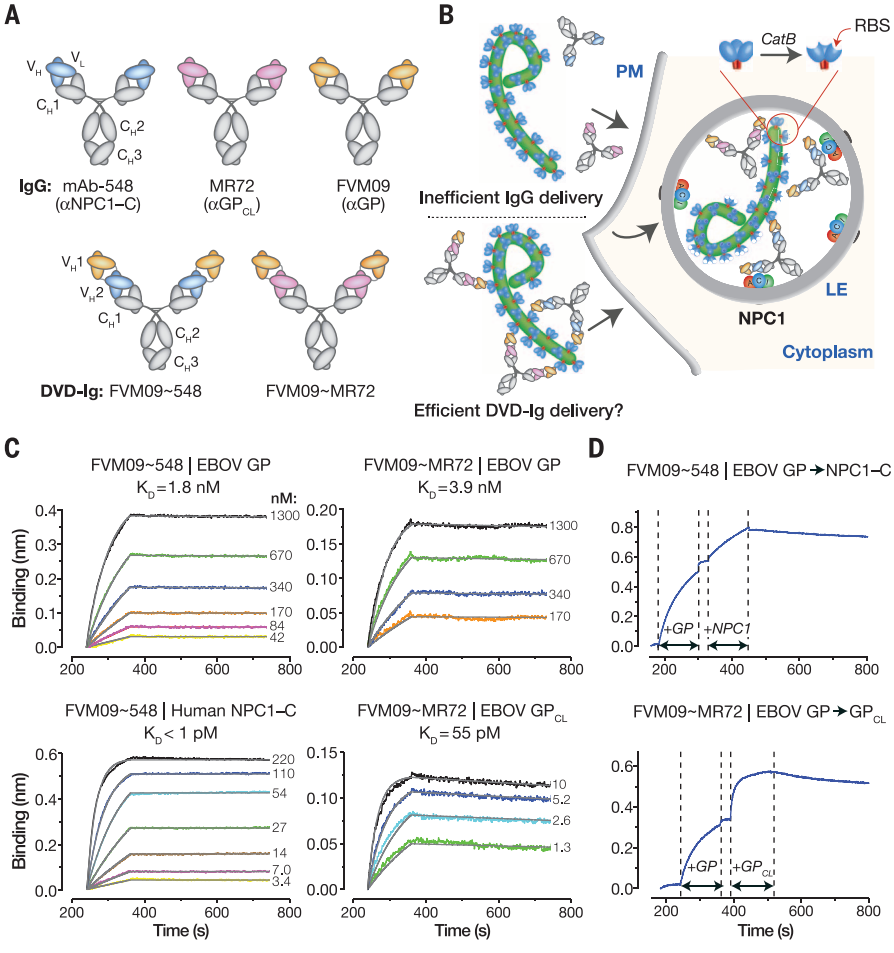

Fig. 1. Dual–variable domain Ig (DVD-Ig) molecules combining extracellular delivery and endosomal receptor–RBS–binding specificities can recognize both of their respective antigens. (**A**) Schematic of mAb-548 and MR72 endosomal receptor or RBS–specific mAbs and FVM09 GP–specific delivery mAb (top row), as well as DVD-Igs engineered to combine them (bottom row). (**B**) A hypothetical mechanism for delivery of DVD-Igs (bottom), but not parent IgGs (top), to the endosomal sites of GP_{CL}-NPC1 interaction. LE, late endosomes. (**C**) Kinetic binding curves for DVD-Ig–antigen interactions were determined by BLI. FVM09~548 (left) and FVM09~MR72 (right) were loaded onto probes, which were then dipped in analyte solutions (FVM09~548: EBOV GP and human NPC1-C; FVM09~MR72: EBOV GP and GP_{CL}). Gray lines show curve fits to a 1:1 binding model. See table S1 for kinetic binding constants. (**D**) Two-phase binding experiments for the DVD-Igs by BLI. Each DVD-Ig–bearing probe was sequentially dipped in analyte solutions containing EBOV GP and then NPC1-C (FVM09~548), or EBOV GP and then GP_{CL} (FVM09~MR72). (C) and (D) Representative curves from two independent experiments are shown.

Downloaded from http://science.sciencemag.org/ on October 20, 2016

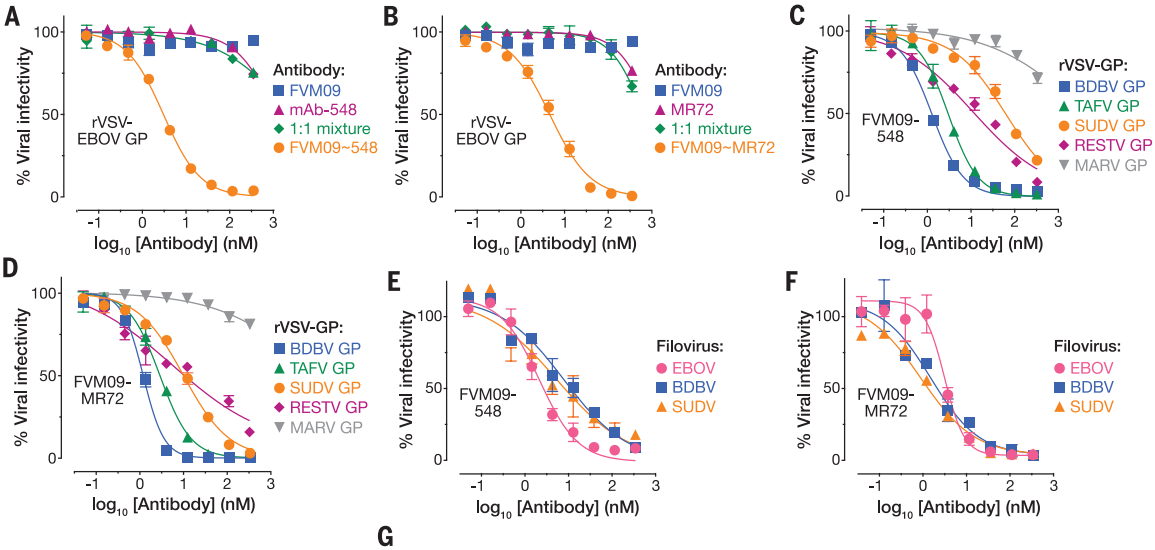

Fig. 2. DVD-Igs, but not parent IgGs or their mixtures, have broad neutralizing activity against ebolaviruses. (**A** to **D**) Neutralization of rVSVs encoding enhanced green fluorescent protein (eGFP) and bearing filovirus GP proteins in human U2OS osteosarcoma cells. Virions were preincubated with increasing concentrations of each parent IgG, DVD-Ig, or equimolar mixtures of parent IgGs (e.g., FVM09 + mAb-548) (1:1 mixture) and then exposed to cells for 12 to 14 hours at 37°C. Infection was measured by automated counting of $eGFP^+$ cells and normalized to infection obtained in the absence of Ab. TAFV, Taï forest virus; RESTV, Reston virus; MARV, Marburg virus. (**E** to **F**) Neutralization of authentic filoviruses in human U2OS osteosarcoma cells, measured in microneutralization assays. Infected cells were immunostained for viral antigen at 48 hours postinfection and enumerated by automated fluorescence microscopy. (A) to (F) Averages ± SD for four to six technical replicates pooled from two or three independent experiments. (**G**) Data in (A) to (F) were subjected to nonlinear regression analysis to derive Ab concentrations at half-maximal neutralization (IC_{50} ± 95% confidence intervals for nonlinear curve fit). *IC_{50} values derived from curves that did not reach 90% neutralization at the highest concentration tested in the experiments are shown.

G

Antibody	rVSV-GP IC_{50} (nM) (±95% CI)						Filovirus IC_{50} (nM) (±95% CI)		
	EBOV	BDBV	TAFV	SUDV	RESTV	MARV	EBOV	BDBV	SUDV
FVM09~548	2.9±0.2	1.3±0.1	3.0±0.3	60±10*	12±3*	>350	2.1±0.4	8±3	5±2
FVM09~MR72	4.7±0.5	1.1±0.1	2.9±0.3	10±1	6±1*	>350	3.6±0.7	1.0±0.2	1.8±0.7

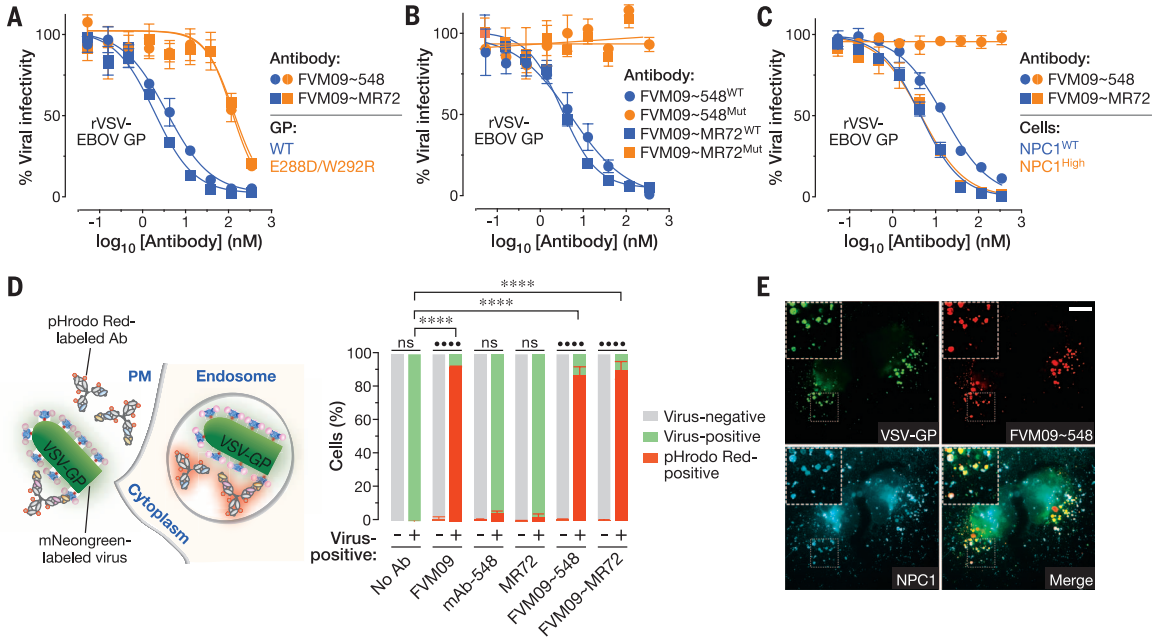

Fig. 3. Roles of delivery and endosomal receptor–RBS–targeting specificities in ebolavirus neutralization by DVD-Igs. (**A**) Neutralizing activity of DVD-Igs against rVSVs bearing WT GP or a GP(E288D/W292R) mutant, in which Asp replaces Glu^{288} and Arg replaces Trp^{292} (see fig. S9). (**B**) Neutralizing activity of mutant DVD-Igs bearing mAb-548 or MR72 combining sites with mutations in the third V_H complementarity determining region ($FVM09\text{~}548^{Mut}$ and $FVM09\text{~}MR72^{Mut}$, respectively). (**C**) Neutralizing activity of DVD-Igs against rVSV–EBOV GP in U2OS cells bearing endogenous levels of NPC1 ($NPC1^{WT}$) or ectopically overexpressing NPC1 ($NPC1^{High}$). (A) to (C) Averages ± SD for six technical replicates pooled from two independent experiments. (**D**) Internalization of labeled Abs into cells in the absence or presence of viral particles. A schematic of the experiment is shown at the left. Parent IgGs and DVD-Igs covalently labeled with the acid-dependent fluorophore pHrodo Red were incubated with rVSV–EBOV GP particles and exposed to cells. $Virus^-$ Ab^+ and $virus^+$ Ab^+ populations were measured by flow cytometry. Averages ± SD for four technical replicates pooled from two independent experiments are shown. Group means for the percentage of Ab^+ cells were compared by two-factor analysis of variance (ANOVA) (see fig. S11). Šídák's post hoc test was used to compare the capacity of each Ab to internalize into $virus^-$ versus $virus^+$ cell populations ($^{****}P < 0.0001$; ns, not significant). Dunnett's post hoc test was used to compare the internalization of each Ab to that of the "no Ab" control in $virus^+$ cell populations ($^{****}P < 0.0001$; all other Ab versus no Ab comparisons were not significant). (**E**) Delivery of Abs to $NPC1^+$ endosomes. FVM09~548 was incubated with rVSV–EBOV GP particles and exposed to cells expressing an NPC1–enhanced blue fluorescent protein–2 fusion protein. Viral particles, Ab, and NPC1 were visualized by fluorescence microscopy (also see figs. S12 and S13). Representative images from two independent experiments are shown. Scale bar, 20 μm.

Downloaded from http://science.sciencemag.org/ on October 20, 2016

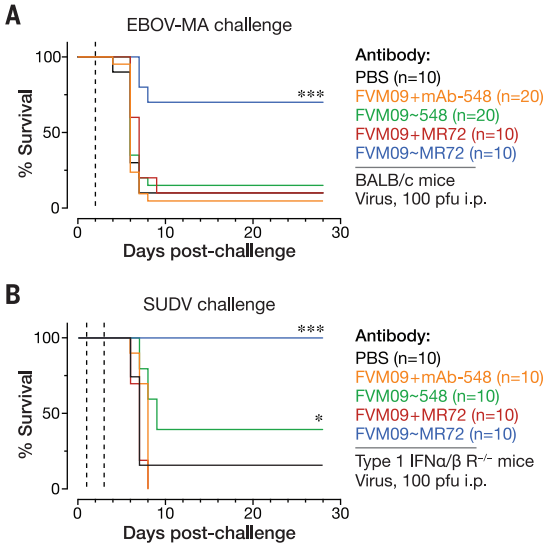

Fig. 4. FVM09~MR72 affords broad postexposure protection from lethal ebolavirus challenge. (**A**) BALB/c mice were challenged with mouse-adapted EBOV (EBOV-MA), and then treated with single doses of parent IgG mixtures [300 μg, ~15 mg per kilogram body weight (mg/kg)] or DVD-Igs (400 μg, ~20 mg/kg, adjusted for molecular weight), or vehicle (phosphate-buffered saline, PBS) at 2 days postchallenge. (**B**) Type 1 IFNα/β $R^{-/-}$ mice were challenged with WT SUDV and then treated with two doses of parent IgG mixtures (300 μg total per dose, ~15 mg/kg); DVD-Igs (400 μg per dose, ~20 mg/kg); or vehicle (PBS) 1 and 3 days post-challenge. "n" indicates the number of animals per group. Data from single cohorts are shown. Survival in each group was compared with that in the PBS group by log-rank (Mantel-Cox) test (*$P < 0.05$; ***$P < 0.001$); all other comparisons to the untreated group were not significant.

Second, DVD-Igs bearing mAb-548 and MR72 variable domains with mutations that abolish binding (FVM09~548^{Mut} and FVM09~$MR72^{Mut}$) lacked neutralizing activity (Fig. 3B). Third, FVM09~548 could not neutralize rVSV–EBOV GP infection in a cell line bearing supraphysiological levels of NPC1, likely because NPC1 overexpression saturates available mAb-548 combining sites (Fig. 3C). Viral neutralization by FVM09~MR72 was unaffected in NPC1-overexpressing cells, consistent with the higher affinity of the GP_{CL}-MR72 complex (55 pM) (table S1), relative to the GP_{CL}–NPC1-C complex (150 μM) (*16*).

We postulated that the bsAbs harness extracellular virions for their delivery to endosomal sites of filovirus-receptor interaction in the context of natural infection. Accordingly, we evaluated the internalization of DVD-Igs and their parent IgGs into cellular endosomes (Fig. 3D and figs. S10 and S11). Each Ab was covalently labeled with the acid-dependent fluorescent probe pHrodo Red and exposed to cells, either alone or following preincubation with fluorescent rVSV–EBOV GP particles (*19*, *26*). Cells were measured for both virus- and Ab-associated fluorescence by flow cytometry. Virus-negative cells displayed little Ab signal; this indicated that neither the DVD-Igs nor their parent IgGs could internalize into cells without virions. By contrast, virus-positive cells were strongly positive for the DVD-Igs but not for the parent mAb-548 and MR72 IgGs. Concordantly, only FVM09 and the DVD-Igs could efficiently colocalize with virions (Fig. 3E and fig. S12) or Ebola virus–like particles (VLPs) (fig. S13) in $NPC1^{+}$ late endosomes, where viral membrane fusion takes place (*19*, *31*). These results, together with the capacity of FVM09 to bind EBOV GP with high affinity between pH 5.5 and 7.5 (fig. S14 and table S1), suggest that virion-bsAb complexes remain associated in early endosomes and traffic together to late endosomes, where proteolytic removal of the GP glycan cap dislodges FVM09, and where mAb-548 and MR72 can engage their respective cellular and viral targets. Collectively, our findings support a two-step "deliver-and-block" mechanism for bsAb neutralization.

Finally, we evaluated the protective efficacy of the DVD-Igs in two murine models of lethal ebolavirus challenge. Because our prior experiments were conducted in human cells, we first tested DVD-Ig neutralization activity in murine NIH/3T3 cells (fig. S15). Whereas FVM09~MR72 retained full activity, FVM09~548 exhibited poor neutralization in murine cells (fig. S15, A and B). This could be readily explained by FVM09~548's reduced binding affinity for the murine NPC1 ortholog (fig. S15C) and consequent reduced capacity to block the GP_{CL}-NPC1 interaction (fig. S15E). The discrepancy between binding of mAb-548 to human and mouse NPC1 likely arises from species-dependent amino acid sequence differences in the mAb-548–binding region of NPC1-C (fig. S16). By contrast, this region in human NPC1-C is identical to those of rhesus macaques and crab-eating (cynomolgus) macaques (fig. S16), which provide the two NHP models of filovirus challenge currently in use. mAb-548 bound strongly to, and inhibited GP_{CL} interaction with, an NHP NPC1 ortholog derived from the mantled guereza, which also shares an identical mAb-548–binding region (fig. S15, D and F). Therefore, although host species–specific differences in NPC1 binding may affect FVM09~548's efficacy in rodents, they are unlikely to do so in NHPs and humans.

Both DVD-Igs were tested for their capacity to protect BALB/c mice when administered 2 days after a lethal challenge with EBOV-MA (Fig. 4A) (*32*). FVM09~MR72 afforded a high level of protection (70%) relative to the untreated group, whereas no significant survival was recorded for FVM09~548 and parent IgG mixtures. We also evaluated the DVD-Igs for postexposure protection against a lethal human SUDV isolate in the immunocompromised, type 1 interferon α/β receptor–deficient (IFNα/β $R^{-/-}$) mouse model (Fig. 4B) (*7*, *33*). FVM09~MR72 was fully protective, and FVM09~548 provided partial protection, relative to the untreated group. The limited in vivo efficacy of FVM09~548 was consistent with its reduced capacity to inhibit the GP_{CL}–murine NPC1 interaction (fig. S15). These findings provide evidence that a bsAb targeting the critical intracellular virus-receptor interaction can confer broad protection against lethal ebolavirus challenge, even under stringent conditions of postexposure treatment.

Recent antibody discovery efforts have demonstrated the existence of conserved GP surface epitopes that can elicit broadly reactive mAbs with cross-protective potential (*3*–*7*, *34*). Herein, we describe a complementary strategy to generate broadly protective Abs that target highly conserved epitopes at the intracellular filovirus-receptor interface, which are normally shielded from GP-specific mAbs. Because the cryptic epitope–targeting components of the bsAbs engineered in this study block endosomal receptor binding by all known filoviruses (*15*) (this study), next-generation molecules combining them with appropriate delivery mAbs of viral or cellular origin may afford coverage against all filoviruses, including newly emerging and engineered variants. This Trojan horse bispecific-antibody approach may also find utility against other viral pathogens known to use intracellular receptors [e.g., Lassa virus (*35*)], or more generally, to target entry-related virus structural rearrangements that occur only in the endolysosomal pathway.

REFERENCES AND NOTES

1. X. Qiu *et al.*, *Nature* **514**, 47–53 (2014).
2. C. D. Murin *et al.*, *Proc. Natl. Acad. Sci. U.S.A.* **111**, 17182–17187 (2014).
3. K. A. Howell *et al.*, *Cell Rep.* **15**, 1514–1526 (2016).
4. A. I. Flyak *et al.*, *Cell* **164**, 392–405 (2016).
5. J. C. Frei *et al.*, *Sci Rep.* **6**, 19193 (2016).
6. W. Furuyama *et al.*, *Sci Rep.* **6**, 20514 (2016).
7. F. W. Holtsberg *et al.*, *J. Virol.* **90**, 266–278 (2016).
8. Z. Y. Keck *et al.*, *J. Virol.* **90**, 279–291 (2016).
9. K. Chandran, N. J. Sullivan, U. Felbor, S. P. Whelan, J. M. Cunningham, *Science* **308**, 1643–1645 (2005).
10. K. Schornberg *et al.*, *J. Virol.* **80**, 4174–4178 (2006).
11. E. H. Miller *et al.*, *EMBO J.* **31**, 1947–1960 (2012).
12. J. E. Carette *et al.*, *Nature* **477**, 340–343 (2011).
13. M. Côté *et al.*, *Nature* **477**, 344–348 (2011).
14. A. S. Herbert *et al.*, *MBio* **6**, e00565-e15 (2015).
15. Z. A. Bornholdt *et al.*, *MBio* **7**, e02154-e15 (2016).
16. H. Wang *et al.*, *Cell* **164**, 258–268 (2016).
17. M. A. Brindley *et al.*, *J. Virol.* **81**, 7702–7709 (2007).
18. B. Manicassamy, J. Wang, H. Jiang, L. Rong, *J. Virol.* **79**, 4793–4805 (2005).
19. J. S. Spence, T. B. Krause, E. Mittler, R. K. Jangra, K. Chandran, *MBio* **7**, e01857-e15 (2016).
20. M. J. Aman, *MBio* **7**, e00346-e16 (2016).
21. M. Ng *et al.*, *Virology* **468-470**, 637–646 (2014).
22. T. Hashiguchi *et al.*, *Cell* **160**, 904–912 (2015).
23. A. I. Flyak *et al.*, *Cell* **160**, 893–903 (2015).
24. J. P. Davies, Y. A. Ioannou, *J. Biol. Chem.* **275**, 24367–24374 (2000).
25. C. Wu *et al.*, *Nat. Biotechnol.* **25**, 1290–1297 (2007).
26. L. M. Kleinfelter *et al.*, *MBio* **6**, e00801-15 (2015).
27. M. Ng *et al.*, *Elife* **4**, e11785 (2015).
28. E. Ndungo *et al.*, *mSphere* **1**, e00007-16 (2016).
29. C. Spiess, Q. Zhai, P. J. Carter, *Mol. Immunol.* **67** (2 Pt A), 95–106 (2015).
30. A. F. Labrijn *et al.*, *Proc. Natl. Acad. Sci. U.S.A.* **110**, 5145–5150 (2013).

Downloaded from http://science.sciencemag.org/ on October 20, 2016

31. J. A. Simmons *et al.*, *J. Virol.* **90**, 605–610 (2016).
32. M. Bray, K. Davis, T. Geisbert, C. Schmaljohn, J. Huggins, *J. Infect. Dis.* **178**, 651–661 (1998).
33. J. M. Brannan *et al.*, *J. Infect. Dis.* **212** (suppl. 2), S282–S294 (2015).
34. Z. A. Bornholdt *et al.*, *Science* **351**, 1078–1083 (2016).
35. L. T. Jae *et al.*, *Science* **344**, 1506–1510 (2014).

ACKNOWLEDGMENTS

The data presented in this manuscript are tabulated in the main paper and in the supplementary materials. We thank C. Harold and T. Alkutkar for technical support. We acknowledge M. D. Scharff, S. Buhl, and the Einstein Macromolecular Therapeutics Development Facility for assistance with generation of mAb-548; E. Ndungo for assistance with hybridoma screening and for provision of purified human-Russell's viper NPC1 chimeras; E. L. Snapp and L. Costantini for generating an NPC1-eBFP2 fusion construct; and A. F. Labrijn, P. W. H. I. Parren, and Genmab for the gift of purified b12*MR72 DuoBody. This work is supported by NIH grants U19 AI109762 (Centers for Excellence in Translational Research) to K.C., J.R.L., J.M.D., and E.O.S.; R01 AI088027 to K.C.; and 1R41 AI122403 to J.R.L. and M.J.A.; Joint Science and Technology Office–Defense Threat Reduction Agency (JSTO-DTRA) project CB04088 to J.M.D.; and a DTRA contract (HDTRA1-13-C-0015) to M.J.A. E.K.N. was also supported by a DAAD (Deutscher Akademischer Austauschdienst, German Academic Exchange Service) fellowship. M.J.A. is president of and owns stocks, and F.W.H. and S.S. own stock options, in Integrated Biotherapeutics. M.J.A., F.W.H., K.A.H., and S.S. are named coinventors on a patent application (WO 2015/200522 A2) submitted by Integrated Biotherapeutics, that covers the endosomal targeting of filovirus bispecific antibodies. A.Z.W., E.K.N., J.R.L., and K.C. are named coinventors on a patent application (PCT/US/16/30652) submitted by Albert Einstein College of Medicine that covers the use of mAb-548 and bispecific antibodies incorporating mAb-548. A.I.F. and J.E.C. are named coinventors on a patent application (PCT/US2016/019644) submitted by Vanderbilt University Medical Center that covers the use of the MR72 antibody and bispecific antibodies incorporating MR72. mAb-548 and bispecific antibodies incorporating it are available from K.C. under a material transfer agreement with Albert Einstein College of Medicine. MR72 antibody and bispecific antibodies incorporating it are available from J.E.C. under a material transfer agreement with Vanderbilt University Medical Center.

SUPPLEMENTARY MATERIALS

www.sciencemag.org/content/354/6310/350/suppl/DC1
Materials and Methods
Figs. S1 to S16
Table S1
References (*36*–*48*)

13 June 2016; accepted 25 August 2016
Published online 8 September 2016
10.1126/science.aag3267

ANTIGEN PRESENTATION

A large fraction of HLA class I ligands are proteasome-generated spliced peptides

Juliane Liepe,[1]* Fabio Marino,[2,3] John Sidney,[4] Anita Jeko,[2,3] Daniel E. Bunting,[1] Alessandro Sette,[4] Peter M. Kloetzel,[5,6] Michael P. H. Stumpf,[1] Albert J. R. Heck,[2,3] Michele Mishto[5,6]*

The proteasome generates the epitopes presented on human leukocyte antigen (HLA) class I molecules that elicit CD8$^+$ T cell responses. Reports of proteasome-generated spliced epitopes exist, but they have been regarded as rare events. Here, however, we show that the proteasome-generated spliced peptide pool accounts for one-third of the entire HLA class I immunopeptidome in terms of diversity and one-fourth in terms of abundance. This pool also represents a unique set of antigens, possessing particular and distinguishing features. We validated this observation using a range of complementary experimental and bioinformatics approaches, as well as multiple cell types. The widespread appearance and abundance of proteasome-catalyzed peptide splicing events has implications for immunobiology and autoimmunity theories and may provide a previously untapped source of epitopes for use in vaccines and cancer immunotherapy.

The presentation of epitopes on the cell surface is a key mechanism by which organisms identify the presence of pathogens, metabolic malfunctioning, or tumors. The HLA class I (HLA-I) immunopeptidome—the set of epitopes allocated onto the HLA-I molecules—impinges on the CD8$^+$ T cell repertoire and the cell-mediated immune response (*1*). HLA-I immunopeptidomes are usually investigated by sequence identification of peptides eluted from HLA-I molecules by means of tandem liquid chromatography–mass spectrometry (LC-MS/MS) (fig. S1). The key step for the transformation of a protein into HLA-I–restricted epitopes is usually processing by the proteasome (*1*), which cuts proteins into peptides; alternatively, the proteasome can also cut and paste peptide sequences, thereby releasing peptide antigens that do not correspond to the original protein sequence (*2*) (fig. S2). This proteasome-catalyzed peptide splicing (PCPS) has long been considered to occur only rarely; partly this has been because the screening of the HLA-I immunopeptidome for proteasome-generated spliced peptides was impeded by methodological challenges.

To overcome these problems, we developed an analytical strategy that accounts for recent discoveries underpinning the PCPS mechanism and can handle the vast proteome-wide human spliced peptide database (fig. S3). With this strategy, we initially analyzed the HLA-I–eluted immunopeptidome of the GR lymphoblastoid cell line (GR-LCL); for a deeper coverage of the immunopeptidome, we adopted a two-dimensional (2D) peptide prefractionation strategy followed by a hybrid peptide fragmentation method [electron-transfer higher-energy collision dissociation (EThcD)] for peptide identification (*3*, *4*) (fig. S1), supplemented by an adapted target-decoy approach (fig. S4). Our analysis led to the identification of 6592 nonspliced and 3417 spliced peptides 9 to 12 amino acid residues in length (9- to 12-mer peptides) (table S1). The latter number represents 34% of the total of identified antigenic peptides (Fig. 1A), thereby increasing the number of identified HLA-I ligands by some 50%. We confirmed the authenticity of the identified spliced antigenic peptides by comparing the LC-MS/MS spectra of 98 exemplary spliced peptides with their corresponding synthetic peptides and computing their correlation score (table S2 and fig. S5). In addition, we verified the proteasome-dependent generation of the spliced antigenic peptides in vitro for three examples by digestions of synthetic polypeptides harboring the corresponding antigenic peptides by purified 20S proteasome (fig. S6).

We queried the HLA-I immunopeptidome mass spectrometry data of GR-LCL against the standard Swissprot human proteome database, which does not account for spliced peptides; this revealed that 655 peptides (i.e., 9% of the total nonspliced antigenic peptides) would be erroneously matched against this incomplete database as nonspliced peptides, because they have much better hits as spliced peptides in our search against the combined spliced and nonspliced peptide database (Fig. 1A). The correct sequences for a set of these antigenic spliced peptides were verified by comparing the LC-MS/MS spectra of the synthetic spliced and nonspliced candidates with the corresponding LC-MS/MS of the GR-LCL HLA-I immunopeptidome (fig. S7, A to I). Our identifications are further supported by the ion score distributions (see fig. S4) of the nonspliced peptides and of those spliced peptides that were wrongly assigned as nonspliced peptides using the standard Swissprot human proteome database, which differ only slightly in their median but not in the overall shape (fig. S7J).

[1]Centre for Integrative Systems Biology and Bioinformatics, Department of Life Sciences, Imperial College London, London SW7 2AZ, UK. [2]Biomolecular Mass Spectrometry and Proteomics, Bijvoet Center for Biomolecular Research and Utrecht Institute for Pharmaceutical Sciences, Utrecht University, 3584 CH Utrecht, Netherlands. [3]Netherlands Proteomics Centre, CH Utrecht, Netherlands. [4]Division of Vaccine Discovery, La Jolla Institute for Allergy and Immunology, La Jolla, CA 92037, USA. [5]Institut für Biochemie, Charité–Universitätsmedizin Berlin, 10117 Berlin, Germany. [6]Berlin Institute of Health, 10117 Berlin, Germany.
***Corresponding author. Email: michele.mishto@charite.de (M.M.); j.liepe@imperial.ac.uk (J.L.)**

Downloaded from http://science.sciencemag.org/ on October 20, 2016

In independent technical replicates of the GR-LCL HLA-I immunopeptidome analyzed without prefractioning (see figs. S1 and S8A) through EThcD or higher-energy collision dissociation (HCD), we identified thousands of peptides; among them, the spliced peptide pools represent 21 to 32% of the HLA-I immunopeptidome diversity (Fig. 1B and table S1A). To corroborate whether this unexpected finding would not be a peculiarity of the GR-LCL cell line, we investigated the HLA-I immunopeptidome of unrelated cell lines. Here, similar results were obtained in the analysis by EThcD of a nonrelated C1R lymphoid cell line (*5*), where 30% of the HLA-I immunopeptidome variety is represented by spliced peptides (Fig. 1A and table S1B). This large prevalence of spliced peptides in the HLA-I immunopeptidome is not a peculiar characteristic of lymphoblastoid cell lines, because in the HLA-I immunopeptidome of primary human fibroblasts (*6*), 29% of the identified antigenic peptides were spliced peptides (Fig. 1A and table S1C). Again, if we were to query those data sets only against the standard Swissprot human proteome database, we would wrongly assign 3.7 to 7.2% of the antigenic peptides as nonspliced peptides (Fig. 1, A and B) while missing all spliced peptides.

Spliced peptides were prevalent not only in the HLA-I immunopeptidome but also in the unsorted pool of GR-LCL cell lysate peptides with molecular weight (MW) smaller than 3 kDa, the maximum size of peptides produced in vitro by the proteasome (*7*) (Fig. 1C). The numbers of both nonspliced and spliced 9- to 12-mer peptides declined when we used an inhibitor of proteasome activity such as epoxomicin (Fig. 1C and fig. S9). Inhibition of proteasome activity led to a longer median length of the nonspliced peptides (fig. S9), which was to be expected since proteasome generates peptides with an average length of 11 residues (*7*, *8*). It also eliminated almost all spliced 9- to 12-mer peptides (Fig. 1C and fig. S9), thereby confirming that the identified spliced peptides are generated by proteasome.

We further verified the proteasome dependency of the spliced peptides by querying the HLA-I immunopeptidome of the T2 cell line, which lacks a functioning transporter associated with antigen processing (TAP). As for other TAP-deficient cell lines, the few antigenic peptides identified so far in the HLA-I immunopeptidome of the T2 cell line derive from both proteasome-mediated and signal peptidase–mediated proteolysis in a similar manner (*9*, *10*). As expected, relative to other HLA-I immunopeptidomes, we identified a drastically reduced number of both spliced and nonspliced peptides eluted from the HLA-I molecules of T2 cells. Among them, spliced peptides represented only 13% of the whole T2 HLA-I immunopeptidome (Fig. 1B). By contrast, the analysis of a cytosolic unsorted pool of 9- to 12-mer peptides of the T2 cells (with MW < 3 kDa) showed a normal frequency of spliced peptides (25%; Fig. 1C). Together, these experiments provide further evidence that spliced peptides presented by HLA-I molecules are produced by the proteasome and that about half of the TAP-independent antigenic peptide pool is generated through proteasome activity (*9*).

As a final (negative) control, we performed LC-MS/MS analysis of a tryptic lysate of the C1R cell line (fig. S8). In this case, the cell lysate was first filtered to include only proteins with MW > 30 kDa to exclude intracellular peptides generated by the proteasome in the mixture. In this tryptic digest, we identified about 1300 9- to 12-mer nonspliced peptides but only a few 9- to 12-mer spliced sequences (Fig. 1C). In fact, only 2.7% of them are (likely incorrectly) annotated as spliced peptides, which provides us with an experimental limit on the overall false discovery rate (FDR) (see fig. S4B). We thus have independent experiments that provide evidence that about one-third of peptides bound to HLA-I are generated by PCPS.

Although spliced peptides represent one-third of the HLA-I immunopeptidome variety, their relevance from an immunological point of view could be undermined if they were not abundantly presented at the cell surface. We thus set out to quantify the abundance of each HLA peptide by label-free quantification based on the intensity of the MS ion peak area. Although this method is not applicable for single peptides (*6*, *8*), it has recently become well accepted when analyzing large proteomics data sets (*6*, *11*, *12*). We substantiated this strategy by titrating two pools of synthetic nonspliced and spliced antigenic peptides; we observed no significant differences between nonspliced and spliced peptides (Fig. 2A). However, label-free quantification did reveal significant differences in the abundance distribution between nonspliced and spliced peptides. Indeed, the spliced antigenic peptides were on average 16 to 26% less abundant than nonspliced peptides in the HLA-I immunopeptidomes of three independent cell lines (Fig. 2, B and C). Therefore, on the basis of our results, we conclude that spliced peptides not only represent one-third of the HLA-I immunopeptidome variety but also approximately one-fourth of the total amount of peptide molecules presented on the HLA-I complex. In agreement with this finding, we recently reported that the abundance of peptides of a small group of melanoma-associated spliced epitopes

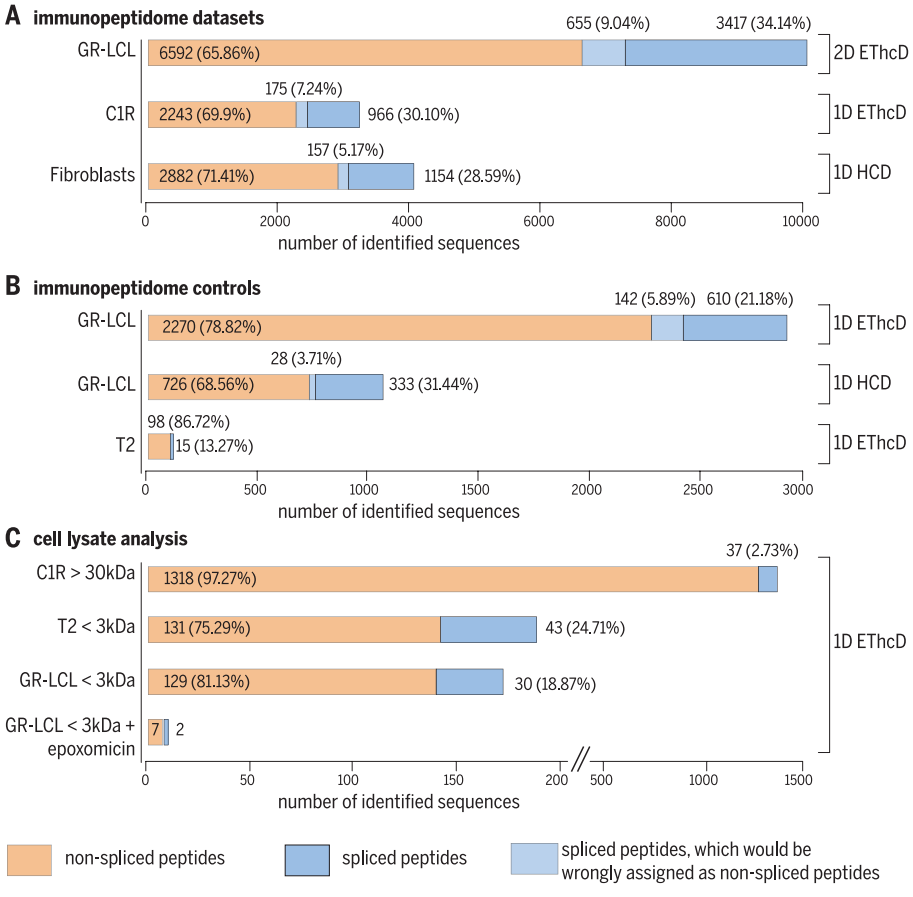

Fig. 1. Sizes and characteristics of spliced and nonspliced peptide pools. (**A** and **B**) Summary of the 9- to 12-mer peptides presented by HLA-I molecules on the GR-LCL and C1R cell lines and human primary fibroblasts (A), or, as controls, on the GR-LCL and T2 cell lines (B). (**C**) Summary of the 9- to 12-mer peptides identified among the cell lysates of T2 and GR-LCL cell lines prefiltered for peptides smaller than 3 kDa not trypsin-digested, or of the C1R cell line prefiltered for polypeptides larger than 30 kDa and trypsin-digested. Samples were analyzed by different LC-MS/MS methods, as depicted. Light blue shaded areas are part of the spliced peptide pool.

Downloaded from http://science.sciencemag.org/ on October 20, 2016

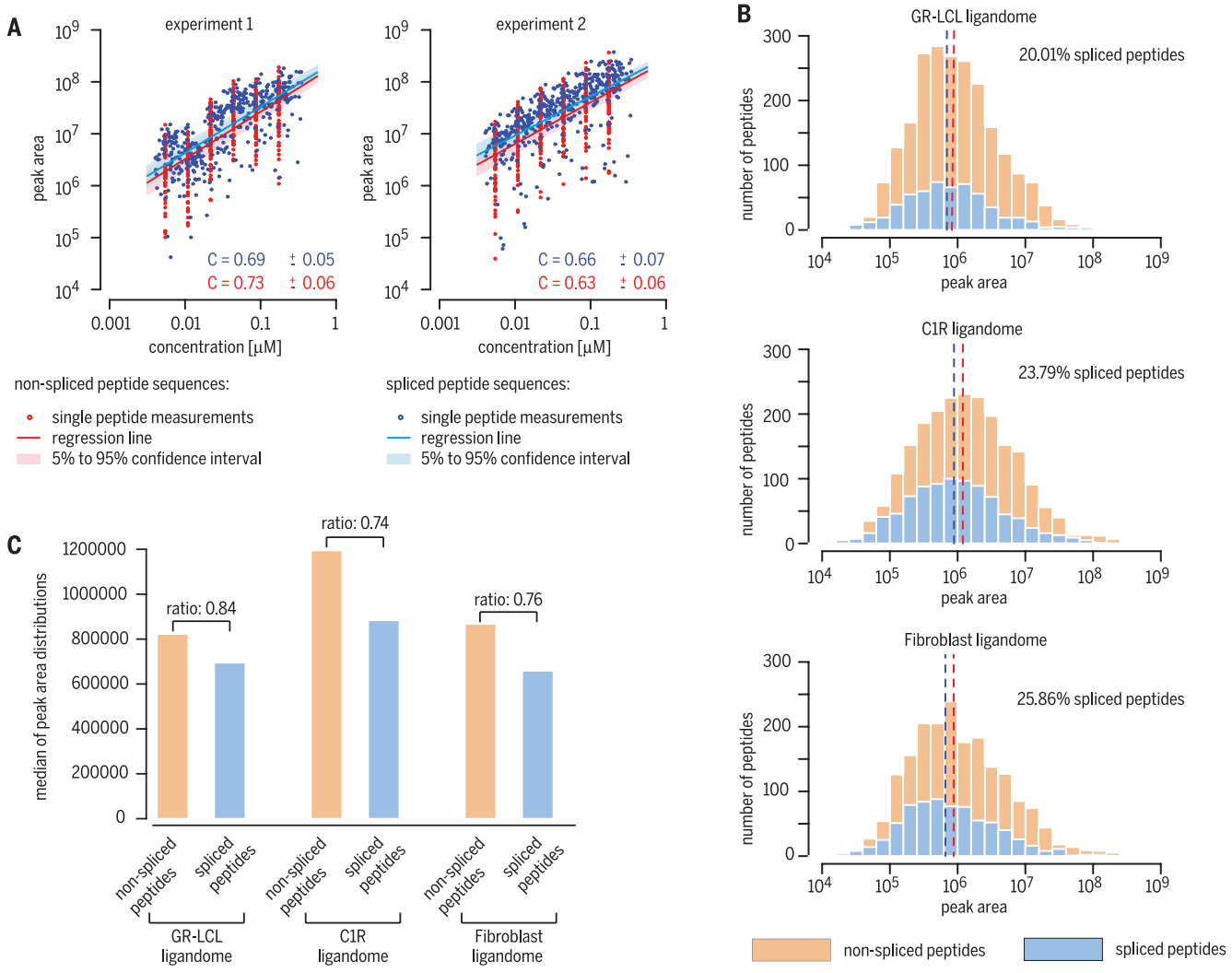

Fig. 2. Semiquantitative comparison of HLA-I–eluted spliced and nonspliced peptides. (**A**) Correlation between MS ion peak area and concentration of a pool of 75 nonspliced and 78 spliced peptides from two experimental replicates. The correlation coefficients with confidence intervals are reported in the charts. Linear regression was applied, and the resulting regression lines with their confidence intervals are depicted for spliced peptides (dark blue line and light blue shaded area) and nonspliced peptides (red line and pink shaded area). Neither the correlation coefficients nor the parameters of the regression lines significantly differ between spliced and nonspliced peptides. (**B**) Distribution of MS ion peak area of spliced and nonspliced peptides eluted from the HLA-I molecules of GR-LCL and C1R cell lines or human fibroblasts. Dashed lines indicate the median of the distribution for spliced peptides (blue) and nonspliced peptides (red). The MS ion peak area distribution of the nonspliced peptides is significantly larger than the distribution of the spliced peptides (Kolmogorov-Smirnov test, $P < 10^{-16}$). The relative proportion of spliced peptides estimated from the integral of the MS ion peak areas of spliced peptides relative to the integral of the peak area of all peptides is reported. (**C**) Medians of MS ion peak area of spliced and nonspliced peptides identified in the HLA-I immunopeptidome of the GR-LCL and C1R cell lines or human primary fibroblasts. Samples were not prefractionated; all samples were analyzed by EThcD (GR-LCL and C1R cell lines and synthetic peptide pools) or by HCD (human fibroblasts).

exposed on the HLA-I complexes is comparable to that of nonspliced melanoma-associated epitopes (*13*). Moreover, we observed a specific response against those spliced epitopes in the peripheral blood of half of the melanoma patients we studied (*13*), highlighting the potential biological impact of the much larger set of spliced epitopes presented in this study.

Spliced epitopes could also represent a distinct pool of antigenic peptides with particular characteristics. The few pioneering studies on PCPS had already provided hints about generative mechanisms. For instance, they suggested that PCPS prefers specific peptide sequences, although the limited number of spliced peptides or epitopes identified has so far precluded an analysis with sufficient statistical power (*2*, *8*, *14*–*21*). With our large pool of spliced antigenic peptides, this became possible. Contrasting the characteristics of the spliced and nonspliced peptides in the GR-LCL HLA-I immunopeptidome, we observed no significant differences in terms of (i) peptide length distribution (fig. S10A), in agreement with our previous observation on in vitro proteasome-catalyzed reactions (*8*); (ii) frequency of the number of putative parental proteins that can generate each spliced or nonspliced peptide (fig. S10B); and (iii) the frequencies of spliced and nonspliced peptides derived from a given antigen (fig. S10C). Remarkably, one-third of self antigens are represented on the GR-LCL cell surface only by spliced peptides (Fig. 3A and fig. S10D), which shows that PCPS increases the antigen exposure and expands the HLA-I immunopeptidome–mediated surveillance of the immune system.

Among the identified spliced antigenic peptides in the GR-LCL 2D HLA-I immunopeptidome, we observed a similar number of spliced peptides generated by the ligation of two splice reactants following their orientation in the parental protein or by inverting their order (i.e., reverse PCPS); 50.1% were normal cis spliced peptides (see fig.

Downloaded from http://science.sciencemag.org/ on October 20, 2016

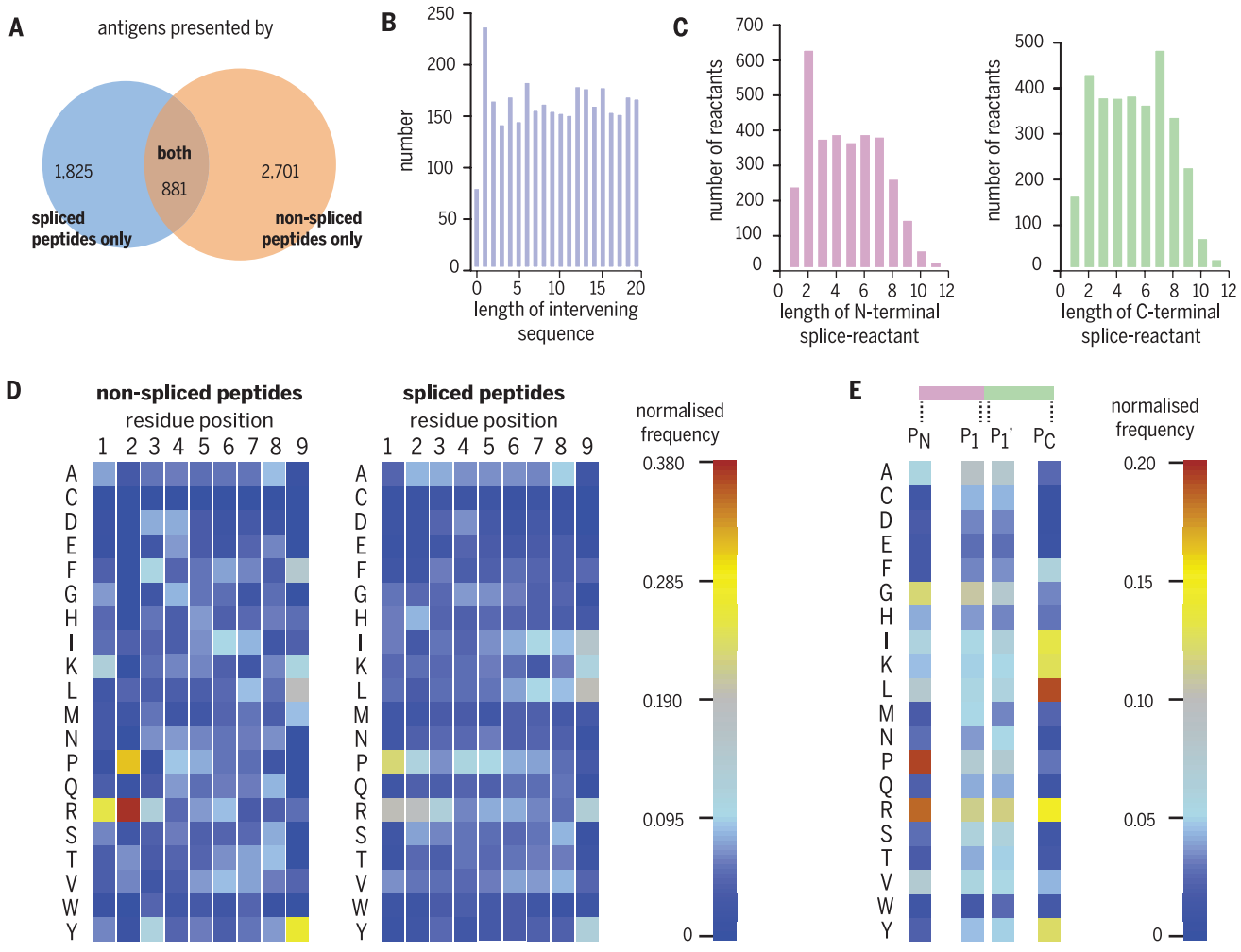

Fig. 3. Antigens, characteristics, and sequence motifs of spliced and nonspliced peptides of the GR-LCL HLA-I immunopeptidome. Data in all panels refer to the GR-LCL 2D-EthcD HLA-I immunopeptidome. (**A**) Number of antigens presented on the HLA-I molecules by only spliced, only nonspliced, or both spliced and nonspliced peptides. (**B**) Length distribution of the sequence between the two splice reactants (i.e., the intervening sequence). (**C**) Length distribution of N- and C-terminal splice reactants generating the antigenic spliced peptides. (**D**) Frequencies of amino acids at each residue of the nonspliced and spliced 9-mer peptides. (**E**) Distribution of amino acids in the P_N, P1, P1′, and P_C positions (see fig. S2) of the spliced peptides. In (D) and (E), all frequency values are normalized for the frequency of the amino acids in the human proteome; that is, they indicate the probability of observing a certain amino acid at a certain position given the frequency of this amino acid in the human proteome. Abbreviations for amino acid residues: A, Ala; C, Cys; D, Asp; E, Glu; F, Phe; G, Gly; H, His; I, Ile; K, Lys; L, Leu; M, Met; N, Asn; P, Pro; Q, Gln; R, Arg; S, Ser; T, Thr; V, Val; W, Trp; Y, Tyr.

S2). We did not observe a clear preference for a specific length of intervening sequences (i.e., the sequences excised between two splice reactants) (Fig. 3B and fig. S2). Also, the length of the N- and C-terminal splice reactants (see fig. S2) was almost equally distributed, with the exception of a seemingly preferred length of two residues in the N-terminal splice reactant, which was most apparent for 9-, 10-, and 11-mer peptides (Fig. 3C and fig. S10E). Because the second residue of the antigenic peptide often corresponds to the anchor site of the specific HLA-I molecules, we speculate that preference for specific amino acids for the ligation could have introduced an evolutionary pressure on the HLA allotype selection, as has previously been hypothesized for the proteasome-dependent peptide hydrolysis and the C terminus of the HLA-I–restricted peptides (*22*).

In the GR-LCL data set, we also compared spliced and nonspliced antigenic peptide motifs in relation to HLA-I haplotypes by applying a neural network–based algorithm (NetMHC ANN) and an algorithm based on the stabilized matrix method (IEDB SMM) (*23*, *24*) to predict in silico their binding to HLA-I molecules. The two algorithms performed similarly when we considered the nonspliced antigenic peptides (fig. S11, A to D). They did, however, differ significantly in the prediction of how efficiently the spliced peptides bind the specific HLA-A and HLA-B variants (fig. S11, A to D). Often, spliced peptides predicted by NetMHC ANN to be barely compatible with the specific HLA-I cleft bound it with an experimentally determined dissociation constant (IC_{50}) below 5000 nM (table S2 and fig. S11E). Such a phenomenon might be due to intrinsic differences in the motifs of spliced and nonspliced antigenic peptides. Indeed, because the algorithms have been trained exclusively on nonspliced epitopes (or nonrandomized peptide libraries), their predictive power for that peptide type could be limited. This hypothesis is also supported by our previous in vitro PCPS analysis (*8*), where we observed that several spliced peptides were produced by proteasomal cutting at rarely used substrate cleavage sites. Such differences emerge when considering the sequence motifs of the spliced and nonspliced 9-mers within the GR-LCL HLA-I immunopeptidome (Fig. 3D) and the other immunopeptidome data sets (fig. S12), especially in positions 2 and 9, which correspond to frequently used anchor sites.

To gather information about the sequence preference of PCPS, we exploited the large number of spliced antigenic peptides available here, and we computed the amino acid distribution at

Downloaded from http://science.sciencemag.org/ on October 20, 2016

the P_N, P1, P1′, and P_C positions (see fig. S2) of the GR-LCL HLA-I immunopeptidome. This outcome matched the data obtained for the replicate GR-LCL immunopeptidome (1D EThcD) but differed from the immunopeptidomes obtained from the C1R cell lineage and human primary fibroblasts (Fig. 3E and fig. S13). The difference between the patterns of the spliced peptide P_N, P1, P1′, and P_C positions could be due to the HLA anchor site differences among the three cell lines. Our more general analysis differs markedly from the HLA-A*02:01-restricted P1-P1′ position pattern recently published by Berkers *et al.* (*20*), thereby confirming that an HLA-unbiased strategy to identify spliced peptide patterns may be essential for developing PCPS prediction algorithms.

Our study shows that the spliced peptides bound to the HLA-I molecules are very frequent and comparable in their amount to the nonspliced peptides but represent a distinct pool of antigens with particular immunological characteristics. One of the key features that may have maintained PCPS through evolutionary history (*8*, *25*, *26*) might be its higher degree of freedom of selecting antigenic peptide sequences. Targeting antigens through nonspliced peptides can be limited by the sequence restrictions that antigens have as a result of their function. PCPS is a solution to this problem, as suggested by the fact that a significant portion of the antigens are represented by spliced peptides only. Of course, the unexpectedly large frequency and amount of HLA-I–restricted spliced peptides may—and, we strongly expect, will—have profound implications for the concept of self/nonself peptide presentation: The large variety of potential spliced antigenic peptides would markedly increase the number of antigenic peptides with overlapping sequences derived from either human or pathogen proteomes, with direct implications for autoimmunity (*25*, *27*, *28*). On the other hand, the frequency of antigenic spliced peptides and their features could also in turn have positive implications for therapies involving HLA-I–restricted epitopes, such as antiviral vaccinations or mutation-specific adoptive T cell therapy against tumors (*29*–*33*); mutant antigens lacking HLA-I–restricted nonspliced epitopes could finally be targeted through spliced epitopes.

REFERENCES AND NOTES

1. M. Groettrup, C. J. Kirk, M. Basler, *Nat. Rev. Immunol.* **10**, 73–78 (2010).
2. N. Vigneron *et al.*, *Science* **304**, 587–590 (2004).
3. C. K. Frese *et al.*, *J. Proteome Res.* **12**, 1520–1525 (2013).
4. G. P. Mommen *et al.*, *Proc. Natl. Acad. Sci. U.S.A.* **111**, 4507–4512 (2014).
5. E. Caron *et al.*, *eLife* **4**, e07661 (2015).
6. M. Bassani-Sternberg, S. Pletscher-Frankild, L. J. Jensen, M. Mann, *Mol. Cell. Proteomics* **14**, 658–673 (2015).
7. A. F. Kisselev, T. N. Akopian, K. M. Woo, A. L. Goldberg, *J. Biol. Chem.* **274**, 3363–3371 (1999).
8. M. Mishto *et al.*, *Mol. Cell. Proteomics* **11**, 1008–1023 (2012).
9. A. O. Weinzierl *et al.*, *Eur. J. Immunol.* **38**, 1503–1510 (2008).
10. E. Lorente *et al.*, *PLOS ONE* **8**, e59118 (2013).
11. J. Cox *et al.*, *Mol. Cell. Proteomics* **13**, 2513–2526 (2014).
12. E. L. de Graaf, P. Giansanti, A. F. Altelaar, A. J. Heck, *Mol. Cell. Proteomics* **13**, 2426–2434 (2014).
13. F. Ebstein *et al.*, *Sci. Rep.* **6**, 24032 (2016).
14. K. Textoris-Taube *et al.*, *J. Biol. Chem.* **290**, 30417–30428 (2015).
15. E. H. Warren *et al.*, *Science* **313**, 1444–1447 (2006).
16. A. Michaux *et al.*, *J. Immunol.* **192**, 1962–1971 (2014).
17. J. Liepe *et al.*, *PLOS Comput. Biol.* **6**, e1000830 (2010).
18. A. Dalet, N. Vigneron, V. Stroobant, K. Hanada, B. J. Van den Eynde, *J. Immunol.* **184**, 3016–3024 (2010).
19. A. Dalet *et al.*, *Proc. Natl. Acad. Sci. U.S.A.* **108**, E323–E331 (2011).
20. C. R. Berkers *et al.*, *J. Immunol.* **195**, 4085–4095 (2015).
21. C. R. Berkers *et al.*, *J. Immunol.* **195**, 4075–4084 (2015).
22. G. Niedermann *et al.*, *Immunol. Rev.* **172**, 29–48 (1999).
23. B. Peters, A. Sette, *BMC Bioinformatics* **6**, 132 (2005).
24. C. Lundegaard, O. Lund, M. Nielsen, *Bioinformatics* **24**, 1397–1398 (2008).
25. A. Grignolio *et al.*, *Front. Immunol.* **5**, 153 (2014).
26. F. A. Steven, *Immunology and Evolution of Infectious Disease* (Princeton Univ. Press, 2002).
27. E. Bellavista *et al.*, *Autoimmune Dis.* **2014**, 739705 (2014).
28. H. G. Rammensee, *Nature* **427**, 203–204 (2004).
29. S. A. Rosenberg, N. P. Restifo, *Science* **348**, 62–68 (2015).
30. S. H. van der Burg, R. Arens, C. J. Melief, *Trends Immunol.* **32**, 97–103 (2011).
31. T. Blankenstein, M. Leisegang, W. Uckert, H. Schreiber, *Curr. Opin. Immunol.* **33**, 112–119 (2015).
32. M. M. Gubin *et al.*, *Nature* **515**, 577–581 (2014).
33. P. G. Coulie, B. J. Van den Eynde, P. van der Bruggen, T. Boon, *Nat. Rev. Cancer* **14**, 135–146 (2014).

ACKNOWLEDGMENTS

Supported by Berlin Institute of Health grant CRG1-TP1 and Einstein Stiftung Berlin grant A2013-174 (P.M.K.); by NC3Rs through David Sainsbury Fellowship NC/K001949/1 (J.L.); by BBSRC grant BB/G007934/1, HFSP grant RGP0061/2011, Leverhulme Trust grant F/07058/BP, and the Royal Society through a Wolfson Research Merit Award (M.P.H.S.); and by Proteins@Work (project number 184.032.201) and the Gravity Program Institute for Chemical Immunology, both funded by the Netherlands Organisation for Scientific Research (F.M., A.J., and A.J.R.H.). We thank P. Henklein, P. Kunert, and B. Brecht-Jachan for the peptide synthesis; C. Keller, M. Bassani-Sternberg, and P. Hitchen for technical support; S. Islam for help in setting up the mass spectrometry analysis pipeline at Imperial College London; and J. Cottrell (Matrix Science Ltd.) for technical support with Mascot. The authors declare no competing financial interests. The RAW files used in this study are available at the Datadryad.org archive (doi:10.5061/dryad.r984n). The scripts for the identification of HLA-I spliced peptides are available upon request.

SUPPLEMENTARY MATERIALS

www.sciencemag.org/content/354/6310/354/suppl/DC1
Materials and Methods
Figs. S1 to S13
Tables S1 and S2
References (*34*–*44*)

12 February 2016; accepted 19 September 2016
10.1126/science.aaf4384

MUCOSAL IMMUNITY

A pathogenic role for T cell–derived IL-22BP in inflammatory bowel disease

Penelope Pelczar,[1]* Mario Witkowski,[1,2]* Laura Garcia Perez,[1]* Jan Kempski,[1] Anna G. Hammel,[1]† Leonie Brockmann,[1] Dörte Kleinschmidt,[1] Sandra Wende,[1] Cathleen Haueis,[1] Tanja Bedke,[1] Marco Witkowski,[3] Susanne Krasemann,[4] Stefan Steurer,[5] Carmen J. Booth,[6] Philipp Busch,[7] Alexandra König,[7]‡ Ursula Rauch,[3] Daniel Benten,[1] Jakob R. Izbicki,[7] Thomas Rösch,[8] Ansgar W. Lohse,[1] Till Strowig,[9] Nicola Gagliani,[1,7]§ Richard A. Flavell,[10]§|| Samuel Huber[1]§||

Intestinal inflammation can impair mucosal healing, thereby establishing a vicious cycle leading to chronic inflammatory bowel disease (IBD). However, the signaling networks driving chronic inflammation remain unclear. Here we report that $CD4^+$ T cells isolated from patients with IBD produce high levels of interleukin-22 binding protein (IL-22BP), the endogenous inhibitor of the tissue-protective cytokine IL-22. Using mouse models, we demonstrate that IBD development requires T cell–derived IL-22BP. Lastly, intestinal $CD4^+$ T cells isolated from IBD patients responsive to treatment with antibodies against tumor necrosis factor–α (anti–TNF-α), the most effective known IBD therapy, exhibited reduced amounts of IL-22BP expression but still expressed IL-22. Our findings suggest that anti–TNF-α therapy may act at least in part by suppressing IL-22BP and point toward a more specific potential therapy for IBD.

Inflammatory bowel disease (IBD) is characterized by chronic intestinal inflammation and dysfunction of the epithelial barrier. The primary cause of the initiation of this disease is unclear. However, it is well accepted that inflammatory responses, most likely driven by the microbiome and defective barrier function, promote a vicious cycle that leads to chronic disease (*1*, *2*). Because IBD is characterized by chronic inflammation, most therapies are directed against the inflammatory responses, but they do not directly promote mucosal healing. Relapsing flares and opportunistic infections that occur as a consequence of immune suppression are the resulting problems. Thus, one major goal is to identify the mechanism that links inflammation and barrier dysfunction. The proinflammatory cytokine tumor necrosis factor–α (TNF-α) is the primary target of IBD therapy at present. There are several potential mechanisms whereby

Downloaded from http://science.sciencemag.org/ on October 20, 2016

therapy with antibodies against TNF-α (anti–TNF-α) might work in IBD. These include the expansion of regulatory T cells, induction of T cell apoptosis, and promotion of the epithelial cell barrier function [reviewed in (*3*)]. However, what determines the response to anti–TNF-α therapy in IBD remains unclear.

Interleukin-22 (IL-22) is up-regulated in the intestine in patients with IBD (*4*, *5*). IL-22 is normally able to promote mucosal healing in the intestine (*6*–*8*); however, when uncontrolled, it can lead to intestinal pathogenesis (*7*, *9*–*12*). Therefore, tight control of IL-22 activity is essential. IL-22 binding protein (IL-22BP) exerts this control by specifically binding IL-22 and preventing it from binding membrane-bound IL-22 receptor 1 (IL-22R1) (*13*–*16*). The binding affinity of IL-22 and IL-22BP is 20- to 1000-fold that of the former and membrane-bound IL-22R1 (*4*, *17*). IL-22 and IL-22BP exhibit an inverse expression pattern upon tissue damage in the intestine in mouse models: IL-22BP is most highly expressed in the colon during homeostasis and tissue repair, whereas IL-22 is most highly expressed at the peak of tissue damage (*4*, *7*, *18*). Thus, careful regulation of IL-22 and IL-22BP controls homeostasis in the intestine; however, the role of IL-22BP in humans in IBD is uncertain.

To address this, we first analyzed IL-22 and IL-22BP expression in intestinal biopsy specimens from patients with ulcerative colitis (UC) or Crohn's disease (CD) (table S1) who either were in remission (UC, n = 13; CD, n = 12) or had active disease based on clinical, endoscopic, and histological findings (UC, n = 18; CD, n = 21). In patients with active IBD, we analyzed samples from both healthy (uninflamed) and diseased (inflamed) areas in the colon and terminal ileum, based on endoscopic and histological findings, which were further validated by analyzing expression of the genes for the inflammatory markers IL-22, IL-17A, and interferon-γ (IFN-γ) (Fig. 1A and fig. S1). In line with previous reports (*4*, *5*), we found increased *IL22* and *IL17A* mRNA expression in the colon and terminal ileum of patients with active CD and UC, compared with that in healthy controls. *IL22BP* mRNA was not decreased, but was rather increased in the colon of these patients (Fig. 1A), suggesting that the activity of IL-22 might be impaired. We also confirmed this finding at the protein level by immunohistochemistry of intestinal biopsy specimens (Fig. 1, B and C). As a control, we analyzed the IL-22 and IL-22BP expression pattern in a non–IBD-related intestinal disease, colonic diverticulitis (n = 5). Colonic diverticulosis is an acquired disease, developing as mucosal and submucosal herniation through the circular muscle layer at vulnerable weak points of the colonic wall. Subsequent inflammation of these diverticula is termed diverticulitis. We obtained tissue specimens from the inflamed area of the colon from patients with diverticulitis and, in line with the studies in mice (*4*, *7*, *18*), we observed increased *IL22* and decreased *IL22BP* expression (Fig. 1A), suggesting that IL-22BP is not generally up-regulated during intestinal inflammation in humans. One possible explanation for the increased expression of IL-22BP in IBD relative to that in diverticulitis might be the chronic versus acute nature of the inflammatory response in these respective diseases.

Next, we aimed to identify the cellular source of IL-22BP in the intestine. To that end, we sorted different cell populations from human intestine. In line with previous publications (*7*, *19*–*21*), we confirmed that dendritic cells (DCs) and eosinophils express high levels of IL-22BP (Fig. 2, A and B, and fig. S2). Unexpectedly, we also observed high IL-22BP expression in $CD4^+CD3^+CD11c^-$ T cells in the small intestine (Fig. 2, A and B). We measured *CD4* and *CD11c* (*ITGAX*) as controls (fig. S3). IL-22BP was also expressed in the colon by T cells, and it was further increased in T cells but not in DCs in the diseased area in patients with active IBD (Fig. 2, C and D, and tables S2 and S3). We found that murine $CD4^+$ T cells in the lymph nodes also expressed *Il22bp* (Fig. 2E). The expression levels were highest in $CD44^+CD4^+$ T cells, reaching levels similar to those in DCs. In the mouse colon, however, we

[1]I. Medizinische Klinik und Poliklinik, Universitätsklinikum Hamburg-Eppendorf, 20246 Hamburg, Germany. [2]Institut für Medizinische Mikrobiologie und Hygiene, Obere Zahlbacherstraße 67, 55131 Mainz, Germany. [3]Department of Cardiology, Charité–Universitätsmedizin Berlin, Campus Benjamin Franklin, Hindenburgdamm 30, 12200 Berlin, Germany. [4]Institut für Neuropathologie, Universitätsklinikum Hamburg-Eppendorf, 20246 Hamburg, Germany. [5]Institut für Pathologie, Universitätsklinikum Hamburg-Eppendorf, 20246 Hamburg, Germany. [6]Section of Comparative Medicine, School of Medicine, Yale University, New Haven, CT 06520, USA. [7]Klinik und Poliklinik für Allgemein-, Viszeral- und Thoraxchirurgie, Universitätsklinikum Hamburg-Eppendorf, 20246 Hamburg, Germany. [8]Klinik und Poliklinik für Interdisziplinäre Endoskopie, Universitätsklinikum Hamburg-Eppendorf, 20246 Hamburg, Germany. [9]Helmholtz-Zentrum für Infektionsforschung, 38124 Braunschweig, Germany. [10]Howard Hughes Medical Institute and Department of Immunobiology, School of Medicine, Yale University, New Haven, CT 06520, USA. *These authors contributed equally to this work. †Present address: Klinik und Poliklinik für Diagnostische und Interventionelle Radiologie, Universitätsklinikum Hamburg-Eppendorf, 20246 Hamburg, Germany. ‡Present address: Zentrum für für Allgemein-, Viszeral-, Thorax- und Gefäßchirurgie, Klinikum Wilhelmshaven, Friedrich-Paffrath-Straße 100, 26389 Wilhelmshaven, Germany. §These authors contributed equally to this work. **||Corresponding author. Email: richard.flavell@yale.edu (R.A.F.); shuber@uke.de (S.H.)**

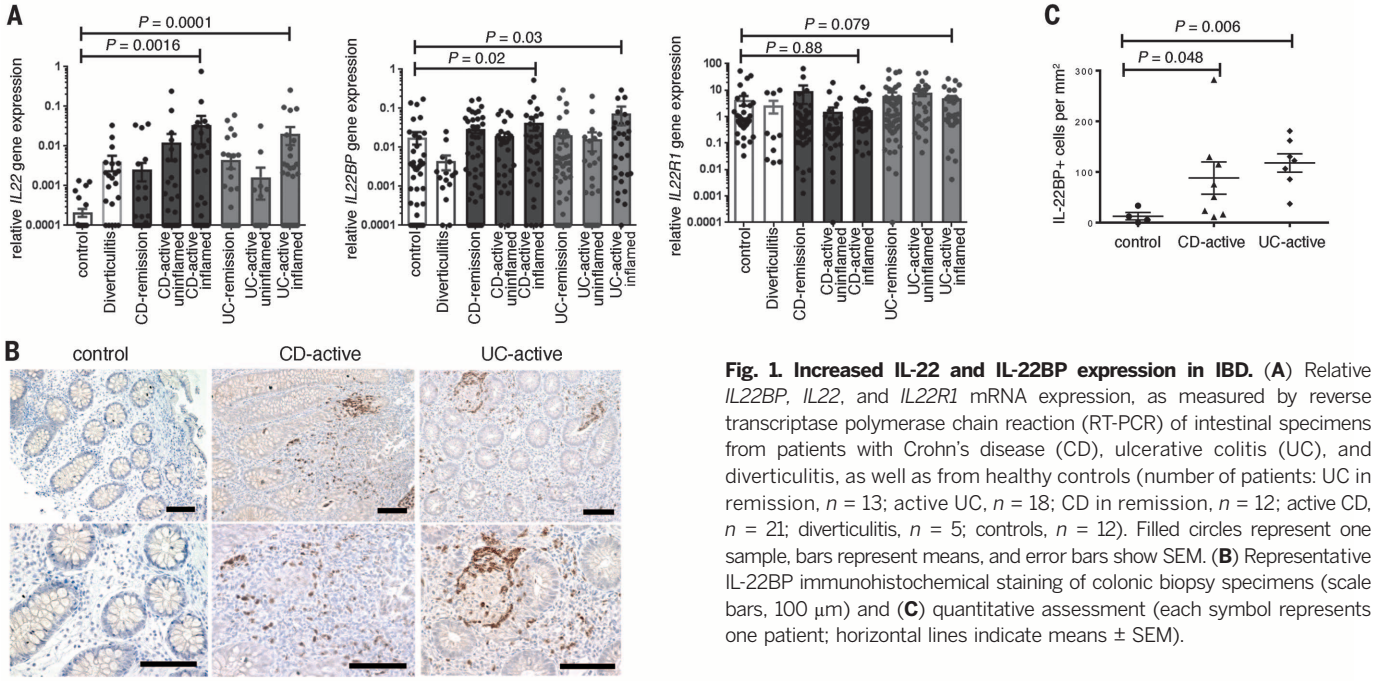

Fig. 1. Increased IL-22 and IL-22BP expression in IBD. (**A**) Relative *IL22BP*, *IL22*, and *IL22R1* mRNA expression, as measured by reverse transcriptase polymerase chain reaction (RT-PCR) of intestinal specimens from patients with Crohn's disease (CD), ulcerative colitis (UC), and diverticulitis, as well as from healthy controls (number of patients: UC in remission, n = 13; active UC, n = 18; CD in remission, n = 12; active CD, n = 21; diverticulitis, n = 5; controls, n = 12). Filled circles represent one sample, bars represent means, and error bars show SEM. (**B**) Representative IL-22BP immunohistochemical staining of colonic biopsy specimens (scale bars, 100 μm) and (**C**) quantitative assessment (each symbol represents one patient; horizontal lines indicate means ± SEM).

Downloaded from http://science.sciencemag.org/ on October 21, 2016

previously did not detect *Il22bp* in bulk populations of TCRβ$^+$ cells in steady-state conditions (*7*). We therefore performed additional analysis of purified CD4$^+$ T cells from the colon. We did detect *Il22bp* in colonic CD4$^+$ T cells, but the expression level was low and close to the detection limit (Fig. 2E). In conclusion, both CD4$^+$ T cells and DCs can produce IL-22BP in mice and humans.

T cell–specific up-regulation of IL-22BP in active IBD suggests a pathogenic role in intestinal inflammation. On the basis of these findings, we aimed to further decipher the relevance of DC- versus T cell–derived IL-22BP in colitis. To that end, we used the murine CD45RB^{high} transfer colitis model, in which IL-22 mediates a protective function (*10*, *22*). To discriminate between CD4$^+$ T cell–derived and innate immune cell–derived IL-22BP, we transferred *Il22bp*$^{-/-}$ and *Il22bp*$^{+/+}$ CD4$^+$CD25$^-$CD45RB^{high} T cells into *Rag1*$^{-/-}$ and *Rag1*$^{-/-}$*Il22bp*$^{-/-}$ mice. Transfer of wild-type T cells into *Rag1*$^{-/-}$ and *Rag1*$^{-/-}$*Il22bp*$^{-/-}$ mice caused equally severe disease, characterized by weight loss and endoscopic and histological scores of colitis (Fig. 3, A to E). However, both *Rag1*$^{-/-}$ and *Rag1*$^{-/-}$*Il22bp*$^{-/-}$ mice that received *Il22bp*-deficient T cells were largely protected from disease development (Fig. 3, A to E). Similar to the results observed in humans (Fig. 2C), the expression of IL-22BP by CD4$^+$ T cells was increased in the murine colitis model (fig. S4). T cells from *Il22bp*$^{-/+}$ mice showed an intermediate level of *Il22bp* expression and caused an intermediate phenotype of colitis development (fig. S5). We also confirmed the pathogenic effect of CD4$^+$ T cell–derived IL-22BP in a bacterial-driven colitis model (fig. S6). T cell–derived IL-22BP thus plays an important pathogenic role in multiple mouse IBD models.

We next sought to address whether the effect of IL-22BP is due to the free activity of IL-22 or to indirect mechanisms. Therefore, we performed the transfer colitis experiment in an IL-22–deficient environment. We transferred *Il22*$^{-/-}$ and *Il22*$^{-/-}$*Il22bp*$^{-/-}$ CD4$^+$CD25$^-$CD45RB^{high} T cells into *Rag1*$^{-/-}$*Il22*$^{-/-}$ mice. In this setting, both *Il22*$^{-/-}$ and *Il22*$^{-/-}$*Il22bp*$^{-/-}$ CD4$^+$CD25$^-$CD45RB^{high} T cells caused equally severe colitis (fig. S7). As a control, we transferred *Il22bp*$^{-/-}$ CD4$^+$CD25$^-$CD45RB^{high} T cells into *Rag1*$^{-/-}$ mice, which again were largely protected from colitis development (fig. S7), indicating that IL-22BP aggravates colitis by blocking IL-22. We furthermore wanted to test whether *Il22bp*-deficient T cells have a cell-intrinsic defect. To this end, we cotransferred congenic wild-type and *Il22bp*-deficient CD4$^+$CD25$^-$CD45RB^{high} T cells into *Rag1*$^{-/-}$ mice and analyzed the transferred T cells upon colitis development. We could not find a significant difference in T cell numbers or cytokine production between wild-type and *Il22bp*-deficient T cells in this setting, arguing against a T cell–intrinsic defect of *Il22bp*-deficient T cells (fig. S8). Taken together, our data suggest that IL-22 is sufficient to protect mice from effector T cell–mediated colitis in the absence of T cell–derived IL-22BP.

Anti–TNF-α therapy is the most effective treatment of IBD at present. We therefore tested whether the efficacy of this therapy is linked to IL-22BP. We found a positive correlation between *IL22BP* and *TNFa* expression in the intestine of IBD patients with active disease (P = 0.004, correlation coefficient r = 0.36; Fig. 4A). Genes encoding other cytokines, such as *IL18*, *IL6*, and *IL23*, did not correlate with *IL22BP* expression (fig. S9). Moreover, *IL22* also positively correlated with *IL22BP* (fig. S9). However, *Il22bp* expression in the colon and lymph nodes of *Il22*$^{-/-}$ mice was

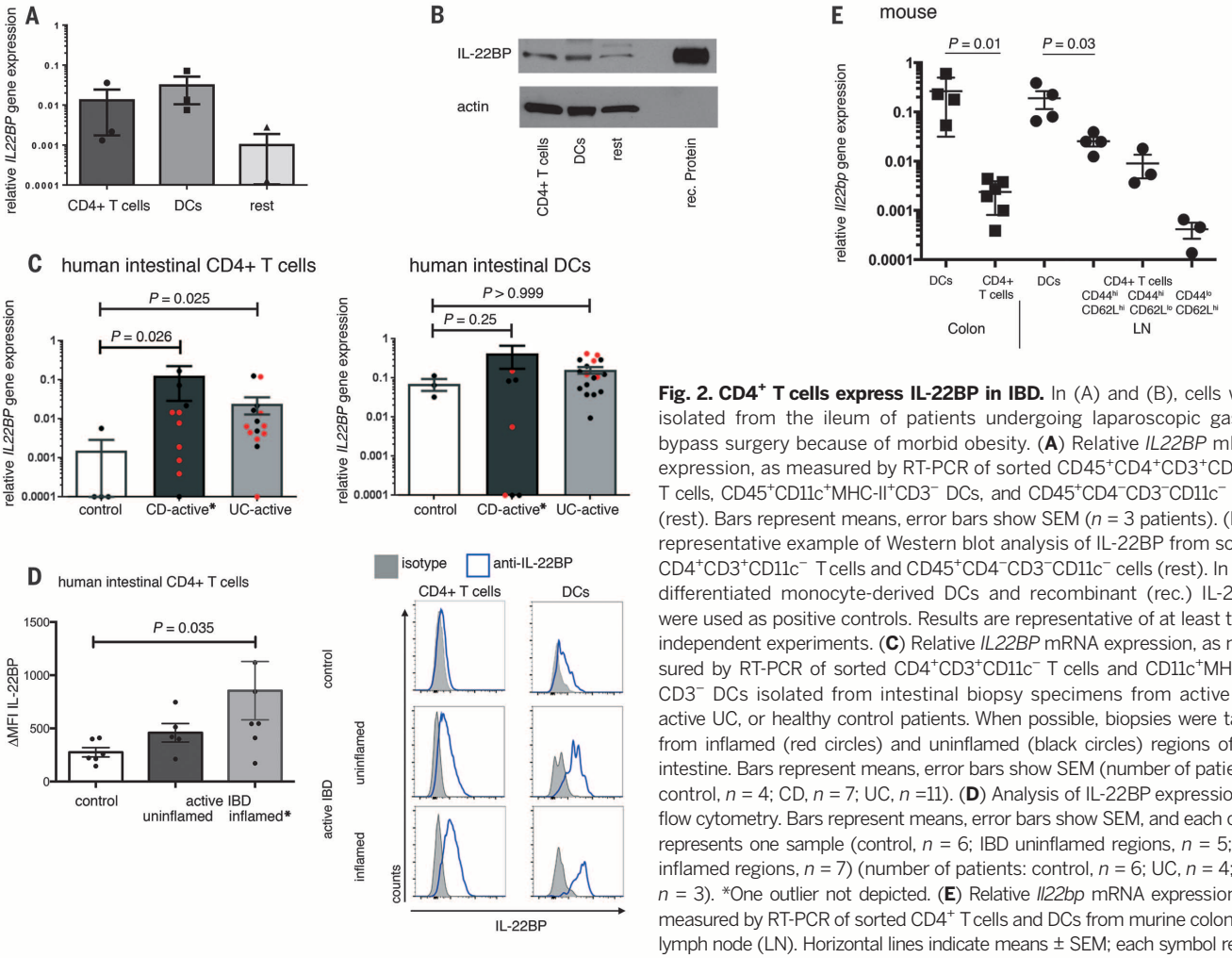

Fig. 2. CD4$^+$ T cells express IL-22BP in IBD. In (A) and (B), cells were isolated from the ileum of patients undergoing laparoscopic gastric bypass surgery because of morbid obesity. (**A**) Relative *IL22BP* mRNA expression, as measured by RT-PCR of sorted CD45$^+$CD4$^+$CD3$^+$CD11c$^-$ T cells, CD45$^+$CD11c$^+$MHC-II$^+$CD3$^-$ DCs, and CD45$^+$CD4$^-$CD3$^-$CD11c$^-$ cells (rest). Bars represent means, error bars show SEM (n = 3 patients). (**B**) A representative example of Western blot analysis of IL-22BP from sorted CD4$^+$CD3$^+$CD11c$^-$ T cells and CD45$^+$CD4$^-$CD3$^-$CD11c$^-$ cells (rest). In vitro differentiated monocyte-derived DCs and recombinant (rec.) IL-22BP were used as positive controls. Results are representative of at least three independent experiments. (**C**) Relative *IL22BP* mRNA expression, as measured by RT-PCR of sorted CD4$^+$CD3$^+$CD11c$^-$ T cells and CD11c$^+$MHC-II$^+$CD3$^-$ DCs isolated from intestinal biopsy specimens from active CD, active UC, or healthy control patients. When possible, biopsies were taken from inflamed (red circles) and uninflamed (black circles) regions of the intestine. Bars represent means, error bars show SEM (number of patients: control, n = 4; CD, n = 7; UC, n =11). (**D**) Analysis of IL-22BP expression by flow cytometry. Bars represent means, error bars show SEM, and each circle represents one sample (control, n = 6; IBD uninflamed regions, n = 5; IBD inflamed regions, n = 7) (number of patients: control, n = 6; UC, n = 4; CD, n = 3). *One outlier not depicted. (**E**) Relative *Il22bp* mRNA expression, as measured by RT-PCR of sorted CD4$^+$ T cells and DCs from murine colon and lymph node (LN). Horizontal lines indicate means ± SEM; each symbol represents one experiment using pooled samples from three to six mice per group.

Downloaded from http://science.sciencemag.org/ on October 21, 2016

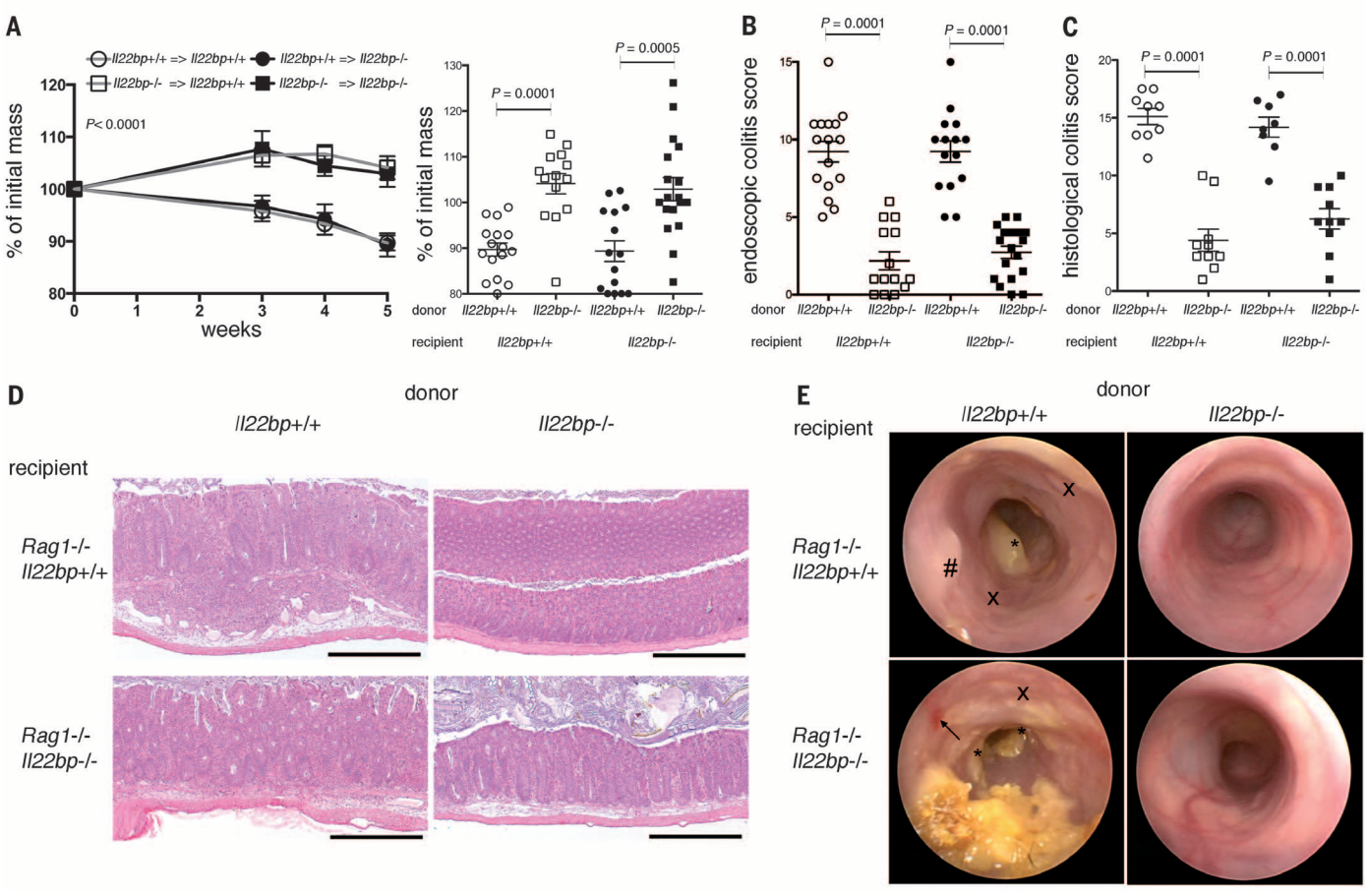

Fig. 3. A pathogenic role of CD4$^+$ T cell–derived IL-22BP in a murine colitis model. CD4$^+$CD25$^-$CD45RB^{high} cells were isolated from the spleen and lymph nodes of *Il22bp*$^{+/+}$ and *Il22bp*$^{-/-}$ mice and transferred into *Rag1*$^{-/-}$ and *Rag1*$^{-/-}$*Il22bp*$^{-/-}$ recipients. Disease development was assessed by (**A**) weight loss, (**B**) endoscopic, and (**C**) histological findings 5 weeks after transfer. Each symbol represents one mouse. Horizontal lines indicate means ± SEM. Results are representative of four independent experiments. (**D**) Representative histological (scale bar, 1 mm) and (**E**) endoscopic findings (asterisks, stool inconsistency; Xs, granularity; pound sign, abundant fibrin; arrow, ulceration).

not significantly reduced (fig. S10), suggesting that IL-22 does not regulate IL-22BP. We therefore further investigated the link between IL-22BP and anti–TNF-α therapy.

To that end, we isolated CD4$^+$ T cells and DCs from intestinal biopsy specimens obtained from IBD patients who were receiving anti–TNF-α therapy (adalimumab or infliximab) or other immunemodulating treatment in order to test whether anti–TNF-α treatment influences the expression of *IL22BP*. *IL22BP* expression was markedly reduced in CD4$^+$ T cells of IBD patients who were responsive to anti–TNF-α treatment, compared with those of patients on other medications (Fig. 4B and table S4). This effect did not seem to be due to differences in disease activity [disease activity index (mean ± SEM) for anti–TNF-α, 0.6 ± 0.25; for other treatment, 0.3 ± 0.13; P = 0.29] and appeared to be specific to CD4$^+$ T cells, because DCs did not show a significant down-regulation of *IL22BP* in IBD patients treated with anti–TNF-α (Fig. 4C). Furthermore, the expression of genes for other T cell signature cytokines and transcriptional regulators, such as *IL17A*, *IL22*, *IFNg*, *IL5*, *FOXP3*, *TBX21*, *GATA3*, and *RORC*, were not different between these groups (Fig. 4D and fig. S11). These data argue against a general and broad effect of anti–TNF-α treatment on CD4$^+$ T cells. However, it remained unclear whether TNF-α would regulate IL-22BP in a direct manner. We found that *IL22bp* expression is not significantly reduced in *Tnfr1*- and *Tnfr2*-deficient T cells in the transfer colitis model, compared with that in wild-type controls (fig. S12). Moreover, TNF-α did not induce *IL22BP* in T cells in vitro (fig. S12). Taken together, these data suggest that TNF-α might regulate IL-22BP in an indirect manner that is as yet unknown.

We next tested whether anti–TNF-α therapy is simply inversely correlated with IL-22BP expression or whether the effect of this treatment is dependent on IL-22BP regulation, and thus on the protective effect of IL-22. In case of the latter, one would expect that this therapy would not work in an *Il22*-deficient environment. To test this point, we transferred wild-type and *Il22*$^{-/-}$ CD4$^+$CD25$^-$CD45RB^{high} T cells into *Rag1*$^{-/-}$ and *Rag1*$^{-/-}$*Il22*$^{-/-}$ mice, respectively, and treated the mice with anti–TNF-α upon colitis development. Anti–TNF-α treatment was not effective in the *Il22*–deficient environment (fig. S13), but anti–TNF-α therapy significantly reduced colitis severity in the *Il22*–sufficient environment. In addition, we transferred *Il22bp*$^{-/-}$ CD4$^+$CD25$^-$CD45RB^{high} T cells into *Rag1*$^{-/-}$*Il22bp*$^{-/-}$ mice and treated the mice with anti–TNF-α upon colitis development. As expected, these mice developed a mild colitis, which, however, was not further improved by anti–TNF-α therapy. To further support these data that we obtained in the murine system, we analyzed CD4$^+$ T cells isolated from the intestine of patients who did not respond to anti–TNF-α therapy. T cell–derived IL-22BP was not down-regulated in these patients (Fig. 4B). Thus, our data indicate that one mechanism whereby anti–TNF-α therapy may reduce disease activity is by down-regulating expression of IL-22BP.

TNF-α antibodies are one of the most effective therapies for IBD, but what determines the response to anti–TNF-α therapy in IBD has remained elusive (*23*, *24*). Our data suggest that anti–TNF-α therapy may block IL-22BP expression by intestinal T cells, thus allowing IL-22–induced mucosal healing. Targeting IL-22BP directly might allow for a more effective and specific

Downloaded from http://science.sciencemag.org/ on October 21, 2016

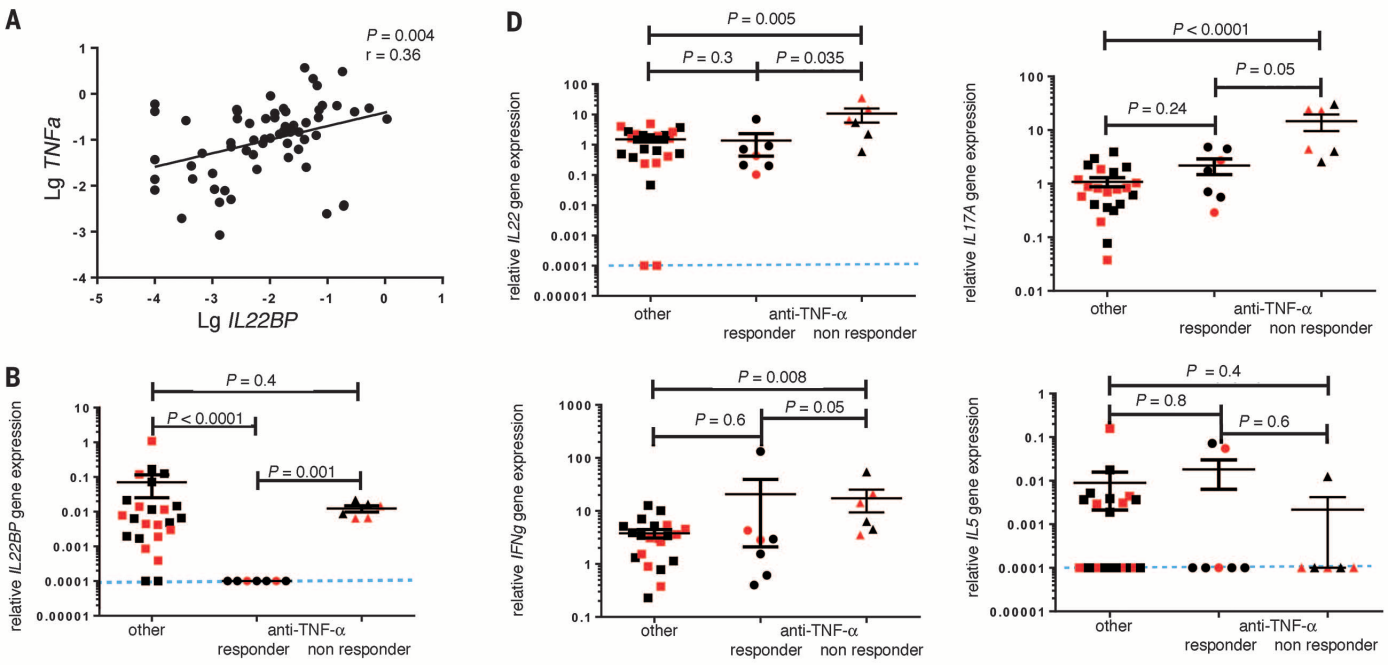

Fig. 4. Anti–TNF-α therapy correlates with reduced IL-22BP expression by CD4$^+$ T cells in IBD (UC and CD) patients. (**A**) Correlation between *TNFα* and *IL22BP* mRNA expression, as measured by RT-PCR (P = 0.004; r = 0.36) of specimens from the intestines of patients with active IBD. In (B) to (D), CD4$^+$CD3$^+$CD11c$^-$ T cells and CD11c$^+$MHC-II$^+$CD3$^-$ DCs were isolated from intestinal biopsy specimens from patients with IBD (CD and UC). When possible, biopsies were taken from inflamed (red circles) and uninflamed (black circles) regions. (**B** and **C**) Relative *IL22BP* mRNA expression, as measured by RT-PCR of (B) CD4$^+$ T cells and (C) DCs isolated from intestinal biopsy specimens from IBD patients being treated with anti–TNF-α therapy or other therapies. (**D**) Relative *IL22*, *IL17A*, *IFNg*, and *IL5* mRNA expression, as measured by RT-PCR of sorted CD4$^+$ T cells from IBD patients being treated with anti–TNF-α therapy or other therapies. Horizontal lines indicate means ± SEM; dotted lines indicate the detection limit (number of patients: other therapies, n = 16; anti–TNF-α responder, n = 5; anti–TNF-α nonresponder, n = 5).

therapy for IBD without invoking the undesirable and potentially dangerous side effects of anti–TNF-α, such as susceptibility to infections. In addition, anti–TNF-α therapy may increase patients' risk of developing cancer. Therefore, long-term anti–IL-22BP treatment might have similar effects, for which these potential patients should be closely screened.

REFERENCES AND NOTES

1. A. Kaser, S. Zeissig, R. S. Blumberg, *Annu. Rev. Immunol.* **28**, 573–621 (2010).
2. N. Gagliani, B. Hu, S. Huber, E. Elinav, R. A. Flavell, *Cell* **157**, 776–783 (2014).
3. M. F. Neurath, *Mucosal Immunol.* **7**, 6–19 (2014).
4. K. Wolk *et al.*, *J. Immunol.* **178**, 5973–5981 (2007).
5. S. Schmechel *et al.*, *Inflamm. Bowel Dis.* **14**, 204–212 (2008).
6. G. F. Sonnenberg, L. A. Fouser, D. Artis, *Nat. Immunol.* **12**, 383–390 (2011).
7. S. Huber *et al.*, *Nature* **491**, 259–263 (2012).
8. K. Sugimoto *et al.*, *J. Clin. Invest.* **118**, 534–544 (2008).
9. M. Kamanaka *et al.*, *J. Exp. Med.* **208**, 1027–1040 (2011).
10. L. A. Zenewicz *et al.*, *Immunity* **29**, 947–957 (2008).
11. S. Kirchberger *et al.*, *J. Exp. Med.* **210**, 917–931 (2013).
12. I. Kryczek *et al.*, *Immunity* **40**, 772–784 (2014).
13. C. C. Wei, T. W. Ho, W. G. Liang, G. Y. Chen, M. S. Chang, *Genes Immun.* **4**, 204–211 (2003).
14. S. V. Kotenko *et al.*, *J. Immunol.* **166**, 7096–7103 (2001).
15. W. Xu *et al.*, *Proc. Natl. Acad. Sci. U.S.A.* **98**, 9511–9516 (2001).
16. L. Dumoutier, D. Lejeune, D. Colau, J. C. Renauld, *J. Immunol.* **166**, 7090–7095 (2001).
17. B. C. Jones, N. J. Logsdon, M. R. Walter, *Structure* **16**, 1333–1344 (2008).
18. K. Moriwaki *et al.*, *Immunity* **41**, 567–578 (2014).
19. P. B. Watchmaker *et al.*, *Nat. Immunol.* **15**, 98–108 (2014).
20. J. C. Martin *et al.*, *Mucosal Immunol.* **7**, 101–113 (2014).
21. J. C. Martin *et al.*, *Mucosal Immunol.* **9**, 539–549 (2016).
22. F. Powrie, R. Correa-Oliveira, S. Mauze, R. L. Coffman, *J. Exp. Med.* **179**, 589–600 (1994).
23. T. J. Ślebioda, Z. Kmieć, *Mediators Inflamm.* **2014**, 325129 (2014).
24. C. Papi *et al.*, *Dig. Liver Dis.* **45**, 978–985 (2013).

ACKNOWLEDGMENTS

The authors thank C. Lieber, P. Musco, J. Alderman, and F. Huber for expert administrative assistance and C. Möller-Koop for performing the immune histochemistry. The authors also thank all members of the Departments of Endoscopy and Surgery at the University Medical Center Hamburg-Eppendorf for their key help in obtaining the human samples involved in this study. This work was supported by the Deutsche Forschungsgemeinschaft (grant SFB841 to S.H., A.W.L, and D.B.), the European Research Council (starting grant 337251 to S.H.), Ernst Jung-Stiftung Hamburg (to S.H.), Stiftung Experimentelle Biomedizin (to S.H.), Werner Otto Stiftung Hamburg (to S.H. and M.W.), and the Howard Hughes Medical Institute (to R.A.F.). All data necessary to understand and assess the conclusions of the manuscript are available in the body of the paper and in the supplementary materials. *Il22-* and *Il22bp*-deficient mice are available from Regeneron under a material transfer agreement with Yale University. S.H., R.A.F., and P.P. are inventors on a patent application (LU 92982) submitted by the University Medical Center Hamburg-Eppendorf together with Yale University that covers the use of IL-22BP as biomarker in anti–TNF-α treatments.

SUPPLEMENTARY MATERIALS

www.sciencemag.org/content/354/6310/358/suppl/DC1
Materials and Methods
Figs. S1 to S13
Tables S1 to S4
References (*25*–*27*)

19 July 2016; accepted 21 September 2016
10.1126/science.aah5903

Downloaded from http://science.sciencemag.org/ on October 21, 2016

AAAS 2017 ANNUAL MEETING

FEBRUARY 16-20 • BOSTON

SERVING SOCIETY THROUGH

SCIENCE POLICY

Advance Registration is Now Open

The 2017 meeting focuses on how to inform policies with the best available scientific evidence.

aaas.org/meetings

See Inside for Details:

President's Address / Registration Rates
Plenary Lectures / Topical Lectures
Seminars / Session Tracks

Downloaded from http://science.sciencemag.org/ on October 20, 2016

AAAS 2017 ANNUAL MEETING

Join us in Boston

Learn about science and technology addressing current and future policy challenges.

- Seminars on gene editing; science and the law; scientific reproducibility and social responsibility; and communicating science
- 120+ symposia in 14 disciplinary tracks covering the latest research advances
- Network with colleagues and attend career development workshops

Connect with us

@AAASmeetings #AAASmtg

facebook.com/AAAS.Science

aaas.org/meetings

Reporters: The AAAS Annual Meeting Newsroom will be hosted on EurekAlert! at eurekalert.org/aaasnewsroom

Dear Colleagues:

On behalf of the AAAS Board of Directors, it is my honor to invite you to join us in Boston for the 2017 AAAS Annual Meeting, February 16-20.

The AAAS Annual Meeting is the most widely recognized global science gathering with cutting-edge scientific sessions, renowned speakers, and valuable networking opportunities.

The 2017 meeting theme—Serving Society Through Science Policy—focuses on how to inform policies with the best available scientific evidence.

We look forward to seeing you in Boston. Advance registration and hotel reservations are now available.

Barbara A. Schaal

Barbara Schaal
AAAS President
Dean of the Faculty of Arts and Sciences
Mary-Dell Chilton Distinguished Professor of Biology
Washington University in St. Louis

PRESIDENT'S ADDRESS

Barbara Schaal
Thursday, February 16
6:00 p.m. – 7:00 p.m.

Dr. Barbara Schaal was among the first plant scientists to use molecular biology-based approaches to understand evolutionary processes in plants, and she has worked to advance understanding of plants' molecular systems and population genetics. Her recent work includes investigating the evolutionary genetics of plants in hopes of enriching crops such as cassava and rice. She holds a bachelor's degree in biology from the University of Illinois at Chicago and received her Ph.D. in population biology from Yale University. A member of the National Academy of Sciences, she was elected as the academy's first woman vice-president in 2005. President Barack Obama appointed Schaal to the President's Council of Advisors on Science and Technology in 2009, and former U.S. Secretary of State Hillary Rodham Clinton appointed her as one of three new science envoys in 2012 to advise the White House, the U.S. Department of State, and the U.S. scientific community about insights gained from travels and interactions abroad. In addition to serving as AAAS President (2016-17), Schaal has been president of the Botanical Society of America and the Society for the Study of Evolution. She has received numerous awards, including a Guggenheim Fellowship, the Key Award from the American Genetics Association, and the American Institute of Biological Sciences Distinguished Scientist Award. At Washington University in St. Louis, where she regularly involves undergraduates in her labs and mentors graduate and postdoctoral students, Schaal has received the Founders Day Distinguished Faculty Award, the Arthur Holly Compton Faculty Achievement Award, and the Graduate Student Senate Outstanding Faculty Mentor Award.

Downloaded from http://science.sciencemag.org/ on October 20, 2016

SERVING SOCIETY THROUGH SCIENCE POLICY

PLENARY LECTURES

Naomi Oreskes
Professor of the History of Science, Harvard University

The Scientist as Sentinel

Friday, February 17
5:00 p.m. – 6:00 p.m.

May Berenbaum
Professor and Department Head of Entomology, University of Illinois, Urbana-Champaign

Can Science Save the Honey Bees?

Saturday, February 18
5:00 p.m. – 6:00 p.m.

S. James Gates Jr.
John S. Toll Professor of Physics, University of Maryland

Science and Evidence-Based Policymaking

Sunday, February 19
5:00 p.m. – 6:00 p.m.

TOPICAL LECTURES

Friday, February 17

Alta Charo
Warren P. Knowles Professor of Law and Bioethics, University of Wisconsin, Madison
Human Gene Editing: Recommendations from U.S. National Academies

Daniel Nocera
Patterson Rockwood Professor of Energy, Harvard University
Global Energy Challenge: Solutions from Science to Technology Transition

MCGOVERN AWARD LECTURE IN THE BEHAVIORAL SCIENCES

Henry L. Roediger, III
James S. McDonnell Distinguished University Professor of Biology
Making It Stick: The Science of Successful Learning

Saturday, February 18

Venki Ramakrishnan
President, Royal Society
Potential and Risks of Recent Developments in Biotechnology

Leila Takayama
Founder and Researcher, Hoku Labs
Robotics: Toward a More Human-Centered Future

SARTON MEMORIAL LECTURE IN THE HISTORY AND PHILOSOPHY OF SCIENCE

Susan Lindee
Janice and Julian Bars Professor of History and Sociology of Science, University of Pennsylvania
The Rise of the Genome: Genetics After the Bomb

Sunday, February 19

Jeremy DeSilva
Associate Professor of Anthropology, Dartmouth College
All Walks of Life: Bipedal Diversity in Early Human Ancestors

John Rickford
J.E. Wallace Sterling Professor of Linguistics, Stanford University
Using Linguistics to Fight Dialect Prejudice in Courtrooms and Beyond

Alan Stern
Principal Investigator, New Horizons mission
The Pluto System as Explored by New Horizons

Downloaded from http://science.sciencemag.org/ on October 20, 2016

SEMINARS

Thursday, February 16

Communicating Science

Science is prevalent in many areas of modern life, and the science-society relationship can be approached in different ways. Interaction between stakeholders, including scientists and non-scientists, is critical to finding common ground on scientific issues affecting society. This seminar builds on connections between scientists, science communication and public engagement professionals who can support their efforts, and social scientists whose research can inform best practices. Attendees will gain actionable knowledge and learn more about the growing public engagement with science community.

Organized by: Emily Cloyd and Elana Kimbrell, AAAS Center for Public Engagement with Science and Technology, Washington, DC

Who's Your Audience?

MODERATOR: Bruce Lewenstein, Cornell University, Ithaca, NY

SPEAKERS: Kirstin Dow, University of South Carolina, Columbia
Kishore Hari, University of California, San Francisco
Matt Leighninger, Public Agenda, New York City

Scientist Motivations, Support, and Challenges for Public Engagement

MODERATOR: Jessica Sickler, J. Sickler Consulting LLC, Pittsburgh, PA

SPEAKERS: Tracey Holloway, University of Wisconsin, Madison
Sriram Sundararajan, Iowa State University, Ames
Ezra Markowitz, University of Massachusetts, Amherst

The Online Scientist: Social Media and Public Engagement

MODERATOR: Erika Shugart, American Society for Cell Biology, Bethesda, MD

SPEAKERS: Raychelle Burks, St. Edward's University, Austin, TX
Nsikan Akpan, PBS NewsHour, Arlington, VA
Sara Yeo, University of Utah, Salt Lake City

Friday, February 17

Gene Editing: Science and Policy Implications

The use of CRISPR-Cas9 as a tool for gene editing has led to a proliferation in research, potential applications, and debates within scientific, policy, and public circles about its ethical implications. In this seminar, speakers share updates on scientific progress in gene editing and potential for its use. Results of recent efforts by the National Academies of Sciences, Engineering, and Medicine and the Hastings Center to assess the safety, ethical, and social implications of gene-editing technology, as well as recommendations for regulation and oversight, are discussed. One session focuses on non-safety ethical issues of human gene editing, including disability rights, dignity, and the relationship between parents and children. Another session delves into the use of gene editing in agricultural research, the potential regulation of these technologies, and social acceptance of genetically-modified food.

CRISPR: A Game Changing Gene-Editing Tool and Implications for Science and Policy

Organized by: Carmen Garcia Fernandez and Eleni Zika, European Research Council, Brussels, Belgium

SPEAKERS: Emmanuelle Charpentier, Max Planck Institute for Infection Biology, Berlin, Germany
Rotem Sorek, Weizmann Institute of Science, Rehovot, Israel
Edze Westra, University of Exeter, Cornwall, United Kingdom

DISCUSSANT: Annelien Bredenoord, University Medical Center Utrecht, Netherlands

Modified Policy for a Genetically Modified World

Organized by: Katherine Bowman and Keegan Sawyer, National Academies of Sciences, Engineering, and Medicine, Washington, DC

MODERATOR: Richard Hynes, Massachusetts Institute of Technology, Cambridge

SPEAKERS: R. Alta Charo, University of Wisconsin Law School, Madison
Jennifer Kuzma, North Carolina State University, Raleigh
Gary Marchant, Arizona State University College of Law, Tempe

The Ethics of Gene Editing: Should Concerns Beyond Safety Matter in Science Policy?

Organized by: Mildred Solomon, The Hastings Center, Garrison, NY

SPEAKERS: George Church, Harvard University, Boston, MA
Josephine Johnston, The Hastings Center, Garrison, NY
Gary Marchant, Arizona State University College of Law, Tempe

The Potential of Gene Editing to Revolutionize Agriculture

Organized by: Donald P. Weeks, University of Nebraska, Lincoln; Martin Spalding, Iowa State University, Ames

MODERATOR: Nina Fedoroff, OFW Law, Washington, DC

SPEAKERS: Dan Voytas, University of Minnesota, St. Paul
Alison Van Eenennaam, University of California, Davis
Mark Cigan, DuPont Pioneer, Johnston, IA

Downloaded from http://science.sciencemag.org/ on October 20, 2016

Saturday, February 18

Science and the Law

This seminar examines the contributions of science to the legal system from a diversity of perspectives. The scientific foundation of forensic science has been called into question in recent years, and one session focuses on progress in two areas of research often key to criminal investigations, latent fingerprint analysis and fire investigation, as well as how judges decide which scientific evidence to permit in court. Another session analyzes how linguistics can both affect and interpret criminal justice outcomes – from innocent people confessing to crimes, to the effects of cross-examination on sexual assault victims. A third session shares research on risk factors for premature mortality and contact with the criminal justice system. Another session discusses scientists' roles in, and reasons for, participating in legal processes.

Science-Based Forensic Evidence: Getting the Science Right in Criminal Investigations

Organized by: Deborah Runkle, AAAS Center of Science, Policy, and Society Programs, Washington, DC

SPEAKERS: Jed Rakoff, U.S. District Court, Southern District of New York, New York City
Jose Almirall, Florida International University, Miami
William Thompson, University of California, Irvine

Discourse Analysis of Criminal Justice

Organized by: Lawrence Solan, Brooklyn Law School, NY

SPEAKERS: Tammy Gales, Hofstra University, Hempstead, NY
Laurence Horn, Yale University, New Haven, CT
Janet Ainsworth, Seattle University, WA

Crime, Justice, and Death

Organized by: William Alex Pridemore, State University of New York, Albany

SPEAKERS: Linda Teplin, Northwestern University, Chicago, IL
William Alex Pridemore, University at Albany, State University of New York
Heather Harris, University of California, Berkeley

DISCUSSANT: Brandon Welsh, Northeastern University, Boston, MA

When the Legal System Seeks Help from Scientists: Successes and Failures

Organized by: Keerthi Shetty, American Academy of Arts and Sciences, Cambridge, MA

SPEAKERS: Shari Diamond, Northwestern University School of Law, Chicago, IL
Richard Lempert, University of Michigan Law School, Ann Arbor
Elizabeth Loftus, University of California, Irvine

Sunday, February 19

Scientific Reproducibility and Social Responsibility

Questions about the reproducibility of scientific research are central in debates about the conduct, outcomes, and funding of science. This seminar includes a panel with the leader of the Open Science Collaboration (OSC)'s 2015 evaluation of 100 psychology studies, a journal editor in which some of those studies were originally published, and a lead author of the subsequent critique of the OSC study. Representatives of both the National Institutes of Health (NIH) and the biomedical research community share their perspectives on the first year of the NIH Rigor and Reproducibility guidelines. Other sessions in this seminar consider internal and external pressures that may influence scientists in producing socially responsible science and the role of ethics in the practice of science across several disciplines.

Ensuring the Reproducibility of Scientific Findings: Where Does Psychology Stand?

Organized by: Robert E. Fay, Westat, Bethesda, MD

SPEAKERS: Brian Nosek, University of Virginia, Charlottesville
D. Stephen Lindsay, University of Victoria, Canada
Prasad Patil, Dana-Farber Cancer Institute Boston, MA

Rigor and Reproducibility One Year Later: How Has the Biomedical Community Responded?

Organized by: Leonard Freedman, Global Biological Standards Institute, Washington, DC

SPEAKERS: Myles Brown, Dana-Farber Cancer Institute, Boston, MA
Michael Lauer, National Institutes of Health, Bethesda, MD

DISCUSSANT: Judith Kimble, University of Wisconsin, Madison

Social Responsibility in Science From the Inside Out

Organized by: Kevin C. Elliott, Michigan State University, East Lansing

SPEAKERS: Heather Douglas, University of Waterloo, Canada
Kevin C. Elliott, Michigan State University, East Lansing
Melinda Gormley, AAAS Science and Technology Policy Fellow, U.S. Environmental Protection Agency, Washington, DC

DISCUSSANT: Marc Saner, University of Ottawa, Canada

How Ethical Science Supports Ethical Policy: Disciplinary Perspectives

Organized by: Rochelle Tractenberg, Georgetown University, Washington, DC

MODERATOR: Andrew Gelman, Columbia University, New York City

SPEAKERS: Richard Maudslay, Royal Academy of Engineering, London, United Kingdom
Rochelle Tractenberg, Georgetown University, Washington, DC
George DeMartino, Denver University, CO

Downloaded from http://science.sciencemag.org/ on October 20, 2016

SESSION TRACKS

Organizers are listed under session titles.

AGRICULTURE AND FOOD

Genetically Engineered Crops: The Evidence and the Unknowns
Organized by Kara Laney, National Academies of Sciences, Engineering, and Medicine, Washington, DC

Innovative Convergence Approaches to Solving Energy and Agricultural Issues
Organized by Katherine Bowman, National Academies of Sciences, Engineering, and Medicine, Washington, DC; Gene Robinson, University of Illinois, Urbana-Champaign

Making the Most of Big Data in Precision Agriculture
Organized by Claire Craig, The Royal Society, London, United Kingdom

Arsenic in Food: From Soil to Plate to Policy
Organized by Mary Lou Guerinot and Laurie Rardin, Dartmouth College, Hanover, NH; Laurie Rardin, Geisel School of Medicine, Hanover, NH

Monitoring Food Security: The Role of New Technologies
Organized by Barbara Rater, U.S. Department of Agriculture, Washington, DC

Phytobiomes: Systems-Level Approaches to Improve Agricultural Productivity
Organized by Jan E. Leach, Colorado State University, Fort Collins; Kellye Eversole, Eversole Associates, Bethesda, MD

Plan Bee: Pollinators, Food Production, and U.S. Policy
Organized by Insu Koh and Taylor Ricketts, University of Vermont, Burlington

ANTHROPOLOGY, CULTURE, AND LANGUAGE

Beringia and the Dispersal of Modern Humans to the Americas
Organized by John Hoffecker, University of Colorado, Boulder; Dennis O'Rourke, University of Kansas, Lawrence

How We Came to Our Senses: Ecology, Evolution, and the Future of Human Sensation
Organized by Nathaniel J. Dominy, Dartmouth College, Hanover, NH; Amanda Melin, University of Calgary, Canada

Language Across the Lifespan: Clues Predicting Alzheimer's Disease
Organized by Suzanne Flynn, Massachusetts Institute of Technology, Cambridge; Barbara Lust, Cornell University, Ithaca, NY

Strengthening Health Systems in Africa: Intersections of Culture and Science
Organized by Crystal Patil, University of Illinois, Chicago; Gillian H. Ice, Ohio University, Athens

BEHAVIORAL AND SOCIAL SCIENCES

A Practical Philosophy of Science: Key to Better Policies
Organized by Pilar Lacruz and Piotr Kwiecinski, European Research Council Executive Agency, Brussels, Belgium

Public Attitudes About Polarized Science: Evolution, Climate Change, Zika, and GMOs
Organized by Deena Weisberg, University of Pennsylvania, Philadelphia; Matthew H. Slater, Bucknell University, Lewisburg, PA

Statistical Issues in Criminology
Organized by David Banks, Duke University, Durham, NC

The Psychology of Decision-Making and Cancer
Organized by Valerie Reyna, Cornell University, Ithaca, NY; Colin Widmer, Miami University, Oxford, OH

The Role of Misinformation in Explaining Public Perceptions of Science
Organized by Nick Allum, University of Essex, United Kingdom; Patrick Sturgis, University of Southampton, United Kingdom

BIOLOGY AND NEUROSCIENCE

Innovative Neurotechnologies and Strategies from the BRAIN Initiative
Organized by Terrence Sejnowski, Salk Institute for Biological Studies, La Jolla, CA; Jane Roskams, Allen Institute for Brain Science, Seattle, WA

Optical Nanoscale Imaging: Unraveling the Chromatin Structure-Function Relationship
Organized by Vadim Backman, Northwestern University, Evanston, IL

RNA Splicing at 40: Reflecting on Scientific Progress, Policy, and Social Justice
Organized by Pnina G. Abir-Am, Brandeis University, Waltham, MA; William C. Summers, Yale University, New Haven, CT

Science, Ethics, and Engagement in the Governance of Gene Drives: It Takes a Village
Organized by Keegan Sawyer and Audrey Thevenon, National Academies of Sciences, Engineering, and Medicine, Washington, DC

The Neuroscience of Time and Memory
Organized by Sheena Josselyn, Hospital for Sick Children, Toronto, Canada

CLIMATE CHANGE

Accelerating Low-Carbon Innovation Through Policy
Organized by Rahel Byland, ETH Zurich, Switzerland

Climate Change and Fisheries: Accounting for Climate Effects in Fisheries Management
Organized by Christopher Costello, University of California, Santa Barbara; Merrick Burden, Environmental Defense Fund, San Francisco, CA

Global Climate Science Imperatives in a Post-Paris Agreement World
Organized by Hope Michelsen, Sandia National Laboratories, Livermore, CA; Manvendra Dubey, Los Alamos National Laboratory, NM

National Climate Assessment: A Sustained Process for Providing Actionable Information
Organized by Tess Carter, U.S. Global Change Research Program, Washington, DC; Jack A. Kaye, National Aeronautics and Space Administration, Washington, DC

The Peril and Promise of Forests and Soils in Achieving the Paris Temperature Goals
Organized by William Moomaw, Tufts University, Medford, MA; Scott Goetz, Woods Hole Research Center, Falmouth, MA

Social Resilience to Climate-Related Disasters
Organized by Peter N. Peregrine, Lawrence University, Appleton, WI; Carol Ember, Human Relations Area Files, New Haven, CT

Solar Geoengineering: What Is It and What Role Could It Play in Climate Policy?
Organized by David Keith, Harvard University, Cambridge, MA

Sustainability in the Changing Arctic: Interdisciplinary Insights for policy
Organized by Philip Loring, University of Saskatchewan, Saskatoon, Canada; S. Craig Gerlach, University of Calgary, Canada

Downloaded from http://science.sciencemag.org/ on October 20, 2016

COMMUNICATION AND PUBLIC PROGRAMS

Aiming for Success from Birth: Community Programs to End the Poverty of Words
Organized by Nan Bernstein Ratner, University of Maryland, College Park

Bringing Scholarly Communication into the 21st Century
Organized by Claire Craig, The Royal Society, London, United Kingdom

The Paris Agreement and Leveraging Religious Support for Climate Policy
Organized by Se Y. Kim and David Buller, AAAS Dialogue on Science, Ethics, and Religion, Washington, DC

From Literacy to Dialogue: How to Best Communicate (Controversial) Science
Organized by Keegan Sawyer, National Academies of Sciences, Engineering, and Medicine, Washington, DC; Dietram Scheufele, University of Wisconsin, Madison

Gravitational Waves: Communicating the Science and Wonder of LIGO
Organized by Peter Saulson, Syracuse University, NY; Gabriela González, Louisiana State University, Baton Rouge

Let's Talk: Learning from Socio-Scientific Conversations Among Scientists and Publics
Organized by Larry Bell, Museum of Science, Boston, MA

The Power and Perils of the News Media in the Use of Scientific Evidence
Organized by Matthew Weber, Rutgers University, New Brunswick, NJ

EDUCATION AND WORKFORCE

Economic Implications of Scientific Training in the Biomedical Research Workforce
Organized by Barbara Natalizio, AAAS Science and Technology Policy Fellow, National Science Foundation, Arlington, VA; Andrew Miklos, National Institutes of Health, Bethesda, MD

Finding Solutions to Implicit Bias in STEM: Thinking Fast Makes Changing Slow
Organized by Lydia Villa-Komaroff, Chestnut Hill, MA

Leveraging Informal Learning Environments to Close Socioeconomic Status-Related Achievement Gaps
Organized by Susan C. Levine, University of Chicago, IL

Downloaded from http://science.sciencemag.org/ on October 20, 2016

AAAS 2017 ANNUAL MEETING
SERVING SOCIETY THROUGH SCIENCE POLICY

Advance Registration Rates until January 27

	AAAS Member Rates for members in good standing	New Member Includes a year of AAAS membership	Non-Member Rates for all other attendees
Professional	$310	$380	$440
Postdoc	$250	$320	$380
K-12 Teacher	$250	$320	$380
Retired Professional	$250	$320	$380
Student	$65	$70	$95
One Day	$175	N/A	$220

aaas.org/meetings

Leveraging Linguistics to Broaden Participation in STEM
Organized by Anne Charity-Hudley, College of William and Mary, Williamsburg, VA

Policies and Practices Affecting the Success of Women in Science and Engineering
Organized by Lynnette D. Madsen, National Science Foundation, Arlington, VA; Darryl Williams, Tufts University, Medford, MA

Using Evidence to Inform Policy for Undergraduate STEM Education
Organized by Jay B. Labov, National Academies of Sciences, Engineering, and Medicine, Washington, DC; Muriel Poston, National Science Foundation, Arlington, VA

Using Existing Evidence to Improve Undergraduate STEM Education
Organized by Judy Dilts, James Madison University, Harrisonburg, VA; Catherine Middlecamp, University of Wisconsin, Madison

ENGINEERING, INDUSTRY, AND TECHNOLOGY

Quantum Computing and Post-Quantum Cryptography
Organized by Charles W. Clark, Joint Quantum Institute, Gaithersburg, MD

Designing and Governing the New Industrial Transformation
Organized by Philip Shapira, Manchester Institute for Innovation Research, United Kingdom

Digital Fabrication in Architecture: The Challenge to Transform the Building Industry
Organized by Rahel Byland, ETH Zurich, Switzerland

Energy Technology Policies in Europe and the US: Learning from Our Differences
Organized by Tajinder Panesor, Institute of Physics, London, United Kingdom

Green Chemistry: 25 Years of Progress
Organized by Teresa Fryberger, National Academies of Sciences, Engineering, and Medicine, Washington, DC

Integrated Cellular Systems: Building Machines with Cells
Organized by Rashid Bashir, University of Illinois, Urbana-Champaign

Urban Mobility as an Engine for Change: European Innovation for Sustainable Cities
Organized by Emily Palmer, EuroTech Universities Alliance, Brussels, Belgium; Ulrich Marsch, Technical University of Munich, Germany

ENVIRONMENT AND ECOLOGY

Should We Mine the Seafloor?
Organized by Thomas Graedel, Yale University, New Haven, CT; Stace Beaulieu, Woods Hole Oceanographic Institution, MA

The Legacy of Deepwater Horizon: New Science Affecting Marine Oil Development Policy
Organized by Steven Murawski, University of South Florida, St. Petersburg

Blue Growth: Conceptualizing Sustainable Development of Marine Environments
Organized by Anne Maria Eikeset, University of Oslo, Norway; Simon A. Levin, Princeton University, NJ

Conservation Paleobiology: Finding Solutions in the Fossil Record
Organized by Susan Kidwell, University of Chicago, IL

Global Environmental Assessments and the Bridge to Environmental Policy
Organized by Jack A. Kaye, National Aeronautics and Space Administration, Washington, DC

Human Impacts on Ecosystems from Fisheries to Forests: Data Informing Decisions
Organized by John Braun, University of British Columbia, Kelowna, Canada; Joanna Flemming, Dalhousie University, Halifax, Canada

Science-Based Strategies for Optimizing Nitrogen Reduction in Northeast U.S. Estuaries
Organized by James Ammerman, Long Island Sound Study, Stamford, CT

Science for the Land-Sea Interface: Informing Coastal and Nearshore Marine Policy
Organized by Michelle Portman, Technion Israel Institute of Technology, Haifa

Protecting the Crown Jewel of the Caribbean: Cuba's Marine Ecosystems
Organized by Dan Whittle, Environmental Defense Fund, Raleigh, NC; Joe Roman, University of Vermont, Burlington, MA

The Effectiveness of Ecosystem Services in Science Decision-Making
Organized by Erica Goldman, COMPASS, Silver Spring, MD

GLOBAL PERSPECTIVES AND ISSUES

Community-Based Social, Ecological, and Health Assessments
Organized by Margaret Murphy, AAAS Science and Technology Policy Fellow, Washington, DC

Global Conference Start-Ups: Inclusive Science and Society Engagement
Organized by Daan Du Toit, South Africa Department of Science and Technology, Pretoria; Miyoko O. Watanabe, Japan Science and Technology Agency, Tokyo

Nuclear Forensics to Combat Terrorism
Organized by Klaus Mayer, European Commission Joint Research Center, Karlsruhe, Germany

Global Principles for Scientific Advice to Governments
Organized by Peter Gluckman, Chief Science Advisor to the Prime Minister of New Zealand, Auckland

Serving Aging Societies Globally Through Science, Technology, and Innovation Policies
Organized by Kuniko Urashima, Japan National Institute of Science and Technology Policy, Tokyo; Naoki Saito, National Institute of Science and Technology Policy, Tokyo, Japan

The Rise of the Rest? High Impact Science in a Multipolar World
Organized by Koen Jonkers, European Commission Joint Research Center, Brussels, Belgium

Think Global, Act Local: Science Diplomacy, Communication, and Advocacy
Organized by Sanjana Patel and Jason Rao, Health Security Partners, Washington, DC

INFORMATION TECHNOLOGY AND COMPUTING

A Pathway Perspective on Expanding the Participation of Women in IT
Organized by Enobong (Anna) Branch, University of Massachusetts, Amherst; Mary Frank Fox, Georgia Institute of Technology, Atlanta

Downloaded from http://science.sciencemag.org/ on October 20, 2016

Artificial Intelligence, People, and Society
Organized by Henry Kautz, University of Rochester, NY; Luke Clarke, The Royal Society, London, United Kingdom

Assistive and Rehabilitative Robotics:
Organized by Nancy Amato, Texas A&M University, College Station

Beyond the Black Box: Toward Transparent and Understandable Machine Learning
Organized by Claire Craig, The Royal Society, London, United Kingdom

Cybersecurity: Mathematics and Policy
Organized by Alice Silverberg, University of California, Irvine

Privacy, Security, and Policy in the Wake of the Apple/FBI Debate
Organized by Daniel Rogers, Terbium Labs, Baltimore, MD; Anice Anderson, Private Engineering Consulting, Carmel, IN

Programming Molecules Using Biology, Chemistry, and Computer Science
Organized by Erik Winfree, California Institute of Technology, Pasadena

The Human Brain and Computing Machines of the Future
Organized by Sankar Basu, National Science Foundation, Arlington, VA

When Everyday Objects Become Internet Devices: A Science Policy Agenda
Organized by Ann Drobnis, Computing Community Consortium, Washington, DC; Elizabeth Mynatt, Georgia Institute of Technology, Atlanta

MEDICAL SCIENCES AND PUBLIC HEALTH

Impact of Drug Shortages and Pricing on the Health of Americans
Organized by William T. Beck, University of Illinois, Chicago; Peter Wipf, University of Pittsburgh, PA

jisha

Thwarting Disease Epidemics and Pandemics with Emerging Technologies
Organized by Duvvur Nageshwar Reddy, Asian Institute of Gastroenterology, Hyderabad, India; Ram D. Sriram, National Institute of Standards and Technology, Gaithersburg, MD

Assessing the Impact of Medical Marijuana: The Grass Could Be Greener
Organized by Ryan Vandrey, Johns Hopkins University School of Medicine, Baltimore, MD; Staci Gruber, McLean Hospital, Belmont, MA

Genomic and Health Data: Global Sharing and Local Governance
Organized by Adrian Thorogood and Bartha Knoppers, McGill University, Montreal, Canada

Mathematical Modeling of Obesity: Integrating Scientific Evidence for Practical Use
Organized by Keisuke Ejima, University of Alabama, Birmingham

Medical Decision-Making: To Screen or Not to Screen?
Organized by Barry Graubard, National Cancer Institute, Rockville, MD

Microbes and Humans: Effects on Health, Disease, and Society
Organized by Janet Rossant, Hospital for Sick Children, Toronto, Canada

Reducing Demographic Disparities in Oral Health Disparities
Organized by Susan Reisine, University of Connecticut School of Dental Medicine, West Hartford

Precision Medicine: New Integrative Paradigms for Disease Modeling
Organized by Kim-Ahn Do, University of Texas MD Anderson Cancer Center, Houston; Arlene Ash, University of Massachusetts Medical School, Worcester

Strategies for Public Health Pandemics: Science, Clinical Practice, and Policy Making
Organized by Eva K. Lee, Georgia Institute of Technology, Atlanta

Supporting Environmental Decision-Daking: Modeling Complex and Noisy Biology
Organized by Nessy Tania, Smith College, Northampton, MA; Richard Judson, U.S. Environmental Protection Agency, Research Triangle Park, NC

The Analysis and Control of Zika and Dengue Virus Epidemics
Organized by Ira M. Longini, University of Florida, Gainesville

Shifting Perspectives on Dementia, Science, and Health Policy
Organized by Ann Lam, Physicians Committee for Responsible Medicine, Washington, DC

PHYSICS AND ASTRONOMY

Scales of Knowledge: From "Action at a Distance" to Black Holes and Quantum Information
Organized by Eva Andrei, Rutgers University, Piscataway, NJ

Cloudy with a Chance of Solar Flares: Quantifying the Risk of Space Weather
Organized by Emily Mobley, U.K. Science and Technology Facilities Council, Didcot

Bringing the Excitement of the 2017 Solar Eclipse to the Public
Organized by Jay Pasachoff, Williams College, Williamstown, MA; Angela Speck, University of Missouri, Columbia

Going Supernova: Stellar Explosions as Objects of and Tools for Discovery
Organized by Lisa Lambert, Canada's National Laboratory for Particle and Nuclear Physics (TRIUMF), Vancouver; Katie Yurkewicz, Fermi National Accelerator Laboratory, Batavia, IL

New Results from Large Hadron Collider Run2: High Precision and Discovery Potential
Organized by Arnaud Marsollier, European Organization for Nuclear Research (CERN), Geneva, Switzerland; Katie Yurkewicz, Fermi National Accelerator Laboratory, Batavia, IL

Opening a New Ear to the Universe with Gravitational Waves
Organized by Terry O'Connor, U.K. Science and Technology Facilities Council, Swindon; Gabriela González, Louisiana State University, Baton Rouge

Particle Therapy and 3-D Imaging: a Roadmap to the Future of Precision Medicine
Organized by Vincenzo Napolano, National Institute for Nuclear Physics, Rome, Italy; Terry O'Connor, U.K. Science and Technology Facilities Council, Swindon

Risk and Benefits in the Astrobiological Exploration of Other Worlds
Organized by John Rummel, SETI Institute, Champlain, NY; Norine Noonan, University of South Florida, St. Petersburg

Downloaded from http://science.sciencemag.org/ on October 20, 2016

PUBLIC POLICY

Evidence-Based Science Advice in the Age of Information: A Canadian Perspective
Organized by Samantha Rae Ayoub and Anna Buczek, Council of Canadian Academies, Ottawa

Ocean Science and Technology: Gathering Input on Federal Research Plan
Organized by Jessica McGrath, National Science Foundation, Arlington, VA

A Practical Philosophy of Science: Key To Better Policies
Organized by Piotr Kwiecinski, European Research Council Executive Agency, Brussels, Belgium; Pilar Lacruz, European Research Council Executive Agency, Brussels, Belgium

Adding the Citizen Voice: Participatory Socio-Scientific Policymaking
Organized by David Sittenfeld, Museum of Science, Boston, MA

Big Data Synthesis for Health Policy
Organized by Erin Faulconer, Institute for Health Metrics and Evaluation, Seattle, WA

Gun Violence Research in the United States: Public Health and Policy Needs
Organized by Sean Gallagher, AAAS Office of Government Relations, Washington, DC

Making Sense of an Abundance of Knowledge to Inform Policymaking
Organized by Stephen Davies, European Commission Joint Research Center, Brussels, Belgium

Supporting Silly-Sounding Science
Organized by Josh Shiode and Erin Heath, AAAS Office of Government Relations, Washington, DC

Engaging People Who Don't Trust Science for Science Policy
Organized by Jane Maienschein, Arizona State University, Tempe

Scientific Advice Mechanisms for Policy
Organized by Johannes Klumpers, European Commission, Brussels, Belgium

The Role of Values in Delivering Science Advice for Policy
Organized by Johannes Klumpers, European Commission, Brussels, Belgium

A New Blueprint for the Ethics and Principles of Science Policymaking
Organized by Aidan Gilligan, SciCom - Making Sense of Science, Brussels, Belgium; Peter Gluckman, Chief Science Advisor to the Prime Minister of New Zealand, Auckland

Unfinished Business: Science Policy for the White House in the New Administration
Organized by Kirstin Matthews, Rice University, Houston, TX

AAAS 2017 ANNUAL MEETING
SERVING SOCIETY THROUGH SCIENCE POLICY

AAAS, publisher of *Science*, thanks the sponsors and supporters of the 2017 Annual Meeting

European Commission

RESEARCH COUNCILS UK

SUBARU

HELMHOLTZ | ASSOCIATION

THE KAVLI FOUNDATION
for its generous support of the Science Journalism Awards

NANYANG TECHNOLOGICAL UNIVERSITY

SNOLAB

Bristol-Myers Squibb

As of September 30, 2016

Downloaded from http://science.sciencemag.org/ on October 20, 2016

siRNA-Validated Antibodies

Proteintech is accelerating its small interfering RNA (siRNA) knockdown program to ensure each one of its 12,000+ antibodies meets rigorous validation standards. siRNA knockdown verifies accurate validation as a negative control to confirm that the antibody binds only to the target protein. These Western blots are performed on whole-cell lysates in which siRNA knocks down expression of the target protein. The original antibody manufacturer became the first company to implement this method in 2014, and continues to push for industry-wide transparency and reproducibility by publishing all of its validation data online. From start to finish, every antibody is made in-house. Proteintech also recently launched its Antibody Upgrade Program, which allows scientists to locate Proteintech equivalents for discontinued or out-of-stock products from all major antibody suppliers.

Proteintech Group
For info: 312-455-8498
www.ptglab.com

Size-Exclusion Chromatography Columns

Superdex 75 Increase is a size-exclusion chromatography resin for fast, reproducible, and high-resolution small-scale purification and analysis of recombinant tagged proteins. Compared with predecessor products, these prepacked columns offer runtimes reduced to one-third with maintained resolution. They are for use with proteins with molecular weights ranging from 3,000 to 70,000, for a variety of applications including preparative protein purification (µg to mg quantities), aggregate analysis, complex formation studies, and sample screening. The 10 × 300 mm column is well suited for high-resolution separations for both preparative and analytical purposes, with 25 µL–500 µL sample volumes. For smaller sample volumes (4 µL–50 µL) and high-resolution preparations and analyses, the 3.2 × 300 mm column is the best choice. The shorter 5 × 150 mm column is suitable for quick purity checks and rapid screening when the highest resolution is not needed.

GE Healthcare Life Sciences
For info: 800-526-3593
www.gelifesciences.com

Magnetic Bead Extraction Platform

EXTRACTMAN is a biomolecule extraction platform enabling researchers to better study complex protein interactions that are critical for drug target identification, as well as numerous topics in proteomics research. The platform can isolate weak interactors and transiently bound complexes that traditional isolation techniques leave behind. These weak interactors represent potentially unseen targets that are integral to fully understanding protein functions, molecular mechanisms, posttranslational modifications, and cell-signaling cascades. Protein isolation using EXTRACTMAN can be performed in significantly less time compared to more traditional tube-based magnetic bead procedures, with up to four samples isolated in parallel in as little as 30 seconds. The platform is ideal for capturing weakly bound protein–protein and cell–protein complexes, because they are not exposed to the high shear forces generated by multiple pipet-based wash steps and require less time in prodissociating wash buffers. EXTRACTMAN uses many commercially available paramagnetic beads, making it easy to adapt existing protocols.

Gilson
For info: 800-445-7661
www.gilson.com/extractman

Chemiluminescent Substrate

Thermo Scientific SuperSignal West Pico PLUS Chemiluminescent Substrate is the newest addition to the SuperSignal product line. Chemiluminescence is the Western blot detection method of choice in many protein laboratories, as it provides high sensitivity and convenience for detection with film or digital imaging equipment. The new formulation allows for brighter, more intense bands that display strong signal stability over the critical time period, allowing for the acquisition of multiple exposures. The high intensity of the light emission is coupled with excellent sensitivity—from the picogram down to the femtogram level—making it easy to obtain publication-quality blot images. SuperSignal West Pico PLUS is used for the detection of horseradish peroxidase and is compatible with different membranes and blocking reagents. It works over a wide range of antibody dilutions and across many different targets, making it an ideal choice for most Western blotting applications.

Thermo Fisher Scientific
For info: 800-955-6288
www.thermofisher.com

UV-Blue Light Converter Screens

Syngene's UV-Blue Light Converter Screens offer a safe, affordable way of using the UV transilluminator in Syngene imaging systems to visualize DNA and protein gels labeled with many commercial fluorescent dyes. The screens come in two sizes (21 cm × 26 cm and 25 cm × 30 cm) and are made of scratch-resistant plastic. Instead of purchasing a new imager or blue light box, researchers can inexpensively convert the transilluminator in their Syngene G:BOX, U:Genius3, InGenius3, and NuGenius systems into a blue-light powerhouse. The screen will alter the 302-nm UV wavelength to 460 nm–470 nm, preventing damage to scientists' skin and eyes while they are visualizing their gels. This adjusted wavelength is optimum for viewing a wide variety of fluorescent colors and gels stained with sensitive dyes, including GelRed, GelGreen, SYBR Safe, SYBR Gold, SYBR Green, SYPRO Ruby, SYPRO Orange, and Coomassie Fluor Orange.

Syngene
For info: +44-(0)-1223-727123
www.syngene.com

Electronically submit your new product description or product literature information! Go to www.sciencemag.org/about/new-products-section for more information.

Newly offered instrumentation, apparatus, and laboratory materials of interest to researchers in all disciplines in academic, industrial, and governmental organizations are featured in this space. Emphasis is given to purpose, chief characteristics, and availability of products and materials. Endorsement by *Science* or AAAS of any products or materials mentioned is not implied. Additional information may be obtained from the manufacturer or supplier.

Downloaded from http://science.sciencemag.org/ on October 20, 2016

ScienceCareers online @sciencecareers.org

There's only one Science

Science Careers Advertising

For full advertising details, go to ScienceCareers.org and click For Employers, or call one of our representatives.

Tracy Holmes
Worldwide Associate Director
Science Careers
Phone: +44 (0) 1223 326525

THE AMERICAS

E-mail: advertise@sciencecareers.org
Fax: +1 (202) 289 6742

Tina Burks
Phone: +1 (202) 326 6577

Nancy Toema
Phone: +1 (202) 326 6578

Online Job Posting Questions
Phone: +1 (202) 312 6375

EUROPE / INDIA / AUSTRALIA / NEW ZEALAND / REST OF WORLD

E-mail: ads@science-int.co.uk
Fax: +44 (0) 1223 326532

Sarah Lelarge
Phone: +44 (0) 1223 326527

Kelly Grace
Phone: +44 (0) 1223 326528

Online Job Posting Questions
Phone: +44 (0) 1223 326528

JAPAN

Katsuyoshi Fukamizu (Tokyo)
E-mail: kfukamizu@aaas.org
Phone: +81 3 3219 5777

Hiroyuki Mashiki (Kyoto)
E-mail: hmashiki@aaas.org
Phone: +81 75 823 1109

CHINA / KOREA / SINGAPORE / TAIWAN / THAILAND

Danny Zhao
E-mail: dzhao@aaas.org
Phone: +86 131 4114 0012

All ads submitted for publication must comply with applicable U.S. and non-U.S. laws. *Science* reserves the right to refuse any advertisement at its sole discretion for any reason, including without limitation for offensive language or inappropriate content, and all advertising is subject to publisher approval. *Science* encourages our readers to alert us to any ads that they feel may be discriminatory or offensive.

ScienceCareers
FROM THE JOURNAL SCIENCE AAAS

ScienceCareers.org

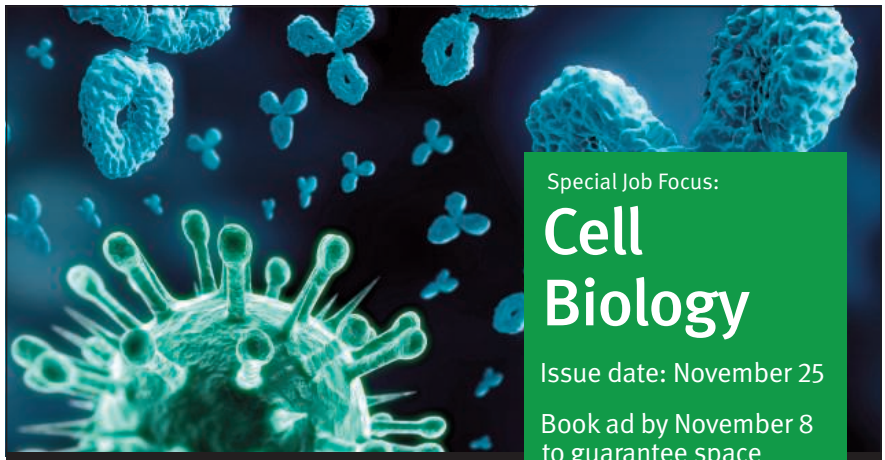

There's only one *Science*.

Special Job Focus:

Cell Biology

Issue date: November 25

Book ad by November 8 to guarantee space

Ads accepted until November 17 if space allows

What makes *Science* the best choice?

- Read and respected by 400,00 readers around the globe
- 75% of readers read *Science* more often than any other journal
- Your ad dollars support AAAS and its programs, which strengthens the global scientific community.

Why choose this job focus for your advertisement?

- Relevant ads lead off the career section with special cell biology banner
- Bonus distribution to American Society for Cell Biology, December 3–7, San Francisco, CA.

Expand your exposure. Post your print ad online to benefit from:

- Link on the job board homepage directly to cell biology jobs
- Dedicated landing page for jobs in cell biology
- Additional marketing driving relevant job seekers to the job board.

Produced by the until *Science*/AAAS Custom Publishing Office.

SCIENCECAREERS.ORG

Science Careers
AAAS

To book your ad: **advertise@sciencecareers.org**

The Americas
202 326 6582

Europe/RoW
+44 (0) 1223 326500

Japan
+81 3 3219 5777

China/Korea/Singapore/Taiwan
+86 131 4114 0012

EMBL

The European Molecular Biology Laboratory (EMBL) is an international research organisation publicly funded by more than 20 member states with a headquarters laboratory in Heidelberg and four sites in Hinxton (the European Bioinformatics Institute, EMBL-EBI), Grenoble, Hamburg and Monterotondo. A sixth EMBL site is being established in Barcelona, Spain. The focus of the new site will be the experimental and computational investigation of tissue biology and disease modelling at the level of tissues and organs. The scientific programme of EMBL emphasises experimental analysis at multiple levels of biological organisation, from the molecule to the organism, as well as computational biology, bioinformatics and systems biology. Within this structure, EMBL Barcelona will add a new dimension in organismal biology.

Head of EMBL Barcelona

at EMBL Barcelona, Spain

The Head of EMBL Barcelona reports directly to the Director General and will have a decisive role in developing the overall strategy for the EMBL Programme in Barcelona, and is accountable for its execution, including the hiring and mentoring of research group leaders. As an active scientist and member of EMBL Faculty, the successful candidate will also maintain personal scientific and technical contacts internationally at the highest level. She/he is expected to contribute greatly to the success of the EMBL Barcelona site and, through participation in EMBL's collegial leadership structure, of EMBL as a whole.

The Head of EMBL Barcelona will:

- be responsible for the setting of programmatic priorities and resource planning;
- lead his/her own research group and select, lead and mentor younger faculty members (six junior research groups by the end of 2021);
- ensure the maintenance of world-class standards of research throughout the site;
- lead the on-site preparation for regular Programme reviews;
- report as required by EMBL Council and other external committees and to the community at large via conferences and special events;
- actively participate in the senior scientific, strategic and administrative leadership of EMBL;
- identify opportunities for improvement/development within EMBL Barcelona.

The tasks are not limited to the above and a flexible approach and ability to adapt to evolving situations in a dynamic organisation is required.

The chosen candidate will have an outstanding record in a field of Tissue, Organ or Organismal Biology, will possess scientific vision and leadership skills, will wish to work in an open, collaborative environment and will possess administrative competence as well as excellent communication and interpersonal skills. Basic requirements for the position include a PhD in the biomedical sciences, a proven record of scientific leadership and at least 10 years' experience in international scientific collaboration. Substantial management and leadership experience within a scientific organisation, preferably international, is also required. Excellent organisational skills and a very good knowledge of English are essential.

Further key competencies are:

- the ability to think strategically, to take effective decisions and provide leadership;
- the capacity to understand the perspective of key decision makers and partners – to think through their needs and interests to identify their agenda;
- the ability to build strong and effective links within and outside the organisation;
- initiative, pro-activeness and very good negotiation skills.

Please note that this is a tenure-eligible appointment.

APPLICATION INSTRUCTIONS

Please apply online through **www.empl.org/jobs** sending a CV and motivation letter at the latest by 6 November 2016.

Questions concerning the role should be sent to the EMBL Director General, Iain Mattaj, at **dg-office@embl.org** and any queries regarding the terms and conditions should be sent to the Head of Human Resources, Roland Block, at **roland.block@embl.de**.

ADDITIONAL INFORMATION

EMBL offers a highly collaborative, uniquely international culture. It fosters top quality, interdisciplinary research by promoting a vibrant environment consisting of young independent research groups with access to outstanding graduate students, postdoctoral fellows and core facilities.

EMBL is an inclusive, equal opportunity employer offering attractive conditions and benefits appropriate to an international research organisation with a very collegial and family-friendly atmosphere. The remuneration package comprises a competitive salary, a comprehensive pension scheme, medical, educational and other social benefits, as well as financial support for relocation and installation, including the family.

www.embl.org

Science Careers online @sciencecareers.org

PennState

The Biology Department at The Pennsylvania State University (www.bio.psu.edu) seeks candidates for an **open-rank tenure-track faculty position** in **Plant Biology**. Candidates using genetic, genomic, phenomic, molecular, cellular, or systems-biology approaches to study fundamental questions in Plant Biology are especially encouraged to apply. The successful candidate is expected to develop and maintain an internationally recognized research program in Plant Biology and contribute to the teaching mission of the University. Candidates should hold a Ph.D. in a life-sciences related subject and have a strong record of prior research accomplishments. Candidates for the ranks of Associate Professor or Professor should additionally have well-established independent research programs and be widely recognized as leaders in their field. Penn State has one of the top US graduate programs in the plant sciences, and a large, vibrant, and collaborative group of faculty in plant biology and the wider life sciences. Penn State`s flagship University Park campus is situated in a community consistently rated as among the most livable small cities in the US. Applications must be submitted electronically at **https://psu.jobs/job/67177** and must include a cover letter, CV, and a third document containing a statement of research interests, a statement of teaching philosophy, and contact information for three potential references. Review of applications will begin immediately and continue until the position is filled. Applications received by **November 7, 2016** will be ensured of full consideration.

CAMPUS SECURITY CRIME STATISTICS: For more about safety at Penn State, and to review the Annual Security Report which contains information about crime statistics and other safety and security matters, please go to http://www.police.psu.edu/clery/ , which will also provide you with detail on how to request a hard copy of the Annual Security Report.

Penn State is an Equal Opportunity, Affirmative Action Employer, and is committed to providing employment opportunities to all qualified applicants without regard to race, color, religion, age, sex, sexual orientation, gender identity, national origin, disability or protected veteran status.

Job URL: https://psu.jobs/job/67177

Keep your job search out of the cheap seats.

- Search thousands of job postings
- Create job alerts based on your criteria
- Get career advice from our Career Forum experts
- Download career advice articles and webinars
- Complete an individual development plan at "myIDP"

Target your job search using relevant resources on **ScienceCareers.org**.

ScienceCareers
FROM THE JOURNAL SCIENCE AAAS

香港科技大學 THE HONG KONG UNIVERSITY OF SCIENCE AND TECHNOLOGY

25 INNOVATING TODAY, EMPOWERING TOMORROW HKUST

Division of Life Science Faculty Positions

Job Posting Details

The Division of Life Science at The Hong Kong University of Science and Technology seeks applications for tenure-track positions at ranks of Assistant Professor and above. We are particularly interested in candidates studying molecular mechanisms related to aging, cancer and stem cell biology. Candidates whose research programs complement or enhance the existing strengths of the Division will also be considered.

Applicants should have a doctoral degree and preferably at least 2 years of postdoctoral experience. They will be expected to establish an independent and internationally recognized research program and to contribute to the missions of the Division in undergraduate and graduate education. The Division of Life Science (life-sci.ust.hk) currently has 40 faculty members working in diverse research areas. The University has a vibrant research environment and is ranked as one of the top universities in Asia. New faculty is provided with competitive start-up funding. The medium of instruction is English.

Starting salary (with full 12-months' coverage) will be commensurate with qualifications and experience. Fringe benefits including medical and dental benefits, annual leave and housing will be provided where applicable. Initial appointment will normally be on a 3-year contract. A gratuity will be payable upon successful completion of contract.

Application Procedure

Application materials including a cover letter, curriculum vitae, research proposal (maximum 3 pages), teaching statement (maximum 1 page), and contact information of three referees should be sent to the Chair of Life Science Search and Appointments Committee (lifssearch@ust.hk). Review of applications will start in November 2016.

(Information provided by applicants will be used for recruitment and other employment-related purposes.)

UCONN

FACULTY POSITION IN STRUCTURAL BIOLOGY, BIOCHEMISTRY, OR BIOPHYSICS

The Department of Molecular and Cell Biology (MCB, http://mcb.uconn.edu) at the University of Connecticut is seeking applicants for a tenure-track position at the assistant professor level with an anticipated start date in August 2017. This position is in the Structural Biology, Biochemistry and Biophysics subgroup (http://sb3.uconn.edu) within the MCB Department (http://mcb.uconn.edu). A priority will be placed on candidates whose research focuses on molecular-level interactions of complex, multi-component biological systems using state-of-the-art experimental approaches, including but not limited to: cryo-electron microscopy, single molecule techniques, mass spectrometry, or NMR. The successful applicant will establish a research program complementing existing areas of research strengths in physical virology, biomembranes/membrane proteins or protein-nucleic acid interactions and develop innovative courses at the graduate and upper-division undergraduate level. For complete details on this position, qualifications, and application instructions please visit the University's *Husky Hire* online application system at **www.jobs.uconn.edu**. (Job Opening ID **#2017168**). For full consideration, applications must be received by **December 15, 2016**. Questions about the position can be addressed to Dr. Nathan Alder (**sb3@uconn.edu**).

The University of Connecticut is an EEO/AA Employer.

Stony Brook Medicine

Postdoctoral/ Sr. Postdoctoral Associate School of Marine and Atmospheric Sciences

The School of Marine and Atmospheric Sciences, Stony Brook University, seeks full-time Postdoctoral Associate with expertise in the application of high throughput sequencing and other molecular techniques to answer questions related to the ecology and the physiology of aquatic plankton and microbes. PhD in Biology, Marine Science, Bioinformatics or related field and a background in analyzing high throughput sequencing data sets required. Background in comparative genomics, experimental approaches with plankton, and/or harmful algal blooms preferred.

Applications due by November 25, 2016.

Visit:
http://www.somas.stonybrook.edu/jobs

for further information. For a full position description or to apply online, visit:
www.stonybrook.edu/jobs
(Req. # 1602665).

Equal Opportunity Employer, females, minorities, disabled, veterans

High-End Global Talents Recruitment

——Job Vacancies in China's Universities and Institutes

Introduction of Job Fairs

The Editorial Department of China Scholars Abroad (CHISA) and China Education Online will jointly hold *the 20th Video Recruitment of High-End Global Talents* to echo the national strategies of strengthening the country through talents and rapidly developing the higher education. **Video and on-spot job fairs are included and the detailed dates are as follows:**

Video Job Fair (Remote)
Oct. 26th, 2016

On-spot Job Fair (Britain, Germany)
Oct. 28th to Nov. 4th, 2016

About the Job Fairs

I. Dates

1) Domestic (China) Video Job Fair:
09:00-11:00, 14:00-16:00, Oct. 26th, 2016 (GMT+8); Website:http://www.edu.cn/cv

2) On-spot Job Fair in Britain and Germany:
Oct. 28th to Nov. 4th, 2016 (GMT+8).
London 29/10/2016, 2:00-5:00pm Octagon Hall, Queen Mary University of London, Mile End Road, London E14NS
Manchester 30/10/2016
Munich 31/10/2016
Berlin 2/11/2016

II. Objects

Overseas scholars, PhD and students ready to graduate.

III. Position Requirements

Mechanical Engineering, Information and Communication Engineering, Power System and Automation, Environmental Science and Ethnology, New Energy Material, Communication and Transportation Engineering, Electronic Science, Biology, Clinical Medicine, Civil Engineering, Instrument Science and Technology, Food Science and Engineering, Mathematics, Geography, Economics, Psychology, Law, Foreign Linguistics and Applied Linguistics, Education, Art, Management, etc.
Special Position Requirements: French Language and Literature, English Language and Literature, Ethnology, etc.

IV. Ways to Participate

1)Please send your CV directly to Zhaojia (zhaojia@eol.cn), Miao Zhilin (miaozl@eol.cn);
2)http://cv.eol.cn Click the entry button named Video Recruitment to have an online face-to-face communication with the specific university. You can choose to talk or write in accordance with your own network and equipment situations.

List of Participated Universities and Organizations

1)Shanghai Municipal Bureau of Human Resources and Social Security;
2)Shanghai Talent Service Center;
3)East China University of Science and Technology;
4)Shanghai Maritime University;
5)Shanghai Normal University;
6)Shanghai University of International Business and Economics;
7)Shanghai University Of Engineering Science;
8)Shanghai Second Polytechnic University;
9)Shanghai Lixin University of Accounting and Finance;
10) Shanghai Dianji University;
11) Bureau of Human Resources and Social Security, Hongkou District, Shanghai;
12) Bureau of Human Resources and Social Security, Minhang District, Shanghai;
13) Shanghai Dajun Tech. Co., Ltd.;
14) Bureau of Human Resources and Social Security, Xuhui District, Shanghai;
15) Shanghai Xufang (Group) Co., Ltd.;
16) Innovation and Entrepreneurship Service Center for High-end Talents, Yangpu District, Shanghai;
17) Shanghai Yangpu Science and Technology Innovation (Group) Co., Ltd.;
18) Innovation and Entrepreneurship Service Center for Overseas High-end Talents, Shanghai International Automobile City;
19) Administration Committee of Shanghai Baoshan City Industrial Park (BSCIP);
20) Shanghai Baojing Science and Technology Industrial Company;
21) Shanghai Electric Group Co., Ltd.;
22) Shanghai Electrical and Power Plant Equipment Group;
23) Southwest University;
24) Northeast Forestry University;
25) Zhengzhou University;
26) Nanjing Institute of Technology;
27) Southwest Jiaotong University;
28) Northwest Agriculture & Forestry University.

ScienceCareers online @sciencecareers.org
OPPORTUNITIES IN CHINA

10 ways that *Science* Careers can help advance your career

1. Register for a free online account on **ScienceCareers.org**.
2. Search thousands of job postings and find your perfect job.
3. Sign up to receive e-mail alerts about job postings that match your criteria.
4. Upload your resume into our database and connect with employers.
5. Watch one of our many webinars on different career topics such as job searching, networking, and more.
6. Download our career booklets, including Career Basics, Careers Beyond the Bench, and Developing Your Skills.
7. Complete an interactive, personalized career plan at "my IDP."
8. Visit our Career Forum and get advice from career experts and your peers.
9. Research graduate program information and find a program right for you.
10. Read relevant career advice articles from our library of thousands.

Visit **ScienceCareers.org** today — all resources are free

ScienceCareers

FROM THE JOURNAL SCIENCE AAAS

SCIENCECAREERS.ORG

香港中文大學
The Chinese University of Hong Kong

Applications are invited for:-

Institute of Tissue Engineering and Regenerative Medicine
Professors / Associate Professors / Assistant Professors
(Ref. 160001UC)

The Chinese University of Hong Kong, an internationally ranked and top tier university in Asia, has recently established an **Institute for Tissue Engineering and Regenerative Medicine (iTERM)**, focused on neuromusculoskeletal medicine.

Research emphases will be on the following programmatic research areas:

- ***stem cells and cell-based therapies***
- ***tissue engineering for regenerative medicine***
- ***3-dimensional microphysiological tissue models***
- ***translational and precision medicine***

Hong Kong is a cosmopolitan city that is rich in culture and has long played a leading role in international commerce, finance and education. The Chinese University of Hong Kong is located on a serene campus that nurtures interaction and collaboration, including the neighboring Hong Kong Science and Technology Park, which houses biotech start-ups and major scientific industries.

iTERM is currently recruiting faculty at all levels, with academic appointments at appropriate departments in the Faculty of Medicine and/or Faculty of Engineering.

Applicants should have a PhD, MD, DVM or an equivalent degree in science, engineering or related disciplines, with a track record of research excellence. In addition to leading a vigorous, independent research program, the appointees are expected to be active participants in educational activities.

Appointments will normally be made on contract basis for up to three years initially, which, subject to mutual agreement, may lead to longer-term appointment or substantiation later. Generous start-up package, competitive salary, and comprehensive core facilities in stem cells, genomics/proteomics, imaging, 3D printing and other areas, are available to support outstanding research programs.

Applications will be considered until the posts are filled.

Application Procedure
Applicants should submit application online, including CV and contact information of three referees. Reference letters can also be sent to the **Director, Dr. Rocky S Tuan,** Institute for Tissue Engineering and Regenerative Medicine, Room 123A, Lo Kwee-Seong Integrated Biomedical Sciences Building, The Chinese University of Hong Kong, Shatin, Hong Kong or by e-mail to iterm@cuhk.edu.hk.

The University only accepts and considers applications submitted online for the post(s) above. For more information and to apply online, please visit http://career.cuhk.edu.hk.

tifr

TATA INSTITUTE OF FUNDAMENTAL RESEARCH
Homi Bhabha Road, Colaba, Mumbai 400005
An Autonomous Institute of the Department of Atomic Energy, Government of India, and a Deemed University

INVITES APPLICATIONS / NOMINATIONS
FOR THE POST OF

CENTRE DIRECTOR, TIFR HYDERABAD

From eminent academics / researchers / scientists with high academic achievement and some experience of administration

For details please visit TIFR Website
http://www.tifr.res.in/positions

Last date for receipt of applications is
November 25, 2016

UC San Diego

Associate or Full Professor (Ladder Rank, Adjunct, In Residence) - Regenerative Medicine

Faculty Position in Regenerative Medicine. The Department of Medicine (http://med.ucsd.edu) at University of California, San Diego is committed to academic excellence and diversity within the faculty, staff, and student body and is currently recruiting outstanding faculty for tenure and non-tenured positions in the Division of Regenerative Medicine.

The Division of Regenerative Medicine, in cooperation with the UC San Diego Health System, the School of Medicine, and the Sanford Stem Cell Clinical Center, seeks faculty applicants to join a highly interdisciplinary effort dedicated to advancing stem cell research to clinical trials. Faculty are sought to conduct strongly interdisciplinary research with clinical applicability in stem cell science and medicine. UC San Diego seeks candidates who will establish, or have established, independent and vigorous extramurally-funded research programs in regenerative medicine, human brain cancer, development of new drugs, and cellular therapeutics. Our top candidates will have innovative approaches and expertise in more than one discipline.

Candidates should have a track record of publications in internationally recognized journals, and a willingness to participate in university service, graduate and undergraduate teaching. Applicants must possess a PhD or MD degree or both.

The Department is interested in candidates who have demonstrated commitment to excellence by providing leadership in teaching, research or service towards building an equitable and diverse scholarly environment.

Rank and Salary is commensurate with qualifications and based on the University of California pay scales.

Review of applications will begin November 4, 2016, and continue until the position is filled.

Interested applicants should upload their CV, statement of research experience and interests, a list of references, and a separate statement summarizing their experiences and their vision for professional contributions in the area of equity and diversity (see: http://facultyexcellence.ucsd.edu/c2d/index.html for more information) to:**http://apptrkr.com/896375**

The University of California is an Equal Opportunity/Affirmative Action Employer. All qualified applicants will receive consideration for employment without regard to race, color, religion, sex, national origin, disability, age or protected veteran status.

Job location
San Diego, CA

Requirements
Documents
- Curriculum Vitae - Your most recently updated C.V.
- Statement of Research
- Statement of Contributions to diversity - Applicants should summarize their past or potential contributions to diversity. See our http://facultyexcellence.ucsd.edu/c2d/index.html site for more information.

References3-5 references required (contact information only)

How to apply
- Create an ApplicantID
- Provide required information and documents
- If any, provide required reference information

To apply, please visit: **http://apptrkr.com/896375**

The University of California is an Equal Opportunity/Affirmative Action Employer. All quali ed applicants will receive consideration for employment without regard to race, color, religion, sex, national origin, disability, age or protected veteran status.

Science Careers online @sciencecareers.org

POSITIONS OPEN

UNIVERSITY OF SOUTH CAROLINASCHOOL OF MEDICINE FACULTY POSITION (Microbiology and Immunology)

The Department of Pathology, Microbiology and Immunology at the University of South Carolina School of Medicine, Columbia invites applications for a non-tenure-track teaching faculty position at the rank of **ASSISTANT PROFESSOR** based on a 12-month appointment. The successful candidate will be responsible primarily for directing, and participating in teaching course/s offered to medical, graduate and post-baccalaureate students. In addition, the candidate will be encouraged to participate in the research efforts of the Department. There are several opportunities to collaborate with departmental faculty. The department is currently ranked 17th among Pathology departments in the nation in NIH funding, and hosts several NIH-funded Research Centers including the Center for Complementary and Alternative Medicine, the Center of Biomedical Research Excellence on Dietary Supplements and Inflammation, and the IDeA Network of Biomedical Research Excellence. Candidates must have a Ph.D., M.D. or M.D./Ph.D., expertise in Immunology and appropriate teaching and research experience. Please submit curriculum vitae and a statement of teaching and research interests with names of 3 references to: **Dr. Mitzi Nagarkatti, Chair, Department of Pathology, Microbiology, and Immunology, University of South Carolina School of Medicine, Columbia, SC 29208** or e-mail: **teachimmunology@uscmed.sc.edu**. The search will start immediately and will continue until the position is filled. *USC Columbia is an EOAA Employer and encourages applications from women and minorities and is responsive to the needs of dual career couples.*

THE DEPARTMENT OF CHEMISTRY AND BIOCHEMISTRY AT THE UNIVERSITY OF MARYLAND, BALTIMORE COUNTY (UMBC)

invites applications for full-time, non-tenure track faculty positions:

(1) Lecturer primarily responsible for instruction and oversight of the physical chemistry and analytical chemistry laboratories beginning August 2017. The successful candidate will have a strong background in chemical instrumentation and methodologies with a desire to teach at the undergraduate level: apply.interfolio.com/38409

(2) Lecturer primarily responsible for teaching general chemistry lecture and laboratory courses as well as analytical chemistry laboratories beginning August 2017. The successful candidate will have experience teaching at the undergraduate level and have a strong commitment to innovative teaching strategies: apply.interfolio.com/38412

Qualifications: Ph.D. in chemistry or a related field preferred; qualified candidates with an M.S. degree and relevant experience will also be considered. We seek candidates who are committed to teaching chemistry at the undergraduate level and to the UMBC mission of increasing diversity in STEM. The application package, including a cover letter, Curriculum Vitae, statement of teaching philosophy, and three letters of recommendation should be submitted electronically at website: **apply.interfolio.com/38409** for the physical/analytical laboratory lecturer position or website: **apply.interfolio.com/38412** for the general chemistry lecturer position. For best consideration, submit application materials by **November 15, 2016**. Consideration of applications will continue until the position is filled.

UMBC is an Equal Opportunity/Affirmative Action Employer. Applications from women, minorities, veterans, individuals with disabilities and other traditionally under-represented groups in the sciences are especially encouraged.

POSITIONS OPEN

FACULTY POSITIONS UC SAN DIEGO DEPARTMENT OF BIOENGINEERING

The Department of Bioengineering in the Jacobs School of Engineering at the University of California, San Diego is inviting applications for a **TENURE-TRACK POSITION** at the Assistant Professor level. A PhD or advancement to candidacy in bioengineering or related engineering disciplines is required for this position. Successful applicants will be expected to teach undergraduate courses in UCSD's Bioengineering, Biotech, Bioinformatics and/or BioSystems Engineering Major tracks and graduate courses in Bioengineering and establish a vigorous program of high-quality federally funded bioengineering research.

To obtain more information or submit your application materials, go to website: **https://apol-recruit.ucsd.edu/apply/JPF01223**.

UCSD is an AA/EOE.

MASSACHUSETTS INSTITUTE OF TECHNOLOGY

The Department of Earth, Atmospheric, and Planetary Sciences at the Massachusetts Institute of Technology invites applications for a tenure-track position in the broad area of Geophysics, including theory, observation, and experimentation. We seek an outstanding scientist with the potential to conduct innovative research and excel in teaching at the undergraduate and graduate levels.

Applicants must hold a Ph.D. in geophysics or a related field by the start of employment. A complete application must include a curriculum vitae, one- to two-page descriptions of research and teaching plans, and three letters of recommendation. Applications are being accepted at Academic Jobs Online website: **https://academicjobsonline.org/ajo/jobs/8065** To receive full consideration, complete applications must be received by **December 15, 2016**.

Search Contact: **Ms. Karen Fosher, HR Administrator, EAPS, 54-924 Massachusetts Institute of Technology, 77 Massachusetts Avenue, Cambridge, MA 02139-4307; email: kfosher@mit.edu**

MIT is an Equal Employment Opportunity Employer. All qualified applicants will receive consideration for employment and will not be discriminated against on the basis of race, color, sex, sexual orientation, gender identity, religion, disability, age, genetic information, veteran status, ancestry, or national or ethnic origin.

INSECT ECOLOGICAL PHYSIOLOGIST

The School of Integrative Biology and the Department of Entomology at the University of Illinois, Urbana-Champaign invite applications for a full-time, **TENURE-TRACK FACULTY POSITION** at the level of Assistant Professor to begin **August 16, 2017**. The School seeks an insect eco-physiologist who works at the interface of some combination of ecology, evolutionary biology, development, behavior, and molecular genetics. Full consideration will be given to applications received by December 1, 2016. For complete details see website: **http://go.illinois.edu/InsectEcoPhys**

The University of Illinois conducts criminal background checks on all job candidates upon acceptance of a contingent offer.

Illinois is an Equal Employment Opportunity Employer/Veteran/Disabled (www.inclusiveillinois.illinois.edu)

POSITIONS OPEN

The Department of Pharmaceutical Chemistry at The University of Kansas (website: https://pharmchem.ku.edu/) invites applications for the Valentino J. Stella **DISTINGUISHED PROFESSOR**. This is an Endowed Position with generous startup funds and highly competitive salary. The successful candidate should be an internationally recognized scholar with interest in the application of physical, physical-organic and/or biophysical chemistry to the characterization of physicochemical properties, formulation and/or drug delivery of small or large molecules, or both, including therapeutics peptides, proteins, antibodies and vaccines. The candidate should demonstrate a strong record of research and scholarship commensurate with a rank for appointment at the level of Distinguished Professor. Screening of applications will begin **January 16, 2017** and applications will be accepted until the position is filled. A complete application includes a letter of interest and a resume should be submitted online at website: **https://employment.ku.edu/academic/7168BR**. Direct additional inquiries about the position to **Dr. Teruna Siahaan at 785-864-7327 (email: siahaan@ku.edu).** *University of Kansas is an EO/AAE, full policy at website: http://policy.ku.edu/IOA/nondiscrimination*

MASSACHUSETTS INSTITUTE OF TECHNOLOGY

The Department of Materials Science and Engineering (DMSE) seeks candidates for open tenure-track faculty positions to begin July 2017 or on a mutually agreed date thereafter. Appointments would be at the assistant or untenured associate professor level. In special cases, a senior faculty appointment may be possible. Faculty duties include teaching at the graduate and undergraduate levels, research, and supervision of student research.

Candidates should hold a Ph.D. in Materials Science and Engineering or a related field by the start of employment. Candidates with deep knowledge of the core of Materials Science and Engineering are desired. DMSE seeks to broaden its research portfolio in two main directions: (1) Computational materials science, including in the areas of materials kinetics, materials synthesis, mesoscale modeling of materials processing and microstructure evolution, and data-driven approaches to materials science for engineered inorganic, organic, or biological materials. (2) Advanced materials characterization, including development and deployment of new and high-resolution methods in microscopy, diffraction, compositional mapping, in situ and in operando techniques for inorganic and organic materials.

However, DMSE has strengths and interests across the full spectrum of materials research, and excellent candidates with expertise in any and all areas of the field are welcomed.

MIT has a number of institute-wide initiatives under way or in development, on topics that include Manufacturing, Energy, Environment, Health, and Data. Individuals who can connect to these initiatives are of interest.

Interested candidates should submit application materials electronically at website: **http://dmsefacsrch.mit.edu**. Each application should include: a curriculum vitae; a statement of research interests; and a statement of teaching interests. We request that each candidate arrange for 3 letters of reference to be uploaded at **http://dmsefacsrch.mit.edu/letters/**. Questions should be addressed to **DMSE-Search-Master@dmsefacsrch.mit.edu**. Responses received by **December 31, 2016** will be given priority. No application received after March 1, 2017 will be considered in this year's search. *We especially encourage minorities and women to apply because of MIT's strong commitment to diversity in engineering education, research and practice.*

Creighton UNIVERSITY
School of Medicine

Department Chair
Biomedical Sciences

Creighton University School of Medicine invites applications and nominations for Professor and Chair of the Department of Biomedical Sciences. The ideal candidate must have a PhD, qualify for appointment as full professor, and possess outstanding interpersonal, leadership, and administrative skills and experience. The candidate should also have an internationally recognized research program supported by extramural funding, and express a strong commitment to mentoring department faculty and fostering collaborative, interdisciplinary research and education, both within the Department and with other basic and clinical science departments. Primary responsibilities of the Chair include developing and implementing strategies to support and enhance the research and educational programs in the department, mentoring and evaluating department faculty, and engaging with various stakeholders to articulate and achieve the missions of the Department, School, and University. The position includes a competitive startup package, renovated research laboratory space and additional resources to significantly expand the teaching and research base by seven faculty positions.

The Department of Biomedical Sciences has a diverse portfolio of federally funded research investigators in the areas of neuroscience, carcinogenesis and cell signaling. Department faculty also participate in graduate and professional education. The School of Medicine is one of nine schools and colleges at Creighton University including professional schools of Business, Law, Nursing, Dentistry, Pharmacy and Health Professions, and the Graduate School. Founded in 1878, Creighton University is a Catholic, Jesuit institution with an enrollment of approximately 7000 students that in 2016 earned the top spot in *U.S. News & World Report* magazine's college rankings for Midwest Regional Universities. This is the 14th year in a row the University has earned the No. 1 ranking in "America's Best Colleges" edition.

Applications received before **December 16th, 2016** will receive full consideration. *Creighton University is an equal opportunity, affirmative action educational Institution and employer, title IX University. Creighton University particularly welcomes applications from minorities, women and persons with disabilities.*

A Curriculum Vitae and letter of application that includes a description of administrative and teaching experiences, current and future research activities, and the names and contact information of three references may be submitted by mail to:

Chair, Search Committee
c/o Lurae McCloskey
Creighton University School of Medicine
2500 California Plaza, Omaha NE 68178
luraemccloskey@creighton.edu
402.280.1135

The newly launched Department of **Applied Physical Sciences (APS)** invites applications for two new faculty positions, prioritizing junior applicants while open to consideration of outstanding candidates at all ranks. The goal of APS is to bridge fundamental research and education in materials science and engineering with translational impact on society's most challenging problems.

This hiring initiative continues a commitment to diversity with an aggressive strategy to build multidisciplinary, team-based research, education, and entrepreneurship at UNC, a top 10 public research university. The Department aims for 20 full-time faculty in addition to joint appointments from partnering departments, with international leadership at the intersection of the physical, life, and energy sciences.

All candidates should have an established record of, or clear potential for, research and teaching excellence, multidisciplinary collaboration, extramural funding including industry, and translational impact in education and entrepreneurship. A PhD in a discipline that contributes to applied physical sciences is required.

Applications will only be accepted online (https://unc.peopleadmin.com/postings/88874). Applicants should submit a CV, research statement, teaching statement, the names of at least 4 persons who are willing to provide a letter of recommendation, and a cover letter outlining potential contributions to APS. Applicants will be notified to have recommendation letters forwarded, or to have pre-interviews.

Applications are reviewed as they are submitted and will continue until the positions are filled. Questions should be directed to: **E. T. Samulski, Chair, Department of Applied Physical Sciences, University of North Carolina at Chapel Hill, Chapel Hill, NC 27599-3050, et@unc.edu**.

The University of North Carolina at Chapel Hill is an Equal Opportunity and Affirmative Action Employer. All qualified applicants will receive consideration for employment without regard to age, color, disability, gender, gender expression, gender identity, genetic information, national origin, race, religion, sexual orientation, or status as a protected veteran.

UNIVERSITY OF MINNESOTA
Driven to Discover℠

UNIVERSITY OF MINNESOTA
INFECTIOUS DISEASES & PROGRAM IN HIV MEDICINE
Physician-Scientists / Basic Scientists

The Division of Infectious Diseases and International Medicine and Program in HIV Medicine of the Department of Medicine at the University of Minnesota invites applications for tenure track positions at the Assistant Professor or tenured Associate Professor ranks. We seek candidates with a MD, PhD, or MD/PhD degree who have a track record of exceptional accomplishment and promise in infectious diseases research. The Program in HIV Medicine's current areas of interest include virus evolution; virus persistence and tissue reservoirs; lymphoid tissue pathology and CD4 T cell depletion and reconstitution; HIV co-morbidities, and HIV-related coinfections, particularly TB; and innate and adaptive immunological responses to infection or co-infections that might eventuate in therapeutic or preventive vaccines. The successful candidate will join a collegial community with outstanding scholarly and scientific resources and opportunities to collaborate with faculty in the Department of Microbiology and Immunology, Center for Immunology, Center for Clinical and Translational Science Institute, Center for Drug Design, and the Institute for Molecular Virology at the University of Minnesota. Individuals licensed to practice medicine in the State of Minnesota will also have the opportunity to provide outpatient care for HIV-infected patients or general ID patients at the University of Minnesota HIV/ID clinic and to provide inpatient ID consultation. Salary will be commensurate with qualifications and expertise and competitive start-up packages are available.

Qualified applicants are invited to apply on-line at **www1.umn.edu/ohr/**.

In addition to the on-line application, applicants should send a 3-page letter describing research interests and expertise, along with a current curriculum vitae and names of three references by e-mail to Scott Povolny **(povo0006@umn.edu)**, addressed to: Timothy Schacker, MD, Director of the Program in HIV Medicine.

The University of Minnesota School of Medicine is an Equal Opportunity, Equal Access, Affirmative Action Employer.

By **Diane Shao**

Knocking on opportunity's door

My research career started when, at 15 years old, I showed up at university laboratories asking for a job. When I told this story to my spouse, another academic, we laughed uproariously at the idea of a kid not even out of high school knocking down the doors of our future laboratories. It sounded utterly clueless. After all, many in the scientific community believe that "talent" alone is the most important ingredient for a successful scientific career. To those with this mindset, people who actively promote themselves or advocate for their careers must be less intelligent or less deserving. But reflecting on my own trajectory, I'm glad that I was bold enough—or clueless enough—to proactively ask for what I needed early in my career.

On that first job search, I had no research experience. But I did have advice from a friend whose enviable jobs as a cashier at both Starbucks and Barnes & Noble proved that he was the authority on getting hired. "The secret," he told me, "is to find a way to talk to the boss." So I emailed 40 principal investigators (PIs) at the nearby university, soliciting a summer position. I strategically included the line, "If I do not receive a response via email, *I will visit you at your office between 2 and 4 p.m. on April 10*," which led to a series of rapid replies kindly turning me down.

"I'm glad that I was bold enough ... to proactively ask for what I needed."

But 10 unsuspecting souls did not respond, so on the designated day, I dressed my best to visit them. My friend was right: Two PIs offered me unpaid internships on the spot. I played it cool, telling them that I would have to think about it. Finally, I met a quirky structural biologist with a friendly smile. He brought me to his lab manager, who eyed me dubiously and offered $8 an hour. "How about $9?" I piped. We shook hands, and I landed my first job ever. I realize now that my actions could have been seen as presumptuous, given the common idea that academia is a meritocracy and good things, such as jobs and higher salaries, naturally go to those who "deserve" them. As a high school student, though, I was blissfully unaware of those cultural norms.

I maintained this mindset in college, where I asked potential advisers whether they had a low-risk project that could lead to a primary authorship for me. Some were disdainful of this goal-oriented approach, declaring that success cannot be planned. But one told me that he had just the project for me: a study whose results would be of importance regardless of the outcome. Three years later, I was his only undergraduate student to have published a first-author paper. I put in a lot of hard work, but I also know that being willing to ask for what I wanted was a crucial contributor to my early success.

As I progressed in my training and started to internalize the academic community's values, it became harder to ask for success on my terms. As a Ph.D. student, for example, I felt uncomfortable speaking up when it looked like I wouldn't get the authorship position I felt I deserved on a paper. I did end up raising the issue. After some opposition I got the appropriate credit, but the fact that I had to ask reinforced my sense that rewards and recognition aren't meted out based solely on merit. Now, as a postdoc, I never tell stories of my youthful, brazen self-advocacy—partly because I wonder whether asking to be given the things I needed means that I don't deserve what I have achieved, and partly because scientists prefer stories of amazing breakthroughs leading to recognition and success.

The reality is that creating opportunities for career advancement is as important as innate scientific talent. I hope to have my own lab one day, and I know that my success—or failure—will be determined by many factors beyond the merit of my projects. I will need to attract trainees, entice funders, and convince the department chair to give me freedom to explore—all of which will require negotiating and advocating for myself. For me, that will mean starting to reharness some of my inner teenager, knocking on doors of opportunity and asking to be let in. ■

Diane Shao is a medical resident and postdoctoral researcher at Boston Children's Hospital. Send your career story to SciCareerEditor@aaas.org.

ILLUSTRATION: ROBERT NEUBECKER

Downloaded from http://science.sciencemag.org/ on October 20, 2016

Published by AAAS